

STUDIES OF BIODIESEL SURROGATES
USING NOVEL SHOCK TUBE TECHNIQUES

A DISSERTATION
SUBMITTED TO THE DEPARTMENT OF MECHANICAL ENGINEERING
AND THE COMMITTEE ON GRADUATE STUDIES
OF STANFORD UNIVERSITY
IN PARTIAL FULFILLMENT OF THE REQUIREMENTS
FOR THE DEGREE OF
DOCTOR OF PHILOSOPHY

Matthew Frederick Campbell
July 2014

© 2014 by Matthew Frederick Campbell. All Rights Reserved.
Re-distributed by Stanford University under license with the author.



This work is licensed under a Creative Commons Attribution-
Noncommercial 3.0 United States License.
<http://creativecommons.org/licenses/by-nc/3.0/us/>

This dissertation is online at: <http://purl.stanford.edu/ms343kp4994>

Includes supplemental files:

1. (*frosh.m*)
2. (*aerofrosh.m*)

I certify that I have read this dissertation and that, in my opinion, it is fully adequate in scope and quality as a dissertation for the degree of Doctor of Philosophy.

Ronald Hanson, Primary Adviser

I certify that I have read this dissertation and that, in my opinion, it is fully adequate in scope and quality as a dissertation for the degree of Doctor of Philosophy.

Craig Bowman

I certify that I have read this dissertation and that, in my opinion, it is fully adequate in scope and quality as a dissertation for the degree of Doctor of Philosophy.

David Davidson

I certify that I have read this dissertation and that, in my opinion, it is fully adequate in scope and quality as a dissertation for the degree of Doctor of Philosophy.

Reginald Mitchell

Approved for the Stanford University Committee on Graduate Studies.

Patricia J. Gumpert, Vice Provost for Graduate Education

This signature page was generated electronically upon submission of this dissertation in electronic format. An original signed hard copy of the signature page is on file in University Archives.

Abstract

In light of the finite supply of fossil fuels, concerns about the impact of combustion engine emissions, and increasing efficiency requirements for on-road vehicles, a search has begun for alternative energy resources. Such fuels would ideally have characteristics such as a high energy density, lower pollutant (hydrocarbon, soot, nitrogen oxide, *etc.*) emissions, domestic origins, and high miscibility with comparable existing fuels. With the possible exception of lower nitrogen oxide emissions, biodiesel fuel realizes all of these qualities and as such has become a leading candidate to blend with, supplement, or in some cases replace traditional fossil diesel fuel. To facilitate such changes in fuel stock, a comprehensive understanding of biodiesel oxidation chemistry is needed.

In the work described herein, the Stanford University Aerosol Shock Tube (AST) was used to measure ignition delay times for six biodiesel surrogate molecules (called Fatty Acid Methyl Esters, or FAMEs) as large as methyl oleate ($C_{19}H_{36}O_2$) at high temperatures (1100-1350 K), moderate pressures (3.5 and 7 atm), and both lean and rich equivalence ratios. This facility was able to make gas-phase measurements of these very-low-vapor-pressure fuels by loading the fuel as a spatially uniform mixture of fuel droplets suspended in an oxidizer/diluent gas blend; the droplets rapidly evaporated behind the incident shock wave. Temperatures behind both incident and reflected shock waves were calculated using a computer code that accounted for the enthalpy loss by the gas as the aerosol droplets changed phase. Moreover, a Fourier Transform InfraRed (FTIR) spectrometer was used to measure the spectra of eleven FAMEs, allowing quantitative fuel measurements during shock experiments.

In addition to these aerosol-based experiments, novel shock tube techniques have been developed. The first involves confining the reactive test gas mixture to a small section of the tube using

a sliding gate valve (called Constrained Reaction Volume (CRV) experimentation), thus enabling the measurement of ignition chemistry under constant-pressure conditions. The second involves expanding available shock tube test times by filling a low-sound-speed gas near the driver section end cap (called staged driver gas filling) to allow moderate-temperature, low-pressure oxidation experiments. Using these techniques, ignition delay times and time histories of intermediate/product species and temperature were measured during *n*-heptane (C_7H_{16}) oxidation at low temperatures (650-800 K) under constant-pressure conditions near 6.5 atm.

The results revealed that many existing biodiesel kinetic mechanisms either under- or over-predict high-temperature ignition times for large biodiesel surrogates; subsequent modifications to high-temperature thermochemistry of biodiesel molecules resulted in more realistic fuel unimolecular decomposition rates and significantly better agreement between model and experiment. Measurements of FAME spectra showed that the absorption cross sections of saturated molecules at 3.39 μm , corresponding to the monochromatic output of a helium-neon (HeNe) laser, can be extrapolated using a simple relationship based on the number of C–H bonds in the molecule. CRV experimentation was shown to almost completely eliminate the pressure changes associated with both first and second stage ignition events during Negative Temperature Coefficient (NTC) region *n*-heptane oxidation. Comparisons between model and experiment indicated that at low temperatures, constant enthalpy-pressure (H-P) constraints are more appropriate for zero-dimensional shock tube simulations than constant internal energy-volume (U-V) constraints. Finally, the staged driver filling technique was found to increase shock tube test times by approximately 20%, while reducing necessary driver helium consumption by up to about 85%.

Acknowledgements

I would first like to thank my advisor, Professor Ron Hanson, for his generous support and wisdom throughout my time at Stanford. He set an inspiring example for me as a scientist, scholar, and family man, which I will carry with me throughout my life. My thanks also go to Dr. Dave Davidson, who patiently gave me good advice about combustion and about life in general. Furthermore, I would like to thank Professor Tom Bowman, whose discussions with me about matters of science and about matters of faith served to both inspire and encourage me. Moreover, I would like to thank Professor Reggie Mitchell, whose enthusiastic teaching style has kindled my enjoyment of thermodynamics.

In addition, I would also like to thank my colleagues in the Hanson Group, including Dr. Dan Haylett, Dr. Megan MacDonald, Dr. Genny Pang, Dr. Brian Lam, Dr. Sijie Li, Andy Tulgestke, Kyle Owen, Luke Zaczek, Rito Sur, Shengkai Wang, Tom Parise, Yangye Zhu, and many others. Stanford would not have been such a wonderful place for me without you.

I also have made many friends outside of the laboratory, who have challenged, encouraged, and prayed for me through the last six years. Thanks especially to Dr. Scott Hsieh, Dr. Jasper Chen, Brian Lee, Clint Fong, Derek Kwan, Jason Ko, Leon Chao, Winston Walker, and others too.

Furthermore, my parents, Drs. Anne and Robb Campbell, have supported me through my entire academic career, as have my sister Dr. Laura Colicchia and brother Ben Campbell. I am grateful to them for seeing the scientist in me and cultivating that pursuit over the years.

Finally and most importantly, I would like to thank my wife Kristen. She has stood beside me from the very beginning of my time at Stanford, and I owe more laughs, smiles, joy, and good memories to her than to anyone else.

Funding

This research was made possible by several generous grants and fellowships, detailed below.

1. The development of the Aerosol Shock Tube (AST) and Constrained Reaction Volume Shock Tube (CRVST) was supported in part by the U.S. Army Research Laboratory and the U.S. Army Research Office (ARO) under Contract/Grant Number W911NF1310206, with Dr. Ralph Anthenien as contract monitor.
2. The development of the CRVST was also supported by the Air Force Office of Scientific Research (AFOSR) under the Basic Research Initiative (BRI) Program under Grant Number FA9550-12-1-0472, with Dr. Chiping Li as program manager.
3. The development of the CRVST was further supported by the AFOSR (BRI Program) under Grant Number FA9550-12-1-0483, under contract monitors Dr. J. Luginsland and Dr. J. Marshall.
4. The development of the laser diagnostics used in this research was supported by the AFOSR through AFOSR Grant Number FA9550-11-1-0217, under the Air Force Research Laboratory (AFRL) Integrated Product Team (IPT), with Dr. Chiping Li as contract monitor.
5. The measurement of ignition delay times of biodiesel surrogates and the measurement of Fatty Acid Methyl Ester (FAME) spectra was supported as part of the Combustion Energy Frontier Research Center (CEFRC), funded by the U.S. Department of Energy (DOE), Office of Science/Office of Basic Energy Sciences, under Award Number DE-SC0001198.
6. The measurement ignition delay times of *n*-heptane was supported by the U.S. DOE, Office of Basic Energy Sciences, under grant number DE-FG02-88ER-13857, with Dr. Wade Sisk as contract monitor.

7. The author was supported from September 2010 through August 2013 by a National Defense Science and Engineering Graduate (NDSEG) Fellowship, under Award Number 32-CFR-168a.
8. The author was also supported from March 2009 through May 2009 by a Dean's Office Fellowship, funded by federal work-study funds and the Stanford University School of Engineering. It was this fellowship that allowed the author to begin working under the direction of Professor Hanson.

Contents

Abstract	v
Acknowledgements	vii
Funding	viii
1 Introduction to biodiesel	1
1.1 Combustion today	1
1.2 Background	3
1.3 Production	4
1.4 Feedstock sources	4
1.5 Benefits	7
1.5.1 High flash point	7
1.5.2 High cetane number	9
1.5.3 Lubricity	9
1.5.4 Solvent properties	9
1.5.5 Biodegradability	9
1.5.6 Domestic origin	10
1.5.7 Miscibility with fossil diesel	10
1.5.8 Lower pollutant emissions	10
1.6 Drawbacks	11
1.6.1 Higher nitric oxide emissions	12
1.6.2 Higher fuel prices	13

1.6.3	Lower energy density	13
1.6.4	Poor oxidative stability	14
1.6.5	Poor cold-flow properties	14
1.7	Previous research on biodiesel combustion	14
1.8	Summary	16
1.9	Scope and organization	18
2	Introduction to shock tubes	19
2.1	Experimental facilities	19
2.2	Types of shock tube measurements	19
2.3	Shock tube operation	20
2.4	Current challenges	22
2.4.1	Fuel loading	22
2.4.2	Test time	23
2.4.3	Energy release	23
2.4.4	Remote ignition	24
2.5	Use of shock tubes for biodiesel research	24
2.6	Summary	24
3	Operation of the aerosol shock tube	26
3.1	Motivation	26
3.2	Experimental setup	27
3.2.1	Aerosol shock tube description	27
3.2.2	Driver insert	30
3.2.3	Calculation of test conditions	30
3.2.4	Fuel measurement	30
3.2.5	Measurement of ignition	32
3.2.6	Example shock experiment	32
3.3	Droplet evaporation	33
3.4	Range of AST	38

3.5	Initial pressures for aerosol loading	40
3.6	Droplet settling time	42
3.7	Estimation of droplet loading	46
3.7.1	Volume fraction estimation	46
3.7.2	Empirical correlation for equivalence ratio	48
3.8	Summary	49
4	AEROFROSH	51
4.1	Introduction	51
4.2	Background	51
4.3	Previous studies	52
4.4	Experimental setup	55
4.5	Outline of algorithm for pure gas-phase flows	56
4.6	Adaptations for shocks in aerosols	56
4.6.1	Presence of droplets in Region 1	57
4.6.2	Modifications to bulk fluid properties	57
4.6.3	Droplet evaporation	58
4.6.4	Quantifying fuel loading	59
4.7	Algorithm: Single-component fuel aerosols	62
4.8	Algorithm: Multi-component fuel aerosols	66
4.8.1	Mixture-averaged liquid properties	67
4.8.2	Accounting for component vapor pressures	67
4.8.3	Determining gas-phase fuel mole fractions	68
4.8.4	Spectroscopic fuel measurement	68
4.8.5	Updating gaseous fuel mole fractions	69
4.9	Validation	69
4.10	Results	72
4.11	Uncertainty analysis	75
4.12	Summary	78

5 Spectroscopy of fatty acid methyl esters	79
5.1 Introduction of FAME infrared spectroscopy	79
5.2 Experimental setup	81
5.3 Data reduction	85
5.4 Results	88
5.4.1 Pressure dependence	88
5.4.2 Concentration dependence	88
5.4.3 Instrument resolution dependence	89
5.4.4 Emission by fuels and by heated cell	90
5.4.5 Evidence of condensation	92
5.4.6 Decomposition study	93
5.4.7 Comparison with PNNL	94
5.4.8 Temperature dependence	94
5.4.9 Molecular size dependence	108
5.4.10 Cross section values at 3.39 microns	110
5.4.11 Integrated area	111
5.5 Discussion	111
5.5.1 Explanation of spectra	111
5.5.2 Comparison with normal alkanes	116
5.5.3 Variation with number of C–H bonds	120
5.5.4 Effects of C=C double bonds	124
5.6 Summary	125
6 Application of the aerosol shock tube to fatty acid methyl ester ignition	127
6.1 Introduction	127
6.2 Previous studies	128
6.2.1 Methyl decanoate	128
6.2.2 Methyl laurate	129
6.2.3 Methyl myristate	129

6.2.4	Methyl palmitate	130
6.2.5	Methyl oleate	130
6.2.6	Methyl linoleate	130
6.2.7	Summary of previous studies	130
6.3	Experimental setup	131
6.3.1	Aerosol Shock Tube (AST)	131
6.3.2	Fuel and gas information	131
6.3.3	Sample experiment	134
6.4	Kinetic modeling	134
6.5	Results and discussion	135
6.5.1	Fully saturated FAMEs	135
6.5.1.1	Methyl decanoate	135
6.5.1.2	Methyl laurate	139
6.5.1.3	Methyl myristate	141
6.5.1.4	Methyl palmitate	142
6.5.1.5	Comparison between methyl laurate and methyl myristate	143
6.5.1.6	Comparison between methyl myristate and methyl palmitate	144
6.5.2	Unsaturated FAMEs	145
6.5.2.1	Methyl oleate	145
6.5.2.2	Methyl linoleate	147
6.5.2.3	Methyl oleate/FAME blend	148
6.5.2.4	Comparison between methyl oleate and methyl linoleate	149
6.5.2.5	Kinetic simulations of methyl oleate and methyl linoleate	149
6.5.3	Overall ignition time correlation	152
6.6	Summary	156
7	Obtaining long shock tube test times	158
7.1	Introduction	158
7.1.1	Motivation	158

7.1.2	Previous research	158
7.1.3	Background	160
7.2	Experimental setup	166
7.3	Application of existing test time extension techniques	167
7.3.1	Driver insert	167
7.3.2	Driver gas tailoring	168
7.3.3	Helium interface gas	171
7.3.4	Driver extensions	171
7.4	Staged driver gas filling	172
7.4.1	Theory	172
7.4.2	Technique	174
7.4.3	Staged versus conventional filling	177
7.4.4	Variation of binary length	179
7.4.5	Variation of filling time	179
7.4.6	Variation of backfill gas sound speed	181
7.4.7	Selection of backfill gas	181
7.5	Combination of techniques	182
7.6	Sample ignition delay time measurement	185
7.7	Heat transfer	187
7.8	Summary	188
8	Operation of the constrained reaction volume shock tube	190
8.1	Introduction	190
8.1.1	Motivation	190
8.1.2	Previous research	191
8.2	Experimental setup	193
8.2.1	Shock tube	193
8.2.2	Gate valve	198
8.2.3	Diagnostics	200

8.3	Results	201
8.3.1	Buffer gas tailoring	202
8.3.2	Buffer/test gas mixing	205
8.3.2.1	Effect of pressure	206
8.3.2.2	Effect of slider speed	207
8.3.2.3	Region 2 contact surface	209
8.3.2.4	Guidelines for gate valve operation	212
8.3.3	Mixing tank/shock tube volume ratio dependence	212
8.4	Comparison of CRV and conventional filling strategies	214
8.5	Summary	217
9	Application of constrained reaction volume shock tube to normal heptane ignition	218
9.1	Introduction	218
9.2	Experimental setup	220
9.2.1	Shock tube facility	220
9.2.2	Laser absorption measurements	220
9.2.2.1	Laser absorption of fuel	220
9.2.2.2	Laser absorption of OH and aldehydes	221
9.2.2.3	Laser absorption of CO ₂	221
9.2.2.4	Laser absorption of H ₂ O and temperature measurement	221
9.2.3	Light emission	222
9.2.4	Ignition measurement	222
9.3	Results	224
9.3.1	Ignition delay times	224
9.3.2	Fuel time-histories and first stage fuel decomposition fraction	227
9.3.3	OH and aldehyde/ketene/formic acid time-histories	230
9.3.4	CO ₂ and H ₂ O time-histories	230
9.3.5	Temperature time-histories and first stage temperature change	231
9.4	Summary	234

10 Conclusion	235
10.1 Summary	235
10.1.1 Extension of AST to very-low-vapor-pressure biodiesel surrogates	236
10.1.2 Multi-fuel-component AEROFROSH	236
10.1.3 Infrared spectra of FAMEs	236
10.1.4 Ignition delay times of FAMEs	237
10.1.5 Long shock tube test times	237
10.1.6 Second-generation CRV shock tube technique	237
10.1.7 Application of CRV technique to <i>n</i> -heptane ignition	238
10.2 Conclusions	238
10.3 Future work	239
10.3.1 Spectra of unsaturated FAMEs	239
10.3.2 New test conditions in the AST	240
10.3.3 Time histories of additional species	240
10.3.4 Further extension of test time	240
10.3.5 CRV length	241
10.4 Final thoughts	241
A FROSH	243
A.1 Introduction	243
A.2 Background	243
A.2.1 Shock tubes	243
A.2.2 Previous Studies	244
A.3 Fundamentals	246
A.3.1 Notation	247
A.3.2 Reference frames	248
A.3.3 Lab time and particle time	249
A.3.4 Governing equations	249
A.3.5 NASA polynomials	250

A.3.6	Newton-Raphson method	252
A.3.7	Numerical constants	253
A.3.8	Frozen chemistry	253
A.4	Code structure	254
A.4.1	Initialization	254
A.4.2	Determination of Region 2 conditions	256
A.4.3	Determination of Region 5 conditions	257
A.4.4	Closing calculations	259
A.5	Vibrational non-equilibrium	259
A.5.1	Background	259
A.5.2	Procedure	262
A.5.3	Summary and demonstration	267
A.6	Validation	269
A.7	Uncertainty analysis	271
A.8	Summary	274
A.9	Derivation of incident shock iteration equations	274
A.10	Derivation of reflected shock iteration equations	279
B	Lab and particle time	284
B.1	Introduction	284
B.2	Derivation	285
B.3	Summary	286
C	Droplet properties	287
C.1	Introduction	287
C.2	Literature review	287
C.3	Thermodynamic expressions	289
C.3.1	Surface tension and density	289
C.3.2	Total energy	289
C.3.3	Inner-droplet pressure	290

C.3.4	Vapor pressure	290
C.3.5	Droplet temperature	290
C.3.6	Sound speed	291
C.4	Results	291
C.5	Summary	292
D	Arrhenius ignition delay expression	294
D.1	Introduction	294
D.2	Derivation	294
D.3	Summary	297
E	Practical considerations for obtaining constant-pressure post-reflected-shock conditions	298
E.1	Introduction	298
E.2	Gas tailoring	298
E.2.1	Driver gas tailoring	298
E.2.2	Buffer gas tailoring	301
E.3	Driver inserts	301
E.4	Staged driver gas filling	307
E.4.1	Effect of P_{4a}	308
E.4.2	Effect of backfill port location	309
E.4.3	Recommendations for backfill gas	309
E.5	Diaphragms	310
E.6	Summary	313
F	Shock tube design	314
F.1	Introduction	314
F.2	Safety factor	314
F.3	Pressure vessels	315
F.3.1	Equations	315

F.3.2	Flanges	317
F.3.3	Bolts	317
F.3.4	Effect of temperature	318
F.3.5	CRVST constraints	319
F.4	Window plug design	319
F.4.1	Equations	319
F.4.2	Transmission	320
F.4.3	Glue	321
F.5	O-rings	322
F.6	Summary	324
G	Determining the fraction of fuel remaining after first stage ignition	325
G.1	Introduction	325
G.2	Procedure	326
G.3	Summary	330
H	Ignition delay time data	332
H.1	Ignition delay time data	332
Bibliography		342

List of Tables

1.1	Fatty acid compositions (weight percent) of several fats and oils.	6
1.2	Several FAME names and corresponding alkane/alkene molecules.	8
1.3	Summary of previous studies concerning saturated FAMEs and the five primary biodiesel components.	17

4.1	Sample input data for AEROFROSH.	74
4.2	Inputs to AEROFROSH and typical values for associated uncertainty.	75
4.3	Results of AEROFROSH uncertainty analysis.	76
5.1	Properties and purity of fuels studied.	82
5.2	Approximate locations of select peaks and valleys for FAMEs.	97
5.3	Peak cross section and FWHM data.	105
5.4	Absorption cross section at $3.392235\text{ }\mu\text{m}$ (2947.909 cm^{-1}) for the FAMEs measured in this study.	112
5.5	Approximate locations of select peaks and valleys for FAMEs.	114
5.6	Fitting parameters for integrated area best-fit lines.	120
5.7	Fitting parameters for integrated area best-fit lines.	122
5.8	R^2 values for $3.39\text{ }\mu\text{m}$ cross section extrapolation best-fit lines based on the absolute number of C–H bonds in the fuel and on the logarithm of the number of C–H bonds in the fuel.	124
6.1	Physical property information for the fuels investigated in this work.	128
6.2	Studies that have developed or modified kinetic mechanisms for the fuels examined in this work.	132
6.3	Gas/fuel purity information, as determined by the supplier.	133
6.4	Gas chromatograph analysis of methyl oleate blend (molar percent).	133
6.5	Best-fit Arrhenius parameters for MD, MLA, MM, and MP.	137
6.6	Best-fit Arrhenius parameters for MO, ML, and the MOB.	146
6.7	Correlation for FAME ignition delay times in terms of pressure, equivalence ratio, carbon number, and saturation.	154
6.8	Correlation for FAME ignition delay times at a common pressure, equivalence ratio, carbon number, unsaturation, and oxygen mole fraction.	155
7.1	Properties of several potential backfill driver gases.	183
8.1	Dimensions of several shock tubes in the literature.	194

8.2 Properties of several potential backfill driver gases.	203
A.1 Sample atomic masses used in FROSH	253
A.2 Output data available from FROSH.	260
A.3 Linear polyatomic molecules.	265
A.4 Inputs to FROSH and typical values for associated uncertainty.	272
A.5 Results of FROSH uncertainty analysis.	273
F.1 Locations of extreme values of principal stresses in pressure vessels.	317
F.2 Maximum operating pressures for CRVST components.	319
F.3 Window material properties.	321
H.1 Ignition delay time data for methyl decanoate.	332
H.2 Ignition delay time data for methyl laurate.	333
H.3 Ignition delay time data for methyl myristate.	334
H.4 Ignition delay time data for methyl palmitate.	335
H.5 Ignition delay time data for methyl oleate.	335
H.6 Ignition delay time data for methyl linoleate.	337
H.7 Ignition delay time data for the methyl oleate/FAME blend.	338
H.8 Ignition delay time data for <i>n</i> -heptane.	340

List of Figures

1.1 Annual world energy consumption by type.	2
1.2 United States average price of fuel per gallon.	3
1.3 Reaction to form three methyl palmitate molecules (MP, C ₁₇ H ₃₄ O ₂) from one triglyceride molecule made of three palmitic acids (C ₁₆ H ₃₂ O ₂).	4
1.4 Reaction to form one triglyceride molecule from three palmitic acids (C ₁₆ H ₃₂ O ₂). . .	5

1.5	Composition of biodiesel	5
1.6	Molecular diagrams of five primary FAMEs in biodiesel fuel.	7
1.7	Average impact of blending biodiesel with fossil diesel on heavy-duty highway engine emissions.	11
1.8	Average quarterly price per Gasoline Gallon Equivalent (GGE) of biodiesel and fossil diesel.	13
1.9	Flow chart summarizing the connection between experimental data and practical engine/emissions/fuel improvements by way of kinetic mechanism development. .	15
2.1	Schematic of conventional shock tube operation.	21
3.1	Schematic of aerosol shock tube operation.	28
3.2	Gantt chart of aerosol shock tube operation.	29
3.3	Schematic of diagnostics in the AST test section.	31
3.4	Example methyl decanoate ignition delay time shock experiment.	33
3.5	Ideal aerosol droplet spacing.	35
3.6	Characteristic timescales for droplet evaporation and diffusion as a function of droplet diameter.	36
3.7	Characteristic timescales for droplet evaporation and diffusion as a function of droplet volume fraction.	37
3.8	Theoretical range of the aerosol shock tube as compared to that of a conventional heated shock tube.	39
3.9	Droplet settling time as a function of droplet diameter.	43
3.10	Methyl palmitate aerosol size distribution.	45
3.11	Schematic of Malvern Particle Sizer setup for measuring the particle size distribution of liquid aerosols.	45
3.12	AGT Mie scattering diagnostic schematic.	50
3.13	Relationship between AGT extinction, pressure, and equivalence ratio.	50

4.1	Control volume used to solve for Region 2 conditions in the presence of evaporating aerosol.	59
4.2	Sample fuel absorbance measurement in Region 2.	61
4.3	Schematic of main loop structure employed by AEROFROSH.	62
4.4	Post-shock (Region 2) temperature in a water droplet/vapor mixture.	71
4.5	Ratio of Region 2 to Region 1 temperature and pressure as a function of incident frozen Mach number.	72
4.6	Ratio of post-to-pre-evaporation properties for <i>n</i> -decane/21%O ₂ /Ar mixtures and for <i>n</i> -hexadecane/21%O ₂ /Ar mixtures as a function of droplet volume fraction. . .	73
4.7	Temperature change as the result of evaporation in Region 2.	73
4.8	Results of AEROFROSH uncertainty analysis for <i>T</i> ₂ and <i>P</i> ₂	77
4.9	Results of AEROFROSH uncertainty analysis for <i>T</i> ₅ and <i>P</i> ₅	77
4.10	Results of AEROFROSH uncertainty analysis for ϕ	78
5.1	Cross section extrapolation model available in the literature.	81
5.2	Molecular diagrams of FAMEs examined in this study.	82
5.3	Experimental setup for FTIR measurements in a heated static cell.	83
5.4	Comparison of spectra for methyl valerate with and without nitrogen dilution. . . .	88
5.5	Spectrum of methyl acetate at 100 °C and fuel partial pressures of 3.8, 5.8, 9.9, and 50.0 Torr.	89
5.6	Spectrum of methyl acetate at 25 °C and 1 atm, measured using instrument resolutions of 0.1 cm ⁻¹ and 1.0 cm ⁻¹	90
5.7	Spectrum of methyl acetate at 100 °C and 1 atm, measured with 5, 10, 25, and 50 scans.	91
5.8	Cell pressure for methyl heptanoate at 100 °C, showing condensation.	92
5.9	Decomposition of methyl heptanoate at 350 °C.	93
5.10	Comparison of spectra of methyl acetate with those measured by PNNL.	94
5.11	Comparison of spectra of methyl propionate with those measured by PNNL.	95
5.12	Comparison of spectrum of methyl butanoate with that measured by PNNL.	95

5.13 Spectrum of methyl acetate.	97
5.14 Spectrum of methyl propionate.	98
5.15 Spectrum of methyl butanoate.	99
5.16 Spectrum of methyl valerate.	99
5.17 Spectrum of methyl hexanoate.	100
5.18 Spectrum of methyl heptanoate.	101
5.19 Spectrum of methyl octanoate.	102
5.20 Spectrum of methyl nonanoate.	102
5.21 Spectrum of methyl decanoate.	103
5.22 Spectrum of methyl crotonate.	104
5.23 Spectrum of methyl-3-nonenanoate.	105
5.24 Peak cross section values of the C–H spectra for the saturated FAMEs examined in this study as a function of temperature.	109
5.25 Full Width at Half Maximum (FWHM) values of the C–H spectra for the saturated FAMEs examined in this study as a function of temperature.	109
5.26 Demonstration of peak cross section and Full Width at Half Maximum (FWHM) for methyl heptanoate at 100 °C.	110
5.27 Comparison of spectra of saturated FAMEs.	111
5.28 Absorption cross sections at 3.392235 μm (2947.909 cm ⁻¹) for the saturated FAMEs examined in this study.	113
5.29 Uncorrected integrated absorbance values for the saturated FAMEs examined in this study.	113
5.30 Contribution of CH ₂ and CH ₃ groups to spectra.	115
5.31 Comparison of the spectrum of propane with those of methyl propionate and methyl butanoate.	117
5.32 Comparison of the spectrum of <i>n</i> -butane with those of methyl butanoate and methyl valerate.	118
5.33 Comparison of the spectrum of <i>n</i> -pentane with those of methyl valerate and methyl hexanoate.	119

5.34 Comparison of the spectrum of <i>n</i> -heptane with those of methyl heptanoate and methyl octanoate.	119
5.35 Demonstration that the number of C–H bonds and integrated area in <i>n</i> -alkanes, 1-alkenes, and saturated FAMEs have a linear relationship.	121
5.36 Demonstration of the linear relationship between a fuel's 3.39 μm cross section and the logarithm of the number of C–H bonds it contains.	123
5.37 C–H bonds present in the vicinity of the C=C double bond in methyl-3-nonenoate. .	125
5.38 Comparison of spectra of MOC, MHP, and M3N at 100 °C.	126
6.1 Molecular diagrams for the FAMEs whose ignition delay times have been measured in this work.	129
6.2 Methyl decanoate ignition delay times.	138
6.3 Methyl laurate ignition delay times.	140
6.4 Methyl myristate ignition delay times.	141
6.5 Methyl palmitate ignition delay times.	142
6.6 Comparison of methyl laurate and methyl myristate ignition delay times.	144
6.7 Comparison of methyl myristate and methyl palmitate ignition delay times.	145
6.8 Methyl oleate ignition delay times.	147
6.9 Methyl linoleate ignition delay times.	148
6.10 Methyl oleate/FAME blend (MOB) ignition delay times.	149
6.11 Comparison of ignition delay times for methyl oleate and methyl linoleate.	150
6.12 Comparison of methyl oleate and methyl linoleate ignition delay times to predictions of the original Westbrook <i>et al.</i> mechanism.	151
6.13 Comparison of methyl oleate and methyl linoleate ignition delay times to predictions of the updated Westbrook <i>et al.</i> mechanism.	152
6.14 Demonstration of overall FAME ignition delay time correlation.	155
7.1 Idealized x-t diagram for a basic shock tube experiment.	161
7.2 Idealized x-t diagram for a tailored shock tube experiment.	162
7.3 Idealized x-t diagram comparing two driver lengths.	163

7.4	Approximate shock tube test time τ at the tailored condition as a function of driver section length.	164
7.5	Shock tube test time τ at the tailored condition as a function of test temperature. . .	165
7.6	Comparison of shocks with and without a driver insert.	169
7.7	Percent increase in test temperature as a function of a non-ideal pressure rise for three test gases at a nominal temperature of 1000 K, assuming isentropic behavior.	169
7.8	Result of driver gas tailoring.	170
7.9	Effect of helium interface gas.	172
7.10	Effect of driver section length.	173
7.11	Test time τ as a function of driver length.	173
7.12	Staged driver filling procedure.	175
7.13	Idealized x-t diagram comparing staged driver filling to conventional driver filling.	176
7.14	Comparison of conventional to staged driver gas filling.	178
7.15	Test time as a function of binary gas length.	180
7.16	Test time as a function of backfill time.	180
7.17	Test time as a function of backfill gas sound speed.	181
7.18	Demonstration of combined test time extension techniques.	184
7.19	Benefit of backfill technique on test time versus Region 5 temperature.	185
7.20	Sample ignition delay time measurement.	186
7.21	Sample ignition delay time measurement.	188
8.1	Shock tube schematic.	193
8.2	CRV shock tube operating procedure.	196
8.3	X-t diagram of CRV shock experiment generated using the WiSTL code.	197
8.4	Exploded view of gate valve.	199
8.5	Locations of diagnostics on shock tube.	200
8.6	Shock wave velocity profile for correctly tailored buffer gas mixture.	204
8.7	Normalized HeNe absorbance traces measured 10.3 cm from the endwall at several pressures during gate valve opening.	207

8.8	Normalized HeNe absorbance traces measured 10.3 cm from the endwall at several gate valve slider speeds.	208
8.9	Effect of slider speed on gate valve timing and buffer/test gas mixing.	209
8.10	HeNe absorbance traces at 10.3 cm-from-endwall observation location showing passage of the buffer/test gas contact surface.	210
8.11	HeNe absorbance trace at 2.0 cm-from-endwall observation location for CRV filling, indicating a constant fuel mole fraction in Region 2.	211
8.12	Range of Stanford shock tube in conventional and CRV operation.	215
8.13	Comparison of conventional and CRV filling shocks.	216
9.1	Comparison between CRV and conventional shock measurements.	223
9.2	<i>n</i> -Heptane ignition delay time values.	225
9.3	HeNe absorbance profiles during <i>n</i> -heptane oxidation, normalized to unity at time zero, for several temperatures (CRV operation).	228
9.4	Fraction of <i>n</i> -heptane remaining after first stage ignition.	229
9.5	Measurements of OH and aldehyde/ketene/formic acid mole fraction during <i>n</i> -heptane oxidation.	231
9.6	Mole fraction time histories of carbon dioxide and water during <i>n</i> -heptane oxidation.	232
9.7	Temperature time-histories during <i>n</i> -heptane oxidation.	233
9.8	Temperature increase during first stage <i>n</i> -heptane ignition.	233
A.1	Velocities and variables in different shock reference frames.	248
A.2	Effect of extrapolating incident shock velocity to different distances from the shock tube endwall.	255
A.3	Ratios of FE-to-EE and FF-to-EE Region 5 (translational) temperature and pressure for shocks in an argon/oxygen mixture.	268
A.4	Ratio of FROSH equilibrium-equilibrium Region 2 and 5 calculations to analytical (ideal shock) relation results of Gaydon and Hurle.	270
A.5	Ratio of FROSH equilibrium-equilibrium Region 2 and 5 calculations to computations done in GasEq.	271

A.6	Results of FROSH uncertainty analysis for T_2 and P_2	273
A.7	Results of FROSH uncertainty analysis for T_5 and P_5	274
B.1	Explanation of terms used in the derivation of the relationship between lab and particle time.	285
C.1	Comparison of droplet properties to bulk fluid properties for methyl decanoate ($C_{11}H_{22}O_2$) at 298.15 K and 200 Torr in argon.	293
E.1	Comparison of actual to theoretical driver gas tailoring.	299
E.2	Diagram showing positive and negative driver inserts.	302
E.3	Section view of the CRVST driver section.	304
E.4	Driver insert for U-joint.	305
E.5	Schematic of driver inserts employed to achieve long test times.	306
E.6	Effect of P_{4a} on Region 5 pressure.	308
E.7	Schematic of diaphragm cutter used in the CRVST.	311
E.8	Example of diaphragm flapping.	312
F.1	Principal stresses in a cylindrical pressure vessel.	316
F.2	Important dimensions for window plug design.	320
F.3	Change in o-ring size due to interaction with methyl decanoate and the methyl oleate blend.	323
G.1	Determination of the time at which the post-first-stage-ignition quantities were evaluated in the <i>n</i> -heptane oxidation simulation.	327
G.2	Simulated temperature and volume increase at first stage ignition.	327
G.3	Simulated absorbance profiles (with similar species grouped together) during <i>n</i> -heptane oxidation.	328
G.4	Simulated <i>n</i> -heptane, interfering species, and total absorbance profiles during <i>n</i> -heptane oxidation.	329
G.5	Fraction of simulated absorbance attributable to <i>n</i> -heptane.	329

Chapter 1

Introduction to biodiesel

1.1 Combustion today

Combustion is a process in which a substance reacts with an oxidizer, giving off heat and producing exhaust. The importance of this process cannot be over-emphasized. In the world today, combustion is the largest energy conversion method, utilized in the transportation, industrial, residential, and electricity-generation spheres. Moreover, the recent International Energy Outlook 2013 report by the United States Energy Information Administration (U.S. EIA) and U.S. Department of Energy (DOE) predicted that in the next 25 years, combustion will continue to increase in importance as the worldwide demand for energy grows [1]. This is depicted in Figure 1.1, which shows that worldwide energy use is expected to increase by 56% from 2010 levels by the year 2040. Also, in 2040, approximately 79% of all energy used is expected to come from fossil fuels (taken in Figure 1.1 to be the sum of liquids, coal, and natural gas), a majority of which will be consumed via combustion [1]. This annual amount of energy, 643 quadrillion Btu, is enough to boil all the water in California's Lake Tahoe, among the top twenty deepest lakes in the world [2, 3], over 11 times!

Among the different energy resources depicted in Figure 1.1, liquid resources comprise approximately 30% of the total consumption each year. Of these liquid fuels, the majority are used in the transportation sector, because liquid fuels are easily transportable and many have a high energy density [4]. More specifically, within the transportation sector, heavy-duty trucks account for

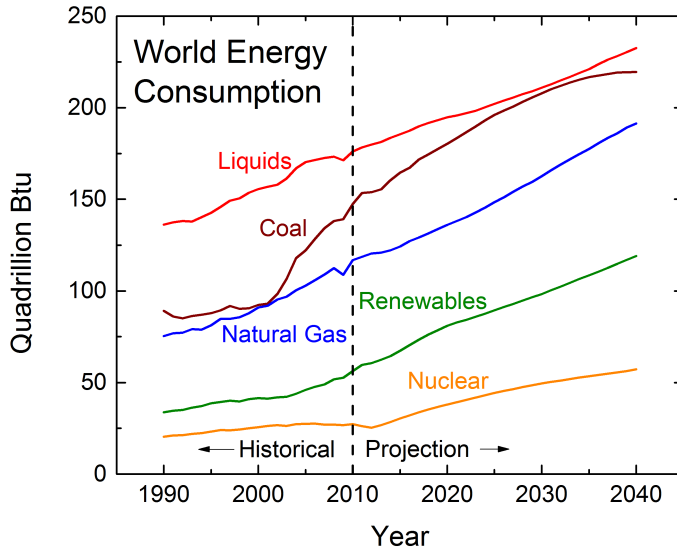


Figure 1.1: Annual world energy consumption by type [1].

a significant fraction of oil consumption and emissions. In 2010, heavy-duty trucks accounted for only 4% of registered vehicles in the U.S., but contributed to roughly 17% of all on-road energy use and 20% of greenhouse gas emissions in the transportation sector [4, 5]. As a result, even small improvements in efficiency and small reductions in emissions across the entire U.S. heavy-duty truck fleet can amount to significant changes at a national level. Given this prominence, it seems that understanding the process of combustion, with specific application to heavy-duty trucks in the transportation sector, is critical.

There are many research-worthy problems related to transportation-sector combustion today. Most noticeably, fuel costs are rising; Figure 1.2 shows the United States average price per gallon of fuel (regular gasoline and number 2 diesel) for several years [6]. These rising costs have driven research of more efficient combustion engine technologies. Moreover, recent regulations by the U.S. Environmental Protection Agency (EPA) have set aggressive targets for large and medium truck fuel economy, carbon (CO_2) and CO) emissions, hydrocarbon (HC) emissions, and soot/particulate matter (PM) emissions [5, 7, 8]. Achieving these standards will require improvements in diesel engine efficiency, modifications to existing engine architecture, and special additives to fossil diesel fuel such as oxygenated species (molecules that contain oxygen). One such oxygenated species,

which is currently being blended with fossil diesel, is a renewable alternative manufactured from vegetable oils, animal fats, and waste fry grease known as biodiesel.

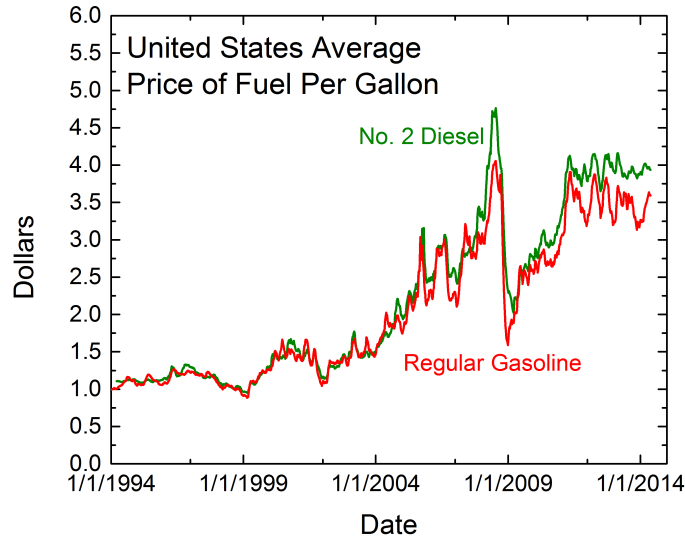


Figure 1.2: United States average price of fuel per gallon [6].

1.2 Background

Biodiesel is a “fuel comprised of mono-alkyl esters of long-chain fatty acids derived from vegetable oils or animal fats,” as defined by the biodiesel standard ASTM D6751 [9]. These mono-alkyl esters are also known as Fatty Acid Methyl Esters (FAMEs), which are produced in a process called transesterification from fatty acids [10–13]. Some of the primary benefits of biodiesel fuel include its high flash point, high cetane number, good lubricity, good solvent properties, renewability, biodegradability, domestic origin, miscibility with fossil diesel, and lower pollutant (hydrocarbon/carbon monoxide/sulfur/soot/particulate matter) emissions [14].

1.3 Production

As mentioned above, biodiesel is produced in a process called transesterification from fatty acids [10–13]. In the most common version of this transformation, shown in Figure 1.3, a fat or oil molecule reacts with three methanol (CH_3OH) molecules to produce three FAME molecules and one glycerol molecule ($\text{C}_3\text{H}_8\text{O}_3$). This process is performed in order to decrease the viscosity of the fat/oil, making it more readily combustible in conventional diesel engines. The yield for this process is usually in excess of 90%. This process typically takes place in the presence of a basic catalyst (*e.g.*, sodium hydroxide, NaOH), which is required in only small amounts (0.5% by weight) [15]. As expected, based on the transesterification graphic (Figure 1.3), the ester composition of biodiesel after the transesterification process closely mirrors that of the fatty acid feedstock [16].

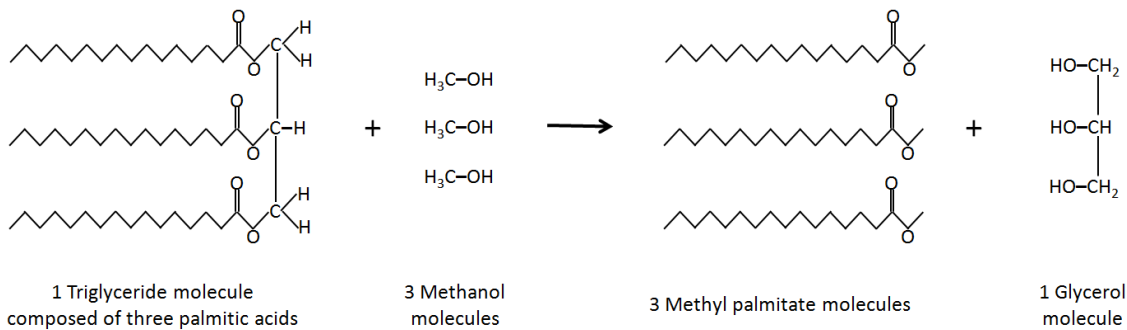


Figure 1.3: Reaction to form three methyl palmitate molecules (MP, $\text{C}_{17}\text{H}_{34}\text{O}_2$) from one triglyceride molecule made of three palmitic acids ($\text{C}_{16}\text{H}_{32}\text{O}_2$).

Note that three fatty acids, when combined, are called a triglyceride (also known as a triester or fat/oil; see Figure 1.4).

1.4 Feedstock sources

Biodiesel fuel can be synthesized from a variety of feedstock oil sources, such as rapeseeds [14], soybeans [14], waste fry grease [17], algae [18, 19], peanuts [20], butter [16], orange seeds [21], tobacco seeds [22], and even waste coffee grounds [23]. Sample compositions for three primary

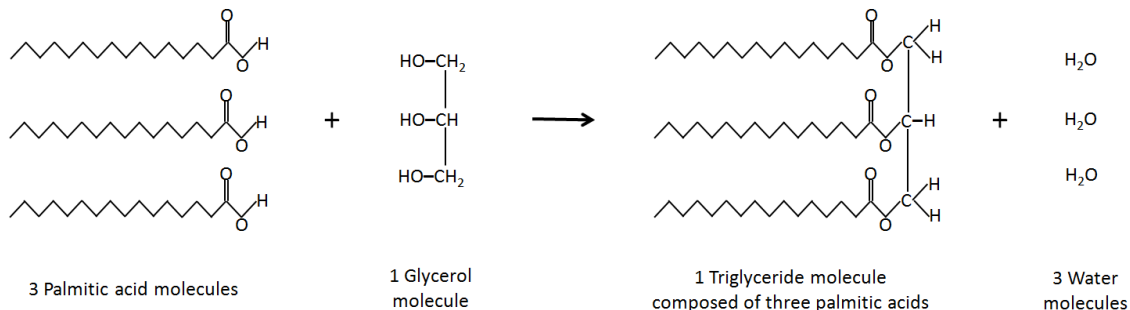


Figure 1.4: Reaction to form one triglyceride molecule from three palmitic acids ($C_{16}H_{32}O_2$).

feedstocks are depicted in Figure 1.5 and several are also listed in Table 1.1. The actual fuel mixture is comprised primarily of five components: methyl palmitate (MP, $C_{17}H_{34}O_2$), methyl stearate (MS, $C_{19}H_{38}O_2$), methyl oleate (MO, $C_{19}H_{36}O_2$), methyl linoleate (ML, $C_{19}H_{34}O_2$), and methyl linolenate (MLN, $C_{19}H_{32}O_2$); molecular diagrams of these molecules can be found in Figure 1.6.

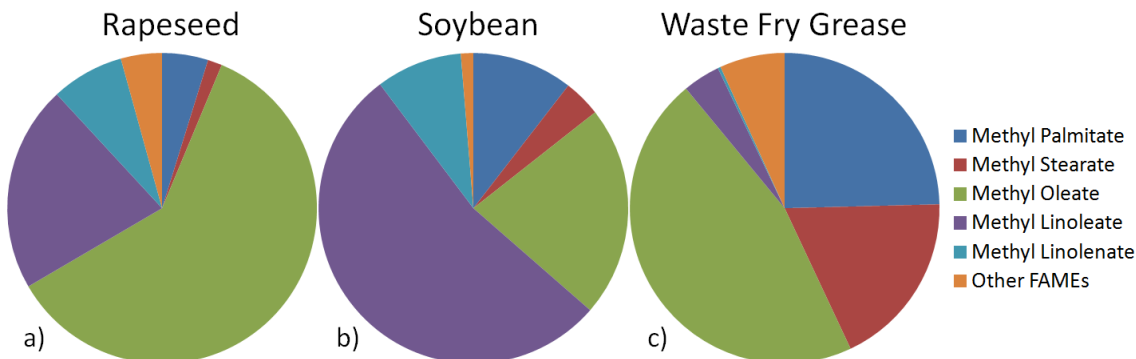


Figure 1.5: Composition of biodiesel (by weight) made from a) rapeseed oil [24], b) soybean oil [24], and c) waste fry grease [17].

Neat (100% pure) biodiesel is often referred to as “B100”, and blends of biodiesel with fossil diesel are noted by their percent volume biodiesel content. One of the most common blends is B20 (*i.e.*, a blend of 20% biodiesel and 80% fossil diesel).

A convenient short hand notation for fatty acid molecular formulas indicates the molecular size and degree of saturation in the form $CA:B$, where A is the number of carbon atoms in the long alkane-like chain and B is the degree of unsaturation. For instance, referring to Figure 1.6, methyl

Table 1.1: Fatty acid compositions (weight percent) of several fats and oils [25–27].

Oil or fat type	C8:0	C10:0	C12:0	C14:0	C16:0	C18:0	C18:1	C18:2	C18:3	C20:0	C22:0	C22:1	C24:0
Soybean				0.1	10.3	4.7	22.5	54.1	8.3				
Rapeseed					2.7	2.8	21.9	13.1	8.6				50.9
Beef tallow	0.1	0.1	3.3		25.2	19.2	48.9	2.7	0.5				
Peanut				10.4	8.9	47.1	32.9	0.5				0.2	
Canola				0.1	3.9	3.1	60.2	21.1	11.1				0.5
Olive					11.0	3.6	75.3	9.5	0.6				
Coconut	8.3	6.0	46.7	18.3	9.2	2.9	6.9	1.7					
Corn					9.9	3.1	29.1	56.8	1.1				
Palm	0.1	0.1	0.9	1.3	43.9	4.9	39.0	9.5	0.3				
Safflower				0.1	6.6	3.3	14.4	75.5	0.1				
Sunflower				0.1	6.0	5.9	16.0	71.4	0.6				
Sunola					3.0	4.4	88.2	4.3	0.1				
Butterfat	5.5	3.0	3.6	11.6	33.4	11.4	27.8	3.1	0.6				
Lard	0.1	0.1	1.4	25.5	15.8	47.1	8.9	1.1					
Cottonseed				0.8	22.9	3.1	18.5	54.2	0.5				
Crambe													
Linseed													
High oleate safflower				0.3	5.5	1.8	79.4	12.9	0.2				
Sesame				13.1	3.9	52.8	30.1						

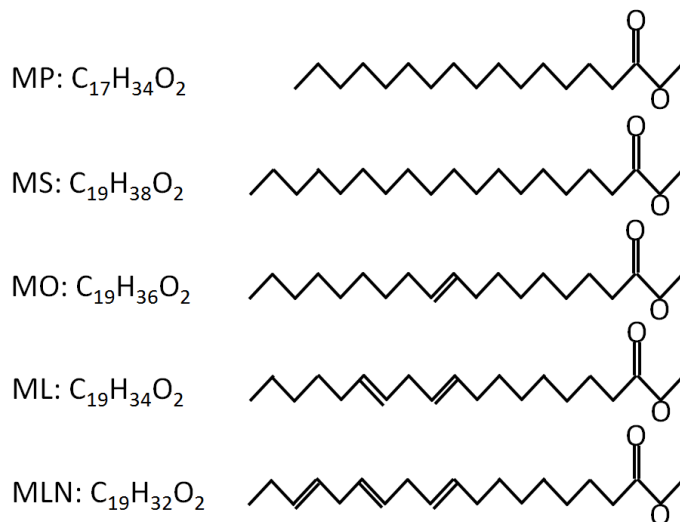


Figure 1.6: Molecular diagrams of five primary FAMEs in biodiesel fuel.

stearate (C₁₉H₃₈O₂) is known as C18:0 since it has an 18-carbon atom chain and is fully saturated, and methyl linolenate (C₁₉H₃₂O₂) is known as C18:3 since it has three double bonds (three degrees of unsaturation). A list of several FAME names and corresponding alkane/alkene molecules is provided in Table 1.2.

1.5 Benefits

There are numerous benefits to biodiesel fuel compared to fossil diesel, as mentioned briefly above. This section will provide details concerning these positive factors.

1.5.1 High flash point

The flash point of a fuel is the lowest temperature at which it can vaporize to form an ignitable mixture in air; generally higher values are preferable, because they imply that the fuel is less likely to explode. Due to their high boiling points and low vapor pressures, biodiesel fuel molecules have very high flash points [12, 27].

CHAPTER 1. INTRODUCTION TO BIODIESEL

Table 1.2: Several FAME names and corresponding alkane/alkene molecules.

Number of Carbon in Chain	FAME (Methyl...)	Short Name	Formula	CA:B	Corresponding Alkane/Alkene	Formula
1	Formate	MF	C ₂ H ₄ O ₂	C1:0	Methane	CH ₄
2	Acetate	MA	C ₃ H ₆ O ₂	C2:0	Ethane	C ₂ H ₆
3	Propionate (Propanoate)	MP	C ₄ H ₈ O ₂	C3:0	Propane	C ₃ H ₈
4	Butyrate (Butanoate)	MB	C ₅ H ₁₀ O ₂	C4:0	Butane	C ₄ H ₁₀
5	Valerate (Pantanate)	MV	C ₆ H ₁₂ O ₂	C5:0	Pentane	C ₅ H ₁₂
6	Hexanoate (Caproate)	MH	C ₇ H ₁₄ O ₂	C6:0	Hexane	C ₆ H ₁₄
7	Heptanoate	MHP	C ₈ H ₁₆ O ₂	C7:0	Heptane	C ₇ H ₁₆
8	Caprylate (Octanoate)	MOC	C ₉ H ₁₈ O ₂	C8:0	Octane	C ₈ H ₁₈
9	Nonanoate	MN	C ₁₀ H ₂₀ O ₂	C9:0	Nonane	C ₉ H ₂₀
10	Caprate (Decanoate)	MD	C ₁₁ H ₂₂ O ₂	C10:0	Decane	C ₁₀ H ₂₂
11	Undecanoate	C11:0			Undecane	C ₁₁ H ₂₄
12	Laurate (Dodecanoate)	MLA	C ₁₂ H ₂₄ O ₂	C12:0	Dodecane	C ₁₂ H ₂₆
13	Tridecanoate	C13:0			Tridecane	C ₁₃ H ₂₈
14	Myristate (Tetradecanoate)	MM	C ₁₄ H ₃₀ O ₂	C14:0	Tetradecane	C ₁₄ H ₃₀
15	Pentadecanoate	C15:0			Pentadecane	C ₁₅ H ₃₂
16	Palmitate (Hexadecanoate)	MP	C ₁₆ H ₃₂ O ₂	C16:0	Hexadecane (Cetane)	C ₁₆ H ₃₄
17	Heptadecanoate	C17:0			Heptadecane	C ₁₇ H ₃₆
18	Stearate (Octadecanoate)	MS	C ₁₈ H ₃₈ O ₂	C18:0	Octadecane	C ₁₈ H ₃₈
19	Nonadecanoate	C ₁₉ H ₄₀ O ₂	C19:0		Nonadecane	C ₁₉ H ₄₀
20	Arachidate (Eicosanoate)	C20:0			Eicosane	C ₂₀ H ₄₂
21	Heneicosanoate	C ₂₁ H ₄₂ O ₂	C21:0		Heneicosane	C ₂₁ H ₄₄
22	Behenate (Docosanoate)	C ₂₂ H ₄₄ O ₂	C22:0		Docosane	C ₂₂ H ₄₆
23	Tricosanoate	C ₂₃ H ₄₆ O ₂	C23:0		Tricosane	C ₂₃ H ₄₈
24	Lignocerate (Tetracosanoate)	C ₂₄ H ₄₈ O ₂	C24:0		Tetracosane	C ₂₄ H ₅₀
25	Pentacosanoate	C ₂₅ H ₅₀ O ₂	C25:0		Pentacosane	C ₂₅ H ₅₂
26	Cerotate (Hexacosanoate)	C ₂₆ H ₅₂ O ₂	C26:0		Hexacosane	C ₂₆ H ₅₄
3	Acrylate	C ₂₇ H ₅₄ O ₂	C27:0			
4	Crotonate (Butenoate)	MC	C ₄ H ₆ O ₂	C3:1	Propene	C ₃ H ₆
9	Nonenoate	M3N	C ₅ H ₈ O ₂	C4:1	Butene	C ₄ H ₈
10	Decenoate	C ₁₀ H ₁₈ O ₂	C9:1		None	C ₉ H ₁₈
16	Palmitoleate	C ₁₁ H ₂₀ O ₂	C10:1		Decene	C ₁₀ H ₂₀
18	Oleate	C ₁₇ H ₃₂ O ₂	C16:1		Hexadecene	C ₁₆ H ₃₂
18	Linoleate	MO	C ₁₉ H ₃₆ O ₂	C18:1	Octadecene	C ₁₈ H ₃₆
18	Linolenate	MLN	C ₁₉ H ₃₄ O ₂	C18:2	Octadecyne	C ₁₈ H ₃₄
20	Eicosenoate	C ₂₁ H ₃₂ O ₂	C18:3		Eicosene	C ₂₀ H ₄₀
22	Erucate	C ₂₃ H ₄₄ O ₂	C22:1		Docosene	C ₂₂ H ₄₄

1.5.2 High cetane number

The cetane number (CN) is a unitless measure of the propensity of a fuel to ignite; cetane (*n*-hexadecane, C₁₆H₃₄) is readily ignitable and is assigned CN = 100, and isocetane (2,2,4,4,6,8,8-heptamethylnonane) is difficult to ignite and is assigned CN = 0. Diesel engines typically burn fuels with cetane numbers ranging from 40 to 55. A higher cetane number implies that a fuel has a shorter ignition delay time, which is desirable, because it provides more time for the fuel to burn in the cylinder. The CN of a fuel is typically larger if it has a longer saturated normal alkane-like carbon chain. Since both methyl stearate and methyl palmitate have such carbon chains, they have high cetane numbers; this makes blending them with lower CN fossil diesel components beneficial [14, 28].

1.5.3 Lubricity

While the sulfur content in fossil diesel fuel results in harmful emissions, it does improve the lubricity of diesel fuel. Thus, new low-sulfur fossil diesel blends are unfortunately associated with increased engine wear. Fortunately, the ester moiety (specifically the O-atoms, which impart polarity) of FAMEs results in high lubricity. For this reason, biodiesel is considered to be an engine lubricant and is often blended with fossil diesel [29].

1.5.4 Solvent properties

Fossil diesel fuel leaves deposits on fuel tanks and hoses. However, biodiesel possesses good solvent properties; it is able to dissolve these deposits. This provides another reason to blend biodiesel with fossil diesel in even small percentages [30].

1.5.5 Biodegradability

When accidentally released into the environment, refined fossil fuels can linger for long periods of time before completely degrading. For instance, gasoline (91 octane) has been found to degrade only about 28% in 28 days, and fossil diesel fuel degrades even more slowly. In contrast, rapeseed

oil methyl ester was shown to degrade as much as 88% in 28 days [30, 31]. A faster degradation time minimizes the impact of accidental spills, making it a positive attribute of biodiesel fuel.

1.5.6 Domestic origin

Since biodiesel can be produced from a wide variety of feedstock sources (see Table 1.1), it can be made virtually worldwide. This contributes to energy security for the biodiesel-producing nation and also reduces the costs of transporting the fuel from its place of origin to its place of consumption. In the United States, biodiesel is produced primarily from soybean oil and waste fry grease, whereas in Europe it is produced from rapeseed oil [32].

1.5.7 Miscibility with fossil diesel

As mentioned above, various blends of biodiesel with fossil diesel (by volume), such as B20, are common. Biodiesel is miscible with fossil diesel in any proportion [14]. Moreover, biodiesel can be transported and handled using the same equipment as fossil diesel fuel [31]. This lowers the capital-related barriers to producing and burning biodiesel fuel.

1.5.8 Lower pollutant emissions

Concentrations of pollutant emissions generated during biodiesel combustion, such as unburned hydrocarbons, carbon monoxide, sulfates, soot, and particulate matter, have generally been shown to be less than concentrations of pollutants generated during fossil diesel combustion (Figure 1.7) [15, 33–36]. Several reasons have been given for these differences. First, biodiesel simply contains lower concentrations of harmful species such as sulfur. Thus, its emissions of harmful pollutants are lower as well [30].

Second, the high cetane number of FAMEs leads to emissions reductions. A higher CN implies a shorter ignition delay time, which leaves more time for complete mixing and combustion of the fuel. Mixtures that are too lean due to insufficient mixing do not support autoignition, meaning that these fuel fragments are swept out with the other exhaust. Thus, since biodiesel's higher CN causes there to be more time for mixing/combustion, lean zones are less frequent, such that emissions of

unburned hydrocarbons are known to be lower when burning biodiesel fuel [36].

Third, the presence of the oxygen atoms contained in FAME molecules also plays an important role [36, 37]. Lower carbon monoxide emissions have been linked with the O-atoms in biodiesel decreasing the local equivalence ratio in parts of the in-cylinder diesel spray flames, allowing more CO to be oxidized to CO₂. Also, the decrease in particulate matter has been explained by the O-atoms contained in FAMEs aiding in the oxidation of soot and its precursors [36]. However, a slight increase in NO_x has been observed by in some cases; this has been discussed extensively in the literature [15, 33–36, 38, 39].

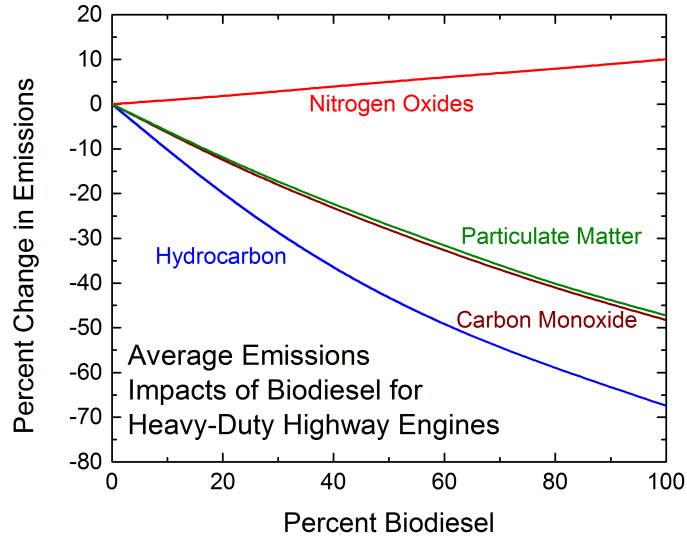


Figure 1.7: Average impact of blending biodiesel with fossil diesel on heavy-duty highway engine emissions [33].

1.6 Drawbacks

While there are many benefits of biodiesel, numerous drawbacks also exist. These are the subject of ongoing research.

1.6.1 Higher nitric oxide emissions

Perhaps the most widely cited drawback of biodiesel is the possible increase in NO_x that has been observed in some studies (see Figure 1.7) [15, 33–36, 38, 39]. The important factors for NO_x formation are the in-cylinder temperature and the duration for which that temperature is sustained. NO_x synthesis is endothermic, such that it forms in very high-temperature environments; the longer the high-temperature environment lasts, the more NO_x that is produced [36].

Several sources for the increase in NO_x emissions when fueling engines with biodiesel (as compared to fossil diesel) have been suggested. First, in older diesel engines that have mechanical injectors (newer models use electronically-controlled fuel injectors), biodiesel injection occurs slightly earlier than fossil diesel injection, because the speed of sound in biodiesel is higher. This results in an increased time for the fuel to be in the cylinder, and may result in an increase in NO_x [36, 40–42].

Second, some researchers have proposed that, in biodiesel combustion, greater amounts of NO_x are formed by the mechanism of Fenimore [43], known as “prompt NO,” than in the case of fossil diesel combustion [44]. Part of the reasoning for this theory has to do with the amount and type of radicals formed in rich premixed biodiesel flames [36].

Third, since the oxygen atoms in biodiesel reduce soot production by lowering the local equivalence ratio in the flame, less heat loss due to soot radiation from the flame occurs. In turn, this contributes to a higher flame temperature and promotes NO_x formation [36, 45].

Fourth, the adiabatic flame temperature of biodiesel is higher than in fossil diesel. It is thought that this again allows more NO_x to form in its endothermic synthesis process [36, 46, 47].

The structure of FAME molecules has also been linked to changes in the amount of in-cylinder NO_x formed during combustion. FAMEs with longer alkane-like hydrocarbon chains are associated with higher NO_x levels, since ignition delay times decrease (higher CN values) with increasing carbon chain length [36]. Moreover, the degree of unsaturation (number of C=C bonds) also has an effect; higher unsaturation leads to longer ignition delay times (lower CN values) [48], and is also known to result in higher peak cylinder pressures and higher heat release rates (and hence higher temperatures) [36, 47].

1.6.2 Higher fuel prices

Historically, the price of biodiesel fuel has been higher than that of fossil diesel. This may have to do with factors of supply/demand and of production/feedstock input costs [31]. Quarterly prices since 2006 for biodiesel and fossil diesel are depicted in Figure 1.8 [49].

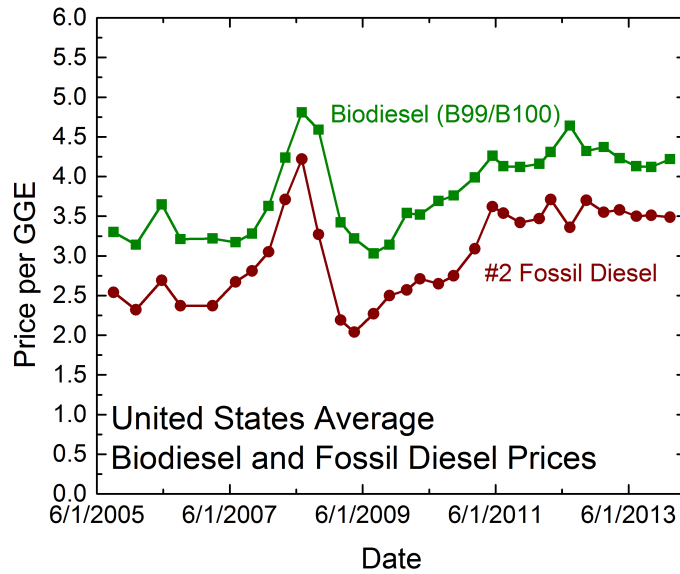


Figure 1.8: Average quarterly price per Gasoline Gallon Equivalent (GGE) of biodiesel and fossil diesel. One GGE is the volume of alternative fuel (in this case biodiesel or fossil diesel) needed to equal the energy content of one gallon of gasoline. 1 GGE for biodiesel is 0.96 gallon biodiesel fuel, and for fossil diesel it is 0.88 gallon fossil diesel fuel (*i.e.*, fossil diesel has a higher energy content than biodiesel, and biodiesel has a higher energy content than gasoline) [49].

1.6.3 Lower energy density

On both a volumetric and a mass basis, biodiesel contains less energy than fossil diesel. Specifically, B100 contains about 91-93% of the energy content of fossil diesel by volume [50]. This is in part because one of the O-atoms in FAMEs is strongly bonded to a C-atom in a double C=O bond, such that there is one fewer carbon atom available to produce carbon monoxide and ultimately form carbon dioxide (a very exothermic process) [37]. The Lower Heating Value (LHV) for fossil diesel is 128,450 Btu/gal, whereas for biodiesel (B100) it is 119,550 Btu/gal [50].

1.6.4 Poor oxidative stability

The oxidative stability of a fuel is a description of its ability to resist oxidation (primarily at room temperatures). Unfortunately, the unsaturated FAMEs in biodiesel (those containing double bonds) are particularly susceptible to a process in which oxygen reacts at double bond sites to form hydroperoxides; this sometimes involves a *cis/trans* isomerization as well. Thus, biodiesel is known for its poor oxidative stability. Various factors have been found to influence biodiesel's oxidative stability, including light exposure, ambient temperature, surface area of liquid fuel exposed to air, and metal contaminants [51, 52]. In addition, various additives to improve biodiesel oxidative stability have been proposed [52, 53].

1.6.5 Poor cold-flow properties

The cold-flow properties of a fuel describe its ability to move/pour/be pumped at low temperatures. Both fossil diesel and biodiesel are known to have somewhat poor cold-flow properties compared to gasoline, but biodiesel's composition makes it particularly susceptible to problems at low temperatures. Though the transesterification process decreases the viscosity (this can be thought of as measure of a fuel's *resistance* to move/pour/be pumped) of biodiesel, its viscosity is still higher than that of fossil diesel. Since viscosity tends to increase with decreasing temperature, at low temperatures the viscosity of biodiesel can become so high that it behaves more like a gel than a liquid. Furthermore, the melting points of FAMEs are generally higher than those of fossil diesel molecules, making solidification (freezing) a potential problem as well [12]. Fortunately, some fuel additives have been proposed to prevent these problems, and also some modern truck engines incorporate fuel heaters to keep viscosity values low [14, 54].

1.7 Previous research on biodiesel combustion

Based on the above overview, it may be surmised that the many advantages of biodiesel make it a promising alternative fuel, but numerous issues still exist that are the subject of ongoing research. In addition to those introduced above, one further area that is receiving particular attention is the

kinetics of biodiesel fuel, or the precise reaction pathways undertaken during FAME oxidation that transform fuel molecules into CO₂ and H₂O while producing heat [32, 37, 55, 56]. Understanding these pathways is of *critical* importance if diesel engine efficiency for biodiesel fueling is to be optimized and pollutant emissions are to be minimized in order to meet new national standards [5, 7, 8].

Combustion models called kinetic mechanisms are used to describe the process of oxidation for fuels. Small mechanisms, such as the mechanism describing the formation of H₂O from H₂ and O₂, contain as few as 20 reactions and 10 species [57]. Others contain many more [58], such as that currently being developed by Lawrence Livermore National Laboratory (LLNL) to describe biodiesel combustion; this mechanism has over 17,000 reactions and 3,500 species [32]. In turn, these mechanisms are used to simulate the process of combustion during the design of diesel engines [59–61]; they can also be used to study pollutant formation and explore the effects of fueling engines with different blends of fuel molecules [37, 55]. (Simulations in other environments, such as jet engines, are also possible [62–64].) More accurate chemical kinetic mechanisms can lead to improvements in heavy-duty truck fuel economy and reductions in pollutant emissions. This process is summarized in Figure 1.9.

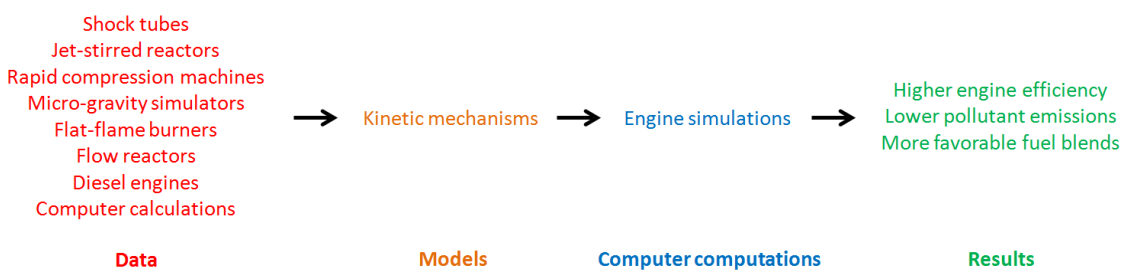


Figure 1.9: Flow chart summarizing the connection between experimental data and practical engine/emissions/fuel improvements by way of kinetic mechanism development.

Chemical kinetic mechanisms are developed and validated using a combination of complex computer-aided molecular computations and experimental data obtained under carefully-controlled conditions. Sources of experimental data include shock tubes, jet-stirred reactors, rapid compression machines, micro-gravity simulators, flat-flame burners, flow reactors, and even actual diesel engines

fitted with exhaust analysis equipment (a gas chromatograph and mass spectrometer, for example). Without high-quality experimental measurements of combustion parameters, developing accurate mechanisms would be impossible, and therefore, realizing the required improvements to modern diesel engines in order to capitalize on the benefits of biodiesel would be very difficult.

Realizing this, numerous researchers have undertaken to measure kinetic data for biodiesel combustion under practical engine conditions. Such conditions include both low and high pressures (2-20 atm), moderate to high temperatures (700-1200 K), and both lean and rich equivalence ratios ($\phi = 0.5 - 4$). A summary of literature studies concerning medium-to-large saturated (no double bonds) FAMEs and the five primary biodiesel components is given in Table 1.3. Note that this table contains many studies, including those contained within this dissertation, which were not available at the start of this project in 2009.

As revealed by Table 1.3, there are very few shock tube studies of biodiesel combustion (in fact, no shock tube studies of large FAMEs existed when this work was commenced in 2009). This represents a *crucial* research need, as shock tubes are uniquely situated to study the high- and moderate-temperature oxidation of practical diesel fuels at engine-relevant pressures and fuel loadings. Therefore, the chief goal of this dissertation is to provide a robust data set of FAME kinetic measurements that can be used to improve combustion mechanisms and ultimately make practical diesel engine improvements.

1.8 Summary

The increasing energy demands of the world require investment in alternative energy resources. In the transportation sector, heavy-duty trucks represent an opportunity for substantial emissions reductions and efficiency improvements. One route toward this end is the use of biodiesel fuel. Biodiesel has advantages over fossil-derived diesel that include lubricity, biodegradability, and lower pollutant emissions; however, the kinetics of its combustion are not yet well-understood. Specifically, a literature review showed a low number of shock tube studies on biodiesel oxidation.

Table 1.3: Summary of previous studies concerning saturated FAMEs and the five primary biodiesel components. Studies that include two or more fuel components have been listed multiple times, as have studies that include multiple experimental techniques. Studies affiliated with Stanford are References [65–68].

FAME (Methyl...)	Formula	Shock Tube	Jet-Stirred Reactor	Flow Reactor / Flame Burner	Rapid Compression Machine / Motored Engine / Droplet Ignition / Other	Kinetic Modeling
Octanoate	C ₉ H ₁₈ O ₂	[69–71]	[72–76]	[74, 77]	[89–93]	[69, 70, 72–76, 78]
Decanoate	C ₁₁ H ₂₂ O ₂	[65, 66, 68, 79–81]	[82, 83]	[77, 84–88]	[36, 89, 92]	[78, 82–85, 87, 92, 94–99, 99, 100]
Laurate	C ₁₃ H ₂₆ O ₂	[67, 68]			[36]	[78, 92, 97]
Myristate	C ₁₅ H ₃₀ O ₂	[67, 68]			[28, 36]	[78, 97]
Palmitate	C ₁₇ H ₃₄ O ₂	[67, 68, 101]	[102]		[28, 36]	[32, 78, 97, 103]
Stearate	C ₁₉ H ₃₈ O ₂	[101]			[28, 36]	[32, 48, 97, 103, 104]
Eicosanoate	C ₂₁ H ₄₂ O ₂					
Behenate	C ₂₃ H ₄₆ O ₂					
Oleate	C ₁₉ H ₃₆ O ₂	[65, 68, 101, 105]	[106]		[36]	[32, 36, 89, 92, 107, 108]
Linoleate	C ₁₉ H ₃₄ O ₂	[101, 105]			[28, 36]	[32, 48, 103]
Linolenate	C ₁₉ H ₃₂ O ₂					[32, 48, 103]

1.9 Scope and organization

This dissertation can roughly be divided into two halves, as follows. The first part of this work deals with measurements undertaken using a facility called the Aerosol Shock Tube (AST). Chapter 2 provides an overview of the conventional gas-phase shock tube, and Chapter 3 provides specific details related to the AST technique, including operating principles and the range of fuels that can be studied using this device. Chapter 4 describes a computer algorithm that has been developed to accurately compute experimental conditions in the AST, and Chapter 5 introduces aspects of FAME spectroscopy that are needed in order to make quantitative fuel measurements during biodiesel combustion. Following this initial development, Chapter 6 demonstrates the application of the AST to ignition delay times of FAMEs under high-temperature conditions.

The second part of this work will focus on the development of improved shock tube techniques, which allow higher-quality shock tube data for biodiesel surrogates to be obtained at engine-relevant conditions. In particular, Chapter 7 introduces techniques for extending shock tube test times to approximately 100 ms, and Chapter 8 introduces a novel Constrained Reaction Volume (CRV) shock tube method, which limits energy release during fuel oxidation. Chapter 9 describes the use of these techniques to measure ignition times for *n*-heptane, a primary reference fuel and diesel fuel surrogate. Finally, Chapter 10 summarizes the work of this dissertation and suggests directions for future research.

Chapter 2

Introduction to shock tubes

2.1 Experimental facilities

As introduced in Chapter 1, many experimental reactors are used to collect high-quality combustion data for the purpose of kinetic mechanism validation. Several devices mentioned in the literature review (Table 1.3) included shock tubes, jet-stirred reactors, rapid compression machines, micro-gravity simulators, flat-flame burners, flow reactors, and actual diesel engines fitted with exhaust analysis equipment. Each of these is able to probe specific aspects of fuel combustion. Unique among all experimental devices, however, is the shock tube, which under some conditions can provide a zero-dimensional environment where the effects of gasdynamics, fluid mechanics, and heat transfer are to first order separate from those of chemical kinetics [109–119]. Various laser, emission, and pressure diagnostics can be used to probe this reactor and ascertain details of chemistry apart from other effects, which allows more straightforward simulation of experimental results [117, 118, 120, 121].

2.2 Types of shock tube measurements

Shock tubes can provide three primary types of data that can be compared to simulations by kinetic mechanisms. First, shock tubes can be used to measure ignition delay times. A fuel's ignition delay time is the time interval that a reactive mixture must be subjected to a high-pressure,

high-temperature environment before it experiences an exponential increase in its overall reaction rate (known as ignition). Such data are called “global validation targets” because they test the ability of a mechanism to simulate the overall combustion reaction of fuel and oxygen combining to form products and release heat. Second, the mole fractions of individual molecules (fuel, products, or intermediates) can be measured throughout the reaction process (temperature and pressure can be measured as well). Such time-histories primarily test the subset of the mechanism that includes reactions relating to the measured species. Third, shock tubes can be used to measure individual reaction rates by carefully selecting reactive mixtures for desired results. Such reaction rates can be directly incorporated into kinetic mechanisms, yielding immediate improvements.

2.3 Shock tube operation

A simplified schematic depicting conventional shock tube operation is given in Figure 2.1. In their most basic form (referred to as a “conventional shock tube” in this work), shock tubes consist of two sections of pipe, separated by a thin diaphragm made of polycarbonate (acrylic) or metal (aluminum or steel). The pipe on one side of the diaphragm is the “driver section,” which is filled with a high-pressure mixture of helium and nitrogen; on the other side is the “driven section,” which is filled with the test gas (usually fuel/oxygen/argon).

Experiments are initiated by strain-induced rupture of the diaphragm owing to the high pressure of the driver section, which results in the formation of an incident shock wave (traveling toward the driven section endwall) and an expansion fan (traveling toward the driver section end cap). As the so-called “incident shock wave” moves through the test gas, it heats and compresses it, sending it in motion toward the endwall. When the incident shock reaches the endwall, it reflects backward and progresses through the test gas once more. This “reflected shock wave” further heats and compresses the test gas to the high temperature/pressure conditions of the experiment, and also stagnates the flow. Diagnostics (*e.g.*, pressure, light emission, laser absorption, Planar Laser-Induced Fluorescence (PLIF), Schlieren imaging, and gas sampling) located near the endwall (usually 2 cm away) subsequently probe the reacting test gas mixture. Meanwhile, the expansion fan reflects from the driver section end cap and travels back toward the driven section endwall. When this expansion fan

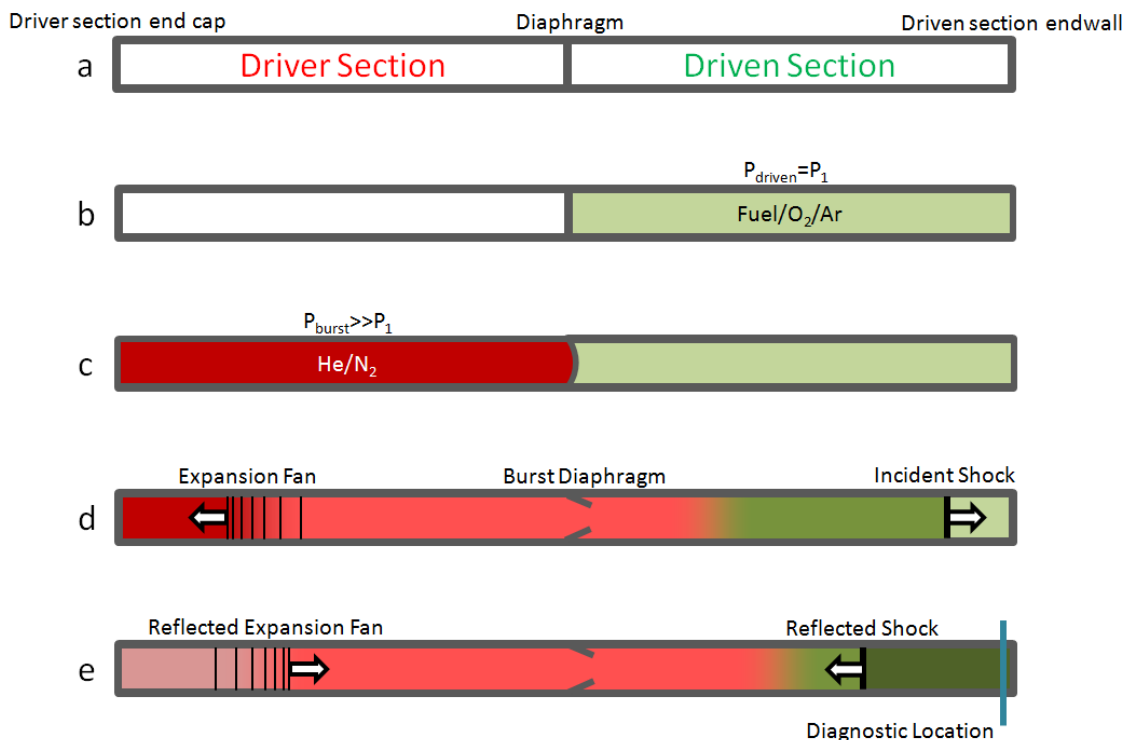


Figure 2.1: Schematic of conventional shock tube operation. a) Labeling of sections. b) Filling of driven section with test gas (fuel/oxidizer/diluent). c) Filling of driver section with driver gas (helium/nitrogen). d) Rupture of diaphragm and formation of incident shock (traveling toward the driven section endwall) and expansion fan (traveling toward the driver section end cap). e) Reflected shock (stagnating the test gas as it travels toward the driver section) and reflected expansion fan (traveling toward the driven section).

reaches the measurement location, it causes a rapid drop in pressure and temperature, quenching reactions and ending the experimental test time.

It is useful to divide a shock experiment into intervals of space-time called “regions” in order to facilitate discussions of gasdynamics. Within the driven gas, the experimental space-time interval prior to diaphragm rupture/passage of the incident shock is termed “Region 1;” that between the incident and reflected shocks is referred to as “Region 2,” and that following passage of the reflected shock is “Region 5.” Likewise, in the driver gas, the interval prior to diaphragm rupture/passage of the incident expansion wave is termed “Region 4,” that between the incident and reflected expansion waves is “Region 3,” and that following the reflected expansion fan is “Region 6.” Throughout this dissertation, variable subscripts (*e.g.*, T_5 and P_5) refer to the region of interest (in this case, the temperature and pressure in Region 5, respectively).

The test conditions in a shock tube are typically computed from the well-established shock-jump equations combined with an equation of state [111]. The most important input to these calculations is the velocity of the incident shock, which is often measured at several axial locations along the length of the shock tube and then extrapolated to the endwall with an uncertainty of better than $\pm 0.2\%$. Several computer algorithms for calculating the post-shock conditions exist (see Appendix A as well as References [113, 122–127]).

2.4 Current challenges

Despite the many advantages of the shock tube technique, several issues exist in these facilities today. These will be outlined below.

2.4.1 Fuel loading

Fuel loading in shock tubes has historically been accomplished in the gas phase. Liquid fuels must be evaporated prior to filling, and the fuel/oxidizer/diluent mixture is typically allowed to fill the entire shock tube volume. The necessity of gas-phase fuel loading represents one important limitation of conventional gas-phase shock tubes, however. Long mixing times and high temperatures

are required in order to vaporize large fuel molecules [79, 101, 128, 129], which can lead to pre-experimental fuel oxidation or partial fuel distillation [130]. Moreover, some large fuels, especially the large FAMEs composing biodiesel fuel, have such low vapor pressures that obtaining sufficient gas-phase fuel molecules for shock tube study is virtually impossible.

2.4.2 Test time

Shock tubes have historically been limited to test times (test time is defined as the interval during which temperature and pressure remain constant) of approximately 10 ms because of various gasdynamic constraints (see Chapter 7). At high temperatures, where kinetic processes are fast, this time is more than sufficient for oxidation measurements. However, at lower temperatures, chemical processes have much longer timescales. Thus, in order to study chemistry at low temperatures, shock tube scientists have conducted studies at high pressures (usually >10 atm), since reaction rates generally increase with pressure and these higher pressures allow available test times to capture the ignition phenomena [131]. For this reason, the low-temperature ignition chemistry of many fuels at low-pressure conditions is not well-understood.

2.4.3 Energy release

As discussed above, under certain conditions, shock tubes are able to provide zero-dimensional combustion environments, making comparisons between model and experiment straightforward. However, during experiments with high fuel loading (*e.g.*, for undiluted measurements in 21%O₂/N₂), the energy release upon ignition significantly changes the experimental conditions in ways that cause measurements to deviate from both constant internal energy-volume (U-V) and constant enthalpy-pressure (H-P) constraints [121, 132]. Not only does this hinder efforts to simulate experimental data, but it also precludes sensitive species measurements (*e.g.*, H₂O, CO₂, CO, *etc.*) following the ignition event.

2.4.4 Remote ignition

An issue related to energy release has to do with where ignition occurs inside a shock tube. Under ideal conditions (*i.e.*, at high temperatures), ignition in shock tubes begins adjacent to the endwall and propagates as a planar detonation wave down the tube toward the burst diaphragm. However, in shock tubes that contain a large “slug” of reacting test gas, ignition has been known to occur far away from the endwall and measurement location (this is known as “remote ignition”). As energy is released far from the endwall, the thermodynamic conditions (T , P) at the measurement location (usually 2 cm from the endwall) change, affecting experimental results [129, 132].

2.5 Use of shock tubes for biodiesel research

Despite the difficulties introduced above, shock tubes have proven to be excellent devices for kinetic measurements of FAMEs. For example, Davidson *et al.* measured ignition delay times of methyl butanoate (MB, $C_5H_{10}O_2$) [133]; Farooq *et al.* studied the decomposition of methyl acetate (MA, $C_3H_6O_2$), methyl propionate (MPI, $C_4H_8O_2$), and MB behind reflected shocks [134]; and Lam *et al.* measured the rate constant of the reaction $OH + Fuel \longrightarrow Products$ for methyl formate (MF, $C_2H_4O_2$), MA, MPI, and MB [135].

Studying surrogates larger than MB in conventional gas-phase shock tubes has proven extremely difficult due to these fuels’ low vapor pressures and associated decomposition issues in preparing gaseous reactant mixtures. Despite these challenges, several recent noteworthy studies include the measurement of ignition delay times of methyl octanoate (MOC, $C_9H_{18}O_2$) [71], methyl decanoate (MD, $C_{11}H_{22}O_2$) [66, 80, 81, 86], and four of the five biodiesel components [101] (see also Table 1.3). Note that at the commencement of this project in 2009, no shock tube studies of large FAMEs existed.

2.6 Summary

In summary, the shock tube has been shown to be a valuable experimental device for obtaining combustion data for the validation and improvement of kinetic mechanisms. Several studies have

already used the shock tube technique to examine smaller FAMEs; however, some difficulties exist that prevent widespread use of shock tubes to study the larger FAMEs actually present in biodiesel.

First, large FAMEs have low vapor pressures, making it difficult to obtain sufficient gas-phase moles of fuel to allow experimentation in conventional shock tubes. Thus, in this work, the Aerosol Shock Tube (AST) technique has been employed to accomplish fuel loading. The AST facility, introduced in Chapter 3, enables study of very-low-vapor-pressure fuels by loading them in the shock tube as micron-sized droplets rather than in the gas phase.

Second, current shock tube test times are limited by gasdynamic effects, preventing studies of biodiesel fuels at low pressure, where reaction timescales are long. For this reason, existing and new techniques to extend the test times of shock tubes have been developed and will be discussed (Chapter 7).

Third, the energy release and remote ignition present in some shock tube experiments makes modeling of biodiesel data difficult and increases the uncertainty in measured results. Therefore, in this work, a new shock tube methodology will be introduced (Chapter 8) in which a sliding gate valve is used to constrain the reactive gas mixture to only a small portion of the shock tube, thereby limiting energy release and rendering remote ignition impossible.

Chapter 3

Operation of the aerosol shock tube

3.1 Motivation

As discussed in Chapter 2, the shock tube is a very useful tool for the study for reaction kinetics and combustion. However, fuel loading in shock tubes has historically been accomplished in the gas phase. Liquid fuels must be evaporated prior to filling, and the fuel/oxidizer/diluent mixture is typically allowed to fill the entire shock tube volume. The necessity of gas-phase fuel loading represents one important limitation of conventional gas-phase shock tubes, however. Historically, to overcome this obstacle, long mixing times and high mixing tank/shock tube temperatures have been employed in order to vaporize large fuel molecules; unfortunately, this can lead to pre-experimental fuel oxidation or partial fuel distillation [130].

An alternative method of studying large molecules in shock tubes involves introducing them in the form of an aerosol of micron-sized fuel droplets in a carrier oxygen/diluent bath gas. This technique allows for high fuel loading of low-vapor-pressure fuels. The Aerosol Shock Tube (AST) at Stanford University [130] is an example of one such facility.

3.2 Experimental setup

3.2.1 Aerosol shock tube description

An aerosol shock tube is a shock tube in which Region 1 contains a mixture of vapor and fuel droplets. Multiple experimental studies regarding the interaction of shock waves with liquid aerosols have been conducted since this device's debut in 1958 [65–68, 105, 128, 130, 136–167] (an aerosol-based rapid compression machine has also been developed [168]). Several strategies exist for loading aerosol fuel droplets into the shock tube, including a use of a modified diesel fuel injector [136], a mat-screen device [138], an induced condensation technique [145], an entrainment system [167], a nozzle shear device combined with a mixing tank [163], or a turbulent mixing scheme [149]. In contrast to these methods, the AST at Stanford University employs an aerosol generation tank combined with a plug flow to pull a uniform mixture of droplets in a carrier gas into the tube [130].

In the Stanford AST setup (see Figure 3.1), a 25-liter tank (called the Aerosol Generation Tank, or AGT) primarily containing bath gas (1%, 4%, or 21% oxygen in argon) is seated above a 25-milliliter pool of liquid fuel. The AGT is adjacent to the shock tube test section; between the test section and the AGT is a sliding valve known as the “endwall gate valve.” Between the test section and the driver section is a volume called the buffer section. A thin polycarbonate diaphragm separates the high pressure driver section from the low pressure buffer section, and another sliding valve, called the “driven gate valve,” separates the buffer and test sections.

In a shock experiment, a fuel droplet/oxidizer/diluent aerosol is first generated within the AGT using ultrasonic nebulizers (Ocean Mist model DK12NS) residing in the 25-milliliter fuel pool, and is mixed using fan blades until spatially uniform. The size of the droplets follows a lognormal distribution with an approximate 2.5 μm number median diameter as measured using a Malvern Spraytec Particle Sizer (model RTS5214); this small size allows the droplets to evaporate quickly. In order to increase nebulizer output, the liquid fuels are heated to 40 °C prior to nebulization; such mild heating is not known to induce premature fuel decomposition [169]. Additionally, for fuels that are solids at room temperature (*e.g.*, methyl palmitate), a hot water bath is employed to slowly melt the fuel prior to it being introduced to the AGT. The aerosol mixture is ushered into the 1.3 m

test section through the endwall gate valve; the displaced gas is pulled out from the test section through a valve (called the “aerosol pull valve”) located on a port adjacent to the driven gate valve to an outside tank (the “dump tank;” for more information on the filling procedure, see Section 3.5). (Prior to this aerosol filling, the buffer section is filled to an intermediate pressure with the diluent gas.) Following pressure equilibration, the driven gate valve is opened and the endwall gate valve shut, yielding what resembles a conventional gas-phase shock tube.

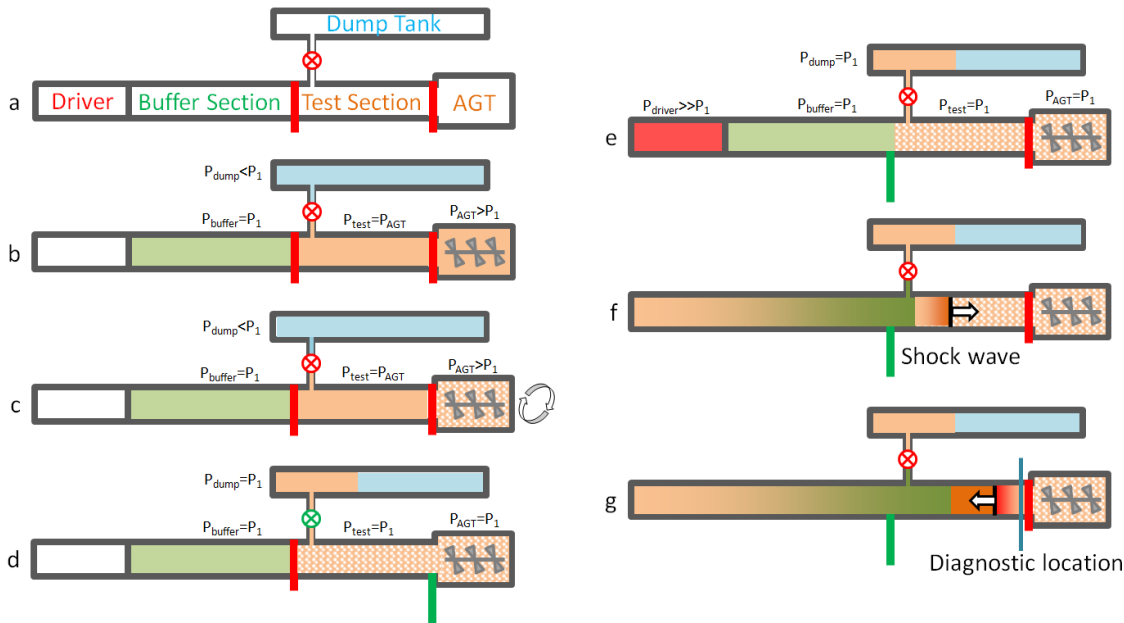


Figure 3.1: Schematic of aerosol shock tube operation. a) Labeling of sections; AGT stands for Aerosol Generation Tank. b) Shock tube sections are set to pre-aerosol-filling pressures. c) Aerosol is generated in the AGT and mixed using a fan. d) Aerosol is pulled into the shock tube through the endwall gate valve (located between the test section and AGT). This is accomplished by first opening the endwall gate valve, and by secondly opening the aerosol pull valve (located between the test section and dump tank). e) The endwall gate and aerosol pull valve are closed, while the driven gate valve (located between the buffer and test sections) is opened and the driver section is filled with helium to a critical high pressure. f) The diaphragm bursts, sending an incident shock propagating down the tube and into the aerosol. The aerosol droplets evaporate and the gaseous fuel diffuses into the bath gas shortly after shock-induced heating. g) The shock reflects off the endwall gate valve and diagnostics probe the resulting high temperature, high pressure gas-phase mixture.

Experiments are initiated when the driver section is filled to a high pressure with helium until

the thin polycarbonate diaphragm bursts, resulting in an incident shock that begins to propagate down the shock tube toward the endwall gate valve. When this wave reaches the location of the (open) driven gate valve, it encounters the fuel aerosol, setting the droplets in motion and causing them to rapidly evaporate, producing a uniform gas-phase fuel/oxidizer/diluent mixture. Eventually, the incident shock reaches the endwall gate valve and reflects back into the evaporated fuel gas/oxidizer/diluent mixture. As the reflected shock passes through, it stagnates the flow and produces a high temperature and high pressure environment for ignition experiments. This technique has been shown to provide high fuel loading with aerosol evenly distributed throughout the test volume [130]. Incident shock velocities are measured using 4-6 pressure transducers (PCB model 132A35) with a typical uncertainty of $\pm 0.5\%$; typical shock attenuation values are $1 - 2\%/\text{m}$. A Gantt chart depicting the timing and coordination of the important aerosol shock tube operation steps is provided in Figure 3.2.

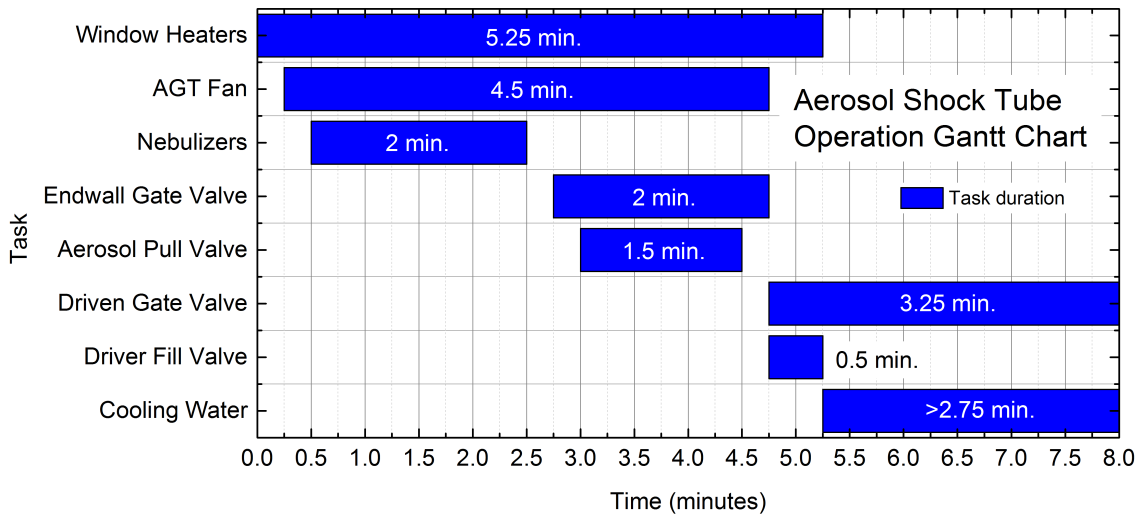


Figure 3.2: Gantt chart of aerosol shock tube operation. The cooling water is run through the test section following each experiment in order to mitigate the temperature increase associated with window heating (the windows are heated to approximately $100\text{ }^{\circ}\text{C}$ in order to prevent fogging/condensation).

3.2.2 Driver insert

A driver insert, constructed according to the method of References [170–172], was used in most of the experiments included in this dissertation in order to mitigate an observed non-ideal pressure rise following the reflected shock wave. The resulting non-reactive (no fuel) pressure trace showed an increase of about 2%/ms at 7.0 atm and 1%/ms at 3.5 atm. This residual non-ideal pressure rise in the presence of the driver insert was thought to be associated with a circular-to-square transition incorporated in this shock tube, which changed the circular 4.5-inch diameter driven section of the tube into a 10-centimeter square (with rounded corners) test section. More information concerning driver inserts can be found in Section 7.3.1.

3.2.3 Calculation of test conditions

The presence of fuel aerosol droplets in the pre-shock test gas mixture poses two challenges. First, as the aerosol droplets evaporate, they reduce the sensible enthalpy of the flow, resulting in a decrease in temperature and an increase in pressure compared to the values for a pure gas-phase flow. As a result, an iterative routine is required to solve for the correct thermodynamic properties following droplet evaporation. This code, called AEROFROSH, is described in Chapter 4 and References [158, 173]. Thermodynamic data, necessary for calculations, is taken from the literature [32, 174]. Uncertainties in computed post-reflected shock temperature and pressure are typically $\pm 1.2\%$ and $\pm 2.4\%$ respectively.

3.2.4 Fuel measurement

The second challenge presented by the presence of the aerosol droplets is as follows. Since mixtures were not prepared manometrically (as in conventional shock tube experimentation), the exact mole fraction of fuel in the test mixture is unknown. Thus, during every experiment, spectroscopic measurements of fuel concentration and droplet scattering are made using a 3.39 μm helium-neon (HeNe) laser and a 650 nm diode laser, respectively. These lasers are co-aligned (in order that they observe an identical volume of evaporating aerosol) and pitched through sidewall windows located 3.6 cm from the endwall (see Figure 3.3). These windows are heated to approximately 100 °C to

prevent fuel condensation.

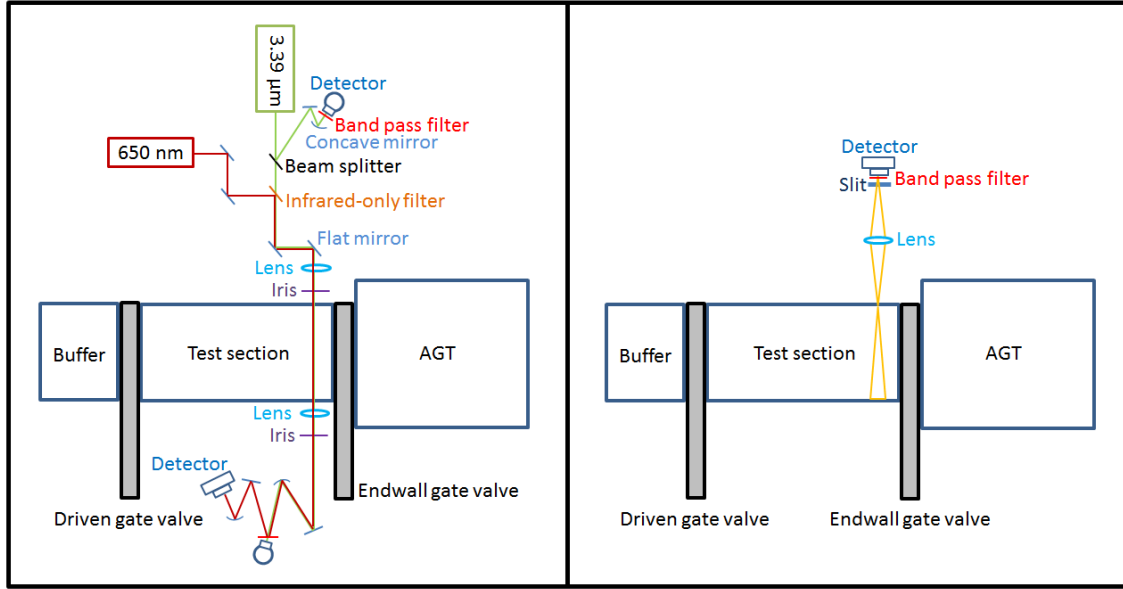


Figure 3.3: Schematic of diagnostics in the AST test section.

Fuel concentration measurements are conducted according to the Beer-Lambert relation (Equation 3.1; see also Equations 4.11, 5.2, 8.4, and 9.1).

$$\alpha = -\ln\left(\frac{I}{I_o}\right) = n_{fuel}\sigma_{fuel}L \quad (3.1)$$

In this equation, α is termed the absorbance, $\frac{I}{I_o}$ is the ratio of transmitted to incident light in the shock tube, n_{fuel} is the fuel concentration [mol/cm^3], σ_{fuel} is the absorption cross section of the fuel [cm^2/mol], and L is the path length over which absorption occurs [cm] (note that in this dissertation, variables on a molar basis are denoted with a hat (^) symbol; however, the absorption cross section σ_{fuel} traditionally is not denoted this way). For the aerosol shock tube experiments reported in this dissertation, $L = 10 \text{ cm}$. Absorption cross section values at $3.39 \mu\text{m}$ for the fuels examined in this work were either taken from the literature [175], measured directly, or estimated with an uncertainty of approximately $\pm 8\%$ based on published data for smaller normal alkanes and methyl esters using a newly developed extrapolation technique (see Chapter 5 and Reference [176]). The resulting

uncertainty in equivalence ratio (accounting for errors such as temperature, pressure, measured absorbance, absorption cross section, *etc.*) is typically $\pm 6\text{-}9\%$.

3.2.5 Measurement of ignition

Ignition in the AST is measured by observing excited OH radical (OH^*) emission at (306 ± 75) nm using a silicon photo-detector and UG-5 Schott Glass band-pass filter positioned at 3.6 cm from the endwall. The ignition delay time is defined as the interval from the arrival of the reflected shock (marked by either the peak or the 50%-rise point of the helium-neon laser Schlieren spike) to the point where the maximum slope of the OH^* emission trace is extrapolated to the OH^* baseline (zero) value. This time is confirmed by sidewall pressure measurements (Kistler model 603B1 transducer) and by helium-neon ($3.39 \mu\text{m}$) fuel absorption data.

3.2.6 Example shock experiment

An example ignition delay time measurement is given in Figure 3.4. Following the incident shock, the droplets rapidly evaporate, as confirmed by the 650 nm laser trace, which shows the extinction dropping to zero at approximately $60 \mu\text{s}$ before arrival of the reflected shock. The $3.39 \mu\text{m}$ signal also decreases while evaporation is taking place, because in this intermediate time the laser is both scattered by aerosol droplets and absorbed by evaporated fuel molecules. At typical post-incident-shock temperatures and pressures (700 K/1.7 atm), the timescale of fuel decomposition is much longer than the particle time (time between shock waves as experienced by individual molecules, typically $400 \mu\text{s}$; see Appendix B), thus fuel molecules enter the post-reflected-shock region intact [32]. After evaporation is complete, the $3.39 \mu\text{m}$ signal registers a uniform pure gas-phase fuel/oxidizer/diluent mixture flowing past the observation window. Typical variation in the $3.39 \mu\text{m}$ signal following complete evaporation is 2%, representing 2% axial non-uniformity in initial gas-phase fuel concentration (evaporation and diffusion times for the fuel droplets, which give a picture of uniformity along the diagnostic line-of-sight, will be discussed in Section 3.3). When the reflected shock arrives, at time zero, the pressure undergoes a step-change and the fuel begins to decompose (notice in Equation 3.1 that absorbance α is proportional to fuel concentration

n_{fuel}). Ultimately, the fuel concentration drops to zero as the OH* radical light emission at 306 nm and pressure rise exponentially, marking the ignition event. The slight pressure rise occurring near 600 μ s is the result of energy release in the shock tube and is characteristic of high-concentration ignition delay experiments.

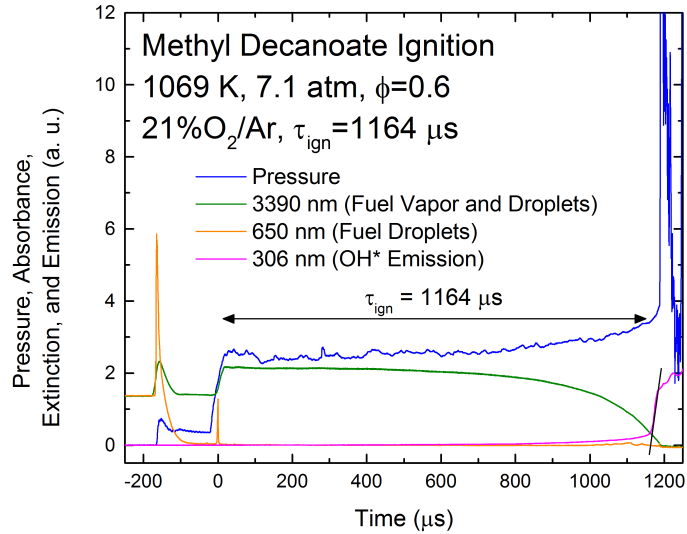


Figure 3.4: Example methyl decanoate ignition delay time shock experiment. Reflected shock initial conditions: 1069 K, 7.1 atm, 21%O₂/Ar, $\phi = 0.6$. The ignition delay time is $\tau_{ign} = 1164 \mu\text{s}$. Initial (Region 1) droplet volume fraction was $F_v = 17 \text{ ppmv}$.

3.3 Droplet evaporation

It is important that the particle time available in Region 2 (that experienced by the particles between the incident and reflected shocks; see Appendix B) is sufficient for complete fuel evaporation and mixing into the carrier gas, such that the resulting mixture has a uniform equivalence ratio (both axially in the shock tube, and along the diagnostic line-of-sight). An analysis of droplet evaporation was carried out by Davidson *et al.* [158] (see also Reference [159]), who found that under most conditions, droplets with diameters less than about 10 μm would rapidly evaporate and that the resulting gas-phase fuel molecules would diffuse into the carrier gas well within the available particle time. In order to elaborate on this finding, an analysis to calculate characteristic evaporation and

diffusion times for aerosol droplets is included here.

Consider an ideal field of spherical droplets, each with diameter \bar{d} , spaced on a cubic grid a distance L_d apart (see Figure 3.5). The total volume within one cube of the grid is

$$V_{tot} = L_d^3 \quad (3.2)$$

and the volume occupied by the one droplet (one eighth in each corner) is

$$V_{drop} = \frac{1}{6}\pi\bar{d}^3 \quad (3.3)$$

Thus, with a droplet volume fraction F_v calculated as

$$F_v = \frac{V_{drop}}{V_{tot}} \quad (3.4)$$

the distance L_d is given by

$$L_d = \left(\frac{\pi}{6F_v} \right)^{\frac{1}{3}} \bar{d} \quad (3.5)$$

Under ideal conditions, the rate of change of the square of droplet diameter d during evaporation is a constant (C) [177–180], *i.e.*,

$$\frac{d}{dt}d^2 = -C \quad (3.6)$$

Solving this equation under the condition that the initial droplet diameter is $d = \bar{d}$ gives

$$d^2 = \bar{d}^2 - 2D\frac{\rho_g}{\rho_l}t \quad (3.7)$$

where D is the diffusion coefficient for the fuel vapor in the carrier gas, $\frac{\rho_g}{\rho_l}$ is the ratio of carrier gas to liquid density, and t is time. This equation can be rearranged to garner a characteristic time at which 95% of the droplet contained in the “droplet cube” has evaporated:

$$\tau_{e,95} = \frac{0.95\bar{d}^2}{2D\frac{\rho_g}{\rho_l}} \quad (3.8)$$

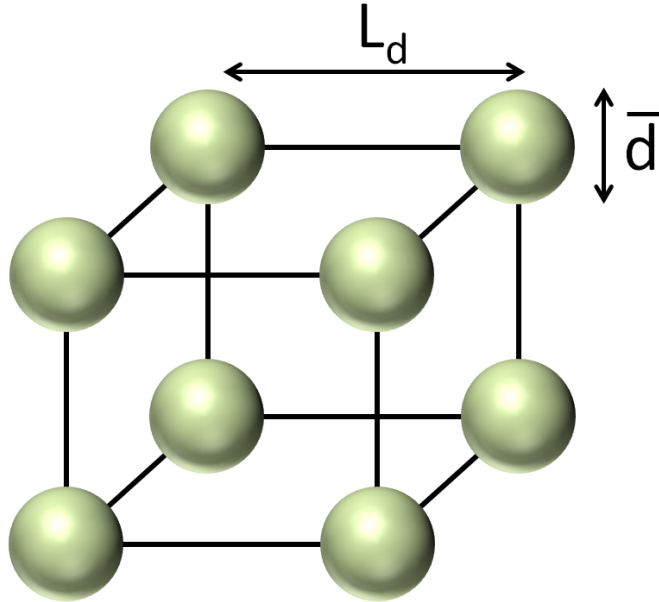


Figure 3.5: Ideal aerosol droplet spacing. All droplets are spherical with diameter \bar{d} and are spaced on a cubic grid a distance L_d apart.

Similarly, the characteristic time for the fuel vapor to diffuse the distance $L_d \frac{\sqrt{3}}{2}$ to the center of the evaporating “droplet cube” (using a binary Fickian diffusion model) is roughly

$$\tau_d = \frac{\left(L_d \frac{\sqrt{3}}{2}\right)^2}{2D} \quad (3.9)$$

As a way to check the usefulness of this simple framework, Equations 3.8 and 3.9 were used to estimate $\tau_{e,95}$ and τ_d for the experiment shown in Figure 3.4. In this figure, the lab-frame evaporation/diffusion time (taken as the time required for the non-resonant laser extinction to drop to zero) is about 107 μs , which corresponds to about 326 μs in the particle frame (see Appendix B for a discussion of lab and particle time). Note that the total particle time in Region 2 for this experiment is about 512 μs (the lab time is about 168 μs). Using the conditions for this experiment ($T_{2,i} = 662 \text{ K}$ (here, subscript i refers to the pre-evaporation value), $P_{2,i} = 1.6 \text{ atm}$, $F_v = 17 \text{ ppmv}$, $\rho_l = 800 \text{ kg/m}^3$, 21%O₂/Ar bath gas), with $\bar{d} = 3 \mu\text{m}$ and $D = 0.3 \text{ cm}^2/\text{s}$, gives a 95%-complete characteristic evaporation time of $\tau_{e,95} \sim 101 \mu\text{s}$ and a characteristic diffusion time of $\tau_d \sim 111 \mu\text{s}$.

Assuming the evaporation and diffusion timescales are completely decoupled (complete evaporation occurs before any diffusion begins), this corresponds to a total time of 212 μs , which shows reasonable agreement between the experiment and the simple model of this section. The difference between the observed and computed values can be attributed to assumptions used in the development of this model, or in estimation errors for the values of \bar{d} and D used above. A similar analysis for a different shock experiment (Figure 4.2) is provided in Section 4.6.4.

Having performed a rough check on the usefulness of this simple model, it can now be employed to simulate evaporation and diffusion in the AST behind incident shock waves. Equations 3.8 and 3.9 have been plotted in Figure 3.6 (variation of \bar{d}) and Figure 3.7 (variation of F_v), respectively. These calculations were performed at typical conditions for a methyl decanoate shock in 21%O₂/Ar ($T_2 = 700 \text{ K}$, $P_2 = 1.6 \text{ atm}$, $\rho_{g,2} = 1.07 \text{ kg/m}^3$, $\rho_l = 800 \text{ kg/m}^3$, and $\bar{d} = 3 \mu\text{m}$; however, a high fuel loading of $F_v = 50 \text{ ppmv}$ was assumed); also, a diffusion coefficient of $D = 0.3 \text{ cm}^2/\text{s}$ was estimated based on data from Reference [181]. In Figure 3.6, τ_d increases with increasing \bar{d} because L_d increases according to Equation 3.5. Similarly, in Figure 3.7, τ_d decreases with increasing F_v because L_d decreases according to Equation 3.5.

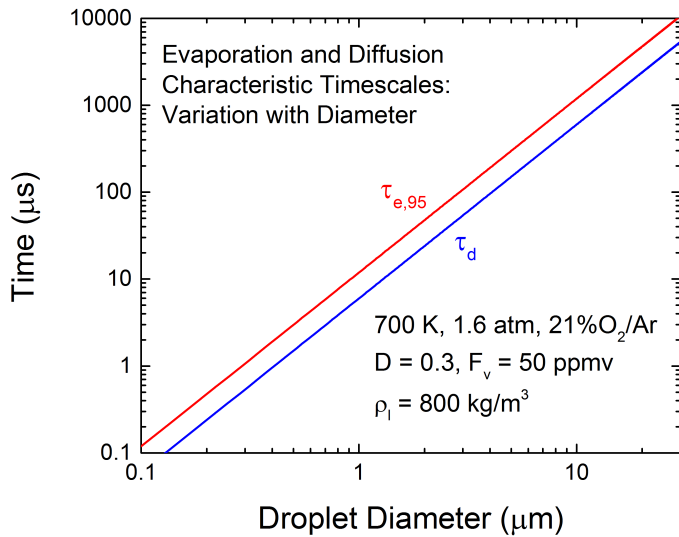


Figure 3.6: Characteristic timescales for droplet evaporation and diffusion as a function of droplet diameter. Conditions: methyl decanoate/21%O₂/Ar, $T_2 = 700 \text{ K}$, $P_2 = 1.6 \text{ atm}$, $\rho_{g,2} = 1.07 \text{ kg/m}^3$, $\rho_l = 800 \text{ kg/m}^3$, $F_v = 50 \text{ ppmv}$, $D = 0.3 \text{ cm}^2/\text{s}$.

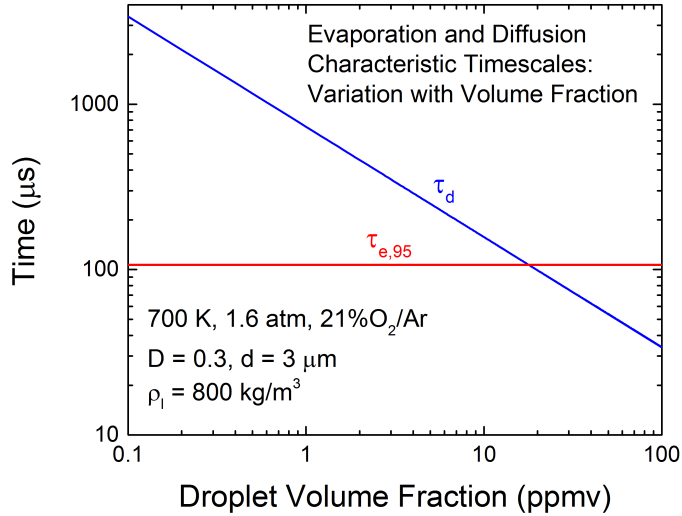


Figure 3.7: Characteristic timescales for droplet evaporation and diffusion as a function of droplet diameter. Conditions: methyl decanoate/21%O₂/Ar, T₂ = 700 K, P₂ = 1.6 atm, ρ_{g,2} = 1.07 kg/m³, ρ_l = 800 kg/m³, \bar{d} = 3 μm, D = 0.3 cm²/s.

These figures show that 3 μm fuel droplets in a 50-ppmv aerosol at typical conditions will evaporate with a characteristic time of $\tau_{e,95} \sim 107 \mu\text{s}$ and diffuse in a characteristic time of $\tau_d \sim 54 \mu\text{s}$; these values are less than the particle time available in these experiments (300-500 μs). Therefore, under the ideal conditions of this analysis, it can be assumed that the resulting post-evaporation mixture is generally quite uniform along the diagnostic line-of-sight.

It should be noted that the diffusion parameter D scales as

$$D \propto \frac{T^{1.8} \left(\frac{1}{M_g} + \frac{1}{M_f} \right)^{1/2}}{P\psi^2} \quad (3.10)$$

where M_g and M_f are the dominant-carrier-gas (usually argon or nitrogen) and fuel molecular weights, and $\psi = \frac{1}{2}(\psi_g + \psi_f)$ is the effective collision diameter for a dominant-carrier-gas molecule/fuel molecule interaction [182, 183]. Thus, evaporation and diffusion rates increase with increasing temperature [158, 159]. Therefore, as pointed out in Reference [158], any droplets remaining in the high-temperature environment following the passage of the reflected shock would evaporate even more rapidly than in the Region 2 environment. Finally, based on Equation 3.10, it

should be noted that droplet evaporation times increase with increasing pressure. As a consequence, aerosol shocks conducted at high Region 2 pressures may not experience full droplet evaporation before the arrival of the reflected shock wave at the test location. In this case, using more dilute mixtures (meaning that fewer droplets are required for the same equivalence ratio) or a measurement location further from the endwall (allowing more time in Region 2 for evaporation) may be required.

3.4 Range of AST

Using aerosol fuel loading significantly extends the size range of fuels that can be studied beyond that of conventional heated shock tubes. This is shown schematically in Figure 3.8. In this graphic, the red curved line shows, for a conventional shock tube with a shock-tube-to-mixing-tank volume ratio of $\frac{V_{ST}}{V_{MT}} = 10$, the vapor pressure required as a function of the number of carbon atoms in the molecular chain of the FAME fuel molecule (*e.g.*, for C₁₁H₂₂O₂ the number of carbons in the chain is 10) to achieve a shock at 1000 K and 10 atm in air (the governing formula, Equation 8.19, is derived in Section 8.3.3). The blue straight line shows the available vapor pressure at a temperature of 25 °C, and the intersection of the red and blue lines (shown in the blue circle) marks the largest FAME fuel that can be studied using the conventional technique. Likewise, the green circle shows the largest FAME fuel that can be studied when the shock tube and mixing tank are heated to 150 °C.

Now, observe the black line, which shows the fuel melting temperature as a function of fuel size. As long as a fuel can be melted, it can be nebulized; thus, the intersection of the grey dotted line (which shows the normal nebulizer operating temperature) with the black line (this point is called out with the black circle) marks the range of AST with unheated nebulizers. Heating the nebulizers further increases this range; the maximum operating temperature of the nebulizers is about 330 K. Thus, the AST is able to study much larger fuels than conventional heated shock tubes.

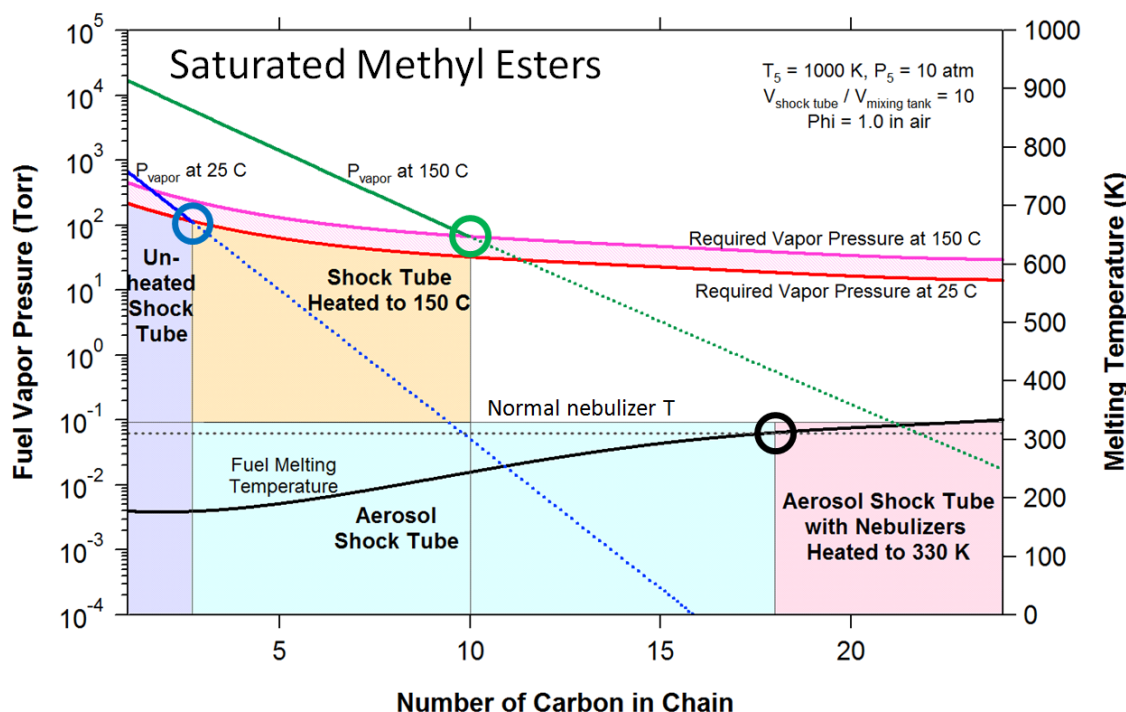


Figure 3.8: Theoretical range of the aerosol shock tube as compared to that of a conventional heated shock tube with a shock-tube-to-mixing-tank volume ratio of $\frac{V_{ST}}{V_{MT}} = 10$. Simulated shock conditions: 1000 K, 10 atm, $\phi = 1$ in 21%O₂/N₂.

3.5 Initial pressures for aerosol loading

The procedure for pulling the aerosol mixture from the AGT into the test section involves a series of pressure ratios. In these calculations, the volume occupied by the droplets is neglected, which is reasonable since most droplet volume fractions are $F_v < 100$ ppmv (in this work, $0.6 < F_v < 17$ ppmv, and a typical value was $F_v = 5$ ppmv). Disregarding evaporation and condensation, the total number of moles of gas N in the dump tank (subscript d), the test section (t), and the AGT (a) combined is constant throughout the aerosol filling procedure (Equation 3.11; here subscripts i and f denote the initial and final conditions, respectively).

$$N_{d,i} + N_{t,i} + N_{a,i} = N_{d,f} + N_{t,f} + N_{a,f} \quad (3.11)$$

Moreover, neglecting compressibility effects and allowing sufficient time (~ 30 seconds) for equilibration, temperature can also be regarded as constant. The ideal gas equation of state (Equation 3.12; see also Equation 4.4) can be used to recast Equation 3.11 in terms of desirable quantities.

$$PV = N\hat{R}_u T \quad (3.12)$$

Here, V represents volume and \hat{R}_u is the ideal gas constant. Thus, applying the ideal gas relationship while holding $\hat{R}_u T$ constant yields

$$P_{d,i}V_d + P_{t,i}V_t + P_{a,i}V_a = P_{d,f}V_d + P_{t,f}V_t + P_{a,f}V_a \quad (3.13)$$

Additionally, in order to avoid disrupting the flow as the gate valve opens and also prevent valve o-ring malfunction, the pressures on both sides of the sliding piece must be equal (ideally within 0.5 Torr) prior to valve actuation. Therefore, for the endwall gate valve,

$$P_{t,i} = P_{a,i} \quad (3.14)$$

and for the driven gate valve,

$$P_{t,f} = P_1 \quad (3.15)$$

where P_1 is the Region 1 pressure of the shock experiment, to which the buffer section is filled. Finally, given sufficiently long filling time (~ 1.5 minutes), after all valves are opened, an equilibrium pressure will be reached such that

$$P_{d,f} = P_{t,f} = P_{a,f} = P_1 \quad (3.16)$$

Substituting Equations 3.14 and 3.16 into Equation 3.13 and solving for $P_{d,i}$ yields

$$P_{d,i} = \frac{P_1 (V_d + V_t + V_a) - P_{t,i} (V_t - V_a)}{V_d} \quad (3.17)$$

A critical parameter when filling the shock tube is the fraction of moles of gas displaced from the test section to the dump tank, X_m (Equation 3.18). This fraction governs the length (as measured from the endwall) to which the aerosol extends in the test section, and also determines the speed at which the aerosol flows into the test section from the AGT.

$$X_m = \frac{N_{d,f} - N_{d,i}}{N_{v,i}} = \frac{P_{d,f}V_d - P_{d,i}V_d}{P_{t,i}V_t} = \frac{V_d(P_{d,f} - P_{d,i})}{P_{t,i}V_t} = \frac{V_d(P_1 - P_{d,i})}{P_{t,i}V_t} \quad (3.18)$$

Note that if $X_m > 1$, all of the moles of gas originally in the test section are pulled into the dump tank. Substituting Equation 3.17 into Equation 3.18 results in

$$X_m = \frac{V_d \left(P_1 - \left(\frac{P_1(V_d + V_t + V_a) - P_{t,i}(V_t - V_a)}{V_d} \right) \right)}{P_{t,i}V_t} \quad (3.19)$$

Finally, solving for $P_{t,i}$ and $P_{d,i}$ gives the initial pressures of the test section and dump tank in terms of the initial experimental pressure P_1 and the X_m parameter.

$$P_{t,i} = P_{a,i} = -P_1 \frac{V_t + V_a}{X_m V_t - (V_t + V_a)} \quad (3.20)$$

$$P_{d,i} = P_1 - P_{t,i} X_m \frac{V_t}{V_d} \quad (3.21)$$

The above framework has enabled the test section to be filled with the aerosol mixture predictably and repeatably, with a high degree of spatial droplet uniformity.

A slightly different derivation of the initial filling pressures, assuming compressible effects, was undertaken by Haylett *et al.* [130, 162]. The equations developed by this author rely on another filling parameter that is based on the displaced volume, X_v .

$$X_v = \frac{V_{displaced}}{V_a} \quad (3.22)$$

This can be related to X_m using Equation 3.23.

$$X_v = 1 - \frac{P_{t,i}}{P_1} (1 - X_m) = 1 + \frac{(1 - X_m)(V_t + V_a)}{X_m V_t - (V_t + V_a)} \quad (3.23)$$

While the framework of Haylett *et al.* [130, 162] and that presented here yield slightly different filling pressures, good aerosol uniformity has been observed by filling the shock tube using either technique (X_m or X_v).

3.6 Droplet settling time

It is important to compute the settling time for the aerosol droplets in order to ensure that they remain “airborne” during the filling process. For sufficiently small droplets of viscous fluids, the aerosol droplets may be treated as solid spheres undergoing Stokes Flow [184, 185]. Under these conditions, the drag (due to pressure and viscous effects) and gravitational forces on the droplet balance one another (buoyancy and electromagnetic forces are said to be negligible), yielding the useful result displayed in Equation 3.24.

$$v_{droplet} = \frac{F_{gravity}}{3\pi\mu d} \quad (3.24)$$

In this equation, $v_{droplet}$ is the terminal velocity of the aerosol droplet, $F_{gravity} = V_{drop}\rho_l g$ is the weight of the droplet (g is the acceleration due to gravity), μ is the dynamic viscosity of the carrier gas, and d is the droplet diameter. This equation is strictly valid for Reynolds numbers $Re \ll 1$,

although it agrees with experimental data up to $Re \approx 1$. Thus, the time t_{settle} for a droplet to fall from an initial height h_0 is

$$t_{settle} = \frac{h_0}{v_{droplet}} \quad (3.25)$$

For water droplets with a diameter of 3 μm in nitrogen at 20 °C and 1 atm, the settling time from an initial height of $h_0 = 10$ cm is about 6 minutes; for 3 μm methyl decanoate ($\text{C}_{11}\text{H}_{22}\text{O}_2$) droplets, the time is about 7 minutes; and for 3 μm *n*-decane ($\text{C}_{10}\text{H}_{22}$) droplets, the time is about 8 minutes (see Figure 3.9). Thus, in the time necessary for filling the shock tube (~ 1.5 minutes), droplet settling will be relatively small.

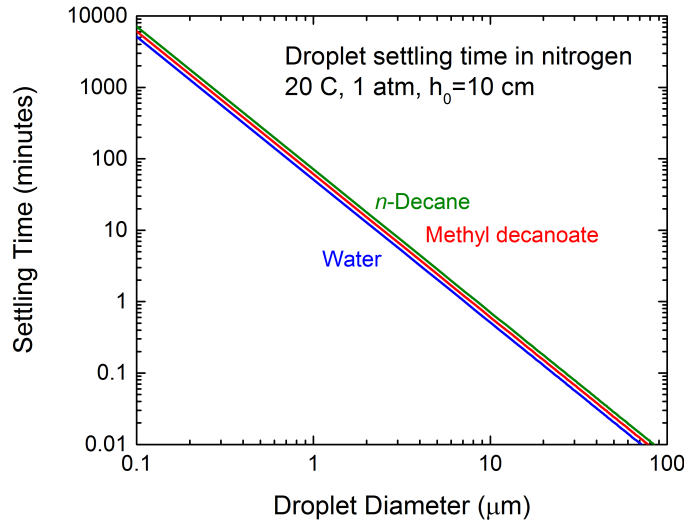


Figure 3.9: Droplet settling time as a function of droplet diameter, for water ($\rho_l = 1.0 \text{ g/cm}^3$), methyl decanoate ($\rho_l = 0.85 \text{ g/cm}^3$), and *n*-decane ($\rho_l = 0.73 \text{ g/cm}^3$) droplets at 20 °C and 1 atm from an initial height $h_0 = 10$ cm. The settling time increases with decreasing liquid density.

Fuels that have large heats of vaporization can take more time to evaporate than that which is available between the incident and reflected shocks (the particle time; see Appendix B). In this case, the diameter-dependence of the droplet settling time (Equation 3.24) can be advantageous. As mentioned above, ultrasonic nebulizers like those used in the Stanford AST produce droplets whose diameters d follow a lognormal size distribution (Equation 3.26, wherein \bar{d} is the count median diameter of the distribution and k is a constant) [151, 186–188] (the number median diameter $d_{n,50}$

of the droplets created by these nebulizers is approximated by Lang's formula, Equation 3.27 [189], where $\kappa = 0.34$ is a constant, σ_l and ρ_l are the surface tension and density of the liquid, and F is the nebulizer excitation frequency).

$$f(d) = \frac{1}{\sqrt{2\pi}d \ln k} \exp\left(-\frac{1}{2}\left[\frac{\ln d - \ln \bar{d}}{\ln k}\right]^2\right) \quad (3.26)$$

$$d_{n,50} = \kappa \left(\frac{8\pi\sigma_l}{\rho_l F^2}\right)^{\frac{1}{3}} \quad (3.27)$$

A typical particle distribution for an aerosol generated using ultrasonic nebulizers, in this case for methyl palmitate aerosol, is shown in Figure 3.10. The distribution shown was measured using a Malvern Spraytec Particle Sizer (model RTS5214) immediately after nebulization (Ocean Mist model DK12NS) without a waiting/settling period. A flow-type geometry was employed in this experiment, in which the aerosol was pulled through a transparent test chamber, through which the particle sizer was aligned, by way of a gas pressure differential that was controlled by a valve connected to a vacuum pump. See Figure 3.11 for details; additional information can also be found in Reference [130]. Though this distribution was not measured in the aerosol shock tube, it is similar to that which would be found in the test section after expansion/filling from the AGT, with the exception that some of the larger droplets could have settled out during the shock tube test section filling process.

According to the diameter-squared droplet evaporation law (Equation 3.7), the larger droplets in the distribution will take longer to evaporate than the smaller ones. Fortunately, according to Equation 3.24, the larger droplets in the distribution will also settle much more quickly than the smaller droplets. Thus, should a size distribution with a very small number median diameter be desired, it can be achieved by simply waiting extended periods of time (~ 2 hours) after generating an aerosol in the AGT while the larger droplets settle. As a result, the evaporation time for the resulting aerosol will be much shorter, allowing evaporation to complete between the incident and reflected shocks. While such a technique was not necessary for the experiments described in this dissertation, it may be useful for future experiments at higher pressure conditions.

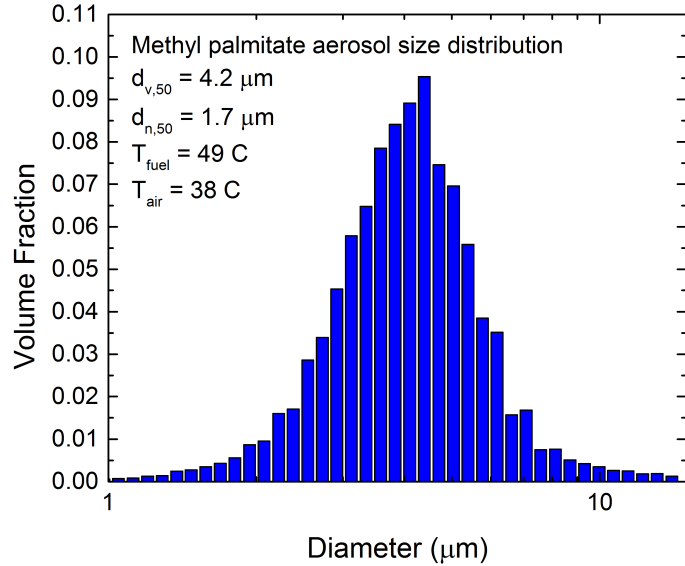


Figure 3.10: Methyl palmitate aerosol size distribution, as measured using a Malvern Spraytec Particle Sizer (model RTS5214), immediately after nebulization (no waiting/settling period). The volume median diameter is $d_{v,50} = 4.2 \mu\text{m}$, the number median diameter is $d_{n,50} = 1.7 \mu\text{m}$, the fuel temperature is $T_{fuel} = 49 \text{ }^\circ\text{C}$, and the air temperature is $T_{air} = 38 \text{ }^\circ\text{C}$.

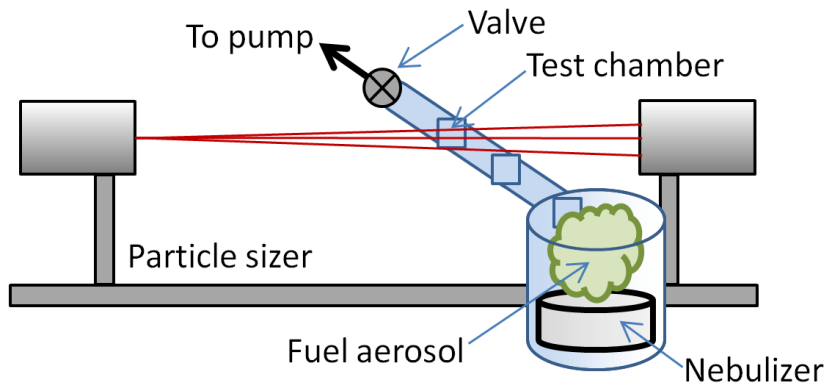


Figure 3.11: Schematic of Malvern Particle Sizer setup for measuring the particle size distribution of liquid aerosols. Aerosols are generated in a container using ultrasonic nebulizers, and then pulled through an optical chamber through which the particle sizer is aligned. The aerosol flow rate through the chamber is controlled by a valve that is connected to a vacuum pump. Figure adapted from Reference [130].

3.7 Estimation of droplet loading

In conventional shock tubes, the exact equivalence ratio is established manometrically by measuring the partial pressures of gaseous fuel, oxidizer, and diluent. However, in the aerosol shock tube, the equivalence ratio depends on the volume fraction of droplets in the final mixture that is encountered by the incident shock wave. Therefore, it is helpful to have a correlation that can be used to predict the necessary droplet loading prior to experimentation, in order to achieve the desired equivalence ratio.

There are two general correlations available. One is best applied to the aerosol after it has been pulled into the shock tube; this serves as a second check on the aerosol concentration measured using the 3.39 μm laser diagnostic. The other is employed in the AGT during the nebulization process; this is most helpful for determining how long the nebulizers need to be active to generate sufficient fuel loading, or for determining the waiting interval necessary for large droplets to settle out of the mixture.

Both correlations rely upon Mie scattering, which describes how light is affected when it encounters small particles. The Mie scattering diagnostic involves a simple 650 nm (visible) laser that passes through the aerosol. In the presence of droplets, the laser light is attenuated as the collimated light is scattered away from the detector. The resulting extinction $\epsilon = -\ln\left(\frac{I}{I_o}\right)$ can be related to the droplet volume fraction F_v according to Equation 3.28,

$$-\ln\left(\frac{I}{I_o}\right) = \epsilon = F_v \frac{\int_0^\infty Q_{ext}(d, n(\lambda)) f(d) \frac{\pi}{4} d^2 L dd}{\int_0^\infty f(d) \frac{4\pi}{3} d^3 dd} \quad (3.28)$$

wherein L is the path length over which the extinction occurs, $Q_{ext}(d, n(\lambda))$ is the Mie coefficient (dependent on droplet diameter d and droplet index of refraction n at light wavelength λ), and $f(d)$ is the aerosol size distribution (*e.g.*, Equation 3.26) [130, 162, 190].

3.7.1 Volume fraction estimation

Knowledge of the particle size distribution and the index of refraction can simplify the Mie scattering equation (Equation 3.28). At first this can seem a daunting task, because such information

may not be readily available. Fortunately, however, the particle size distributions $f(d)$ for most fuels of practical interest, when aerosolized using ultrasonic nebulizers, are very similar and follow Equation 3.26. Moreover, most fuels of practical interest also have similar indices of refraction ($n \sim 1.33 - 1.42$). Haylett *et al.* used these facts to simplify Equation 3.28, producing a straightforward relationship:

$$\epsilon = CLF_v \quad (3.29)$$

Here, $C = 0.31 \pm 0.01 \frac{1}{\text{m}}$ is a constant, the units of path length L are [m], and the particle volume fraction F_v is expressed in parts per million by volume [ppmv].

The F_v obtained from this relationship can be used to translate the Region 1 (pre-incident shock) 650 nm laser extinction value ϵ_1 (measured in the test section; see Figure 3.3) into an equivalence ratio ϕ by way of the droplet cube framework from Section 3.3. This serves as a check on the ϕ value measured at the end of Region 2 via the 3.39 μm laser diagnostic. Calculation of the equivalence ratio requires knowledge of the number of oxygen molecules (O_2) needed for complete combustion ($N_{\text{O}_2,\text{stoich}}$; *i.e.*, all H-atoms form H_2O , all C-atoms form CO_2 , all S-atoms form SO_2 , *etc.*), as well as the number of O_2 present in the actual mixture ($N_{\text{O}_2,\text{mix}}$).

$$\phi = \frac{N_{\text{O}_2,\text{stoich}}}{N_{\text{O}_2,\text{mix}}} \quad (3.30)$$

Note that this derivation will neglect the fuel vapor present in the gas phase. This is appropriate in light of the other simplifications employed to achieve the desired equivalence ratio estimation.

The quantity $N_{\text{O}_2,\text{stoich}}$ can be determined from Equation 3.31,

$$N_{\text{O}_2,\text{stoich}} = N_{\text{fuel}} \left(N_{\text{C,fuel}} + \frac{1}{4} N_{\text{H,fuel}} + N_{\text{S,fuel}} \right) \quad (3.31)$$

where $N_{\text{C,fuel}}$, $N_{\text{H,fuel}}$, and $N_{\text{S,fuel}}$ are the number of C, H, and S atoms in one fuel molecule, respectively, and N_{fuel} is calculated on a basis of total volume V_{tot} in Equation 3.32.

$$N_{\text{fuel}} = F_v V_{\text{tot}} \rho_l \frac{1}{\hat{M}_l} \quad (3.32)$$

In this equation, ρ_l and \hat{M}_l are the liquid density and molar mass, respectively, and $F_v V_{tot}$ represents the volume of the droplets.

The quantity $N_{O_2,mix}$ can have contributions from both the bath gas and the fuel itself (in the case of oxygenated fuels like FAMEs).

$$N_{O_2,mix} = N_{O_2,bath} + N_{O_2,fuel} \quad (3.33)$$

The contribution from the bath gas can be derived from the ideal gas equation of state (Equation 3.12):

$$N_{O_2,bath} = x_{O_2} \frac{P}{\hat{R}_u T} V_{tot} (1 - F_v) \quad (3.34)$$

Here, x_{O_2} is the mole fraction of oxygen in the bath gas, and $V_{tot} (1 - F_v)$ represents the volume of the gas. Finally, the contribution from fuel is given by

$$N_{O_2,fuel} = N_{fuel} \left(\frac{1}{2} N_{O,fuel} \right) \quad (3.35)$$

where $N_{O,fuel}$ is the number of oxygen atoms contained in one molecule of the fuel.

Combining the above equations together and noting that V_{tot} drops out of the result allows the equivalence ratio ϕ to be estimated from the Region 1 650 nm extinction value ϵ_1 . Applying this framework to the example shown in Figure 3.4 yields an estimate of $\phi_{est} \sim 1.4$, which is more than two times the value measured using the infrared laser diagnostic ($\phi_{meas} = 0.6$). The difference can be explained by the simplifications employed in this derivation, including the use of $C = 0.31 \frac{1}{m}$ in Equation 3.29. It could also be evidence of slight axial non-uniformity of the aerosol in the test section, where the droplet volume fraction F_v in Region 1 is higher near the endwall than at the location corresponding to the gas/droplet mixture that is ultimately swept down to the test location following the incident shock.

3.7.2 Empirical correlation for equivalence ratio

The Mie scattering framework introduced in Equation 3.28 can also be applied to estimate the extinction required by a non-resonant laser in the aerosol generation tank in order to achieve the

desired equivalence ratio following fuel loading (aerosol expansion into the test section) and droplet evaporation. This diagnostic relies on a 650 nm laser that is aligned through the AGT (shown in Figure 3.12). The resulting extinction $\epsilon = -\ln\left(\frac{I}{I_o}\right)$, together with the desired initial experiment Region 1 pressure P_1 , can be related to the equivalence ratio ϕ according to Equation 3.36.

$$\frac{-\ln\left(\frac{I}{I_o}\right)}{P_1} = \frac{\epsilon}{P_1} = a\phi + b \quad (3.36)$$

Here, $a > 0$ and b are two empirical constants that depend on the fraction of moles of gas displaced from the test section to the dump tank X_m , the post-reflected-shock pressure P_5 , the bath gas mixture, and the fuel type. Since $a > 0$, as ϕ increases at constant P_1 , ϵ must also increase (*i.e.*, more fuel droplets are present to scatter the light). Moreover, as P_1 increases at constant ϕ , ϵ increases as well, reflecting the fact that more droplets are needed as the concentration of oxidizer increases with pressure. The dependence on X_m arises because the volume fraction of droplets (which are incompressible) changes as the carrier gas in the AGT expands into the test section. This relationship is plotted in Figure 3.13 for methyl linoleate data with $X_m = 1.25$. Of course, the equivalence ratio in every shock experiment is precisely measured in the test section following complete droplet evaporation using the Beer-Lambert relationship and the 3.39 μm HeNe laser diagnostic (Equation 3.1); however, Equation 3.36 is useful for creating the aerosol mixture prior to experimentation.

3.8 Summary

In this chapter, details of the operation of the aerosol shock tube have been presented. The aerosol-fuel-loading technique has been shown to increase the size range of fuels that can be studied using the shock tube technique, and the pressures of each shock tube volume necessary for filling the desired quantity of aerosol have been outlined. Important timescales for droplet evaporation and diffusion have also been introduced, and shown to be less than available Region 2 particle times. Settling times for droplets have been shown to be long enough to allow droplet loading with minimal fuel loss to the tube wall. Finally, two relationships for estimating the fuel loading based on Mie scattering by the aerosol droplets have been set forth.

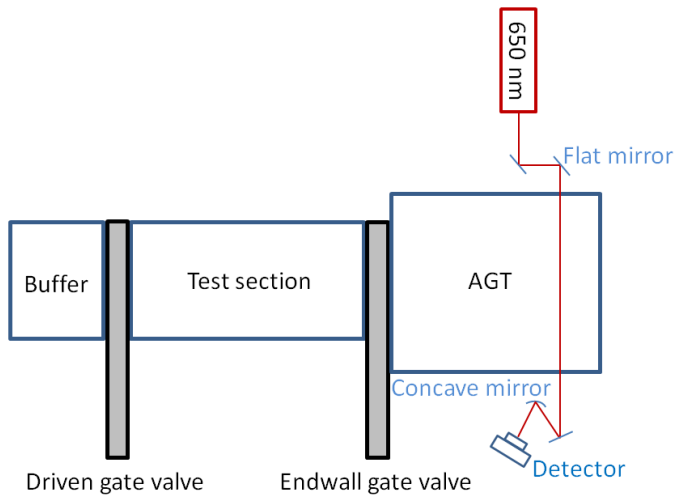


Figure 3.12: AGT Mie scattering diagnostic schematic.

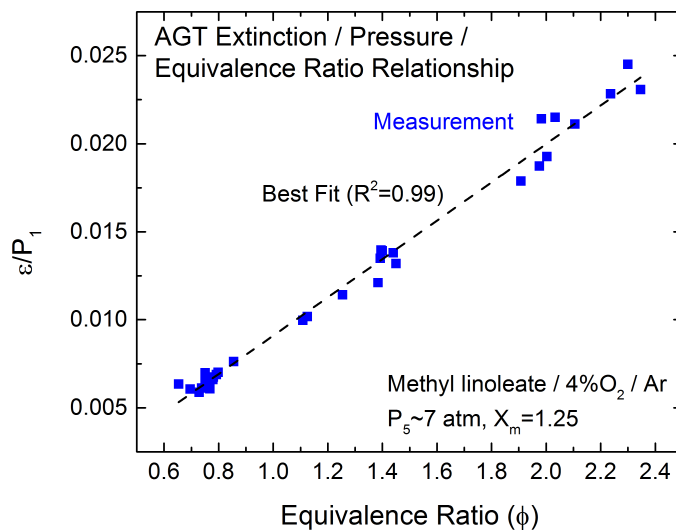


Figure 3.13: Relationship between AGT extinction, pressure, and equivalence ratio. Extinction measurements were made immediately after nebulization was complete (no waiting/settling time).

Chapter 4

AEROFROSH

*The contents of this chapter have been submitted to the journal **Shock Waves** [173].*

4.1 Introduction

Shock tubes provide an excellent platform for studying reaction kinetics and fuel ignition processes. Fuel loading in the shock tube for these experiments can either be accomplished completely in the gas phase, or in two-phase mixtures such as aerosols. Regardless of the loading method, accurate determination of temperature, pressure, and density conditions in the test environment are needed for precise measurement of test quantities such as ignition delay times or species mole fractions. This chapter presents a code, called AEROFROSH, which has been used in the High Temperature Gasdynamics Laboratory (HTGL) at Stanford to calculate the test conditions behind incident and reflected shocks for evaporating aerosol mixtures in shock tubes. Furthermore, new adaptations to this algorithm that allow the use of multi-fuel-component aerosols (such as five-component biodiesel blends or jet fuels like JP-8/Jet-A) will be introduced as well.

4.2 Background

The interaction of shocks with aerosols is quite complex, and an understanding of the underlying and competing processes will facilitate comprehension of the computational algorithm discussed in

this work. Consider the scenario in which an incident shock propagates into a fuel-droplet-laden gas mixture (*i.e.*, an aerosol composed of fuel droplets, fuel vapor, and carrier (bath) gas). First, the incident shock heats and accelerates the gas surrounding the droplets as in a fully gas-phase mixture. Immediately following this heating and acceleration, some condensation of vapor back to liquid form may take place because the pressure has suddenly increased [191]. Next, relaxation processes occur in which droplets break apart and are accelerated to the velocity of the carrier gas. The carrier gas velocity decreases somewhat in this process, causing compression and a slight pressure rise [192]. During and following this droplet breakup and acceleration, three processes, namely heat transfer from the gas into the droplets, droplet evaporation, and fuel vapor diffusion into the gas mixture, transform the aerosol into a fully gaseous medium. After these processes are complete, the gas temperature, pressure, and density have decreased, increased, and increased, respectively, from the immediate post-shock conditions. The post-incident-shock environment is termed Region 2, and that prior to the incident shock is termed Region 1.

Ultimately in shock tube experiments the incident shock reflects off of the endwall and travels back through the mixture, stagnating, heating, and compressing it to the desired test conditions as in a conventional pure gas-phase shock. The reflected shock moves through two different mediums in its propagation. Immediately after reflection, the shock wave travels into a short but finite still-heating, evaporating, and diffusing mixture. This mixture's length is governed by the time needed for the three processes above together with the incident and reflected shock velocities. After passing through this short volume in close vicinity to the endwall, the reflected shock propagates through a fully evaporated and uniform gas-phase mixture. The environment following the reflected shock is termed Region 5.

4.3 Previous studies

Experimentally measuring the temperature, pressure, and density conditions behind the reflected shock wave (in Region 5) of a shock experiment (*e.g.*, using laser diagnostics, pressure transducers, *etc.*) has historically been quite difficult to do with a high degree of accuracy. For this reason, the conservation equations of mass, momentum, and energy, combined with an equation of state,

have often been used to compute the conditions behind incident and reflected shocks using the measured incident shock velocity as the primary input parameter. Early researchers employed analytical relationships to this end, such as those of Gaydon and Hurle, which assume constant gaseous heat capacities [111]. Many different numerical routines have been developed, including those of Gordon and McBride [122], Mitchell and Kee [113], Esser [123], Davidson *et al.* [124–126], and Morley [127]. Another routine, called FROSH (FROzen SHock), is described in Appendix A. This chapter will only discuss the adaptations necessary for computations in aerosol-laden flows rather than outline all of the algorithms for pure gas-phase calculations.

Numerous theoretical and experimental studies have been published discussing the interaction between droplets and gaseous mixtures. Bahn produced an early overview of literature regarding the so-called diameter-squared evaporation law and states parameters for computing mass and energy diffusion coefficients [177]. A review of studies through 1979 regarding flows with nucleation and condensation was performed by Kotake and Glass [193]. A more recent literature review of fuel droplet heating and evaporation was conducted by Sazhin [194].

Much theoretical work has been done to study shock waves and liquid aerosols. One of the earliest studies was performed by Lu and Chiu, who investigated the shock structure of two-phase flows with droplet evaporation [195]. An important feature of their numerical method was incorporation of mass transfer between phases. Panton and Oppenheim expanded upon Lu and Chiu's results, performing numerical simulations in the limit where mass transfer between phases was diffusion-limited [191]. Their results showed that in the immediate post-shock environment for certain test conditions, large droplets could grow in size due to condensation and small droplets could simultaneously shrink from evaporation. This example highlights the importance of droplet diameter-dependent properties, a discussion of which is provided in Appendix C. Soon after these initial studies, Marble reviewed the subject of shocks in aerosols, including fundamental relations and a discussion of significant experimental results from an analytical standpoint [196, 197]. One important finding discussed in that work is that the conditions immediately behind shocks in aerosols, before droplet evaporation and relaxation have occurred, can be accurately described by pure gas-phase conservation equations.

Narkis and Gal-Or explored the differences between high and low particle loading [198]. Their

results showed that the error induced by neglecting particle volume becomes especially significant at the end of the relaxation period, but before this time the solutions including and excluding this volume are quite similar. Rakib *et al.* studied shock waves in water aerosols [199, 200]. They found that even for very strong shocks (in this case with Mach number equal to 15), the presence of water droplets significantly reduced the post-shock temperature due to the enthalpy of vaporization.

Guha and Young produced a number of studies describing the interaction of shock waves and aerosols. In Reference [201] they introduced several governing equations applicable to two-phase flows (specifically, wet steam), and set forth three expressions for sound speed in two-phase mixtures. They also presented analytical expressions to describe the structure of normal shock waves in steady vapor-droplet flows [202]. Guha applied the Rankine-Hugoniot relationships to shocks in aerosols and examined the internal structures of these waves using analytical and numerical approaches [203]. Guha also applied the Rankine-Hugoniot relations specifically to gas-droplet mixtures, employing the assumption of small droplet volume fraction to simplify some of the expressions [204]. One important finding was that the gas-phase ideal shock relations (*e.g.*, those in Gaydon and Hurle [111]), when applied to shocks in aerosols, provide accurate estimations of numerically-obtained post-shock properties. Young composed detailed conservation equations for gas-droplet interactions, and included a number of important terms such as droplet surface energy [205].

An extensive analysis was undertaken by Tambour and Zehavi to analyze the flow field behind normal shocks in aerosols [206], in which they gave an in-depth explanation of droplet coalescence. However, because the droplet sizes were chosen to be small, droplet breakup was not included as a process in their model. Chang and Kailasanath constructed a computational model to investigate shock interactions with aerosols, which allowed for droplet breakup and employed an axisymmetric rather than traditional one-dimensional platform [207]. The authors found that their model results compared well with previous simulations and experiments [208, 209], and also showed that droplet breakup results in greater shock attenuation. Sychevskii recommended a method for processing liquid droplets using shock tubes [210] that includes methods for accommodating droplets that have varying composition, for example a salt-water solution. Finally, two recent papers by Petersen [211] and Von Dongen [212] concerning shock waves in two-phase flows provide useful overviews.

Though only briefly summarized above, an enormous amount of work has been done in the area of shock waves in two-phase flows. However, the literature does not yet contain a software package that has applied the fundamental principles governing these environments with the *sole and express* purpose of computing post-shock conditions in shock tubes. Furthermore, a significant limitation also exists in two-phase shock calculation methods, as to the author's knowledge, no routine is available that can account for multi-component fuel mixtures. In this chapter, details are provided concerning a computer code, called AEROFROSH, which performs shock calculations in evaporating multi-component fuel aerosol environments across both incident and reflected shocks in shock tubes. This code has been composed in MATLAB computer software [213].

4.4 Experimental setup

The shock tube employed in this work was described in Section 3.2. Details of the algorithm that accounts for the presence of aerosol droplets are somewhat dependent on the specific experimental configuration, although the general procedure described herein is applicable to a wide variety of aerosol shock tubes. Briefly, this shock tube produces a spatially-uniform mixture of fuel droplets and bath gas in a 25-liter tank (called the Aerosol Generation Tank, or AGT) adjacent to the endwall using a bank of ultrasonic nebulizers that reside in a 25-milliliter pool (total volume) of liquid fuel below the bath gas. This mixture is ushered into the tube through a sliding endwall gate valve. An incident shock wave evaporates the aerosol droplets to produce a uniform gaseous fuel/bath gas mixture, which the reflected shock further heats and compresses. A laser-based spectroscopic measurement of fuel concentration is performed immediately before the reflected shock, and a non-resonant laser is used to verify complete droplet evaporation. This experimental configuration allows gas-phase ignition and pyrolysis studies to be performed on very-low-vapor-pressure fuels, such as biodiesel, without problems such as pre-experimental fuel decomposition or partial fuel distillation [130].

4.5 Outline of algorithm for pure gas-phase flows

This section will provide a very brief review of the traditional algorithm employed by most codes to solve for post-shock conditions in pure gas-phase flows. More details concerning this method can be found in Appendix A.

The conservation equations for mass, momentum, and energy are given in Equations 4.1, 4.2, and 4.3 (subscripts a and b indicate the applicable shock region). Taken in combination with the ideal gas equation of state (Equation 4.4; see also Equation 3.12), they allow temperature and pressure behind a shock to be calculated. Here, ρ represents gas density, u is the shock-frame gas velocity, P and T are the gas pressure and temperature, and h is the gas mass-specific enthalpy. Also, $R_g = \frac{\hat{R}_u}{\hat{M}_{gas}}$ is the specific gas constant where \hat{R}_u is the universal gas constant, \hat{M}_{gas} is the molar mass of the mixture, and the hat (^) symbol denotes molar units.

$$\rho_a u_a = \rho_b u_b \quad (4.1)$$

$$P_a + \rho_a u_a^2 = P_b + \rho_b u_b^2 \quad (4.2)$$

$$h_a + \frac{1}{2} u_a^2 = h_b + \frac{1}{2} u_b^2 \quad (4.3)$$

$$P = \rho R_g T = \frac{R_g T}{v} \quad (4.4)$$

Two iteration routines are typically required - one to solve for the post-incident-shock conditions, and another to solve for those following the reflected shock. These routines usually assume that chemistry is frozen throughout the shock process, *i.e.*, that the mole fractions of gases remain unchanged throughout the entirety of Regions 1 and 2, and in the immediate beginning of Region 5.

4.6 Adaptations for shocks in aerosols

In this section, important differences between shocks in pure gases and shocks in aerosols, as well as the methods employed by AEROFROSH to account for them, will be presented. A detailed analysis of the effects of the droplets on bulk fluid properties is provided in Appendix C.

4.6.1 Presence of droplets in Region 1

The presence of a liquid phase in Region 1 is the first and most important source of difference between shocks in pure gas-phase flows and shocks in liquid aerosols. Effects include temperature-dependent changes in mixture enthalpy and density, as well as changes in gaseous mole fractions due to evaporation. A quantity to monitor the amount of matter in liquid and gaseous phases within the shock tube is needed in order to accurately account for the liquid-induced property changes in Regions 1 and 2; one simple method to obtain such a value is to track the total number of moles in the liquid and gas phases within a differentially small volume in the shock tube. The derived quantity, C_m , is defined in Equation 4.5, where $N_{1,d}$ is the number of moles in the droplets (liquid phase) in this volume, and $N_{1,g}$ is the number of moles in the gas phase within this volume. In Region 1, C_m is computed for a volume of gas and droplets that begins far away from the measurement location, but ultimately is swept toward the endwall and stagnated at the test location by the reflected shock. The C_m ratio is essential in precisely determining the density, heat capacity, and enthalpy of Regions 1 and 2.

$$C_m = \frac{N_{1,d}}{N_{1,d} + N_{1,g}} = \frac{\frac{N_{1,d}}{N_{1,g}}}{\frac{N_{1,d}}{N_{1,g}} + 1} \quad (4.5)$$

4.6.2 Modifications to bulk fluid properties

The second difference between shocks in gases and shocks in aerosols is that the aerosol droplets modify the fluid's sound speed. Guha identified the frozen speed of sound in an aerosol as a good parameter for computing shock Mach numbers in two-phase environments [204]. The correlation of Chu and Temkin for frozen sound speed a_{frozen} is easily applied as it depends not on droplet diameter, but on the mass and volume fractions of the liquid phase [214–216]. It is repeated in Equation 4.6, where a_{gas} is the sound speed of the carrier gas (as given for an ideal gas in Equation 4.7), ϕ_v is the volume (V) concentration (*i.e.*, volume fraction; $\phi_v = F_v$ (Equation 3.4)) of fuel droplets given in Equation 4.8, and ϕ_m is the mass concentration of fuel droplets given in Equation 4.9. The Mach number $M_{IS,frozen}$ for a shock traveling at velocity U_{IS} in an aerosol should be computed according to Equation 4.10 using the modified sound speed a_{frozen} , rather than the sound speed of the carrier gas alone (here the subscript IS denotes the incident shock). Note that

there is some disagreement in the literature as to the exact expression for frozen sound speed, especially between the values given in References [214] and [217]. A brief discussion on the differences was given by Temkin [216], who ultimately chose the form shown below. Changes to sound speed and shock Mach number as described in this section become important for droplet volume fractions $\phi_v = F_v > 10^{-6}$ (1 ppmv).

$$a_{frozen} = a_{gas} \frac{\sqrt{1 - \phi_m}}{1 - \phi_v} \quad (4.6)$$

$$a_{gas} = \sqrt{\frac{\gamma P}{\rho_{gas}}} = \sqrt{\gamma R_g T} \quad (4.7)$$

$$\phi_v = \frac{V_{liq}}{V_{liq} + V_{gas}} \quad (4.8)$$

$$\phi_m = \frac{\phi_v \frac{\rho_{drops}}{\rho_{gas}}}{1 + \left(1 - \frac{\rho_{gas}}{\rho_{drops}}\right) \phi_v \frac{\rho_{drops}}{\rho_{gas}}} \quad (4.9)$$

$$M_{IS,frozen} = \frac{U_{IS}}{a_{frozen}} \quad (4.10)$$

In these equations, $\gamma = \frac{c_p}{c_v}$ is the specific heat ratio of the carrier gas, and ρ_{gas} and ρ_{drops} are the densities of the carrier gas and droplets, respectively.

4.6.3 Droplet evaporation

Droplet evaporation in Region 2 is the third source of difference between shocks in pure gases and shocks in liquid aerosols. The latent heat of vaporization of the liquid fuel decreases the sensible enthalpy of the gas, which in turn alters the final temperature, pressure, and density of the Region 2 fully-evaporated gaseous mixture. As a result, the initial Region 2 temperature (immediately after the incident shock passes and before evaporation has occurred) is higher than the final Region 2 temperature (immediately before the reflected shock passes and after evaporation has completed). AEROFROSH is able to report both the pre-evaporation and post-evaporation Region 2 conditions. Note that the pre-evaporation test conditions only reflect the gaseous species because, among other reasons, it is impossible for most fuels to exist as liquids at Region 2 temperatures and pressures.

Figure 4.1 shows the control volume used to solve for the final Region 2 conditions. In the

schematic, notice that the control volume extends beyond the area where evaporation is occurring, such that the only important conditions are those before and after complete evaporation. Since properties of the gas are only easily well-defined in the pre- and post-evaporation regions, AEROFROSH requires that evaporation be complete by the end of Region 2. This allows the program to completely account for the gas's sensible enthalpy loss due to the fuel's heat of vaporization. Should evaporation not be complete by the end of Region 2, the problem becomes much more complex and a transient solution similar to that of References [201], [206], or [207] would be required.

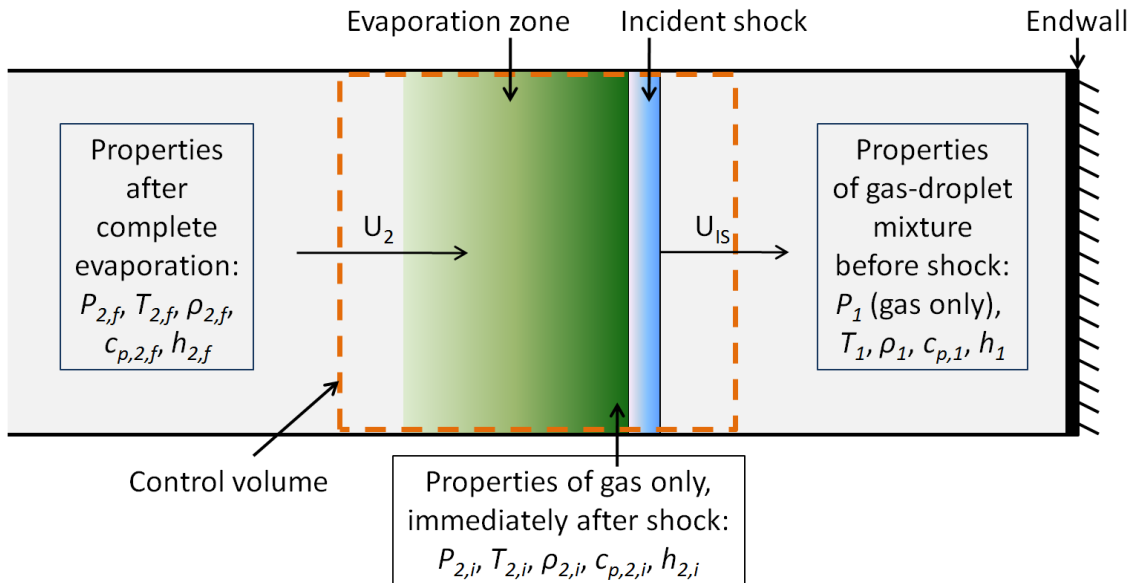


Figure 4.1: Control volume used to solve for Region 2 conditions in the presence of evaporating aerosol, shown in the lab reference frame. Initial and final Region 2 conditions are denoted by subscripts i and f , respectively. Note that the control volume is chosen such that final Region 2 state has no liquid phase present.

4.6.4 Quantifying fuel loading

The fourth important difference between shocks in gases and shocks in aerosols is the technique for fuel loading. Conventional gas-phase shock tubes use a manometric method of determining fuel concentration prior to experimentation. In contrast, shocks in aerosols require a fuel measurement after droplet evaporation is complete, because techniques of quantifying the amount of fuel aerosol

in the Region 1 mixture (*e.g.*, using Mie scattering [152]) are difficult. This is best accomplished by way of a spectroscopic laser diagnostic using the Beer-Lambert relation. The Beer-Lambert equation relates the absorption of light by a resonant species, in this case the fuel molecule, to the concentration of that species, according to Equation 4.11 (see also Equations 3.1, 5.2, 8.4, and 9.1).

$$\alpha_2 = -\ln\left(\frac{I_2}{I_o}\right) = n_{2,fuel}\sigma_{2,fuel}L \quad (4.11)$$

In this equation, α_2 is called the absorbance, I_2 is the transmitted light intensity in Region 2 following droplet evaporation, I_o is the light intensity incident upon the shock tube, $n_{2,fuel}$ is the Region 2 gas phase fuel concentration, $\sigma_{2,fuel}$ is the temperature-dependent absorption cross section of the fuel in Region 2, and L is the path length over which the absorption takes place inside the evaporated gas mixture. When combined with the ideal gas equation of state, the Beer-Lambert relation can be used to calculate the fuel mole fraction $x_{2,fuel}$ according to Equation 4.12 (here, T_2 and P_2 are the Region 2 temperature and pressure respectively).

$$x_{2,fuel} = \frac{n_{2,fuel}}{n_{2,total}} = \frac{\alpha_2 \hat{R}_u T_2}{\sigma_{2,fuel} P_2 L} \quad (4.12)$$

The temperature-dependence of the absorption cross section can be well-described by a third-order polynomial of the form given in Equation 4.13, where coefficients a through d , determined by either experiment or theory, and are inputs to AEROFROSH. An extra iteration step is required in the code as a result of this temperature dependence.

$$\sigma_{2,fuel} = aT^3 + bT^2 + cT + d \quad (4.13)$$

A sample absorbance measurement in which two lasers have been employed is given in Figure 4.2. The first, non-resonant laser (650 nm) senses the presence of droplets due to Mie scattering, and the second, resonant laser measures fuel concentration using a 3.39 μm helium-neon (HeNe) laser. In this figure, the non-resonant laser extinction drops to zero at about 95 μs , indicating that no droplets remain. The absorbance measurement by the resonant laser is extrapolated to the Region 5 Schlieren spike, yielding $\alpha_2 = 0.727$ as the final absorbance value. Temperature and pressure data

at the initial and final Region 2 conditions are denoted on the plot.

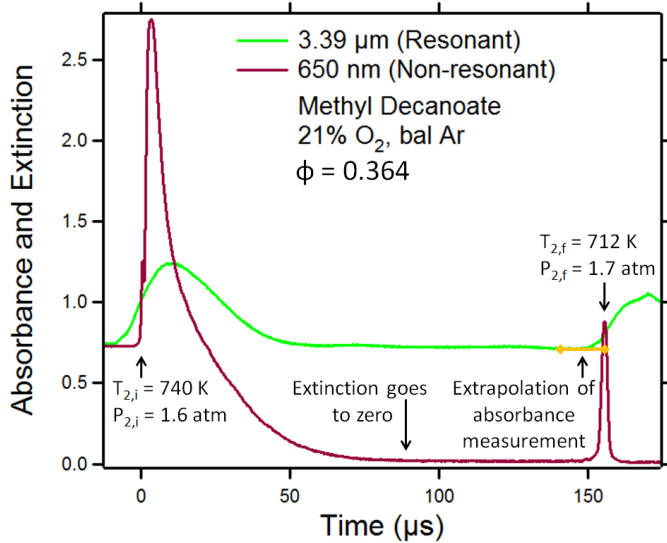


Figure 4.2: Sample fuel absorbance measurement in Region 2 for a methyl decanoate shock in 21% oxygen/argon with $\phi = 0.364$ (initial droplet volume fraction: $F_v = 9.0$ ppmv).

For the experiment shown in Figure 4.2, the evaporation/diffusion time in the lab frame (taken as the time required for the non-resonant laser extinction to drop to zero) is approximately 95 μs , which corresponds to about 300 μs in the particle frame (see Appendix B for a discussion of lab and particle time). The total particle time in Region 2 for this experiment is about 490 μs . Using the framework developed in Section 3.3 to estimate characteristic evaporation and diffusion times at the conditions of this experiment ($T_{2,i} = 740$ K, $P_{2,i} = 1.6$ atm, $F_v = 9.0$ ppmv, $\rho_l = 800 \text{ kg/m}^3$, 21%O₂/Ar bath gas), with $\bar{d} = 3 \text{ } \mu\text{m}$ and $D = 0.3 \text{ cm}^2/\text{s}$, gives a 95%-complete characteristic evaporation time of $\tau_{e,95} \sim 113 \text{ } \mu\text{s}$ and a characteristic diffusion time of $\tau_d \sim 169 \text{ } \mu\text{s}$. Assuming the evaporation and diffusion timescales are completely decoupled (complete evaporation occurs before any diffusion begins), this corresponds to a total time of 282 μs , which shows good agreement between the experiment and the simple model of Section 3.3. A similar analysis based on Figure 3.4 is available in Section 3.3 as well.

4.7 Algorithm: Single-component fuel aerosols

The main structure of AEROFROSH is shown schematically in Figure 4.3. Notice that solving for the conditions behind the incident shock requires two loops; the inner loop solves for the Region 2 post-droplet-evaporation temperature and pressure ($T_{2,f}$ and $P_{2,f}$), and the outer loop solves for the post-droplet-evaporation fuel mole fraction $x_{2,fuel}$. This chapter will focus on the outer loop, which is unique to shocks in aerosols; details concerning the algorithms found within the inner incident shock loop and the reflected shock loop are available in Appendix A.

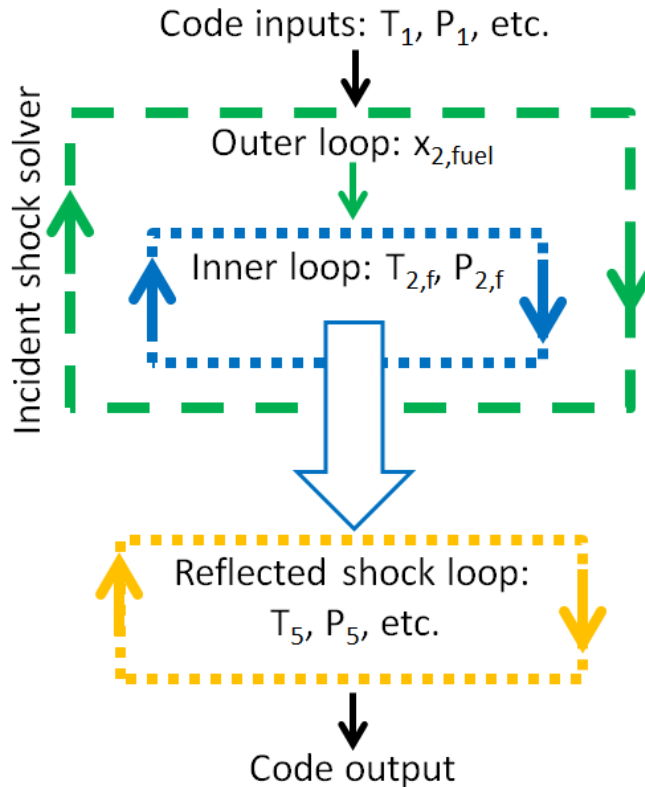


Figure 4.3: Schematic of main loop structure employed by AEROFROSH. The incident shock iteration procedure involves an outer loop to solve for fuel mole fraction, and an inner Newton-Raphson loop to ascertain post-incident-shock, post-evaporation temperature and pressure. To solve for conditions following the reflected shock, only one Newton-Raphson iteration loop is required. A separate Newton-Raphson iteration loop, not shown, solves for the pre-evaporation (gas phase only) conditions immediately following the incident shock.

Prior to entering the outer loop, AEROFROSH accepts input data and performs some preliminary calculations related to the Region 1 gas phase carrier gas (excluding droplets) mixture. Table 4.1 at the end of this chapter summarizes the required inputs; note that thermodynamic data for each gaseous species in the seven-coefficient polynomial NASA format is required [122, 174]. Preliminary calculations include determination of the gas's molecular weight ($\hat{M}_{1,gas}$), ideal constant ($R_{g,1,gas}$), specific volume ($v_{1,gas}$), enthalpy ($h_{1,gas}$), and heat capacity ($c_{p,1,gas}$). In these calculations, the vapor of the liquid fuel droplets is allowed to modify the Region 1 gas mole fractions by assuming that the fuel possesses its saturated vapor pressure at T_1 ; these modified mole fractions $x_{1,bath,i}$ and $x_{1,fuel}$ are computed according to Equations 4.14 and 4.15. In these expressions, the modifier “bottle” is used to signify that the mixture is in the “as-purchased” state, *i.e.*, that which is received new from a supplier. Furthermore, in this work the index subscript i is used to denote bath gas species (*e.g.*, argon, nitrogen, oxygen).

$$x_{1,bath,i} = x_{bottle,i} \frac{P_1 - P_{sat,fuel}}{P_1} \quad (4.14)$$

$$x_{1,fuel} = \frac{P_{sat,fuel}}{P_1} \quad (4.15)$$

This input data is passed to the outer loop, which performs two functions. First, it combines the properties of the carrier gas and the properties of the fuel droplets, and passes these combined properties to the inner iteration loop. Second, it receives fully-evaporated gas Region 2 properties from the inner loop, checks the calculated fuel mole fraction against the Beer-Lambert spectroscopic fuel measurement, and decides whether or not to continue the iteration process.

There are four pre-evaporation Region 1 mixture properties that must be computed by the outer loop: the sound speed a_{frozen} , the incident shock Mach number $M_{IS,frozen}$, the density $\rho_{1,mix}$, and the enthalpy $h_{1,mix}$. The sound speed is computed according to Equations 4.6-4.9, and the Mach number by Equation 4.10. The density and enthalpy are computed according to Equations 4.16 and 4.17, using the variable C_m together with gas and fuel molar masses, \hat{M}_{gas} and \hat{M}_{fuel} , to perform a mass-weighted summation. In these equations, ρ_{fuel} is the density of the fuel, $h_{1,fuel}^{liq}$ is the enthalpy of the liquid fuel droplets, $h_{1,gas}$ is the enthalpy of the Region 1 gas mixture, and

$\hat{M}_{2,evap}$ is the molecular weight of the fully evaporated Region 2 gas mixture.

$$\rho_{1,mix} = \frac{m_{gas} + m_{liq}}{V_{gas} + V_{liq}} = \frac{\left((1 - C_m) \hat{M}_{gas} \right) + \left(C_m \hat{M}_{fuel} \right)}{\left((1 - C_m) \frac{\hat{R}_u T_1}{P_1} \right) + \left(C_m \hat{M}_{fuel} \frac{1}{\rho_{fuel,avg}} \right)} \quad (4.16)$$

$$h_{1,mix} = \left(\frac{C_m \hat{M}_{fuel}}{\hat{M}_{2,evap}} \right) h_{1,fuel}^{liq} + \left(\frac{(1 - C_m) \hat{M}_{1,gas}}{\hat{M}_{2,evap}} \right) h_{1,gas} \quad (4.17)$$

Note that adding in the enthalpy of the liquid fuel $h_{1,fuel}^{liq}$ is equivalent to adding the enthalpy of the fuel vapor $h_{1,fuel}^{vap}$ and subtracting out the fuel's enthalpy of vaporization $h_{1,fuel}^{fg}$ (Equation 4.18).

$$h_{1,fuel}^{liq} = h_{1,fuel}^{vap} - h_{1,fuel}^{fg} \quad (4.18)$$

As mentioned above, these values are all passed to the inner iteration loop, together with a guess as to the actual post-evaporation fuel mole fraction $x_{2,fuel}^{guess}$. The inner loop uses the guessed fuel mole fraction and other input properties to solve for the post-evaporation Region 2 temperature and pressure. After completion, it passes the iteration results back to the outer loop, which checks the guessed fuel mole fraction against the spectroscopically-measured value $x_{2,fuel}^{spec}$. Since the spectroscopic value depends on the post-evaporation temperature and pressure according to Equations 4.12 and 4.13, the Beer-Lambert relation provides closure to the three-unknown problem and allows $T_{2,f}$, $P_{2,f}$, and $x_{2,fuel}$ to be determined.

Should the spectroscopic and guessed fuel mole fractions be sufficiently close, the algorithm exits and the reflected shock iteration routine, described in Appendix A, commences. However, if these values differ significantly, the outer loop updates the C_m variable according to Equations 4.5, 4.19, and 4.20, produces new gas phase mole fraction guesses via Equations 4.21 and 4.22, and commences another iteration cycle. In these equations, $x_{2,bath,i}^{guess}$ and $x_{2,fuel}^{guess}$ are the guessed post-evaporation Region 2 mole fractions of bath gas components and fuel, respectively (i is the bath gas component index); these are sent to the next cycle of the loop. Furthermore, $x_{2,bath}$ is the total mole fraction of non-fuel gases in the post-evaporation Region 2 mixture and C_{bath} is the number of bath

gas components.

$$x_{2,bath} = 1 - x_{2,fuel}^{spec} = \sum_{i=1}^{C_{bath}} x_{2,bath,i} \quad (4.19)$$

$$\frac{N_{1,d}}{N_{1,g}} = \frac{x_{1,bath} - x_{2,bath}}{x_{2,bath}} \quad (4.20)$$

$$x_{2,bath,i,guess} = \frac{N_{2,bath,i}}{N_{2,g}} = \frac{N_{1,bath,i}}{N_{2,g}} = \frac{N_{1,g}x_{1,bath,i}}{N_{1,g} + N_{1,d}} = \frac{x_{1,bath,i}}{1 + \frac{N_{1,d}}{N_{1,g}}} \quad (4.21)$$

$$x_{2,fuel,guess} = \frac{N_{2,fuel}}{N_{2,g}} = \frac{N_{1,fuel,vap} + N_{1,d}}{N_{1,g} + N_{1,d}} = \frac{N_{1,g}x_{1,fuel} + N_{1,d}}{N_{1,g} + N_{1,d}} = \frac{x_{1,fuel} + \frac{N_{1,d}}{N_{1,g}}}{1 + \frac{N_{1,d}}{N_{1,g}}} \quad (4.22)$$

Equations 4.23-4.27 are used to derive Equation 4.20. Equation 4.23 states that the total number of moles in the gas phase following evaporation $N_{2,g}$ is equal to the number of moles of carrier gas (the carrier gas consists of bath gas plus fuel vapor) in Region 1 $N_{1,g}$ plus the number of moles in the droplets in Region 1 $N_{1,d}$. Equation 4.24 determines the number of moles of bath gas (non-fuel vapor components) in Region 1 $N_{1,bath}$ from the total number of moles of carrier gas in Region 1 and the mole fraction of bath gas in Region 1 $x_{1,bath}$; Equation 4.25 accomplishes the same goal in Region 2. Equation 4.26 is a statement of mass conservation for the bath gas components between Regions 1 and 2. Finally, Equation 4.27 combines the previous results into Equation 4.23; rearranging Equation 4.27 produces Equation 4.20.

$$N_{2,g} = N_{1,g} + N_{1,d} \quad (4.23)$$

$$N_{1,bath} = N_{1,g}x_{1,bath} \quad (4.24)$$

$$N_{2,bath} = N_{2,g}x_{2,bath} \quad (4.25)$$

$$N_{1,bath} = N_{2,bath} \quad (4.26)$$

$$\frac{N_{1,g}x_{1,bath}}{x_{2,bath}} = N_{1,g} + N_{1,d} \quad (4.27)$$

In addition to those formulas above, Equations 4.28 and 4.29 are also needed to derive Equations 4.21 and 4.22. Equation 4.28 is used to determine the moles of fuel vapor in Region 1 based

on the (gas phase) fuel vapor mole fraction $x_{1,fuel}$, and Equation 4.29 is a statement of mass conservation for the fuel molecules, stating that the total number of moles of fuel in Region 2 $N_{2,fuel}$ has contributions from the fuel vapor $N_{1,fuel,vap}$ and from the droplets $N_{1,d}$.

$$N_{1,fuel,vap} = N_{1,g}x_{1,fuel} \quad (4.28)$$

$$N_{2,fuel} = N_{1,fuel,vap} + N_{1,d} \quad (4.29)$$

Finally, it is sometimes useful to determine the pre-evaporation Region 2 conditions present in the gas (not the droplets) immediately after the incident shock wave passes. This is accomplished by simply solving Equations 4.1-4.4 using only the gas properties instead of the aerosol mixture properties. A comparison between the Region 2 pre-evaporation conditions (denoted with subscript i) and post-evaporation conditions (denoted with subscript f) is provided in Figures 4.6 and 4.7, to be discussed later in this chapter.

The reflected shock iteration routine assumes that the mixture and incident shock conditions are that of the fully evaporated gas in Region 2 and that the gas in Region 5 is also fully evaporated and stagnated. Because of the high temperatures that occur behind the reflected shock wave, these assumptions are expected to be valid except at the earliest times (*i.e.*, for the first several microseconds) in the test gas closest to the end wall (*i.e.*, in the first several millimeters from the endwall).

4.8 Algorithm: Multi-component fuel aerosols

The previous section introduced an algorithm that can determine the post-reflected-shock conditions for shocks in aerosols containing a single fuel component. While studies of a single fuel component in shock tubes are useful, interest also exists in the interaction of shocks with multi-fuel-component aerosols. For instance, shock tube studies of biodiesel fuel must account for at least five different fuel molecules that comprise this mixture. In this section, several adaptations to the previous algorithm are provided, which allow it to compute post-reflected-shock conditions for multi-component fuels.

4.8.1 Mixture-averaged liquid properties

First, ideal solution mixing rules are used to compute the specific volume $v_{fuel,avg}$, density $\rho_{fuel,avg}$, and mass-average enthalpy $h_{fuel,avg}^{liq}$ for the liquid fuel mixture. These formulas are presented in Equations 4.31-4.32; subscript j will be used to index liquid components (i was used for gaseous components). The liquid-phase mass fractions of the fuel components z_j are computed through Equation 4.30, in which the liquid-phase mole fractions of the fuel components are denoted y_j . C_{fuel} is the number of fuel components.

$$z_j = \frac{y_j \hat{M}_j}{\sum_{j=1}^{C_{fuel}} y_j \hat{M}_j} \quad (4.30)$$

$$v_{fuel,avg} = \frac{1}{\rho_{fuel,avg}} = \sum_{j=1}^{C_{fuel}} z_j v_{fuel,j} \quad (4.31)$$

$$h_{fuel,avg}^{liq} = \sum_{j=1}^{C_{fuel}} z_j h_{fuel,j} \quad (4.32)$$

4.8.2 Accounting for component vapor pressures

The second difference is that Dalton and Raoult's laws are used to compute the average vapor pressure of the fuel $P_{vap,fuel,avg}$ using the saturated vapor pressures of each fuel component $P_{sat,j}$. Dalton's law of partial pressures states that the total pressure P_{total} of an ideal mixture of gases is the sum of the partial pressures P_j of the individual gases within that mixture (Equation 4.33). Raoult's law states that, given an ideal mixture of ideal gases in contact with an ideal liquid solution, the partial pressure of each component in the gas phase is related to its mole fraction in the liquid solution y_j and its saturation vapor pressure, $P_{j,sat}$ (Equation 4.34). Combining Dalton and Raoult's laws, the average vapor pressure in the presence of an ideal liquid fuel solution is given by Equation 4.35.

$$P_{total} = \sum_{j=1}^{C_{fuel}} P_j \quad (4.33)$$

$$P_j = P_{total}x_j = P_{sat,j}y_j \quad (4.34)$$

$$P_{vap,fuel,avg} = \sum_{j=1}^{C_{fuel}} P_j = \sum_{j=1}^{C_{fuel}} P_{sat,j}y_j \quad (4.35)$$

4.8.3 Determining gas-phase fuel mole fractions

The third change is that the fuel vapor pressures give rise to new gas-phase mole fractions of bath gas molecules $x_{1,bath,i}$ and fuel molecules $x_{1,fuel,j}$ according to Equations 4.36 and 4.37. Recall that the term “bottle” refers to mole fractions in the as-purchased mixture. The sum of $x_{bath,i}$ and $x_{fuel,j}$ over all of the C_{bath} and C_{fuel} components is 1.0 as expected (Equation 4.38).

$$x_{1,bath,i} = x_{bottle,i} \frac{P_1 - P_{vap,fuel,avg}}{P_1} \quad (4.36)$$

$$x_{1,fuel,j} = \frac{P_{sat,j}y_j}{P_1} \quad (4.37)$$

$$\sum_{i=1}^{C_{bath}} x_{1,bath,i} + \sum_{j=1}^{C_{fuel}} x_{1,fuel,j} = 1.0 \quad (4.38)$$

4.8.4 Spectroscopic fuel measurement

The fourth difference is that the spectroscopic fuel concentration measurement in Region 2 results from absorption by all fuel components rather than just one fuel component. The total mole fraction of fuel can be determined by Equation 4.39, which employs the average absorption cross section as given in Equation 4.40. Here, $\sigma_{2,fuel,j}$ is the Region 2 absorption cross section of fuel component j according to Equation 4.13.

$$x_{2,fuel} = \sum_{j=1}^{C_{fuel}} x_{2,fuel,j} = \frac{n_{2,fuel}}{n_{2,total}} = \frac{\alpha_2 \hat{R}_u T_2}{\sigma_{2,fuel,avg} P_2 L} \quad (4.39)$$

$$\sigma_{2,fuel,avg} = \sum_{j=1}^{C_{fuel}} \frac{x_{2,fuel,j}}{x_{2,fuel}} \sigma_{2,fuel,j} \quad (4.40)$$

4.8.5 Updating gaseous fuel mole fractions

Finally, the fully-evaporated gas-phase mole fractions of individual fuel components $x_{2,fuel,j}$ must be updated following each iteration cycle of the outer loop. One constraint is required for each fuel component, and one constraint (the total fuel mole fraction $x_{2,fuel}$) is known via Equation 4.39. The remaining $C_{fuel} - 1$ constraints come by assuming that the mole fractions of the fuel components in the evaporating droplets $y_{fuel,droplet,j}$ are identical to those in the bottle $y_{fuel,bottle,j}$, resulting in Equation 4.41. In the experimental geometry used at Stanford University as described above, this assumption is well-founded since the droplet size and yield from ultrasonic nebulizers depends largely on liquid surface tension and viscosity [188], which, in ideal solutions, are properties of the liquid mixture rather than the individual fuel components. The quantity $\frac{N_{1,d}}{N_{1,g}}$ is still given by Equation 4.20, and the bath gas mole fractions $x_{2,bath,i,guess}$ are still computed by Equation 4.21. Finally, C_m is still given in Equation 4.5.

$$\begin{aligned} x_{2,fuel,j,guess} &= \frac{N_{2,fuel,j}}{N_{2,g}} = \frac{N_{1,fuel,vap,j} + N_{1,d,j}}{N_{1,g} + N_{1,d}} \\ &= \frac{N_{1,g}x_{1,fuel,j} + N_{1,d}y_{fuel,bottle,j}}{N_{1,g} + N_{1,d}} = \frac{x_{1,fuel,j} + \frac{N_{1,d}}{N_{1,g}}y_{fuel,bottle,j}}{1 + \frac{N_{1,d}}{N_{1,g}}} \end{aligned} \quad (4.41)$$

4.9 Validation

It is important to compare numerical results with both theory and experiment in order to validate computational models. This section provides several theoretical comparisons, and will refer the reader to Reference [158] (Figure 6), Reference [218] (Figures 7, 9, and 10), Reference [219] (Figures 13 and 14), and Reference [220] (Figures 11 and 12), which provide an in-depth comparison of calculations by AEROFROSH with experimental shock tube results.

Guha's analytical shock relationships for mixtures of water vapor and water droplets [204] can be compared to the numerical results of AEROFROSH. The relevant figures and expressions in Guha's work are explicit in terms of a quantity called y_1 (referred to henceforth for clarity as y_1^G), which is the mass fraction of liquid droplets in the total mixture. For a single component vapor-droplet mixture (*e.g.*, water droplets in water vapor), dividing by that component's molar mass can

demonstrate that the quantity C_m discussed in this work is identical to Guha's term y_1^G . In order to compare results with Guha, a modified version of AEROFROSH was produced in which the Region 2 absorbance input was replaced with the value of $C_m = y_1^G$. Rather than an outer loop to determine droplet loading, the code acknowledged that the mole fraction of water was $x_{water} = 1.0$ and proceeded to solve the incident shock relations using the specified C_m . Guha's work was mostly concerned with shocks in low pressure industrial steam turbines, and as such reflected shock conditions were not addressed.

Two plots similar to those of Guha have been replicated here (Guha's Figure 4 and Figure 7) [204]. Figure 4.4 shows post-shock (Region 2) temperature T_2 as a function of droplet loading for a constant pressure ratio $\frac{P_2}{P_1} = 3.0$. $C_m = 0$ corresponds to no droplets, and beyond $C_m = 0.0684$ droplets are not fully evaporated, leading to the saturated solution at the post-shock pressure $T_2 = T_{2,sat}(P_2)$. Not surprisingly, when no drops are present, the analytical results of Guha and Gaydon [111] converge, and the numerical results of a pure gas-phase solver (in this case, an in-house code called FROSH, see Appendix A) and AEROFROSH also converge. The difference between the analytical and numerical results at $C_m = 0$ is due to the gas-phase heat capacity being fixed in the former and transient in the latter solution methods. For the condition of maximum droplet loading, both Guha and AEROFROSH correctly predict that $T_2 = T_{2,sat}(P_2)$.

The second comparison with Guha's work, shown in Figure 4.5, examines the ratio of Region 2 to Region 1 temperature and pressure as predicted by Guha and by AEROFROSH for water droplet/vapor mixtures as a function of incident shock frozen Mach number. The plot is given for $C_m = y_1^G = 0.001$. While the results follow similar trends, Guha's predictions for post-shock temperature and pressure are consistently higher than the numerical values of AEROFROSH. This could be caused by a number of effects, including assumptions regarding constant heat capacity ratios and constant water enthalpy of vaporization values in temperature.

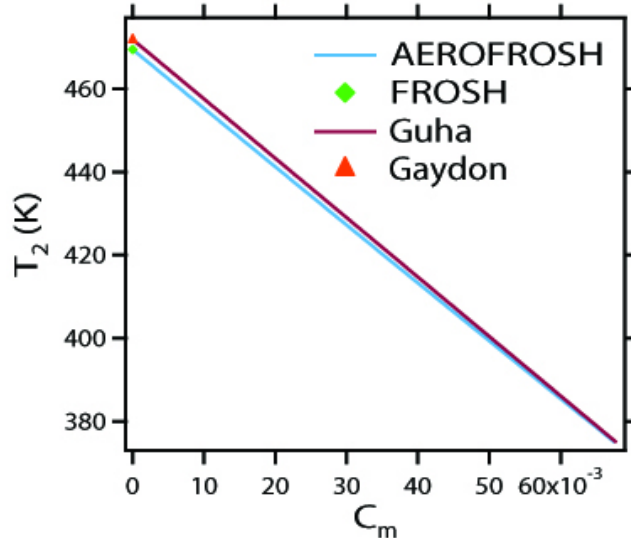


Figure 4.4: Duplication of Figure 4 in Guha [204]. Post-shock (Region 2) temperature in a water droplet/vapor mixture for constant pressure ratio $\frac{P_2}{P_1} = 3.0$ as a function of droplet loading C_m . Region 1 conditions are $T_1 = 74.8$ °C and $P_1 = 262.5$ Torr. When no droplets are present, the analytical results of Guha [204] and Gaydon [111] converge, as do the predictions of a pure gas-phase solver (FROSH, see Appendix A) and AEROFROSH. For maximum droplet loading while still maintaining complete droplet evaporation, Guha and AEROFROSH correctly predict that $T_2 = T_{2,sat}(P_2)$.

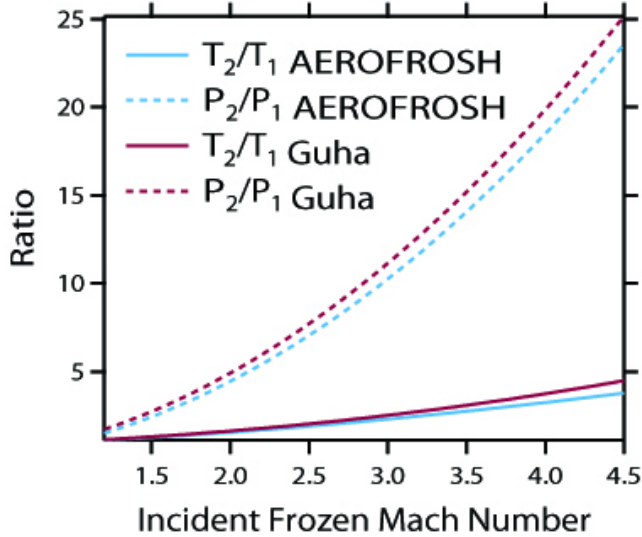


Figure 4.5: Duplication of Figure 7 in Guha [204]. Ratio of Region 2 to Region 1 temperature and pressure as a function of incident frozen Mach number in water droplet/vapor mixtures for the analytical results of Guha [204] and for AEROFRSH. Region 1 conditions are $T_1 = 66.4$ °C, $P_1 = 200$ Torr, and $C_m = 0.001$.

4.10 Results

AEROFRSH can be used to model the effect of droplet evaporation on the properties of a post-shock flow. Calculations have been performed for *n*-decane/21%O₂/Ar mixtures and for *n*-hexadecane/21%O₂/Ar mixtures, and the results are displayed in Figures 4.6 and 4.7 as a function of initial droplet volume fraction. As expected, temperature decreases during evaporation, while pressure and density increase. The extent of the temperature change predicted demonstrates the importance of accounting for the presence of droplets in the flow.

It is useful to examine the importance of a multi-component version of AEROFRSH by carrying out a practical example. Bax *et al.* studied stoichiometric 26% methyl oleate (MO)-74% *n*-decane (ND) by mole mixtures diluted in helium at 800 Torr and between 550 and 1000 K in a jet-stirred reactor [106]. This same fuel blend can be examined in a calculation for a hypothetical aerosol shock tube experiment in 10% oxygen (balance argon) to illustrate the importance of a multi-component calculation.

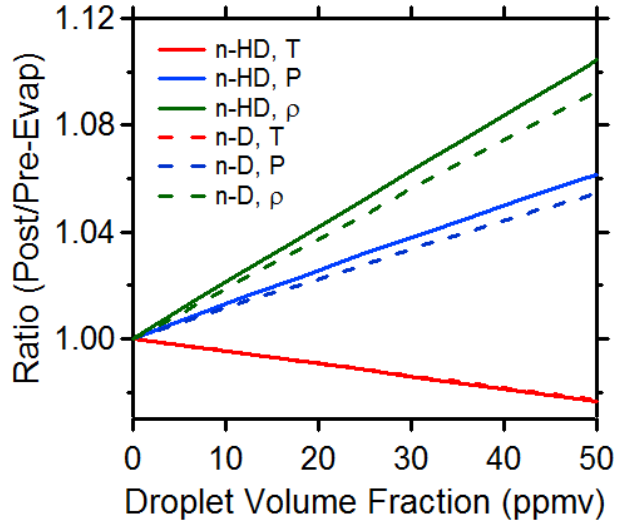


Figure 4.6: Ratio of post-to-pre-evaporation properties for *n*-decane/21%O₂/Ar mixtures and for *n*-hexadecane/21%O₂/Ar mixtures as a function of droplet volume fraction. Conditions: $U_{IS} = 800$ m/s; $M_{IS} \sim 1.88$; $T_1 = 300$ K; $P_1 = 1000$ Torr; $T_{2,i} \sim 541$ K; $P_{2,i} \sim 5.4$ atm; $T_5 \sim 800$ K; $P_5 \sim 16$ atm. At a fuel loading of $F_v = 50$ ppmv, the equivalence ratio for the *n*-decane mixture is approximately 0.5, and that for the *n*-hexadecane mixture is 0.4; the *n*-decane has a higher equivalence ratio despite being a smaller molecule because of its high vapor pressure.

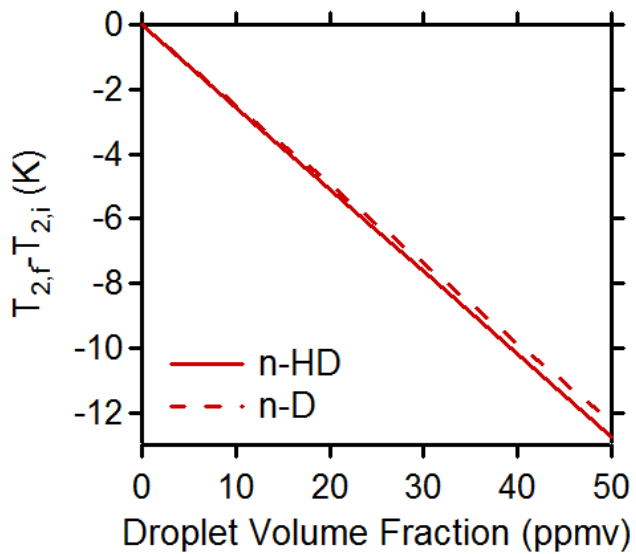


Figure 4.7: Temperature change as the result of evaporation in Region 2. Conditions are the same as those in Figure 4.6.

Consider a shock wave experiment with an incident shock velocity $U_{IS} = 700$ m/s, Region 1 temperature and pressure $T_1 = 22$ °C and $P_1 = 150$ Torr, and a Region 2 absorbance of $\alpha_2 = 0.7$. With these initial conditions, in order to yield Region 5 conditions of $T_5 = 1059$ K and $P_5 = 4.5$ atm with the same gas-phase fuel ratio as that studied by Bax *et al.* [106] ($\frac{x_{2,MO}}{x_{2,fuel}} = 0.26$, $\frac{x_{2,ND}}{x_{2,fuel}} = 0.74$), a liquid fuel mixture (by mole) of $y_{MO} = 0.62$ and $y_{ND} = 0.38$ would be required. This liquid-phase mixture is extremely different to the ultimate gas-phase mixture because the vapor pressures of MO and ND are so different; at 22 °C the first is about 4.2 microTorr while that of the second is 1.3 Torr. It is difficult to estimate the composition and equivalence ratio that would have been achieved had the liquid-phase mole fractions been $y_{MO} = 0.26$ and $y_{ND} = 0.74$ because the Region 2 absorbance experienced would also change, but a conservative estimate is that the gas-phase fuel mole fractions would be approximately $\frac{x_{2,MO}}{x_{2,fuel}} = 0.02$ and $\frac{x_{2,ND}}{x_{2,fuel}} = 0.98$, with a rich equivalence ratio of $\phi = 1.1$. This example demonstrates the importance of accurately accounting for the different properties of individual fuel components. Sample input data for the Bax *et al.* example are given in Table 4.1.

Table 4.1: Sample input data for AEROFROSH based on example discussed above of emulating experiments by Bax *et al.* [106]. $C_{19}H_{36}O_2$ is methyl oleate and $C_{10}H_{22}$ is *n*-decane.

Input	Variable	Units	Example
Incident shock velocity	U_{IS}	m/s	700
Region 1 temperature	T_1	K	295.15
Region 1 pressure	P_1	Torr	150
Bath gas species names			{'Ar', 'O ₂ '}
Bath gas mole fractions			[0.90, 0.10]
Liquid fuel species names			{'C ₁₉ H ₃₆ O ₂ ', 'C ₁₀ H ₂₂ '}
Liquid fuel mole fractions			[0.622, 0.378]
Fuel vapor pressure values	$P_{sat,fuel,j}$	Torr	[4.2×10 ⁻⁶ , 1.3]
Fuel density values	$\rho_{fuel,j}$	g/cm ³	[0.872, 0.730]
Fuel enthalpy values	$h_{fuel,j}$	J/kg	[-2.46×10 ⁶ , -2.13×10 ⁶]
Fuel abs. cross sect. polynoms.	a, b, c, d	m ² /mol	[1.38×10 ⁻⁷ , -4.08×10 ⁻⁴ , 0.34, -2.67; 0, -1.72×10 ⁻⁴ , 0.173, 3.63]
Region 2 fuel absorbance	α_2		0.700
Region 5 fuel absorbance	α_5		0.900
Optical path length	L	m	0.100

4.11 Uncertainty analysis

Uncertainty analyses are useful tools in determining accuracy of calculations. Typically these are conducted by changing input parameters and monitoring the change in important output results. Important inputs to AEROFROSH and their associated uncertainties are summarized in Table 4.2. For simplicity, heat capacity and enthalpy values from the NASA polynomials [122, 174] were assumed to change in the same direction (positive or negative) during one AEROFROSH temperature/pressure calculation. Temperature-dependent values of fuel density, vapor pressure, and enthalpy were computed only at the nominal Region 1 temperature, then modified by their associated uncertainties. Nominal Region 1 values used in this analysis were $T_1 = 300$ K, $P_1 = 200$ Torr, $U_{IS} = 800$ m/s, $\alpha_2 = 1.07$, $P_{sat,fuel} = 0.041$ Torr, $\rho_{fuel} = 0.87$ g/cm³, and $h_{fuel} = -3.5 \times 10^6$ J/kg [221–224]. The bath gas was 10%O₂/Ar, and the fuel was modeled as 100% pure methyl decanoate. These initial conditions produce incident fully-evaporated post-incident-shock conditions of $T_2 = 755$ K and $P_2 = 2.14$ atm, and post-reflected-shock conditions of $T_5 = 1311$ K and $P_5 = 9.13$ atm ($\phi = 1.0$). Errors in bath gas composition, contaminants in the fuel, and variations in shock tube optical path length were not considered.

Table 4.2: Inputs to AEROFROSH and typical values for associated uncertainty.

Input	Variable	Units	Uncertainty
Region 1 temperature	T_1	K	± 1.1 K
Region 1 pressure	P_1	Torr	± 0.15 %
Incident shock velocity	U_{IS}	m/s	± 0.5 %
NASA enthalpy	a_1-a_7	J/mol	± 0.5 %
NASA heat capacity	a_1-a_7	J/mol-K	± 0.5 %
Region 2 absorbance	α_2	(none)	± 2 %
Region 2 cross section polynomial	a, b, c, d	m ² /mol	± 8 %
Fuel vapor pressure	$P_{sat,fuel,j}$	Torr	± 5 %
Fuel density	$\rho_{fuel,j}$	g/cm ³	± 0.5 %
Fuel enthalpy	$h_{fuel,j}$	J/kg	± 0.3 %

The results of the uncertainty analysis on an input-by-input basis are shown graphically in Figures 4.8, 4.9, and 4.10. These plots show the error induced in the specified output by individually perturbing each input in the positive direction by the amount of its maximum uncertainty. Using these values, a Root-of-Sum-of-Squares (RSS) analysis was performed according to Equation 4.42

in order to determine the combined uncertainty (here, ε_{RSS} is the RSS uncertainty, $\frac{\Delta R_m}{R}$ is the fractional change in the output result when input m is varied in the positive direction, and N is the number of inputs (in this case, $N = 9$)). In addition, results for all combinations of the input variables, perturbed in both positive and negative directions for a total of $2^9 = 512$ trials, were computed using an automated routine in order to determine the worst-case uncertainty. The results are provided in Table 4.3 for T_2 , P_2 , T_5 , P_5 , and ϕ . As expected, the worst-case uncertainty values are larger than those for the RSS analysis, since the RSS analysis does not consider second-order interactions between the input variables. Major contributors to T_5 uncertainty (RSS: $\pm 1.03\%$ overall) are U_{IS} ($\pm 0.82\%$), $\sigma_{2,fuel}$ ($\pm 0.51\%$), and the thermodynamic data (c_p and h ; $\pm 0.30\%$). For ϕ , the major contributors to uncertainty are $\sigma_{2,fuel}$ ($\pm 6.09\%$) and α_2 ($\pm 1.62\%$). Note that when thermodynamic polynomial data from the Burcat database [174] are employed, the actual uncertainty of the fits are specified therein, and are often much lower than the conservative 0.5% used in this analysis. Furthermore, if more precise shock velocity determination techniques are employed, the temperature errors decrease still further. In summary, this uncertainty analysis shows that Region 2 and 5 conditions can be computed with a good degree of accuracy, despite conservative estimates as to the uncertainty of AEROFROSH input data.

$$\varepsilon_{RSS} = \sqrt{\sum_{m=1}^N \left(\frac{\Delta R_m}{R} \right)^2} \quad (4.42)$$

Table 4.3: Results of AEROFROSH uncertainty analysis. The Root-of-Sum-of-Squares (RSS) analysis was conducted according to Equation 4.42, and the worst case analysis was conducted by perturbing all inputs simultaneously to find the maximum change in the output variable. Conditions: $T_2 = 755$ K, $P_2 = 2.14$ atm, $T_5 = 1311$ K, $P_5 = 9.13$ atm, methyl decanoate/10%O₂/Ar ($\phi = 1.0$).

Output Variable	Nominal Value	Root-of-Sum-of-Squares		Worst Case	
		%	Value	%	Value
T_2	755 K	$\pm 0.78\%$	± 5.873 K	$\pm 1.43\%$	± 10.80 K
P_2	2.14 atm	$\pm 1.20\%$	± 0.026 atm	$\pm 2.27\%$	± 0.049 atm
T_5	1311 K	$\pm 1.03\%$	± 13.44 K	$\pm 1.83\%$	± 23.97 K
P_5	9.13 atm	$\pm 1.87\%$	± 0.171 atm	$\pm 3.71\%$	± 0.339 atm
ϕ	1.00	$\pm 6.33\%$	± 0.063	$\pm 9.12\%$	± 0.091

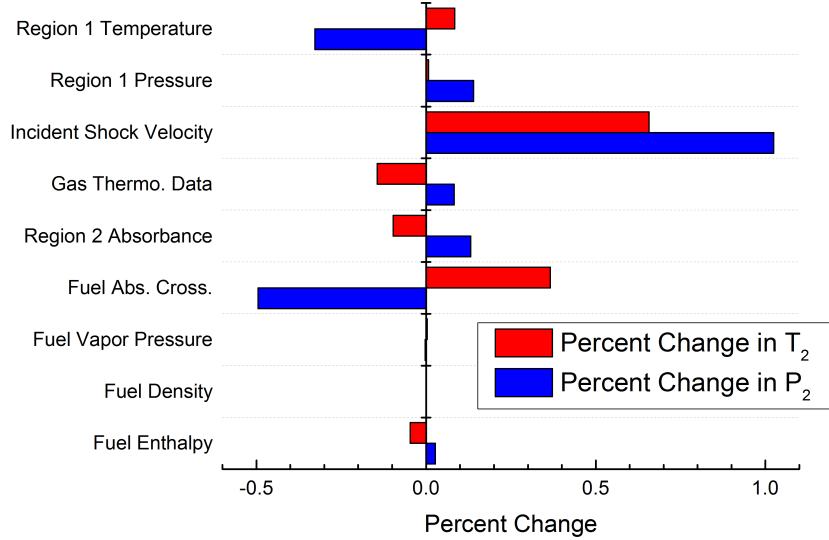


Figure 4.8: Results of AEROFROSH uncertainty analysis for T_2 and P_2 . Errors are shown for the case when the input listed is perturbed in the *positive* direction. Conditions: $T_2 = 755$ K, $P_2 = 2.14$ atm, $T_5 = 1311$ K, $P_5 = 9.13$ atm, methyl decanoate/10%O₂/Ar ($\phi = 1.0$).

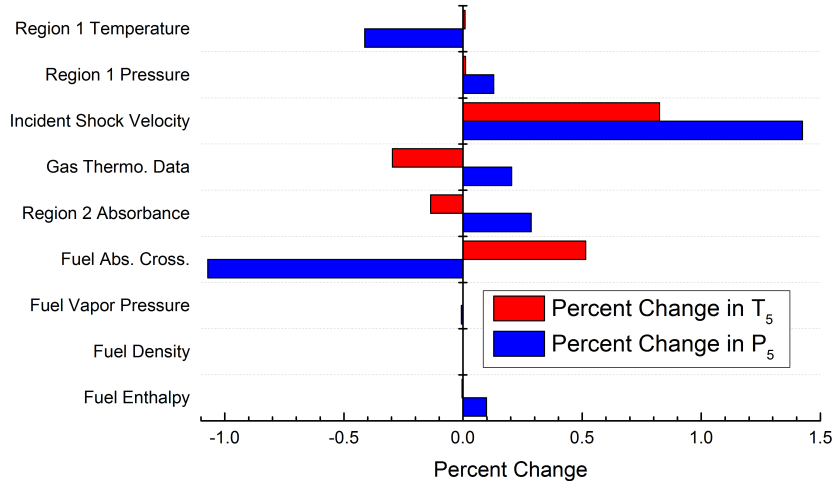


Figure 4.9: Results of AEROFROSH uncertainty analysis for T_5 and P_5 . Errors are shown for the case when the input listed is perturbed in the *positive* direction. Conditions: $T_2 = 755$ K, $P_2 = 2.14$ atm, $T_5 = 1311$ K, $P_5 = 9.13$ atm, methyl decanoate/10%O₂/Ar ($\phi = 1.0$).

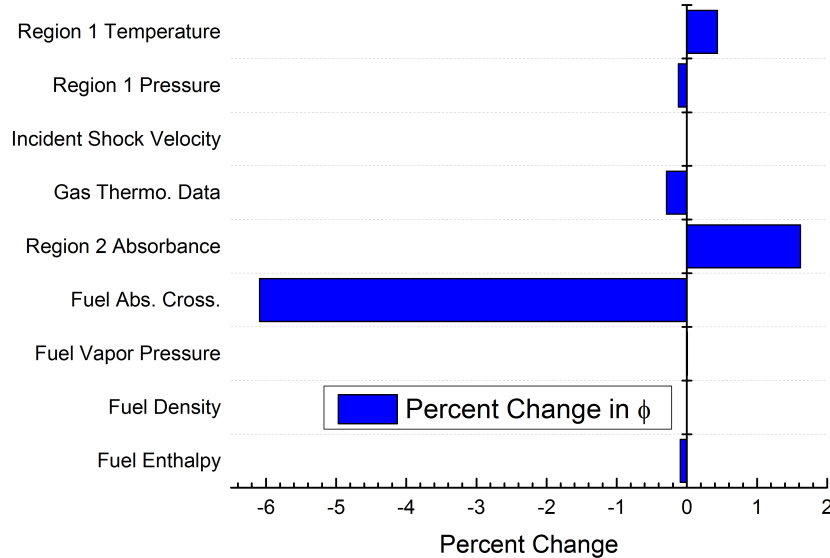


Figure 4.10: Results of AEROFROSH uncertainty analysis for ϕ . Errors are shown for the case when the input listed is perturbed in the *positive* direction. Conditions: $T_2 = 755$ K, $P_2 = 2.14$ atm, $T_5 = 1311$ K, $P_5 = 9.13$ atm, methyl decanoate/10%O₂/Ar ($\phi = 1.0$).

4.12 Summary

A shock calculator for gaseous flows, AEROFROSH, has been introduced. Adaptations for the multi-component fuel version of AEROFROSH have been also been shown. Validation based on previous numerical and analytical studies has been demonstrated, and multiple experimental studies that have validated post-shock temperature and pressure values calculated using the algorithm have been cited. An error analysis of the program shows that even with conservative estimates of input uncertainty, post-shock conditions can be computed with a good degree of accuracy. This code should prove useful for scientists wishing to perform accurate calculations of post-shock conditions for studies of kinetics and combustion in aerosols.

Chapter 5

Spectroscopy of fatty acid methyl esters

*The contents of this chapter have been published in the **Journal of Quantitative Spectroscopy and Radiative Transfer (JQSRT)** [176].*

5.1 Introduction of FAME infrared spectroscopy

Optical, non-invasive diagnostics for quantitative fuel sensing in combustion applications such as scramjets and diesel engines have become important analysis tools in the testing and improvement of advanced propulsion systems [118]. As such, optically probing the mid-InfraRed (mid-IR) C–H stretch feature ($2500\text{--}3400\text{ cm}^{-1}$) has gained special attention as a method of detecting fuel molecules, since many fuels of practical importance are hydrocarbons. In order to make quantitative spectroscopic measurements of gas-phase fuel concentration, the absorption cross section of each fuel (σ), which specifies how much light is absorbed by one mole of a particular molecule per meter of absorbing distance, must be well-characterized. Specifically, cross section values at $3.39\text{ }\mu\text{m}$ (more precisely, $3.392235\text{ }\mu\text{m}$ or 2947.909 cm^{-1}), corresponding to the monochromatic output of a helium-neon (HeNe) laser, are of special importance due to the prevalence and simplicity of this specific laser diagnostic technique [225–229].

One particular class of hydrocarbons that is being considered for its renewable aspects is Fatty Acid Methyl Esters (FAMEs), which are a primary component of biodiesel fuel [12, 31, 230]. These molecules consist of a long hydrocarbon chain ending in an ester group $\text{O}=\text{C}-\text{O}-\text{CH}_3$. FAMEs

can be either saturated or unsaturated. While normal alkanes and 1-alkenes have been extensively studied (see References [175, 225–227, 231–233] and references therein), according to a recent literature review, no quantitative data exist for gas-phase mid-IR cross sections of FAMEs at temperatures above 50 °C. Cross section data at elevated temperatures are important for diagnostic use in heated shock tubes [128], aerosol shock tubes [68, 105, 218], internal combustion engines [234–237], pulse detonation engines [238], and other combustion reactors.

A disadvantage to studying FAMEs compared to most normal alkanes and alkenes is that FAMEs have very low vapor pressures and fast decomposition rates. This inhibits high-temperature study of the large FAMEs actually present in biodiesel fuel (such as methyl stearate, C₁₉H₃₈O₂) in the gas phase due to the long experimental times required for spectroscopic study over the full (2500–3400 cm⁻¹) C–H stretch IR spectrum. Instead, extrapolations of cross sections for large FAMEs must be made based on available data for smaller and medium-sized FAMEs. Models to predict cross section values of hydrocarbon molecules by extrapolation based on similar geometric features and trends in temperature dependence have been proposed previously [227, 239, 240]. In particular, the model of Mével *et al.* [227] employs a linear additive extrapolation method for predicting the 3.39 μm HeNe cross section (up to $T = 140$ °C), which was shown to work well for small and mid-sized hydrocarbons (Equation 5.1, with $\sigma_{\text{alkane}} = 2.70 \text{ m}^2/\text{mol}$ and N_{CH} being the number of C–H bonds in the molecule). Unfortunately, this model only approximately captures the trends seen in normal alkane 3.39 μm cross section data for molecules larger than those observed in the Mével *et al.* study (Figure 5.1).

$$\sigma_{Mével} = N_{\text{CH}}\sigma_{\text{alkane}} \quad (5.1)$$

Based on the above discussion, there is a clear need to expand the current knowledge base of mid-IR hydrocarbon fuel spectra to include FAME data. Moreover, an updated prediction model is needed to enable extrapolation of 3.39 μm cross section data for small and medium-sized FAMEs to larger molecular sizes, including those of actual biodiesel components. Therefore, the gas-phase mid-infrared absorption spectra of eleven FAMEs have been quantitatively measured between 25 °C

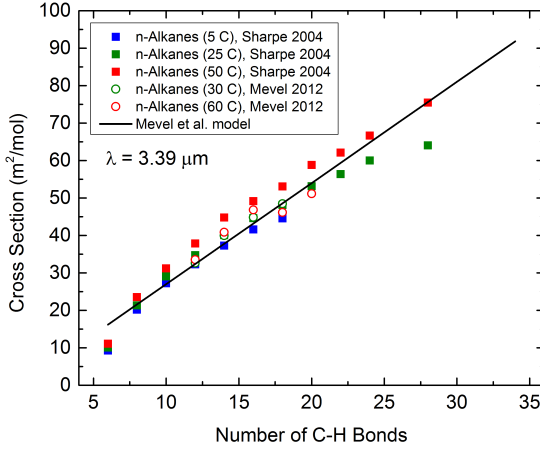


Figure 5.1: Comparison of $3.39 \mu\text{m}$ cross section data from Sharpe *et al.* [175] and Mével *et al.* [227] with the Mével linear extrapolation model.

and 500°C using a Fourier Transform InfraRed (FTIR) spectrometer with a resolution of 1 cm^{-1} . These FAMEs, shown in Figure 5.2 and detailed in Table 5.1, include nine fully-saturated compounds: methyl acetate (MA, $\text{C}_3\text{H}_6\text{O}_2$), methyl propionate (MPI, $\text{C}_4\text{H}_8\text{O}_2$), methyl butanoate (MB, $\text{C}_5\text{H}_{10}\text{O}_2$), methyl valerate (MV, $\text{C}_6\text{H}_{12}\text{O}_2$), methyl hexanoate (MH, $\text{C}_7\text{H}_{14}\text{O}_2$), methyl heptanoate (MHP, $\text{C}_8\text{H}_{16}\text{O}_2$), methyl octanoate (MOC, $\text{C}_9\text{H}_{18}\text{O}_2$), methyl nonanoate (MN, $\text{C}_{10}\text{H}_{20}\text{O}_2$), and methyl decanoate (MD, $\text{C}_{11}\text{H}_{22}\text{O}_2$); and two mono-unsaturated compounds: methyl crotonate (MC, $\text{C}_5\text{H}_8\text{O}_2$) and methyl-3-nonenate (M3N, $\text{C}_{10}\text{H}_{18}\text{O}_2$). Furthermore, using these spectra, the absorption cross section at $3.39 \mu\text{m}$ has been determined for these fuels as a function of temperature. Finally, a new extrapolation method for estimating the cross sections of large linear hydrocarbons has been developed using an empirical relationship between the $3.39 \mu\text{m}$ cross section and the logarithm of the number of C–H bonds in the molecule.

5.2 Experimental setup

The full experimental setup employed in this study is very similar to that which was used and described in detail by Klingbeil *et al.* in the High Temperature Gasdynamics Laboratory (HTGL) at

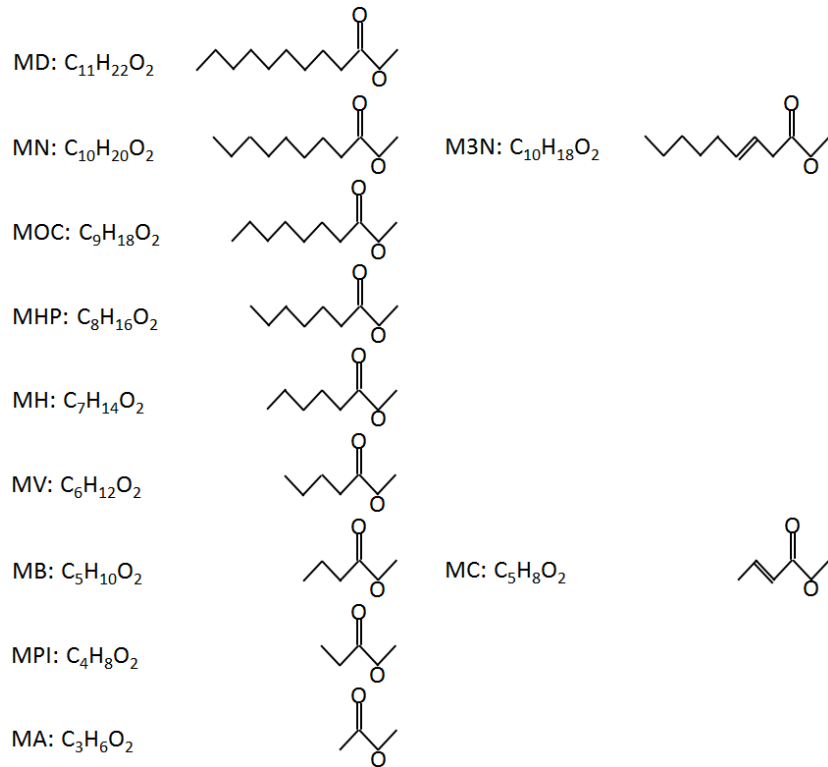


Figure 5.2: Molecular diagrams of FAMEs examined in this study. Fully saturated FAMEs are shown on the left, and mono-unsaturated FAMEs are displayed on the right next to their saturated counterparts.

Table 5.1: Properties and purity of fuels studied. Vapor pressure information is taken from Reference [222].

Fuel	Abbreviation	Formula	Molecular Weight [g/mol]	Vapor Pressure at 100 °C [Torr]	Purity [%]
Methyl acetate	MA	$\text{C}_3\text{H}_6\text{O}_2$	74.1	2814.8	99.87
Methyl propionate	MP	$\text{C}_4\text{H}_8\text{O}_2$	88.1	1425.1	99.99
Methyl butanoate	MB	$\text{C}_5\text{H}_{10}\text{O}_2$	102.1	698.0	99.7
Methyl valerate	MV	$\text{C}_6\text{H}_{12}\text{O}_2$	116.2	316.1	99.99
Methyl hexanoate	MH	$\text{C}_7\text{H}_{14}\text{O}_2$	130.2	148.1	99.9
Methyl heptanoate	MHP	$\text{C}_8\text{H}_{16}\text{O}_2$	144.2	56.9	99.8
Methyl octanoate	MOC	$\text{C}_9\text{H}_{18}\text{O}_2$	158.2	33.9	99.9
Methyl nonanoate	MN	$\text{C}_{10}\text{H}_{20}\text{O}_2$	172.3	17.4	98.8
Methyl decanoate	MD	$\text{C}_{11}\text{H}_{22}\text{O}_2$	186.3	6.5	99.7
Methyl crotonate	MC	$\text{C}_5\text{H}_8\text{O}_2$	100.1		99.4
Methyl 3-nonenanoate	M3N	$\text{C}_{10}\text{H}_{18}\text{O}_2$	170.2		99.2

Stanford [225, 241]; hence, only a brief overview of this setup will be presented here. Figure 5.3 is a schematic of the apparatus.

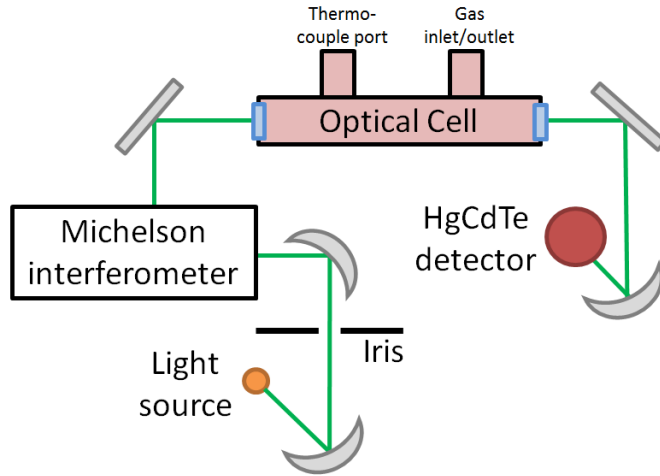


Figure 5.3: Experimental setup for FTIR measurements in a heated static cell. Figure adapted from Reference [225].

Measurements were performed using a Nicolet model 6700 FTIR spectrometer with moderate (1 cm^{-1}) resolution. This assembly was equipped with an XT-KBr beam splitter, IR light source, and HgCdTe detector. In this arrangement, radiation exited the light source, was focused through an iris, was collimated, passed through a Michelson interferometer that resulted in wavelength modulation, and passed through the heated optical cell. Light emerging from the cell was collected and focused onto the detector. The short path length employed by this setup minimized interference from atmospheric water and carbon dioxide in the frequency range studied ($2500\text{-}3400 \text{ cm}^{-1}$) and thus negated the need for spectral subtraction of ambient interference. Small corrections (in most cases $<0.5 \text{ m}^2/\text{mol}$) were applied to the observed spectra in order to negate a finite DC-offset and achieve a zero-baseline at the extremes of the spectra (near 2500 cm^{-1} and near 3400 cm^{-1}); these artifacts may have been associated with pressure-induced stresses on the windows of the cell. Measurements were conducted using Mertz phase correction and a boxcar apodization function.

With the exception of MV at 25°C , MN at 400°C , and MHP at 400°C , at least two samples of each fuel were tested at each temperature, and results were averaged to produce one aggregated

scan at each temperature. For each sample, three measurements consisting of either 25 scans (at low temperatures) or 5 scans (at high temperatures, with fewer scans to avoid decomposition) were conducted. Comparison of the three measurements in each sample gave insight as to whether the fuel was decomposing and verified experimental repeatability, while comparison of different samples provided corroboration that the correct mixture had been obtained. Moreover, averaging several measurements resulted in a higher Signal-to-Noise Ratio (SNR) for each reported spectrum. Measurements consisting of 25 scans lasted approximately 1 minute (for a total in-cell gas test time of 3 minutes per sample), and measurements consisting of 5 scans lasted approximately 20 seconds (for a total in-cell gas test time about 60 seconds per sample). Before introducing the sample to the optical cell, a baseline intensity measurement was recorded in the evacuated cell. Finally, after the three measurements were recorded for the sample, the cell was evacuated and a second baseline intensity measurement was recorded. Measuring the baseline before and after the sample measurements allowed the intensity drift of the light source to be quantified.

The optical cell used in this study had a path length of 20.95 cm and employed stainless steel construction with copper gaskets. Windows were made from sapphire, which exhibits high transmission over the frequency range studied (>80%) at the temperatures of interest in this work [242]. An oven was specially modified to completely enclose the cell, perform uniform heating, and allow optical access through open ports. Convection through these open oven window ports resulted in a temperature drop of the cell wall of approximately 10 K near the cell windows. Prior to entering the cell, the gas was made to flow through a 20-cm coiled tube inside the oven in order to ensure complete and uniform heating. A K-type thermocouple inside the cell was used to measure gas temperature, and this value was corroborated by the oven set-point temperature. Pressure in the cell was continuously monitored using a low-pressure Baratron (MKS 628B) and/or a high-pressure Setra Systems transducer (Setra 280E). In order to reduce uncertainty in cell pressure, a static cell technique such as that employed in References [128, 225, 227] was employed (rather than a flow-type cell as in References [226, 243]).

Preparation of gas-phase fuel samples in the mixing manifold adjacent to the oven was accomplished using three different techniques. First, for MA, MPI, MB, and MC, fuel vaporization was achieved by direct evaporation from a fuel flask attached to the manifold. This fuel flowed into

a stainless steel mixing tank with a magnetically actuated stirring system that was maintained at approximately 100 °C. Nitrogen (99.99%, Praxair Inc.) was then added to achieve a pressure exceeding 1000 Torr and a fuel mole fraction of ~0.2-0.5%. The resulting mixture was allowed to stir for at least 10 minutes prior to experimentation, at which point it was introduced into the optical cell at a pressure of 1 atm; a fixed pressure was chosen to remove possible pressure dependencies exhibited by these small fuels. Second, for MV and MH, which have high vapor pressures but whose spectra at the conditions observed are not pressure-dependent, fuel was evaporated directly from the fuel flask into the manifold and optical cell. Third, for MHP, MOC, MN, MD, and M3N, which have low vapor pressures, fuel was injected directly into the mixing tank using a Suba-Seal Rubber Septa injection system. The leak rate (of air) through this injection system was measured to be 0.006 Torr/minute, which was considered small for the 10-second fuel injection time required. Fuels were allowed to evaporate in the mixing tank for at least 10 minutes prior to being introduced to the manifold and optical cell. Prior to evaporation or fuel injection, the entire rig was evacuated to pressure less than 0.010 Torr (as measured using the Baratron transducer) by way of a mechanical pump (pump oil was changed between fuels). Furthermore, fuels evaporated from fuel flasks were subjected to freeze-pump-thaw cycles to remove dissolved air, but were otherwise used without further purification. Fuel purity information is provided in Table 5.1. All fuels in this study were supplied by Sigma-Aldrich Corp.

5.3 Data reduction

The ratio of incident to transmitted light in a gaseous absorbing medium is related to the concentration of that medium by the Beer-Lambert relation (Equation 5.2; see also Equations 3.1, 4.11, 8.4, and 9.1). In this equation, α is called the absorbance, I is the transmitted light intensity, I_o is the incident light intensity, n is the concentration [mol/m³] of the absorbing species, x_f is the fuel mole fraction, P is the total gas pressure [Pa], $\hat{R}_u = 8.3144621 \frac{\text{Pa}\cdot\text{m}^3}{\text{mol}\cdot\text{K}}$ is the ideal gas constant [244, 245], T is the gas temperature [K], $\sigma_{\nu,T}$ is the temperature-dependent absorption cross section [m²/mol] at frequency ν , and L is the optical path length [m]. By measuring α and n for a known L and T , the cross section $\sigma_{\nu,T}$ can be determined. Peak absorbance values for these measurements typically

ranged from $\alpha = 0.03$ to $\alpha = 0.50$.

$$\alpha = -\ln\left(\frac{I}{I_o}\right) = n\sigma_{\nu,T}L = \frac{x_f P}{\hat{R}_u T} \sigma_{\nu,T} L \quad (5.2)$$

As thoroughly described by References [226, 246–249], the IR C–H absorption band is the result of rovibrational transitions in which molecules undergo simultaneous rotational and vibrational quantum number changes while absorbing radiation. Since the C–H rotational energy level spacing is small ($\sim 1 \text{ cm}^{-1}$), the population of molecules in excited rotational levels increases significantly as the temperature is increased above standard conditions; this causes the overall rovibrational feature to broaden. However, the C–H vibrational energy level spacing is much larger ($\sim 3000 \text{ cm}^{-1}$), such that at the temperatures of interest in this study (25–500 °C), thermodynamic equilibrium dictates that the fractional population in the ground vibrational state remains approximately constant. This yields the useful result that integrating the frequency-dependent cross section over the entire absorption feature (in this case, from 2500 to 3400 cm^{-1}) produces a value (termed the integrated area, $\Psi [\text{cm}^{-1}\text{cm}^2\text{mol}^{-1}]$), which is very nearly constant with temperature (Equation 5.3; note that the term $\frac{\hat{R}_u T}{x_f P L}$ is not temperature-dependent because for a given gas molar concentration, the ratio $\frac{T}{P}$ is constant).

$$\Psi = \int_{\text{C-H band}} \sigma_{\nu,T} d\nu = \int_{\text{C-H band}} \frac{\alpha \hat{R}_u T}{x_f P L} d\nu = \frac{\hat{R}_u T}{x_f P L} \int_{\text{C-H band}} \alpha d\nu \neq f(T) \quad (5.3)$$

The constant integrated area property at the conditions of interest is advantageous because it allows the manometrically derived mole fraction of fuel $x_f^{\text{manometric}}$ and the computed (observed) cross section $\sigma_{\nu,T}^{\text{observed}}$ to be corrected in the case of fuel condensation, fuel adsorption/desorption to/from cell walls, contaminant adsorption/desorption to/from cell walls, or moderate (<15%) fuel decomposition. Specifically, Ψ is proportional to $\sigma_{\nu,T}$ and inversely proportional to x_f . Thus, if the true integrated area Ψ_{true} is known based on experiments in which condensation, absorption, desorption, and decomposition are absent, the true cross section $\sigma_{\nu,T}^{\text{true}}$ and true mole fraction x_f^{true} may be computed from the observed cross section $\sigma_{\nu,T}^{\text{observed}}$ and $x_f^{\text{manometric}}$ using Equation 5.4. The cross sections and spectra reported in this study have been corrected according to this technique,

using the integrated area values (averaged over several conditions) reported in Table 5.5.

$$\frac{\Psi_{true}}{\Psi_{observed}} = \frac{x_f^{manometric}}{x_f^{true}} = \frac{\sigma_{\nu,T}^{true}}{\sigma_{\nu,T}^{observed}} \quad (5.4)$$

It should be noted that in the case of fuel decomposition, fragment molecules may still absorb light and contribute to the overall C–H absorption spectrum. However, the combined contribution of these products will be small if the fuel’s mole fraction is still close to its original value (within 15%). Furthermore, features of smaller molecules (for instance, methane) will begin to show in other parts of the spectrum if these molecules are present in sufficient quantity [226]. Since in these experiments no features of other smaller species could be found, it was concluded that decomposition was sufficiently small to allow integrated area compensation to be done.

A sensitivity analysis was performed according to Equation 5.5 to estimate the error in these cross section measurements. In general, the measurement temperature and mixture composition were found to be the primary sources of error. Uncertainty values for the 3.39 μm cross section values of MA are generally less than 15%, those for MPI <4%; those for MB and MV <6%; those for MH <3%; those for MHP, MOC, and MN <4%; for MD <5%; for MC <7%, and for M3N <4%. Uncertainties at low and high temperatures are slightly larger due to uncertainty in fuel concentration as a result of condensation and decomposition, respectively. Values for integrated area were within 2% of the average value at most conditions, varying to within 15% in the case of the most extreme fuel decomposition (MHP and MOC at 400 °C). The reproducibility of this data is generally within the calculated uncertainty.

$$\frac{\Delta\sigma}{\sigma} = \sqrt{\left(\frac{\Delta T}{T}\right)^2 + \left(\frac{\Delta x_f}{x_f}\right)^2 + \left(\frac{\Delta P}{P}\right)^2 + \left(\frac{\Delta L}{L}\right)^2 + \left(\frac{\Delta I}{I} \frac{1}{\ln\left(\frac{I}{I_o}\right)}\right)^2 + \left(\frac{\Delta I_o}{I_o} \frac{1}{\ln\left(\frac{I}{I_o}\right)}\right)^2} \quad (5.5)$$

5.4 Results

5.4.1 Pressure dependence

Spectra for MA, MPI, MB, MV, MH, MHP, MOC, MN, MD, MC, and M3N were measured with 1 cm^{-1} spectral resolution between 2500 and 3400 cm^{-1} at temperatures ranging from $25\text{ }^{\circ}\text{C}$ to $500\text{ }^{\circ}\text{C}$. Since the spectra/ $3.39\text{ }\mu\text{m}$ cross section values of small hydrocarbons are often pressure-dependent [225, 226], MA, MPI, MB, and MC were measured at 1 atm by dilution in nitrogen. The spectra of molecules the size of and larger than MV were found to be independent of pressure (for instance, the measured spectra of MV at 1.2 Torr (pure fuel) and 757 Torr (by N_2 dilution) are identical; see Figure 5.4); thus, spectra of molecules the size of and larger than MV were measured at low pressure without dilution.

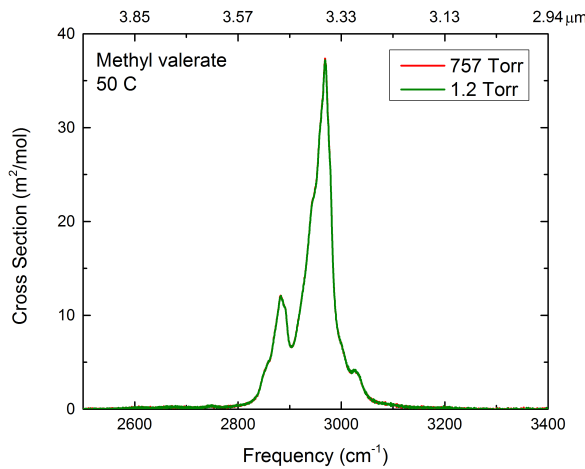


Figure 5.4: Comparison of spectra for methyl valerate at $50\text{ }^{\circ}\text{C}$ at 1.2 Torr (pure fuel) and at 757 Torr (diluted in nitrogen with a partial pressure of 0.98 Torr).

5.4.2 Concentration dependence

In order to quantify the effects of fuel concentration on the data, spectra of methyl acetate were measured at partial pressures of 3.8 Torr, 5.8 Torr, 9.9 Torr, and 50.0 Torr by dilution in nitrogen at

an overall pressure of 1 atm. The spectra at 3.8, 5.8, and 9.9 Torr agree closely, while that taken at 50.0 Torr agrees to within 10% of the other spectra (see Figure 5.5). This variation can be attributed to differences in the pressure measurement schemes used in the different experiments: a capacitance manometer (Baratron) was used below 20 Torr and a silicon sensor (Setra Systems) was used above 20 Torr. Based on these measurements, it was concluded that for the measurements performed, the observed spectra were not significantly dependent on fuel concentration.

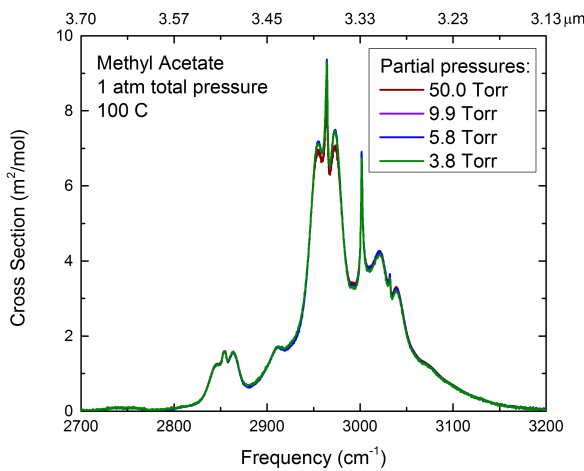


Figure 5.5: Spectrum of methyl acetate at 100 °C and fuel partial pressures of 3.8, 5.8, 9.9, and 50.0 Torr.

5.4.3 Instrument resolution dependence

The spectrum for methyl acetate was measured using high sensitivity settings (100 averaged scans at 0.1 cm^{-1} resolution) at $25\text{ }^{\circ}\text{C}$ and 1 atm; this spectrum was then compared with another measurement at lower resolution (25 averaged scans at 1 cm^{-1} resolution) taken at the same temperature and pressure in order to quantify the effects of instrument broadening (Figure 5.6). At these conditions, the spectrum of MA exhibits fine structures, especially at 2964 cm^{-1} and 3002 cm^{-1} , which can be used to gage whether instrument broadening is occurring. Since the spectra measured using the fine and coarse resolutions yielded identical spectra even in these fine features, it

was concluded that 1.0 cm^{-1} resolution was sufficient for these measurements. Using a lower resolution decreases the in-cell measurement time and errors associated with decomposition and/or condensation.

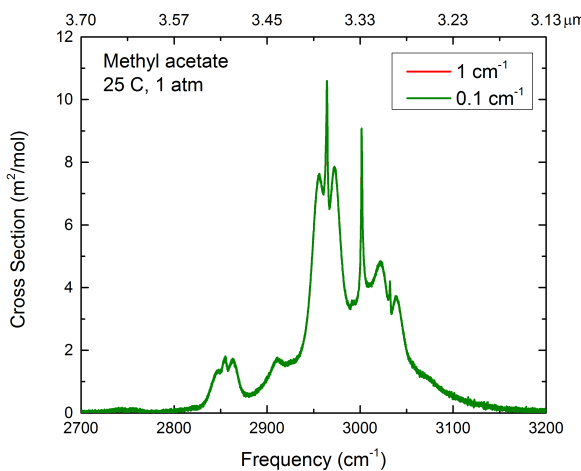


Figure 5.6: Spectrum of methyl acetate at $25\text{ }^{\circ}\text{C}$ and 1 atm, measured using instrument resolutions of 0.1 cm^{-1} and 1.0 cm^{-1} .

Recall that each spectrum is actually the averaged result of several scans measured using the FTIR. Using a greater number of scans results in a higher signal-to-noise ratio, but requires a longer measurement interval during which fuel condensation and/or decomposition can occur. In order to ensure that the number of scans did not affect the measured data, the spectrum of methyl acetate was measured at $100\text{ }^{\circ}\text{C}$ and 1 atm using 5, 10, 25, and 50 scans with 1 cm^{-1} resolution. As expected, as the number of scans increases, the signal-to-noise ratio was found to decrease; however, the overall spectrum exhibited the same features and shape.

5.4.4 Emission by fuels and by heated cell

Other researchers have used FTIR spectrometers to measure emission by hot samples [250–254]. In order to ensure that emission from the hot optical cell components and gaseous fuel was insignificant in these absorption experiments, measurements were taken between 2400 cm^{-1} and

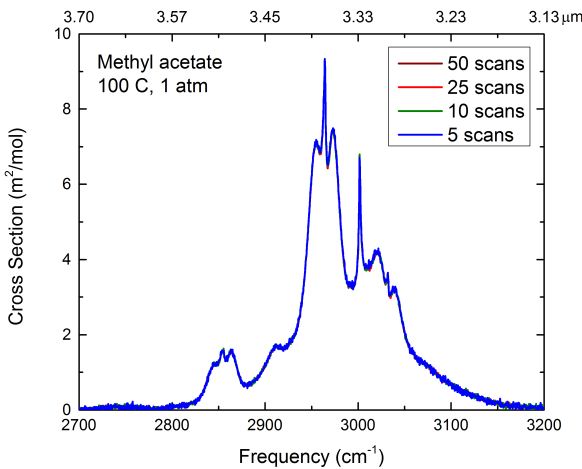


Figure 5.7: Spectrum of methyl acetate at 100 °C and 1 atm, measured with 5, 10, 25, and 50 scans.

3400 cm⁻¹ at 100, 200, 300, 400, and 500 °C with the infrared light source blocked. To observe emission from the cell components alone, the cell was evacuated and the infrared light source blocked while the frequency range 2400-3400 cm⁻¹ was probed. To observe emission from the gaseous fuel, the cell was filled to typical pressures of these experiments (2-3 Torr) with neat MV and the same frequency range was again probed with the light source blocked. Experiments were also conducted with normal heptane (C₇H₁₆), a representative alkane fuel. Emission was not observed in any of these experiments (the detector signal was negligible in the entire spectral range), confirming that the spectra reported herein represent pure absorption measurements. The lack of observed emission can be attributed in part to the optical geometry employed in the apparatus; in order to observe emission, past researchers have employed special collection optics such as large ellipsoidal mirrors [250–254]. Also, these findings confirm predictions by other researchers, that at low temperatures, the adverse effects of fuel emission are not problematic for FTIR measurements in the frequency range of interest (2400-3400 cm⁻¹) at the reported resolution (1 cm⁻¹) [255].

5.4.5 Evidence of condensation

Pressure within the cell was measured as a function of time for a pure methyl heptanoate sample at 100 °C in order to determine the extent of condensation occurring in the test cell (Figure 5.8). Measured cell pressure exhibited a sharp decrease during the first minute then stabilized over time; the total pressure drop across the 10-minute trial was 0.27 Torr, or 6.5%. The spectra measured when the fuel was first introduced to the cell and after 10 minutes agree to within 1%.

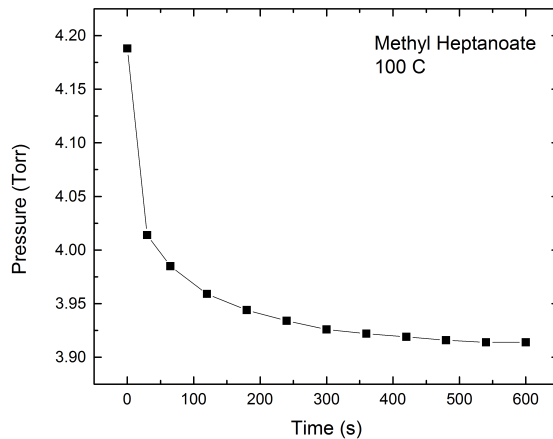


Figure 5.8: Cell pressure for methyl heptanoate at 100 °C, showing condensation.

In order to account for observed pressure changes during fuel measurements, the pressure values before and after each 25-scan (~60 seconds) or 5-scan (~20 seconds) measurement were averaged to determine a mean pressure for the trial. This mean pressure was then used to compute the reported absorption cross section value and the integrated area value. Also, in some cases, more than three measurements (each consisting of either 25 or 5 scans) per sample were taken if measurements performed immediately after filling the optical cell exhibited large changes in pressure.

5.4.6 Decomposition study

As described above, the constant integrated area property of the C–H stretch absorption feature can be used to correct measured cross section values in the case of mild (up to $\sim 15\%$) decomposition according to Equation 5.4. In order to demonstrate this, the spectrum of methyl heptanoate was measured at 60 second intervals for approximately 20 minutes, holding a cell temperature of $350\text{ }^{\circ}\text{C}$; fuel pressure in the cell was also recorded. The results of this experiment are shown in Figure 5.9, which depicts both the unscaled cross section at $3.39\text{ }\mu\text{m}$, the scaled cross section at this wavelength, and the fuel pressure. Notice that initially the fuel pressure drops (this can be attributed to condensation of fuel on the cell/manifold walls), but around 175 seconds it begins to increase (this can be attributed to an increase in number of moles in the cell as MHP decomposition occurs). While the unscaled cross section falls, the corrected cross section, compensated using the integrated area measured at time zero, remains approximately constant for the duration. At the end of the experiment, the fuel mole fraction was computed to be approximately 85%. This gives confidence to the integrated area compensation method employed in this study.

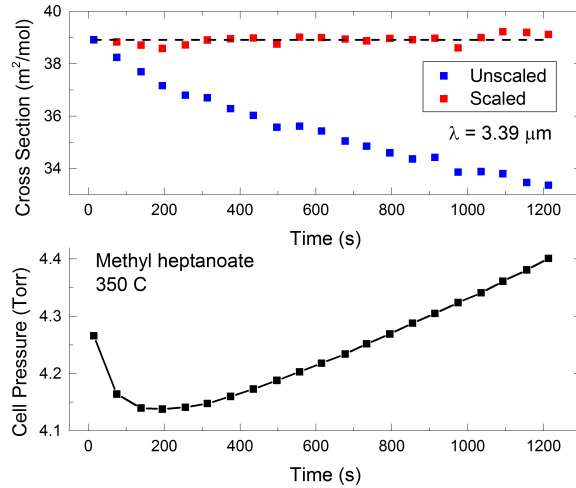


Figure 5.9: Decomposition of methyl heptanoate at $350\text{ }^{\circ}\text{C}$. The top graphic shows the scaled and unscaled cross section values at $3.39\text{ }\mu\text{m}$, and the bottom graphic depicts the cell pressure as a function of time.

5.4.7 Comparison with PNNL

The Pacific Northwest National Laboratory (PNNL) uses an FTIR experimental rig that is similar to that at Stanford University, allowing researchers there to make ultra-high-purity measurements of the cross sections of many species with 0.1 cm^{-1} resolution at atmospheric pressure [175, 231–233]. Comparisons were performed of the spectra from this study of MA at 25 °C and 50 °C and 1 atm (Figure 5.10), the spectra of MPI at 25 °C and 50 °C and 1 atm (Figure 5.11), and the spectrum of MB at 25 °C and 1 atm (Figure 5.12) to those measured by PNNL. In general, agreement between the measurements is excellent; however, in some cases the spectra (cross section values) agree to within a scaling factor difference of ~10%. Note that since the spectra observed were resolvable even with 1 cm^{-1} resolution (see Section 5.4.3), the differences between the PNNL data and that of this work are likely not related to apodization or resolution effects.

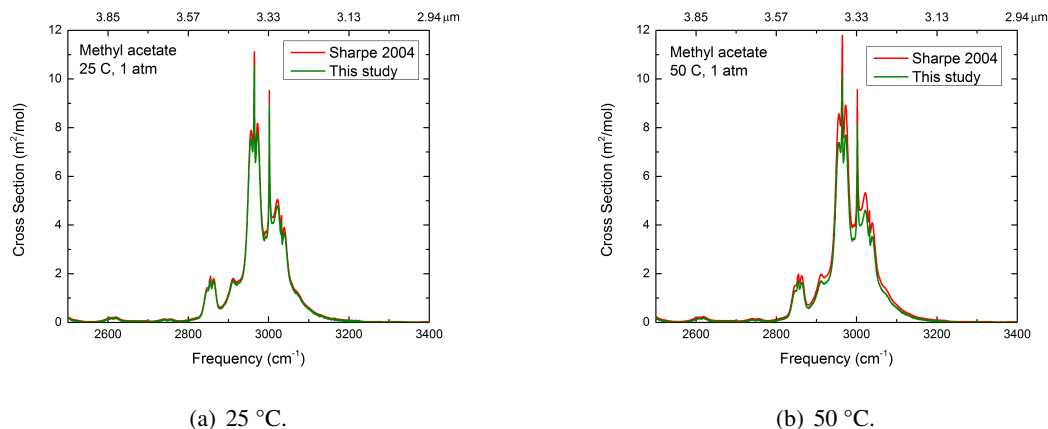


Figure 5.10: Comparison of spectra of methyl acetate at (a) 25 °C and (b) 50 °C and approximately 1 atm with spectra measured by Sharpe *et al.* [175]. The spectra agree to within 16 percent.

5.4.8 Temperature dependence

The spectra of methyl acetate at 25 °C, 100 °C, and 250 °C are shown in Figure 5.13. Several features of this plot are noteworthy. First, at 25 °C there are many fine structures visible; however, at elevated temperatures these give way to broader, smoother features. Important peaks (local maxima) for MA occur at 2856 cm^{-1} , 2863 cm^{-1} , 2911 cm^{-1} , 2956 cm^{-1} , 2964 cm^{-1} , 2973 cm^{-1} , 3002 cm^{-1} ,

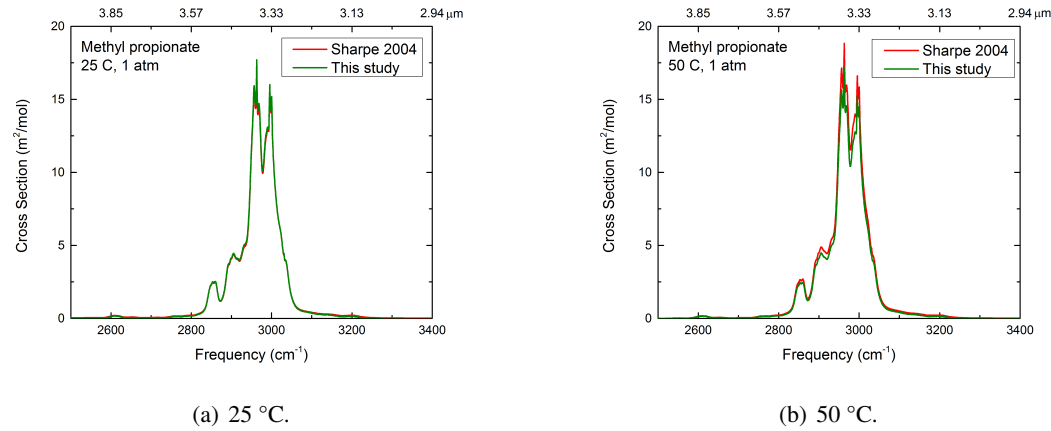


Figure 5.11: Comparison of spectra from methyl propionate at (a) 25 °C and (b) 50 °C and approximately 1 atm with spectra measured by Sharpe *et al.* [175]. The agreement at 25 °C is excellent, while the spectra at 50 °C agree to within 10 percent.

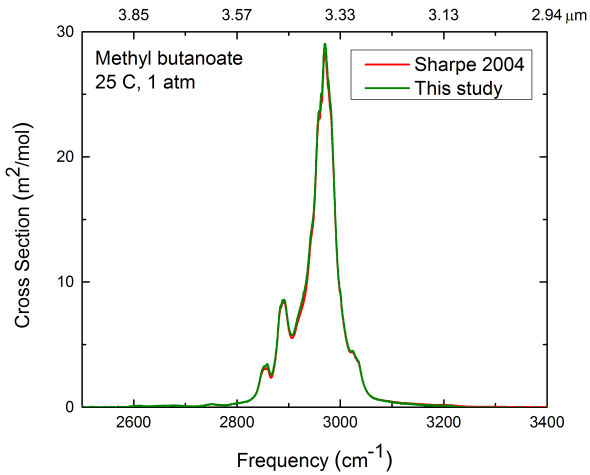


Figure 5.12: Comparison of spectrum of methyl butanoate measured in this study at 25 °C and 1 atm to that of Sharpe *et al.* [175]. The spectra show excellent agreement.

3022 cm^{-1} , and 3039 cm^{-1} ; select values among these for MA as well as the other FAMEs studied in this chapter are listed in Table 5.2 in order to assist in comparisons between FAME species (this table also provides the locations of local minima, or valleys, in the spectra). Second, the magnitude of the prominent peak located at 3002 cm^{-1} decreases drastically as temperature increases, as do the peaks at 3022 cm^{-1} and 3039 cm^{-1} . A dramatic shift in the spectrum with temperature such as this is common in the C–H absorption band (see, for instance, the work of Klingbeil *et al.* [225]), illustrating the necessity for high-quality temperature-dependent spectral data at these conditions. Third, the peak value of the spectrum decreases with temperature, and the spectrum also broadens with temperature. This can be seen more clearly in Figures 5.24 and 5.25 (discussed extensively later in this chapter), which show the peak cross section value and Full Width at Half Maximum (FWHM) for the FAMEs studied at various temperatures (the FWHM is defined as the difference between the greatest and least frequencies corresponding to one-half of the peak cross section value of the spectrum, as shown in Figure 5.26 later in this chapter). Moreover, these plots reveal that for each FAME, the peak cross section and FWHM change linearly with temperature. Fourth, in the wings of the spectra (between 2700 cm^{-1} and 2880 cm^{-1} , and between 3050 cm^{-1} and 3200 cm^{-1}), the cross section increases with temperature. This is consistent with the fact that more rotational energy levels in these molecules become populated as temperature rises; this increase, together with the increase in FWHM, serves to counteract the decrease in peak cross section and keep the total integrated area Ψ of the C–H spectrum constant. Finally, the frequency of the HeNe laser, shown by a dashed black line in Figure 5.13 and subsequent FAME spectral depictions, falls at a fortuitous location wherein the $3.39\text{ }\mu\text{m}$ cross section is relatively independent of temperature. Cross section values at the HeNe wavelength for the saturated FAMEs examined in this work are plotted in Figure 5.28 (also addressed more extensively later in this chapter).

The spectrum of methyl propionate at temperatures of $25\text{ }^\circ\text{C}$, $150\text{ }^\circ\text{C}$, and $300\text{ }^\circ\text{C}$ is displayed in Figure 5.14. This spectrum, like that of MA, displays numerous fine features; important peaks for MPI occur at 2855 cm^{-1} , 2906 cm^{-1} , 2956 cm^{-1} , 2963 cm^{-1} , 2969 cm^{-1} , 2995 cm^{-1} , and 3000 cm^{-1} . MPI's spectrum also displays sharp temperature dependence within some frequency bands, as can be seen near 2995 cm^{-1} . Notice that the peak cross section of MPI is greater than that of MA, consistent with the fact that MPI has two more C–H bonds than MA. Also, as with MA, the cross

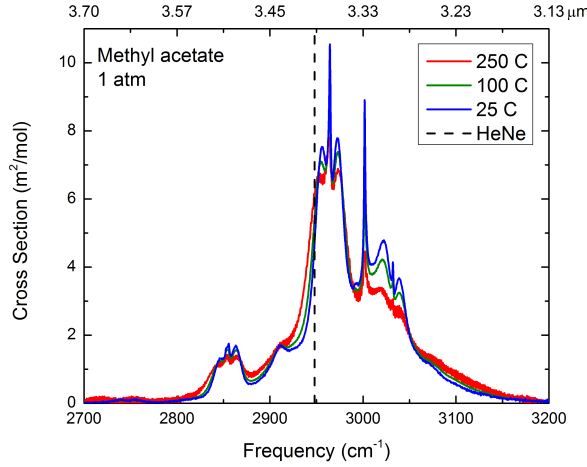


Figure 5.13: Spectrum of methyl acetate at three temperatures and 1 atm (partial pressure of fuel is approximately 3.6 Torr, diluted in nitrogen). Also shown in this and subsequent spectrum plots is a dashed line denoting the 2947.909 cm^{-1} frequency of the HeNe laser.

Table 5.2: Approximate locations of select peaks and valleys for FAMEs examined in this work. Features listed in the same column of the table appear to be correlated.

Fuel	Formula	Number of CH_2 Groups	Number of CH_3 Groups	Peak Locations [cm^{-1}]	Valley Locations [cm^{-1}]
Methyl acetate	$\text{C}_3\text{H}_6\text{O}_2$	0	2	2964 3002	2990
Methyl propionate	$\text{C}_4\text{H}_8\text{O}_2$	1	2	2963 2995	2978
Methyl butanoate	$\text{C}_5\text{H}_{10}\text{O}_2$	2	2	2890 2970	2907
Methyl valerate	$\text{C}_6\text{H}_{12}\text{O}_2$	3	2	2881 2968	2903
Methyl hexanoate	$\text{C}_7\text{H}_{14}\text{O}_2$	4	2	2882 2942 2967	2901 2950
Methyl heptanoate	$\text{C}_8\text{H}_{16}\text{O}_2$	5	2	2871 2940 2967	2897 2953
Methyl octanoate	$\text{C}_9\text{H}_{18}\text{O}_2$	6	2	2868 2936 2967	2899 2954
Methyl nonanoate	$\text{C}_{10}\text{H}_{20}\text{O}_2$	7	2	2867 2934 2965	2897 2955
Methyl decanoate	$\text{C}_{11}\text{H}_{22}\text{O}_2$	8	2	2865 2933 2964	2896 2954
Methyl crotonate	$\text{C}_5\text{H}_8\text{O}_2$	0	2	2859 2936 2956	2888 2944
Methyl 3-nonenanoate	$\text{C}_{10}\text{H}_{18}\text{O}_2$	5	2	2868 2935 2966	2894 2955

section value at the HeNe wavelength remains approximately constant as temperature changes.

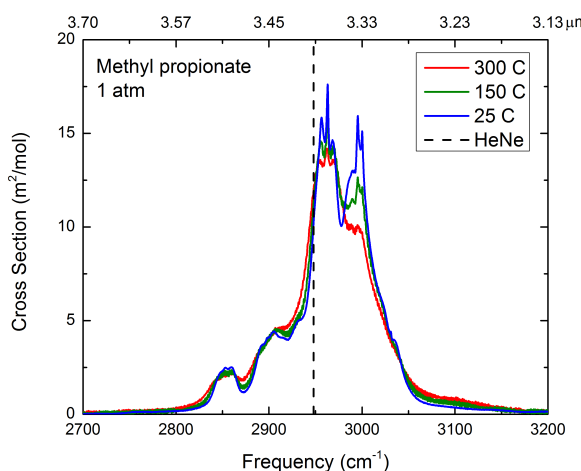


Figure 5.14: Spectrum of methyl propionate at three temperatures and 1 atm (partial pressure of fuel is approximately 2.7 Torr, diluted in nitrogen).

The spectrum of methyl butanoate is plotted at temperatures of 25 °C, 200 °C, and 300 °C in Figure 5.15. Peaks occur at approximately 2857 cm⁻¹, 2890 cm⁻¹, and 2970 cm⁻¹; like those in the spectrum of MPI, the peaks at 2857 cm⁻¹ and 2890 cm⁻¹ disappear as temperature increases. While the frequency of the HeNe laser lies in a qualitatively similar part of the spectrum as it does in MPI, the cross section seems to show a slight increase with temperature in the range studied (see Figure 5.28). Overall, the temperature-dependence of the spectrum of MB is similar to those of MA and MPI; this observation can be made of all of the FAMEs studied in this work.

Spectra for methyl valerate at 25 °C, 150 °C, and 350 °C are shown in Figure 5.16. The MV spectrum exhibits peaks at 2881 cm⁻¹, 2968 cm⁻¹, and 3027 cm⁻¹. A key feature of this spectrum occurs near the HeNe laser frequency; at this location the slope of the cross section plot appears to decrease slightly. This marks the point where another peak will begin to appear in larger molecules such as MH.

The spectrum of methyl hexanoate is plotted in Figure 5.17 at temperatures of 100 °C, 200 °C, and 350 °C. This molecule was not studied at temperatures lower than 100 °C because its low vapor pressure results in excessive condensation. Other techniques besides that used in this study,

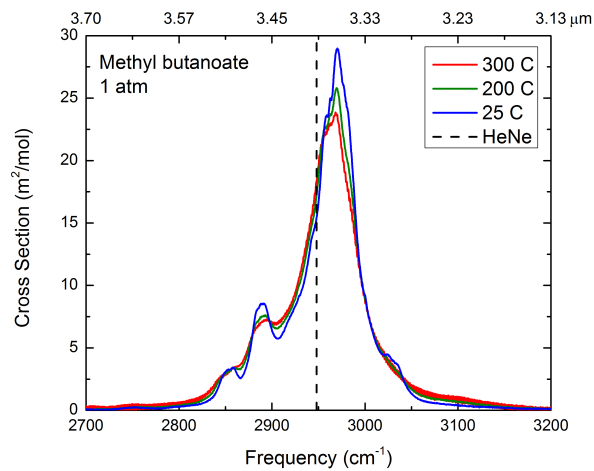


Figure 5.15: Spectrum of methyl butanoate at three temperatures and 1 atm (partial pressure of fuel is approximately 2.8 Torr, diluted in nitrogen).

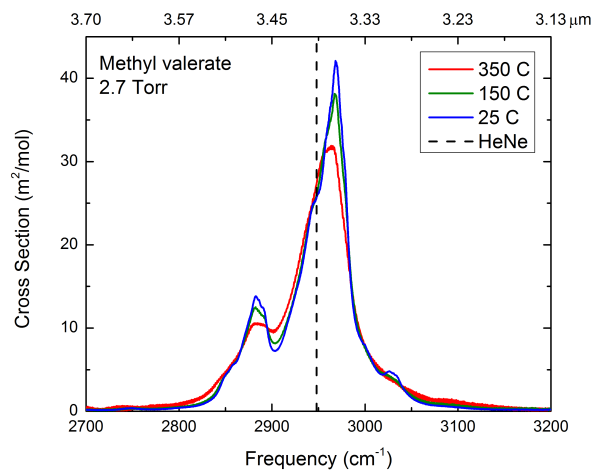


Figure 5.16: Spectrum of pure methyl valerate at three temperatures and an average pressure of 2.7 Torr. As temperature increases, the peak cross section decreases.

however, are available to make high-quality, low-temperature measurements of low-vapor-pressure molecules [243]. Several peaks are visible in the MH spectrum, at 2882 cm^{-1} , 2943 cm^{-1} , 2967 cm^{-1} , and 3025 cm^{-1} . The small peak at 2943 cm^{-1} is indistinguishable by about $200\text{ }^{\circ}\text{C}$, consistent with the fact that spectra tend to broaden and smoothen as temperature rises. Close observation reveals that the peak of the spectrum shifts to lower frequencies as temperature increases, such that at $450\text{ }^{\circ}\text{C}$ (not shown in Figure 5.17) it is within 6 cm^{-1} of the 2947.909 cm^{-1} HeNe laser frequency. Based on Figure 5.24, it appears that the peak cross section of MH will continue to drop as temperature rises; this is evidence that the $3.39\text{-}\mu\text{m}$ cross section may also exhibit strong temperature dependence at temperatures above $450\text{ }^{\circ}\text{C}$ due to its close proximity to the peak frequency.

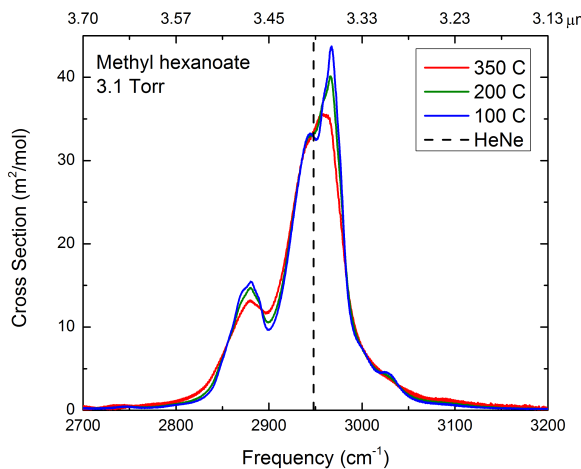


Figure 5.17: Spectrum of pure methyl hexanoate at three temperatures and an average pressure of 3.1 Torr .

Spectra of methyl heptanoate are shown at temperatures of $100\text{ }^{\circ}\text{C}$, $200\text{ }^{\circ}\text{C}$, and $350\text{ }^{\circ}\text{C}$ in Figure 5.18. In these spectra, peaks are visible at 2871 cm^{-1} , 2940 cm^{-1} , and 2967 cm^{-1} ; the peak at 2967 cm^{-1} disappears above $350\text{ }^{\circ}\text{C}$ (note that a typographical error in Reference [176] said 350 K instead). Interestingly, the HeNe laser frequency (2947.909 cm^{-1}) falls just to the left of the valley at 2953 cm^{-1} , which yields the HeNe cross section temperature-independent in the temperature range studied. Were the HeNe laser frequency to coincide with the valley, the cross section values at $100\text{ }^{\circ}\text{C}$ and $350\text{ }^{\circ}\text{C}$ would have differed by about $3\text{ m}^2/\text{mol}$.

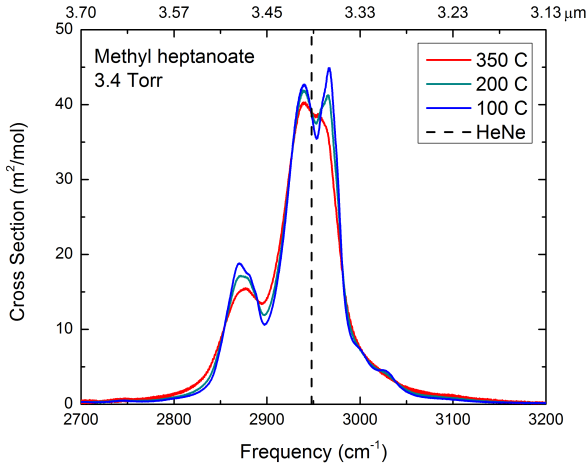


Figure 5.18: Spectrum of pure methyl heptanoate at three temperatures and an average pressure of 3.4 Torr.

The spectrum of methyl octanoate is shown at temperatures of 100 °C, 200 °C, and 350 °C in Figure 5.19. Peaks exist at approximately 2868 cm⁻¹, 2936 cm⁻¹, 2967 cm⁻¹, and 3025 cm⁻¹. The peak at 2967 cm⁻¹ can be seen until about 350 °C, but the peak at 2868 cm⁻¹ remains distinguishable up to 400 °C (not shown in Figure 5.19). Notice that the frequency of the HeNe laser is on the right side of the peak in MOC, whereas for molecules the size of and smaller than MV it was on the left side. Despite this change, the HeNe laser frequency still falls at a point where the 3.39 μm cross section is relatively temperature-independent at the conditions studied.

The spectrum of methyl nonanoate is shown in Figure 5.20 at temperatures of 100 °C, 200 °C, and 350 °C. Several peaks are visible at 2867 cm⁻¹, 2934 cm⁻¹, 2965 cm⁻¹, and 3026 cm⁻¹. The peak at 2965 cm⁻¹ can be seen until about 250-300 °C (plots at these temperatures are not shown in Figure 5.20), and the 3.39 μm cross section is relatively temperature-independent within the range studied.

With a vapor pressure of only 6.5 Torr at 100 °C [222], methyl decanoate posed a difficult challenge for heated cell experimentation due to the occurrence of condensation and decomposition at some conditions. Nevertheless, its spectrum has been successfully measured between 100 °C and 350 °C, as shown in Figure 5.21. Peaks are visible at 2865 cm⁻¹, 2933 cm⁻¹, 2964 cm⁻¹, and

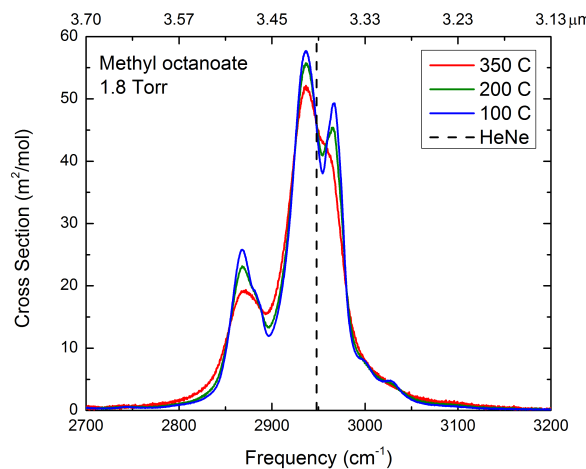


Figure 5.19: Spectrum of pure methyl octanoate at three temperatures and an average pressure of 1.8 Torr.

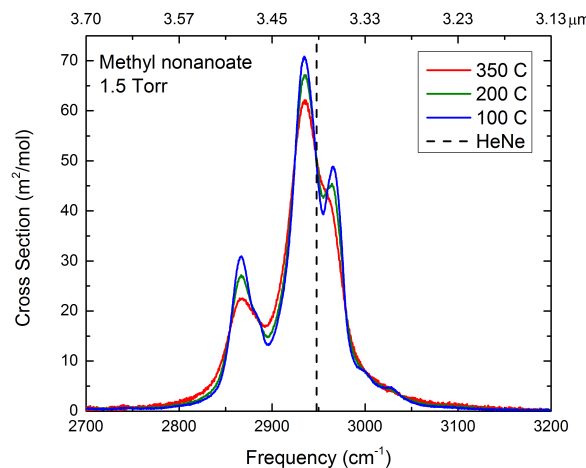


Figure 5.20: Spectrum of pure methyl nonanoate at three temperatures and an average pressure of 1.5 Torr.

3026 cm^{-1} . The peak at 2964 cm^{-1} disappears at about $250\text{ }^{\circ}\text{C}$ (not shown in Figure 5.21), and the HeNe laser frequency again lies at a point in the spectrum that causes it to be relatively temperature-independent. In general, the temperature-dependence of this spectrum is similar to that of the other FAMEs examined in this study.

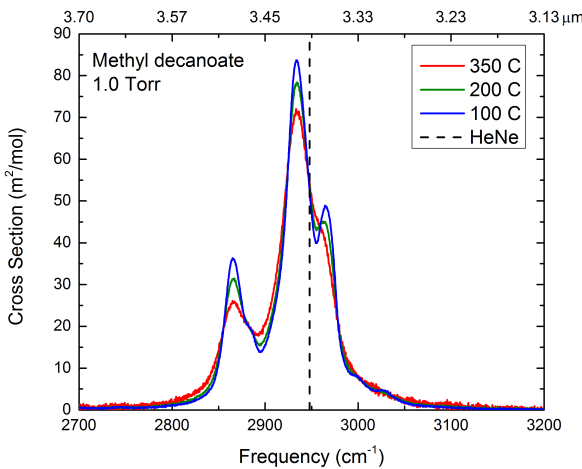


Figure 5.21: Spectrum of pure methyl decanoate at three temperatures and an average pressure of 1.0 Torr.

Methyl crotonate is a mono-unsaturated FAME molecule formed by replacing the single C–C bond at the second carbon atom location in the alkane-like carbon chain in MB with a double C=C bond (see Figure 5.2). Spectra of MC are plotted in Figure 5.22 at temperatures of $25\text{ }^{\circ}\text{C}$, $150\text{ }^{\circ}\text{C}$, and $300\text{ }^{\circ}\text{C}$. Numerous peaks can be seen; the most prominent occur at approximately 2859 cm^{-1} , 2926 cm^{-1} , 2936 cm^{-1} , 2956 cm^{-1} , 2966 cm^{-1} , 2988 cm^{-1} , and 2999 cm^{-1} . Unlike the other FAMEs examined in this study, MC's cross section at the HeNe wavelength (shown as a dashed line in Figure 5.22) increases significantly with temperature. Were a laser with a frequency of about 2954 cm^{-1} rather than the HeNe frequency of 2947.909 cm^{-1} used to detect MC, however, the variation with temperature would be greatly reduced. This provides motivation for the use of wavelength-tunable infrared lasers to probe the C–H stretch spectrum, as these light sources can be tuned to more favorable areas of the absorption spectrum [256].

Methyl-3-nonenoate is a mono-unsaturated FAME molecule formed by replacing the single

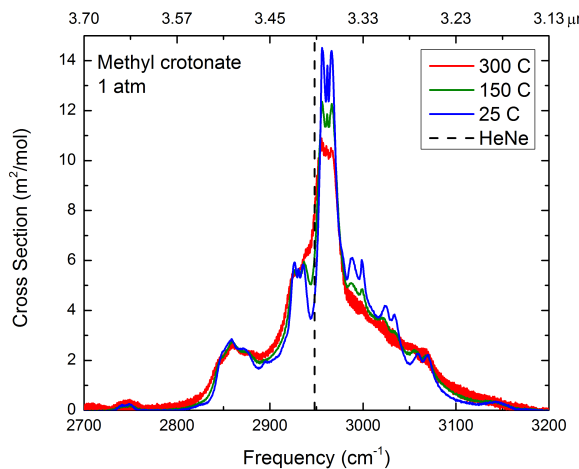


Figure 5.22: Spectrum of methyl crotonate at three temperatures and 1 atm (partial pressure of fuel is approximately 3.6 Torr, diluted in nitrogen).

C–C bond at the third carbon atom location in the alkane-like carbon chain in MN with a double C=C bond (see Figure 5.2). Spectra of M3N are plotted in Figure 5.23 at temperatures of 100 °C, 250 °C, and 350 °C. This spectrum shows peaks at 2868 cm⁻¹, 2935 cm⁻¹, and 2966 cm⁻¹; the cross section at the HeNe wavelength is temperature-independent in the range examined.

As introduced above, Figure 5.24 depicts the change in peak cross section values of the spectra of the saturated FAMEs studied as a function of temperature (these values are also tabulated in Table 5.3). Several observations can be made. First, the peak cross section in each spectrum increases with FAME carbon chain length; this is consistent with the fact that longer FAMEs have more C–H bonds, allowing them to absorb more light. Second, peak cross sections decrease linearly with temperature. Third, it appears that the data for FAMEs larger than MPI can be divided into two groups. The first consists of MB, MV, and MH, whose maxima occur around 2965 cm⁻¹; the second consists of MOC, MN, and MD, whose maxima result from a different peak that is located around 2935 cm⁻¹. Overlapping these two groups is MHP, whose peak at about 2965 cm⁻¹ has the greatest magnitude below 200 °C, whereas at and above 200 °C its peak at 2935 cm⁻¹ dominates. In both of these groups, the best-fit line's slope becomes more negative as molecular size increases. Moreover, it appears that as each peak (that at 2935 cm⁻¹ and that at 2965 cm⁻¹) increases in height with

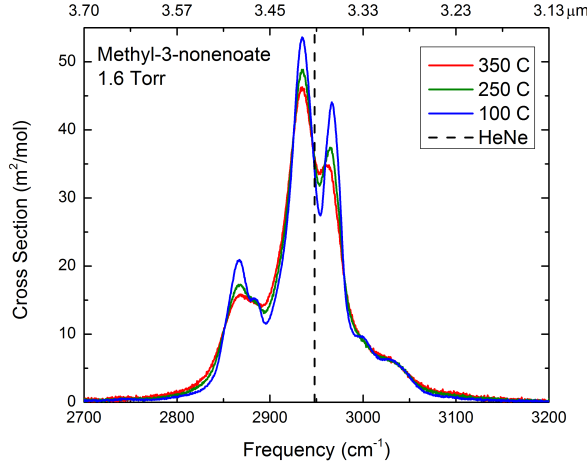


Figure 5.23: Spectrum of pure methyl-3-nonenate at three temperatures and an average pressure of 1.6 Torr.

molecular size, peak cross section falls faster with temperature. Fourth, observe that the differences in peak height between MH, MV, and MHP are smaller than those between the other FAMEs examined. This is likely due to the emergence of the new peak at 2935 cm^{-1} in MH and MHP, which competes with that at 2965 cm^{-1} for absorbance.

Table 5.3: Peak cross section (σ_{peak}) and FWHM data.

N_{CH}	Fuel	T [°C]	σ_{peak} [m ² /mol]	$\frac{1}{2}\sigma_{peak}$ [m ² /mol]	FWHM [cm ⁻¹]	Frequency at Peak [cm ⁻¹]
6	MA	25	10.5	5.3	54.36	2964.34
6	MA	50	10.1	5.1	55.32	2964.34
6	MA	100	9.1	4.6	58.10	2964.34
6	MA	150	8.7	4.3	59.90	2964.22
6	MA	200	8.2	4.1	62.07	2964.22
6	MA	250	7.8	3.9	64.12	2964.10
6	MA	300	7.5	3.8	65.93	2963.74
6	MA	350	7.3	3.6	67.98	2963.26
6	MA	400	6.8	3.4	69.67	2962.29
8	MPI	25	17.6	8.8	62.92	2963.02
8	MPI	50	17.1	8.5	64.36	2963.02
8	MPI	100	16.3	8.2	66.53	2962.90

Table 5.3: (continued)

N_{CH}	Fuel	T [°C]	σ_{peak} [m ² /mol]	$\frac{1}{2}\sigma_{peak}$ [m ² /mol]	FWHM [cm ⁻¹]	Frequency at Peak [cm ⁻¹]
8	MPI	150	15.6	7.8	68.82	2962.53
8	MPI	200	15.0	7.5	70.27	2962.65
8	MPI	250	14.7	7.3	71.48	2962.05
8	MPI	300	14.2	7.1	73.40	2962.41
8	MPI	350	14.1	7.0	75.21	2961.93
8	MPI	400	13.8	6.9	76.54	2961.21
10	MB	25	29.0	14.5	45.68	2970.25
10	MB	100	27.7	13.9	49.66	2970.13
10	MB	200	25.8	12.9	54.36	2969.28
10	MB	250	24.9	12.5	56.41	2968.32
10	MB	300	23.9	11.9	59.42	2968.32
10	MB	350	22.7	11.3	62.68	2968.08
10	MB	400	21.8	10.9	66.29	2967.23
12	MV	25	42.1	21.1	43.87	2968.32
12	MV	50	41.7	20.8	44.60	2968.32
12	MV	100	39.9	20.0	46.77	2968.32
12	MV	150	38.1	19.1	48.82	2967.36
12	MV	200	36.3	18.1	51.23	2967.23
12	MV	250	34.9	17.4	53.76	2967.23
12	MV	300	33.1	16.6	56.89	2966.15
12	MV	350	31.9	16.0	59.06	2963.38
12	MV	400	31.0	15.5	61.23	2961.21
12	MV	450	30.4	15.2	62.92	2958.56
12	MV	500	28.9	14.4	66.78	2954.58
14	MH	100	43.7	21.9	55.44	2967.23
14	MH	150	42.0	21.0	57.01	2967.23
14	MH	200	40.1	20.1	59.06	2966.27
14	MH	250	38.4	19.2	61.23	2965.31
14	MH	300	36.7	18.3	63.16	2964.34
14	MH	350	35.6	17.8	64.73	2956.75
14	MH	400	35.1	17.5	65.93	2955.90
14	MH	450	34.8	17.4	67.14	2953.74
16	MHP	100	44.9	22.4	61.35	2966.27
16	MHP	150	43.0	21.5	62.92	2966.27
16	MHP	200	41.9	20.9	64.12	2938.43
16	MHP	250	41.4	20.7	64.97	2940.24

Table 5.3: (continued)

N_{CH}	Fuel	T [°C]	σ_{peak} [m ² /mol]	$\frac{1}{2}\sigma_{\text{peak}}$ [m ² /mol]	FWHM [cm ⁻¹]	Frequency at Peak [cm ⁻¹]
16	MHP	300	40.9	20.4	65.69	2940.24
16	MHP	350	40.3	20.2	66.53	2939.39
16	MHP	400	39.6	19.8	67.86	2939.27
18	MOC	100	57.7	28.8	58.70	2936.38
18	MOC	150	56.7	28.4	59.18	2936.38
18	MOC	200	55.7	27.9	59.54	2936.38
18	MOC	250	55.0	27.5	60.27	2937.34
18	MOC	300	53.2	26.6	61.47	2936.50
18	MOC	350	52.1	26.1	62.07	2936.38
18	MOC	400	51.0	25.5	63.40	2934.57
20	MN	100	70.8	35.4	55.08	2934.57
20	MN	150	69.2	34.6	55.44	2934.57
20	MN	200	67.1	33.6	55.81	2935.41
20	MN	250	65.8	32.9	56.53	2934.45
20	MN	300	63.9	31.9	57.25	2935.41
20	MN	350	62.1	31.1	58.10	2936.38
20	MN	400	61.3	30.7	58.58	2934.45
22	MD	100	83.7	41.9	51.11	2933.73
22	MD	150	81.2	40.6	51.11	2934.45
22	MD	200	78.4	39.2	51.83	2934.57
22	MD	250	76.5	38.2	52.07	2934.45
22	MD	300	73.8	36.9	52.79	2933.61
22	MD	350	72.0	36.0	53.64	2933.37
8	MC	25	14.5	7.3	22.30	2955.90
8	MC	50	13.9	6.9	23.99	2955.90
8	MC	100	13.1	6.5	26.76	2955.78
8	MC	150	12.4	6.2	29.05	2955.78
8	MC	200	11.8	5.9	41.10	2955.90
8	MC	250	11.3	5.6	44.11	2955.78
8	MC	300	10.9	5.4	54.72	2955.42
8	MC	350	10.1	5.1	57.01	2954.82
8	MC	400	9.2	4.6	63.40	2955.66
18	M3N	100	53.6	26.8	57.74	2934.57
18	M3N	150	51.8	25.9	59.06	2935.41
18	M3N	200	50.2	25.1	60.15	2934.57
18	M3N	250	48.8	24.4	61.23	2934.21

Table 5.3: (continued)

N_{CH}	Fuel	T [°C]	σ_{peak} [m ² /mol]	$\frac{1}{2}\sigma_{\text{peak}}$ [m ² /mol]	FWHM [cm ⁻¹]	Frequency at Peak [cm ⁻¹]
18	M3N	300	47.6	23.8	62.44	2933.61
18	M3N	350	46.3	23.1	64.36	2934.57
18	M3N	400	44.8	22.4	65.33	2934.33

Figure 5.25 shows, as function of temperature, the Full Width at Half Maximum (FWHM) values of the spectra of the saturated FAMEs studied (the FWHM is demonstrated in Figure 5.26; these values are also tabulated in Table 5.3). Again, numerous observations may be made. First, the FWHM increases with temperature; this mirrors the fact that the peak cross section decreases such that the total integrated area Ψ of each molecule's C–H absorption spectrum remains constant (Equation 5.3). Second, with the exception of MA and MPI, the slope of each best-fit line decreases (become less positive) as molecular size increases. Third, the same two groups visible in Figure 5.24 (MB-MV-MH and MOC-MN-MD) can be seen in Figure 5.25. However, there are some striking differences between these collections. Within the MOC-MN-MD group, the rate of increase of the FWHM with temperature is less than that in the MB-MV-MH group; this could be because MOC-MN-MD display three prominent peaks rather than just two. In the MOC-MN-MD group, the FWHM decreases with molecular size, but in the MB-MV-MH group, the FWHM of MH is greater than those of MB and MV. This could be a mathematical phenomenon; since the peak height of MH is lower than expected as discussed above, its half-maximum height is also lower (and closer to the wide base of the spectrum), yielding a FWHM that is larger. Finally, it appears that MPI is an outlier in this graphic, with FWHM values much larger than the other saturated FAMEs studied.

5.4.9 Molecular size dependence

Figure 5.27 displays the spectra of MA, MB, MHP, and MD at 100 °C and 300 °C in order to illustrate the dependence of the C–H absorption band on molecular size. Since many details of these spectra have been discussed above, only a brief overview of these plots will be provided here. First, observe that the frequencies of the spectral peaks decrease as molecular size increases (see

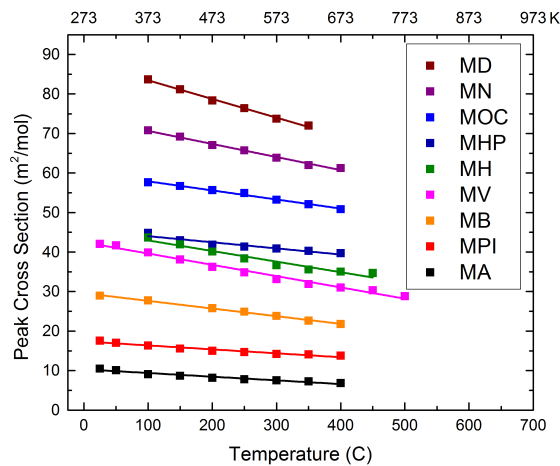


Figure 5.24: Peak cross section values of the C–H spectra for the saturated FAMEs examined in this study as a function of temperature.

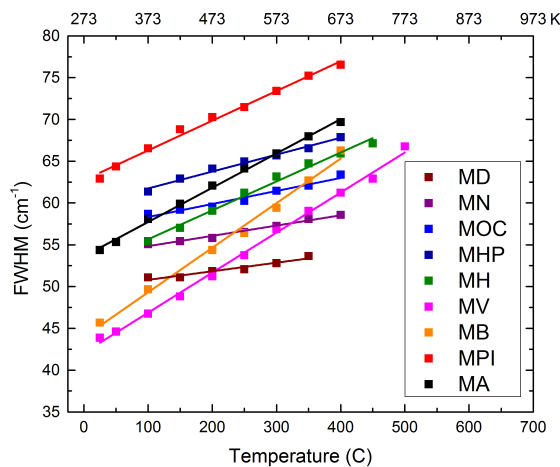


Figure 5.25: Full Width at Half Maximum (FWHM) values of the C–H spectra for the saturated FAMEs examined in this study as a function of temperature.

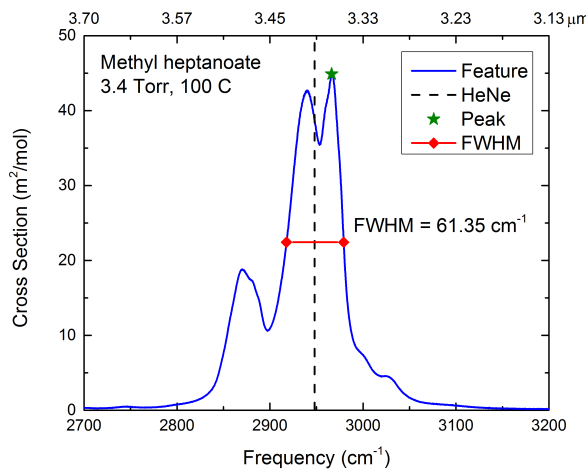


Figure 5.26: Demonstration of peak cross section and Full Width at Half Maximum (FWHM) for methyl heptanoate at 100 °C. The FWHM is defined as the difference between the greatest and least frequencies corresponding to one-half of the peak cross section value of the spectrum.

also Table 5.2). Second, notice that at each temperature, cross sections increase with molecular size below about 2970 cm^{-1} , but above 3040 cm^{-1} the opposite is true (as molecular size increases, the cross section actually decreases slightly). Finally, it can be seen that the spectra of larger molecules bear striking resemblance to those of their smaller counterparts, as if lengthening the carbon chain in these FAMEs serves to exaggerate smaller molecules' features. Such comparisons are useful in anticipating the nature of the spectra of even larger molecules, such as the five primary components of biodiesel fuel: methyl palmitate (MP, $\text{C}_{17}\text{H}_{34}\text{O}_2$), methyl stearate (MS, $\text{C}_{19}\text{H}_{38}\text{O}_2$), methyl oleate (MO, $\text{C}_{19}\text{H}_{36}\text{O}_2$), methyl linoleate (ML, $\text{C}_{19}\text{H}_{34}\text{O}_2$), and methyl linolenate (MLN, $\text{C}_{19}\text{H}_{32}\text{O}_2$).

5.4.10 Cross section values at 3.39 microns

Cross section values at $3.392235\text{ }\mu\text{m}$ for the FAMEs observed in this study are provided in Table 5.4 and are plotted (for the saturated molecules) in Figure 5.28. It appears that the HeNe laser cross section varies linearly with temperature within the range studied; this was also observed by Klingbeil *et al.* [225, 226] and Mével *et al.* [227]. However, since the variation in cross sections was smaller than the uncertainty in the data, average $3.39\text{ }\mu\text{m}$ cross section values between $150\text{ }^\circ\text{C}$

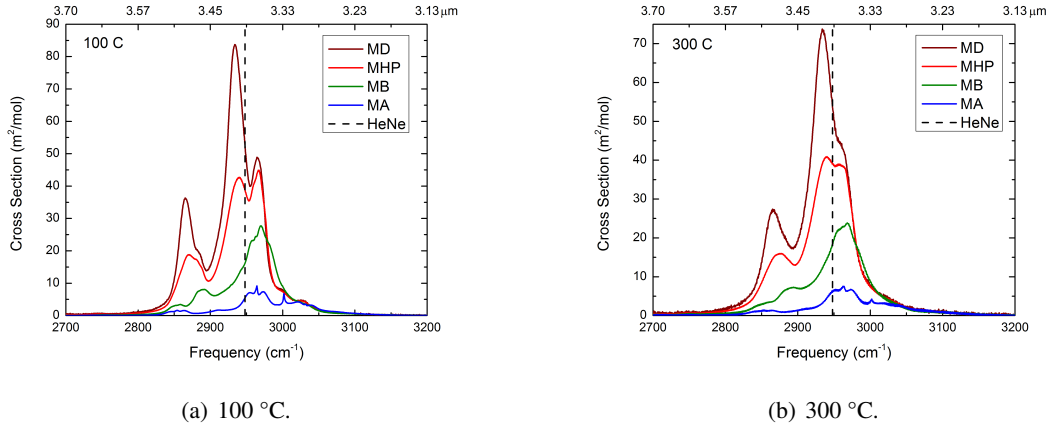


Figure 5.27: Comparison of spectra of saturated FAMEs at (a) 100 °C and (b) 300 °C.

and 400 °C have also been reported in Table 5.4, together with uncertainty percentages for each of these values.

5.4.11 Integrated area

Integrated area values as a function of temperature are plotted in Figure 5.29, demonstrating the constant integrated area property of the C–H absorption band. Values that are smaller than the suggested integrated area values (shown in solid lines) are instances where fuel condensation (low temperatures) or fuel decomposition (high temperatures) is suspected. Average integrated area values for each fuel are provided in Table 5.5, together with values derived from the results of Sharpe *et al.* [175]. The agreement between these values is within the combined uncertainties of the measurements.

5.5 Discussion

5.5.1 Explanation of spectra

The C–H absorption spectra of the FAMEs studied reflect these fuels’ molecular structures in terms of the number of CH₂ and CH₃ groups each possesses. In particular, the Handbook of Spectroscopy [257] states that CH₂ groups typically absorb light in the intervals 2850–2900 cm⁻¹

Table 5.4: Absorption cross section at 3.392235 μm (2947.909 cm^{-1}) for the FAMEs measured in this study. Units are m^2/mol . Average cross section values between 150 °C and 400 °C, together with uncertainty percentages for these average values, are given in the last two columns of the table. Since the cross section of MC exhibits a relatively large change between 150 °C and 400 °C, no average value is given; however, the average uncertainty for the data in this temperature range is still provided.

Temperature / Molecule	25 °C	50 °C	100 °C	150 °C	200 °C	250 °C	300 °C	350 °C	400 °C	450 °C	500 °C	150-400 °C	Uncertainty [%]
	298 K	323 K	373 K	423 K	473 K	523 K	573 K	523 K	673 K	723 K	773 K	Average	
Methyl acetate	4.7	5	5.4	5.8	6.1	6.1	6.1	6.4	6.1	6.1	6.1	6.1	10.5
Methyl propionate	10.2	10.5	10.9	11.3	11.6	11.9	12	12.2	12.1	11.8	11.8	3.8	
Methyl butanoate	15.4	16.2	17.3	18	18.4	18.5	18.9			18.2	18.2	7.8	
Methyl valerate	25.7	25.8	25.9	26.1	26.3	26.8	27.3	27.4	27.7	27.7	27.3	26.9	3.9
Methyl hexanoate	32.9	33	33.2	33.4	33.5	33.4	33.5	33.4	33.4	33.4	33.4	33.4	2.4
Methyl heptanoate	38.8	38.9	39.1	39.2	39.1	39	38.4			39	39	4.7	
Methyl octanoate	45.4	45.9	46.1	46.4	46.2	46.1	45.4			46	46	5	
Methyl nonanoate	49.3	50.1	50.4	50.6	50.5	50.5	50.7			50.5	50.5	4.5	
Methyl decanoate	52.5	53	53.5	53.9	53.6	54.5				53.7	53.7	6.6	
Methyl crotonate	4.5	4.8	5.5	6.2	6.9	7.3	7.7	8.2	7.9			4.6	
Methyl-3-nonenanoate			33.9	34.6	34.8	35.4	35.7	36	36			35.4	4.1

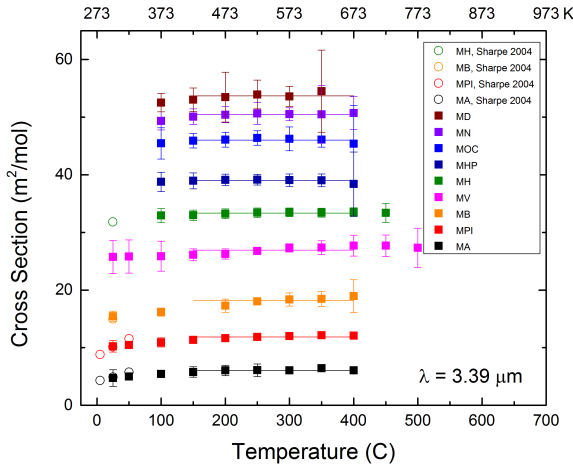


Figure 5.28: Absorption cross sections at $3.392235\text{ }\mu\text{m}$ (2947.909 cm^{-1}) for the saturated FAMEs examined in this study. The recommended average cross section values for the range 150 to $400\text{ }^{\circ}\text{C}$ are shown as solid lines. Comparison is given with data from Sharpe *et al.* [175].

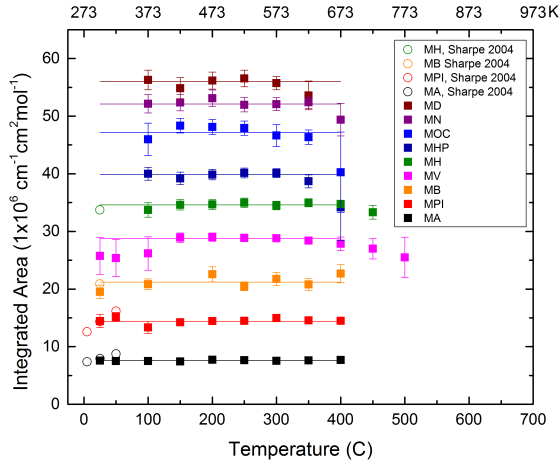


Figure 5.29: Uncorrected integrated absorbance values for the saturated FAMEs examined in this study. The average integrated absorbance values from Table 5.5 are shown as solid lines as well. Values that are lower than the average indicate the presence of condensation or decomposition. Spectra and $3.39\text{ }\mu\text{m}$ cross section values reported in this chapter have been adjusted to the average integrated absorbance values here according to Equation 5.4. Comparison is given with data from Sharpe *et al.* [175].

CHAPTER 5. SPECTROSCOPY OF FATTY ACID METHYL ESTERS

Table 5.5: Integrated area information for the fuels studied, together with comparison to results of Sharpe *et al.* [175]. Uncertainty values for Sharpe *et al.* data are quoted for Type-B errors.

Fuel	Formula	This study		Sharpe <i>et al.</i>		Difference [%]
		Integrated area [$1 \times 10^6 \text{ cm}^{-1} \text{cm}^2 \text{mol}^{-1}$]	Uncertainty [%]	Integrated area [$1 \times 10^6 \text{ cm}^{-1} \text{cm}^2 \text{mol}^{-1}$]	Uncertainty [%]	
Methyl formate	C ₂ H ₄ O ₂			9.6	<3	
Methyl acetate	C ₃ H ₆ O ₂	7.6	3.0	8.01	<3	5.6
Methyl propionate	C ₄ H ₈ O ₂	14.4	4.4	14.4	<3	0.0
Methyl butanoate	C ₅ H ₁₀ O ₂	21.2	5.3	20.9	<3	1.4
Methyl valerate	C ₆ H ₁₂ O ₂	28.8	2.4			
Methyl hexanoate	C ₇ H ₁₄ O ₂	34.6	2.5	33.7	<7	2.6
Methyl heptanoate	C ₈ H ₁₆ O ₂	39.9	2.4			
Methyl octanoate	C ₉ H ₁₈ O ₂	47.2	3.6			
Methyl nonanoate	C ₁₀ H ₂₀ O ₂	52.1	2.5			
Methyl decanoate	C ₁₁ H ₂₂ O ₂	56.0	2.7			
Methyl acrylate	C ₄ H ₆ O ₂					
Methyl crotonate	C ₅ H ₈ O ₂	10.2	2.8			
Methyl-3-nonenate	C ₁₀ H ₁₈ O ₂	43.0	2.5			

and $2925\text{-}2975\text{ cm}^{-1}$, and CH_3 groups typically absorb light in the intervals $2875\text{-}2925\text{ cm}^{-1}$ and $2950\text{-}3000\text{ cm}^{-1}$. These intervals are depicted in Figure 5.30, together with the spectra of MD, MHP, MB, MA, and MC at $100\text{ }^\circ\text{C}$. Notice from Figure 5.2 and Table 5.2 that each FAME contains two CH_3 groups, but the number of CH_2 groups increases with the length of the carbon chain. Also from Figure 5.2 and Table 5.2, observe that MA and MC have no CH_2 groups.

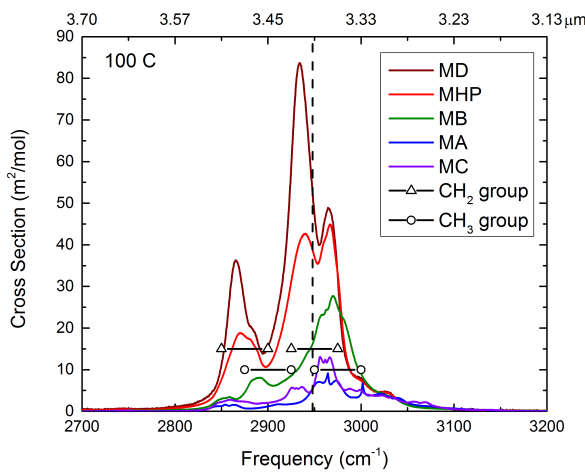


Figure 5.30: Contribution of CH_2 and CH_3 groups to spectra of MD, MHP, MB, MA, and MC at $100\text{ }^\circ\text{C}$ based on recommended ranges from the Handbook of Spectroscopy [257].

By observation of Figure 5.30, it appears that the peaks at approximately 2865 cm^{-1} and 2935 cm^{-1} can be attributed to contributions by CH_2 groups; this seems reasonable given that these peaks' heights increase as the carbon chain length increases. Observations by Klingbeil *et al.* corroborate this finding; these authors observed that normal pentane has a CH_2 -related peak at 2940 cm^{-1} , normal heptane has a CH_2 -related peak at 2936 cm^{-1} , and normal dodecane has CH_2 -related peaks at about 2866 cm^{-1} and 2933 cm^{-1} [225]. Note that the small peak observable in MC at about 2935 cm^{-1} is obviously not due to CH_2 group absorption since MC has no CH_2 groups; however, it may be due to absorption by the single C–H bonds adjacent to the C=C double bond.

The peaks in MA and MC near 2965 cm^{-1} must be attributed primarily to CH_3 group absorption, since MA and MC have no CH_2 groups. That MC has a higher peak cross section value than MA

at this wavelength indicates that the single C–H bonds adjacent to the C=C double bond in MC may contribute to total absorbance at this wavelength as well. Also, from MB to MD, the peak near 2965 cm^{-1} increases in magnitude still further; this indicates that the CH_2 groups in these fully saturated FAMEs can contribute to absorbance at 2965 cm^{-1} . However, the amount of increase of the 2965 cm^{-1} peak cross section seems to decrease as molecular size increases; the change from MB (2 CH_2 groups) to MHP (5 CH_2 groups) is $17.2\text{ m}^2/\text{mol}$, whereas from MHP to MD (8 CH_2 groups) is only $4\text{ m}^2/\text{mol}$. Klingbeil *et al.* attributed the peaks of normal pentane, heptane, and dodecane at 2966 cm^{-1} , 2968 cm^{-1} , and 2970 cm^{-1} respectively primarily to CH_3 group absorption, because they found these to have a similar magnitude cross section [225]. Finally, the relatively low cross sections of the valley located at about 2900 cm^{-1} may be attributable to CH_3 group absorption, since these values remain relatively constant between all saturated FAMEs studied.

5.5.2 Comparison with normal alkanes

As discussed above, the features of a molecule's absorption spectrum reflect the structure of that molecule. Thus, comparisons between two classes of molecules that have identifiable structural differences can reveal information about the source of spectral features that differ between the two molecular classes' spectra. In particular, the structure of FAMEs is similar to that of normal alkanes in that both classes possess a long hydrocarbon chain; however, FAMEs differ in that their chain is interrupted by a $\text{O}=\text{C}–\text{O}$ group, where a CH_3 function is bonded to the last O-atom. Therefore, comparisons between FAMEs and *n*-alkanes are useful because they reveal information concerning the effects of this $\text{O}=\text{C}–\text{O}$ group on the spectra. Furthermore, since spectral information for *n*-alkanes is more widely available due to their higher vapor pressures and common use as combustion fuels, knowledge of how FAME spectra differ from *n*-alkane spectra could allow useful extrapolations where no other knowledge is obtainable in the literature.

Spectra of propane (C_3H_8) [175], MPI, and MB are compared in Figure 5.31; keep in mind that propane and MPI have the same number of C–H bonds but MB has two more. Immediately obvious is that the overall magnitude of the MPI spectrum is smaller than that of propane; however, at frequencies greater than about 3000 cm^{-1} , the magnitude of MPI is greater than that of propane. In contrast, the magnitude of the MB spectrum more closely matches that of propane, especially

between 2950 cm^{-1} and 3000 cm^{-1} . As an example, at the frequency of the HeNe laser, the cross section of propane is about $22.3\text{ m}^2/\text{mol}$ and that of MPI is less than half of this value ($10.2\text{ m}^2/\text{mol}$), whereas that of MB is $15.4\text{ m}^2/\text{mol}$. It appears that one-to-one comparisons between the spectra of propane and MPI are not easily done because the two are so distinct. Overall, it seems that the spectrum of propane contains more fine structures than that of MPI, as if the $\text{O}=\text{C}-\text{O}$ function serves to dampen out and smooth over C–H oscillations.

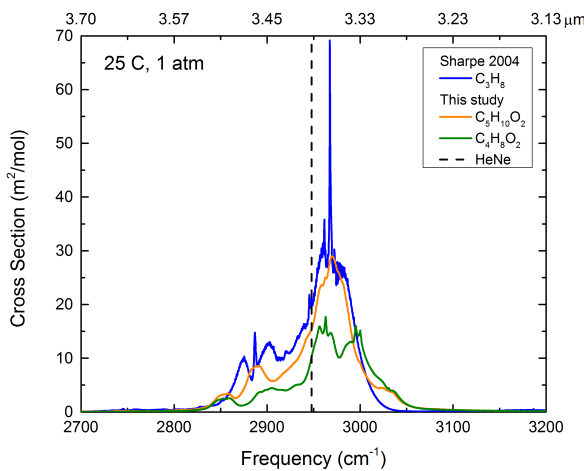


Figure 5.31: Comparison of the spectrum of propane (C_3H_8) as measured by Sharpe *et al.* [175] to those of methyl propionate ($\text{C}_4\text{H}_8\text{O}_2$) and methyl butanoate ($\text{C}_5\text{H}_{10}\text{O}_2$) at $25\text{ }^\circ\text{C}$ and 1 atm .

Spectra of normal butane (C_4H_{10}) [175], MB, and MV are compared in Figure 5.32; *n*-butane and MB have the same number of C–H bonds while MV has two more. While the magnitude of the MB spectrum is generally lower than that of *n*-butane, the spectrum of MB exceeds that of *n*-butane above about 3000 cm^{-1} , as it did in the case of propane and MPI. Though the spectrum of MB displays fewer fine features than of *n*-butane, it is able to mimic the overall *n*-butane feature trend much better than MPI was able to mimic that of propane. As in Figure 5.31, the spectrum of MV more closely resembles that of *n*-butane in the range 2950 cm^{-1} to 3000 cm^{-1} than does that of MB; at the HeNe wavelength the cross section values of *n*-butane, MB, and MV are $29.0\text{ m}^2/\text{mol}$, $15.4\text{ m}^2/\text{mol}$, and $25.7\text{ m}^2/\text{mol}$, respectively.

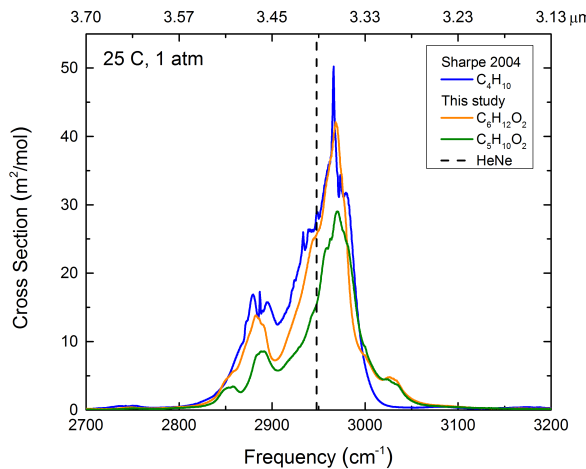


Figure 5.32: Comparison of the spectrum of *n*-butane (C_4H_{10}) as measured by Sharpe *et al.* [175] to those of methyl butanoate ($\text{C}_5\text{H}_{10}\text{O}_2$) and methyl valerate ($\text{C}_6\text{H}_{12}\text{O}_2$) at 25 °C and 1 atm.

A comparison between the spectra of *n*-pentane (C_5H_{12}) [225], MV, and MH is given in Figure 5.33. At some frequencies, namely less than 2850 cm^{-1} and between 2970 cm^{-1} and 3000 cm^{-1} , the three spectra follow the same trends. However, outside these small intervals, the spectra differ significantly. Overall, MH matches the spectrum of *n*-pentane better than MV; at the HeNe laser wavelength the cross sections of *n*-pentane, MV, and MH are 34.5 m^2/mol , 25.9 m^2/mol , and 32.9 m^2/mol , respectively.

Figure 5.34 offers a comparison between the spectra of *n*-heptane (C_7H_{16}) [225], MHP, and MOC. Not surprisingly, the same trends found in Figure 5.33 hold for this trio of fuels as well. At the HeNe laser wavelength, the cross section values of *n*-heptane, MHP, and MOC are 45.7 m^2/mol , 38.8 m^2/mol , and 45.4 m^2/mol , respectively.

Several observations can be made by reflecting on these normal alkane-FAME comparisons. First, it seems that as molecular size increases, the cross section values of normal alkanes and saturated methyl esters, which have two more C–H bonds, begin to coincide. Second, in the larger FAMEs studied, the O=C–O group appears to have a dampening effect on the spectrum between about 2850 cm^{-1} and 2970 cm^{-1} , such that the cross section values of FAMEs with the same number

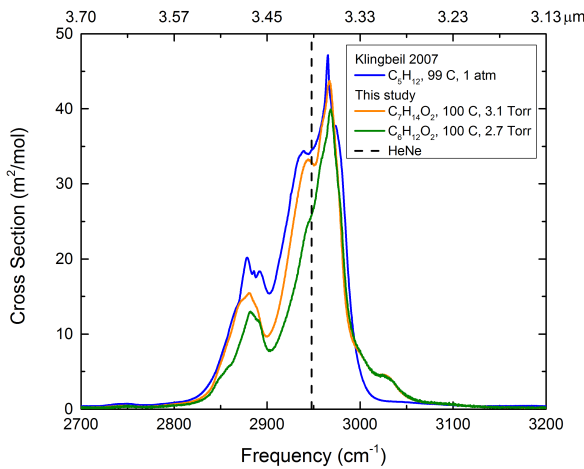


Figure 5.33: Comparison of the spectrum of normal pentane (C_5H_{12}) as measured by Klingbeil *et al.* [225] with the spectra of MV ($C_6H_{12}O_2$) and MH ($C_7H_{14}O_2$) at approximately 100 °C.

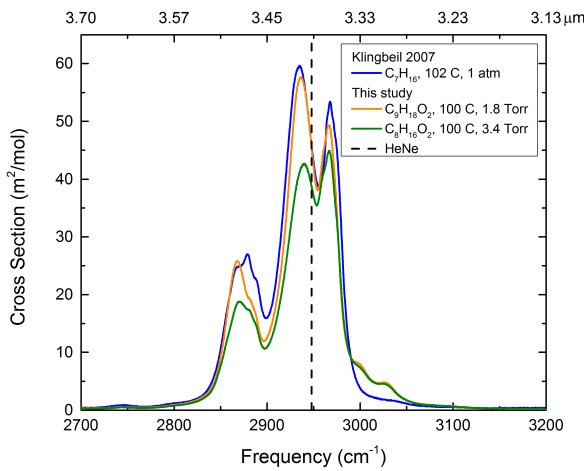


Figure 5.34: Comparison of the spectrum of normal heptane (C_7H_{16}) as measured by Klingbeil *et al.* [225] with the spectra of MHP ($C_8H_{16}O_2$) and MOC ($C_9H_{18}O_2$) at approximately 100 °C.

of C–H bonds as the corresponding normal alkane have lower cross section values. Third, the presence of the O=C–O group has a smoothing effect on FAME spectra relative to normal alkanes, such that fine features present in normal alkanes are not visible in the spectra of FAMEs. It is not thought that the absence of fine features in the FAME spectra relative to the normal alkane spectra is the result of apodization or instrument resolution effects.

5.5.3 Variation with number of C–H bonds

As mentioned in the introduction, many FAMEs of practical importance, such as those present in biodiesel fuel, have vapor pressures that are so low and decomposition rates that are so high that they are unsuitable for heated cell experimentation. In this case, an alternative to direct measurement of cross section values must be used; one technique is to extrapolate cross sections based on information from smaller FAMEs. Two properties of FAMEs are of primary interest: the integrated area Ψ , and the cross section $\sigma_{\nu,T}$ at the HeNe wavelength ($\nu = 3.39 \mu\text{m}$).

Figure 5.35 suggests that for normal alkanes, 1-alkenes, and saturated FAMEs, the integrated area of the C–H absorption band increases linearly with the number of C–H bonds N_{CH} in the fuel; this observation was also made by Klingbeil [241]. Interestingly, the rate of increase is greatest for normal alkanes and smallest for saturated FAMEs. Parameters for each of the best-fit lines in this figure according to Equation 5.6 are provided in Table 5.6.

$$\Psi = aN_{\text{CH}} + b \quad (5.6)$$

Table 5.6: Fitting parameters for integrated area best-fit lines in Figure 5.35 according to Equation 5.6. The \pm numbers are standard error values for the fitting parameters. $\Psi = aN_{\text{CH}} + b$.

Category	a [$1 \times 10^6 \text{ cm}^{-1}\text{cm}^2\text{mol}^{-1}(\text{N}_{\text{CH}})^{-1}$]	b [$1 \times 10^6 \text{ cm}^{-1}\text{cm}^2\text{mol}^{-1}$]	R^2	Source
n-Alkanes	3.54 ± 0.06	-3.32 ± 1.12	0.997	[Sharpe 2004] [175]
1-Alkenes	3.40 ± 0.22	-11.27 ± 2.82	0.975	[Sharpe 2004] [175]
Sat. FAMEs	3.21 ± 0.01	-11.29 ± 0.14	0.999	[Sharpe 2004] [175]
Sat. FAMEs	3.01 ± 0.10	-8.37 ± 1.49	0.993	This study

The second property for which extrapolation can be useful is the $3.39 \mu\text{m}$ HeNe laser cross section. Interestingly, the data of Sharpe *et al.* [175], of Mével *et al.* [227], and of this study

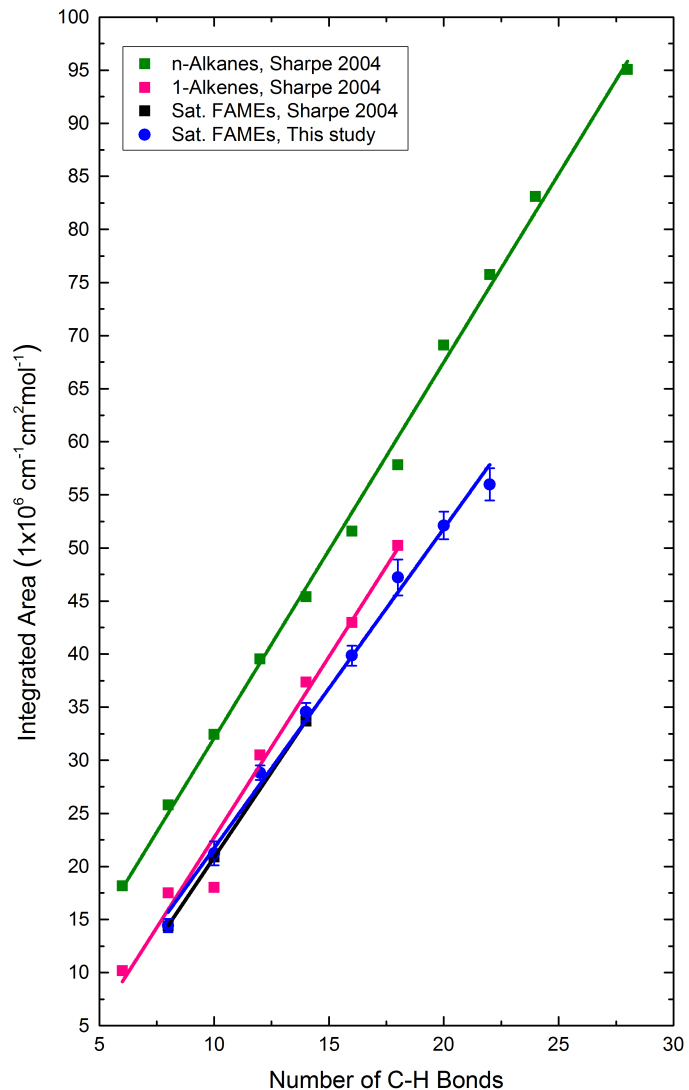


Figure 5.35: Demonstration that the number of C–H bonds and integrated area in *n*-alkanes, 1-alkenes, and saturated FAMEs have a linear relationship. Comparison is given with data from Sharpe *et al.* [175]. A similar trend was observed by Klingbeil [241].

indicate that the 3.39 μm cross section does not vary linearly with the absolute number of C–H bonds in the fuel N_{CH} (as proposed by Mével *et al.* in Equation 5.1), but rather varies linearly with the *logarithm* of the number of C–H bonds in the fuel $\log_{10}(N_{\text{CH}})$ (Equation 5.7).

$$\sigma_{\nu,T} = c \log_{10}(N_{\text{CH}}) + d \quad (5.7)$$

Figure 5.36 illustrates this concept. Furthermore, the rate of increase of the 3.39 μm cross section is approximately constant for all three hydrocarbon classes, as demonstrated by the best-fit line parameters in Table 5.7. A constant rate of increase across multiple molecular classes was also observed by Mével *et al.* [227] in the authors' predictive framework (Equation 5.1). Table 5.8 compares the R^2 values for best-fit lines to the absolute number of C–H bonds (Equation 5.1) and to the logarithm of the number of C–H bonds. In all cases except the data by Mével *et al.* [227], the R^2 value is 1–3% higher for the logarithm-based fit, which is an indication of the usefulness of the framework based on $\log_{10}(N_{\text{CH}})$ (the R^2 value for the logarithm-based fit to the Mével *et al.* data is only 0.5% less). The logarithmic variation is relatively unique to the 3.39 μm wavelength; not all parts of the C–H absorption spectrum exhibit this trend. Note that MA and MPI, with qualitatively different spectra from saturated FAMEs the size of MB and larger, have not been included in Figure 5.36. This simple linear relationship allows extrapolations of 3.39 μm cross section values to larger FAMEs to be made with greater confidence.

Table 5.7: Fitting parameters for 3.39 μm cross section best-fit lines in Figure 5.36 according to Equation 5.7. The \pm numbers are standard error values for the fitting parameters. Since only two data points were plotted for saturated FAME data from Sharpe *et al.* [175], no error statistics for this linear fit are given. $\sigma_{\nu,T} = c \log_{10}(N_{\text{CH}}) + d$.

Category	c [$\text{m}^2\text{mol}^{-1}(\log_{10}(N_{\text{CH}}))^{-1}$]	d [$\text{m}^2\text{mol}^{-1}$]	R^2	Source
n-Alkanes (140 °C)	95.40 ± 5.53	-71.24 ± 6.78	0.983	[Mevel 2012] [227]
n-Alkanes (50 °C)	92.65 ± 1.97	-61.43 ± 2.33	0.996	[Sharpe 2004] [175]
1-Alkenes (50 °C)	101.25 ± 7.31	-83.22 ± 8.08	0.974	[Sharpe 2004] [175]
Sat. FAMEs (25 °C)	115.04	-100.05		[Sharpe 2004] [175]
Sat. FAMEs	105.08 ± 2.17	-86.83 ± 2.46	0.997	This study

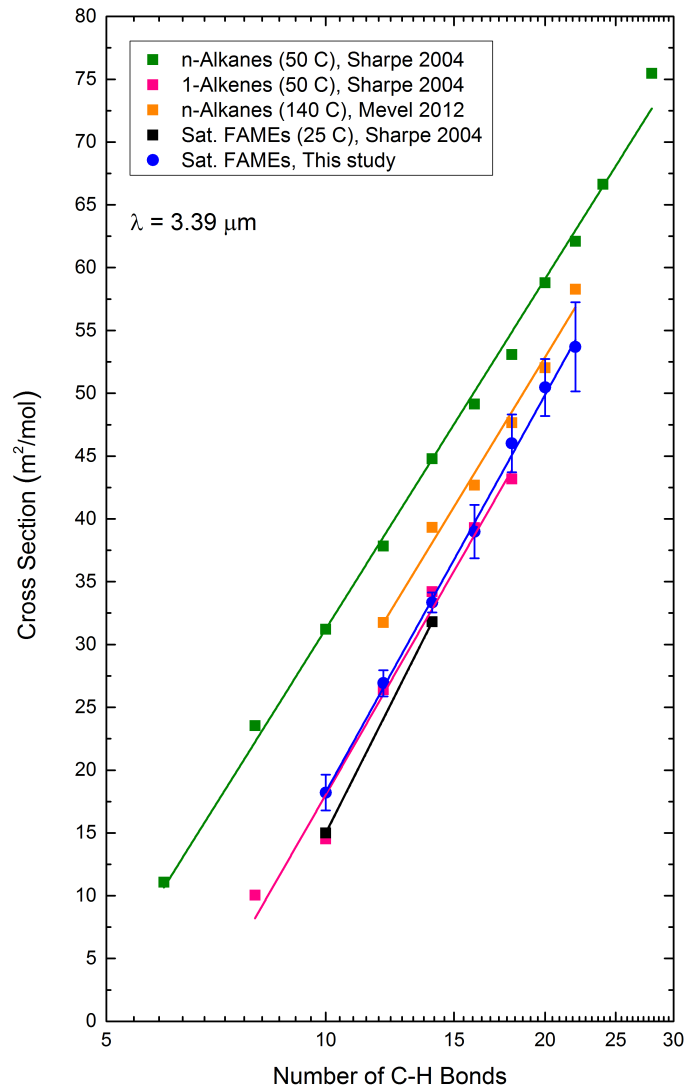


Figure 5.36: Demonstration of the linear relationship between a fuel's $3.39 \mu\text{m}$ cross section and the logarithm of the number of C–H bonds it contains. Shown here are the average cross section values (between 150 and 400°C) for the saturated FAMEs examined in this study, as well as values from Sharpe *et al.* [175] and Mével *et al.* [227].

Table 5.8: R^2 values for $3.39\text{ }\mu\text{m}$ cross section extrapolation best-fit lines based on the absolute number of C–H bonds in the fuel N_{CH} (as proposed by Mével *et al.* [227] in Equation 5.1) and on the logarithm of the number of C–H bonds in the fuel $\log_{10}(N_{\text{CH}})$ (Equation 5.7). Since only two data points were plotted for saturated FAME data from Sharpe *et al.* [175], no error statistics for this linear fit are given.

Category	$R^2(N_{\text{CH}})$	$R^2(\log_{10}(N_{\text{CH}}))$	Source
<i>n</i> -Alkanes (140 °C)	0.988	0.983	[Mevel 2012] [227]
<i>n</i> -Alkanes (50 °C)	0.966	0.996	[Sharpe 2004] [175]
1-Alkenes (50 °C)	0.964	0.974	[Sharpe 2004] [175]
Sat. FAMEs (25 °C)			[Sharpe 2004] [175]
Sat. FAMEs	0.981	0.997	This study

5.5.4 Effects of C=C double bonds

As introduced above, M3N ($\text{C}_{10}\text{H}_{18}\text{O}_2$) is a variant of MN ($\text{C}_{10}\text{H}_{20}\text{O}_2$), formed by inserting a C=C double bond in place of a C–C single bond at the third carbon site in the long hydrocarbon chain. This C=C bond affects the C–H spectrum in two ways. First, since both of the double-bonded carbon atoms may only bond to one hydrogen atom rather than to two, there are two fewer C–H bonds absorbing and contributing to the magnitude of the spectrum. Second, the hydrogen atoms attached to the double-bonded carbon atoms are held in vinylic bonds, as shown in Figure 5.37. These vinylic bonds have dissociation energies of $\sim 108\text{ kcal/mol}$, which is greater than the nearby values of $\sim 98\text{ kcal/mol}$ for secondary atoms and $\sim 88\text{ kcal/mol}$ for allylic bonds [48]. The greater bond dissociation energy of the vinylic bonds prevents them from vibrating as freely and thus hinders their ability to absorb energy in the $2500\text{--}3400\text{ cm}^{-1}$ frequency range. Conversely, the weakly bonded allylic hydrogen atoms are able to vibrate more freely, causing them to absorb more radiation. Combining these two effects, one might expect the effective number of C–H bonds of M3N to be greater than 16 (the effective number if M3N's vinylic bonds did not contribute) but less than 20 (the number of C–H bonds of MN). Using the observed integrated area for M3N ($\Psi = 43.0 \times 10^6\text{ cm}^{-1}\text{cm}^2\text{mol}^{-1}$) in Equation 5.6 and the parameters given in Table 5.6 to solve for the effective number of C–H bonds yields $N_{\text{CH}} = 17$, which is in good agreement with the framework introduced above.

Figure 5.38 offers a comparison between the spectra of MOC ($\text{C}_9\text{H}_{18}\text{O}_2$), MHP ($\text{C}_{10}\text{H}_{20}\text{O}_2$),

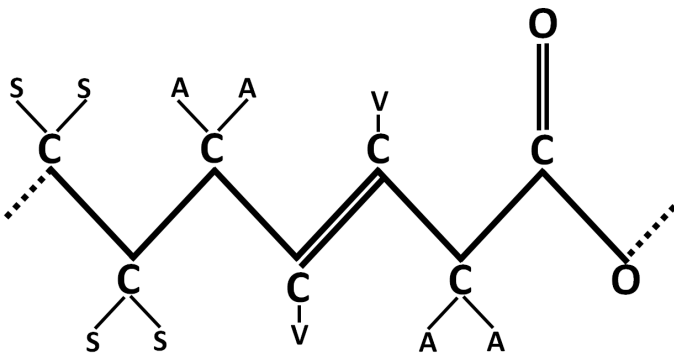


Figure 5.37: C–H bonds present in the vicinity of the C=C double bond in methyl-3-nonenate. “V” stands for vinylic bond (~108 kcal/mol), “A” stands for allylic bond (~88 kcal/mol), and “S” stands for secondary bond (~98 kcal/mol) [48].

and M3N ($C_{10}H_{18}O_2$) at 100 °C. Notice that all three spectra exhibit three primary peaks and two primary valleys, and that the frequency locations of these peaks/valleys are approximately the same. Near 2867 cm^{-1} , the peak values of MHP and M3N agree closely, whereas that of MOC is higher. However, the three fuels display the same cross section in the 2897 cm^{-1} valley. Near 2936 cm^{-1} , MOC and M3N agree more closely than MHP does; however, in the valley at 2953 cm^{-1} , M3N has a cross section that is much lower than those of MOC and MHP. At 2966 cm^{-1} , the spectra of MHP and M3N agree very closely while MOC has a slightly higher cross section; however, at frequencies above 2986 cm^{-1} in the wing of the spectra, M3N yields higher cross section values than MOC and MHP. Finally, at the HeNe laser wavelength, M3N displays a cross section significantly lower than those of MOC and MHP. These complex differences in spectra make it difficult to precisely pinpoint the effects of C=C double carbon bonds on measured spectra. Additional mono-unsaturated fuels were unavailable for experimentation at the time of this work; future studies should examine more unsaturated FAMEs.

5.6 Summary

Spectra of MA, MPI, MB, MV, MH, MHP, MOC, MN, MD, MC, and M3N have been measured at 1 cm^{-1} resolution between 2500 cm^{-1} and 3400 cm^{-1} and at temperatures ranging from 25 °C to

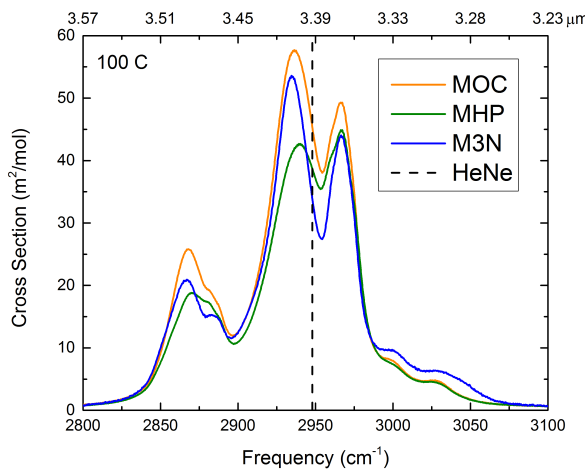


Figure 5.38: Comparison of spectra of MOC, MHP, and M3N at 100 °C.

500 °C using an FTIR spectrometer. Integrated area values and cross section values at 3.39 μm have been reported. The integrated area values were found to be independent of temperature in the absence of condensation/decomposition, and the 3.39 μm cross section values were found to be independent of temperature between 150 °C and 400 °C within the measurement uncertainty. Peak cross section values of these spectra were found to decrease linearly with temperature, and the FWHM values of these spectra were found to increase linearly with temperature. For both normal alkanes, 1-alkenes, and saturated FAMEs, the integrated area of the C–H absorption spectrum was found to increase linearly with the number of C–H bonds in the fuel; moreover, the 3.39 μm cross section values were found to increase linearly with the *logarithm* of the number of C–H bonds in the fuel. Finally, the presence of C=C double bonds in unsaturated FAMEs was found to decrease the cross section values compared to fully saturated counterpart molecules because unsaturated FAMEs possess two fewer hydrogen atoms and also the two hydrogen atoms caught in vinylic bonds are prevented from full oscillation. These spectra will be useful in the development of biodiesel-sensing diagnostics for use in a variety of combustion and chemistry-related applications.

Chapter 6

Application of the aerosol shock tube to fatty acid methyl ester ignition

*The contents of this chapter have been published in the journal **Proceedings of the Combustion Institute** [105] and in the journal **Fuel** [68]. They have also been presented at the **28th International Symposium on Shock Waves** [65], the **34th International Symposium on Combustion** [258], and the **8th United States Combustion Meeting** [67].*

6.1 Introduction

As mentioned in Chapter 1, biodiesel fuel possesses a number of unique advantages that make it a plausible alternative to conventional fossil fuels. In order to make use of biodiesel in modern day engines, a comprehensive understanding of its oxidation chemistry is needed. One key component of such an understanding is a fuel's ignition delay time at elevated temperatures and pressures. In this chapter, ignition delay times for several biodiesel surrogate molecules, measured behind reflected shock waves using the Stanford aerosol shock tube, are reported. These molecules are methyl decanoate, methyl laurate, methyl myristate, methyl palmitate, methyl oleate, methyl laurate, and a blend of methyl oleate and other Fatty Acid Methyl Esters (FAMEs).

6.2 Previous studies

6.2.1 Methyl decanoate

Of the surrogate fuels examined in this study, methyl decanoate (MD, $C_{11}H_{22}O_2$; see Figure 6.1) has been the subject of the majority of research efforts to date. This is because its vapor pressure at 315 K (186 milliTorr) makes it experimentally accessible using traditional techniques [27]; its melting point is 260 K [14] (more fuel property information can be found in Table 6.1). Moreover, it is the largest component in cuphea biodiesel (65% by mass), hailed for its beneficial properties [259]. Previous studies of MD include microgravity experimentation [89, 92, 93], motored engine studies [90], pre- and non-pre-mixed flame examinations [77, 84–88], pyrolysis studies [260], and jet-stirred reactor analyses [82, 83]. Shock tube studies were performed by Wang and Oehlschlaeger, who worked at pressures of 15–16 atm in 21% O_2 / N_2 mixtures with lean, stoichiometric, and rich equivalence ratios [79]; Haylett *et al.*, who worked at a pressure of 8 atm in 21% O_2 /Ar mixtures with very lean equivalence ratios [66]; and Li *et al.*, who examined methyl decanoate autoignition at engine exhaust gas recirculation (EGR) conditions in air [80] (see also Wang *et al.* [81], who measured several methyl decenoate (MDE, $C_{11}H_{20}O_2$) isomers). Other researchers have conducted modeling studies [91, 94–100], and some of the experimental papers also include sections concerning mechanism development or reduction [84, 85, 87, 92]. A summary of kinetic mechanisms designed for the fuels explored in this work is given in Table 6.2.

Table 6.1: Physical property information for the fuels investigated in this work [14, 27, 261].

Fuel	Molecular formula	Molecular weight [g/mol]	Vapor pressure (315 K) [Torr]	Melting point (1 atm) [K]
Methyl decanoate	$C_{11}H_{22}O_2$	186.3	186×10^{-3}	260
Methyl laurate	$C_{13}H_{26}O_2$	214.3	20.9×10^{-3}	278
Methyl myristate	$C_{15}H_{30}O_2$	242.4	3.27×10^{-3}	292
Methyl palmitate	$C_{17}H_{34}O_2$	270.5	327×10^{-6}	304
Methyl oleate	$C_{19}H_{36}O_2$	296.5	96.7×10^{-6}	254
Methyl linoleate	$C_{19}H_{34}O_2$	294.5	4.65×10^{-6}	238

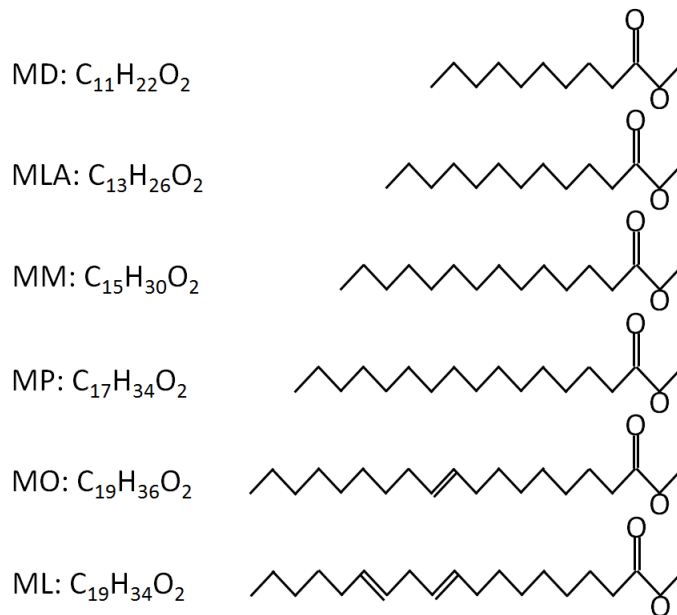


Figure 6.1: Molecular diagrams for the FAMEs whose ignition delay times have been measured in this work.

6.2.2 Methyl laurate

Methyl laurate (MLA, $\text{C}_{13}\text{H}_{26}\text{O}_2$) has been studied by far fewer researchers. Its vapor pressure at 315 K is 20.9 milliTorr [27] and its melting point is 278 K [14]. Vaughn *et al.* [89] and Marchese *et al.* [92] studied MLA droplets in microgravity environments, Schönborn *et al.* examined it in an engine study [36], and Herbinet *et al.* [97] developed a kinetic mechanism for this fuel using an automatic compilation program known as EXGAS.

6.2.3 Methyl myristate

Methyl myristate (MM, $\text{C}_{15}\text{H}_{30}\text{O}_2$) has also been relatively untouched in the literature. Its vapor pressure at 315 K is 3.27 milliTorr [27] and its melting point is 292 K [261]. One motored engine study [36] and one modeling study [97] have addressed this fuel.

6.2.4 Methyl palmitate

Despite being one of the five primary components of real biodiesel blends, methyl palmitate (MP, $C_{17}H_{34}O_2$) has been the subject of very few published experimental or kinetic modeling studies. Its low vapor pressure (327 microTorr at 315 K) [27] and its high melting point (304 K) [261] make it inaccessible to typical experimental techniques. However, Knothe *et al.* measured the cetane number of MP [28], Schönborn *et al.* studied MP in an engine using PID-controlled heaters to melt this waxy fuel [36], Hakka *et al.* dissolved MP in *n*-decane (at a ratio of 26:74 mol:mol respectively) in order to examine it using a jet-stirred reactor [102], and Wang *et al.* used a high pressure shock tube heated to 200 °C in order to make ignition delay time measurements [101]. Two relevant modeling studies are Herbinet *et al.* [97] and Westbrook *et al.* [32].

6.2.5 Methyl oleate

Methyl oleate (MO, $C_{19}H_{36}O_2$) has been the subject of multiple studies. Its vapor pressure at 315 K is 96.7 microTorr [27] and its melting point is 254 K [14]. Early work from the food industry is summarized by Porter *et al.* [262]. More recent work includes tubular reactor studies [107, 108], cetane number determination work [28], microgravity experimentation [89, 92], a motored engine study [36], a jet-stirred reactor analysis [106], a heated shock tube study [101], and kinetic modeling [32, 48, 103, 104].

6.2.6 Methyl linoleate

Methyl linoleate (ML, $C_{19}H_{34}O_2$) has been studied by fewer researchers than MO. Its vapor pressure at 315 K is 4.65 microTorr [27] and its melting point is 238 K [14]. Knothe *et al.* determined the cetane number for ML [28], Schönborn *et al.* studied ML in an engine, Wang *et al.* studied ML in a heated shock tube [101], and Westbrook *et al.* performed kinetic modeling [32, 48].

6.2.7 Summary of previous studies

The literature review above demonstrates that a solid base of research in the area of large biodiesel surrogates has been established. However, key pieces of information that are necessary

to improve kinetic mechanism accuracy are still lacking. In the case of MD, shock tube studies at oxygen contents other than 21% are needed. For MLA, MM, MP, MO, and ML, only scarce shock tube data is currently available. Additionally, for MO, shock tube data demonstrating the effect of blending this methyl ester with other FAMEs would be enlightening. The current work has sought to explore these research problems.

6.3 Experimental setup

6.3.1 Aerosol Shock Tube (AST)

The ignition delay time measurements discussed in this chapter were performed using the Aerosol Shock Tube (AST). Details of this facility can be found in Section 3.2.

6.3.2 Fuel and gas information

Research-grade gases employed in these experiments (1%, 4%, or 21% oxygen in argon) were obtained from Praxair Inc. FAMEs studied were obtained from Sigma-Aldrich Corp. and from Nu-Check Prep Inc.; these were subject to degassing prior to use by way of a mechanical vacuum pump over the surface of the liquid but were otherwise used without further purification (gas/fuel supplier and purity information can be found in Table 6.3).

One of the fuels studied was blend of (nominally) 70% methyl oleate and 30% other FAME components by mole (known as the Methyl Oleate Blend, MOB), obtained from Sigma-Aldrich Corp. A Gas-Chromatograph (GC) analysis was conducted by Inspectorate America (now known as Bureau Veritas - Commodities Division) to determine the composition of the MOB; the results (on a molar basis) are provided in Table 6.4. The analysis revealed the presence of 6.67% non-ester components; these were assumed to be glycerol ($C_3H_8O_3$), a product of the transesterification process used to produce FAMEs from fatty acids [10–13]; see also Figure 1.3. Interestingly, the measured percent of MO (62.98%) in the blend was less than that quoted by Sigma-Aldrich Corp. (>69.5%), which could be attributed to measurement error or to production problems. A separate estimation based on the GC certification analysis provided by Sigma-Aldrich Corp. revealed a 66.8%

Table 6.2: Studies that have developed or modified kinetic mechanisms for the fuels examined in this work.

Fuel	Authors	Year	Reference	Mechanism Type
Methyl decanoate	Herbinet <i>et al.</i>	2008	[96]	Detailed chemical kinetic mechanism
	Seshadri <i>et al.</i>	2009	[84]	Skeletal mechanism
	Glaude <i>et al.</i>	2010	[82]	EXGAS automatically-generated mechanism
	Herbinet <i>et al.</i>	2010	[96]	Modifications for monounsaturated variants of MD
	Luo <i>et al.</i>	2010	[95]	Skeletal mechanism
	Herbinet <i>et al.</i>	2011a	[83]	EXGAS automatically-generated mechanism
	Herbinet <i>et al.</i>	2011b	[97]	EXGAS automatically-generated mechanism
	Sarathy <i>et al.</i>	2011	[87]	Detailed chemical kinetic mechanism and skeletal mechanism
	Diévert <i>et al.</i>	2012	[98]	Detailed chemical kinetic mechanism
	Grana <i>et al.</i>	2012	[99]	Lumped kinetic mechanism
	Luo <i>et al.</i>	2012	[100]	Skeletal mechanism
Methyl laurate	Herbinet <i>et al.</i>	2011b	[97]	EXGAS automatically-generated mechanism
Methyl myristate	Herbinet <i>et al.</i>	2011b	[97]	EXGAS automatically-generated mechanism
Methyl palmitate	Herbinet <i>et al.</i>	2011b	[97]	EXGAS automatically-generated mechanism
	Westbrook <i>et al.</i>	2011	[32]	Detailed chemical kinetic mechanism
Methyl oleate	Naik <i>et al.</i>	2011	[104]	Detailed chemical kinetic mechanism
	Westbrook <i>et al.</i>	2011	[32]	Detailed chemical kinetic mechanism
	Westbrook <i>et al.</i>	2013	[48]	Detailed chemical kinetic mechanism
	Campbell <i>et al.</i>	2013	[105]	Updates to thermochemistry in Westbrook 2011 mechanism
	Saggese <i>et al.</i>	2013	[103]	Lumped kinetic mechanism
Methyl linoleate	Westbrook <i>et al.</i>	2011	[32]	Detailed chemical kinetic mechanism
	Westbrook <i>et al.</i>	2013	[48]	Detailed chemical kinetic mechanism
	Campbell <i>et al.</i>	2013	[105]	Updates to thermochemistry in Westbrook 2011 mechanism
	Saggese <i>et al.</i>	2013	[103]	Lumped kinetic mechanism

Table 6.3: Gas/fuel purity information, as determined by the supplier. The methyl oleate blend (MOB) is a mixture, obtained and used as-supplied from Sigma-Aldrich Corp., which consists of about 70% (by mole) methyl oleate, along with about 30% other FAME components. Fuels were subjected to mechanical pumping to remove dissolved oxygen but were otherwise used as-is without further purification.

Component	Supplier	Purity
Helium	Praxair Inc.	99.99%
1% Oxygen in argon	Praxair Inc.	99.99+%
4% Oxygen in argon	Praxair Inc.	99.99+%
21% Oxygen in argon	Praxair Inc.	99.99+%
Methyl decanoate (MD)	Sigma-Aldrich Corp.	99.4%
Methyl laurate (MLA)	Sigma-Aldrich Corp.	99.1%
Methyl myristate (MM)	Sigma-Aldrich Corp.	99.6%
Methyl palmitate (MP)	Sigma-Aldrich Corp.	99.4%
Methyl oleate blend (MOB)	Sigma-Aldrich Corp.	70% MO, 30% other FAMEs
Methyl oleate (MO)	Nu-Check Prep Inc.	99.9%
Methyl linoleate (ML)	Nu-Check Prep Inc.	99.9%

MO content, which is more consistent with the analysis by Inspectorate America. Regardless, high-temperature ignition delay time simulations conducted using the Saggese *et al.* mechanism revealed no significant change in reactivity with the inclusion of these other species as compared to assuming the blend was 100% MO [103].

Table 6.4: Gas chromatograph analysis of methyl oleate blend (molar percent).

Component	Molecular formula	Molar Percent
Methyl myristate	C ₁₅ H ₃₀ O ₂	2.99%
Methyl palmitoleate	C ₁₇ H ₃₂ O ₂	4.68%
Methyl palmitate	C ₁₇ H ₃₄ O ₂	4.13%
Methyl linolenate	C ₁₉ H ₃₂ O ₂	8.40%
Methyl linoleate	C ₁₉ H ₃₄ O ₂	8.34%
Methyl oleate	C ₁₉ H ₃₆ O ₂	62.98%
Methyl stearate	C ₁₉ H ₃₈ O ₂	0.75%
Methyl erucate	C ₂₃ H ₄₄ O ₂	0.16%
Methyl behenate	C ₂₃ H ₄₆ O ₂	0.31%
Methyl lignoceritate	C ₂₅ H ₅₀ O ₂	0.58%
Glycerol	C ₃ H ₈ O ₃	6.67%

Due to concerns about the oxidative stability of methyl oleate and the other FAMEs [52], the following precaution was taken. Two containers of the methyl oleate/FAME blend (MOB) were

acquired from the same production lot. One jar was kept sealed in nitrogen in a light-proof package, while the other was used in ignition delay time studies. On the last day of experimentation, the other sealed jar was opened and ignition delay times of its liquid were measured. Ignition delay times for the two jars were found to be effectively identical, indicating that the fuel that had been opened longer had not oxidized during the testing period.

Finally, equivalence ratios specified in this work are based on the total oxygen content in the mixture, including the two O-atoms possessed by these oxygenated fuels.

6.3.3 Sample experiment

A sample ignition delay time measurement shock experiment is provided in Section 3.2.6. The diagnostics employed allowed the measurement of pressure, OH* emission at (306 ± 75) nm, droplet scattering using a laser at 650 nm, and fuel/hydrocarbon absorption using a helium-neon (HeNe) laser at $3.39 \mu\text{m}$.

Ignition delay time data are plotted in Arrhenius form. The uncertainty in the reported ignition delay times is typically $\pm 30\%$, conservatively estimated by considering individual error contributions from temperature, pressure, and equivalence ratio.

6.4 Kinetic modeling

Ignition delay times were simulated using Chemkin-II (used for EXGAS mechanisms to avoid convergence problems) and Chemkin-Pro [263] (employed for all other mechanisms) by extrapolating the maximum gradient in the OH-radical concentration to the baseline (pre-ignition) value. Simulations did not include the experimental residual non-ideal pressure rise (mentioned in Section 3.2.2); at elevated temperatures this small increase has little effect on ignition delay, as illustrated in the methyl decanoate experiments/modeling of Wang and Oehlschlaeger [79].

Results for MD were simulated using three mechanisms: Herbinet *et al.* [94], Glaude *et al.* [82], and Diévert *et al.* [98]. These mechanisms are described and compared extensively in Li *et al.* [80]. Ignition delay times for MLA, MM, and MP were simulated using the Herbinet *et al.* [97] mechanism, which was automatically generated using the EXGAS software package and validated against

methyl palmitate jet-stirred reactor experiments [102]. Data for MP were also simulated using the Westbrook *et al.* [32] mechanism, which included thermochemistry updates discussed in Section 6.5.2.5 [105] (in this chapter, the updated mechanism will be referred to as the “updated Westbrook *et al.* mechanism”). Finally, results for MO, ML, and the MOB were simulated using the original Westbrook *et al.* [32] and updated Westbrook *et al.* [32, 105] mechanisms.

6.5 Results and discussion

6.5.1 Fully saturated FAMEs

6.5.1.1 Methyl decanoate

Ignition delay times for methyl decanoate were measured at a pressure of 7 atm in 1% and 21% oxygen/argon bath gas at equivalence ratios ranging from 0.29 to 0.81 and at temperatures ranging from 1026 to 1388 K. These data, together with data for other FAMEs in this dissertation, are available in Appendix H. Using these results, Arrhenius expressions in the form

$$\tau_{ign} = A \exp\left(\frac{\hat{E}_A}{\hat{R}_u T}\right) \quad (6.1)$$

were determined from the experimental data for the 1% and 21% oxygen/argon/MD mixtures. In this expression, τ_{ign} is the ignition delay time [ms], A is a constant [ms], \hat{E}_A is the activation energy [kcal/mol], $\hat{R}_u = 1.9872041 \times 10^{-3} \frac{\text{kcal}}{\text{mol}\cdot\text{K}}$ is the ideal gas constant [244, 245], and T is the temperature of the experiment [K]. The values of A and \hat{E}_A were determined by linear regression analysis of the natural logarithm of Equation 6.1, *i.e.*,

$$\ln(\tau_{ign}) = \ln(A) + \frac{\hat{E}_A}{\hat{R}_u} \left(\frac{1}{T} \right) \quad (6.2)$$

The \hat{E}_A variable should be considered a fitting parameter rather than a constant with physical meaning (as elementary reaction activation energy values can be). However, a derivation of Equation 6.1 based on fundamental principles can be found in Appendix D. Data used to compute A and \hat{E}_A by way of Equation 6.2 were first scaled to a common pressure P and equivalence ratio ϕ (see

Equation 6.3 below), in order to eliminate second-order scaling dependencies.

Arrhenius parameters were also determined based on ignition delay times simulated using the Herbinet *et al.* [94], Glaude *et al.* [82], and Diévert *et al.* [98] mechanisms for 1% and 21% oxygen/argon/MD mixtures at the conditions of this study. Additionally, data from Wang and Oehlschlaeger [79], which were obtained using a heated high pressure shock tube at 15-16 atm in 21% oxygen/nitrogen/MD mixtures, were scaled to 7 atm using a simple $\tau_{ign} \sim P^{-1}$ rule; an Arrhenius expression for this scaled data set has also been determined. The Arrhenius parameters mentioned above, along with the Arrhenius data determined by both mechanism and experiment for the other fuels pertinent to this study, are listed in Table 6.5. Arrhenius correlations for individual equivalence ratio-pressure combinations, rather than one overall correlation, are supplied because of the wide variation in activation energy across the conditions studied.

Ignition delay time data measured in this study for methyl decanoate are plotted in Arrhenius form in Figure 6.2. On this and all subsequent plots, error bars are reported in temperature only (*i.e.*, horizontally) because post-reflected shock temperature is the primary source of uncertainty in these measurements. By way of reference, for fuels with activation energies of roughly 45 kcal/mol, a 1.2% uncertainty in temperature results in a 25% uncertainty in ignition time.

Small corrections to ignition delay times have been applied to scale individual points to a common pressure P^{common} and common equivalence ratio ϕ^{common} in Figure 6.2 and all subsequent Arrhenius figures according to Equation 6.3 (note that in the form given by Equation 6.3 below, exponents a and b will be negative the exponents that would be computed using Equation 2 in Reference [68]). For methyl decanoate, scaling exponents a and b were obtained by perturbing P and ϕ by small amounts in the Westbrook *et al.* kinetic mechanism [32] (this mechanism is based in part on the Herbinet *et al.* (2008) methyl decanoate mechanism [94]) and observing the change in τ_{ign} . For all other fuels, scaling exponents were obtained through linear regression analysis on the experimental data.

$$\tau_{ign}^{scaled} = \tau_{ign}^{unscaled} \left(\frac{P^{common}}{P^{unscaled}} \right)^a \left(\frac{\phi^{common}}{\phi^{unscaled}} \right)^b \quad (6.3)$$

In Figure 6.2, noteworthy is the negative oxygen mole fraction scaling shown on the plot; as oxygen content increases, ignition delay times decrease. Moreover, activation energy, visible in

Table 6.5: Best-fit Arrhenius parameters for MD, MLA, MM, and MP according to Equation 6.1. Comparisons are also given, where appropriate, with predictions from the Diévert *et al.* [98], Glaude *et al.* [82], Herbinet *et al.* [94], Herbinet *et al.* [97], and updated Westbrook *et al.* [32, 105] mechanisms. Arrhenius information is given as well for the scaled methyl decanoate data of Wang and Oehlschlaeger [79]. The \pm numbers are computed from the standard error values for the fitting parameters. $T_{ign} = A \exp\left(\frac{\hat{E}_A}{R_u T}\right)$.

Fuel	Data Set	Pressure [atm]	Equivalence Ratio	x_{O_2}	A [ms]	\hat{E}_A [kcal/mol]	R^2	Temperature Range [K]
MD	This Study	7	0.5	0.01	$4.95 \pm 73.34 \times 10^{-9}$	47.3 ± 7.3	0.914	1262-1388
MD	Herbinet 2008 [94]	7	0.5	0.01	2.10×10^{-8}	44.6		1262-1388
MD	Glaude 2010 [82]	7	0.5	0.01	1.70×10^{-11}	63.5		1262-1388
MD	Diévert 2012 [98]	7	0.5	0.01	8.70×10^{-10}	53.8		1262-1388
MD	This Study	7	0.5	0.21	$7.11 \pm 16.02 \times 10^{-6}$	26.0 ± 2.6	0.935	1026-1213
MD	Wang 2012 (in air; scaled) [79]	7	0.5	0.21	$2.28 \pm 1.73 \times 10^{-6}$	28.9 ± 1.2	0.985	1001-1314
MD	Herbinet 2008 [94]	7	0.5	0.21	1.18×10^{-7}	34.9		1026-1213
MD	Glaude 2010 [82]	7	0.5	0.21	3.48×10^{-7}	33.8		1026-1213
MD	Diévert 2012 [98]	7	0.5	0.21	9.02×10^{-7}	31.7		1026-1213
MLA	This Study	3.5	1.25	0.04	$2.71 \pm 23.10 \times 10^{-8}$	43.2 ± 5.7	0.905	1217-1351
MLA	Herbinet 2011 [97]	3.5	1.25	0.04	7.53×10^{-9}	49.3		1300-1354
MLA	This Study	7	0.75	0.04	$4.74 \pm 4.96 \times 10^{-8}$	40.8 ± 1.8	0.987	1163-1320
MLA	Herbinet 2011 [97]	7	0.75	0.04	3.56×10^{-9}	48.6		1163-1354
MLA	This Study	7	1.25	0.04	$2.95 \pm 2.81 \times 10^{-6}$	30.9 ± 1.7	0.974	1171-1354
MLA	Herbinet 2011 [97]	7	1.25	0.04	6.37×10^{-8}	42.3		1163-1354
MM	This Study	3.5	0.75	0.04	$1.32 \pm 4.06 \times 10^{-8}$	44.2 ± 3.6	0.951	1207-1334
MM	Herbinet 2011 [97]	3.5	0.75	0.04	3.12×10^{-9}	50.1		1162-1357
MM	This Study	7	0.75	0.04	$1.57 \pm 3.09 \times 10^{-8}$	43.1 ± 2.7	0.952	1162-1317
MM	Herbinet 2011 [97]	7	0.75	0.04	4.81×10^{-9}	47.9		1162-1357
MM	This Study	7	1.25	0.04	$5.26 \pm 6.18 \times 10^{-7}$	34.9 ± 1.9	0.968	1162-1357
MM	Herbinet 2011 [97]	7	1.25	0.04	9.99×10^{-8}	41.3		1162-1357
MP	This Study	3.5	0.75	0.04	$4.14 \pm 12.20 \times 10^{-10}$	52.4 ± 3.4	0.972	1180-1309
MP	Herbinet 2011 [97]	3.5	0.75	0.04	3.67×10^{-9}	49.9		1180-1311
MP	Updated Westbrook 2011 [32, 105]	3.5	0.75	0.04	2.46×10^{-8}	41.8		1180-1311
MP	This Study	7	0.375	0.04	$3.29 \pm 3.91 \times 10^{-7}$	35.1 ± 1.9	0.976	1191-1311
MP	Herbinet 2011 [97]	7	0.375	0.04	2.99×10^{-10}	53.6		1180-1311
MP	Updated Westbrook 2011 [32, 105]	7	0.375	0.04	3.12×10^{-9}	46.0		1180-1311

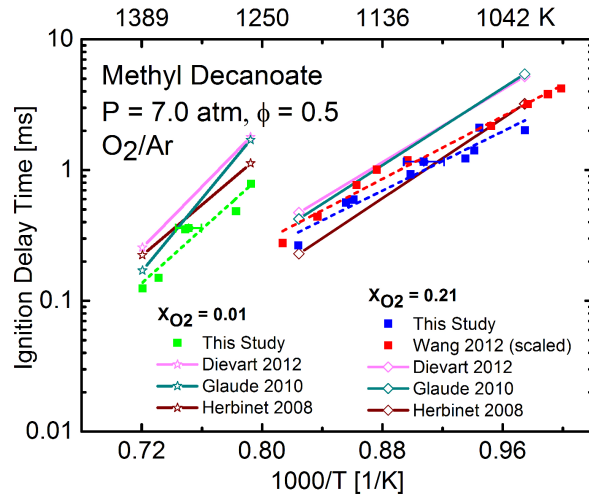


Figure 6.2: Methyl decanoate ignition delay times at $\phi = 0.5$ and 7 atm for oxygen mole fractions of 0.01 and 0.21 in argon. Solid lines are predictions by Diévert *et al.* [98], Glaude *et al.* [82], Herbinet *et al.* [94] mechanisms, and short-dashed lines (in this and all other figures) represent best-fits to data from this study. Data from Wang and Oehlschlaeger [79] were taken in air at 15-16 atm and have been scaled to 7 atm using a simple $\tau_{ign} \sim P^{-1}$ rule; a short-dashed best-fit line has also been included for this data as well.

the slope $\left(\frac{d\tau_{ign}}{d(\frac{1}{T})}\right)$ of the data points and numerically in Table 6.5, decreases as oxygen content increases. Also shown in this figure are the scaled 21% oxygen/nitrogen/MD data from Wang and Oehlschlaeger [79]. Notice the similarity, given experimental uncertainty, in ignition delay times and activation energy between the scaled Wang and Oehlschlaeger data and the 21% oxygen/argon/MD data presented in the current study. This gives confidence in the aerosol shock tube technique and supports comparisons between the two shock tube facilities. As expected, the diluent of the experiment (nitrogen vs. argon) has little effect on the measured ignition delay times [264]; however, a slightly shorter ignition delay time in the argon-diluted data is observable.

Ignition delay time predictions made using the mechanisms of Herbinet *et al.* [94], Glaude *et al.* [82], and Diévert *et al.* [98] have also been plotted in Figure 6.2 in solid lines. First, observe the 1% oxygen/argon/MD mixture data. At low temperatures, the Herbinet mechanism predicts ignition times more closely; however, at higher temperatures, the Glaude mechanism predicts ignition times more closely. For all temperatures, the Diévert mechanism's predictions are too slow by an approximate factor of two. At high temperatures, hydrocarbon fuel ignition is highly sensitive to fuel unimolecular decomposition reaction rates. It is thus likely that the single largest source of difference between measured and simulated ignition times are these decomposition rates, making them a good target for future experimental and modeling efforts.

Next, observe the 21% oxygen/argon/MD mixture data. The Herbinet mechanism under-predicts ignition delay times at high temperatures but reproduces them well at low temperatures. Conversely, the Glaude and Diévert mechanisms over-predict ignition delay times at low temperatures but do a good job at high temperatures. Finally, notice that, true to the experimental data presented here, all of the mechanisms predict a decrease in ignition delay time and activation energy as oxygen content increases.

6.5.1.2 Methyl laurate

Ignition delay times for methyl laurate were measured at pressures of 3.5 and 7 atm in 4% oxygen/argon bath gas at equivalence ratios ranging from 0.67 to 1.44 and at temperatures ranging

from 1163 to 1354 K. Results are displayed in Figure 6.3. First observe the data at a common pressure of 7 atm. For these data, at high temperatures, positive equivalence ratio scaling is evident, in which an increase in equivalence ratio results in an increase in ignition delay time (in Equation 6.3, $b > 0$). However, notice that at low temperatures, the data seem to be insensitive to equivalence ratio. Next observe the data at a common equivalence ratio of $\phi = 1.25$. Within this subset of the data, negative pressure scaling is evident; as pressure increases, ignition delay time decreases (in Equation 6.3, $a < 0$).

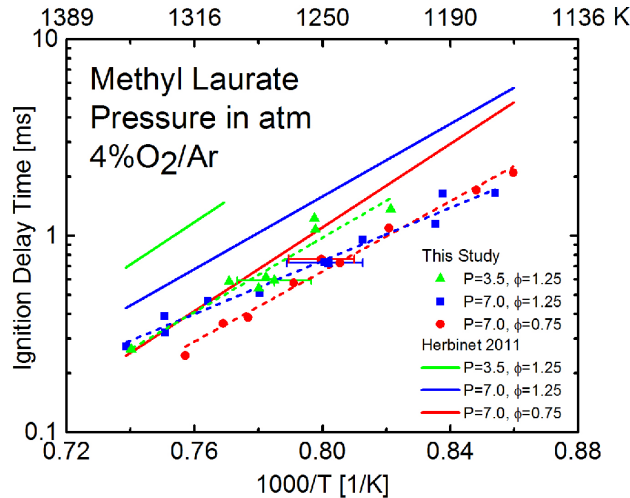


Figure 6.3: Methyl laurate ignition delay times taken in 4% oxygen/argon mixtures. Comparison is given with the Herbinet *et al.* mechanism [97], shown in solid lines.

Ignition delay time predictions calculated using the Herbinet *et al.* mechanism [97] are also shown in Figure 6.3. Notice that the Herbinet mechanism generally over-predicts ignition delay times; its predictions at 3.5 atm are too long by an approximate factor of two. However, for the higher-temperature data at 7 atm, the mechanism's predictions are closer to the experimental results. The mechanism seems to accurately capture the positive equivalence ratio scaling and negative pressure scaling. Focusing on the predictions at 7 atm, it is observable that the mechanism emulates the experimentally-seen low-temperature equivalence ratio independence.

6.5.1.3 Methyl myristate

Ignition delay times for methyl myristate were measured at pressures of 3.5 and 7 atm in 4% oxygen/argon bath gas at equivalence ratios ranging from 0.54 to 1.35 and at temperatures ranging from 1162 to 1357 K. The results, displayed in Figure 6.4, show striking resemblance to those of methyl laurate. Similar to MLA, the MM data display positive equivalence ratio scaling (observable at high temperatures) and negative pressure scaling. Also similar to MLA, the MM data show insensitivity to equivalence ratio at low temperatures.

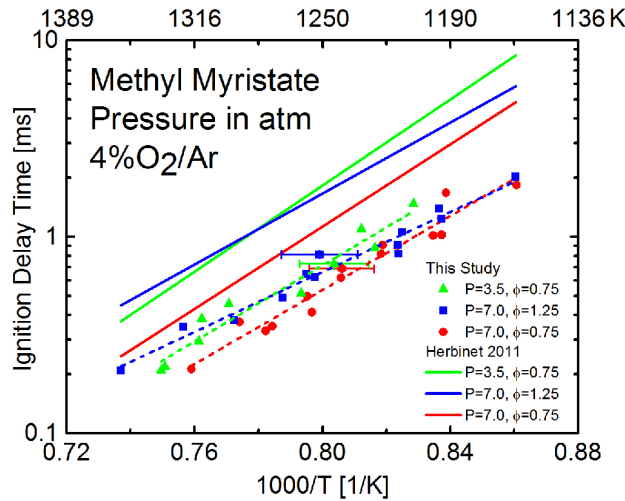


Figure 6.4: Methyl myristate ignition delay times taken in 4% oxygen/argon mixtures. Comparison is given with the Herbinet *et al.* mechanism [97], shown in solid lines.

Comparisons with the methyl myristate mechanism of Herbinet *et al.* [97] are also shown in Figure 6.4. At all temperatures studied the Herbinet mechanism over-predicts ignition delay time data by a factor of approximately two. As in the MLA mechanism predictions, the MM mechanism seems to capture the positive equivalence ratio scaling and negative pressure scaling accurately. In addition, the mechanism correctly captures the equivalence ratio independence shown in the MM data at low temperatures.

6.5.1.4 Methyl palmitate

Ignition delay times for methyl palmitate were measured at pressures of 3.5 and 7 atm in 4% oxygen/argon bath gas at equivalence ratios ranging from 0.27 to 0.81 and at temperatures ranging from 1180 to 1311 K. Results are displayed in Figure 6.5. While the two sets of data displayed have neither pressure nor equivalence ratio in common, several important comparisons can nevertheless still be made. Observe that ignition delay times taken at lower pressure and higher equivalence ratio are longer than those taken at higher pressure and lower equivalence ratio; however, a convergence of the two trends can be seen at high temperatures.

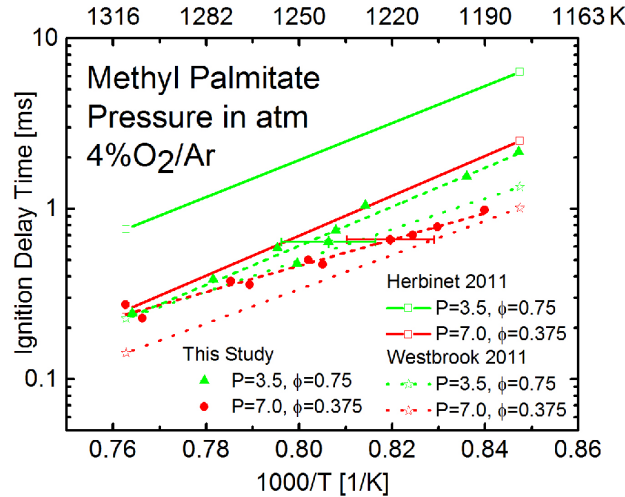


Figure 6.5: Methyl palmitate ignition delay times taken in 4% oxygen/argon mixtures. Comparison is given with the Herbinet *et al.* [97] (solid lines) and updated Westbrook *et al.* [32, 105] (dotted lines) mechanisms.

Comparison is given in Figure 6.5 with predictions from the Herbinet *et al.* [97] and updated Westbrook *et al.* [32, 105] mechanisms. (Though the updates to the Westbrook *et al.* [32] mechanism are not introduced until Section 6.5.2.5, the updated mechanism, rather than the original, will nonetheless be used for simulations here.) Both mechanisms correctly predict that the data taken at low pressure and high equivalence ratio should have longer ignition delay times than those taken at high pressure and low equivalence ratio. Within the 3.5 atm data, at all temperatures studied, the

Herbinet mechanism over-predicts ignition delay times by an approximate factor of four. In contrast, the updated Westbrook mechanism predicts ignition delay times correctly at high temperatures, but under-predicts them by approximately twofold at lower temperatures. Observations may also be made by focusing solely on the 7 atm data. At high temperatures, the Herbinet mechanism accurately captures ignition delay time data; however, at lower temperatures its predictions are too large. In contrast, the Westbrook mechanism under-predicts ignition delay times at high temperatures, but correctly simulates them at low temperatures.

6.5.1.5 Comparison between methyl laurate and methyl myristate

A comparison between the ignition delay time results for MLA and MM at a pressure of 7 atm and equivalence ratios of $\phi = 0.75$ and $\phi = 1.25$ is given in Figure 6.6. This comparison is insightful because it helps elucidate the effect of carbon chain length on ignition delay time; the structures of MLA and MM are identical except that the carbon chain length of MLA is 12, whereas that of MM is 14. First observe the data points for MLA and MM that occur at an equivalence ratio of $\phi = 0.75$. A comparison between these two sets of data reveals that, at high temperatures, ignition delay time may decrease as carbon chain length increases from MLA to MM (although the temperature error bars on the data, shown on Figures 6.3 and 6.4, obscure this fact slightly). This effect is also seen in large normal alkanes. This decrease could be due to the effect of carbon chain length on C–H and C–C bond strength [24, 265]. Also, this effect is most pronounced at high temperatures, and is less apparent as temperature decreases. A comparison of these two fuels at an equivalence ratio of $\phi = 1.25$ also reveals that ignition delay time decreases as carbon chain length increases from MLA to MM.

Ignition delay times simulated using the Herbinet *et al.* [97] mechanism are also shown in Figure 6.6. The mechanism does not capture the increase in reactivity with carbon chain length; in fact, it seems to predict a slight decrease in reactivity as carbon chain length increases from MLA to MM.

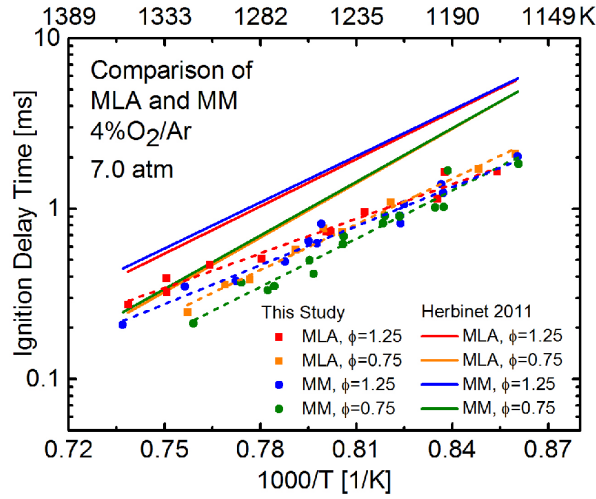


Figure 6.6: Comparison of methyl laurate and methyl myristate ignition delay times at 7 atm and equivalence ratios of $\phi = 0.75$ and $\phi = 1.25$, together with simulations performed using the Herbinet *et al.* [97] mechanism.

6.5.1.6 Comparison between methyl myristate and methyl palmitate

A comparison between the ignition delay time results for MM and MP at a pressure of 3.5 atm and an equivalence ratio of $\phi = 0.75$ is given in Figure 6.7. This graph further emphasizes the effect of carbon chain length on reactivity; MM has a carbon chain length of 14 and MP has a carbon chain length of 16. Similar to the MLA-MM comparison, at high temperatures this figure may indicate that reactivity increases (ignition delay time decreases) as carbon chain length increases from MM to MP (although the temperature error bars on the data, shown on Figures 6.4 and 6.5, obscure this fact slightly). Moreover, in the same way this change is more pronounced at high temperatures and less noticeable as temperature decreases.

Figure 6.7 also includes ignition delay time predictions performed using the Herbinet *et al.* [97] mechanism. As in the MLA-MM comparison, the mechanism fails to capture the increase in reactivity as chain length increases from MM to MP, and in fact a slight reduction in reactivity can be seen.

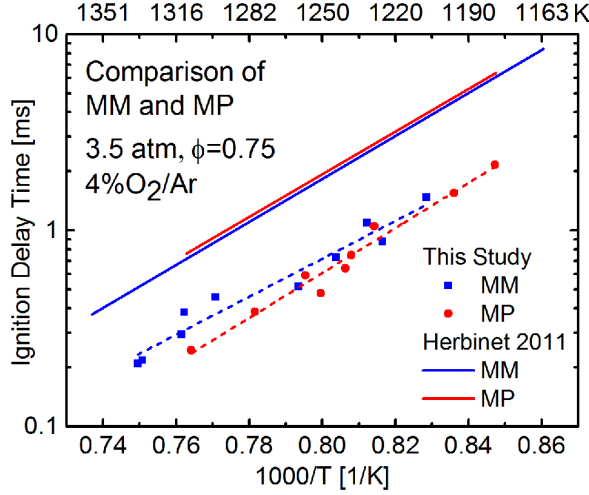


Figure 6.7: Comparison of methyl myristate and methyl palmitate ignition delay times at 3.5 atm and $\phi = 0.75$, together with simulations performed using the Herbinet *et al.* [97] mechanism.

6.5.2 Unsaturated FAMEs

6.5.2.1 Methyl oleate

Ignition delay times for methyl oleate were measured in 4% oxygen/argon bath gas at pressures of 3.5 and 7 atm, equivalence ratios from 0.6 to 2.4, and temperatures from 1115 to 1370 K. Using these data, Arrhenius expressions were determined for methyl oleate for several pressure and stoichiometry conditions, as shown (together with predictions by the original Westbrook *et al.* [32] and updated Westbrook *et al.* [32, 105] mechanisms) in Table 6.6. This table also includes values for methyl linoleate and the methyl oleate/FAME blend.

Ignition delay times for methyl oleate are plotted in Figure 6.8, where best-fits to the data are shown as dotted or dashed lines. Negative pressure scaling (increasing pressure decreases ignition time) and positive equivalence ratio scalings are immediately evident, although close inspection reveals that both scalings are not constant but vary with temperature. The pressure ratio scaling exhibits a crossover temperature near 1450 K (*i.e.*, where the ignition delay time shows no sensitivity to pressure). The equivalence ratio scaling exhibits a cross-over temperature near 1150 K.

In the case of the equivalence ratio scaling, at temperatures higher than 1150 K, the equivalence

Table 6.6: Best-fit Arrhenius parameters for MO, ML, and the MOB according to Equation 6.1. Comparisons are also given, where appropriate, with predictions from the original Westbrook *et al.* [32] and updated Westbrook *et al.* [32, 105] mechanisms. The \pm numbers are computed from the standard error values for the fitting parameters. $\tau_{ign} = A \exp\left(\frac{\hat{E}_A}{R_u T}\right)$.

Fuel	Data Set	Pressure [atm]	Equivalence Ratio	x_{O_2}	A [ms]	\hat{E}_A [kcal/mol]	R^2	Temperature Range [K]
MO	This Study	3.5	1.25	0.04	$3.03 \pm 5.52 \times 10^{-8}$	42.8 ± 2.6	0.970	1196-1370
MO	Original Westbrook 2011 [32]	3.5	1.25	0.04	4.62×10^{-7}	34.7		1196-1370
MO	Updated Westbrook 2011 [32, 105]	3.5	1.25	0.04	7.44×10^{-8}	40.1		1136-1333
MO	This Study	7	0.75	0.04	$9.37 \pm 14.03 \times 10^{-8}$	38.2 ± 2.2	0.980	1152-1314
MO	Original Westbrook 2011 [32]	7	0.75	0.04	1.47×10^{-7}	36.4		1152-1314
MO	Updated Westbrook 2011 [32, 105]	7	0.75	0.04	2.40×10^{-8}	41.8		1136-1333
MO	This Study	7	1.25	0.04	$7.32 \pm 4.50 \times 10^{-7}$	33.6 ± 1.2	0.987	1131-1339
MO	Original Westbrook 2011 [32]	7	1.25	0.04	1.91×10^{-7}	35.7		1131-1339
MO	Updated Westbrook 2011 [32, 105]	7	1.25	0.04	4.89×10^{-8}	40.2		1136-1333
MO	This Study	7	2.00	0.04	$1.17 \pm 0.66 \times 10^{-5}$	27.1 ± 1.1	0.984	1115-1316
MO	Original Westbrook 2011 [32]	7	2.00	0.04	5.11×10^{-7}	33.6		1115-1316
MO	Updated Westbrook 2011 [32, 105]	7	2.00	0.04	1.17×10^{-7}	38.2		1136-1333
ML	This Study	3.5	1.25	0.04	$1.10 \pm 0.99 \times 10^{-7}$	39.4 ± 1.6	0.989	1179-1350
ML	Original Westbrook 2011 [32]	3.5	1.25	0.04	3.44×10^{-7}	35.1		1179-1350
ML	Updated Westbrook 2011 [32, 105]	3.5	1.25	0.04	4.43×10^{-8}	41.4		1136-1333
ML	This Study	7	0.75	0.04	$1.86 \pm 1.48 \times 10^{-7}$	36.7 ± 1.4	0.986	1141-1334
ML	Original Westbrook 2011 [32]	7	0.75	0.04	1.27×10^{-7}	36.7		1141-1334
ML	Updated Westbrook 2011 [32, 105]	7	0.75	0.04	2.91×10^{-8}	41.5		1136-1333
ML	This Study	7	1.25	0.04	$1.95 \pm 1.15 \times 10^{-6}$	31.4 ± 1.2	0.989	1143-1378
ML	Original Westbrook 2011 [32]	7	1.25	0.04	1.62×10^{-7}	35.9		1143-1378
ML	Updated Westbrook 2011 [32, 105]	7	1.25	0.04	4.62×10^{-8}	40.3		1136-1333
ML	This Study	7	2.00	0.04	$6.06 \pm 5.04 \times 10^{-6}$	28.6 ± 1.5	0.984	1128-1332
ML	Original Westbrook 2011 [32]	7	2.00	0.04	3.62×10^{-7}	34.1		1128-1332
MOB	Updated Westbrook 2011 [32, 105]	7	2.00	0.04	1.16×10^{-7}	38.2		1136-1333
MOB	This Study	7	0.75	0.04	$3.42 \pm 2.60 \times 10^{-7}$	35.6 ± 1.4	0.977	1158-1358
MOB	This Study	7	1.25	0.04	$2.32 \pm 1.10 \times 10^{-6}$	31.0 ± 1.0	0.986	1141-1360

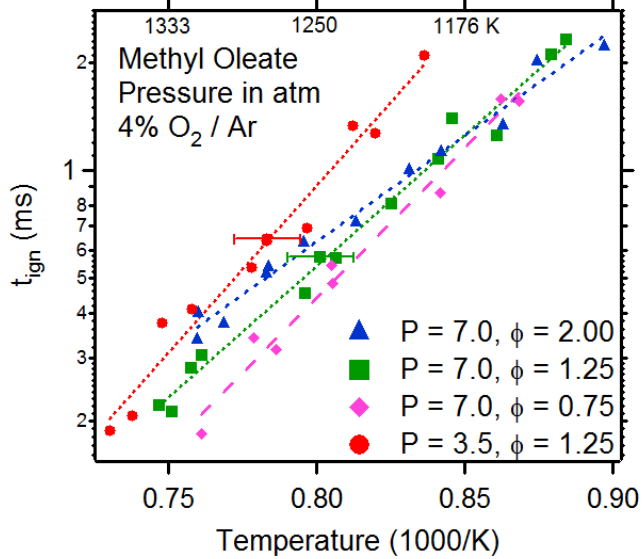


Figure 6.8: Methyl oleate ignition delay times taken in 4% oxygen/argon mixtures. Best-fits to data are shown in dotted or dashed lines.

ratio scaling is positive, and at lower temperatures, scaling is expected to become negative. Such a cross-over point is observable in high-temperature results for other fuels, including experimental data for methyl decanoate by Wang and Oehlschlaeger [79].

6.5.2.2 Methyl linoleate

Ignition delay times for methyl linoleate were measured in 4% oxygen/argon bath gas at pressures of 3.5 and 7 atm, equivalence ratios from 0.7 to 2.3, and temperatures from 1128 to 1378 K; data are plotted in Figure 6.9. The figure shows that, as for methyl oleate, pressure and equivalence ratio scaling are temperature-dependent for methyl linoleate. The pressure and equivalence ratio crossover temperatures are 1400 and approximately 1170 K, respectively. The high-temperature methyl linoleate data at $\phi = 2.0$ and $\phi = 1.25$ have closer values than in the case of methyl oleate.

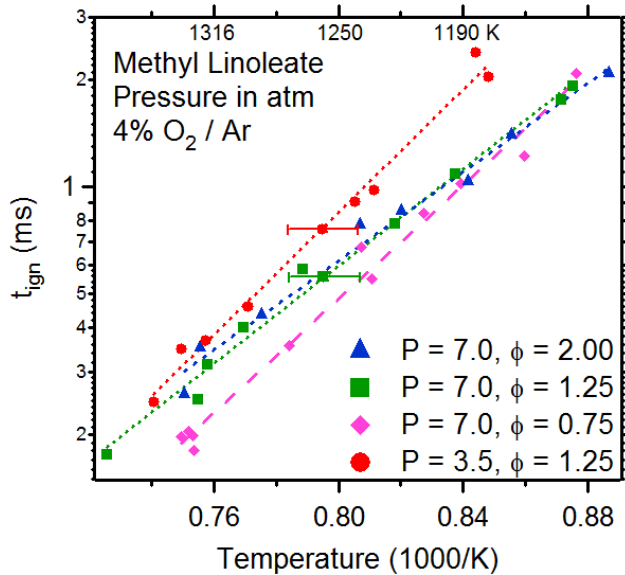


Figure 6.9: Methyl linoleate ignition delay times taken in 4% oxygen/argon mixtures. Best-fits to data are shown in dotted or dashed lines.

6.5.2.3 Methyl oleate/FAME blend

Ignition delay times for the methyl oleate/FAME blend were measured at a pressure of 7 atm in 4% oxygen/argon bath gas at equivalence ratios ranging from 0.32 to 1.42 and at temperatures ranging from 1141 to 1360 K. These results are displayed in Figure 6.10. In addition to these data, ignition delay times for pure methyl oleate at the same conditions are also shown. There are multiple noteworthy attributes of this comparison. First, both of the MO and MOB data sets show positive equivalence ratio scaling at high temperatures. Moreover, for both MO and MOB, a region at low temperatures exists wherein the sensitivity of ignition delay time to equivalence ratio vanishes. By comparing ignition delay time values between the MO and MOB data sets, it can be seen that the MOB may have slightly reduced reactivity as compared to the pure MO; however, the uncertainty in the data sets makes this difficult to confirm. Overall, it appears that the 30% non-MO components in the MOB did not significantly affect the reactivity of the blend.

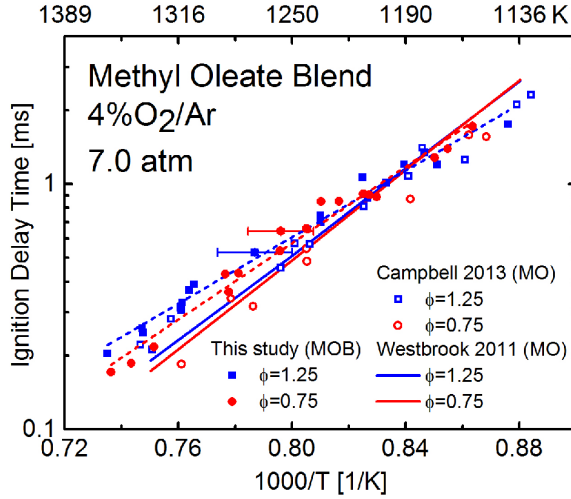


Figure 6.10: Methyl oleate/FAME blend (MOB) ignition delay times taken in 4% oxygen/argon mixtures. Ignition delay times for pure methyl oleate are also shown for comparison.

6.5.2.4 Comparison between methyl oleate and methyl linoleate

A comparison between the ignition delay times of methyl oleate and methyl linoleate is given in Figure 6.11. Ignition delay times for the two fuels are very similar. Furthermore, activation energies for the two fuels at common pressures are similar, consistent with the simulations using the original Westbrook *et al.* [32] and updated Westbrook *et al.* [32, 105] mechanisms, as can be seen in Table 6.6.

6.5.2.5 Kinetic simulations of methyl oleate and methyl linoleate

Arrhenius plots in Figure 6.12 have been constructed to compare the experimental ignition delay data for methyl oleate and methyl linoleate, at a single equivalence ratio of $\phi = 1.25$, to predictions by the original Westbrook *et al.* mechanism [32] (shown as solid lines). Several facts are clear upon inspection. Most importantly, the original Westbrook *et al.* mechanism under-predicts ignition delay times by about 50%. Secondly, the mechanism fails to capture the pressure scaling evident in the experimental data, namely a convergence of ignition delay times at higher temperatures. Finally, in the case of both methyl oleate and methyl linoleate, the mechanism's predictions at 3.5 atm

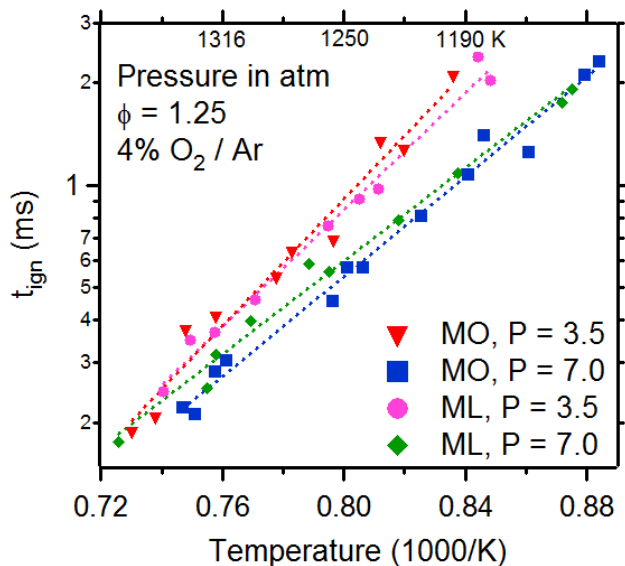


Figure 6.11: Comparison of ignition delay times for methyl oleate and methyl linoleate. Best-fits to data are shown in dotted or dashed lines.

are closer to experimental values at high temperatures than at low temperatures, but at 7 atm the opposite is true. Details of the effects of equivalence ratio for both model and experiment at all measured stoichiometries are provided in Table 6.6.

The original Westbrook *et al.* mechanism [32] was validated by comparisons with results from a variety of experimental devices, but there were no shock tube data available for mechanism testing before the present work. A major group of reactions that are particularly dependent upon shock tube results for rate validations are the unimolecular decomposition reactions, which are important for reaction initiation at high initial temperatures but often relatively unimportant in most other combustion environments. Using the Reaction Path Analysis tool in Chemkin-Pro [263], the sensitivity of the present computed results to rates of these reactions was calculated to determine if they could explain the observed discrepancies in the mechanism predictions.

A large family of unimolecular initiation reactions is present in the current mechanisms, representing fission of each fuel at the C–C, C–O and C–H bonds in each fuel molecule. For methyl oleate, there are 16 C–C bonds, one C=C double bond, one C=O double bond, and two C–O bonds (see Figure 6.1). There are also 36 C–H bonds, but in general the rupture of C–H bonds

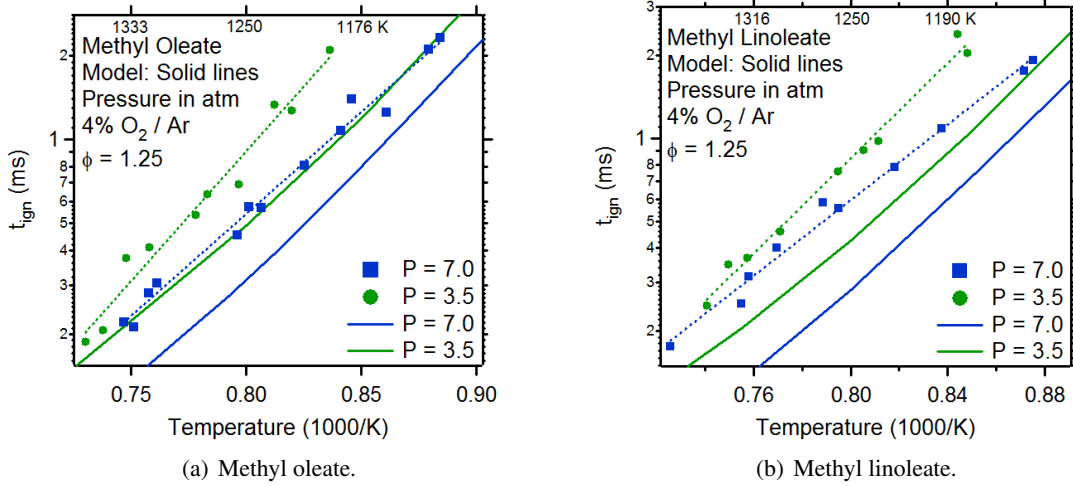


Figure 6.12: Comparison of a) methyl oleate and b) methyl linoleate ignition delay times to predictions of the original Westbrook *et al.* mechanism [32], shown as solid lines.

does not contribute to initiation due to the higher strength of C–H bonds relative to C–C and other bonds in each fuel. The kinetic mechanism includes bond fission of all 16 C–C bonds and both C–O bonds, while the significantly higher bond strength of the C=C and C=O bonds make their fission extremely slow and of no importance. Elementary sensitivity analysis showed that all of the 18 remaining initiation reactions (*i.e.*, the 16 C–C and 2 C–O bond fissions) had significant influence on the computed ignition delay times of the present study.

The decomposition rates of all of these 18 reactions are determined in the mechanism by specifying the rates of the reverse, recombination reactions and permitting the rates in the decomposition direction to be computed from knowledge of the equilibrium constants and the reverse rates. This generally produces the most reliable decomposition rates, since the rates of the recombination reactions, which are exothermic and have little or no activation energy barriers, are usually better known than the decomposition rates. Unfortunately, in the case of the present fuel molecules, for which thermochemical quantities had not previously been determined, there were systematic errors in the information that had been used to compute the equilibrium constants in the original Westbrook *et al.* mechanism [32] for the reactions involving both methyl oleate and methyl linoleate using the THERM program of Ritter and Bozzelli [266].

Recent work by Burke [267] to analyze and optimize the bond energies included in THERM, using error-analysis techniques similar to those of Frenklach (see, for instance, Reference [268]), resulted in thermochemical values that showed significantly improved agreement with experimentally measured and theoretically calculated data. Making approximate corrections to these parameters based on Burke's results [267], for both the fuel molecules and their radicals produced by H-atom abstraction, resulted in lower decomposition rates for the initiation reactions, significantly improving the agreement between the computed and experimentally measured results. The corrected results, computed using this improved mechanism (the updated Westbrook *et al.* mechanism [32, 105]), are shown in Figure 6.13. Overall, this process is an excellent demonstration of the importance of availability of many different types of experimental results for kinetic mechanism development and validation. Satisfactory comparisons give better credibility to both the experimental results and to the kinetic mechanism.

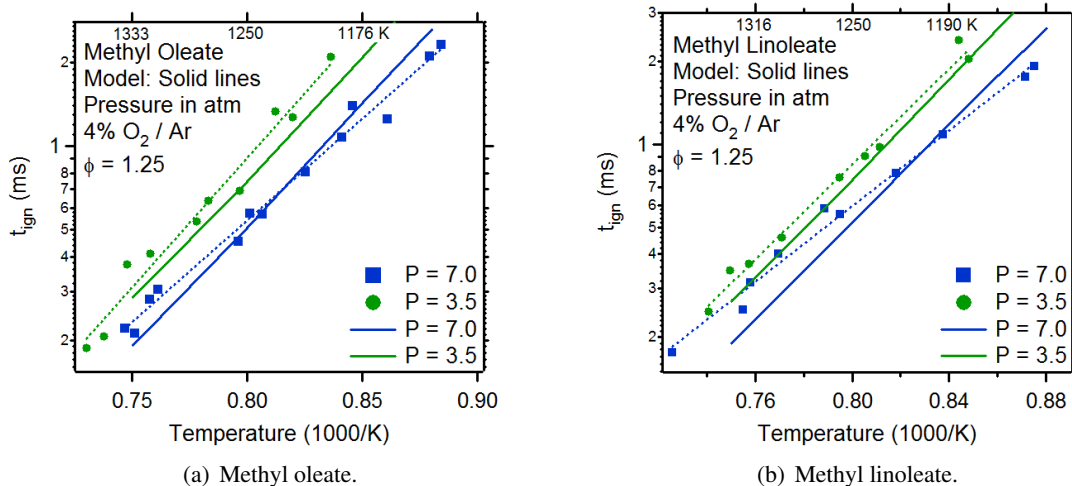


Figure 6.13: Comparison of a) methyl oleate and b) methyl linoleate ignition delay times to predictions of the updated Westbrook *et al.* mechanism [32, 105], shown as solid lines.

6.5.3 Overall ignition time correlation

Ignition delay time data can be summarized by correlations that serve to reveal the underlying dependence of ignition time on important parameters such as pressure or equivalence ratio [269].

Several authors have suggested correlations for various fuels (normal alkanes, oxygenates, *etc.*), including those listed in References [66, 133, 269–273]. A correlation for the FAME ignition data taken in 4%O₂/Ar (for MLA, MM, MP, MO, ML, and the MOB) was formed in this manner by taking into account the effects of pressure (P) [atm], equivalence ratio (ϕ), the carbon number (carbon chain length, $C_{\#}$), and the degree of unsaturation (U_d ; a fully saturated molecule has $U_d = 0$, and $U_d = 2$ corresponds to two degrees of unsaturation, *i.e.*, two double bonds in the carbon chain). Data for MD, which were not taken at an oxygen mole fraction of $x_{O_2} = 0.04$, were not included. This correlation assumed the form of Equation 6.4,

$$\tau_{ign} = A' P^a \phi^b C_{\#}^c (U_d + 1)^d \exp\left(\frac{\hat{E}'_A}{\hat{R}_u T}\right) \quad (6.4)$$

wherein A' [ms] is a constant and \hat{E}'_A [kcal/mol] is the activation energy. The dash ($'$) on the A' and \hat{E}'_A terms serves to differentiate these values (determined from the data before scaling to a common $P/\phi/C_{\#}/U_d$) from the A and \hat{E}_A values of Equation 6.1 (determined from data for one fuel (one $C_{\#}$ and one U_d) that *has* been scaled to a common P/ϕ). Values for A' , a , b , c , d , and \hat{E}'_A were determined by linear regression on the natural logarithm of Equation 6.4, *i.e.*,

$$\ln(\tau_{ign}) = \ln(A') + a \ln(P) + b \ln(\phi) + c \ln(C_{\#}) + d \ln(U_d + 1) + \frac{\hat{E}'_A}{\hat{R}_u} \left(\frac{1}{T}\right) \quad (6.5)$$

Notice that the addition of unity to U_d in Equations 6.4 and 6.5 is performed such that fully saturated molecules ($U_d = 0$) could be included in the linear regression ($\ln(0)$ is undefined). Values for the parameters in this equation, as well as the range of values over which it is valid, are provided in Table 6.7. The values of exponents a , b , c , and d reveal an overall negative pressure scaling (ignition delay time decreases as pressure increases), positive equivalence ratio scaling, negative carbon number scaling, and positive unsaturation scaling for the FAMEs studied. The positive unsaturation scaling may be explained by the fact that the double C=C bond changes the bond strength of the neighboring C–H and C–C bonds [24, 265].

Additionally, ignition times taken in 4%O₂/Ar (for MLA, MM, MP, MO, ML, and the MOB) were scaled to a common pressure $P = 6$ atm, equivalence ratio $\phi = 1$, carbon number $C_{\#} = 16$,

Table 6.7: Correlation (τ_{ign} , [ms]) for FAME ignition delay times (at oxygen mole fraction $x_{O_2} = 0.04$) in terms of pressure (P) [atm], equivalence ratio (ϕ), carbon number ($C_\#$), and saturation (U_d), according to Equation 6.4. The \pm numbers are computed from the standard error values for the fitting parameters. For this fit, $R^2 = 0.941$.

Quantity	Value
A'	$(7.96 \pm 4.62 \times 10^{-6})$ ms
a	-0.366 ± 0.043
b	0.197 ± 0.029
c	-0.693 ± 0.152
d	0.104 ± 0.057
\hat{E}'_A	(34.3 ± 0.6) kcal/mol
T range	1115-1378 K
P range	3.2-7.3 atm
ϕ range	0.27-2.39
$C_\#$ range	12-18
U_d range	0-2
x_{O_2}	0.04

and unsaturation $U_d = 1$ using Equation 6.6 below, which has a form similar to that of Equation 6.3, introduced earlier in this chapter.

$$\tau_{ign}^{scaled} = \tau_{ign}^{unscaled} \left(\frac{P^{common}}{P^{unscaled}} \right)^a \left(\frac{\phi^{common}}{\phi^{unscaled}} \right)^b \left(\frac{C_\#^{common}}{C_\#^{unscaled}} \right)^c \left(\frac{(U_d + 1)^{common}}{(U_d + 1)^{unscaled}} \right)^d \quad (6.6)$$

Using the scaled data, a correlation at $P = 6$ atm, $\phi = 1$, $C_\# = 16$, $U_d = 1$, and $x_{O_2} = 0.04$ was determined in the form of Equation 6.1. Values for A and \hat{E}_A for this equation are provided in Table 6.8. In this case, $\hat{E}_A = \hat{E}'_A$; however, this need not necessarily be so, since these values depend on the spread/scatter of the original unscaled data and the scaling exponents used. Both the unscaled data and the scaled data have been plotted in Figure 6.14, demonstrating the usefulness of the correlation introduced above. Interestingly, the FAMEs examined in this study have very similar ignition times; unscaled ignition delay times for different fuels differ by only about a factor of 2-3 at any given temperature. This has been observed for other classes of hydrocarbons as well [274].

It should be noted that the correlation introduced above assumes that the pressure, equivalence ratio, carbon number, and unsaturation scaling are not a function of temperature. In reality, the data show that at certain temperatures, the ignition delay time values for the FAMEs studied are

Table 6.8: Correlation (τ_{ign} , [ms]) for FAME ignition delay times at a common pressure $P = 6$ atm, equivalence ratio $\phi = 1$, carbon number $C_{\#} = 16$, unsaturation $U_d = 1$, and oxygen mole fraction $x_{O_2} = 0.04$, according to Equation 6.1. The \pm numbers are computed from the standard error values for the fitting parameters. For this fit, $R^2 = 0.942$.

Quantity	Value
A	$(6.50 \pm 1.79 \times 10^{-7})$ ms
\hat{E}_A	(34.3 ± 0.6) kcal/mol
T range	1115-1378 K
P	6 atm
ϕ	1
$C_{\#}$	16
U_d	1
x_{O_2}	0.04

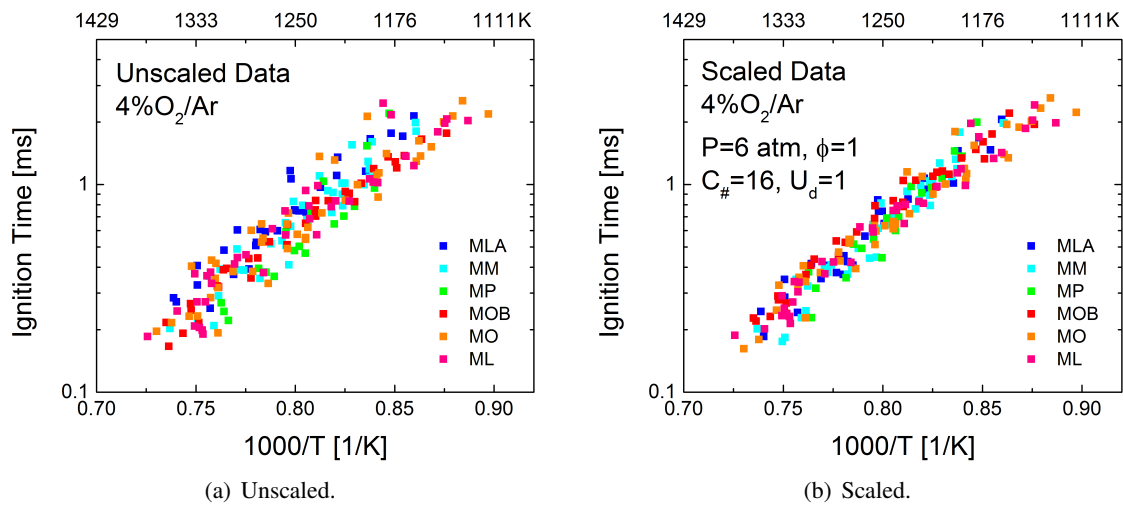


Figure 6.14: Demonstration of overall FAME ignition delay time correlation. Part (a) shows unscaled data, and part (b) shows scaled data. Data for MLA, MM, MP, MO, ML, and the MOB ($x_{O_2} = 0.04$) were scaled to $P = 6$ atm, $\phi = 1$, $C_{\#} = 16$, and $U_d = 1$ according to Equation 6.6 using exponents given in Table 6.7.

insensitive to these parameters, or even that the scaling may reverse (negative instead of positive, *etc.*). A third fitting equation that allowed parameters a , b , and c (the data for coefficient d did not warrant a temperature dependence) to vary as linear functions of temperature was also developed. The resulting correlation did not significantly improve the fitting results (an R^2 value of ~ 0.95 was achieved, compared to a value of ~ 0.94 for the previous fits, and moreover the scatter of the scaled ignition delay time values was still generally within the uncertainty in temperature for these measurements). Thus, while in principle a temperature-dependent scaling should be employed to summarize these data, such a regression has not been proposed here.

6.6 Summary

Methyl decanoate ignition delay time data in 1% oxygen/argon bath gas mixtures have been reported at 7 atm and an equivalence ratio of $\phi = 0.5$ at temperatures between 1262 and 1388 K, showing that available mechanisms generally over-predict ignition delay times at these conditions. Also, methyl decanoate ignition delay time data in 21% oxygen/argon bath gas mixtures were found to compare favorably with existing mechanisms, and moreover good agreement was found with scaled data from Wang and Oehlschlaeger [79]. The first shock tube ignition delay time measurements for neat methyl laurate, methyl myristate, and methyl palmitate were reported at pressures of 3.5 and 7 atm, equivalence ratios ranging from $\phi = 0.27$ to $\phi = 1.44$, and temperatures ranging from 1162 to 1357 K. Comparisons with available mechanisms at these conditions showed that in general simulated ignition delay times were too long. Furthermore, comparisons between these three fuels at common pressure and equivalence ratio conditions showed that ignition delay time decreases as carbon chain length increases. Methyl oleate and methyl linoleate were also studied in 4% oxygen/argon mixtures at pressures of 3.5 and 7 atm, equivalence ratios from $\phi = 0.6$ to $\phi = 2.4$, and temperatures of 1100 to 1400 K. A comparison was first made with the original Westbrook *et al.* mechanism [32], showing an under-prediction of ignition delay times by about 50%. This under-prediction was attributed to errors in methyl oleate and methyl linoleate thermochemistry, which, when refined, resulted in significant performance improvements for the mechanism [32, 105]. Methyl oleate has also been studied in a blend of other FAMEs, showing

that the presence of the 30% other FAMEs had little effect on reactivity. Additionally, an overall ignition delay time correlation was determined, which revealed details of the pressure, equivalence ratio, carbon number, and unsaturation scaling of the FAMEs studied in 4%O₂/Ar. Finally, these data provide targets for the validation of reduced kinetic mechanisms for these surrogates, or for future improvements to detailed mechanisms for biodiesel fuels.

Chapter 7

Obtaining long shock tube test times

*The contents of this chapter have been submitted to the journal **Shock Waves** [275].*

7.1 Introduction

7.1.1 Motivation

The use of shock tubes for studies of combustion chemical kinetics has enabled the precise determination of reaction rates, the measurement of ignition delay times, and studies of other combustion phenomena for the past 60 years. To date, most of these studies have employed test times less than about 15 ms (*e.g.*, [131, 276]) and often times less than 2 ms (see the results presented in Chapter 6). Although this short duration has been sufficient to examine the chemistry of hydrocarbon fuels of practical significance at elevated temperatures (>900 K) and high pressures, recent interest in low-temperature combustion at practical engine conditions (between 600 and 900 K at moderate pressures and a range of equivalence ratios), which is characterized by much longer timescales, has created a need for greater test times in shock tubes.

7.1.2 Previous research

Several researchers have contributed to the extension of shock tube test times. For instance, Amadio *et al.* [277] and Hong *et al.* [278] developed driver gas tailoring relationships for use with

low-sound-speed gases and convergent shock tubes, respectively. Additionally, Dumitrescu [170], Stotz *et al.* [171], and Hong *et al.* [172] modified the geometry of the driver section to achieve either non-attenuating incident shock waves or to mitigate pressure increases in the post-reflected-shock region. Rossmann *et al.* [279] developed a shock tunnel with a plunger in the driver section, which allowed the driver section length to be modified in order to reduce high pressure helium use. However, this helium consumption reduction came at the expense of a decrease in test time as well. Similarly, Pang *et al.* [280], Lam *et al.* [281], and Gates *et al.* [156] used driver section extensions together with driver gas tailoring to achieve test times approaching 20 ms, 25 ms, and 45 ms, respectively (see also Reference [117]). Also, Hanson *et al.* [132] and Zhu *et al.* [129] demonstrated a Constrained Reaction Volume (CRV) approach to confine the reactive gas volume to an area very close to the endwall of the shock tube, reducing the adverse effects of reactions occurring far from the test location at long test times (see Chapter 8).

Several groups have studied shock propagation phenomena numerically or theoretically. Hooker [282] and Polacheck and Seeger [283] examined shock interactions at gas interfaces; their work led to better understanding of driver/driven gas mixing and the need for a light-weight interface gas (*e.g.*, helium) in the shock tube's driven section near the diaphragm [278]. Frazier *et al.* [284] numerically examined the effects of heat transfer on post-reflected-shock average gas temperature, and concluded that heat transfer did not significantly reduce area-averaged temperature for test times up to (and longer) than 20 ms in 8 cm diameter or larger shock tubes. Jacobs [285] developed a quasi-one-dimensional Lagrangian code for the simulation of transient flow facilities such as free-piston-driven shock tunnels, and a similar code, called KASIMIR, was developed by Esser [123]. Also, a second order, Muscl-Hancock-Method finite volume code with an exact Riemann solver has been developed by the University of Wisconsin Shock Tube Lab (WiSTL) [286]. This code is able to generate x-t diagrams, which graphically depict wave propagation in shock tubes and help predict test time. Finally, Rossmann *et al.* developed an empirically-informed computer routine capable of generating x-t diagrams [279]. The routine used experimental incident shock attenuation data to better model the incident shock trajectory, and also accounted for the acceleration of the contact surface due to boundary layer growth.

7.1.3 Background

As introduced in Section 2.3, a pressure-driven shock tube consists of two parts: the driver section, filled with high-pressure driver gas (often helium), separated by a thin polycarbonate or metal diaphragm from the driven section, which contains a low-pressure driven gas (often argon). The experiment commences when the diaphragm bursts due to pressure-induced strain, and an incident shock wave propagates in the driven section toward the shock tube endwall, located at the end of the driven section. As it moves, the shock wave heats and compresses the gas, setting it in motion in the direction of the incident shock. When the incident shock reaches the endwall, it reflects back toward the driver section, further compressing and heating the driven gas, and also stagnating the flow. The arrival of the reflected shock at the test location (typically 1-2 cm from the endwall) marks the beginning of the test time. Meanwhile, an expansion wave moves in the driver section away from the burst diaphragm toward the driver section's end cap. After reaching the driver section end cap, this wave is reflected and moves toward the driven section endwall. When the expansion wave arrives at the test location, it causes a decrease in pressure, ending the test time.

An x-t diagram can be used to clarify the various interactions between the waves introduced above, as shown in Figure 7.1. On this plot, the use of straight lines implies that ideal shock tube behavior is assumed (*i.e.*, shock and expansion wave velocity attenuation is neglected); this results in a slight under-prediction of test time. The black line represents the incident and reflected shock waves, the blue and purple lines denote the expansion head and tail waves respectively, and the red line represents the contact surface between the driver and driven gases. In this figure, the dimensions shown represent those of the shock tube used in this study, with its shortest driver section. This shock tube has a driven section length of $L_{driven} = 9.73$ m, and a driver length of $L_{driver} = 3.63$ m. The test time shown in this figure is denoted τ .

Several areas in this figure are denoted with numbers, which correspond to different regions in space-time during the shock experiment. The initial, undisturbed driven section is termed Region 1, and that in the driver section is termed Region 4. Likewise, the interval behind the incident shock wave and bounded first by the contact surface and then by the expansion wave head is Region 2. The region behind the reflected shock is Region 5. Finally, Region 3 denotes the conditions in the

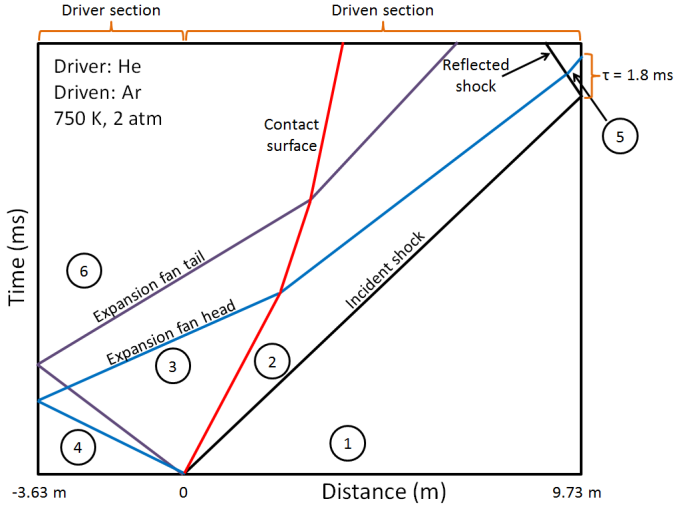


Figure 7.1: Idealized x-t diagram for a basic shock tube experiment, generated based on the WiSTL code [286] with thermodynamic data taken from Reference [174]. Conditions: $M_{IS} = 1.68$ (incident shock Mach number), $T_1 = T_4 = 22^\circ\text{C}$, $P_4 = 1.2 \text{ atm}$, $P_1 = 179 \text{ Torr}$, $P_5 = 2.0 \text{ atm}$, $T_5 = 750 \text{ K}$, $A_{driver} = A_{driven}$ (identical driver and driven cross sectional areas). Driver: 100% He; driven: 100% Ar.

driver gas between the contact surface and the expansion fan, and Region 6 refers to the driver gas conditions following the reflected expansion wave.

When test times longer than a few milliseconds are attempted, a new phenomenon occurs wherein the reflected shock interacts with the contact surface, sending either a shock or an expansion wave back to the test location. This causes either a pressure increase (shock wave) or a pressure drop (expansion wave). Both of these conditions are undesirable and result in the termination of the test time (for detailed x-t diagrams of these cases, see Figures 3 and 4 of Reference [277]). In order to counteract this contact surface interaction, driver gas tailoring, made possible by blending a lower-sound-speed gas such as nitrogen, argon, carbon dioxide, or propane with the helium, is used such that the pressures on both sides of the contact surface, following the passage of the reflected shock, are identical. This stagnates the contact surface and as a result no wave is reflected back to the test section (see References [277, 278, 287]). Ultimately, the test time is ended by the arrival of the expansion wave, reflected from the driver section end cap, at the test location.

An idealized x-t diagram showing a shock experiment at the tailored condition is shown in

Figure 7.2. Region 8 refers to the time behind the reflected shock, bounded by the expansion wave head. Notice that the contact surface is motionless (vertical dashed line between Regions 5 and 8) after interacting with the reflected shock wave but before encountering the expansion wave head. Also, the test time in this case is almost 10 times longer than in the untailored example. In this figure, a driver mixture of helium and propane (see Reference [277]) was chosen in order to enlarge the area of Region 8 at the given temperature, making the plot easier to read (tailoring is also possible using helium/nitrogen at this temperature, although this results in a smaller Region 8 area).

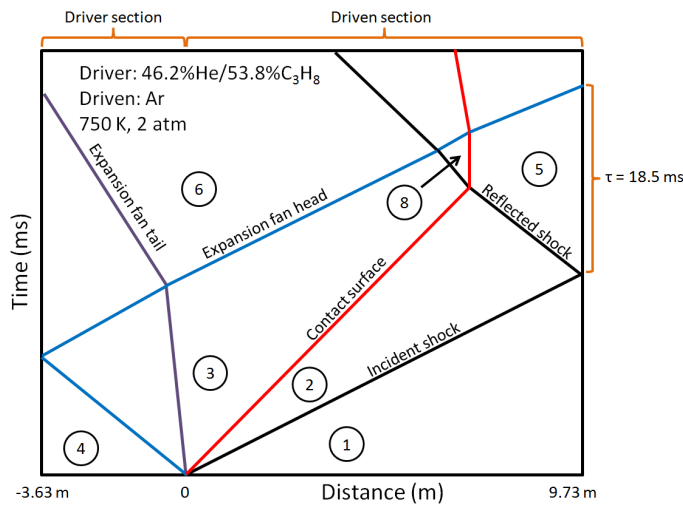


Figure 7.2: Idealized x-t diagram for a tailored shock tube experiment, generated based on the WiSTL code [286] with thermodynamic data taken from Reference [174] and driver gas tailoring generated using the methodology of Amadio *et al.* [277]. Conditions: $M_{IS} = 1.68$, $T_1 = T_4 = 22^\circ\text{C}$, $P_4 = 2.0$ atm, $P_1 = 179$ Torr, $P_5 = 2.0$ atm, $T_5 = 750$ K, $A_{\text{driver}} = A_{\text{driven}}$. Driver: 46.2% He/53.8% C_3H_8 ; driven: 100% Ar.

An x-t diagram can also be used to predict test time as a function of the length of a shock tube's driver section. For instance, consider Figure 7.3, an idealized x-t plot showing two different driver section lengths (3.63 m and 9.57 m, representing two driver lengths available for the shock tube in this study). As is evident, expanding the driver section length increases test time.

Now consider a fictitious shock tube whose total length, driven plus driver, is 20 m. Using an idealized x-t diagram allows the test time of such a shock tube to be easily estimated as a function of the driver length. An in-house computer algorithm has been developed for this purpose that relies

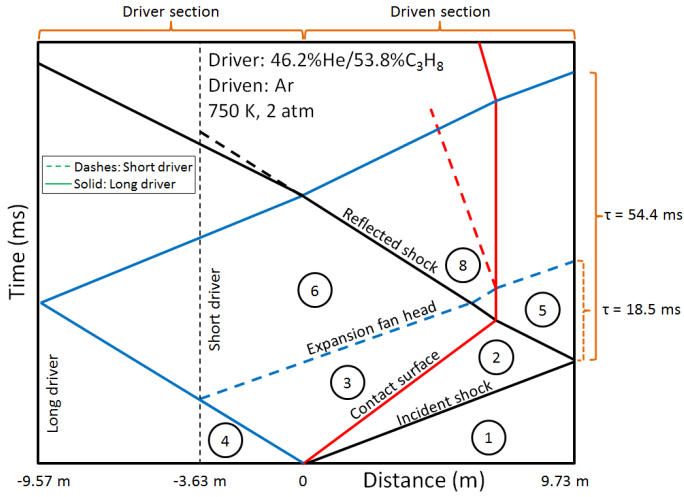


Figure 7.3: Idealized x-t diagram comparing two driver lengths (3.63 m and 9.57 m), generated based on the WiSTL code [286] with thermodynamic data taken from Reference [174] and driver gas tailoring generated using the methodology of Amadio *et al.* [277]. Conditions are identical to those in Figure 7.2.

on ideal shock relations taken from References [277, 287]. Similar to the code developed by Rossmann *et al.* [279], this routine employs several simplifications that cause its test time predictions to deviate slightly from experiment. Despite this shortcoming, this code is introduced here because it is a useful tool for both understanding trends observed in experiments and for aiding shock tube design. Figure 7.4 shows, at one particular test pressure and three test temperatures, the effect of increasing the driver length, while decreasing the driven length to keep the total shock tube length constant. Notice that increasing the driver length, rather than driven length, results in the longest test time at all Region 5 temperatures (T_5) shown. This figure also provides values predicted by the WiSTL code [286]. The values of both programs are in good agreement, although the simple assumption in the current Stanford calculations that the expansion wave velocity remains constant results in a longer test time prediction. It is also important to note that both the WiSTL and Stanford codes assume a driver-to-driven section area ratio of $\frac{A_{\text{driver}}}{A_{\text{driven}}} = 1$. As a consequence, these codes predict a driver gas helium mole fraction that is higher than that necessary in the Stanford tube, which has a convergent driver-driven design with $\frac{A_{\text{driver}}}{A_{\text{driven}}} = 2.38$ [278, 288] (see dimensions in Section 7.2). This results in higher driver gas sound speeds and corresponds to an under-prediction

of test time relative to times observed in the Stanford facility (the sound speeds and other properties of several gases at 20 °C are provided in Table 7.1).

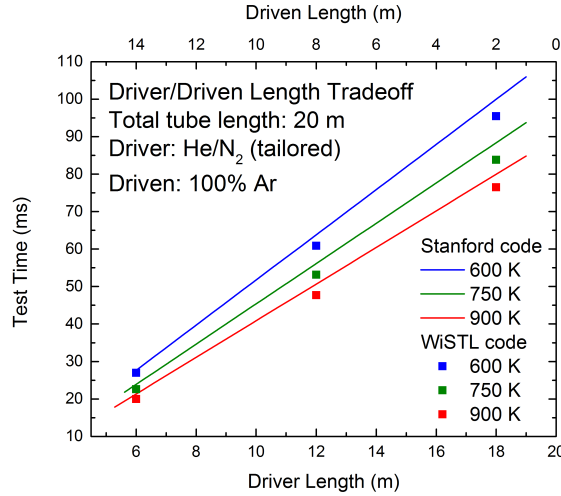


Figure 7.4: Approximate shock tube test time τ at the tailored condition [277, 278] as a function of driver section length, for a total shock tube length of 20 m. Lines are computations by the Stanford code, and individual points are values obtained using the WiSTL code [286], with thermodynamic data taken from Reference [174]. The positively sloped lines indicate that increasing driver section length is more effective at increasing test time than increasing driven section length. As discussed in Amadio *et al.* [277], tailoring is not possible at the shortest driver lengths at some low temperatures. Conditions: $T_1 = T_4 = 22$ °C, $P_5 = 2.0$ atm, $A_{\text{driver}} = A_{\text{driven}}$. Driver: He/N₂ (tailored); driven: 100% Ar.

Plots can also be generated to estimate the available test time as a function of Region 5 temperature T_5 , for different driver section lengths and a fixed driven section length. This is shown in Figure 7.5. Note again the good agreement between the WiSTL code's predictions and those of the Stanford code. As temperature increases, available test time decreases because at the tailored condition more helium is required in the driver gas, thereby increasing the speed of the expansion wave head. Conveniently, above about 900 K the timescale for kinetic processes generally decreases with temperature as well. This implies that a shock tube with sufficient driver length operating at the tailored condition is able to observe kinetic processes over a very large range of temperatures. Plots such as Figure 7.5 are useful in determining the driver length necessary to obtain the required test time.

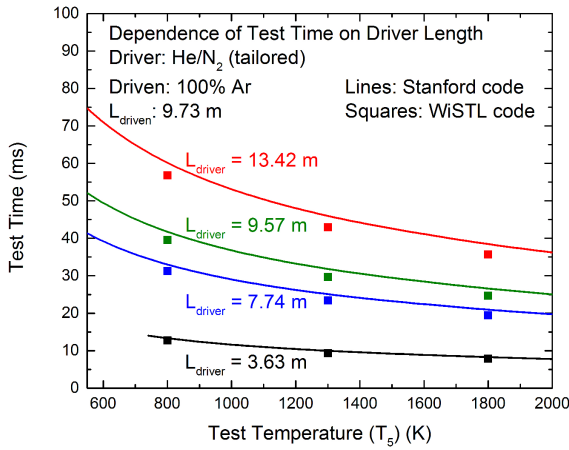


Figure 7.5: Shock tube test time τ at the tailored condition [277, 278] as a function of test temperature, for $L_{driven} = 9.73\text{ m}$ and several values of L_{driver} (corresponding to available Stanford shock tube driver section configurations). Lines are computations by the Stanford code, and individual points are values obtained using the WiSTL code [286], with thermodynamic data taken from Reference [174]. As discussed in Amadio *et al.* [277], tailoring is not possible at the shortest driver lengths at some low temperatures. Conditions: $T_1 = T_4 = 22\text{ }^\circ\text{C}$, $P_5 = 2.0\text{ atm}$, $A_{driver} = A_{driven}$. Driver: He/N₂ (tailored); driven: 100% Ar.

In the High Temperature Gasdynamics Laboratory (HTGL) at Stanford, numerous techniques for extending the test time in shock tubes have been developed, including driver inserts [172], driver gas tailoring [278], the use of helium interface gas in front of the diaphragm [278], driver extensions [156, 280, 281], and staged driver gas filling [289]. The goal in this work is to use these tools sequentially to achieve and even exceed the test time predictions offered by the x-t diagrams shown above.

7.2 Experimental setup

As introduced above, the shock tube employed in this study was initially composed of a 9.73-meter driven section with a round cross section-internal diameter of 11.53 cm, and a driver section composed of a 3.63-meter driver section with a round internal diameter of 17.8 cm. Using driver extensions, which had internal diameters of 15.4 cm, the driver section length was extendable to a maximum of 13.42 m. The driver and driven sections were separated by a polycarbonate diaphragm with a thickness of 0.010 inch, and a four-blade cutter was used to decrease shock-to-shock variation in burst pressure and minimize the occurrence of diaphragm fragments released in the tube. Driver inserts, discussed later in this chapter, were constructed according to the methodology of Hong *et al.* [172] in order to counteract the non-ideal pressure rise in the test section associated with boundary layer formation and shock attenuation.

Diagnostics were located 2 cm away from the endwall of the driven section. Sidewall pressures were monitored using a Kistler model 603B1 transducer covered in Room Temperature Vulcanizing silicone (RTV) mounted at this location, and shock speeds were measured using the time-of-arrival technique via a series of seven PCB model 113A26 transducers (with a PCB model 483B08 amplifier) and extrapolated to the endwall with an accuracy of better than $\pm 0.2\%$. Data from these instruments were recorded using a LabVIEW data acquisition system with a measurement rate of 10 MHz. Note that test times measured at the 2 cm location (as in these experiments) and on the endwall (as in the simulations performed in this study) are essentially identical. Temperature and pressure at the endwall behind the incident and reflected shocks were computed using 1-D shock relations (for instance, see Reference [125] and Appendix A) to an accuracy of better than $\pm 0.6\%$.

and $\pm 1.6\%$, respectively, using thermodynamic data taken from the Burcat database [174].

Prior to each experiment, the driven section was mechanically pumped to a pressure of less than 0.1 Torr, and the driver section was rough-pumped to a pressure of less than 1 Torr. Research-grade argon, helium, nitrogen, propane, and carbon dioxide were obtained from Praxair Inc. Spectroscopic-grade normal heptane, used in ignition experiments, was obtained from Sigma-Aldrich Corp. and was degassed prior to use. Binary (tailored) driver section mixtures were prepared in the driver section by alternately filling two components (usually in three cycles) and allowing the mixture to settle for at least two minutes prior to bursting the diaphragm; this technique has been found to work satisfactorily by other researchers [277, 290]. Due to shock-to-shock variations in filling pressures, the actual driver gas tailoring varied slightly between individual experiments, as the reported values in the plots contained in this chapter suggest. Finally, to initiate the experiment, the non-helium component (usually nitrogen) was filled until the diaphragm ruptured. Because filling ports in the shock tube are located near the driver section end cap in all driver section configurations, this had the side effect of prolonging test time by pushing the helium-containing mixture toward the diaphragm, much like in the staged driver filling technique described in detail in Section 7.4.

7.3 Application of existing test time extension techniques

In this section, the use of driver inserts [170–172], driver gas tailoring [277, 278], helium interface gas in front of the diaphragm [278], and driver extensions [117, 156, 280, 281] will be demonstrated in order to achieve a long test time with uniform pressure throughout the shock experiment. Details of these individual techniques may be found in greater detail in the referenced papers. Additional information may also be found in Appendix E.

7.3.1 Driver insert

Pressure profiles from two baseline cases are shown in Figure 7.6: one experiment using a driver insert, and the other without. In both experiments, the driver gas was 100% nitrogen and the driven gas was 100% argon. Also, the driver and driven lengths were 3.63 m and 9.73 m, respectively,

and the driver-to-driven cross section area ratio was $\frac{A_{\text{driver}}}{A_{\text{driven}}} = 2.38$. At time zero, both pressure records show a step change corresponding to the arrival of the incident and reflected shocks at the 2 cm test location (the resolution of the plot's abscissa is insufficient to differentiate the two shocks). Notice that in the shock taken without the driver insert, a subsequent normalized pressure increase of approximately $\frac{dP^*}{dt} = 1.8\%/\text{ms}$ is observable. (The non-uniform increase occurring at about 9 ms in this trace will be discussed later.) Pressure increases such as this are highly undesirable, since they isentropically increase the experimental temperature according to Equation 7.1 [291, 292] (representative values of this equation at 1000 K are shown in Figure 7.7).

$$T = T_0 \left(\frac{P}{P_0} \right)^{\frac{\gamma-1}{\gamma}} \quad (7.1)$$

In this equation, T_0 and P_0 are the initial temperature and pressure in Region 5, and $\gamma = \frac{c_p}{c_v}$ is the temperature-dependent heat capacity ratio of the driven gas. The pressure increases shown in Figure 7.6 are caused by factors such as shock attenuation and boundary layer growth behind the incident and reflected shock waves, and can be removed by use of a driver insert (see References [170–172]). The driver insert serves to gradually decrease the area of the driver section (as a function of distance) from the diaphragm toward the driver section endwall. This area change prematurely reflects part of the expansion wave back to the test section to counteract the non-ideal pressure increase, resulting in constant post-reflected-shock pressure. Thus, in contrast to the record without an insert, the pressure trace with an insert shown in Figure 7.6 exhibits a normalized pressure change of $\frac{dP^*}{dt} = 0\%/\text{ms}$ in the time before and after the non-uniform increase (from about 6 to 11 ms in this trace). Finally, the pressure drop in both pressure traces shown near 19 ms represents the arrival of the expansion fan, reflected from the end cap of the driver section, at the 2 cm measurement location.

7.3.2 Driver gas tailoring

The non-ideal pressure increase seen at a time of about 9 ms in the no-insert pressure trace of Figure 7.6 is caused by a driver/driven gas tailoring mismatch. This is the result of the interaction between the contact surface and the reflected shock wave, as discussed in Section 7.1.3. Typically,

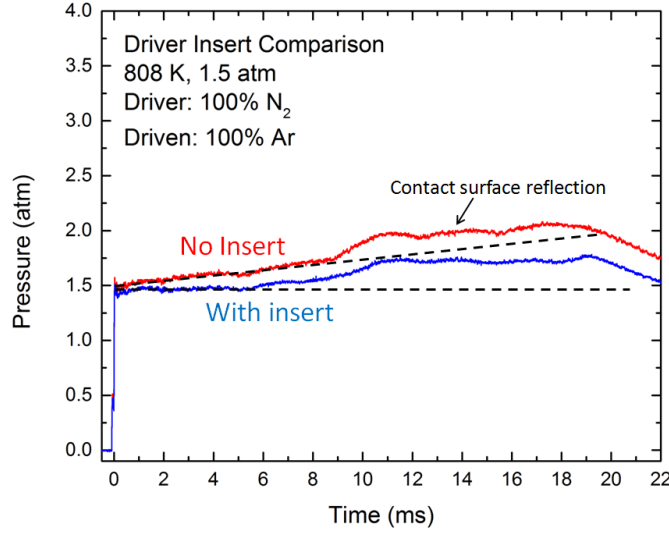


Figure 7.6: Comparison of shocks with and without a driver insert. The pressure increase around 9 ms is caused by a driver gas tailoring mismatch. Notice that before and after this increase the pressure in the presence of the driver insert is constant to within $\pm 5\%$. Conditions: $T_5 = 808$ K, $P_5 = 1.5$ atm, $\frac{A_{driver}}{A_{driven}} = 2.38$, $L_{driver} = 3.63$ m, $L_{driven} = 9.73$ m. Driver: 100% N₂; driven: 100% Ar.

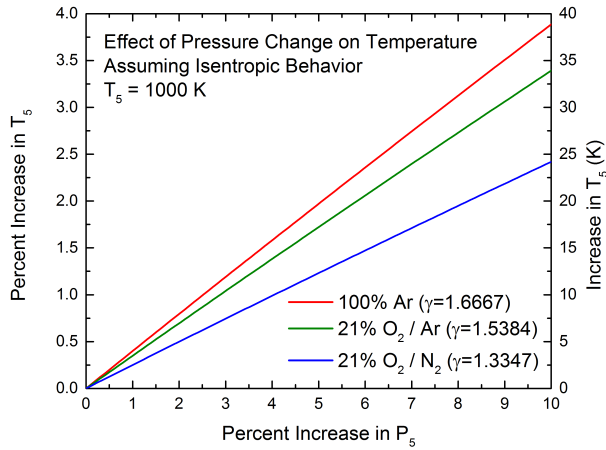


Figure 7.7: Percent increase in test temperature as a function of a non-ideal pressure rise (associated with a gas tailoring mismatch, a contact surface bump, general $\frac{dP^*}{dt}$, etc.) for three test gases at a nominal temperature of 1000 K, assuming isentropic behavior according to Equation 7.1. Gas properties computed using thermodynamic data obtained from Reference [174].

pressure increases such as this indicate that the driver gas requires more helium at the given Region 5 temperature (likewise, a pressure decrease indicates a need for a higher mole fraction of the low-sound speed gas, in this case, nitrogen). Figure 7.8 compares the untailored shock experiment (driver gas of 100% N₂) with a tailored experiment, taken using a driver gas of 31% He/N₂ (the shock tube geometry is identical to that of Figure 7.6). At the tailored condition, the pressure in Regions 5 and 8 in the shock tube are matched [277, 278, 287] (see Figure 7.2), such that neither an expansion wave nor a shock wave is transmitted back to the test section. Not surprisingly, a sustained pressure increase is not visible, indicating that a shock wave did not reflect back to the test location from the driver/driven gas contact surface. However, a pressure hump (contact surface bump) can still be seen near about 10 ms. Finally, the test time at the tailored condition is slightly reduced, indicated by the arrival of the expansion wave at the 2 cm measurement location about 2 ms earlier. This is the result of helium increasing the sound speed of the driver gas, allowing the expansion wave head to move more quickly.

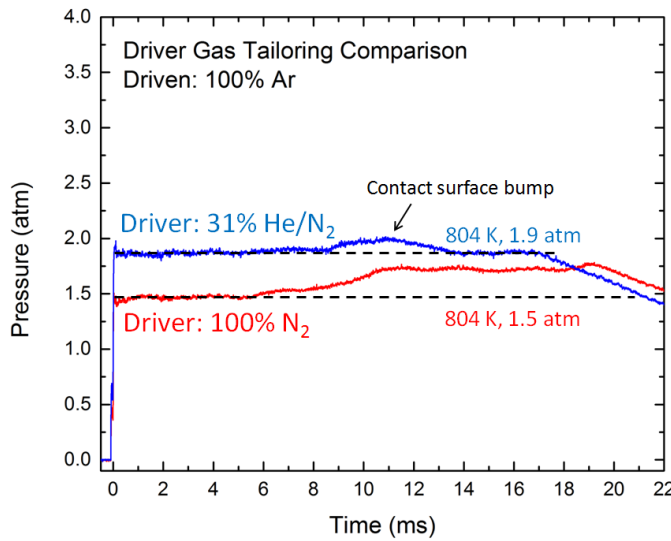


Figure 7.8: Result of driver gas tailoring. The 31%He/N₂ driver gas corresponds to the tailored condition at $T_5 \sim 800$ K in a shock tube that has a driver/driven area ratio $\frac{A_{\text{driver}}}{A_{\text{driven}}} = 2.38$ [278]. Shock tube dimensions are identical to those given in Figure 7.6, and a driver insert was used to mitigate non-ideal pressure increases.

7.3.3 Helium interface gas

In an ideal shock tube, the contact surface between the driver and driven gases would have zero thickness and no mixing would occur between these fluids. However, for a variety of reasons related to the physics of diaphragm rupture, some driver/driven gas mixing does occur, which results in a contact mixing zone of finite length. The contact surface bump observable in Figure 7.8 is the result of the reflected shock interacting with this mixing zone, as described in detail in References [278, 282, 283]. Use of a lightweight gas such as helium as a buffer between the driver and driven gases greatly reduces the influence of this interaction. In these experiments, helium gas is introduced through a port immediately in front of the diaphragm by first filling the tube with the driven gas mixture (argon) to a pressure very close to the initial pressure (called P_1), then by filling helium until the pressure is P_1 . Figure 7.9 shows the impact of a helium interface gas that is 2.4% of P_1 (corresponding to a length in the driven section of about 23 cm) on the contact surface bump. Helium percentages ranging from about 2 to 10 percent have been found to give the best performance (*i.e.*, elimination of the contact surface bump) in these experiments. Note that other researchers using different shock tubes have reported values as high as 20% [278]; this large range is likely due to differences in shock tube geometry and diaphragm material (polycarbonate versus metal). Finally, observe that the flat, $\frac{dP^*}{dt} = 0\%/\text{ms}$ test time in the resulting shock is about 16.5 ms.

7.3.4 Driver extensions

As introduced in Figure 7.3, lengthening the driver section can greatly increase test time (see References [117, 156, 280, 281]). Figure 7.10 shows the result of increasing the driver section length from 3.63 m to 7.74 m, and then to 9.57 m. True to expectations, increasing driver section length delays the arrival of the expansion wave at the endwall; test time is plotted as a function of length in Figure 7.11. Also shown in Figure 7.11 are test time predictions made by the Stanford code. Notice that the measured test times are longer than the predicted times, which is likely due to two factors. First, bursting the diaphragm with nitrogen tends to increase test time as discussed in Section 7.2; the model assumed that the entire driver section was filled with the tailored gas mixture. Second, the shock tube employed has a convergent design with $\frac{A_{\text{driver}}}{A_{\text{driven}}} = 2.38$, which allows less

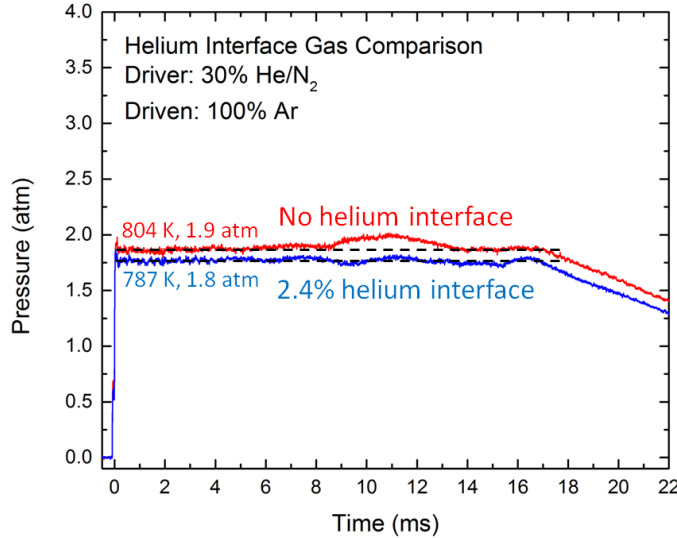


Figure 7.9: Effect of helium interface gas. Shock tube geometry is identical to that provided in Figure 7.6, and a driver insert was used to mitigate non-ideal pressure increases.

driver gas helium to be used as compared to $\frac{A_{\text{driver}}}{A_{\text{driven}}} = 1$ (as assumed by the models) in order to achieve the same Region 5 temperature, thus decreasing the driver gas sound speed and delaying the arrival of the expansion fan at the test section [278, 288].

7.4 Staged driver gas filling

7.4.1 Theory

Returning to Figure 7.2, it is evident that the expansion wave head originates at the diaphragm, propagates toward the driver section end cap and then is reflected. While undergoing this process, this wave travels at the local sound speed (relative to the gas) of the tailored driver gas mixture [287]. Thus, the use of helium, which has a high sound speed (see Table 7.1), in the driver gas mixture impedes efforts to achieve long test times because it causes the expansion wave to travel more quickly and reach the test section sooner. Moreover, helium is an expensive noble gas [293], making it costly to fill the entire driver section (especially once this section is elongated to expand test time). However, helium is a desirable driver gas because of its propensity to create strong shocks with

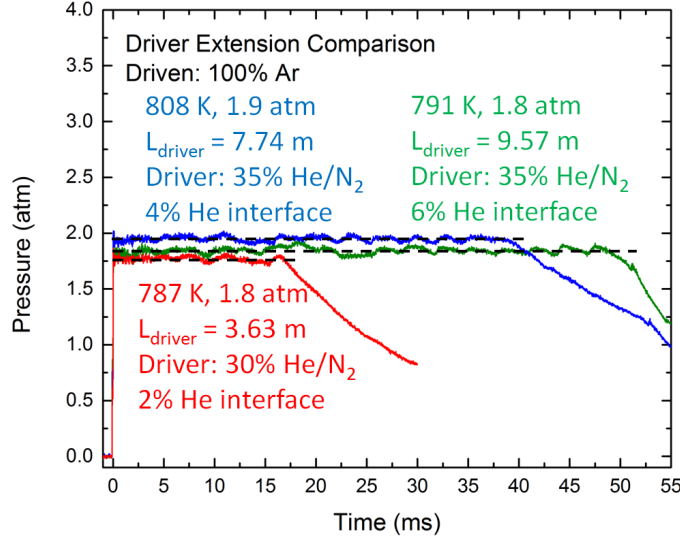


Figure 7.10: Comparison of pressure profiles for $\frac{A_{\text{driver}}}{A_{\text{driven}}} = 2.38$, $L_{\text{driven}} = 9.73 \text{ m}$, with L_{driver} values of 3.63 m, 7.74 m, and 9.57 m. Driven gas is 100% Ar, and driver gases are tailored He/N₂ mixtures. A driver insert was used to mitigate non-ideal pressure increases.

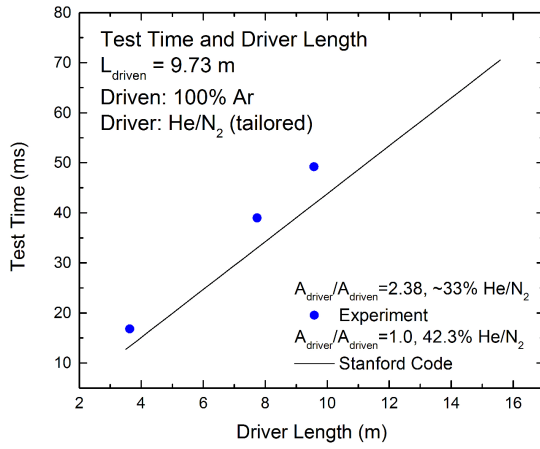


Figure 7.11: Test time τ as a function of driver length, for $L_{\text{driven}} = 9.73 \text{ m}$ at $T_5 = 800 \text{ K}$ and $P_5 = 1.9 \text{ atm}$. Driven gas is 100% Ar, and driver gases are tailored He/N₂ mixtures. These experiments employed a driver insert. The line is a computation by the Stanford code using thermodynamic data taken from Reference [174].

moderate driver section pressures (the other alternative sometimes considered is hydrogen [294–296], which is not commonly used in the United States because of its explosive potential). In order to accommodate the need for strong shocks (obtained by having the tailored helium/low-sound-speed gas adjacent to the diaphragm) while achieving the longest possible test time (obtained by filling a majority of the driver section with a low-sound-speed gas), a staged driver gas filling technique has been developed.

Note that using a lower-sound-speed gas (such as nitrogen, krypton, or xenon) in the driven section could also result in increased test time. However, nitrogen has a finite vibrational relaxation time behind shock waves that can affect data analysis [297–299], and is also known for causing various shock wave bifurcation phenomena [300, 301]. Moreover, krypton and xenon are prohibitively expensive. For these reasons, argon is often the preferred inert driven bath gas for shock tube experiments.

7.4.2 Technique

In a conventional shock tube experiment that employs driver gas tailoring, such as those introduced above, the driver section is filled with a binary mixture, often consisting of helium and nitrogen, until the diaphragm ruptures. The staged filling technique involves one additional step, and is performed as follows (see also Figure 7.12). First, the driver section is filled to an intermediate pressure P_{4a} as in the conventional filling technique with a tailored binary mixture of helium and nitrogen. The ideal gas equation of state (Equation 3.12) can be used to relate this pressure to the driver length L_{driver} using the driver cross sectional area A_{driver} , the number of moles of binary gas N_{binary} , the initial temperature T_4 , and the ideal gas constant \hat{R}_u .

$$P_{4a}A_{driver}L_{driver} = N_{binary}\hat{R}_uT_4 \quad (7.2)$$

Second, the driver section is filled until diaphragm rupture (said to occur at pressure P_4) using a port near to the driver section end cap (far from the diaphragm) with a third, low-sound-speed (backfill) gas. As this low-sound-speed gas fills, it pushes the binary mixture toward the diaphragm. (A mixing zone also develops between the backfill and binary gases during this process.) The idealized

length of binary gas, as measured from the diaphragm, is called L_{binary} . Applying the ideal gas law to the compressed binary gas alone yields

$$P_4 A_{driver} L_{binary} = N_{binary} \hat{R}_u T_4 \quad (7.3)$$

Dividing Equation 7.2 by Equation 7.3 and rearranging yields an expression (Equation 7.4) for the ratio $\frac{P_{4a}}{P_4}$, which governs the extent to which the driver section is filled with the binary mixture.

$$\frac{P_{4a}}{P_4} = \frac{L_{binary}}{L_{driver}} \quad (7.4)$$

Note that this equation ignores the presence of the driver insert, which slightly decreases the driver section area as discussed above. The L_{binary} values provided in this chapter do, however, account for the slight change in diameter of the driver section as it changes from 17.8 cm over the first 3.63 m to 15.4 cm over the next 9.79 m (the total maximum driver length is 13.42 m).

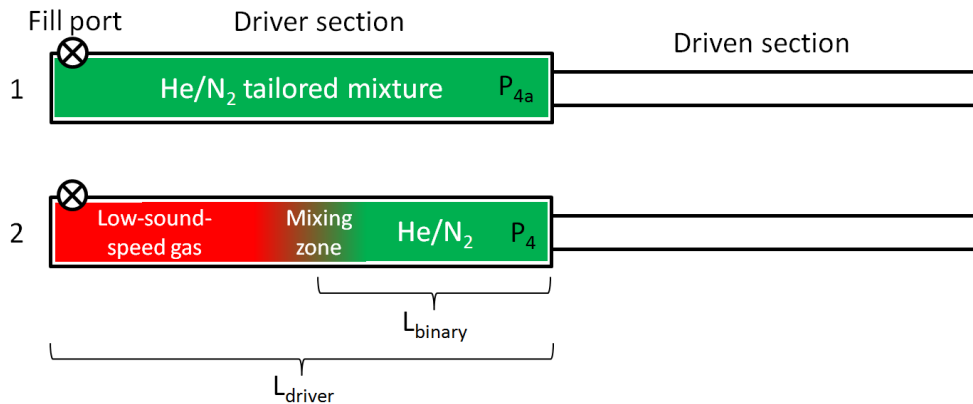


Figure 7.12: Staged driver filling procedure (in this case, tailored (binary) mixture is He/N₂). The driver section is first filled to pressure P_{4a} with the binary mixture, and then is filled from a port near the driver end cap with the low-sound-speed (backfill) gas until diaphragm rupture at pressure P_4 .

An idealized x-t diagram comparing staged driver filling to conventional driver filling is shown in Figure 7.13. In this plot, $L_{binary} = 3.63$ m, $L_{driver} = 9.57$ m, and $L_{driven} = 9.73$ m. For clarity, regions labeled “a” correspond to the backfilled gas and those labeled “b” correspond to the binary (tailored) gas. In the staged driver gas shock (shown in solid lines), within the driver section,

notice that the lines denoting the expansion fan wave head propagating in the backfilled (low sound speed) gas have a greater slope (time divided by distance) than those showing the conventional driver filling shock expansion fan wave head (shown in dashed lines). This reflects the fact that in the staged driver gas shock, the expansion fan travels more slowly. Also notice that within the tailored gas, the initial slope of the expansion head and tail lines are low, reflecting the fact that the driver gas immediately adjacent to the diaphragm has a high sound speed. This high sound speed allows a strong shock wave to be generated. The net effect of this staged driver gas filling procedure is that a strong shock wave is produced via the binary mixture, but the expansion wave head is delayed in reaching the test location at the end of the driven section because it must first pass through the low-sound-speed backfilled gas in the driver section. Moreover, helium gas is only needed in a short length of the driver section next to the diaphragm; the rest of the driver section can be filled with a much less expensive alternative such as nitrogen, argon, or carbon dioxide [277].

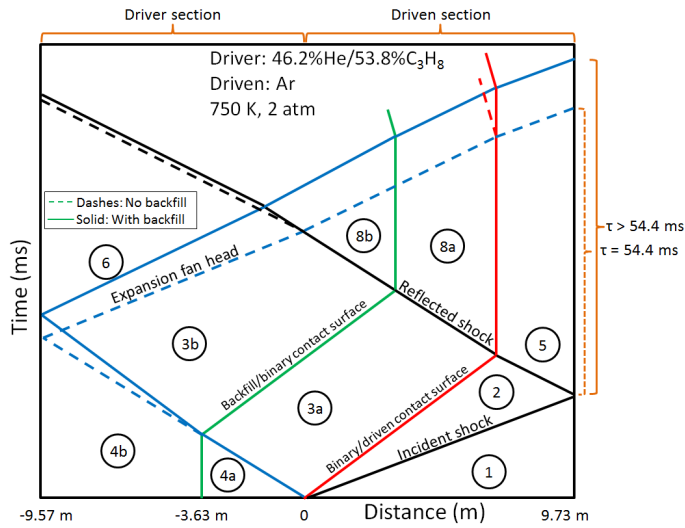


Figure 7.13: Idealized x-t diagram comparing staged driver filling (solid lines) to conventional driver filling (dashes), with $L_{binary} = 3.63 \text{ m}$, $L_{driver} = 9.57 \text{ m}$, and $L_{driven} = 9.73 \text{ m}$. Notice that the expansion wave travels more slowly in the low-sound-speed backfill gas, delaying the arrival of the expansion wave at the endwall. Conditions are identical to those in Figure 7.2.

In the current experiments, no evidence that abrupt expansion or shock waves are reflected back to the test section as the reflected shock interacts with the backfill/binary gas contact surface

was found. In contrast, a tailoring mismatch at the tailored driver/driven gas interface generates a distinct pressure change in the test section, such as that demonstrated in Figure 7.8. One possible explanation for this discrepancy is that the mixing zone that develops between the backfill and binary gases as the backfill gas flows into the driver section is much more extensive than that which develops between the binary and driven gases as the diaphragm bursts. Because this mixing zone is longer, the transition in gas properties as seen by the reflected shock entering the backfill/binary mixing zone is gradual, and a reflected expansion or shock wave is not generated and sent back to the test section. For this reason, Figure 7.13 is drawn with a vertical contact surface line between Regions 8a and 8b, meaning that the backfill/binary gas contact surface is stagnated by the reflected shock. Interestingly, no contact surface bump, as in that shown in Figure 7.9, has been observed as the result of the backfill/binary gas contact mixing zone; this is attributable to the similarity in properties between these gases (in the case of the binary/driven gas contact mixing zone, gas properties can vary significantly, and the mixing of these gases does not necessarily result in linearly varying conditions). Finally, in these staged driver gas filling experiments, significantly lower non-ideal pressure change $\frac{dP^*}{dt}$ has been observed when the expansion wave is propagating through the backfill gas as compared to $\frac{dP^*}{dt}$ measured during conventional driver filling (no backfill). This can be attributed to the interaction of the expansion wave with the mixing zone between the backfill and tailored gases; however, further experimentation is necessary to fully understand this phenomenon.

7.4.3 Staged versus conventional filling

Figure 7.14 offers a comparison between the pressure traces of a shock with conventional driver filling ($L_{binary} = L_{driver} = 7.74$ m) and a shock with $L_{binary} = 1.1$ m where the backfill gas was pure nitrogen. The conventional filling shock was accomplished by filling a pre-mixed 30% He/N₂ mixture into the driver section. By observing the delayed arrival of the expansion wave, it becomes evident that staged driver gas filling expanded the available test time by approximately 8 ms, or about 22%. Moreover, the staged driver filling shock required about 85% less helium than its counterpart.

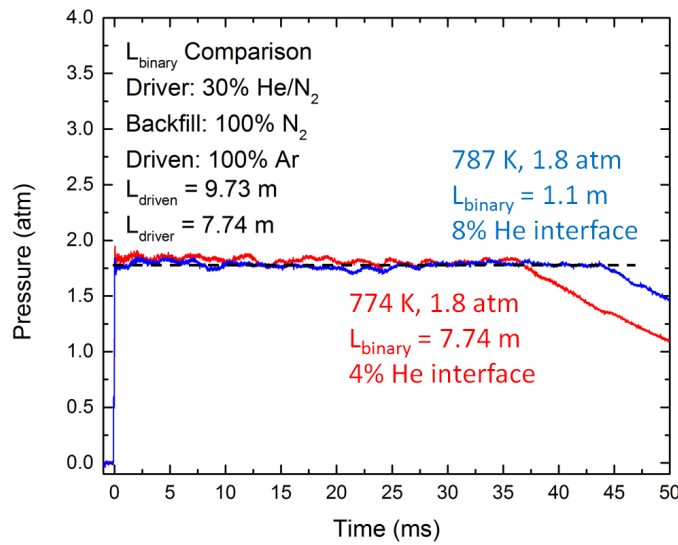


Figure 7.14: Comparison of conventional to staged driver gas filling. The use of staged driver gas filling increased test time by roughly 8 ms (22%) and used 85% less helium, compared to its conventional counterpart. Conditions: $\frac{A_{driver}}{A_{driven}} = 2.38$, $L_{driver} = 7.74$ m, $L_{driven} = 9.73$ m. Driver: 30% He/N₂; driven: 100% Ar; backfill: 100% N₂. A driver insert was used to mitigate non-ideal pressure increases.

7.4.4 Variation of binary length

Figure 7.15 shows the relationship between test time and L_{binary} for tailored He/N₂ binary gas and pure nitrogen backfill gas. As L_{binary} decreases, a greater proportion of the driver section is filled with the low-sound-speed backfill gas, and test time increases. Note that experimental L_{binary} values greater than about 5 m (except the case of filling the entire driven section with a pre-mixed binary mixture) were unachievable because the corresponding intermediate pressure P_{4a} was too close to the diaphragm burst pressure P_4 . Also shown in this figure are predictions by the Stanford code. Agreement between the Stanford model and experiment is reasonable, given the assumptions employed in the computer algorithm. Notably, the model correctly predicts the approximate rate of test time increase as L_{binary} is decreased. The under-prediction of test times by the Stanford code can be attributed in part to the driver/driven area ratio once again; at this temperature, the simulation required more helium in the binary gas mixture, thus increasing the expansion wave's velocity and reducing predicted test times. Finally, the change in character of the simulation near $L_{binary} = 5$ m occurs because for shorter L_{binary} the reflected expansion fan wave head first encounters the reflected shock, whereas for longer L_{binary} the reflected expansion fan wave head first encounters the backfill/binary gas interface.

7.4.5 Variation of filling time

In order to further investigate binary/backfill gas mixing, the flow rate of backfill gas was varied; this resulted in different filling times for the backfill gas. Presumably, as the backfill gas flow rate is increased (*i.e.*, shorter backfill time), the rate of turbulent mixing between the binary and backfill gases should increase, causing the binary/backfill mixing zone to be longer and affecting the resulting test time. However, in these experiments, over a wide range of backfilling times, test time remained constant (see Figure 7.16). Moreover, the non-ideal pressure change $\frac{dP^*}{dt}$ remained approximately constant as well. This could be an indication that the length of the mixing zone has little effect on test time, or that other factors besides backfill gas flow rate are more important in determining the extent of binary/backfill gas mixing.

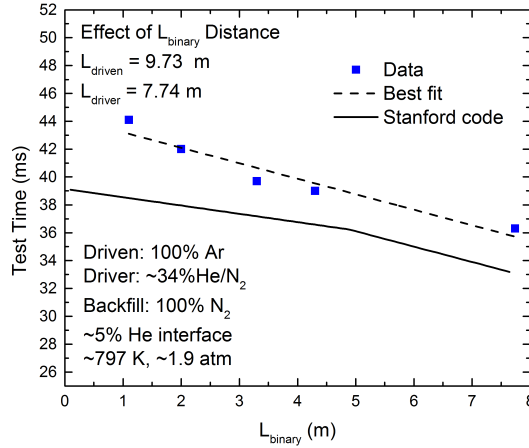


Figure 7.15: Test time as a function of binary gas length in the driver section for $\frac{A_{driver}}{A_{driven}} = 2.38$. As L_{binary} decreases, test time increases. Also, within the scatter of the data, this relationship is approximately linear. A comparison is given with backfill test time predictions made by the Stanford code ($\frac{A_{driver}}{A_{driven}} = 1$) as well.

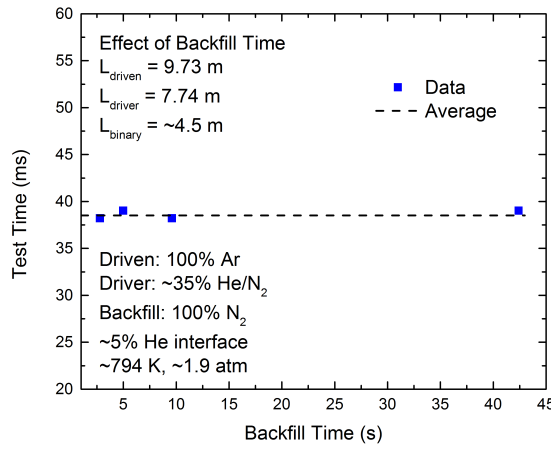


Figure 7.16: Test time as a function of backfill time. Within the range of values studied, there seems to be no effect of backfill time (*i.e.*, backfill gas flow rate) on test time.

7.4.6 Variation of backfill gas sound speed

In order to investigate the effect of backfill gas sound speed, a series of experiments were conducted using different backfill gases. These gases, in order of lowest sound speed to highest sound speed at 20 °C, were 100% CO₂, 21% O₂/Ar, 100% Ar, 21% O₂/N₂, 100% N₂, and 30% He/N₂. A plot relating test time to backfill gas sound speed is provided in Figure 7.17. As expected, test time increases as sound speed decreases.

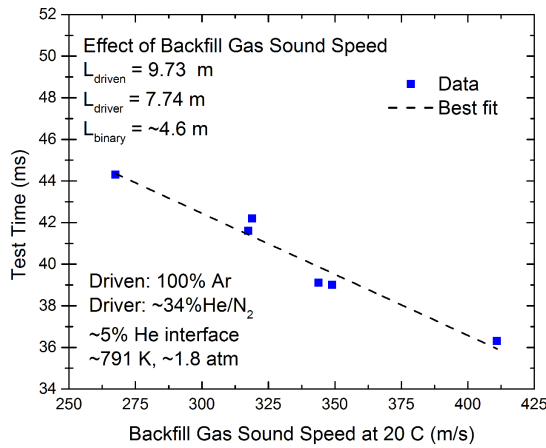


Figure 7.17: Test time as a function of backfill gas sound speed at 20 °C. The test time is seen to increase linearly with a decrease in the backfill gas sound speed.

7.4.7 Selection of backfill gas

The selection of appropriate backfill gas depends on a number of factors, including the desired test time, price of backfill gas, component vapor pressure, and environmental considerations (several potential backfill gases and their properties are provided for reference in Table 7.1). First, Figure 7.17 can be used as a selection guide for determining the backfill gas necessary to obtain the desired test time, holding other factors (*e.g.*, L_{driver} , L_{driven} , and L_{binary}) constant. Second, backfill gas prices are somewhat dependent on geographical location. However, in general, gases obtained from the atmosphere (*e.g.*, N₂ and Ar), from natural gas (*e.g.*, CH₄ and C₃H₈), and from

combustion products (*e.g.*, CO₂) have reliably low prices. Third, in terms of gas properties, the driver section burst pressure (P_4) is limited by the vapor pressure of the backfill gas [277]. For example, C₃H₈ and CO₂ have vapor pressures of about 9 atm and 57 atm at 20 °C, meaning that the maximum P_4 values when backfilling with these species are 9 atm and 57 atm, respectively. Since driver burst pressure P_4 generally scales with reflected shock pressure P_5 [287], these gases may be excluded for very high pressure experiments. Finally, environmental considerations are important factors in choosing a backfill gas. As evident from Table 7.1, sound speed generally decreases with gas molecular weight, making larger molecules attractive candidates. Several examples include large hydrocarbons (*e.g.*, C₃H₈), noble gases (*e.g.*, Kr and Xe), and insulators/refrigerants (*e.g.*, SF₆ and C₄F₁₀). However, these groups possess some notable drawbacks. In particular, pressurized hydrocarbons have explosive potential, noble gases are often prohibitively expensive unless a trace gas exhaust recovery system is implemented, and insulators/refrigerants are known as being potent greenhouse gases. Moreover, some agents such as CO are known to be poisonous, making even small leaks very dangerous. As such, care must be exercised in selecting the most appropriate backfilling gas for experimentation.

7.5 Combination of techniques

Figure 7.18 provides a demonstration of the use of the above techniques in concert. This experiment employed pure argon in the 9.73 m driven section. The 13.42 m driver section was filled with pure nitrogen gas as the tailored “binary” gas mixture (0%He/100%N₂) and pure carbon dioxide as the backfill gas. A short L_{binary} value of 1.2 m was used. Moreover, a series of driver inserts were employed to mitigate non-ideal pressure changes. These included a conical insert similar to that used by Stotz *et al.* [171] in order to reduce the driver section diameter such that $\frac{A_{driver}}{A_{driven}} = 1$, allowing the reflected shock wave to pass back into the driver section with no immediate area change. (For $\frac{A_{driver}}{A_{driven}} > 1$, an expansion wave is generated and propagates back to the test location when the reflected shock passes back into the driver section; likewise, for $\frac{A_{driver}}{A_{driven}} < 1$, a shock wave is generated and propagates back to the test section.) In this experiment, the resulting post-reflected-shock temperature was sufficiently low that no helium interface gas was required, as discussed

Table 7.1: Properties of several backfill driver gases at 20 °C using data obtained from the Burcat database [174].

Species	Molecular weight [g/mol]	$\gamma = \frac{c_p}{c_v}$ (20 °C)	Gas constant [J/kg-K]	Sound speed (20 °C) [m/s]	Category
H ₂	2.02	1.41	4124.5	1303.8	Diatomeric
He	4.00	1.67	2077.3	1007.4	Noble gas
Ne	20.18	1.67	412.0	448.7	Noble gas
CH ₄	16.04	1.31	518.3	445.6	Hydrocarbon
H ₂ O	18.02	1.33	461.5	424.1	Triatomic
N ₂	28.01	1.40	296.8	349.0	Diatomeric
CO	28.01	1.40	296.8	349.0	Diatomeric
NO	30.01	1.39	277.1	335.5	Diatomeric
O ₂	32.00	1.40	259.8	326.0	Diatomeric
Ar	39.95	1.67	208.1	318.9	Noble gas
C ₂ H ₆	30.07	1.19	276.5	310.7	Hydrocarbon
CO ₂	44.01	1.29	188.9	267.4	Triatomic
C ₃ H ₈	44.10	1.13	188.6	249.8	Hydrocarbon
Kr	83.80	1.67	99.2	220.2	Noble gas
SO ₂	64.06	1.27	129.8	219.4	Triatomic
Xe	131.29	1.67	63.3	175.9	Noble gas
C ₂ HF ₅	120.02	1.10	69.3	149.2	Refrigerant
Rn	222.00	1.67	37.5	135.3	Noble gas
SF ₆	146.06	1.09	56.9	135.2	Insulator
C ₂ Cl ₆	236.74	1.07	35.1	104.7	Refrigerant
C ₄ F ₁₀	238.03	1.05	34.9	103.5	Refrigerant

by Hong *et al.* [278]. The resulting pressure trace shows a test time of 102 ms. To the author's knowledge, this is the longest constant-pressure test time to have been achieved in a laboratory reflected-shock experiment.

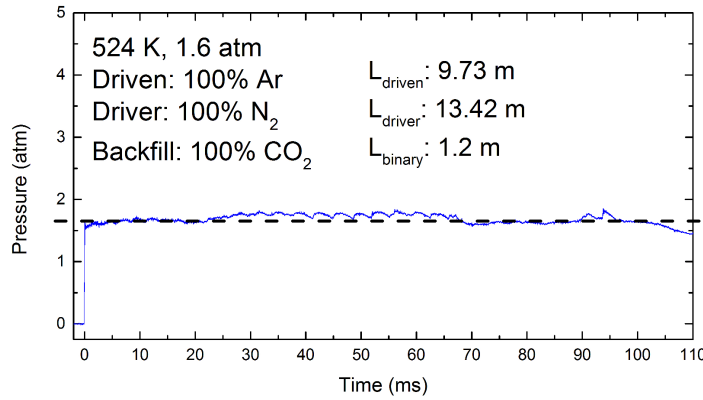


Figure 7.18: Demonstration of combined test time extension techniques. This shock shows 102 ms (0.102 s) of test time at $T_5 = 524$ K and $P_5 = 1.6$ atm; the dashed line shows the average pressure (1.695 atm). Conditions: $\frac{A_{driver}}{A_{driven}} = 1$, $L_{driven} = 9.73$ m, $L_{driver} = 13.42$ m, $L_{binary} = 1.2$ m. Driver: 100% N_2 (at this temperature, the correct tailoring requires no helium); driven: 100% Ar; backfill: 100% CO_2 . No helium interface gas was needed. A series of driver inserts was used to mitigate non-ideal pressure increases.

Figure 7.19 shows the Stanford code's estimate as to the test time obtainable as a function of T_5 with and without backfilling, for $L_{driven} = 9.73$ m, $L_{driver} = 13.42$ m, $L_{binary} = 1.2$ m, tailored He/ N_2 driver gas, argon driven gas, and carbon dioxide backfill gas. Importantly, the introduction of staged driver gas filling can substantially increase the available test time at all temperatures. Relative to the experiment shown in Figure 7.18, the model under-predicts the measured test time. Again, this is likely due to the idealized assumptions implicit in the computer code, such as zero backfill/binary gas mixing, but could also be the result of uncertainty in the experimental value of $L_{binary} = 1.2$ m, since this value does not account for the volume occupied by the inserts employed. Note that the code predicts that backfilling allows for greater increases in test time at higher temperatures as compared to at low temperatures. This reflects the fact that at high temperatures, a majority of the tailored driver gas consists of helium, implying that replacing this gas with a low-sound-speed

alternative can yield great performance enhancements.

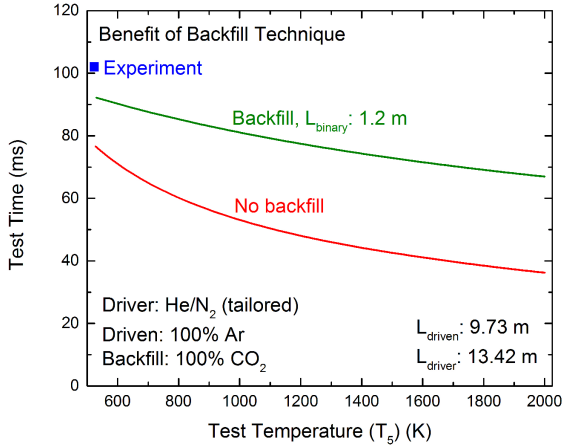


Figure 7.19: Benefit of backfill technique on test time versus Region 5 temperature T_5 . Lines show Stanford code predictions and the blue square shows experimental measurement. Conditions: $\frac{A_{driver}}{A_{driven}} = 1$, $L_{driven} = 9.73\text{ m}$, $L_{driver} = 13.42\text{ m}$, $L_{binary} = 1.2\text{ m}$. Driver: He/N₂ (tailored); driven: 100% Ar; backfill: 100% CO₂. No helium interface gas was used. Note that these test times are longer than those of Figure 7.15 because, in this case, a longer L_{driver} and a lower-sound-speed backfill gas were employed. Also, they are longer than the values of Figure 7.17 because, in this case, a longer L_{driver} and a shorter L_{binary} were employed.

7.6 Sample ignition delay time measurement

An example application of the long constant pressure test time concept will now be introduced by examining a problem of practical interest, namely the measurement of ignition delay time. A sample ignition delay time measurement for a *n*-heptane/21%oxygen/argon ($\phi = 0.5$) mixture at 4.6 atm and 648 K is provided in Figure 7.20. Details of the diagnostics employed in this experiment are available in Section 9.2.2 and Reference [289], hence only a concise summary will be provided here. At these conditions, *n*-heptane exhibits two-stage ignition. The first stage ignition was monitored by observing the fuel decay according to the Beer-Lambert relation (see Equations 3.1, 4.11, 5.2, 8.4, and 9.1) using a continuous wave helium neon (HeNe) laser at 3.39 μm that probes

Region 5 at a location 2 cm from the endwall; the decline in absorbance near 50 ms clearly marks this event. Second stage ignition is monitored by emission from excited OH (OH^*) radicals near 306 nm through a port in the shock tube endwall; the rise in the emission signal near 65 ms indicates this occasion and is corroborated by the rise in pressure and the final drop in HeNe absorbance. The second stage ignition delay time shown is greater than 65 ms, making it, to the author's knowledge, one of the longest ignition delay times ever measured in a shock tube. This experiment would not have been possible without the test time extension techniques discussed in this work and the results provide a good example of the Negative Temperature Coefficient (NTC) region behavior exhibited by many large alkane fuels at practical engine conditions. It is worth noting that these experiments provide data similar to that obtainable in a Rapid Compression Machine (RCM), but without ambiguity associated with the finite compression time and gradual pressure decays in such facilities [302–304].

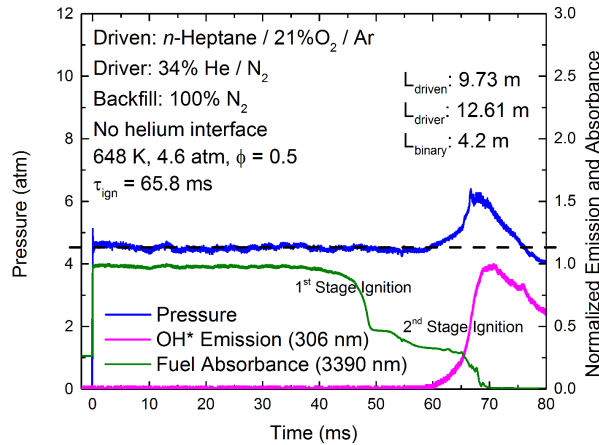


Figure 7.20: Sample ignition delay time measurement. The first drop in fuel absorbance indicates first stage ignition; the rise in OH^* emission, rise in pressure, and further drop in fuel absorbance indicate second stage ignition. Conditions: $\frac{A_{\text{driver}}}{A_{\text{driven}}} = 1$, $L_{\text{driven}} = 9.73 \text{ m}$, $L_{\text{driver}} = 12.61 \text{ m}$, $L_{\text{binary}} = 4.2 \text{ m}$. Driver: 34% He/N_2 ; driven: n -heptane/21% O_2/Ar ($\phi = 0.5$); backfill: 100% N_2 . A driver insert was employed to eliminate non-ideal pressure increases, and no helium interface gas was used. $\tau_{\text{ign},1} = 48.0 \text{ ms}$; $\tau_{\text{ign},2} = 65.8 \text{ ms}$.

7.7 Heat transfer

As mentioned in Section 7.1.2, a numerical analysis by Frazier *et al.* [284] concluded that wall heat transfer does not reduce area-averaged temperature at long times, for shock tubes with 8-cm or larger internal diameters. In order to examine this statement, gas pressure and temperature were measured *in situ* for several carbon dioxide-seeded experiments (4%CO₂/Ar) over long test durations. Like the ignition measurement, details of the CO₂-based spectroscopic temperature diagnostic are available elsewhere [289, 305] so only a brief overview is provided here. The temperature diagnostic was based on a two-color absorption technique, which exploited the steep inverse temperature dependence between CO₂ transitions in different infrared absorption bands to achieve high sensitivity. Spectroscopic measurement uncertainty is estimated to be less than 2% for the reflected shock conditions in these experiments.

Figure 7.21 depicts one of these shocks, taken at 635 K and 5.1 atm. During this experiment, a very small residual non-ideal pressure change of $\frac{dP^*}{dt} = 0.22\%/\text{ms}$ was allowed in order to examine the isentropic relationship between gas temperature and pressure (Equation 7.1); near the end of the test time this amounted to an 11% overall increase in pressure. Several important notes can be made about this graphic. First, the initial post-reflected-shock temperature computed based on incident shock speed matches the spectroscopically-obtained value to within 0.5%, which is the approximate uncertainty in the measured temperature; this underscores the reliability of the velocity-based calculation technique used widely in shock tube studies. Moreover, the uncertainty in shock-speed-based temperature for this experiment is conservatively estimated to be only about 0.3% by accounting for errors in measured incident shock-speed (0.14% in this trial), initial (pre-shock) temperature and pressure, and thermodynamic properties (heat capacity and enthalpy). At this stage of development of the laser-based diagnostic, there is slightly less uncertainty in the shock-speed-based temperature value than that measured spectroscopically, but the important message is that these values agree within their (small) experimental uncertainties. Second, the subsequent measured temperature change tracks that calculated from the change in pressure (assuming isentropic compression according to Equation 7.1) very closely. This gives confidence to use of the isentropic relationship to estimate changes to post-reflected-shock temperature based on observed pressure profiles.

Hence, the conclusion of Frazier *et al.* [284] that wall heat transfer is not a significant concern in large-diameter shock tubes, like that employed in this work, at conditions similar to those of this study, seems well-founded. Were heat transfer a problem, one might expect a significant temperature and pressure drop over the course of the experiment. Note that the spectroscopic diagnostic yields a path-average temperature value; due to conduction heat transfer, the temperature of the gas in the thin boundary layer at the edges of the shock tube will be lower than the bulk temperature. Further work is needed to investigate the role of heat transfer over a wider range of conditions.

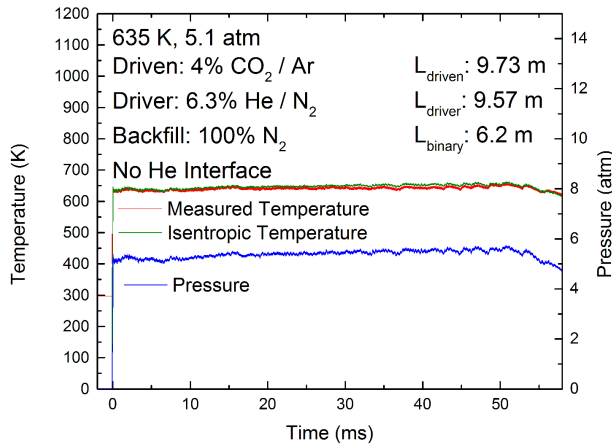


Figure 7.21: Sample CO₂-based spectroscopic temperature measurement, and comparison with isentropically-computed temperature (Equation 7.1). Conditions: $\frac{A_{driver}}{A_{driven}} = 2.38$, $L_{driven} = 9.73$ m, $L_{driver} = 9.57$ m, $L_{binary} = 6.2$ m. Driver: 6.3% He/N₂; driven: 4%CO₂/Ar ($\gamma_5 = 1.6128$); backfill: 100% N₂. A driver insert was employed to control the non-ideal pressure increase, and no helium interface gas was used. The shock tube test section diameter is 11.53 cm.

7.8 Summary

The use of several shock tube techniques for achieving extended reflected-shock test times with uniform pressure have been demonstrated, including driver inserts, driver gas tailoring, the use of helium interface gas in front of the diaphragm, driver extensions, and staged driver gas filling. The latter method, which involves first filling the driver section with a tailored binary gas mixture, and

secondly backfilling a low-speed-of-sound gas near the driver section end cap, can increase test times by approximately 20% while reducing necessary driver helium consumption by up to about 85%. By combining the above techniques together, an experiment with 102 ms of test time at 524 K and 1.6 atm has been achieved. The value of these strategies has been demonstrated by measuring long *n*-heptane/21%O₂/Ar ($\phi = 0.5$) ignition delay times at pressures near 4.5 atm and temperatures near 650 K. Also, a novel spectroscopic CO₂-based temperature diagnostic has been employed to demonstrate the viability of using isentropic relations to predict changes in test temperature based on the measured pressure profile for each shock, and hence have shown that temperature remains constant throughout the entire test duration in long shocks when pressure is held constant. The techniques introduced herein will allow use of shock tubes to explore low-temperature, moderate-pressure chemistry that is of practical importance to a variety of combustion devices in use today.

Chapter 8

Operation of the constrained reaction volume shock tube

*The contents of this chapter have been published in the journal **Review of Scientific Instruments** [306].*

8.1 Introduction

8.1.1 Motivation

As introduced in Chapter 2, the shock tube has been an important reactor for studies of high-temperature combustion kinetics for at least the last 60 years. At high temperatures (>1000 K) and for dilute fuel mixtures, where ignition delay times are typically short (<2 ms) and pre-ignition chemical energy release is small, these devices are able to provide a near-constant internal energy and specific volume (U-V) environment up to the time of ignition, with well-defined initial conditions at time zero [111, 117, 118, 120, 287]. However, numerous non-ideal phenomena can occur at lower temperatures where ignition delay times and related chemical processes have longer timescales. These include ignition first occurring at remote locations (away from the endwall), that then affects conditions at the test location (typically 1-2 cm from the endwall) [132]. Also, except for highly dilute reactive mixtures, the pressure increase due to energy release during the ignition

event causes experiments to deviate sharply from the constant U-V behavior generally assumed in modeling the flow field [129, 280, 281, 289]. Here an improved shock tube design to obviate these problems is reported.

It has been previously shown that remote ignition events and the effects of energy release can be significantly reduced by employing a Constrained Reaction Volume (CRV) technique, in which the reactive gas mixture is confined to a small fraction of the entire shock tube near the endwall [129, 132]. In initial CRV experiments performed in the High Temperature Gasdynamics Laboratory (HTGL) at Stanford, a staged driven-section filling technique has been employed in which the test gas was pushed into a small volume in the test section at the end of the shock tube using a second inert component, called the buffer gas. However, mixing between the buffer and test gases resulted in higher uncertainty in the test gas composition [129, 132]. The primary goal of the current work was to introduce a removable physical barrier (specifically, a sliding gate valve) between the test gas and buffer gas that could limit the extent of mixing in the time before the incident shock wave passed by the buffer/test gas contact surface. In this way, smaller volumes of well-defined reactive mixtures can be prepared and will remain intact for experimentation.

8.1.2 Previous research

Several noteworthy experiments have been conducted previously in which the test gas mixture was constrained to a section of the shock tube. The earliest facilities to accomplish this were single pulse shock tubes [294, 307, 308], which used a ball valve to confine the post-reflected-shock test gas mixture within the test section after it was cooled by the arrival of the expansion wave. In this way, post-shock gas samples could be obtained and analyzed without being diluted by other gases in the shock tube.

Later experiments used sliding gate valves rather than ball valves. According to a recent literature review, the first researchers to use a sliding gate valve in a shock tube were Brown and Thomas [309], whose valve was located between a 0.82 m long test gas section and a 3.17 m long buffer section (these had internal diameters of 7.6 cm). This valve enabled the shock wave to stabilize in the inert buffer gas before entering the test gas mixture and also prevented what the authors referred to as “spurious ignition”. The authors commented that great care was taken to equalize the

pressures on both sides of the valve prior to its opening, that the buffer and test gases were acoustically matched to prevent refraction effects, and that the gate valve was opened less than 0.5 seconds prior to diaphragm rupture in order to prevent buffer/test gas mixing. In their study, the shock velocity was measured to within $\pm 0.6\%$, resulting in a post-reflected-shock temperature uncertainty of $\pm 1.3\%$, or 22 K at 1700 K.

A gate valve was also employed by Haylett, Davidson, and Hanson [66, 130, 160] in order to confine a fuel aerosol/oxidizer/diluent mixture close to the endwall in their low-vapor-pressure diesel surrogate experiments. In that work, the buffer gas was chosen to be the same as that of the test gas but with no fuel aerosol droplets, and the gate valve was located approximately 1.2 m from the shock tube endwall. These researchers measured the incident shock velocity to within approximately $\pm 0.4\%$. This technique was also discussed in Chapter 3.

A different application of the Haylett *et al.* gate valve [66, 130, 160] was demonstrated by Gates *et al.* [155], who employed it to confine a post-reflected-shock gas/endospore aerosol mixture after expansion wave-induced cooling in order to collect samples of biological aerosols. The technique used by Gates *et al.* was similar to that used in single pulse shock tubes [294, 307, 308], except a sliding gate valve was used instead of a ball valve.

To summarize the above review, two separate techniques have generally been employed to confine a gas mixture to part of a shock tube: a ball valve [294, 307, 308] and a gate valve [66, 130, 155, 160] (note that the use of thin diaphragms for gas separation in shock tube driven sections [310, 311] is uncommon because the diaphragm fragments created as the incident shock wave shatters the diaphragm interfere with diagnostics located in the test section). Of the two techniques, the gate valve has been found to be superior for the current application because it is thinner and occupies less volume than a ball valve (particularly for the relatively large 11.53 cm diameter tube employed in this work). Additionally, past efforts to measure incident shock speed in the presence of a gas interface have resulted in increased velocity uncertainties [66, 130, 160]; however, for kinetics applications where accurate knowledge of post-shock temperature (computed primarily based on incident shock velocity) is imperative, small error margins ($<0.2\%$) are desirable. In this study, it has been sought to minimize this velocity error through careful gas tailoring [309] and the sliding valve has been placed closer to the endwall so as to limit the axial extent of the reactive mixture more than in

previous studies.

8.2 Experimental setup

8.2.1 Shock tube

The shock tube employed in this work (known as the Constrained Reaction Volume Shock Tube, CRVST), shown in Figure 8.1, consists of a 9.57 m driver section filled with a high-pressure tailored [277, 278] helium/nitrogen mixture separated by a 0.030-inch polycarbonate diaphragm from a 9.32 m buffer section filled with a specially tailored carbon dioxide/nitrogen/argon buffer gas mixture (for comparison purposes, the dimensions of several shock tubes found in the literature are provided in Table 8.1). A sliding gate valve, described below, separates this buffer section from a 39.5 cm test section that contains the test gas mixture (fuel/oxygen/argon). The length of this test section can be increased or decreased by the insertion of different endwall plates and several assorted spacers. Both the buffer and test sections have internal diameters of 11.53 cm. As in Brown and Thomas [309], the pressures in the buffer and test gas sections are carefully matched prior to the experiment.

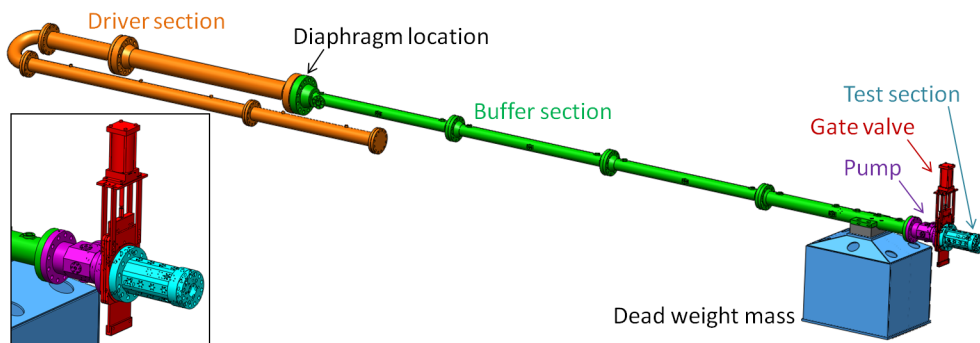


Figure 8.1: Shock tube schematic. The driver length shown is 9.57 m, and the combined length of the buffer section, gate valve, and test section is 9.73 m.

As introduced in Section 2.3, experiments are initiated when the high-pressure driver gas ruptures the diaphragm. A four-blade cutter in the form of a cross, mounted on the tube centerline, is also used to decrease shock-to-shock variation in the burst pressure and minimize the occurrence

CHAPTER 8. OPERATION OF THE CRVST

Table 8.1: Dimensions of several shock tubes in the literature. Abbreviations: CRVST = Constrained Reaction Volume Shock Tube, HPST = High Pressure Shock Tube, KST = Kinetics Shock Tube, LPST = Low Pressure Shock Tube, KIT = Karlsruhe Institute of Technology, RPI = Rensselaer Polytechnic Institute, NUI = National University of Ireland, RWTH = Rheinisch-Westfälische Technische Hochschule, KAUST = King Abdullah University of Science and Technology. “CRV” refers to filling only the CRVST test section with test gas, and “Conv.” refers to filling the entire CRVST volume with test gas. The lengths of the Stanford KST, NASA tube, and CRVST driver sections are given as their longest values; the shortest values (standard configurations) are 3.35 m, 3.70 m, and 3.63 m respectively. The diameter of the CRVST driver section is taken as the length-weighted average of its 17.8 cm and 15.4 cm diameter parts (see Section 7.2). A similar compilation of shock tube geometries can be found in Reference [303].

Institution	Description	Country/State	Diameter [cm]	Length [m]	Volume [L]	Diameter [cm]	Length [m]	Volume [L]	Mixing Tank Volume [L]	Reference
University of Illinois at Chicago		Illinois	5.08	1.52	3.1	2.54	4.10	2.1	[312]	
KIT	HPST	Germany	3.14	1.98	1.5	3.14	2.97	2.3	[313]	
Stanford University	CRVST (CRV)	California	16.05	13.42	271.5	11.53	0.40	4.1	44.9	[306]
McGill University	Quebec	Quebec	5.00	3.00	5.9	5.00	4.20	8.2	90.0	[314]
Stanford University	HPST	California	7.62	3.00	13.7	5.00	5.00	9.8	12.8	[315]
RPI	NUI Galway	New York	2.59	5.70	3.0	5.70	4.11	10.5	[316]	
RWTH Aachen		Ireland	6.30	3.03	9.4	6.30	5.73	17.9	[317]	
University of Duisburg-Essen		Germany	8.70	5.30	31.5	8.70	6.30	37.5	[131]	
KAUST	HPST	Germany	9.00	6.10	38.8	9.00	6.40	40.7	[318]	
Texas A&M University	CRVST (Conv.)	Saudi Arabia	10.00	7.00	55.0	10.00	7.00	55.0	[319]	
Stanford University	KST	Texas	7.62	2.46	11.2	15.24	4.72	86.1	55.6	[71, 320]
Stanford University	LPST	California	16.05	13.42	271.5	11.53	9.73	101.6	44.9	[306]
KAUST		California	14.13	7.12	111.6	14.13	8.54	133.9	12.0	[321, 322]
RWTH Aachen		Saudi Arabia	14.00	9.00	138.5	14.00	9.00	138.5	95.0	[323]
Stanford University	NASA Tube	Germany	14.00	4.50	69.3	14.00	11.00	169.3	260.0	[290, 324]
University of Central Florida		California	15.24	7.55	137.7	15.24	10.51	191.7	14.5	[321]
		Florida	7.62	3.50	16.0	16.20	10.70	220.5		[165]

of diaphragm fragments released in the tube. This rapid bursting results in the formation of an incident shock wave that moves toward the test section, and an expansion wave that moves back into the driver section. In the current experiments, the velocity of the shock wave is measured using a series of seven PCB model 113A26 transducers. This velocity is extrapolated to the shock tube endwall with an accuracy of $\pm 0.2\%$ and is used to calculate the initial post-shock temperature and pressure to within $\pm 0.6\%$ and $\pm 1.6\%$, respectively, using an in-house code (FROSH) that employs standard shock jump relations and thermodynamic properties of the constituent gases [125, 174] (see Appendix A). The pressure in the test section is measured *in situ* using a Kistler model 601B1 transducer covered in Room Temperature Vulcanizing silicone (RTV) located in the test section 2 cm from the endwall, consistently confirming the computed conditions.

A few seconds prior to diaphragm rupture, the sliding gate valve is opened, which allows the incident shock wave to pass into the test section (refer to Figure 8.2). As the shock wave propagates into the test gas, it heats the gas and compresses it from its original volume, which spans a distance $L_1 = 39.5$ cm between the endwall and the gate valve, to a smaller volume close to the endwall. Ultimately, the incident shock wave reflects from the endwall of the test section; the reflected shock wave then moves back through the test gas toward the diaphragm, further heating and compressing the test gas. This results in the test gas being stagnated and confined to a volume with a length L_5 as measured from the endwall, enabling spectroscopic and pressure diagnostics, discussed below, to probe the reactive test gas at a location 2 cm from the endwall (note that the distance from the endwall at which diagnostics are located is typically kept to a minimum; however, at most conditions, similar results are expected for distances up to about 5 cm (the aerosol shock tube uses an endwall distance of about 3.6 cm)). Typical values of L_5 in the CRV experiments in this study are between 5 and 10 cm, whereas values of L_5 for a similar conventionally-filled shock tube (in which the entire buffer and test gas sections are filled with reactive test gas) might vary between about 130 and 240 cm.

An x-t diagram, as introduced in Section 7.1.3, provides a graphical depiction of wave propagation in a shock tube. The University of Wisconsin Shock Tube Lab (WiSTL) has developed a second order Muscl-Hancock-Method finite volume code with an exact Riemann solver, capable of generating such diagrams for shock tubes with both a buffer gas and a test gas [286]. Figure 8.3 is an

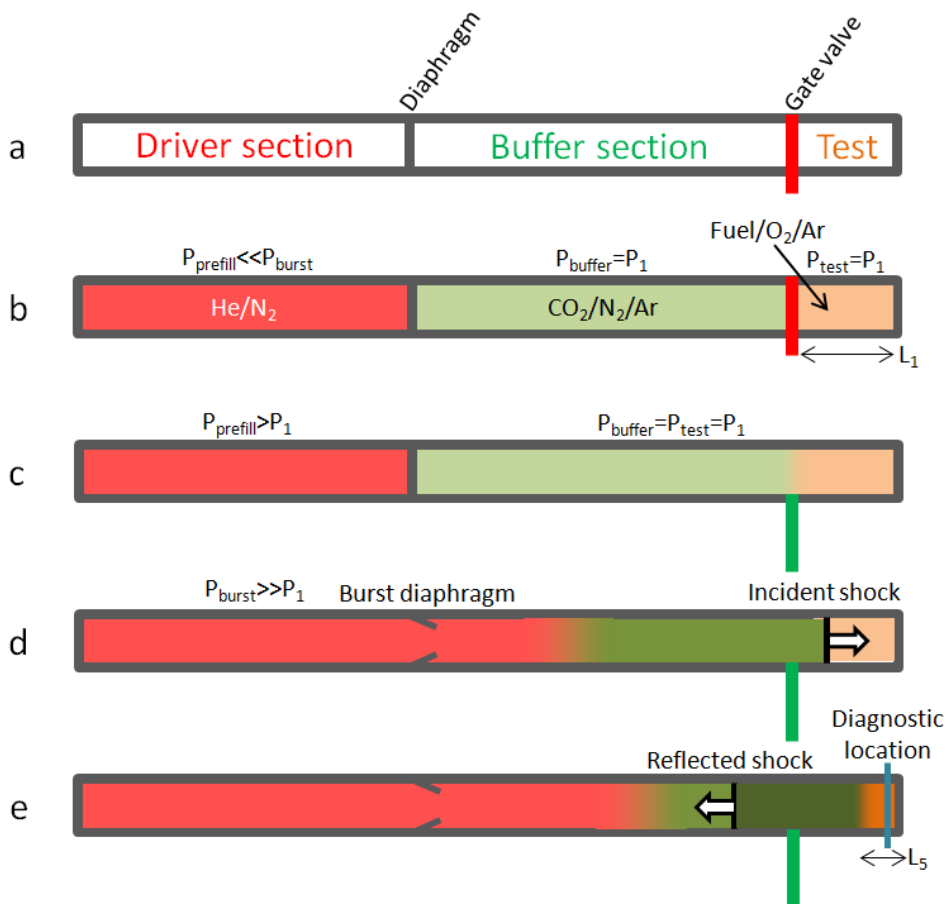


Figure 8.2: CRV shock tube operating procedure. (a) Labeling of shock tube sections (b) Initial gas filling (c) Opening of gate valve (d) Rupture of diaphragm and passage of incident shock (e) Passage of reflected shock and stagnation of gas flow.

example of one such plot, showing correctly matched (*i.e.*, tailored) driver/buffer gas and buffer/test gas interfaces. In this figure, the circled numbers show different regimes of the shock experiment. For instance, Region 4 refers to the driver gas prior to diaphragm rupture. The letters “a” and ”b” denote the buffer and test gases, respectively; for example, Regions 5a and 5b are the buffer and test gases following the passage of the reflected shock. Notice that the contact surface lines, shown in red, between Regions 8, 5a, and 5b are vertical, denoting stagnated contact surfaces with equal gas pressure on both sides.

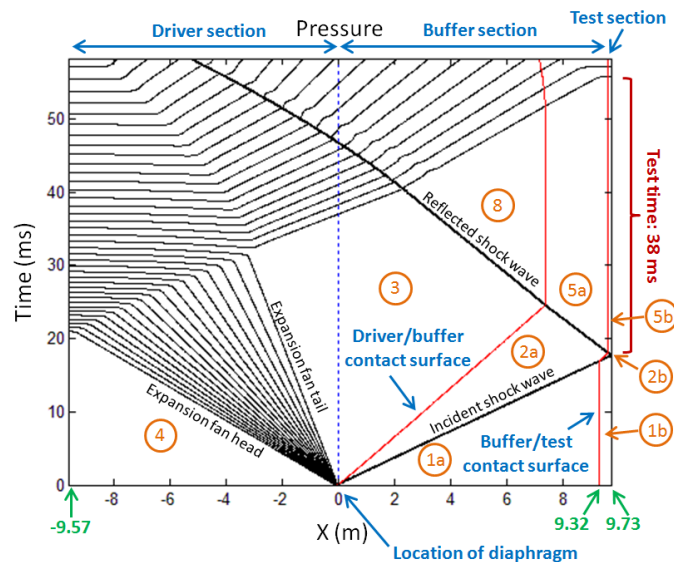


Figure 8.3: X-t diagram of CRV shock experiment generated using the WiSTL code [286], showing movement of driver/buffer gas and buffer/test gas interfaces. Solid lines are constant pressure contours. Experimental conditions: $M_{IS} = 1.77$, $T_1 = T_4 = 22\text{ }^{\circ}\text{C}$, $P_4 = 6.6\text{ atm}$, $P_1 = 492\text{ Torr}$, $L_1 = 39.5\text{ cm}$, $P_5 = 6.5\text{ atm}$, $T_5 = 750\text{ K}$, $L_5 = 10.0\text{ cm}$. Driver: 45%He/55%N₂, Buffer: 10%CO₂/7%N₂/83%Ar, Test: 0.9%C₇H₁₆/9.91%O₂/89.19%Ar ($\phi = 0.75$).

In Figure 8.3, the test gas was compressed from a length $L_1 = 39.5\text{ cm}$ to $L_5 = 10.0\text{ cm}$. The ideal gas equation of state (Equation 3.12) can be used to relate these lengths to the thermodynamic shock conditions in Regions 1 and 5 (this derivation closely resembles that outlined for staged driver gas filling in Section 7.4.2). In Region 1,

$$P_1 A_{test} L_1 = N_{test} \hat{R}_u T_1 \quad (8.1)$$

where P_1 and T_1 are the Region 1 pressure and temperature, respectively, A_{test} is the cross sectional area of the test section, N_{test} is the number of moles of test gas filling the test section, and \hat{R}_u is the ideal gas constant. Similarly, in Region 5,

$$P_5 A_{test} L_5 = N_{test} \hat{R}_u T_5 \quad (8.2)$$

where P_5 and T_5 are the Region 5 pressure and temperature, respectively. Dividing Equation 8.1 by Equation 8.2 and solving for L_5 yields Equation 8.3 below [132],

$$L_5 = L_1 \frac{\rho_1}{\rho_5} = L_1 \frac{T_5 P_1}{T_1 P_5} \quad (8.3)$$

wherein ρ_1 and ρ_5 (see Equation 4.4) are the Region 1 and Region 5 densities, respectively.

Lastly, it should be noted that a driver insert [170–172] is generally used to eliminate the non-ideal pressure increase caused by shock attenuation and boundary layer growth. Also, test gas mixtures are prepared manometrically in stainless steel mixing tanks (one for the buffer gas and another for the test gas). The shock tube is turbo-mechanically pumped to a pressure lower than 10^{-5} Torr prior to most experiments, with a negligible subsequent leak-plus-outgassing rate. Normal heptane used in the ignition experiments was obtained from Sigma-Aldrich Corp. (99.3%) and was subject to degassing prior to use, while research-grade oxygen, carbon dioxide, nitrogen, propane, and argon were obtained from Praxair Inc.

8.2.2 Gate valve

An exploded view of the custom-built stainless steel gate valve employed by this shock tube is shown in Figure 8.4. The valve employs a pneumatic piston that smoothly moves the sliding piece at a speed that can be adjusted between about 4 and 11 cm/s, giving an actuation time of 1 to 4 seconds. These slow speeds are chosen to minimize turbulent mixing of the buffer and test gases.

In order to facilitate laser diagnostic alignment in the test section, the gate valve has a vertical orientation when mounted to the shock tube. Two ground tool steel spacer pieces are employed to ensure that the two halves of the valve remain perfectly parallel while supporting the weight of the

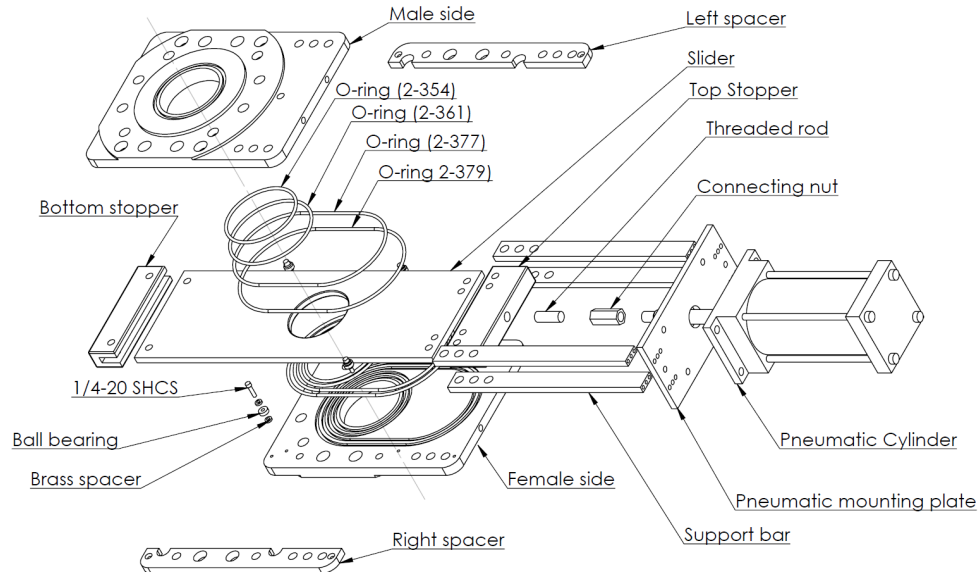


Figure 8.4: Exploded view of gate valve. O-ring sizes are provided for reference.

test section.

O-rings on each side of the slider provide the vacuum and overpressure sealing, and each o-ring has a backup in case of failure during gate valve motion. The o-ring gland depths and spacer thicknesses were carefully chosen in order to provide about 10% o-ring compression and 77% gland fill, a combination that yields a good vacuum/overpressure seal while allowing the gate valve to slide uninhibited. When the valve is shut, the circular cutout in the slider is contained within the oval-shaped o-ring (see Figure 8.4), and when open, the circular cutout is centered on the round o-rings. Also, a tightly-toleranced 0.030-inch clearance is present between both faces of the slider and the gate valve sides, in order to avoid metal-to-metal contact but ensure a high-integrity seal.

The slider piece is constructed from a 0.5-inch thick cold-rolled steel plate in order to withstand a pressure of up to 150 atm while heated to 100 °C (up to 200 atm if unheated (25 °C)) in the unlikely event of a strong shock wave colliding with the gate valve while it is closed. Brass ball bearings are used to guide the slider as it travels, and set screws allow precise tuning of the slider such that the cutout circle is correctly aligned to the shock tube's circular bore. Also, the slider cutout features slight bevels on its edges to avoid snipping the o-rings during its travel. No evidence

that these bevels influence the behavior of the incident and reflected shocks has been found.

A gas line, equipped with a secondary ball valve, connects the buffer section of the shock tube to the inner chamber of the gate valve. This line allows the slider cutout volume (0.133 liters) to be vacuum-pumped when the valve is shut, and also allows the cutout volume to be filled with buffer gas prior to each experiment as a further protection against buffer/test gas mixing as the slider opens. In order to pump out the small volume between the concentric o-rings, the gate valve is cycled twice prior to each shock experiment while under vacuum. Additional details concerning the design of the CRVST (and other shock tubes in general) can be found in Appendix F.

8.2.3 Diagnostics

The diagnostics employed in this work are depicted in Figure 8.5. As mentioned above, a Kistler pressure transducer located at 2 cm from the endwall is used to monitor pressure. This transducer's half-rise during the reflected shock serves as the indicator of the beginning of post-reflected-shock test time. Also, the PCB transducers located at intervals away from the endwall, though not quantitative indicators of absolute pressure, provide qualitative measures of pressure changes such as that associated with ignition.

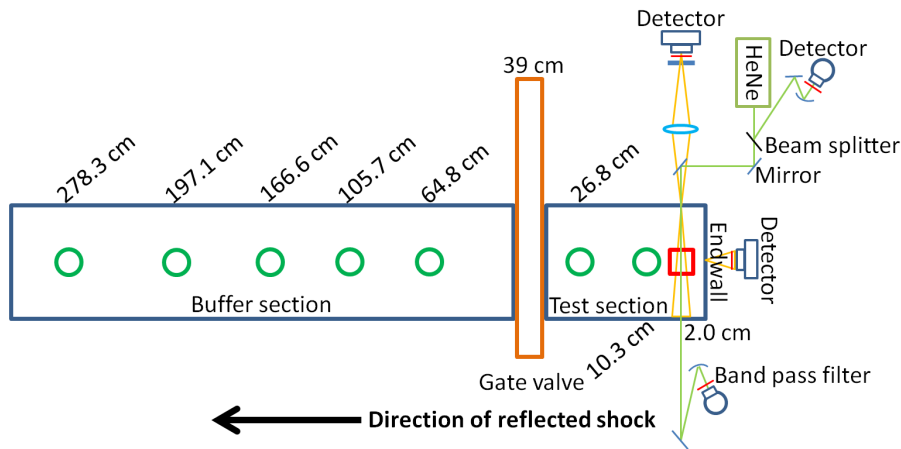


Figure 8.5: Locations of diagnostics on shock tube (diagram not to scale). Circles denote PCB transducers and the square denotes the Kistler transducer. Also shown are the HeNe 3.39 μm laser absorption diagnostic (green lines) and 306 nm OH* emission diagnostic (yellow triangles).

Also passing through two optical access ports at 2 cm from the end wall is a 3.39 μm continuous wave helium-neon (HeNe) laser beam, which is used to measure fuel concentration via the Beer-Lambert relation (Equation 8.4; see also Equations 3.1, 4.11, 5.2, and 9.1).

$$\alpha = -\ln\left(\frac{I}{I_o}\right) = n\sigma_\nu L \quad (8.4)$$

In this equation, α is the absorbance, I_o is the incident monochromatic light intensity at frequency ν , I is the transmitted light intensity at frequency ν , $n = \frac{P}{R_u T}$ is the number density [mol/cm³] of absorbing species, σ_ν is the absorption cross section [cm²/mol], and L is the path length [cm]. This diagnostic is used to corroborate the manometrically prepared fuel mole fraction value prior to every experiment. Furthermore, this diagnostic provides a record of fuel decomposition and can be used as a reliable indicator of ignition. Absorption cross section values for *n*-heptane were obtained from the literature [175, 225, 226] and were confirmed using shock tube experiments.

Finally, emission from excited OH radicals at (306 \pm 75) nm (OH* emission) is monitored using a series of focusing lenses, slits, and Schott Glass UG-5 band-pass filters at both 2 cm from the endwall and through a port in the endwall of the shock tube. Ignition times garnered from both positions yield consistent results, although the endwall OH* sensor serves to integrate the axial emission distribution and thus has slightly different temporal behavior than that of the sidewall sensor [325].

8.3 Results

Four aspects of the CRV shock tube are discussed below. First, new methodology for buffer gas tailoring is introduced; second, buffer/test gas mixing after the gate valve is opened is examined; third, the implications of the ratio of mixing tank volume to shock tube volume are discussed; and fourth, a side-by-side comparison between shocks taken using the CRV and conventional filling techniques is provided. A thorough discussion of the influence of CRV length L_1 is provided elsewhere [132] and thus will not be addressed in this chapter.

8.3.1 Buffer gas tailoring

In shock tube kinetics experiments, where accurate knowledge of temperature is imperative, precise measurement of incident shock velocity is critical because the calculated Region 5 temperature T_5 depends on the square of this quantity [111]. Thus, the incident shock velocity is measured at several locations along the length of the shock tube and extrapolated to the endwall assuming a constant attenuation rate (an in-depth discussion of shock velocity measurement is available elsewhere [165]). However, for short CRV lengths (small L_1), only one velocity measurement is possible in the test gas. Thus, as mentioned by Brown and Thomas [309], it is important to acoustically match the buffer and test gases (*i.e.*, tailoring) in order to achieve a consistent shock velocity and attenuation rate across the buffer/test gas interface. This allows the shock velocity to be measured over a greater distance (in both the buffer gas and in the test gas), enabling an extrapolation of the shock velocity to the endwall with much greater confidence.

Shock wave theory dictates that proper buffer gas tailoring can be accomplished by closely matching the molecular weight \hat{M} (Equation 8.5) and heat capacity ratio $\gamma = \frac{\hat{c}_p}{\hat{c}_v}$ (Equation 8.6) of the buffer and test gases. In particular, the sound speed a [m/s], which depends on \hat{M} and γ , governs wave propagation in gases (Equation 8.7), and the shock attenuation rate Γ [%/ms] is proportional to the square root of shock Mach number $M_{IS} = \frac{U_{IS}}{a}$ (Equation 8.8) [315].

$$\hat{M} = \sum_{i=1}^C x_i \hat{M}_i \quad (8.5)$$

$$\gamma = \frac{\hat{c}_p}{\hat{c}_v} = \frac{\sum_{i=1}^C x_i \hat{c}_{p,i}}{\sum_{i=1}^C x_i \hat{c}_{v,i}} \quad (8.6)$$

$$a = \sqrt{\frac{\gamma \hat{R}_u T}{\hat{M}}} \quad (8.7)$$

$$\Gamma \propto P_1^{-0.14} M_{IS}^{0.5} \propto P_1^{-0.14} U_{IS}^{0.5} \left(\frac{\gamma \hat{R}_u T_1}{\hat{M}} \right)^{-0.25} \quad (8.8)$$

In these equations, C is the number of gaseous species, x_i is the mole fraction of species i , \hat{M}_i is the molar mass of species i , and $\hat{c}_{p,i}$ and $\hat{c}_{v,i}$ are the molar heat capacity values at constant pressure

and constant volume of species i , respectively. Also, U_{IS} is the incident shock velocity, \hat{R}_u is the ideal gas constant, and P_1 and T_1 are the Region 1 pressure and temperature. Since a particular test gas is often chosen to achieve experimental goals, the buffer composition must be varied to meet the tailoring constraints. It has been found that in order to match both \hat{M} and γ for fuel/oxygen/argon test gas mixtures, a three-component buffer gas mixture consisting of carbon dioxide, nitrogen, and argon is convenient. For fuel/oxygen/nitrogen test gas mixtures, the three buffer gas components can consist of carbon dioxide, nitrogen, and a small hydrocarbon such as methane or propane. Properties of oxygen, argon, nitrogen, carbon dioxide, and several representative fuels are provided in Table 8.2.

Table 8.2: Region 1 gas properties for several gases and fuels ($T_1 = 20^\circ\text{C}$, $P_1 = 300$ Torr). In this table, $R_g = \frac{\hat{R}_u}{\hat{M}}$ is the mass-specific gas constant and ρ is density. Data obtained from the Burcat database [174].

Gas / Fuel	\hat{M} [g/mol]	$\gamma = \frac{\hat{c}_p}{\hat{c}_v}$	R_g [J/kg-K]	\hat{c}_p [J/mol-K]	\hat{c}_v [J/mol-K]	a [m/s]	ρ [kg/m ³]
CH ₄	16.042	1.314	518.279	34.821	26.506	446.757	0.263
N ₂	28.013	1.400	296.803	29.121	20.807	348.965	0.460
O ₂	31.999	1.397	259.837	29.272	20.958	326.176	0.525
Ar	39.948	1.667	208.132	20.786	12.472	318.889	0.656
CO ₂	44.010	1.290	188.924	36.976	28.662	267.300	0.722
C ₃ H ₈	44.096	1.130	188.555	72.506	64.192	249.869	0.724
n-C ₇ H ₁₆	100.202	1.054	82.977	163.066	154.751	160.099	1.644
n-C ₁₀ H ₂₂	142.282	1.038	58.437	228.703	220.389	133.330	2.335

Applying Equations 8.5 and 8.6 to the constraints that $\hat{M}_{test} = \hat{M}_{buffer}$ and $\gamma_{test} = \gamma_{buffer}$ and solving algebraically provides an analytical solution for the three buffer gas component mole fractions (x_1 , x_2 , and x_3). The results are presented in Equations 8.9, 8.10, and 8.11, where subscripts 1, 2, and 3 denote the first, second, and third buffer components, respectively.

$$x_1 = \frac{\left(\frac{\hat{M}_3 - \hat{M}_{test}}{\hat{M}_3 - \hat{M}_2}\right) (\gamma_{test} (\hat{c}_{v,2} - \hat{c}_{v,3}) - (\hat{c}_{p,2} - \hat{c}_{p,3})) - (\hat{c}_{p,3} - \gamma_{test} \hat{c}_{v,3})}{\left(\frac{\hat{M}_3 - \hat{M}_1}{\hat{M}_3 - \hat{M}_2}\right) (\gamma_{test} (\hat{c}_{v,2} - \hat{c}_{v,3}) - (\hat{c}_{p,2} - \hat{c}_{p,3})) - (\gamma_{test} (\hat{c}_{v,1} - \hat{c}_{v,3}) - (\hat{c}_{p,1} - \hat{c}_{p,3}))} \quad (8.9)$$

$$x_2 = \left(\frac{\hat{M}_3 - \hat{M}_{test}}{\hat{M}_3 - \hat{M}_2} \right) - x_1 \left(\frac{\hat{M}_3 - \hat{M}_1}{\hat{M}_3 - \hat{M}_2} \right) \quad (8.10)$$

$$x_3 = 1 - x_1 - x_2 \quad (8.11)$$

A sample shock velocity measurement demonstrating correct buffer gas tailoring is shown in Figure 8.6. In this experiment, the test gas was 0.9%*n*-heptane/20.8%O₂/Ar ($\phi = 0.5$), and the buffer gas was 12%CO₂/13%N₂/Ar. Here, the shock wave is traveling from right-to-left, where the distance of $x = 0$ denotes the endwall position. Notice that the shock wave shows no change in its attenuation as it enters the vicinity of the gate valve (denoted by the vertical red dotted line), as indicated by the fact that the left two velocity measurement points are consistent with the trend set by the first (right most) four measurements. In particular, the velocity error (one standard deviation) at the endwall is only $\pm 0.072\%$, allowing the Region 5 temperature (658.8 K) and pressure (4.45 atm) to be computed to $\pm 0.3\%$ and $\pm 1.2\%$, respectively, for this particular experiment.

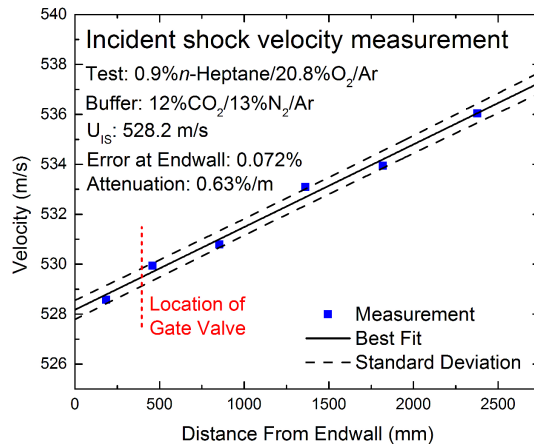


Figure 8.6: Shock wave velocity profile for correctly tailored buffer gas mixture. The shock velocity was extrapolated to the endwall ($x = 0$ mm), yielding a value of $U_{IS} = 528.2$ m/s.

Note that the buffer and test gases are only identically matched at the initial (Region 1) experimental temperature. As temperature increases, the heat capacity values' dependence on temperature will cause the γ values of the test and buffer gases to differ slightly. Thus, perfect buffer gas tailoring is accomplished for the incident shock only, not the reflected shock. However, for most gas mixtures, even at Region 5 temperatures over 1000 K, the γ values of the buffer and test gases continue

to match to within about 1%. Furthermore, these mixtures' densities, which depend only on \hat{M} given the same T and P , will remain closely matched as well. As a result, no reflected expansion or reflected shock waves originating from this interface are expected [326, 327] or have been observed in these measurements.

In separate experiments using 4.0% C_3H_8 /20.2% O_2 /Ar ($\phi = 1$) test gas, other buffer tailoring methods were also explored. For instance, only the buffer/test gas molecular weights were matched using 4.0% CO_2 /20.2% O_2 /Ar buffer gas, and only the heat capacity ratio values were matched using 4.0% C_3H_8 /20.2% N_2 /Ar buffer gas. In both cases, a significant velocity change was observed as the incident shock wave entered the test section. This is evidence that matching both test gas and buffer gas molecular weight and specific heat ratio is important for proper buffer gas tailoring.

Finally, it should be noted that the condition for buffer gas tailoring ($\hat{M}_{test} = \hat{M}_{buffer}$ and $\gamma_{test} = \gamma_{buffer}$), detailed above, is different to that for driver gas tailoring ($P_5 = P_8$; see Section 7.1.3 and Figure 7.2). This is the result of different goals for the tailoring methods. Buffer gas tailoring seeks to match the velocity and attenuation rate of the incident shock, whereas driver gas tailoring seeks to prevent reflected expansion or shock waves from originating at the driver/buffer gas interface during its interaction with the reflected shock. Additional information concerning gas tailoring can be found in Appendix E.

8.3.2 Buffer/test gas mixing

In CRV experiments that employ the gate valve, mixing between the test and buffer gases occurs after the slider is opened due to both Fickian diffusion and turbulent mixing (the slider induces velocity in the gas when it moves). Directly adjacent to the slider piece, the buffer/test gas mixing happens immediately; further from the valve, the mixing begins later. Thus, the mixing zone expands outward from the gate valve into the test section. When L_5 ranges between 5 and 10 cm, at the conditions of many shock experiments, the test gas that ultimately is compressed to the 2 cm measurement location originates between 8 and 16 cm from the endwall (between about 32 and 24 cm from the slider). Thus, in order to ensure negligible test gas dilution in shock experiments, the mixing zone must be confined to a critical length within approximately 24 cm of the gate valve, or further than about $L_{1,crit} = 16$ cm from the endwall. Since the mixing zone expands at a finite

rate, this distance corresponds to a critical time $\tau_{1,crit}$ as measured from the time when the gate valve slider begins to move, at which time buffer/test gas mixing becomes problematic. Preventing the mixing zone from reaching $L_{1,crit}$ can be accomplished by ensuring that the time between gate valve opening and diaphragm rupture, τ_{gv} , is less than $\tau_{1,crit}$ (*i.e.*, $\tau_{gv} < \tau_{1,crit}$; note that a typographical error in Reference [306] incorrectly had this inequality reversed).

8.3.2.1 Effect of pressure

In order to quantify $\tau_{1,crit}$, spectroscopic fuel absorption measurements using the HeNe laser diagnostic were conducted through a set of windows located $L_{meas} = 10.3$ cm from the endwall (29.2 cm from the gate valve) in the test section. These tests followed the following procedure. The test section was filled with 1% *n*-heptane in argon, and the buffer section was filled with 100% argon; both sections were filled to identical pressures. The data acquisition software was started at time zero, and the gate valve slider began moving at a time of 3 seconds (at the slider speed chosen for these experiments, the actuation time necessary for the gate valve to completely open was $\tau_{act} = 1.4$ seconds). As the mole fraction of fuel at $L_{meas} = 10.3$ cm decreases due to mixing, the HeNe absorbance also declines (see Equation 8.4). Thus, an observable mixing interval, τ_{mix} , can be obtained by noting the time between when the slider begins to move and when the HeNe absorbance begins to fall. Note that at the 10.3 cm observation location, since $L_{meas} < L_{1,crit}$, the observed mixing time τ_{mix} will be slightly longer than the actual time at which buffer/test gas mixing becomes problematic, $\tau_{1,crit}$ (*i.e.*, $\tau_{mix} > \tau_{1,crit}$).

Trials were conducted at several representative Region 1 pressures, and results are shown in Figure 8.7. In this figure, the HeNe absorbance values have been normalized to unity prior to time zero in order to facilitate comparison. Notice that the HeNe absorbance falls more quickly as pressure increases, which might be expected since the fuel concentration gradient $\frac{\Delta n_f}{\Delta L} = \left(\frac{P}{R_u T} \right) \left(\frac{\Delta x_f}{\Delta L} \right)$ scales with pressure (here, L is the axial distance in the shock tube [cm], n_f is the fuel concentration [mol/cm³], R_u is the ideal gas constant [atm-cm³/mol-K], and x_f is the fuel mole fraction). Despite this change in gradient, however, the observed time at which mixing begins τ_{mix} remains essentially independent of pressure. For a slider speed $U_{slider} = 10.9$ cm/s (corresponding to an actuation time $\tau_{act} = 1.4$ seconds) and $L_{meas} = 10.3$ cm, $\tau_{mix} \sim 8$ seconds. Similar measurements

were also conducted at windows located $L_{meas} = 18.5$ cm from the endwall, or 21.0 cm from the slider, yielding $\tau_{mix} \sim 7$ seconds for $U_{slider} = 10.9$ cm/s.

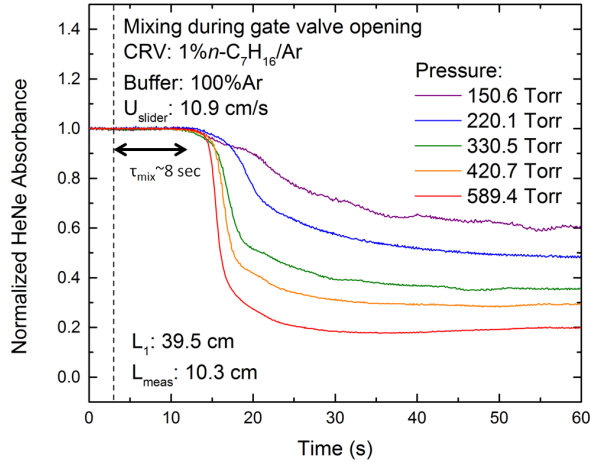


Figure 8.7: Normalized HeNe absorbance traces measured 10.3 cm from the endwall at several pressures $P = P_{buffer} = P_{test}$ during gate valve opening at a slider speed of $U_{slider} = 10.9$ cm/s. At this speed, the activation time for the valve is $\tau_{act} = 1.4$ seconds. The dashed line denotes the time when the slider started moving. As buffer/test gas mixing occurs, the concentration of fuel decreases, causing the absorbance to drop as well. Test gas: 1%*n*-heptane/Ar; buffer gas: 100%Ar.

8.3.2.2 Effect of slider speed

Similar spectroscopic measurements were performed with 1%*n*-heptane/Ar test gas mixtures (100%Ar buffer) at $L_{meas} = 10.3$ cm for $P = 330$ Torr in order to understand the effect of the speed of the moving gate valve slider U_{slider} on buffer/test gas mixing. Figure 8.8 summarizes these findings. Notice that the measured mixing interval (τ_{mix}) increases with decreasing U_{slider} ; however, the effect is not very pronounced. Thus, the critical time before buffer/test gas mixing becomes problematic ($\tau_{1,crit}$) may be thought to not be sensitive to U_{slider} .

In order to understand the mechanism for the buffer/test gas mixing, an analysis examining both binary Fickian diffusion and turbulent mixing was performed. First, binary diffusivity data for *n*-heptane/nitrogen mixtures, taken from Reference [181], was scaled to the conditions of this experiment (including diluting in argon rather than nitrogen; see Equation 3.10), and a characteristic

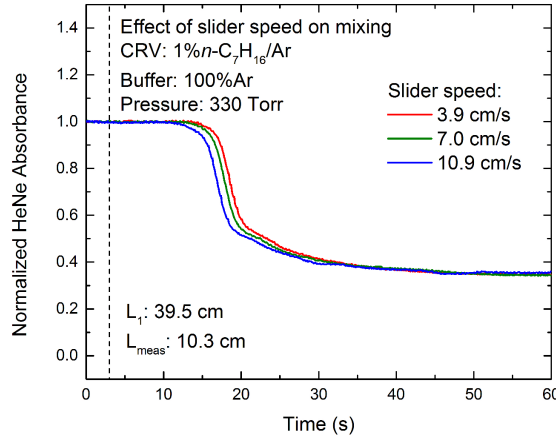


Figure 8.8: Normalized HeNe absorbance traces measured 10.3 cm from the endwall at several gate valve slider speeds at 330 Torr. The dashed line denotes time when the slider started moving. Test gas: 1%*n*-heptane/Ar; buffer gas: 100%Ar.

time for diffusion τ_d for these experiments was calculated according to Equation 8.12.

$$\tau_d = \frac{(L_1 - L_{meas})^2}{2D_{FA}} \quad (8.12)$$

Here, $L_1 - L_{meas}$ represents the distance over which diffusion must take place to reach the measurement location, and D_{FA} is the binary diffusion coefficient for *n*-heptane in argon. The results showed that, as expected, the timescale for binary diffusion alone was orders of magnitude larger than the experimentally observed τ_{mix} values. Similarly, using turbulent diffusivity and dimensional arguments, the timescale for turbulent mixing τ_t was found to be

$$\tau_t = \frac{(L_1 - L_{meas})^2}{U_{slider}d_{st}} \quad (8.13)$$

Here, d_{st} is the shock tube diameter (note that d_{st} is equivalent to the optical path length in the shock tube L from the Beer-Lambert relation, Equation 8.4). Equation 8.13 is plotted in Figure 8.9 against slider speed U_{slider} , together with experimentally measured mixing time values τ_{mix} and the actuation time of the valve τ_{act} . As U_{slider} decreases, slightly more time is available before mixing

becomes problematic (τ_t increases); however, the valve actuation time τ_{act} also increases to a point where operation is inconvenient. The theoretical timescale for turbulent mixing (τ_t) has the same order of magnitude as the experimental data (τ_{mix}) and values agree well for fast slider speeds; thus, the turbulent mixing timescale (τ_t) appears to be a good approximation to the critical time before buffer/test gas mixing becomes problematic $\tau_{1,crit}$). However, at slow slider speeds the agreement between model and experiment is poor. This is likely caused by the simplifying assumptions used in this analysis, as well as secondary effects that were not accounted for.

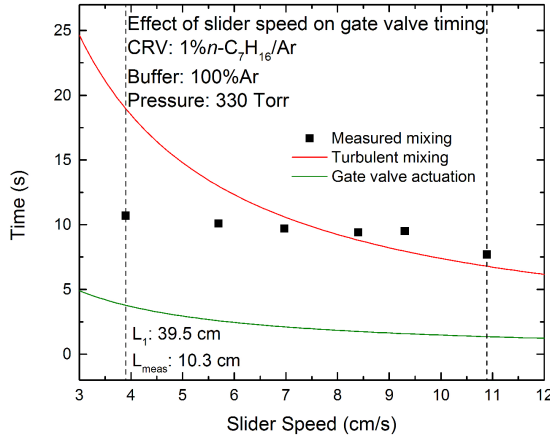


Figure 8.9: Effect of slider speed on gate valve timing and buffer/test gas mixing. As slider speed decreases, τ_t (the characteristic turbulent mixing timescale) increases but τ_{act} (the actuation, or opening, time for the valve) also increases. Conditions are identical to those of Figure 8.8.

8.3.2.3 Region 2 contact surface

Finally, HeNe absorbance profiles in *n*-heptane/15%O₂/Ar mixtures were measured through the 10.3 cm windows following incident shock waves in order to gain more insight into the extent of the buffer/test gas mixing zone as it is swept past this location. A comparison between two shocks, one showing significant mixing and the other showing little mixing, is provided in Figure 8.10. First observe the pressure trace measured at 10.3 cm from the endwall. The first pressure rise in this trace corresponds to the passage of the incident shock (said to occur at time zero), and the second rise

corresponds to the arrival of the reflected shock.

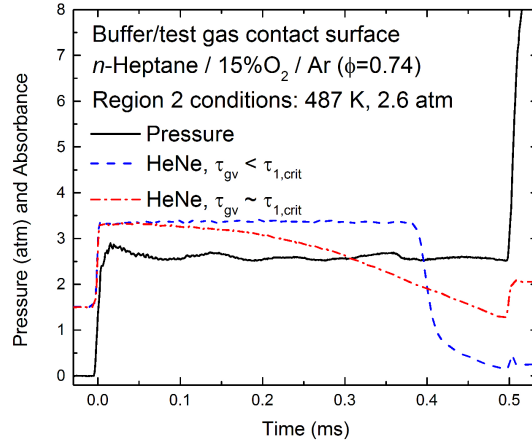


Figure 8.10: HeNe absorbance traces at 10.3 cm-from-endwall observation location showing passage of the buffer/test gas contact surface, where time zero corresponds to the incident shock passing the 10.3 cm location (blue dashes: $\tau_{gv} < \tau_{1,crit}$, red dash-dot: $\tau_{gv} \approx \tau_{1,crit}$). Also shown is a pressure trace taken at the 10.3 cm location (black solid line) using a PCB model 113A26 transducer. τ_{gv} is the time interval between gate valve actuation and diaphragm rupture, and $\tau_{1,crit}$ is the time at which buffer/test gas mixing becomes problematic.

Prior to time zero, the HeNe absorbance in both traces represents the fuel concentration in the stationary test gas. At time zero, both HeNe absorbance traces experience a step-increase following the pressure jump induced by the incident shock (see Equation 8.4). Following time zero, the HeNe absorbance represents the fuel concentration in the gas that is rushing past the 10.3 cm location toward the endwall. Notice in the dashed blue trace that the absorbance stays constant until about 0.38 ms, at which point it exhibits a sharp decline corresponding to the passage of the buffer/test gas contact surface. In this experiment, the time between gate valve actuation and diaphragm rupture τ_{gv} was much less than $\tau_{1,crit}$ (the critical time at which buffer/test gas mixing becomes problematic), such that very little buffer/test gas mixing occurred. Contrast this with the dash-dotted red trace, which exhibits a gradual decline beginning at about 0.04 ms. In this latter experiment, $\tau_{gv} \approx \tau_{1,crit}$, such that significant buffer/test gas mixing was allowed to occur. By converting particle time to lab time (see Appendix B) and using the computed post-incident-shock gas velocity,

the starting locations of the contact surfaces were calculated to be 33.7 cm and 12.8 cm from the endwall in the first and second shocks, respectively. These values corroborate the experimentally measured mixing time (τ_{mix}) intervals measured in the gate valve opening experiments performed at $L_{meas} = 10.3$ cm and $L_{meas} = 18.5$ cm from the endwall. Finally, the HeNe absorbance jump occurring at about 0.5 ms in both traces corresponds to the concentration step-change caused by the reflected shock. Note that no *n*-heptane decomposition is expected to occur at these relatively low-temperature (<800 K), low-pressure (<3 atm) conditions in the short duration of Region 2 [328]; hence, all changes in HeNe absorbance can be attributed to gasdynamic phenomena as discussed above. This can be seen in Figure 8.11, which displays a Region 2 HeNe absorbance trace taken for CRV filling, measured at the 2-cm-from-endwall observation location. The absorbance shown remains flat, indicating a constant fuel mole fraction (no decomposition or evidence of mixing).

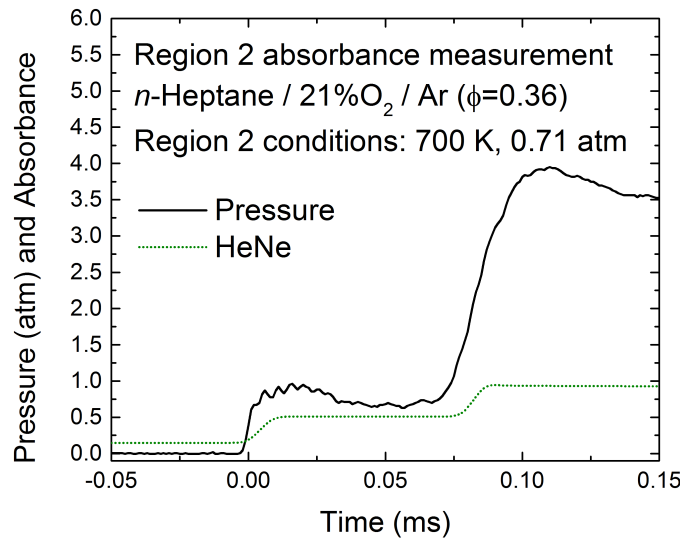


Figure 8.11: HeNe absorbance trace at 2.0 cm-from-endwall observation location for CRV filling, indicating a constant fuel mole fraction in Region 2. Also shown is a pressure record taken at this location using a Kistler model 601B1 transducer; the pressure overshoots are a non-physical transducer effect (the real pressure during Region 2 is relatively constant, like that measured by the PCB transducer shown in Figure 8.10; the difference can generally be attributed to the different temporal responses of the sensors).

8.3.2.4 Guidelines for gate valve operation

Considering the investigation of gate valve operating parameters outlined above, the following guidelines for experimental configurations similar to those of the Stanford facility are proposed. First, since the mixing timescale that would dilute the test gas is approximately $\tau_{1,crit} \sim 7$ seconds at most post-reflected-shock temperature/pressure conditions, the time between opening the gate valve and bursting the diaphragm (τ_{gv}) should be kept less than about five seconds (in order to allow a small buffer time). This can be accomplished by pre-filling the driver section to a pressure $P_{prefill}$ very close to but less than the burst pressure P_4 , opening the gate valve, and finally filling the driver section until diaphragm rupture at P_4 . Second, since the gate valve slider speed U_{slider} is only loosely correlated with the buffer/test gas mixing time, a fast slider speed (in this case, $U_{slider} = 10.9$ cm/s) is advisable, since this minimizes the time at which the driver section remains at intermediate pressure $P_{prefill}$. Third, spectroscopic fuel measurements conducted at the measurement location during Region 2 should be used to monitor the axial fuel concentration as in Figures 8.10 and 8.11; such measurements give increased confidence that no fuel dilution has occurred and have the added benefit of confirming manometric mixture mole fractions. Finally, as a practical matter, vibrations in the shock tube occurring as the gate valve opens can prematurely trigger shock velocity transducer counter timers. In order to avoid this problem, the entire transducer signal from all PCB transducers should be recorded on every experiment. Constrained reaction volume shock experiments conducted according to this methodology are straightforward and repeatable.

8.3.3 Mixing tank/shock tube volume ratio dependence

In gas-phase shock tube methodology, all fuels must be completely vaporized prior to experimentation. Since fuel vapor pressure values generally decrease as fuel molecular weight increases, it is critical to understand how the geometry (*i.e.*, volumes) of the mixing tanks and shock tube affects the size range of fuels that can be studied.

Mole conservation can be used to determine both the number of shocks obtainable per mixing tank mixture N_{shocks} and the minimum mixing tank pressure required to fill the shock tube for one

experiment $P_{m,i}$. N_{shocks} can be found by Equation 8.14,

$$N_{shocks} = \frac{N_{m,i} - N_{m,f}}{N_s} \quad (8.14)$$

where $N_{m,i}$ is the initial number of moles of the gas mixture in the mixing tank (at initial pressure $P_{m,i}$ and held at temperature T_m), $N_{m,f}$ is the number of moles in the tank once it has been depleted to the initial shock experimental pressure P_1 (the residual gas in the mixing tank cannot be forced into the shock tube and is thus wasted), and N_s is the number of moles needed to fill the shock tube to pressure P_1 (the shock tube is held at temperature T_1). The ideal gas equation of state (Equation 3.12) can be used to determine these molar quantities,

$$N_{m,i} = \frac{P_{m,i}V_m}{\hat{R}_u T_m} \quad (8.15)$$

$$N_{m,f} = \frac{P_1 V_m}{\hat{R}_u T_m} \quad (8.16)$$

$$N_s = \frac{P_1 V_s}{\hat{R}_u T_1} \quad (8.17)$$

where V_m is the mixing tank volume and V_s is the shock tube volume that is filled with test gas (for conventional operation, V_s is the entire shock tube volume, but for CRV operation, V_s is only the volume of the test section). Combining Equations 8.14 through 8.17 together yields the desired result:

$$N_{shocks} = \frac{V_m}{V_s} \frac{T_1}{T_m} \left(\frac{P_{m,i}}{P_1} - 1 \right) \quad (8.18)$$

Lastly, by rearranging Equation 8.18 for the case where $N_{shocks} = 1$, an expression can be obtained that gives the minimum mixing tank pressure necessary to perform just one shock experiment.

$$P_{m,i} = P_1 \left(\frac{V_s}{V_m} \frac{T_m}{T_1} + 1 \right) = \frac{P_{fuel}}{x_{fuel}} \quad (8.19)$$

Here, P_{fuel} is the fuel's vapor pressure at the mixing tank temperature T_m , and x_{fuel} is the mole fraction of fuel in the test gas mixture.

From Equations 8.18 and 8.19, it is evident that increasing the ratio $\frac{V_m}{V_s}$ increases the number of

shocks possible for each mixture, and decreases the fuel vapor pressure required to perform at least one shock. Thus, for a given mixing tank volume, using the CRV concept to decrease the volume of the shock tube to be filled with test gas provides more shock-to-shock mixture repeatability since one mixing tank mixture can provide test gas for a greater number of shock experiments. Furthermore, this technique also increases the size of fuel molecules that can be studied, since even the low vapor pressures of many large hydrocarbons of practical combustion interest can provide enough gas-phase molecules for one shock. By this method, shock tube researchers can avoid using extreme mixing tank and shock tube heating in order to increase the fuel vapor pressure and generate enough fuel vapor for experimentation, as has been done historically [79, 101, 128, 129]. Such heating is problematic because it can introduce issues of partial fuel distillation and pre-experimental fuel decomposition [130].

Figure 8.12 applies Equations 8.18 and 8.19, together with vapor pressure information obtained from the literature [222], to demonstrate the range of the Stanford CRVST under conventional (full shock tube; $\frac{V_m}{V_s} = 0.44$) and CRV ($\frac{V_m}{V_s} = 10.9$) operation for normal alkanes in a shock experiment with *n*-alkane/21%O₂/Ar ($\phi = 1$) test gas at 10 atm and 837 K. When operating in CRV mode, molecules as large as *n*-dodecane (C₁₂H₂₆) can be studied (a fuel can be examined when at least one shock can be performed per mixing tank mixture). Note that this figure was generated assuming that the full vapor pressure of the fuel is obtained in the mixing tank. In practice, to avoid fuel condensation, the fuel pressure is typically limited to two thirds of its saturation vapor pressure value (see MacDonald *et al.* [128] for details).

8.4 Comparison of CRV and conventional filling strategies

A sample *n*-heptane shock experiment using CRV filling, together with a comparison at the same conditions using conventional filling, is shown in Figure 8.13. Only a brief discussion of this graphic will be given here; a complete treatment is available in Section 9.2.4 and in Reference [289]. First, consider the three pressure traces shown, in the top panel. In this graphic, the step increase at time zero corresponds to the arrival of the reflected shock at the measurement location. (Note that in Figures 8.10 and 8.11, time zero was taken to be the time when the *incident* shock reached the

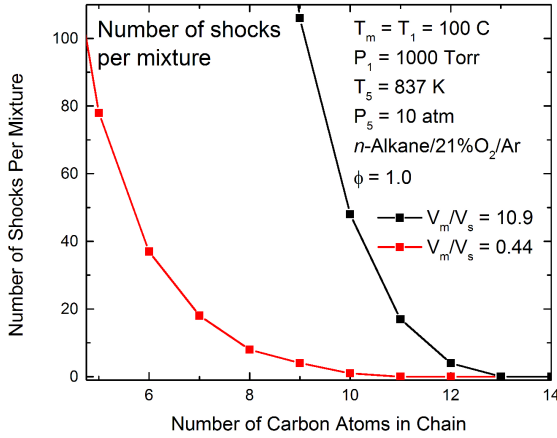


Figure 8.12: Range of Stanford shock tube in conventional ($\frac{V_m}{V_s} = 0.44$) and CRV ($\frac{V_m}{V_s} = 10.9$) operation (a fuel can be studied when at least one shock can be performed per mixing tank mixture). When operating in CRV mode, molecules as large as *n*-dodecane ($C_{12}H_{26}$) can be studied. Conditions: $T_m = T_1 = 100$ °C, $P_1 = 1000$ Torr, $T_5 = 837$ K, $P_5 = 10$ atm, test gas: fuel/21%O₂/Ar ($\phi = 1$). Vapor pressure information obtained from Reference [222].

observation location.) The pressure profiles remain constant until about $t = 8$ ms, at which point the conventional pressure trace rises sharply, corresponding to a first stage ignition event (at these conditions, *n*-heptane exhibits two-stage ignition). In contrast, notice that the pressure rise in the CRV shock is almost nonexistent during this event, hereby enabling constant-pressure modeling of the reactive flow. (Figure 8.13 also includes a non-reactive pressure record, and the CRV pressure trace returns to this almost perfectly after both first and second stage ignition events.) However, spectroscopic fuel measurements, shown in the third panel, confirmed that fuel consumption during first stage ignition was identical in both filling techniques (note that absorbance appears higher in the conventional trace because the pressure is higher).

After the first stage ignition event, the pressure in the conventional experiment remains higher until the second stage ignition event, which is marked by a very large and sustained increase in pressure at about 22 ms (the conventional shock ignition pressure spike reaches a maximum value of about 26 atm, almost four times the nominal shock pressure). This event is corroborated by the

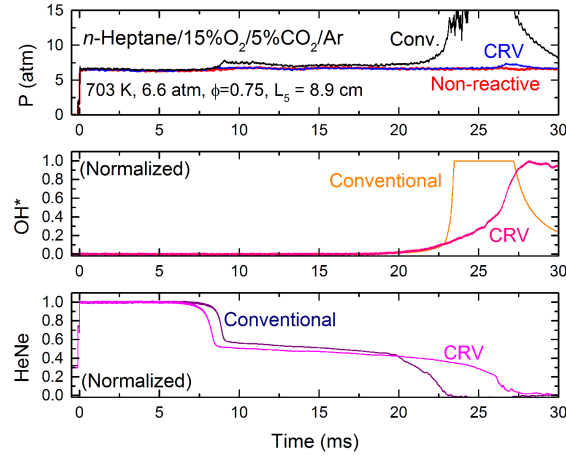


Figure 8.13: Comparison of conventional and CRV filling shocks. Top panel: pressure (atm); middle panel: normalized endwall OH^* emission at 306 nm; lower panel: normalized HeNe laser absorbance at 3390 nm (fuel). Conditions: $T_5 = 703 \text{ K}$, $P_5 = 6.6 \text{ atm}$, $L_5 = 8.9 \text{ cm}$. Buffer gas: 17.5%CO₂/11.5%N₂/Ar, Test gas: *n*-heptane/15%O₂/5%CO₂/Ar ($\phi = 0.75$). Figure adapted from Campbell *et al.* [289].

increase in endwall OH^* emission (second panel) and the decay of the fuel absorbance. In contrast, the CRV shock shows a very slight rise near 25 ms, corresponding to ignition; this quickly relaxes back to the non-reactive pressure once more.

This difference in the pressure behavior during ignition in the conventional shock experiment, as compared to the CRV shock experiment, is very important in terms of enabling correct modeling of the reacting flow field behind a reflected shock in reactive gases. The large pressure changes characteristic of conventional shocks make both constant internal energy-volume (U-V) and constant enthalpy-pressure (H-P) modeling, which are commonly used for lack of better models, inappropriate. In contrast, the near-constant-pressure conditions produced by the CRV shock tube technique allow for constant H-P modeling throughout the entire ignition event.

8.5 Summary

A second-generation constrained reaction volume shock tube that employs a sliding gate valve to constrain the reactive gas mixture to a small portion of the shock tube near the endwall has been demonstrated. This technique has been shown to produce near-constant pressure post-reflected-shock ignition conditions, thereby allowing constant enthalpy-pressure (H-P) modeling of experiments. This is in contrast to conventional reflected shock experiments that are not properly modeled using commonly-used constant internal energy-volume (U-V) or H-P models. In this work, proper buffer gas tailoring was shown to produce linear shock velocity attenuation, allowing precise calculation of post-reflected-shock conditions. Moreover, buffer/test gas mixing was investigated using a spectroscopic technique, showing a time interval following gate valve actuation that avoids dilution of the test gas that is ultimately swept to the test location. Finally, the size range of fuels examinable in this facility was discussed, showing further benefits of filling only a small portion of the shock tube with test gas. This shock tube and the CRV technique should prove useful for future studies of hydrocarbon chemistry and reactive shock wave gasdynamics.

Chapter 9

Application of constrained reaction volume shock tube to normal heptane ignition

*The contents of this chapter have been accepted for publication in the journal **Proceedings of the Combustion Institute** [289].*

9.1 Introduction

Recent efforts to improve internal combustion engine efficiency have resulted in the need for better kinetic mechanisms that describe fuel oxidation chemistry at practical conditions. One important fuel that has been the subject of numerous experimental (*e.g.*, [90, 91, 131, 269, 271, 272, 318, 329–362]) and modeling (*e.g.*, [59, 274, 328, 363–387]) studies is normal heptane, as it is a primary reference fuel. (Note that a more comprehensive listing of *n*-heptane studies published before 2004 was performed by Babushok and Tsang [381]. Also, it should be noted that several recent studies have addressed general low-temperature hydrocarbon oxidation chemistry, including References [388–393].)

n-Heptane has also received attention as it has particular relevance to research on biodiesel

fuel. First, since it is a primary reference fuel, it has been compared with simulations of biodiesel ignition delay time data [48]. Second, since the combustion characteristics of normal alkanes like *n*-heptane are similar to those of biodiesel, molecules like *n*-heptane have been used for lack of other kinetic data for biodiesel kinetic mechanism validation [48]. Third, *n*-heptane has been used as a surrogate for fossil diesel fuel, making it an important molecule with which comparisons to FAMEs can be made [394]. Fourth, it is the basis for the Lawrence Livermore National Laboratory methyl decanoate mechanism [94]. Finally, it is frequently blended with or compared to FAMEs for experimentation in other reactor types [90, 91, 355, 358, 395], meaning that a better understanding of neat (pure) *n*-heptane combustion characteristics will aid in understanding the unique aspects of biodiesel oxidation.

To date, most shock tube ignition delay time studies of *n*-heptane at Negative Temperature Coefficient (NTC) region temperatures (between 600 and 900 K) (*e.g.*, [131, 334, 346]) have been performed at pressures above 10 atm, since available test times for shock tubes have historically been restricted to about 10 ms and ignition delay times are longer than this at lower pressures. As a result, leading kinetic mechanisms (*e.g.*, that of Lawrence Livermore National Laboratory, LLNL [328]) have not been validated at NTC region temperatures and moderate pressures using shock tube data. Moreover, long ignition delay times experimentally measured in shock tubes have been subject to pre-ignition phenomena occurring away from the test location, which have been known to cause an increase in pressure and temperature and ultimately decrease measured ignition delay times [334]. This creates challenges in simulating measured ignition delay times, as conditions during each experiment cannot be properly classified as possessing constant internal energy and constant volume (U-V) [129, 132] as has been commonly assumed.

The need for experimental data that are easy to simulate at engine-relevant (moderate-pressure/low-temperature) conditions is evident. Thus, the newly developed Constrained Reaction Volume (CRV) shock tube, described in Chapter 8 and Reference [306], and the capability of achieving long test times, described in Chapter 7 and Reference [275], have been applied to the measurement of *n*-heptane ignition delay times, mole fraction time-histories (fuel, OH, aldehydes, CO₂, and H₂O), and temperature histories at NTC region conditions.

9.2 Experimental setup

9.2.1 Shock tube facility

The facility used in these studies, including the CRV concept and capacity for achieving long test times, has been described extensively in Sections 7.2 and 8.2. Thus, additional details will not be provided here.

9.2.2 Laser absorption measurements

Laser diagnostics are able to make quantitative measurements of gaseous species because the ratio of monochromatic light intensity at frequency ν incident upon an absorbing gas mixture I_o to that exiting the mixture I is related to the number density of absorbing species n according to the Beer-Lambert relation (see also Equations 3.1, 4.11, 5.2, and 8.4).

$$\alpha = -\ln\left(\frac{I}{I_o}\right) = n\sigma_\nu L \quad (9.1)$$

In this equation, α is known as the absorbance, σ_ν is the propensity for light absorption by the molecule at frequency ν (called the absorption cross section) and L is the path length along which the absorption occurs.

9.2.2.1 Laser absorption of fuel

Measurements of fuel concentration were made using the 3.39 μm output of a continuous wave (CW) helium-neon (HeNe) laser. Cross section values were obtained from References [175, 225, 226] and were confirmed using shock tube experiments. Before each shock experiment, the mole fraction of fuel was measured using this spectroscopic technique; measured values were typically 3% lower than manometric values, attributed to fuel loss to the walls of the unheated shock tube. Fuel mole fraction values were also measured between the incident and reflected shocks on each experiment, confirming that mixing of buffer and test gases had not diluted the reactive mixture.

9.2.2.2 Laser absorption of OH and aldehydes

OH concentration was measured using the output of a narrow-linewidth CW laser at 306.7 nm, the peak of the well-characterized $R_1(5)$ absorption line in the OH $A - X(0, 0)$ band [396, 397]. The laser light was obtained by intracavity frequency-doubling of 613.4 nm light generated by a Spectra Physics model 380 ring dye laser that was pumped by a 5 W Coherent Verdi at 532 nm. Common mode rejection was used to reduce laser intensity noise, resulting in a minimum detectivity of 5 ppm at the conditions of this work, with an estimated uncertainty of $\pm 10\%$. Measurements were also performed with the laser tuned off the OH line to observe other absorbing species, enabling use of a simple subtraction scheme to cancel spectrally broad interference. At the conditions of these experiments, interference is largely due to molecules possessing a C=O bond, *i.e.*, aldehydes, ketenes, and formic acid. Kinetic simulations performed using the LLNL mechanism [328] revealed that CH₂O is the dominant aldehyde produced during first stage ignition of *n*-heptane. Therefore, the cross section of CH₂O [398] was assumed to represent that of aldehydes/ketenes/formic acid, and time-histories of these species' total concentration have thus been inferred and reported here. Finally, emission by OH at 306 nm in the laser absorption scheme, which used a series of irises to limit radiation reaching the detector, was found to be negligible.

9.2.2.3 Laser absorption of CO₂

Carbon dioxide mole fraction measurements were attained by a fixed-wavelength direct absorption method near 4.2 μm using a CW external-cavity quantum cascade laser [305]. The laser was tuned to the $R(66)$ transition in the fundamental band near 2387.24 cm⁻¹, which offers minimal absorption temperature sensitivity over the temperature range 700-1000 K. The measurement uncertainty is $< 10\%$, and the minimum detectivity is approximately 5 ppm.

9.2.2.4 Laser absorption of H₂O and temperature measurement

Water mole fraction and temperature measurements were acquired along a single line-of-sight using two frequency-multiplexed tunable diode lasers centered upon H₂O absorption transitions near 3920.09 cm⁻¹ and 4029.52 cm⁻¹. The wavelength of each laser was scanned

across the transition linecenter at 20 kHz and modulated at 90 and 112 kHz, respectively, to monitor first-harmonic-normalized wavelength-modulation spectroscopy with second-harmonic detection (WMS-2f/1f) signals at linecenter. Details regarding the experimental setup and select spectroscopic parameters are given in References [399, 400].

9.2.3 Light emission

The emission from kinetically excited OH radicals (OH^*) at (306 ± 75) nm was also measured during ignition using a silicon photo-detector and a UG-5 Schott Glass band-pass filter. This diagnostic was positioned at both a window located 2 cm from the endwall and at a port in the endwall; ignition delay time measurements at the two locations generally agreed to within 10%.

9.2.4 Ignition measurement

Ignition delays were measured relative to the time of arrival of the reflected shock, taken here as the time of the half-rise in pressure caused by the reflected shock. First and second stage ignition events in the NTC region were measured by observing the fuel decay process by way of the $3.39\ \mu\text{m}$ HeNe diagnostic. The time of first stage ignition was taken to be the instant of maximum slope in the initial decline of the fuel absorbance, and the time of second stage ignition was taken to be the instant when the absorbance declined to 5% of its initial post-reflected-shock value. At high temperatures, the maximum OH^* emission slope was extrapolated to the baseline (zero) value to determine the ignition delay time.

A sample ignition measurement, including a comparison between CRV and conventional shock tube-filling experimentation, is shown in Figure 9.1 (see also Section 8.4). Observe that the decreasing HeNe absorbance provides a clear indication of the two stages of ignition. Moreover, comparing the reactive pressure traces to the non-reactive trace near these ignition events serves to illustrate the differences between CRV and conventional experimentation. Near the first ignition event, the conventional shock exhibits a clearly visible and sustained pressure increase, whereas the CRV experiment shows virtually no rise relative to the nonreactive pressure. Furthermore, at the second ignition event, the conventional shock shows an exponential pressure rise to a level roughly four

times that of the non-reactive experiment, whereas the CRV experiment shows only a small pressure increase that quickly relaxes to the non-reactive pressure. Importantly, since the CRV shock remains at nearly constant pressure up to and even throughout its ignition process, this experiment can be effectively modeled as a constant enthalpy-pressure (H-P) reactor. In contrast, the conventional-fill experiment cannot be correctly modeled in a simple way, *e.g.*, as a zero-dimensional reactor at constant energy-volume (U-V), though such an approach may be adequate in many cases for simulating first stage ignition, or in strong ignition cases with no pre-ignition energy change. The slight difference in first stage ignition time, between conventional and CRV experiments, can be linked to small mismatches in shock conditions, such as equivalence ratio and initial reaction temperature.

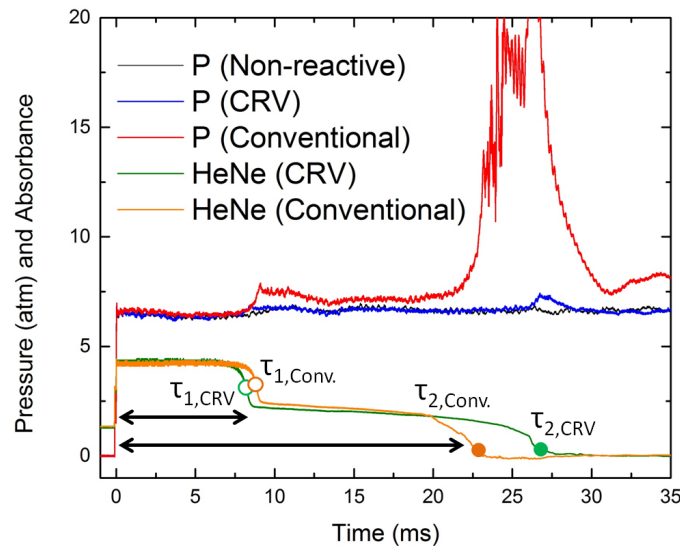


Figure 9.1: Comparison between CRV and conventional shock measurements. Reflected shock initial conditions: $\phi \sim 0.75$ (*n*-heptane/15%O₂/5%CO₂/Ar), $P_5 \sim 6.6$ atm, $T_5 \sim 703$ K, $L_5 = 9$ cm. Ignition delay times (indicated by open and solid circles): $\tau_{1,CRV} = 8.2$ ms, $\tau_{2,CRV} = 26.8$ ms, $\tau_{1,conventional} = 8.8$ ms, $\tau_{2,conventional} = 22.7$ ms.

9.3 Results

9.3.1 Ignition delay times

Ignition delay times for *n*-heptane were measured using the CRV strategy at an equivalence ratio of $\phi = 0.75$ in 15%O₂/5%CO₂/Ar and in 15%O₂/Ar mixtures at 6.5 atm and temperatures between 651 and 823 K. (CO₂ was included in mixtures in support of a new CO₂-absorption based temperature diagnostic, briefly discussed in Section 7.7 and in Reference [305]. Additionally, CO₂ was not included in the determination of equivalence ratio, and simulations [328] revealed that the presence of CO₂ had negligible effect on ignition kinetics). Measurements were also conducted using the conventional filling strategy throughout this range for purposes of comparison. In addition to these low temperature tests, experiments were conducted using both the CRV and conventional strategies at higher temperatures and a pressure of 7 atm. These ignition delay data are summarized in Figure 9.2, and are also tabulated in Appendix H. Small scaling corrections, obtained from the LLNL mechanism [328] by perturbing pressure and equivalence ratio at several temperatures and observing the effect on τ_1 and τ_2 , to ignition delay times have been applied to normalize individual points to a common P and ϕ according to Equation 6.3 (note that these scaling factors are temperature-dependent). Furthermore, ignition delay time predictions made using the LLNL [328] mechanism have been included in this figure.

Several observations can be made about Figure 9.2. First, compare the constant U-V and constant H-P modeling methods. Observe that at high temperatures, the U-V and H-P simulations yield nearly identical results. However, in the NTC region, the U-V simulation yields strikingly lower second stage (*i.e.*, complete) ignition delay times than the H-P simulation, while the two predict identical first stage times. This paradox is the result of an ignition-accelerating pressure increase that occurs in U-V simulations during first stage ignition but that does not occur in H-P simulations. Since the increase occurs during the first stage ignition but not before, differences between U-V and H-P trials exhibit themselves in the second stage ignition delay times rather than in the first.

Next, compare the CRV and conventional shock tube experiments. Notice that at high temperatures, CRV and conventional data agree closely with one another (as well as with simulations); this similarity was expected, as non-ideal effects in shock tubes typically become important at long

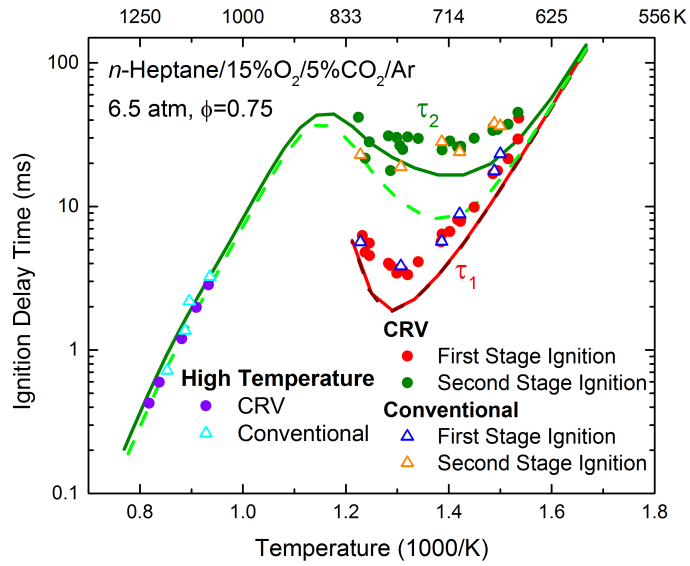


Figure 9.2: n -Heptane ignition delay time values (n -heptane/15% O_2 /5% CO_2 /Ar, $\phi = 0.75$, 6.5 atm). Solid lines: constant H-P modeling; dashed lines: constant U-V modeling (LLNL/Mehl *et al.* mechanism [328]). NTC region data are presented at the initial post-reflected-shock temperature, prior to the temperature increase associated with first stage ignition. Error bars are not visible at the resolution used in this plot.

times, *i.e.*, at lower temperatures [281]. Also in agreement are the CRV and conventional first stage ignition delay times in the NTC (between 825 and 650 K), consistent with the fact that CRV and conventional pressure traces looked identical up to the point of first stage ignition. Furthermore, at temperatures below about 725 K, the CRV and conventional techniques yield similar second stage ignition delay times with low scatter, in contrast with expectation based on simulations. However, between about 825 and 725 K, the second stage ignition data show significantly more scatter; one possible explanation is that ignition phenomena at these temperatures are more sensitive to the small deviations in pressure present in these experiments relative to the nominal value of 6.5 atm. The LLNL mechanism [328] supports this hypothesis; it gives a pressure scaling of $P^{-2.2}$ at 800 K, whereas at 675 K it is $P^{-0.9}$ (this shift is likely caused by changes in the governing kinetic reactions for the ignition process). In general, it appears that conventional shocks performed between 825 and 725 K have slightly lower second stage ignition times relative to CRV shocks - currently attributed to the influence of the first stage ignition pressure increase.

Finally, compare the experimental data to the simulations. At high temperatures, the CRV and conventional data are described well by both the U-V and H-P computations. This reflects the accuracy of both the LLNL mechanism [328] and the suitability of simulating single-stage ignition delay times using the U-V constraint when the times are relatively short and non-ideal shock tube effects and pre-ignition energy release are minimal. (Nonetheless, H-P modeling may be regarded as physically more correct in reactive experiments where the measured pressure is constant.) At temperatures below 725 K, it appears that the CRV and conventional complete ignition data are more closely modeled by the H-P simulation than by the U-V modeling. In contrast, above 725 K, there is slight evidence that the U-V simulation may more closely match the conventional data, while the H-P model more closely tracks the CRV points. The difference between the measured second stage ignition delay times and the U-V simulations, at temperatures below 725 K, can once again be linked to the pressure profiles of the two experiment types. At these low temperatures, the LLNL U-V simulation predicts a first stage ignition pressure increase of as much as 40%, whereas that observed in the CRV experiments was negligible and that in the conventional experiments was typically only 10% at all temperatures, reflecting the reality that reflected shock ignition is really not a constant U-V process. In the regime above 725 K, the U-V model predicts a first stage ignition

pressure increase of only about 10%, which more closely matches that observed in the conventional experiments, whereas the CRV data were taken in constant pressure conditions. Finally, observe that the LLNL mechanism predicts a slightly higher temperature (775 K) than the measurements (765 K) at which the minimum first stage ignition time occurs. Further experiments, including species and temperature time-histories, are needed to fully characterize this interesting NTC region.

9.3.2 Fuel time-histories and first stage fuel decomposition fraction

Additional information on the details of ignition can be obtained by measuring time-histories of important reactants, radicals, intermediates, and products during oxidation. In the present work, initial measurements of fuel, OH, aldehydes, CO₂, and H₂O, as well as temperature time-histories, all conducted in the CRV mode of operation, are reported. These measurements should provide stronger constraints on the kinetic mechanism, allowing improvements to be made with more precision than by simply matching global validation targets, *e.g.*, ignition delay times.

HeNe laser absorbance time-histories are plotted at several different NTC region temperatures in Figure 9.3. Profiles have been normalized to unity at time zero in order to facilitate comparison. Prior to first stage ignition, some of these measurements have high uncertainty due to high absorbance values (around $\alpha = 4$ in some cases). However, after first stage ignition, absorbance values have fallen due to fuel decomposition such that accurate fuel mole fraction values can be deduced after accounting for interfering species (that also absorb at 3.39 μm) and for the effect of first stage ignition temperature rise on the absorption cross section σ_ν .

Several observations can be made from Figure 9.3. First, the traces show that first stage ignition delay time decreases with increasing temperature until about 765 K, at which point first stage ignition delay time increases. A similar pattern can be deduced for second stage ignition, although some shocks showed scatter in ignition time, as discussed above. Furthermore, though convoluted by temperature change and interference, it appears that the fraction of fuel remaining after first stage ignition increases with increasing temperature.

In order to clarify this latter observation, an analysis was performed to quantify the fraction of fuel remaining after first stage ignition. Using the LLNL mechanism [328] with H-P modeling, intermediate hydrocarbon mole fractions, as well as the temperature and volume increase

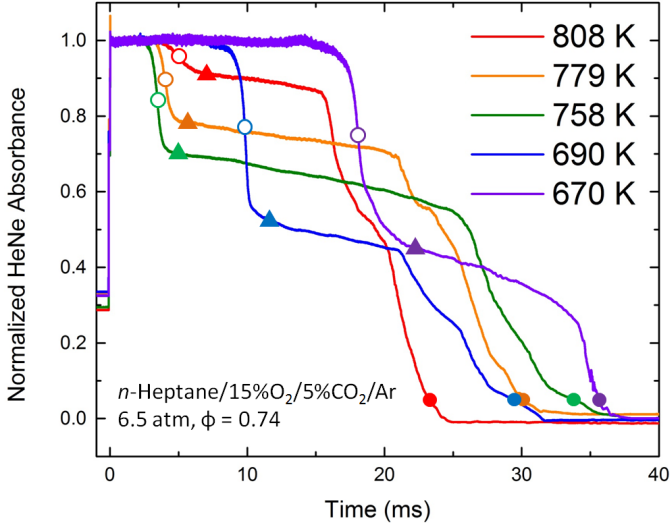


Figure 9.3: HeNe absorbance profiles during *n*-heptane oxidation, normalized to unity at time zero, for several temperatures (CRV operation). Conditions: *n*-heptane/15%O₂/5%CO₂/Ar, $\phi = 0.74$, 6.5 atm. Open circles denote first stage ignition (defined as the point of maximum slope), solid triangles denote post-ignition fuel absorbance, and solid circles denote second stage ignition.

upon first stage ignition, were estimated. Also, using cross section values measured by Klingbeil *et al.* [225, 226, 241], high-temperature absorbance values of interfering species were specified and used to correct the observed HeNe absorbance. Details of this analysis can be found in Appendix G. Values for the fraction of fuel remaining after first stage ignition have been plotted in Figure 9.4. As also noticed by Karwat *et al.* [360], the fraction of fuel remaining after first stage ignition increases with temperature. Both the data and the model follow an exponential trend, as shown in the semilog scale of this plot. Within the uncertainty of the data, the LLNL mechanism agrees with the values measured in this work; however, there is evidence that the mechanism under-predicts the fraction of fuel remaining at low temperatures. This under-prediction was also observed by other researchers [335, 339, 357, 360], and Karwat *et al.* [360] provide an excellent discussion about this discrepancy. Finally, it should be noted that the humps/bumps present in the laser records at later times (near the second stage ignition event) in Figure 9.3 are likely caused laser beam fluctuation due to density gradients in the shock tube (sometimes called “beam steering”), rather than kinetic effects; this is supported by the smooth simulated absorbance profiles provided

in Appendix G.

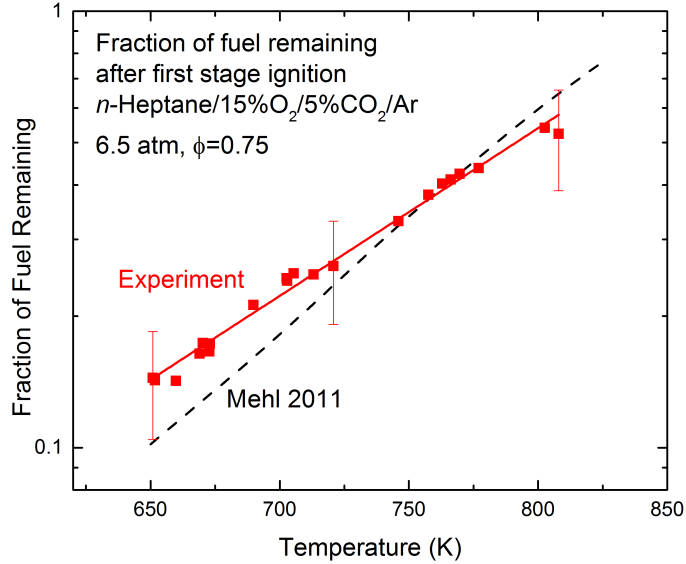
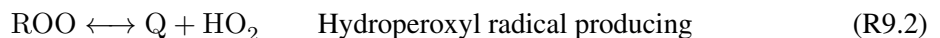


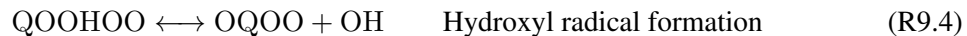
Figure 9.4: Fraction of *n*-heptane remaining after first stage ignition in CRV operation (points), along with comparison with H-P simulation using LLNL mechanism [328] (dashed line) and best-fit line to data (solid line; $R^2 = 0.989$). Conditions: *n*-heptane/15%O₂/5%CO₂/Ar, $\phi = 0.75$, 6.5 atm.

A sensitivity analysis performed using the LLNL mechanism [328] with H-P constraints at 700 K and 7 atm ($\phi = 0.75$) revealed that during first stage ignition the *n*-heptane mole fraction is subject to strong competition between rearrangement reactions (promoting ignition, Reaction R9.1) and hydroperoxyl radical-producing reactions (inhibiting ignition, Reaction R9.2).



Further analysis is necessary to determine the extent to which this competition determines the fraction of fuel remaining after first stage ignition. The analysis also revealed that the fuel mole fraction during first stage ignition is sensitive to reactions of the form of Reactions R9.3 and R9.4.





9.3.3 OH and aldehyde/ketene/formic acid time-histories

Absorbance profiles of OH and aldehyde/ketene/formic acid were measured during *n*-heptane oxidation at initial temperatures of 669 and 705 K in *n*-heptane/15%O₂/5%CO₂/Ar mixtures with an equivalence ratio of $\phi = 0.72$ using the CRV strategy. To quantify these measurements, the LLNL mechanism was used to predict the post-ignition temperatures, enabling specification of the proper absorption cross section values. The results at 705 K are shown in Figure 9.5, together with H-P simulations by the LLNL mechanism [328]. In this figure, first stage ignition is marked by a rapid rise in aldehyde concentration, and second stage ignition is marked by the rapid rise in OH concentration (to a predicted plateau level for OH that is dictated by equilibrium thermodynamics) and a characteristically rapid consumption of intermediates. Notice that at these conditions the LLNL mechanism under-predicts these times, consistent with the under-prediction of ignition times shown in Figure 9.2. However, the measured plateau values of aldehyde and OH mole fraction match those of the model to within 10%.

9.3.4 CO₂ and H₂O time-histories

Mole fractions of carbon dioxide and water were measured during *n*-heptane oxidation at initial temperatures of 699 and 744 K in *n*-heptane/15%O₂/Ar mixtures (no seeded CO₂) with an equivalence ratio of $\phi = 0.74$ using the CRV strategy. The results at 699 K are shown in Figure 9.6, together with H-P simulations by the LLNL mechanism [328]. First, notice that the first stage ignition delay time, as indicated by the rapidly rising H₂O and CO₂ mole fractions around 9 ms, is under-predicted by the mechanism, consistent with other measurements. Moreover, the complete ignition time, indicated by the second CO₂ step increase, is also under-predicted. (Unfortunately, strong infrared emission obscured the second stage ignition measurement of water.) Note that the CO₂ plateau values following first and second stage ignition closely match those predicted by the mechanism, while the measured initial H₂O plateau value is about 16% lower than the LLNL prediction. Sensitivity analysis performed for this experiment revealed that the mole fraction of CO₂ is

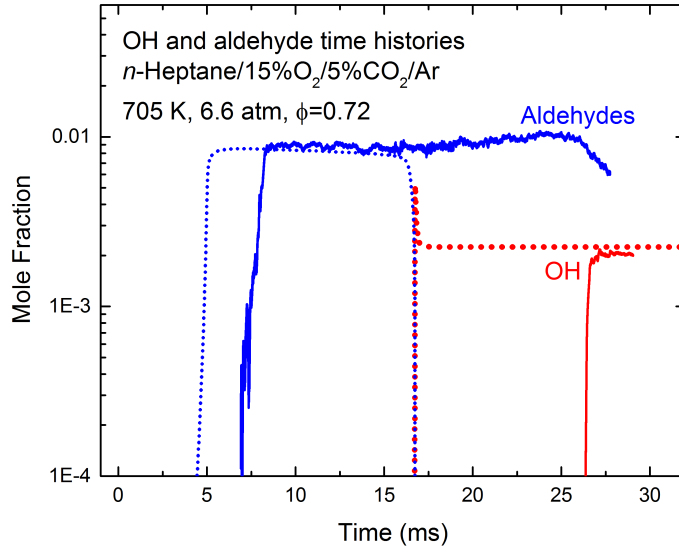


Figure 9.5: Measurements of OH and aldehyde/ketene/formic acid mole fraction during *n*-heptane oxidation at an initial (pre-first stage ignition) temperature of 705 K (solid lines), together with H-P simulation by the LLNL mechanism [328] (dotted lines). Conditions: *n*-heptane/15%O₂/5%CO₂/Ar, $\phi = 0.72$, 6.6 atm.

sensitive to a competition between Reactions R9.1 and R9.3 (see Section 9.3.2), but further analysis is needed to quantitatively determine the effect of this competition on the post-first stage ignition plateau level of CO₂.

9.3.5 Temperature time-histories and first stage temperature change

First stage temperature measurements were carried out using the water produced in two experiments. (Unfortunately, strong infrared emission in these experiments obscured the second stage ignition event.) These temperature traces, for experiments with initial temperatures of 699 K and 744 K, are shown in Figure 9.7, together with H-P-constrained simulations performed with the LLNL mechanism. Several points are evident. First, observe that in both experimental traces, the temperature measured after first stage ignition very closely matches that of the simulations. Second, despite beginning at a lower initial temperature, the post-first stage ignition temperature of the 699 K (initial T) experiment is essentially identical to that of the 744 K (initial T) experiment; this is shown in both the simulation and the experiment. Finally, notice that the measured temperature

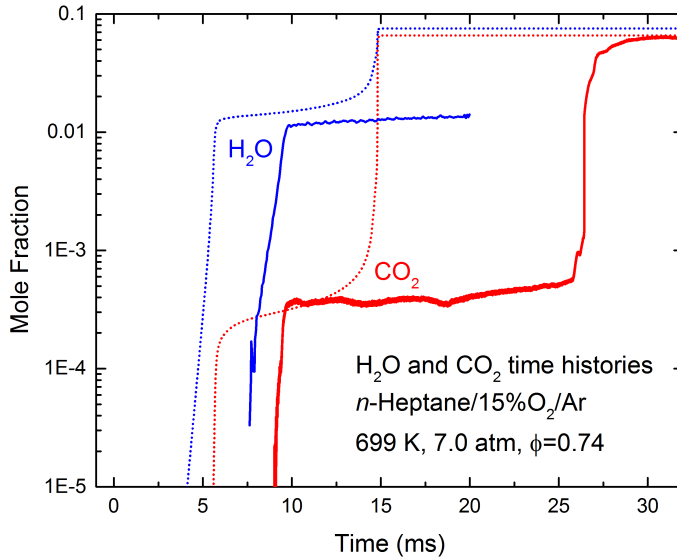


Figure 9.6: Mole fraction time histories of carbon dioxide and water during *n*-heptane oxidation at an initial (pre-first stage ignition) temperature of 699 K (solid lines), together with H-P simulation by the LLNL mechanism [328] (dotted lines). Conditions: *n*-heptane/15%O₂/Ar, $\phi = 0.74$, 7.0 atm.

remains relatively constant after first stage ignition, whereas that predicted by the H-P modeling increases steadily with time, presumably due to incorrect parameters of the mechanism.

Using the thermodynamically calculated pre-ignition temperature (based on the measured incident shock velocity) as a baseline, the temperature increase during first stage ignition was computed for the two temperature measurements (at initial temperatures of 699 K and 744 K) discussed above. The results, together with H-P predictions by the LLNL mechanism [328], are shown in Figure 9.8. Interestingly, the simulation predicts an essentially linear relationship in the temperature increase with the initial pre-first stage ignition temperature. The two experimental data points match very closely to the simulation (dashed black line in the graphic), giving confidence in the LLNL mechanism-based temperature-compensation technique used to determine absorption cross section values after the first ignition event in the species time-history analyses above. Although only limited temperature data were observed in this study, the value of such data is seen to be high, and hence in future work this method will be refined and employed widely.

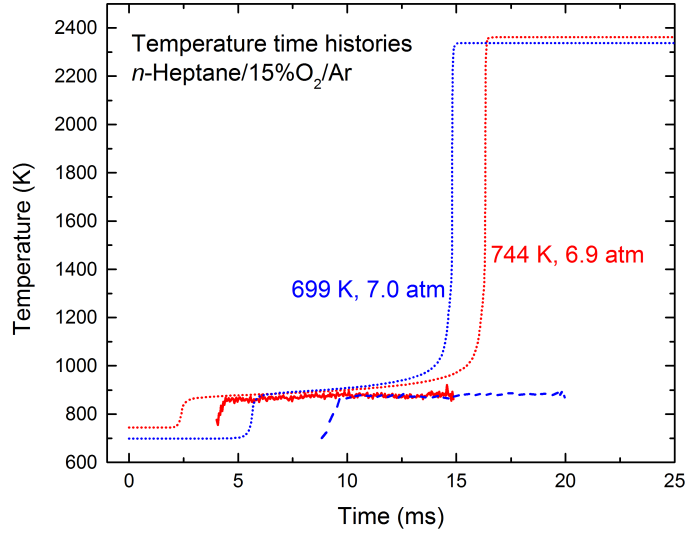


Figure 9.7: Temperature time-histories during *n*-heptane oxidation at initial conditions (pre-first stage ignition) of 699 K/7.0 atm (blue dashes) and 744 K/6.9 atm (red solid line), together with H-P simulation using the LLNL mechanism [328] (blue and red dotted lines). Mixture: *n*-heptane/15%O₂/Ar, $\phi = 0.74$.

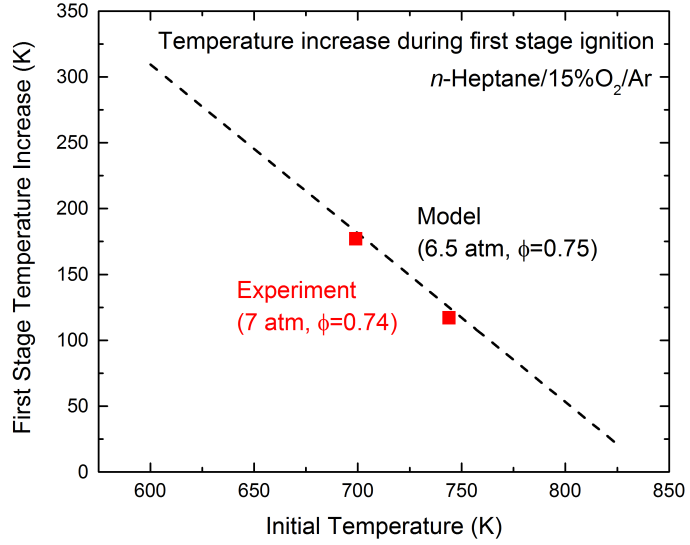


Figure 9.8: Temperature increase during first stage *n*-heptane ignition as a function of initial (pre-first stage ignition) temperature (points), together with H-P simulation with the LLNL mechanism [328] (dashed line). Conditions are identical to those in Figure 9.7.

9.4 Summary

The first constant-pressure *n*-heptane ignition delay time data taken at 6.5-7.4 atm in the NTC region using a second-generation CRV technique combined with staged driver gas filling have been reported here. Using these techniques, test times of up to 55 ms have been achieved, and both first and second stage ignition phenomena have been observed under near-constant-pressure conditions. Comparisons between the conventional and CRV filling strategies reveal that ignition delay data taken using these strategies, for the current reactive mixtures and test conditions, agree reasonably well within the scatter of the measurements. In addition to ignition delay times, time-histories of fuel, OH, aldehydes, CO₂, H₂O, and temperature have been measured in the NTC region. At high temperatures, it was found that the LLNL mechanism [328] with either U-V or H-P modeling agrees well with the measured single stage ignition delay data. In the NTC region, two stages of ignition were observed. Constant U-V and H-P simulations for first stage ignition times are indistinguishable, and the LLNL mechanism consistently under-predicts the measured times. Significant differences were seen between H-P and U-V modeling of second stage ignition times, with H-P simulations generally in better agreement with data. The multi-species and temperature capabilities demonstrated in this study, together with the staged driver filling technique enabling long test times and the CRV strategy allowing improved gasdynamic modeling, should prove very useful in future studies of combustion chemistry.

Chapter 10

Conclusion

10.1 Summary

Over the next 25 years, diesel combustion will remain a major method of energy conversion in the transportation sector. In order to meet increasingly stringent emissions and fuel economy requirements, improvements to existing engine architectures and alternative (non-petroleum) feedstock sources are required. The design of new engines and fuel blends requires accurate knowledge of the detailed combustion kinetics of diesel fuel and its alternatives. Such information takes the form of detailed kinetic mechanisms, which can be used to simulate engine performance and emissions, allowing critical improvements to be made more readily. One promising alternative fuel is biodiesel; however, the detailed chemistry of its combustion is still not well-understood.

The focus of this dissertation was to enlarge the experimental shock tube database of biodiesel surrogate combustion measurements. In order to accomplish this, the Aerosol Shock Tube (AST) technique was used to allow measurements of very-low-vapor-pressure biodiesel surrogate fuels. Also, the staged driver gas filling and Constrained Reaction Volume (CRV) strategies were developed in order to extend available test times and limit energy release upon ignition, allowing ignition experiments of *n*-heptane at engine-relevant conditions.

10.1.1 Extension of AST to very-low-vapor-pressure biodiesel surrogates

Chapter 3 described the operation of the AST and its use in measuring ignition delay times of large, very-low-vapor-pressure biodiesel surrogates. Importantly, the aerosol fuel loading technique was found to significantly extend the size range of fuels that could be studied using the shock tube technique (Section 3.4). Moreover, a simple Mie scattering laser diagnostic was demonstrated that was shown to be useful for predicting post-droplet-evaporation equivalence ratio (Section 3.7.2).

10.1.2 Multi-fuel-component AEROFROSH

A multi-fuel-component version of AEROFROSH was developed (Chapter 4) in order to more accurately study blends of liquid molecules such as actual biodiesel fuel, which consists primarily of five Fatty Acid Methyl Esters (FAMEs). This routine was found to accurately determine post-droplet-evaporation temperature and pressure, and moreover compared favorably with another aerosol shock calculator (Section 4.9). Furthermore, an uncertainty analysis found that post-shock temperature, pressure, and equivalence ratio could be accurately determined for biodiesel experimentation, despite conservatively large estimates for uncertainties to algorithm inputs (Section 4.11).

10.1.3 Infrared spectra of FAMEs

The infrared spectra of eleven FAMEs were measured using an FTIR spectrometer (Chapter 5). Spectra were found to compare favorably with those measured by the Pacific Northwest National Laboratory (PNNL) (Section 5.4.7). Using these spectra, absorption cross section data at $3.39\text{ }\mu\text{m}$ (Section 5.4.10) and integrated area values (Section 5.4.11) have been reported. Comparisons between the FAME spectra and spectra of normal alkanes have been performed (Section 5.5.2), as well as comparisons between saturated and mono-unsaturated FAMEs (Section 5.5.4). Finally, a new extrapolation model for $3.39\text{ }\mu\text{m}$ absorption cross section data has been found to accurately capture the data from this work and that of other researchers, as well (Section 5.5.3). The spectra presented in this dissertation will allow high-quality, quantitative measurements of gaseous FAMEs to be conducted in a variety of reactors such as diesel engines and shock tubes.

10.1.4 Ignition delay times of FAMEs

Ignition delay times for six FAMEs have been measured using the AST technique (Chapter 6). The data indicate that high-temperature reactivity increases with the length of the long carbon chain in these FAMEs, consistent with findings for normal alkanes (Sections 6.5.1.5 and 6.5.1.6). Comparisons with ignition delay time predictions by existing kinetic mechanisms have also been performed, showing in some cases significant differences between model and experiment. Modifications to the high-temperature thermochemistry of the Westbrook *et al.* mechanism [32] based on the measurements in this work have resulted in significantly lower deviation between model and experiment (Section 6.5.2.5). Also, a correlation for the ignition delay time data in 4%O₂/Ar mixtures was determined and successfully used to scale/normalize these measurements (Section 6.5.3).

10.1.5 Long shock tube test times

A number of techniques have been employed to achieve ultra-long shock tube test times in order to measure biodiesel kinetics at practical engine conditions (Chapter 7). Theoretical predictions of test time using x-t diagrams have resulted in good agreement with experimental data (Section 7.3.4). A novel staged driver gas filling technique has also been introduced and characterized, showing significant increases in test time above previously existing methods, together with a reduction in required driver section helium (Section 7.4). Using these techniques, shocks with test times as long as 102 ms have been achieved (Section 7.5). Finally, initial spectroscopic measurements of gas temperature suggested that heat transfer is insignificant at long test times for experiments in the Stanford CRVST (Section 7.7).

10.1.6 Second-generation CRV shock tube technique

A second-generation Constrained Reaction Volume (CRV) technique has been developed that employs a sliding gate valve to confine the reactive test gas mixture to a small section of the shock tube (Chapter 8). Special buffer gas tailoring has been developed in order to enable low-uncertainty incident shock velocity measurements (Section 8.3.1). Moreover, spectroscopic fuel measurements

have been performed to characterize buffer gas/test gas mixing upon gate valve actuation. This technique has been shown to significantly reduce energy release during shock tube ignition experiments, enabling model simulations under a constant enthalpy-pressure (H-P) constraint. Because of this, biodiesel combustion data obtained using this facility can be more readily compared with calculations by existing kinetic mechanisms, allowing improvements to be made with greater certainty.

10.1.7 Application of CRV technique to *n*-heptane ignition

Finally, the CRV shock tube technique has been applied to measure *n*-heptane ignition (Chapter 9); *n*-heptane is an important diesel surrogate and is also relevant to biodiesel combustion. Importantly, ignition delay time results obtained using the CRV and conventional filling techniques agreed at high temperatures, but at some lower temperatures showed evidence that the large energy release characteristic of conventional shocks resulted in lower ignition times. As a result, at these low temperatures, CRV ignition times seemed to agree better with H-P constrained simulations than with constant internal energy-volume (U-V) simulations (Section 9.3.1). Also, a helium-neon (HeNe) laser-based fuel sensor was used to produce low-scatter measurements of first stage ignition in the Negative Temperature Coefficient (NTC) region (Section 9.3.2). Finally, measurements of OH, aldehydes, CO₂, H₂O, and temperature at NTC region conditions have also been conducted using sensitive spectroscopic diagnostics, revealing possible sources of the underlying differences between the kinetic mechanism of Mehl *et al.* [328] and these ignition delay time data (Sections 9.3.3, 9.3.4, and 9.3.5).

10.2 Conclusions

Based on the above summary, several conclusions can be drawn.

1. The aerosol fuel loading technique extends the size range of fuels that can be studied in shock tubes, allowing the chemistry of large biodiesel surrogate molecules to be investigated.
2. The infrared C–H stretch spectra of FAMEs and other hydrocarbons exhibit similar spectral features, reflecting the number and location of the CH₂ and CH₃ groups that these molecules contain.

3. The high-temperature ignition delay times of large FAMES are very similar; within the temperature/pressure range studied (1100-1400 K and 3.5-7 atm in 4%O₂/Ar mixtures), values for different fuels were found to differ by only about a factor of 2-3 at any given temperature.
4. The staged driver gas filling technique significantly extends the post-reflected-shock test time available in shock tubes.
5. The constrained reaction volume fuel loading technique reduces the energy release in shock tubes during the ignition process.
6. The Mehl *et al.* [328] kinetic mechanism for normal heptane oxidation under-predicts both first and second stage ignition times for fuel/15%O₂/Ar ($\phi = 0.75$) mixtures near 6.5 atm at temperatures between 650 and 800 K, but accurately captures ignition of these mixtures at high temperatures.

10.3 Future work

10.3.1 Spectra of unsaturated FAMEs

While much has been accomplished in the course of this dissertation, the work has revealed many more interesting research opportunities. Of these, the first has to do with measuring more spectra of unsaturated FAMEs. Only two such molecules (methyl crotonate (MC, C₅H₈O₂) and methyl-3-nonenoate (M3N, C₁₀H₁₈O₂)) were available for experimentation in sufficient purity at the time of this study, but as fuel synthesis methods improve, more will become available. These spectral measurements will help reveal the influence of C=C bonds on FAME absorption cross sections. Understanding this influence is particularly important for measurements involving methyl oleate (MO, C₁₉H₃₆O₂), methyl linoleate (ML, C₁₉H₃₄O₂), and methyl linolenate (MLN, C₁₉H₃₂O₂), which have one, two, and three degrees of unsaturation (see Table 1.2). These fuels' cross section values can be estimated by modifying the cross section of their fully-saturated counterpart, methyl stearate (MS, C₁₉H₃₈O₂), to account for the effect of unsaturation degree.

10.3.2 New test conditions in the AST

The ignition delay time measurements conducted in the AST during this work were performed at high temperatures. However, many combustion devices such as diesel engines operate at significantly lower temperatures. As such, it will be important to extend the range of the AST to long test times, using the techniques introduced in this work, because at lower temperatures chemical reaction timescales are longer. In addition, performing experiments at very high pressures (20-30 atm) will be useful. Operating at these new conditions presents new challenges, however. Droplet evaporation takes more time at lower temperatures and higher pressures. Possible solutions could involve measuring fuel concentration further from the endwall (in order to increase the time in Region 2 when droplet evaporation takes place) [130]; employing a higher-molecular-weight diluent gas (*e.g.*, Kr rather than Ar), since this would allow a slower shock wave to produce an identical temperature increase (hence allowing more time in Region 2) [111]; or allowing an extended pre-shock waiting period whereby larger aerosol droplets would settle out of the flow to leave only small droplets that evaporate more quickly (Section 3.6).

10.3.3 Time histories of additional species

As discussed in Section 2.2, shock tubes are able to make a variety of measurements, including species mole fraction time history profiles, which can be used to improve kinetic mechanisms. The initial species and temperature time history measurements performed in this thesis provide strong constraints for mechanism development. Using additional laser diagnostics developed in the High Temperature Gasdynamics Laboratory (HTGL), different species can be measured as well, providing more information for mechanism validation and improvement.

10.3.4 Further extension of test time

Another opportunity for future study involves pursuing even longer shock tube test times. This could be done using unconventional driver section designs that resemble flexible hoses, rather than the usual rigid pipe employed by most shock tubes today. Achieving even longer test times has the

advantage of allowing less reactive mixtures to be studied; such mixtures exhibit smaller temperature changes throughout the ignition process, which decreases the uncertainty in absorption cross sections necessary for species-specific laser diagnostics.

10.3.5 CRV length

Finally, modifications to the existing CRV test section in order to extend or reduce its length are possible, but have not yet been performed. Such changes would further-optimize the CRV concept for making more refined measurements of combustion chemistry.

10.4 Final thoughts

In this dissertation, a wealth of kinetic data relevant to biodiesel combustion has been collected and analyzed. In the course of this work, the AST technique has been extended to measure very-low-vapor-pressure FAME ignition, and the mid-IR spectra of multiple FAMEs have been characterized. Moreover, methods for extending test times in shock tubes and for limiting energy release upon ignition have been developed and used to study *n*-heptane ignition during low-pressure, low-temperature oxidation. The biodiesel kinetic data acquired in this work has already resulted in and will continue to allow the improvement of existing combustion models. Also, the new shock tube techniques introduced will allow more precise and more easily simulated kinetic data to be acquired, further-enhancing mechanism development. Ultimately, with better kinetic mechanisms for biodiesel surrogates in hand, diesel engine designers will be able to craft motors and fuel blends that capitalize on the benefits of biodiesel fuel in order to realize critical efficiency and emissions improvements over the next 25 years. Finally, other researchers have also seen the importance of biodiesel fuel and have begun making similar measurements to those in this dissertation; a recent bibliometric study revealed that the number of publications related to both biodiesel and biodiesel emissions has increased exponentially [35].

The work summarized above has shown promise to allow shock tube measurements in new combustion regimes, as well as to make improvements to chemical kinetic mechanisms. It is my

hope that these data indeed prove useful for such ends. However, by far the most significant accomplishment of my time at Stanford is simply the wealth of relationships I have formed with faculty, labmates, and friends. There is no way to place a value on these, and I will continue to treasure each person I have met here long after my time is through.

Appendix A

FROSH

A.1 Introduction

In modern shock tube experiments, temperature, pressure, and density conditions in behind both incident and reflected shocks are computed rather than measured. Computations typically involve solving the mass, momentum, and energy conservation equations combined with an equation of state [111]. This appendix will introduce a computer code, known as FROSH, which performs these calculations in chemically frozen (no chemical reactions) gas phase environments.

A.2 Background

A.2.1 Shock tubes

The shock tube was introduced in Chapter 2. A schematic showing the operation of a conventional gas phase shock tube is provided in Figure 2.1. Definitions of the different space-time intervals involved in a shock experiment, called “regions,” are given in Section 2.3. Finally, an x-t diagram, which provides a graphical depiction of wave propagation in a shock tube, is provided for a simple shock experiment in Figure 7.1.

A.2.2 Previous Studies

Measuring the temperature, pressure, and density conditions in Region 5 of a shock experiment has historically been quite difficult to do experimentally. For this reason, the conservation equations of mass, momentum, and energy, combined with an equation of state, have often been used to compute the conditions behind incident and reflected shocks using the measured incident shock velocity as a primary input parameter. Early researchers employed analytical relationships to this end. In particular, Gaydon and Hurle published ideal relationships, which assume constant gaseous heat capacities, to compute post-shock conditions [111]. The authors comment that these relationships work well for monatomic gases up to about 8000 K (where ionization and electronic excitation become important), but deviate rapidly for diatomic and polyatomic gases whose specific heats change with temperature. The fact that gaseous heat capacities change with temperature necessitates an iterative numerical solution method for precise temperature and pressure prediction behind shock waves.

Many different numerical routines have been written. Gordon and McBride produced a code capable of computing various shock properties while accounting for shock attenuation [122] that has been used in numerous studies (*e.g.*, References [401, 402]). Another often-used program is that of Bittker and Scullin [403], which calculates species concentrations, reaction rates, temperature, pressure, density, and other properties as a function of time, given initial conditions, the incident shock speed, governing chemical reactions, and applicable rate constants (see, for instance, References [404, 405]). McLain and Rao improved on the algorithm of this program to allow its use for many chemical species simultaneously [406]. Gardiner *et al.* composed equations suitable for numerical iteration for determination of shock properties [407], and these relationships have been used in several studies (*e.g.*, References [408, 409]). A routine called KASIMIR has also been developed by Esser for this purpose [123]; validation based on Chemkin-Pro [263] simulations and shock tube experiments was performed by Heufer and Olivier [290]. Mitchell and Kee developed a code to predict chemical kinetic behavior behind shocks that accounted for real gas effects and boundary layer effects [113] when coupled with the Chemkin-II solver. Reynolds developed a chemical equilibrium

solver called STANJAN that employs the element potential method to solve for species concentration, sound speed, and other mixture properties in gaseous mixtures [410]. A newer program, called GasEq [127], has been cited in more recent publications [314, 411–414], and its computational routines are similar to those cited above. Finally, algorithms that generate x-t diagrams often employ the ideal shock relations to compute flow properties (see References [285, 286]).

Several scientists have worked to quantify real gas effects in shock tubes. In particular, Davidson *et al.* wrote a routine to solve the shock equations using several real gas state equations, which required knowledge of real gas parameters for all gaseous species in test gas mixtures [124–126]. Davidson’s work included a comparison of real gas temperature and pressure to ideal gas temperature and pressure in Region 5 for nominal Region 5 pressures of 100, 300, and 1000 atm. This analysis showed that the temperature and pressure values predicted by ideal gas and real gas equations of state are very similar for temperatures above 1000 K and pressures less than 100 atm.

Several studies have also been conducted to predict the change in temperature and pressure in Region 5 due to non-ideal gasdynamic effects (*e.g.*, boundary layer formation, shock attenuation, *etc.*) [291, 292, 415–421]. Notably, Petersen *et al.* [291] found that these effects in Region 5 are most significant for low pressures (less than 10 atm) and high temperatures (above 1400 K), as determined by the change in Region 5 temperature after 500 μs of test time.

A common theme among shock tube studies is that accurate determination of Region 5 temperature is of utmost importance, because reaction rates scale so drastically with temperature [291]. This motivates careful application of governing equations, boundary conditions, and assumptions in order to calculate post-shock conditions. As such, multiple studies have been performed using laser diagnostics to verify that results predicted by shock condition calculators are accurate [220, 292, 422–430].

A primary source of concern in early shock tube research was quantifying the effects of molecular vibration at high temperatures. The breadth of work on this subject is immense, so only the most pertinent references are included in this review and the reader may consult them for more background information. Millikan and White studied the time necessary for vibrational relaxation in several gas mixtures [297, 431]. Lambert, Taylor, and Rapp studied intermolecular transfer of vibrational energy [432–434]. Cottrell, Clarke, and Vincenti produced excellent books of vibrational

processes in gases [435–437]. Lastly, the Handbook of Shock Waves has a profound discussion concerning gas vibration in shock environments [115].

Enthalpy and heat capacity data for gaseous species are required in order to solve the conservation of energy equation. In most numerical methods, these are obtained from the 7-coefficient NASA (National Aeronautics and Space Administration) polynomials [122, 174], which allow computation of thermodynamic data within 0.5 percent error [403, 406, 438]. Another common source are the JANAF (Joint Army Navy Air Force) tables [439].

Clearly, an enormous amount of work has been done in the area of calculating conditions behind shock waves. However, the literature does not yet contain a software package that has applied the fundamental principles governing these environments with the *sole and express* purpose of computing post-shock conditions in shock tubes. A computer code like this would be of great use to many researchers who use shock tubes as a tool for studying other phenomena, for example kinetics and combustion processes. As such, a computer code, FROSH, has been implemented to solve the conservation equations of mass, momentum, and energy, combined with the ideal gas equation of state, in gaseous environments across both incident and reflected shocks in shock tubes. This code has been composed in MATLAB computer software, which is known for its fast computational speed and vector-manipulation abilities [213].

A.3 Fundamentals

Before presenting the algorithms, it is necessary to introduce several concepts. These include important notation used in this appendix, two significant reference frames, the relationship between lab time and particle time, several governing equations and relevant expressions for propagating shocks, the NASA polynomial thermodynamic property equations, the Newton-Raphson computational iteration method, values for important numerical constants, and the assumption of frozen chemistry.

A.3.1 Notation

As a matter of notation, ρ denotes density, v denotes specific volume (and $v = \frac{1}{\rho}$), P denotes pressure, T denotes temperature, h denotes enthalpy, and c_p and c_v denote heat capacity at constant pressure and constant volume, respectively. Also, u (lower case) denotes velocity in the particle frame (see below in Section A.3.2), U (upper case) denotes velocity in the lab frame, and numerical subscripts denote the regions (1-5) where the conditions apply (see Section 2.3).

A variable is often termed “specific” if it is on a per-mole or per-mass basis; such variables are written in lower case. Specific variables with a hat ($\hat{\cdot}$) symbol are on a mole basis, and specific variables without a hat are on a mass basis. The subscript IS denotes “incident shock,” and likewise RS denotes “reflected shock.” In gas-phase mixtures, x_i and w_i are the mole and mass fractions of component i . Equations A.1 and A.2 can be used to convert between these forms, where \hat{M}_i is the molecular weight of each component and the summation is over all C components in the mixture.

$$x_i = \frac{\frac{1}{\hat{M}_i} w_i}{\sum_{i=1}^C \frac{1}{\hat{M}_i} w_i} \quad (\text{A.1})$$

$$w_i = \frac{x_i \hat{M}_i}{\sum_{i=1}^C x_i \hat{M}_i} \quad (\text{A.2})$$

\hat{R}_u denotes the universal (molar) gas constant, and R_g denotes the gas mixture-specific mass-based gas constant; the two are related by the molar mass of the gas mixture \hat{M}_g according to Equations A.3 and A.4.

$$\hat{M}_g = \sum_{i=1}^C x_i \hat{M}_i \quad (\text{A.3})$$

$$R_g = \frac{\hat{R}_u}{\hat{M}_g} \quad (\text{A.4})$$

The letter N is used to denote some number of moles; for instance N_{bath} denotes moles of bath gas species. Finally, the term “bottle” will be used to refer to species mole fractions in their purchased mixture form. For example, in a n -heptane/21%O₂/Ar ($\phi = 1$) mixture, the bottle-mixture

mole fractions would be 21%O₂/79%Ar, but in the mixture these would be 20.61%O₂/77.51%Ar because the remaining 1.88% is *n*-heptane.

A.3.2 Reference frames

Figure A.1 introduces two reference frames. The lab frame assumes the observer is watching the shock move past a fixed point in the shock tube, whereas the shock frame assumes the observer is “riding” on the wave. Note that if $U_5 = 0$ (in the case of test gas stagnation behind the reflected shock), then $u_5 = U_{RS}$; this condition will be used to solve for the reflected shock temperature and pressure.

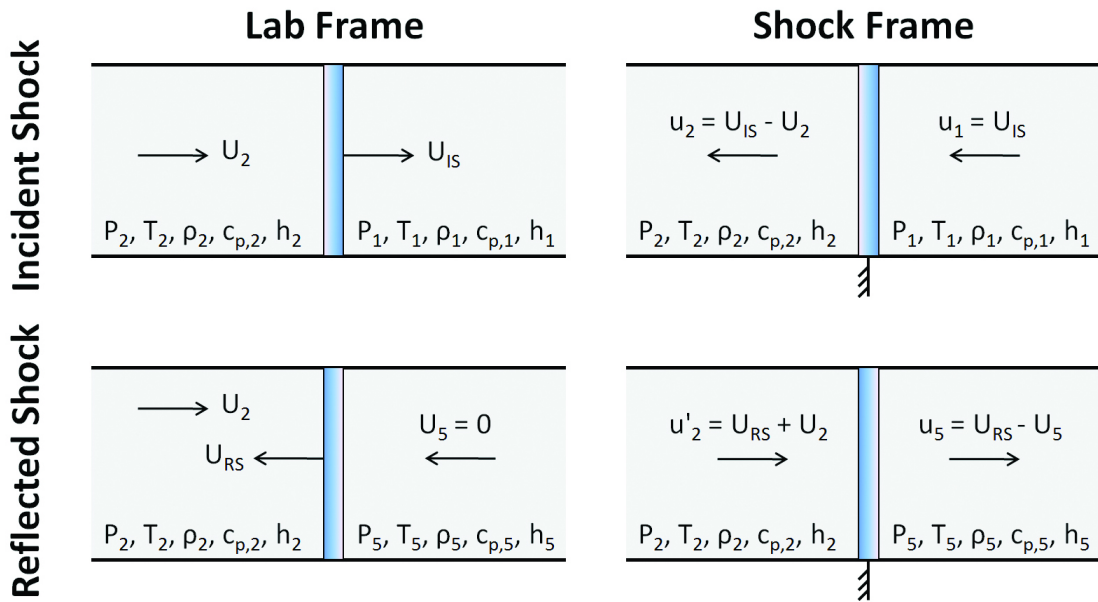


Figure A.1: Velocities and variables in different shock reference frames. Ideally, $U_5 = 0$ such that $u_5 = U_{RS}$. All arrows show velocities in the *positive* direction. The variable u'_2 denotes the incoming gas velocity experienced by the reflected shock wave in the shock reference frame. Figure adapted from References [111, 113].

It is useful to define several relationships using Figure A.1. These are detailed in Equations A.5 through A.10. The variable u'_2 denotes the incoming gas velocity experienced by the reflected shock wave in the shock reference frame. Equation A.10 is an explicit statement of the stagnation

condition introduced above.

$$u_1 = U_{IS} \quad (\text{A.5})$$

$$u_2 = U_{IS} - U_2 \quad (\text{A.6})$$

$$u'_2 = U_{RS} + U_2 \quad (\text{A.7})$$

$$u_5 = U_{RS} - U_5 \quad (\text{A.8})$$

$$= U_{RS} - 0 \quad (\text{A.9})$$

$$= U_{RS} \quad (\text{A.10})$$

A.3.3 Lab time and particle time

Instrumentation fitted to a shock tube at a particular location records experimental events in lab time t_{lab} , but molecules within the shock tube experience particle time $t_{particle}$. A simple conversion between these two reference frames in Region 2 assuming ideal shock behavior (*i.e.*, no attenuation) is given in Equation A.11, and later derived in Appendix B. Of course, the reflected shock wave stagnates the gas mixture such that lab and particle time are identical in Region 5.

$$\frac{t_{particle}}{t_{lab}} = \frac{\rho_2}{\rho_1} \quad (\text{A.11})$$

A.3.4 Governing equations

Equations 4.1 through 4.4, first introduced in Section 4.5, are the conservation equations for mass, momentum, and energy, respectively, as well as the ideal gas equation of state. The subscripts a and b refer to Regions 1 and 2, or 2 and 5. The ideal gas equation of state is generally appropriate at Region 5 temperatures above 1000 K and pressures less than 100 atm, where real gas effects can be neglected [124]. At low pressures, the ideal gas equation of state is also appropriate below 1000 K.

$$\rho_a u_a = \rho_b u_b \quad (4.1)$$

$$P_a + \rho_a u_a^2 = P_b + \rho_b u_b^2 \quad (4.2)$$

$$h_a + \frac{1}{2}u_a^2 = h_b + \frac{1}{2}u_b^2 \quad (4.3)$$

$$P = \rho R_g T = \frac{R_g T}{v} \quad (4.4)$$

The following relationships are also important for propagating shocks. Equation A.12 defines the heat capacity at constant volume c_v relative to the heat capacity at constant pressure c_p for an ideal gas, Equation A.13 defines the ratio of heat capacities γ , Equation 4.7 (repeated from Section 4.6.2) defines the speed of sound a in an ideal gas mixture, and Equation A.14 defines the Mach number M for a shock (note the use of the shock-frame velocity, u). Note that Equations A.12 and A.13 are also valid on a molar basis, *i.e.*, using \hat{c}_p , \hat{c}_v , and \hat{R}_u .

$$c_v = c_p - R_g \quad (A.12)$$

$$\gamma = \frac{c_p}{c_v} \quad (A.13)$$

$$a = \sqrt{\frac{\gamma P}{\rho}} = \sqrt{\gamma R_g T} \quad (4.7)$$

$$M = \frac{u}{a} \quad (A.14)$$

Finally, two other useful relationships that relate heat capacity values to the heat capacity ratio and ideal gas constant are

$$c_v = \frac{R_g}{\gamma - 1} \quad (A.15)$$

$$c_p = \frac{\gamma R_g}{\gamma - 1} \quad (A.16)$$

A.3.5 NASA polynomials

As introduced above, the NASA 7-coefficient polynomials allow the computation of gaseous heat capacity, enthalpy, and entropy as a function of temperature (for ideal gases, heat capacity and enthalpy are a function of temperature only; a slight correction to entropy for pressure is given

later). A description of the file format for this data is provided in Reference [122], and the polynomial equations are repeated below in Equations A.17, A.18, and A.19 (the entropy equation is included here for completeness, but is not used in FROSH). The coefficients a_1 through a_7 are read by FROSH from the NASA polynomial file. Note that these equations are mole-specific values (denoted by the $\hat{\cdot}$); achieving mass-specific values can be done by simply dividing by the molar mass \hat{M} (Equation A.3).

$$\hat{c}_p = \hat{R}_u (a_1 + a_2 T + a_3 T^2 + a_4 T^3 + a_5 T^4) \quad (\text{A.17})$$

$$\hat{h} = \hat{R}_u \left(a_1 T + \frac{1}{2} a_2 T^2 + \frac{1}{3} a_3 T^3 + \frac{1}{4} a_4 T^4 + \frac{1}{5} a_5 T^5 + a_6 \right) \quad (\text{A.18})$$

$$\hat{s} = \hat{R}_u \left(a_1 \ln(T) + a_2 T + \frac{1}{2} a_3 T^2 + \frac{1}{3} a_4 T^3 + \frac{1}{4} a_5 T^4 + a_7 \right) \quad (\text{A.19})$$

Mixing rules for ideal mixtures of ideal gases can be used to compute properties in the case where more than one species is present. These are outlined in Equations A.20, A.21, and A.22. As before, the mixture entropy equation is included for completeness and is not used in the programs. The reference pressure for the NASA polynomial data is $P_{ref} = 1$ atm. The variable x_i denotes the mole fraction of each component, and summation is over all C components in the mixture. Note that these equations are mole-specific values; achieving mass-specific values can be done by simply dividing by the mixture molar mass \hat{M}_g .

$$\hat{c}_{p,mix} = \sum_{i=1}^C x_i \hat{c}_{p,i} \quad (\text{A.20})$$

$$\hat{h}_{mix} = \sum_{i=1}^C x_i \hat{h}_i \quad (\text{A.21})$$

$$\hat{s}_{mix} = \sum_{i=1}^C x_i (\hat{s}_i - \hat{R}_u \ln(x_i)) - \hat{R}_u \ln\left(\frac{P}{P_{ref}}\right) \quad (\text{A.22})$$

A.3.6 Newton-Raphson method

The Newton-Raphson method is commonly used to quickly solve multiple equations concurrently. What follows is a brief theoretical outline to the strategy in two dimensions. In this system, there are two equations f_1 and f_2 in two variables, a and b . The iterative algorithm calls for guesses to a and b , called a_{guess} and b_{guess} . The values of f_1 and f_2 are computed at a_{guess} and b_{guess} , and also the four partial derivatives $\left(\frac{\partial f_1}{\partial a}\right)_b$, $\left(\frac{\partial f_1}{\partial b}\right)_a$, $\left(\frac{\partial f_2}{\partial a}\right)_b$, $\left(\frac{\partial f_2}{\partial b}\right)_a$ are computed at a_{guess} and b_{guess} as well. These values are arranged into two vectors and a matrix called $\tilde{\mathbf{v}}_{guess}$, $\tilde{\mathbf{g}}(\tilde{\mathbf{v}}_{guess})$, and $\mathbf{g}'(\tilde{\mathbf{v}}_{guess})$ (here the tilde (\sim) denotes a vector or matrix). The partial derivative matrix $\mathbf{g}'(\tilde{\mathbf{v}}_{guess})$ can be identified as a Jacobian \mathbf{J} [440]. These are described in Equations A.23, A.24, and A.25.

$$\tilde{\mathbf{v}}_{guess} = \begin{bmatrix} a_{guess} \\ b_{guess} \end{bmatrix} \quad (\text{A.23})$$

$$\tilde{\mathbf{g}}(\tilde{\mathbf{v}}_{guess}) = \begin{bmatrix} f_1(a_{guess}, b_{guess}) \\ f_2(a_{guess}, b_{guess}) \end{bmatrix} \quad (\text{A.24})$$

$$\mathbf{g}'(\tilde{\mathbf{v}}_{guess}) = \begin{bmatrix} \left(\frac{\partial f_1}{\partial a}\right)_b & \left(\frac{\partial f_1}{\partial b}\right)_a \\ \left(\frac{\partial f_2}{\partial a}\right)_b & \left(\frac{\partial f_2}{\partial b}\right)_a \end{bmatrix} = \mathbf{J} \quad (\text{A.25})$$

Next, the inverse of the Jacobian, \mathbf{J}^{-1} is computed using standard linear algebraic methods, and the new vector $\hat{\mathbf{v}}_{new}$, containing the new values of a and b (a_{new} and b_{new}), is computed according to Equation A.26.

$$\hat{\mathbf{v}}_{new} = \tilde{\mathbf{v}}_{guess} - \mathbf{J}^{-1} \tilde{\mathbf{g}}(\tilde{\mathbf{v}}_{guess}) = \begin{bmatrix} a_{new} \\ b_{new} \end{bmatrix} \quad (\text{A.26})$$

The values within $\tilde{\mathbf{v}}_{guess}$ and $\hat{\mathbf{v}}_{new}$ are compared, and a decision is made. If the values of a and b have changed less than some iterative threshold, the algorithm exits and the new values of a_{new} and b_{new} are considered the solutions to f_1 and f_2 . If, however, the values of a and b change by an amount greater than the threshold, the algorithm loops back to Equation A.24, using a_{new} and b_{new} as new guesses a_{guess} and b_{guess} . Ultimately the solution values of a and b will minimize the

absolute values of f_1 and f_2 .

A.3.7 Numerical constants

Values for numerical constants used in algorithms can have a large effect on the projected outcomes. Hence, a brief overview of the values of constants used in FROSH is in order. The value of the ideal gas constant was taken to be $\hat{R}_u = 8.3144621 \frac{\text{J}}{\text{mol}\cdot\text{K}}$, as determined by the National Institute of Standards and Technology (NIST) [244, 245]. The value of the reference temperature, T_{ref} , was taken to be 298.15 K. Though no reference pressure is explicitly needed in FROSH, throughout this appendix the reference pressure is taken as $P_{ref} = 1 \text{ atm}$. Finally, values of the atomic masses \hat{M}_i of elements included in the program were taken from NIST (2010) [441]. Atomic masses for all known elements were included in the program, but a sample of the most important atomic masses are displayed in Table A.1.

Table A.1: Sample atomic masses used in FROSH [441].

Element Name	Symbol	Atomic Mass \hat{M}_i [g/mol]
Argon	Ar	39.948
Bromine	Br	79.904
Carbon	C	12.0107
Chlorine	Cl	35.453
Fluorine	F	18.9984032
Hydrogen	H	1.00794
Helium	He	4.002602
Iodine	I	126.90447
Krypton	Kr	83.798
Nitrogen	N	14.0067
Neon	Ne	20.1797
Oxygen	O	15.9994
Sulfur	S	32.065
Silicon	Si	28.0855
Xenon	Xe	131.293

A.3.8 Frozen chemistry

The chemical composition of a reactive gas mixture begins to change when it experiences high temperatures. As a consequence, new gaseous species are created and the heat capacity, density,

pressure, and temperature of that mixture change. Were this to occur in Region 2 of a shock experiment, the conditions predicted by shock calculators in Region 5 would not be accurate. Either the chemical kinetics of gaseous species would need to be accounted for during the shock calculation, or an assumption of no chemical reactivity in Region 2 would be needed. In order to employ the second option, it is important that the timescale of chemical reactivity at Region 2 temperatures and pressures be much longer than the time particles experience in Region 2. Typical Region 2 temperatures, pressures, and particle residence times are 500-800 K, 0.5-2 atm, and 100-400 μ s respectively. Under these conditions, it is reasonable to assume that no chemical reactions occur in Region 2 [328]. Many other researchers have also assumed frozen Region 2 chemistry (see, for instance, References [442–444]). Furthermore, a simple laser diagnostic or emission measurement during Region 2 can be used to verify the absence of chemistry during every experiment (no change in laser absorbance and no emission are expected during Region 2 if chemistry is frozen; see Figures 8.10 and 8.11). This assumption is called the “frozen chemistry” assumption, and is the origin of the “FRO” in the name FROSH.

A.4 Code structure

A.4.1 Initialization

The algorithm of FROSH is presented in the following section. Several inputs are required by the code: the incident shock velocity U_{IS} [m/s], the Region 1 temperature T_1 [K], the Region 1 pressure P_1 [Torr], an array of gas species names (*e.g.*, {’C₇H₁₆’, ’O₂’, ’Ar’}), an array of gas mole fractions corresponding to the gas species names (*e.g.*, [0.0188, 0.2061, 0.7751]), and the name of the file containing the NASA polynomial coefficients for the constituents of the gas mixture. An additional input discussing the vibrational equilibration of the gas mixture behind the shock is also necessary; this will be discussed in the next section.

As discussed in Sections 8.2.1 and 8.3.1, incident shock velocities are typically measured at several axial locations along the length of the shock tube. Most researchers extrapolate this incident shock velocity to the endwall of the shock tube, where the condition that the gas behind the reflected shock wave is stagnated is without question fulfilled (the shock velocity at the endwall is actually

zero due to the non-penetration boundary condition, but this extrapolation yields what it would have been had the endwall not existed) and where the attenuation of the reflected shock wave is unimportant. Other researchers choose to extrapolate the velocity to the location of the optical diagnostics used on the shock tube, usually 1-5 cm from the endwall. A comparison of computed Region 2 and 5 temperature and pressure for a mixture of 10% oxygen in argon, an endwall incident shock velocity of 800 m/s, and a shock attenuation of $\Gamma = 2.5\%/m$ is given in Figure A.2.

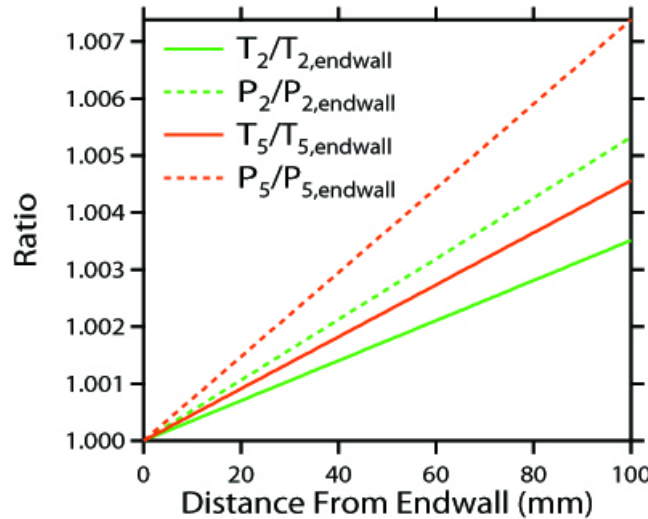


Figure A.2: Effect on T_2 , P_2 , T_5 , and P_5 of extrapolating incident shock velocity to different distances from the shock tube endwall. The figure shows that extrapolating conditions to a point not at the endwall results in slight increases to predicted temperature and pressure as compared to endwall values (because the incident shock velocity is higher at distances further from the endwall), but these changes are small. Computation conditions are $T_1 = 298.15$ K, $P_1 = 30$ Torr, $U_{IS,endwall} = 800$ m/s, and a shock attenuation of $\Gamma = 2.5\%/m$. The test gas mixture is 10%O₂/Ar. Nominal conditions modeled at the endwall are $T_2 = 798$ K, $P_2 = 0.296$ atm, $T_5 = 1428$ K, and $P_5 = 1.15$ atm.

A number of initializing routines must be completed prior to iterating for the Region 2 and 5 conditions. These include reading thermodynamic parameters, computing species and mixture molar masses, and computing Region 1 gas mixture enthalpy and heat capacity. The details of these subroutines will not be described in detail here, save to say that FROSH reads the NASA polynomials from an input text file as specified in Reference [122], the molar mass \hat{M}_g and gas

constant R_g of the mixture are computed according to Equations A.3 and A.4 and Table A.1, and the thermodynamic properties are computed according to Equations A.17, A.18, A.20, and A.21.

A.4.2 Determination of Region 2 conditions

The program's Newton-Raphson procedure, outlined above in Equations A.23 through A.26, iterates upon Region 2 variables temperature T_2 and pressure P_2 . Initial guesses for these values are required in order to start the routine. The initial guesses are computed using the ideal shock relations, detailed in Equations A.27 and A.28. These equations and their derivation from fundamental principles can be found in Reference [111].

$$P_{2,ideal} = P_1 \left(\frac{2\gamma_1 M_{IS}^2 - (\gamma_1 - 1)}{\gamma_1 + 1} \right) \quad (\text{A.27})$$

$$T_{2,ideal} = T_1 \left(\frac{\left(\gamma_1 M_{IS}^2 - \frac{\gamma_1 - 1}{2} \right) \left(\frac{\gamma_1 - 1}{2} M_{IS}^2 + 1 \right)}{\left(\frac{\gamma_1 + 1}{2} \right)^2 M_{IS}^2} \right) \quad (\text{A.28})$$

The iteration routine can now commence. First, Equations 4.4, A.17, A.18, A.20, and A.21 are used to compute the Region 2 mixture specific volume, heat capacity, and enthalpy from $P_{2,guess}$ and $T_{2,guess}$. Next, the values of the functions f_1 and f_2 , as well as the values of their partial derivatives, are computed at $P_{2,guess}$ and $T_{2,guess}$. These functions are presented for the Region 1-Region 2 shock jump below in Equations A.29 through A.34 (they are derived in Section A.9).

$$f_1 = \left(\frac{P_{2,guess}}{P_1} - 1 \right) + \left(\frac{u_1^2}{P_1 v_1} \right) \left(\frac{v_2}{v_1} - 1 \right) \quad (\text{A.29})$$

$$f_2 = \left(\frac{h_2 - h_1}{\frac{1}{2} u_1^2} \right) + \left(\frac{v_2^2}{v_1^2} - 1 \right) \quad (\text{A.30})$$

$$\left(\frac{\partial f_1}{\partial P_2} \right)_{T_2} = \left(\frac{1}{P_1} \right) + \left(\frac{u_1^2}{P_1 v_1^2} \right) \left(\frac{-v_2}{P_{2,guess}} \right) \quad (\text{A.31})$$

$$\left(\frac{\partial f_1}{\partial T_2} \right)_{P_2} = \left(\frac{u_1^2}{P_1 v_1^2} \right) \left(\frac{v_2}{T_{2,guess}} \right) \quad (\text{A.32})$$

$$\left(\frac{\partial f_2}{\partial P_2} \right)_{T_2} = \left(\frac{2v_2}{v_1^2} \right) \left(\frac{-v_2}{P_{2,guess}} \right) \quad (\text{A.33})$$

$$\left(\frac{\partial f_2}{\partial T_2} \right)_{P_2} = \left(\frac{2}{u_1^2} \right) c_{p,2} + \left(\frac{2v_2}{v_1^2} \right) \left(\frac{v_2}{T_{2,guess}} \right) \quad (\text{A.34})$$

The algorithm computes the new P_2 and T_2 using Equation A.26, and then checks to see how the computed values differ from the guesses according to Equations A.35 and A.36. If the values of κ_{P_2} and κ_{T_2} are less than the specified tolerance, the algorithm exits. If not, it loops and continues iterating until convergence is reached.

$$\kappa_{P_2} = \left| \frac{P_{2,guess} - P_{2,new}}{P_{2,new}} \right| \quad (\text{A.35})$$

$$\kappa_{T_2} = \left| \frac{T_{2,guess} - T_{2,new}}{T_{2,new}} \right| \quad (\text{A.36})$$

After completing the iteration, several properties are computed for Region 2. These include the gas velocity u_2 from Equation 4.1, the ratio of heat capacities γ_2 from Equations A.12 and A.13, and the speed of sound V_2 from Equation 4.7.

A.4.3 Determination of Region 5 conditions

The program now begins to iterate upon the Region 5 conditions in a similar manner. The ideal conditions $P_{5,ideal}$ and $T_{5,ideal}$, computed from Equations A.37 through A.39 (derived in Reference [111]), serve as the initial guesses. Equations 4.4, A.17, A.18, A.20, and A.21 are used to compute Region 5 gas properties using these ideal values. The reader may notice that γ was recomputed in Region 2 rather than assumed to be equal to its Region 1 value (in Reference [111], γ was assumed to be constant).

$$\eta = \frac{\gamma_2 + 1}{\gamma_2 - 1} \quad (\text{A.37})$$

$$P_{5,ideal} = P_2 \left(\frac{\eta + 2 - \frac{P_1}{P_2}}{1 + \eta \frac{P_1}{P_2}} \right) \quad (\text{A.38})$$

$$T_{5,ideal} = T_2 \left(\frac{P_{5,ideal}}{P_2} \right) \left(\frac{\eta + \frac{P_{5,ideal}}{P_2}}{1 + \eta \frac{P_{5,ideal}}{P_2}} \right) \quad (\text{A.39})$$

Iteration functions f_3 and f_4 and their derivatives are specified in Equations A.40 through A.45.

Derivations for these equations are presented in Section A.10. Finally, convergence criteria are given in Equations A.46 and A.47.

$$f_3 = \left(\frac{P_{5,guess}}{P_2} - 1 \right) + \left(\frac{(u_1 - u_2)^2}{P_2(v_5 - v_2)} \right) \quad (\text{A.40})$$

$$f_4 = \left(\frac{h_5 - h_2}{\frac{1}{2}(u_1 - u_2)^2} \right) + \left(\frac{v_5 + v_2}{v_5 - v_2} \right) \quad (\text{A.41})$$

$$\left(\frac{\partial f_3}{\partial P_5} \right)_{T_5} = \left(\frac{1}{P_2} \right) + \left(\frac{-(u_1 - u_2)^2}{P_2(v_5 - v_2)^2} \right) \left(\frac{-v_5}{P_{5,guess}} \right) \quad (\text{A.42})$$

$$\left(\frac{\partial f_3}{\partial T_5} \right)_{P_5} = \left(\frac{-(u_1 - u_2)^2}{P_2(v_5 - v_2)^2} \right) \left(\frac{v_5}{T_{5,guess}} \right) \quad (\text{A.43})$$

$$\left(\frac{\partial f_4}{\partial P_5} \right)_{T_5} = \left(\frac{-2v_2}{(v_5 - v_2)^2} \right) \left(\frac{-v_5}{P_{5,guess}} \right) \quad (\text{A.44})$$

$$\left(\frac{\partial f_4}{\partial T_5} \right)_{P_5} = \left(\frac{1}{\frac{1}{2}(u_1 - u_2)^2} \right) c_{p,5} + \left(\frac{-2v_2}{(v_5 - v_2)^2} \right) \left(\frac{v_5}{T_{5,guess}} \right) \quad (\text{A.45})$$

$$\kappa_{P_5} = \left| \frac{P_{5,guess} - P_{5,new}}{P_{5,new}} \right| \quad (\text{A.46})$$

$$\kappa_{T_5} = \left| \frac{T_{5,guess} - T_{5,new}}{T_{5,new}} \right| \quad (\text{A.47})$$

$$(A.48)$$

A.4.4 Closing calculations

After finishing the Region 5 iteration routine, the program performs a few small calculations. The reflected shock velocity is computed in Equation A.49. Shock-frame velocity u'_2 is computed using Equation A.50, and is used to compute the reflected shock Mach number by Equation A.14. Equations A.49 and A.50 will be derived in Section A.10. Finally, the ratio of heat capacities γ_5 is found from Equations A.12 and A.13, and the speed of sound V_5 is computed using Equation 4.7.

$$U_{RS} = u_5 = \frac{v_5}{v_2 - v_5} (u_1 - u_2) = \frac{\rho_2}{\rho_5 - \rho_2} (u_1 - u_2) \quad (\text{A.49})$$

$$u'_2 = u_5 + u_1 - u_2 \quad (\text{A.50})$$

Lastly, the equivalence ratio of the shock is computed. This subroutine computes the stoichiometric molar number of oxygen atoms required for complete combustion $N_{O,stoich}$ by assuming that all carbon atoms in the mixture $N_{C,mix}$ form CO_2 , all hydrogen atoms $N_{H,mix}$ form H_2O , and all sulfur atoms $N_{S,mix}$ form SO_2 . It then divides the number of oxygen atoms needed by the number of oxygen atoms in the mixture $N_{O,mix}$ to find the equivalence ratio according to Equation A.51. Note that if fuel (*e.g.*, $\text{C}_{11}\text{H}_{22}\text{O}_2$) or other molecules (*e.g.*, CO_2) contain oxygen atoms, these will be included in the total oxygen count (neat $\text{C}_{11}\text{H}_{22}\text{O}_2$ has an equivalence ratio of $\phi = 16.5$, and neat CO_2 has $\phi = 1$). The output data available from FROSH are listed in Table A.2.

$$\phi = \frac{N_{O,stoich}}{N_{O,mix}} = \frac{2N_{C,mix} + \frac{1}{2}N_{H,mix} + 2N_{S,mix}}{N_{O,mix}} \quad (\text{A.51})$$

A.5 Vibrational non-equilibrium

A.5.1 Background

Gases “store” energy in translational, rotational, vibrational, and electronic energy modes. After a shock propagates through a gas, the relative fractions of translational energy (TE), rotational

Table A.2: Output data available from FROSH.

Data	Units	Variables
Temperature	K	T_2, T_5
Pressure	Pa	P_2, P_5
Density	kg/m ³	ρ_1, ρ_2, ρ_5
Heat Capacity Ratio	(none)	$\gamma_1, \gamma_2, \gamma_5$
Sound Speed	m/s	a_1, a_2, a_5
Mach Number	(none)	M_{IS}, M_{RS}
Velocity	m/s	U_{RS}
Stoichiometry	(none)	ϕ

energy (RE), and vibrational energy (VE) quickly adjust via intramolecular (within one molecule) transfer to obtain three Boltzmann population fraction distributions, described in Equations A.52 through A.54 (in many cases, electronic energy can be neglected). In these equations, $\frac{N_i}{N_{tot}}$ is the fraction of molecules in energy level i , ϵ_i is the energy of that particular level, g_i is the degeneracy of that energy level, k_B is the Boltzmann constant, and $Q(T)$ is the temperature-dependent partition function of that mode, evaluated at temperature T . Each of these Boltzmann population fraction distributions yields a temperature for that energy mode: T_{trans} , T_{rot} , and T_{vib} . Initially, these temperatures are not equal ($T_{trans} \neq T_{rot} \neq T_{vib}$) such that an overall temperature T is undefined.

$$\frac{N_{i,trans}}{N_{tot}} = \frac{g_i \exp\left(\frac{-\epsilon_i}{k_B T_{trans}}\right)}{Q_{trans}(T_{trans})} \quad (\text{A.52})$$

$$\frac{N_{i,rot}}{N_{tot}} = \frac{g_i \exp\left(\frac{-\epsilon_i}{k_B T_{rot}}\right)}{Q_{rot}(T_{rot})} \quad (\text{A.53})$$

$$\frac{N_{i,vib}}{N_{tot}} = \frac{g_i \exp\left(\frac{-\epsilon_i}{k_B T_{vib}}\right)}{Q_{vib}(T_{vib})} \quad (\text{A.54})$$

Following (even during) this initial redistribution within each molecule, energy transfer occurs between molecules (intermolecular transfer) in order to achieve thermal equilibrium in which $T_{trans} = T_{rot} = T_{vib} = T$. Energy transfer between two molecules occurs when they collide. In a collision, one energy mode of the first molecule gains energy, and one mode of the second molecule loses energy. Notation for intermolecular transfer in this appendix is written in the form M_1-M_2 ,

where M_1 is the energy mode of the molecule gaining energy and M_2 is the energy mode in the molecule losing energy. The process of energy transfer between modes is termed “relaxation.”

For small gaseous molecules (two to four atoms), energy transfer between molecules in translational and rotational modes ($TE-TE$, $RE-TE$, and $RE-RE$) is much faster than vibrational energy transfer ($VE-TE$ or $VE-RE$). This is because vibrational energy level spacing is larger than translational and rotational energy level spacing, such that more energetic collisions (and hence, less likely collisions) are required to transfer sufficient vibrational energy for vibrational mode excitation (see References [115, 297, 431–437, 445] for more details on this phenomenon). Thus, vibrational relaxation is often delayed relative to translational and rotational relaxation, which necessitates special treatment in the FROSH algorithm.

If vibrational relaxation cannot occur in the finite time of Region 2 or Region 5, the temperature of translation and rotation is not the same as that of vibration (for a discussion of the time available in Region 2, see Equation A.11 and Appendix B). This is significant because the temperature specified for chemical reactions is the translational temperature, and it is of utmost importance to accurately determine this parameter.

FROSH accounts for vibrational non-equilibrium by “freezing” the constant volume vibrational heat capacity $\hat{c}_{v,vib}$ and vibrational energy \hat{e}_{vib} such that these cannot change across a shock, while allowing the translational and rotational constant volume heat capacities and enthalpies to change. Thus, if the gas cannot equilibrate vibrationally in Region 2, $\hat{c}_{v,2,vib} = \hat{c}_{v,1,vib}$ and $\hat{e}_{2,vib} = \hat{e}_{1,vib}$, but $\hat{c}_{v,trans}$, $\hat{c}_{v,rot}$, \hat{e}_{trans} , and \hat{e}_{rot} are allowed to change. Likewise, if the gas cannot equilibrate vibrationally in both Region 2 and 5, $\hat{c}_{v,5,vib} = \hat{c}_{v,2,vib} = \hat{c}_{v,1,vib}$ and $\hat{e}_{5,vib} = \hat{e}_{2,vib} = \hat{e}_{1,vib}$ but $\hat{c}_{v,trans}$, $\hat{c}_{v,rot}$, \hat{e}_{trans} , and \hat{e}_{rot} are allowed to change.

Note that, as will be discussed below, the heat capacities for translation and rotation are essentially constant at temperatures near and above T_{ref} , so for shocks modeled as vibrationally frozen, $\hat{c}_{v,trans}$ and $\hat{c}_{v,rot}$ will stay constant and only the \hat{e}_{trans} and \hat{e}_{rot} will change. Also note that if vibrational equilibrium is possible in the time of Region 2, it is certainly possible in the time of Region 5 because vibrational relaxation proceeds more quickly as temperature increases [445]. The vibrational equilibration condition is specified to FROSH by selecting one of three options: EE (vibrationally equilibrated in both Region 2 and Region 5), FE (vibrationally frozen in Region 2 but

equilibrated in Region 5), or FF (vibrationally frozen in both Region 2 and Region 5).

Selecting the vibrational condition for calculations correctly is important. A reliable method, demonstrated by Gauthier *et al.* [346], involves comparing the measured pressure values (P_2 and P_5) to those computed by FROSH. Alternatively, in some shocks, vibrational equilibrium can be generally assumed in all cases. Large hydrocarbons (*e.g.*, normal alkanes larger than pentane, C₅H₁₂) have many more vibrational modes than smaller molecules (*e.g.*, diatomics). Thus, the energy level spacing of vibrational modes in large molecules is quite small compared to the vibrational energy level spacing of smaller (*e.g.*, diatomic) molecules. This allows rotational/translational-vibrational transfer (*TE-VE* and *RE-VE*) to occur more readily for large molecules. After these large hydrocarbons become vibrationally excited, they quickly transfer their vibrational energy to other smaller diatomic bath gas molecules such as oxygen and nitrogen (*VE-VE* transfer). In consequence, shocks performed in mixtures containing large molecular species can be considered in vibrational equilibrium (EE) in both Region 2 and Region 5. This is supported by the results of Gauthier *et al.* [346]. Also, shocks in which the bath gas is argon, which does not have vibrational energy modes, may in many cases not be subject to vibrational relaxation phenomena.

A.5.2 Procedure

This section will now outline the procedure for accounting for vibrational nonequilibrium. The basic strategy followed in the FROSH program is to separate the energy in the translational and rotational modes from that in the vibrational modes, and account for each separately.

A gas molecule's molar enthalpy is given by the integral in Equation A.55, where, as mentioned above, T_{ref} is taken to be 298.15 K, and $\hat{h}_{form}^{T_{ref}}$ is the molar heat of formation of the molecule at the reference temperature.

$$\hat{h}_i(T) = \hat{h}_{form,i}^{T_{ref}} + \int_{T_{ref}}^T \hat{c}_{p,i}(T) dT \quad (\text{A.55})$$

The molar heat capacity at constant pressure \hat{c}_p is related to the molar heat capacity \hat{c}_v at constant volume by Equation A.56 (this Equation A.12 on a molar basis).

$$\hat{c}_{p,i} = \hat{c}_{v,i} + \hat{R}_u \quad (\text{A.56})$$

Furthermore, according to the molecular theory of gases, the constant volume heat capacity \hat{c}_v of a gas is the sum of contributions from the translational, rotational, and vibrational energy modes [446], as written in Equation A.57.

$$\hat{c}_{v,i} = \hat{c}_{v,trans,i} + \hat{c}_{v,rot,i} + \hat{c}_{v,vib,i} \quad (\text{A.57})$$

Lastly, recasting Equation A.55 with the aid of Equation A.21 gives the molar enthalpy for the entire gas mixture in Equation A.58.

$$\hat{h}_{mix}(T) = \sum_{i=1}^C x_i \left(\hat{h}_{form,i}^{T_{ref}} + \int_{T_{ref}}^T \hat{c}_{p,i}(T) dT \right) \quad (\text{A.58})$$

What remains is to compute each of these heat capacities, and then integrate to achieve the gaseous enthalpy. Note that these equations are derived on a mole-basis due to the simplicity of using mole-fraction-weighted summations; FROSH converts the mole-basis values to a mass-basis before using them.

Each degree of freedom in motion that a molecule has yields one energy mode, and each mode contributes $\frac{1}{2}\hat{R}_u$ to the total heat capacity for a given molecule (per mole). For translational motion, there are three degrees of freedom, one for each X , Y , and Z movement direction. Hence the translational constant volume heat capacity is given by Equation A.59. This equation is valid when all translational energy modes are fully excited, which is true for essentially all temperatures where molecules are gaseous.

$$\hat{c}_{v,trans,i} = \frac{3}{2}\hat{R}_u \quad (\text{A.59})$$

A similar summation can be done for rotational energy. However, the calculation is more difficult because the shape of the molecule changes the available rotational degrees of freedom. When a molecule has a small moment of inertia about an axis, the rotational energy level spacing becomes exceedingly large; as a result this rotational mode is essentially non-active. Small moments of inertia occur on all three axes of a monatomic molecule, and along the inter-nuclear axis for linear molecules. Thus, monatomic molecules have no rotational freedom, those that are linear have two degrees of freedom in rotation, and nonlinear molecules have three rotational degrees of freedom.

For example, noble gases such as argon and helium have no rotational energy modes, diatomic molecules such as oxygen and nitrogen have two rotational energy modes, and most polyatomic molecules have three rotational energy modes.

There are a number of exceptions, however, for species that have three or more atoms and yet are linear. Such molecules have only two rotational degrees of freedom. Perhaps the most common of these exceptions is carbon dioxide (bond structure O=C=O). A list of common linear polyatomic molecules is given in Table A.3. The FROSH program checks all species with three or more atoms against this list to ensure that the rotational heat capacity calculations are correct. Note that the list in Table A.3 is not exhaustive, but can be easily edited in the source code of FROSH to add other linear polyatomic molecules. Data concerning the number and identity of atoms in gaseous species is read into FROSH from the NASA polynomial tables. Ultimately, the rotational constant volume specific heat for a molecule is given by Equation A.60, where $M_{rot,i}$ is the number of rotational degrees of freedom. This equation is valid when all rotational energy modes are fully excited, which is true at temperatures near and higher than T_{ref} .

$$\hat{c}_{v,rot,i} = \frac{1}{2} \hat{R}_u M_{rot,i} \quad (\text{A.60})$$

From the above discussion it is evident that the translational and rotational heat capacities at constant volume are independent of temperature for temperatures near and above T_{ref} , because translational and rotational modes are fully excited. Thus, the integral in Equation A.58 can be combined with Equations A.56 and A.57 then recast in Equation A.61.

$$\hat{h}_{mix}(T) = \sum_{i=1}^C x_i \left(\hat{h}_{form,i}^{T_{ref}} + (\hat{c}_{v,trans,i} + \hat{c}_{v,rot,i} + \hat{R}_u)(T - T_{ref}) + \int_{T_{ref}}^T \hat{c}_{v,vib,i}(T) dT \right) \quad (\text{A.61})$$

Table A.3: Linear polyatomic molecules.

Three Atoms	Four Atoms	Five Atoms
BeCl ₂	C ₂ H ₂	C ₃ H ₂
C ₃	C ₂ N ₂	C ₃ N ₂
CCN	CCCC	C ₃ O ₂
CCO	HCCCl	
CH ₂		
CNC		
CNN		
CO ₂		
F ₂ Xe		
HCC		
HCN		
N ₂ O		
N ₃		
NCN		
NCO		
OCS		

Pulling out the heat of formation and integral terms yields Equation A.62.

$$\begin{aligned} \hat{h}_{mix}(T) = & \sum_{i=1}^C x_i \left(\hat{h}_{form,i}^{T_{ref}} \right) \\ & + \sum_{i=1}^C x_i \left(\left(\hat{c}_{v,trans,i} + \hat{c}_{v,rot,i} + \hat{R}_u \right) (T - T_{ref}) \right) \\ & + \sum_{i=1}^C x_i \left(\int_{T_{ref}}^T \hat{c}_{v,vib,i}(T) dT \right) \end{aligned} \quad (\text{A.62})$$

The integral in Equation A.62 can be thought of as the vibrational contribution to the enthalpy. When conditions are modeled as frozen, this quantity does not change across the shock. Hence, FROSH computes this quantity in Region 1 by integrating from T_{ref} to T_1 and carries it through any frozen shock computations, as shown in Equation A.63. Note that since this is an integral of constant volume heat capacity, the result is internal energy rather than enthalpy (hence the \hat{e} designation as opposed to \hat{h}). The superscript “frozen” is a reminder that this equation should be

applied for shocks modeled as vibrationally frozen.

$$\hat{e}_{1,vib,mix}^{frozen} = \sum_{i=1}^C x_i \left(\int_{T_{ref}}^{T_1} \hat{c}_{v,vib,i}(T) dT \right) \quad (\text{A.63})$$

The method of computing this integral requires further explanation. One method for determining the vibrational contribution to heat capacity is by summing degrees of freedom, as with the translational and rotational calculations above. Each vibrational mode contributes $2\left(\frac{1}{2}\hat{R}_u\right)$ to the heat capacity because vibration involves both kinetic and potential energy. The total number of vibrational modes for a gaseous species $M_{vib,i}$ is given by Equation A.64, where $N_{atoms,i}$ is the number of atoms in the molecule and the subtracted 3 represents the number of translational degrees of freedom. Thus, the total contribution to constant volume specific heat is given by Equation A.65.

$$M_{vib,i} = 3N_{atoms,i} - 3 - M_{rot,i} \quad (\text{A.64})$$

$$\hat{c}_{v,vib,i} = \hat{R}_u M_{vib,i} \quad (\text{A.65})$$

Using the degrees of freedom summation method produces significant errors at temperatures near the reference temperature T_{ref} , however, because the vibrational modes are only partially excited at low temperatures. This means that near T_{ref} , $\hat{c}_{v,vib,i} \ll \hat{R}_u M_{vib,i}$. Because of this, FROSH computes the vibrational contribution to enthalpy by a rearrangement of Equation A.62, given in Equation A.66. In this equation, $\hat{h}_{1,mix}^{NASA}(T_1)$ is the molar enthalpy in Region 1 computed using the NASA polynomials (Equations A.18 and A.21) at T_1 . The NASA polynomials account for partial vibrational excitation at low temperatures, and hence correctly specify enthalpy at all temperatures within their usable range (usually 200-3000 K). Thus, the true Region 1 vibrational energy is found by subtracting the translational and rotational contributions from the overall enthalpy.

$$\hat{e}_{1,vib,mix}^{frozen} = \hat{h}_{1,mix}^{NASA}(T_1) - \sum_{i=1}^C x_i \left(\hat{h}_{form,i}^{T_{ref}} \right) - \sum_{i=1}^C x_i \left(\left(\hat{c}_{v,trans,i} + \hat{c}_{v,rot,i} + \hat{R}_u \right) (T_1 - T_{ref}) \right) \quad (\text{A.66})$$

What remains is to compute the enthalpy of formation term, which easily accomplished by noting that the integral in Equation A.58 disappears when $T = T_{ref}$. This allows use of the NASA

polynomial data, and is shown explicitly in Equation A.67.

$$\sum_{i=1}^C x_i \left(\hat{h}_{form,i}^{T_{ref}} \right) = \hat{h}_{form,mix}^{T_{ref}} = \hat{h}_{1,mix}^{NASA}(T_{ref}) \quad (\text{A.67})$$

Combining Equations A.67 and A.66 yields Equation A.68, the final expression for the vibrational contribution to the gas energy.

$$\hat{e}_{1,vib,mix}^{frozen} = \hat{h}_{1,mix}^{NASA}(T_1) - \hat{h}_{1,mix}^{NASA}(T_{ref}) - \sum_{i=1}^C x_i \left(\left(\hat{c}_{v,trans,i} + \hat{c}_{v,rot,i} + \hat{R}_u \right) (T_1 - T_{ref}) \right) \quad (\text{A.68})$$

Lastly, by inserting terms into Equation A.62, the enthalpy of the gas mixture behind a frozen shock is given by Equation A.69.

$$\hat{h}_{mix}^{frozen}(T) = \hat{h}_{1,mix}^{NASA}(T_{ref}) + \sum_{i=1}^C x_i \left(\left(\hat{c}_{v,trans,i} + \hat{c}_{v,rot,i} + \hat{R}_u \right) (T - T_{ref}) \right) + \hat{e}_{1,vib,mix}^{frozen} \quad (\text{A.69})$$

In addition to the enthalpy, the heat capacity of the gas mixture is also required. Equations A.56, A.57, A.59, and A.60 taken together show that the constant pressure molar heat capacity of the gas mixture does not change across a shock that is modeled as frozen. This is because by definition $\hat{c}_{v,2,vib} = \hat{c}_{v,1,vib}$, and both $\hat{c}_{v,trans}$ and $\hat{c}_{v,rot}$ are independent of temperature for temperatures near and above T_{ref} . Hence, Equation A.70 gives the specific heat behind a vibrationally frozen shock, where $\hat{c}_{p,1,mix}^{NASA}(T_1)$ is the heat capacity computed from the NASA polynomials (Equations A.17 and A.20) at T_1 .

$$\hat{c}_{p,mix}^{frozen}(T) = \hat{c}_{p,1,mix}^{NASA}(T_1) \quad (\text{A.70})$$

A.5.3 Summary and demonstration

The following summarizes the methodology employed by FROSH in modeling vibrationally frozen shocks. For a FE (frozen-equilibrated) shock, Region 1 enthalpy and heat capacity are computed using the NASA polynomials, outlined in Equations A.17, A.18, A.20, and A.21. Region 2 enthalpy is computed by Equation A.69 at $T = T_2$, where the terms within are given in

Equations A.59, A.60, A.68, and the NASA polynomials. Region 2 heat capacity is given by Equation A.70. Region 5 enthalpy and heat capacity are computed using the NASA polynomials because vibrational equilibrium is assumed. For a FF (frozen-frozen) shock, Region 1 and Region 2 data are computed as in a FE shock, and Region 5 data are computed in the same way as for the FE Region 2 conditions. For a EE shock, only the NASA polynomials are used to compute enthalpy and heat capacities.

As a demonstration of the impact that vibrational equilibrium changes can have on computed conditions, the ratios of FE-to-EE and FF-to-EE Region 5 temperature and pressure have been plotted for shocks in an argon/oxygen mixture as a function of the oxygen mole fraction in the bath gas in Figure A.3. Oxygen, being a diatomic molecule, must undergo vibrational relaxation after encountering a shock wave; however, argon, as a monatomic, does not. Significant changes in calculated conditions can be observed for neat oxygen shocks. Therefore, for mixtures with a high oxygen content, it is critical to correctly identify the vibrational model most appropriate to the experiment.

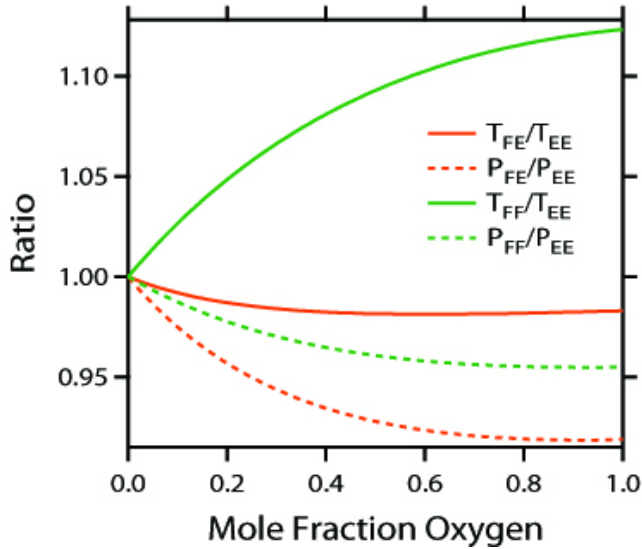


Figure A.3: Ratios of FE-to-EE and FF-to-EE Region 5 (translational) temperature and pressure for shocks in an argon/oxygen mixture. Initial conditions are $T_1 = 298.15$ K, $P_1 = 300$ Torr, and $U_{IS} = 1000$ m/s. Region 5 conditions for 100%Ar are $T_5 = 2304$ K and $P_5 = 20.7$ atm, and EE Region 5 conditions for 100%O₂ are $T_{5,trans} = 1288$ K and $P_5 = 22.1$ atm.

Figure A.3 does present one interesting result that should be clarified. One might expect that $T_{5,FE} > T_{5,EE}$ because the vibrationally frozen incident shock condition yields $T_{2,FE} > T_{2,EE}$; however, the opposite is observed. This may be understood at a high level using the ideal shock relationships set forth in Gaydon and Hurle [111] (Equations A.27, A.28, A.37, A.38, and A.39). The ratio $\frac{T_5}{T_2}$ increases with increasing γ and also increases with increasing $\frac{P_2}{P_1}$. Vibrational relaxation causes γ to decrease, such that $\gamma_{5,FF} > \gamma_{5,FE}$; in frozen shocks this promotes a higher T_5 value. Additionally, as mentioned above, for vibrationally frozen incident shocks, $T_{2,FF} = T_{2,FE} > T_{2,EE}$, which also promotes a higher T_5 value. However, the vibrationally frozen incident shock condition yields $P_{2,FF} = P_{2,FE} < P_{2,EE}$; in frozen shocks this promotes a lower T_5 value. These forces are conflicting, and the balance of power changes between FF and FE shocks. In the case of FF shocks, the fact that $\gamma_{5,FF} = \gamma_1 > \gamma_{5,EE}$ overwhelms the decrease in P_2 caused by the frozen incident shock condition, and the result is that $T_{5,FF} > T_{5,EE}$. In contrast, for FE shocks, $\gamma_{5,FE} = \gamma_{5,EE}$. The resulting competition over T_5 is that $T_{2,FE} > T_{2,EE}$ (working to increase T_5), but $P_{2,FE} < P_{2,EE}$ (working to decrease T_5). The latter factor dominates in FE shocks, and as a result $T_{5,FE} < T_{5,EE}$.

Finally, it should be noted that this code assumes that the rotational modes are completely excited at the Region 1 temperature T_1 . This is generally a good assumption, although there are a handful of exceptions. For example, hydrogen (H_2), a diatomic molecule with large rotational level spacing, has a true total heat capacity at constant volume of $\hat{c}_v = 2.4725\hat{R}_u$ rather than $\hat{c}_v = \frac{5}{2}\hat{R}_u$ at T_{ref} , as computed using the NASA polynomials. There are also other degrees of freedom for energy storage in molecules, notably electronic modes. One important example is nitric oxide (NO), whose electron in the anti-bonding molecular orbital has energy transitions contributing to heat capacity even at T_{ref} [447]. While the difference in calculated values under FE and FF conditions due to these anomalies might be small, it is important to be cognizant that such discrepancies exist.

A.6 Validation

It is important to compare numerical results with both theory and experiment in order to validate computational models. This section provides several theoretical comparisons, and will refer the

reader to References [292, 305, 346, 429] (see also Sections 7.7 and 9.3.5 in this work) that provide an in-depth comparison of FROSH's calculations to experimental shock tube results.

Figure A.4 shows the ratio of results from FROSH to those of Gaydon and Hurle [111] for various Mach numbers and a 10%O₂/Ar mixture. In this case, the numerical and analytical results agree well for weak shocks, though as shock strength (as indicated by Mach number) increases, the deviation is more significant. The difference between the analytical and numerical values is due to gaseous heat capacity; Gaydon and Hurle's relationships do not allow heat capacity to increase with temperature, while FROSH iterates in order to allow this to take place.

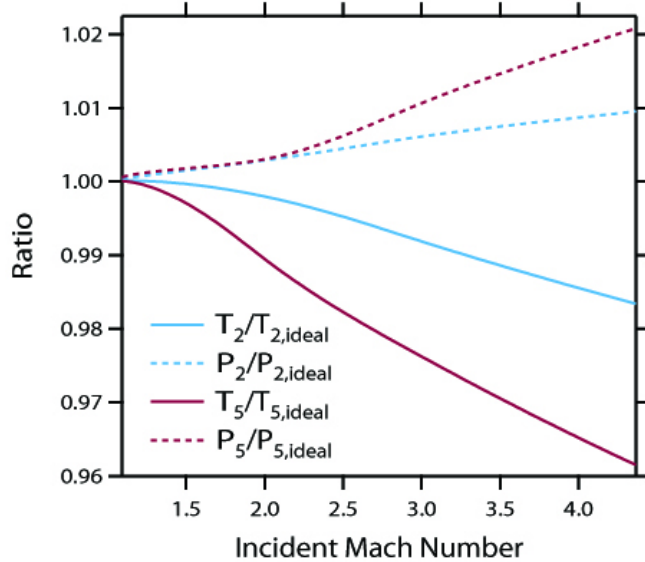


Figure A.4: Ratio of FROSH equilibrium-equilibrium Region 2 and 5 calculations to analytical (ideal shock) relation results of Gaydon and Hurle [111] for various Mach numbers and a 10%O₂/Ar mixture. Initial conditions are $T_1 = 298.15$ K, $P_1 = 30$ Torr. The slight bifurcation in Region 5 conditions at $M = 2.1$ occurs when the heat capacity of oxygen begins to increase with temperature at a slower rate at around $T = 945$ K.

A similar comparison of FROSH to another program, GasEq [127], is given in Figure A.5. Some differences in results exist, but these are very small and it appears that the codes agree quite well.

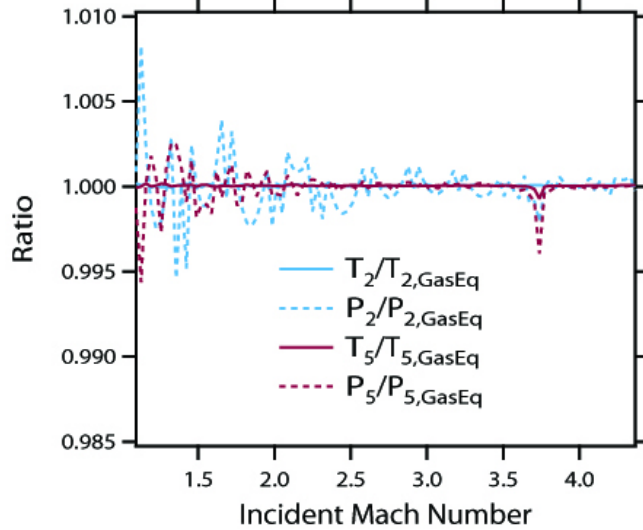


Figure A.5: Ratio of FROSH equilibrium-equilibrium Region 2 and 5 calculations to computations done in GasEq [127] for various Mach numbers and a 10%O₂/Ar mixture. Initial conditions are $T_1 = 298.15$ K, $P_1 = 30$ Torr. Though some discrepancies exists, these are insignificant and the two codes agree quite well.

A.7 Uncertainty analysis

As introduced in Section 4.11, uncertainty analyses are useful tools in determining accuracy of calculations. Typically these are conducted by changing input parameters and monitoring the change in important output results. Important inputs to FROSH and their associated uncertainties are reported in Table A.4. For simplicity, heat capacity and enthalpy values were assumed to change in the same direction (positive or negative) during one FROSH temperature/pressure calculation. Nominal Region 1 values used in this analysis were $T_1 = 300$ K, $P_1 = 200$ Torr, and $U_{IS} = 800$ m/s. An uncertainty in the fuel concentration of $\pm 4\%$ was also allowed. The test gas mixture was *n*-heptane/21%O₂/Ar ($\phi = 1.0$), and vibrational modes were assumed to be equilibrated in both Region 2 and Region 5 (EE). These initial conditions produce post-incident-shock conditions of $T_2 = 722$ K and $P_2 = 2.14$ atm, and post-reflected-shock conditions of $T_5 = 1179$ K and $P_5 = 9.27$ atm.

Table A.4: Inputs to FROSH and typical values for associated uncertainty.

Data	Units	Uncertainty
Region 1 temperature	K	± 1.1 K
Region 1 pressure	Torr	± 0.15 %
Incident shock velocity	m/s	± 0.2 %
NASA heat capacity	J/mol-K	± 0.5 %
NASA enthalpy	J/mol	± 0.5 %
Fuel mole fraction		± 4 %

The results of the uncertainty analysis on an input-by-input basis are shown graphically in Figures 4.8, and 4.9. These plots show the error induced in the specified output by individually perturbing each input in the positive direction by the amount of its maximum uncertainty. Using these values, a Root-of-Sum-of-Squares (RSS) analysis was performed according to Equation 4.42 (repeated below) in order to determine the combined uncertainty (here, ε_{RSS} is the RSS uncertainty, $\frac{\Delta R_m}{R}$ is the fractional change in the output result when input m is varied in the positive direction, and N is the number of inputs (in this case, $N = 5$)). In addition, results for all combinations of the input variables, perturbed in both positive and negative directions for a total of $2^5 = 32$ trials, were computed using an automated routine in order to determine the worst-case uncertainty. The results are provided in Table A.5 for T_2 , P_2 , T_5 , and P_5 . As expected, the worst-case uncertainty values are larger than those for the RSS analysis, since the RSS analysis does not consider second-order interactions between the input variables. Major contributors to T_5 uncertainty (RSS: $\pm 0.61\%$ overall) are x_{fuel} ($\pm 0.42\%$), the thermodynamic data (c_p and h ; $\pm 0.32\%$), and U_{IS} ($\pm 0.30\%$). Note that when thermodynamic polynomial data from the Burcat database [174] are employed, the actual uncertainty of the fits are specified therein, and are often much lower than the conservative 0.5% used in this analysis. Also, a spectroscopic fuel measurement in Region 1 of experiments can decrease the uncertainty associated with x_{fuel} . Furthermore, if more precise shock velocity determination techniques are employed, the temperature errors decrease still further. In summary, this uncertainty analysis shows that Region 2 and 5 conditions can be computed with a good degree of accuracy,

despite conservative estimates as to the uncertainty of FROSH input data.

$$\varepsilon_{RSS} = \sqrt{\sum_{m=1}^N \left(\frac{\Delta R_m}{R} \right)^2} \quad (4.42)$$

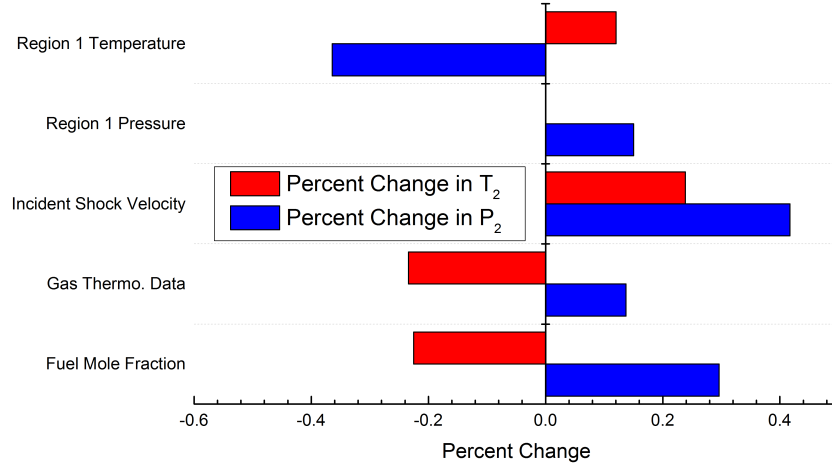


Figure A.6: Results of FROSH uncertainty analysis for T_2 and P_2 . Errors are shown for the case when the input listed is perturbed in the *positive* direction. Conditions: $T_2 = 722$ K, $P_2 = 2.14$ atm, $T_5 = 1179$ K, $P_5 = 9.27$ atm, n -heptane/21%O₂/Ar ($\phi = 1.0$).

Table A.5: Results of FROSH uncertainty analysis. The Root-of-Sum-of-Squares (RSS) analysis was conducted according to Equation 4.42, and the worst case analysis was conducted by perturbing all inputs simultaneously to find the maximum change in the output variable. Conditions: $T_2 = 722$ K, $P_2 = 2.14$ atm, $T_5 = 1179$ K, $P_5 = 9.27$ atm, n -heptane/21%O₂/Ar ($\phi = 1.0$).

Output Variable	Nominal Value	Root-of-Sum-of-Squares		Worst Case	
		%	Value	%	Value
T_2	722 K	$\pm 0.42\%$	± 3.038 K	$\pm 0.82\%$	± 5.923 K
P_2	2.14 atm	$\pm 0.66\%$	± 0.014 atm	$\pm 1.37\%$	± 0.029 atm
T_5	1179 K	$\pm 0.61\%$	± 7.212 K	$\pm 1.10\%$	± 13.00 K
P_5	9.27 atm	$\pm 1.10\%$	± 0.102 atm	$\pm 2.30\%$	± 0.213 atm

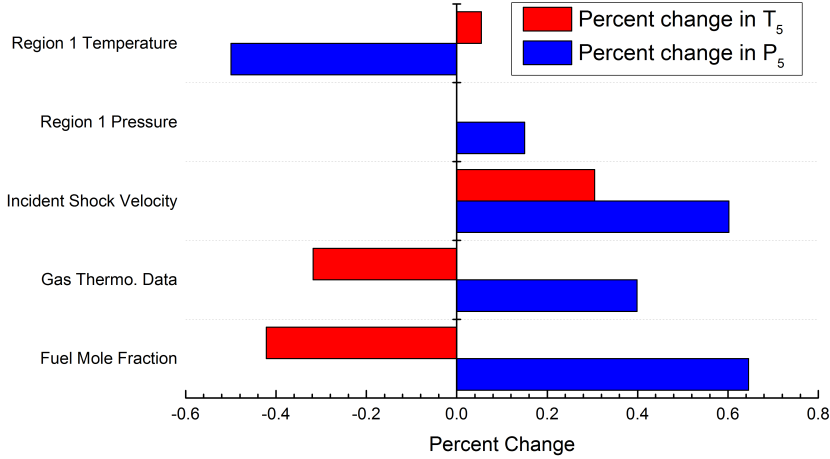


Figure A.7: Results of FROSH uncertainty analysis for T_5 and P_5 . Errors are shown for the case when the input listed is perturbed in the *positive* direction. Conditions: $T_2 = 722$ K, $P_2 = 2.14$ atm, $T_5 = 1179$ K, $P_5 = 9.27$ atm, *n*-heptane/21%O₂/Ar ($\phi = 1.0$).

A.8 Summary

A shock calculator for gaseous mixtures, FROSH, has been introduced. Algorithms to compute Region 2 and 5 conditions have been outlined and the problem of vibrational equilibration has been addressed. Validation based on previous numerical and analytical studies has been demonstrated, and several experimental studies that have validated post-shock temperature and pressure have been cited. An error analysis of the program showed that even with conservative estimates of input uncertainty, post-shock conditions can be computed with a good degree of accuracy. This code will prove useful for scientists wishing to perform accurate calculations of post-shock conditions for studies of kinetics and combustion.

A.9 Derivation of incident shock iteration equations

In this section, the iteration equations f_1 and f_2 (Equations A.29 and A.30), as well as their derivatives (Equations A.31 through A.34), will be explained and derived. While the ultimate expressions shown and related forms can be found in various publications [113, 124–126, 407],

the published journal literature disturbingly lacks an outlined derivation of them from fundamental principles. Thus, in this appendix, these quantities have been derived from basic conservation relations and are presented below.

In a two-dimensional Newton-Raphson scheme, two equations must be chosen and their absolute values minimized in order to numerically solve for the two unknowns. Since mass, momentum, and energy are conserved across a shock wave, a natural choice is to choose two of these relationships, subtract terms in order to equate each to zero, and minimize the two resulting equations. Any two of the three conservation equations may be chosen, but as shown below the momentum and energy equations are favorable.

In order to minimize the two iteration equations, derivatives in the two iteration variables must be computed. Three classes of derivatives can be identified. The first is between pre- and post-shock variables, for example $\left(\frac{\partial v_1}{\partial P_2}\right)_{T_2}$ or $\left(\frac{\partial u_1}{\partial T_2}\right)_{P_2}$. These derivatives are all zero, because the pre-shock properties are constant.

The second is between post-shock variables that are related by the equation of state or ideal gas relationships, for example $\left(\frac{\partial v_2}{\partial P_2}\right)_{T_2}$ or $\left(\frac{\partial h_2}{\partial T_2}\right)_{P_2}$. In this case, such derivatives can be easily found, as detailed later in this section.

The third case is the partial derivative of post-shock velocity in terms of post-shock pressure or temperature, *e.g.*, $\left(\frac{\partial u_2}{\partial P_2}\right)_{T_2}$ or $\left(\frac{\partial u_2}{\partial T_2}\right)_{P_2}$. These quantities are quite difficult to determine alone, but fortunately the conservation of mass relation (Equation 4.1) can recast these derivatives in terms of pre-shock velocity, and pre-and post-shock density. Such partial derivatives can then easily be computed.

As a result of needing the conservation of mass relation to compute partial derivatives of post-shock velocity, the best choice of equations to minimize (f_1 and f_2) are derived from the conservation of momentum and energy relations (Equations 4.2 and 4.3).

One more numerical choice is of note before proceeding. The quantities contained within the minimization equations can often be quite large. Historically, subtracting two large numbers in a numerical algorithm was unwise because finite machine precision occasionally resulted in loss of information. Thus it has become commonplace to take ratios of large quantities rather than directly subtract them. This convention has been upheld in the algorithms presented here. For example,

rather than subtract pre- from post-shock pressure, the two are divided and compared to unity.

With these considerations in mind, f_1 is obtained as follows from the momentum conservation equation (Equation 4.2). First, the mass conservation equation (Equation 4.1) is used to substitute for u_2^2 and recast the equation in terms of only velocity u_1 .

$$P_1 + \rho_1 u_1^2 = P_2 + \rho_2 u_2^2 \quad (\text{A.71})$$

$$P_1 + \rho_1 u_1^2 = P_2 + u_1^2 \frac{\rho_1^2}{\rho_2} \quad (\text{A.72})$$

The result is divided by P_1 , then the terms are rearranged and equated to zero.

$$1 + \frac{\rho_1 u_1^2}{P_1} = \frac{P_2}{P_1} + \frac{u_1^2 \rho_1^2}{P_1 \rho_2} \quad (\text{A.73})$$

$$0 = \frac{P_2}{P_1} - 1 + \frac{u_1^2 \rho_1^2}{P_1 \rho_2} - \frac{\rho_1 u_1^2}{P_1} \quad (\text{A.74})$$

Finally, the equation is factored and specific volume v is substituted for inverse density $\frac{1}{\rho}$, yielding the final expression (Equation A.29).

$$f_1 = 0 = \left(\frac{P_2}{P_1} - 1 \right) + \left(\frac{u_1^2}{P_1 v_1} \right) \left(\frac{v_2}{v_1} - 1 \right) \blacksquare \quad (\text{A.29})$$

Likewise, f_2 is derived by the following method. The conservation of energy relation (Equation 4.3) is first divided by $\frac{1}{2}u_1^2$.

$$h_1 + \frac{1}{2}u_1^2 = h_2 + \frac{1}{2}u_2^2 \quad (\text{A.75})$$

$$\frac{h_1}{\frac{1}{2}u_1^2} + 1 = \frac{h_2}{\frac{1}{2}u_1^2} + \frac{u_2^2}{u_1^2} \quad (\text{A.76})$$

Next, all the terms are rearranged, factored, and equated to zero.

$$0 = \left(\frac{h_2 - h_1}{\frac{1}{2}u_1^2} \right) + \left(\frac{u_2^2}{u_1^2} - 1 \right) \quad (\text{A.77})$$

Equation 4.1 (mass conservation) is used to transform the ratio of squared velocities into a ratio

of squared densities.

$$0 = \left(\frac{h_2 - h_1}{\frac{1}{2}u_1^2} \right) + \left(\frac{\rho_1^2}{\rho_2^2} - 1 \right) \quad (\text{A.78})$$

Finally, specific volume v is substituted for inverse density $\frac{1}{\rho}$, yielding the final expression (Equation A.29).

$$f_2 = 0 = \left(\frac{h_2 - h_1}{\frac{1}{2}u_1^2} \right) + \left(\frac{v_2^2}{v_1^2} - 1 \right) \quad \blacksquare \quad (\text{A.30})$$

The partial derivatives of f_1 and f_2 are obtained by differentiating the equation of state (Equation 4.4). Five partial derivatives are necessary: $\left(\frac{\partial v_2}{\partial P_2} \right)_{T_2}$, $\left(\frac{\partial v_2}{\partial T_2} \right)_{P_2}$, $\left(\frac{\partial P_2}{\partial T_2} \right)_{P_2}$, $\left(\frac{\partial h_2}{\partial T_2} \right)_{P_2}$, and $\left(\frac{\partial h_2}{\partial P_2} \right)_{T_2}$. These quantities will be presented first, and after this introduction they will be applied to the partial derivatives of f_1 and f_1 .

To achieve $\left(\frac{\partial v_2}{\partial P_2} \right)_{T_2}$, the ideal gas equation is expressed in terms of v_2 . Next, the partial derivative in P_2 holding T_2 constant is taken, and the ideal gas expression for v_2 is employed to simplify the result. This yields the desired quantity (Equation A.81).

$$v_2 = \frac{R_{g,2}T_2}{P_2} \quad (\text{A.79})$$

$$\left(\frac{\partial v_2}{\partial P_2} \right)_{T_2} = -\frac{R_{g,2}T_2}{P_2^2} \quad (\text{A.80})$$

$$\left(\frac{\partial v_2}{\partial P_2} \right)_{T_2} = -\frac{v_2}{P_2} \quad \blacksquare \quad (\text{A.81})$$

Achieving $\left(\frac{\partial v_2}{\partial T_2} \right)_{P_2}$ is done in largely the same manner (Equation A.84). The ideal gas equation is again expressed in terms of v_2 , and the partial derivative in T_2 holding P_2 constant is computed. Then, the ideal gas equation is used again to simplify the expression because $\frac{R_{g,2}}{P_2} = \frac{v_2}{T_2}$.

$$v_2 = \frac{R_{g,2}T_2}{P_2} \quad (\text{A.82})$$

$$\left(\frac{\partial v_2}{\partial T_2} \right)_{P_2} = \frac{R_{g,2}}{P_2} \quad (\text{A.83})$$

$$\left(\frac{\partial v_2}{\partial T_2} \right)_{P_2} = \frac{v_2}{T_2} \quad \blacksquare \quad (\text{A.84})$$

The next three partial derivatives are much simpler to determine. Equation A.85 is trivial.

$$\left(\frac{\partial P_2}{\partial T_2}\right)_{P_2} = 0 \quad \blacksquare \quad (\text{A.85})$$

The derivative of Region 2 enthalpy h_2 in Region 2 temperature T_2 at constant P_2 is, for ideal gases, the heat capacity at constant pressure $c_{p,2}$ (Equation A.86).

$$\left(\frac{\partial h_2}{\partial T_2}\right)_{P_2} = c_{p,2} \quad \blacksquare \quad (\text{A.86})$$

Finally, for ideal gases, enthalpy is a function of temperature only. Thus, the change in enthalpy with pressure at constant temperature is zero (Equation A.87).

$$\left(\frac{\partial h_2}{\partial P_2}\right)_{T_2} = 0 \quad \blacksquare \quad (\text{A.87})$$

With these partial derivatives in hand, the necessary partial derivatives of f_1 and f_2 can be determined. To achieve $\left(\frac{\partial f_1}{\partial P_2}\right)_{T_2}$, f_1 is first differentiated by P_2 , noting that specific volume v_2 depends on P_2 . This expression is then factored and simplified into its final form in Equation A.31.

$$\left(\frac{\partial f_1}{\partial P_2}\right)_{T_2} = \frac{1}{P_2} + \left(\frac{u_1^2}{P_1 v_1}\right) \left(\frac{1}{v_1}\right) \left(\frac{\partial v_2}{\partial P_2}\right)_{T_2} \quad (\text{A.88})$$

$$= \left(\frac{1}{P_1}\right) + \left(\frac{u_1^2}{P_1 v_1^2}\right) \left(\frac{-v_2}{P_2}\right) \quad \blacksquare \quad (\text{A.31})$$

$\left(\frac{\partial f_1}{\partial T_2}\right)_{P_2}$ is obtained by first differentiating f_2 by T_2 . The result is simplified using the partial derivative relationships $\left(\frac{\partial P_2}{\partial T_2}\right)_{P_2} = 0$ and $\left(\frac{\partial v_2}{\partial T_2}\right)_{P_2} = \frac{v_2}{T_2}$, yielding Equation A.32.

$$\left(\frac{\partial f_1}{\partial T_2}\right)_{P_2} = \frac{1}{P_2} \left(\frac{\partial P_2}{\partial T_2}\right)_{P_2} + \left(\frac{u_1^2}{P_1 v_1}\right) \left(\frac{1}{v_1}\right) \left(\frac{\partial v_2}{\partial T_2}\right)_{P_2} \quad (\text{A.89})$$

$$= 0 + \left(\frac{u_1^2}{P_1 v_1^2}\right) \left(\frac{v_2}{T_2}\right) \quad \blacksquare \quad (\text{A.32})$$

Equation A.33 $\left(\left(\frac{\partial f_2}{\partial P_2}\right)_{T_2}\right)$ is obtained by differentiating f_2 by P_2 . The result is simplified

using the ideal gas partial derivatives computed above.

$$\left(\frac{\partial f_2}{\partial P_2} \right)_{T_2} = \frac{1}{\frac{1}{2}u_1^2} \left(\frac{\partial h_2}{\partial P_2} \right)_{T_2} + \frac{2v_2}{v_1^2} \left(\frac{\partial v_2}{\partial P_2} \right)_{T_2} \quad (\text{A.90})$$

$$= 0 + \left(\frac{2v_2}{v_1^2} \right) \left(\frac{-v_2}{P_2} \right) \quad \blacksquare \quad (\text{A.33})$$

Finally, the partial derivative of f_2 in T_2 (Equation A.34) is obtained by computing this derivative and simplifying the expression using partial derivative expressions for $\left(\frac{\partial h_2}{\partial T_2} \right)_{P_2}$ and $\left(\frac{\partial v_2}{\partial T_2} \right)_{P_2}$.

$$\left(\frac{\partial f_2}{\partial T_2} \right)_{P_2} = \frac{1}{\frac{1}{2}u_1^2} \left(\frac{\partial h_2}{\partial T_2} \right)_{P_2} + \frac{2v_2}{v_1^2} \left(\frac{\partial v_2}{\partial T_2} \right)_{P_2} \quad (\text{A.91})$$

$$= \left(\frac{2}{u_1^2} \right) c_{p,2} + \left(\frac{2v_2}{v_1^2} \right) \left(\frac{v_2}{T_2} \right) \quad \blacksquare \quad (\text{A.34})$$

Thus, the incident shock iteration equations have been derived.

A.10 Derivation of reflected shock iteration equations

In this section, the iteration equations f_3 and f_4 (Equations A.40 and A.41), as well as their derivatives (Equations A.42 through A.45), will be derived. As in f_1 and f_2 , the momentum and energy conservation equations will serve as the basis for these expressions. Expressions for U_{RS} and u'_2 in terms of known quantities are necessary to arrive at this end. Furthermore, a relationship between the four shock-frame velocities, u_1 , u_2 , u_5 , and u'_2 , is needed. These expressions will be derived first, and following this explanation the former quantities will be determined.

The relationship between the four shock-frame velocities is simple to obtain. First, Equation A.6 is solved for U_2 , and Equation A.5 is substituted into this result for U_{IS} .

$$U_2 = U_{IS} - u_2 \quad (\text{A.92})$$

$$= u_1 - u_2 \quad (\text{A.93})$$

Next, Equation A.10 is inserted into Equation A.7. Finally, the expression above for U_2 is

exchanged into the result below, yielding u'_2 in terms of u_1 , u_2 , and u_5 (Equation A.50).

$$u'_2 = U_{RS} + U_2 \quad (\text{A.94})$$

$$= u_5 + U_2 \quad (\text{A.95})$$

$$= u_5 + u_1 - u_2 \quad \blacksquare \quad (\text{A.50})$$

To obtain U_{RS} , the mass conservation expression (Equation 4.1) is applied across the reflected shock wave. Next, Equation A.50 is substituted for u'_2 .

$$\rho_5 u_5 = \rho_2 u'_2 \quad (\text{A.96})$$

$$= \rho_2 (u_5 + u_1 - u_2) \quad (\text{A.97})$$

The u_5 terms are moved to the left hand side of the equation, and the result is factored.

$$\rho_5 u_5 - \rho_2 u_5 = \rho_2 (u_1 - u_2) \quad (\text{A.98})$$

$$u_5 (\rho_5 - \rho_2) = \quad (\text{A.99})$$

Finally, the equation is solved for u_5 , and the stagnation condition (Equation A.10) is employed to equate the result to U_{RS} (Equation A.49).

$$u_5 = U_{RS} = \frac{\rho_2}{\rho_5 - \rho_2} (u_1 - u_2) \quad \blacksquare \quad (\text{A.49})$$

u'_2 can be obtained in a similar manner, or, more simply, from the continuity equation combined with Equation A.49 above. Applying mass conservation across the reflected shock and substituting Equation A.49 for u_5 yields the desired result in Equation A.102.

$$\rho_2 u'_2 = \rho_5 u_5 \quad (\text{A.100})$$

$$= \rho_5 \frac{\rho_2}{\rho_5 - \rho_2} (u_1 - u_2) \quad (\text{A.101})$$

$$u'_2 = \frac{\rho_5}{\rho_5 - \rho_2} (u_1 - u_2) \quad \blacksquare \quad (\text{A.102})$$

With these results in hand, the iteration functions f_3 and f_4 can be found. To obtain f_3 , momentum conservation is applied across the reflected shock. The resulting expression is divided by P_2 and equated to zero.

$$P_2 + \rho_2 (u'_2)^2 = P_5 + \rho_5 u_5^2 \quad (\text{A.103})$$

$$1 + \frac{\rho_2}{P_2} (u'_2)^2 = \frac{P_5}{P_2} + \frac{\rho_5}{P_2} u_5^2 \quad (\text{A.104})$$

$$0 = \left(\frac{P_5}{P_2} - 1 \right) + \frac{\rho_5}{P_2} u_5^2 - \frac{\rho_2}{P_2} (u'_2)^2 \quad (\text{A.105})$$

Next, expressions for u_5^2 and $(u'_2)^2$ from Equations A.49 and A.102 are substituted into the equation, and terms are collected.

$$0 = \left(\frac{P_5}{P_2} - 1 \right) + \frac{\rho_5}{P_2} \left(\frac{\rho_2}{\rho_5 - \rho_2} \right)^2 (u_1 - u_2)^2 - \frac{\rho_2}{P_2} \left(\frac{\rho_5}{\rho_5 - \rho_2} \right)^2 (u_1 - u_2)^2 \quad (\text{A.106})$$

$$= \left(\frac{P_5}{P_2} - 1 \right) - \frac{1}{P_2} (u_1 - u_2)^2 \frac{\rho_2 \rho_5}{(\rho_5 - \rho_2)^2} (\rho_5 - \rho_2) \quad (\text{A.107})$$

$$= \left(\frac{P_5}{P_2} - 1 \right) - \frac{1}{P_2} (u_1 - u_2)^2 \frac{\rho_2 \rho_5}{\rho_5 - \rho_2} \quad (\text{A.108})$$

The final expression for f_3 is obtained by noting that $\frac{\rho_2 \rho_5}{\rho_5 - \rho_2} = \frac{-1}{v_5 - v_2}$ (Equation A.40).

$$f_3 = 0 = \left(\frac{P_5}{P_2} - 1 \right) + \left(\frac{(u_1 - u_2)^2}{P_2 (v_5 - v_2)} \right) \blacksquare \quad (\text{A.40})$$

f_4 is derived beginning with the energy conservation equation applied across the reflected shock. The equation is then rearranged and equated to zero.

$$h_2 + \frac{1}{2} (u'_2)^2 = h_5 + \frac{1}{2} u_5^2 \quad (\text{A.109})$$

$$0 = (h_5 - h_2) + \frac{1}{2} u_5^2 - \frac{1}{2} (u'_2)^2 \quad (\text{A.110})$$

Once again the expressions for u_5^2 and $(u'_2)^2$ from Equations A.49 and A.102 are applied, and

the terms are gathered and simplified.

$$0 = (h_5 - h_2) + \frac{1}{2} \left(\frac{\rho_2}{\rho_5 - \rho_2} \right)^2 (u_1 - u_2)^2 - \frac{1}{2} \left(\frac{\rho_5}{\rho_5 - \rho_2} \right)^2 (u_1 - u_2)^2 \quad (\text{A.111})$$

$$= \frac{h_5 - h_2}{\frac{1}{2} (u_1 - u_2)^2} + \frac{\rho_2^2 - \rho_5^2}{(\rho_5 - \rho_2)^2} \quad (\text{A.112})$$

The final expression is obtained by realizing that $\frac{\rho_2^2 - \rho_5^2}{(\rho_5 - \rho_2)^2} = \frac{v_5 + v_2}{v_5 - v_2}$ (Equation A.41).

$$f_4 = \left(\frac{h_5 - h_2}{\frac{1}{2} (u_1 - u_2)^2} \right) + \left(\frac{v_5 + v_2}{v_5 - v_2} \right) \blacksquare \quad (\text{A.41})$$

Derivatives of f_3 and f_4 are obtained by the same method as in f_1 and f_2 . The ideal gas partial derivatives in Region 2 have parallels in Region 5, as shown below (Equations A.113 through A.117).

$$\left(\frac{\partial v_5}{\partial P_5} \right)_{T_5} = -\frac{v_5}{P_5} \blacksquare \quad (\text{A.113})$$

$$\left(\frac{\partial v_5}{\partial T_5} \right)_{P_5} = \frac{v_5}{T_5} \blacksquare \quad (\text{A.114})$$

$$\left(\frac{\partial P_5}{\partial T_5} \right)_{P_5} = 0 \blacksquare \quad (\text{A.115})$$

$$\left(\frac{\partial h_5}{\partial T_5} \right)_{P_5} = c_{p,5} \blacksquare \quad (\text{A.116})$$

$$\left(\frac{\partial h_5}{\partial P_5} \right)_{T_5} = 0 \blacksquare \quad (\text{A.117})$$

The partial derivative of f_3 in P_2 is obtained by computing this derivative and simplifying using Equation A.113.

$$\left(\frac{\partial f_3}{\partial P_5} \right)_{T_5} = \frac{1}{P_2} - \frac{(u_1 - u_2)^2}{P_2 (v_5 - v_2)^2} \left(\frac{\partial v_5}{\partial P_5} \right)_{T_5} \quad (\text{A.118})$$

$$= \left(\frac{1}{P_2} \right) + \left(\frac{-(u_1 - u_2)^2}{P_2 (v_5 - v_2)^2} \right) \left(\frac{-v_5}{P_5} \right) \blacksquare \quad (\text{A.42})$$

Similarly, $\left(\frac{\partial f_3}{\partial T_5}\right)_{P_5}$ can be found by differentiating f_3 in T_5 , and simplifying according to Equation A.113.

$$\left(\frac{\partial f_3}{\partial T_5}\right)_{P_5} = \frac{1}{P_2} \left(\frac{\partial P_5}{\partial T_5}\right)_{T_5} - \frac{(u_1 - u_2)^2}{P_2 (v_5 - v_2)^2} \left(\frac{\partial v_5}{\partial T_5}\right)_{P_5} \quad (\text{A.119})$$

$$= 0 + \left(\frac{-(u_1 - u_2)^2}{P_2 (v_5 - v_2)^2}\right) \left(\frac{v_5}{T_5}\right) \quad \blacksquare \quad (\text{A.43})$$

Obtaining $\left(\frac{\partial f_4}{\partial P_5}\right)_{T_5}$ is accomplished by computing this derivative according to the product differentiation rule, then substituting the appropriate simplifying ideal gas partial derivative expressions.

$$\left(\frac{\partial f_4}{\partial P_5}\right)_{T_5} = \frac{1}{\frac{1}{2}(u_1 - u_2)^2} \left(\frac{\partial h_5}{\partial P_5}\right)_{T_5} - \frac{v_5 - v_2}{(v_5 - v_2)^2} \left(\frac{\partial v_5}{\partial P_5}\right)_{T_5} + \frac{1}{v_5 - v_2} \left(\frac{\partial v_5}{\partial P_5}\right)_{T_5} \quad (\text{A.120})$$

$$= 0 - \frac{v_5 - v_2}{(v_5 - v_2)^2} \frac{-v_5}{P_5} + \frac{1}{v_5 - v_2} \frac{-v_5}{P_5} \quad (\text{A.121})$$

$$\left(\frac{\partial f_4}{\partial P_5}\right)_{T_5} = \left(\frac{-2v_2}{(v_5 - v_2)^2}\right) \left(\frac{-v_5}{P_5}\right) \quad \blacksquare \quad (\text{A.44})$$

Finally, $\left(\frac{\partial f_4}{\partial T_5}\right)_{P_5}$ can be found by computing this derivative, again with the product rule, substituting partial derivatives, and simplifying.

$$\left(\frac{\partial f_4}{\partial T_5}\right)_{P_5} = \frac{1}{\frac{1}{2}(u_1 - u_2)^2} \left(\frac{\partial h_5}{\partial T_5}\right)_{P_5} - \frac{v_5 - v_2}{(v_5 - v_2)^2} \left(\frac{\partial v_5}{\partial T_5}\right)_{P_5} + \frac{1}{v_5 - v_2} \left(\frac{\partial v_5}{\partial T_5}\right)_{P_5} \quad (\text{A.122})$$

$$= \frac{1}{\frac{1}{2}(u_1 - u_2)^2} c_{p,5} - \frac{v_5 - v_2}{(v_5 - v_2)^2} \frac{v_5}{T_5} + \frac{1}{v_5 - v_2} \frac{v_5}{T_5} \quad (\text{A.123})$$

$$\left(\frac{\partial f_4}{\partial T_5}\right)_{P_5} = \left(\frac{1}{\frac{1}{2}(u_1 - u_2)^2}\right) c_{p,5} + \left(\frac{-2v_2}{(v_5 - v_2)^2}\right) \left(\frac{v_5}{T_5}\right) \quad \blacksquare \quad (\text{A.45})$$

Thus, the reflected shock iteration equations have been derived.

Appendix B

Lab and particle time

B.1 Introduction

During Region 2 in a shock experiment, gas is being swept past the observation location. The gas that was situated at the test location at the beginning of Region 2 is compressed closer to the endwall by the end of Region 2 (see Section 2.3). Likewise, gas that is ultimately swept down to the test location and stagnated there by the reflected shock (at the end of Region 2) originated much further away from the endwall. This implies that in Region 2, the particle-frame time (that experienced by the gas in the tube) is different to the lab-frame time (that observed by a measurement device fixed to the side of the shock tube).

The difference between lab and particle time has important ramifications. Namely, in aerosol shocks, droplet evaporation times measured during Region 2 must be scaled from the observed lab time into the actual particle time. Also, when using chemical kinetic mechanisms to verify that no fuel decomposition/chemistry occurs in Region 2, the simulation duration must be governed by the particle time, rather than observed lab time.

Fortunately, a simple correction (Equation A.11, derived below) can be used to translate particle time into lab time, and vice versa. This derivation follows that originally set forth by Haylett [162].

B.2 Derivation

Begin by considering Figure B.1, which shows ideal (non-attenuating) shock waves, a particle path, and the measurement location (the cartoon is drawn to best show the distances and times discussed and is not to scale). Traveling at lab-frame velocity U_{IS} , the incident shock hits a particle beginning a distance d from the measurement location and accelerates it to lab-frame velocity U_2 toward the endwall. Ultimately the particle is stagnated at the measurement location by the reflected shock.

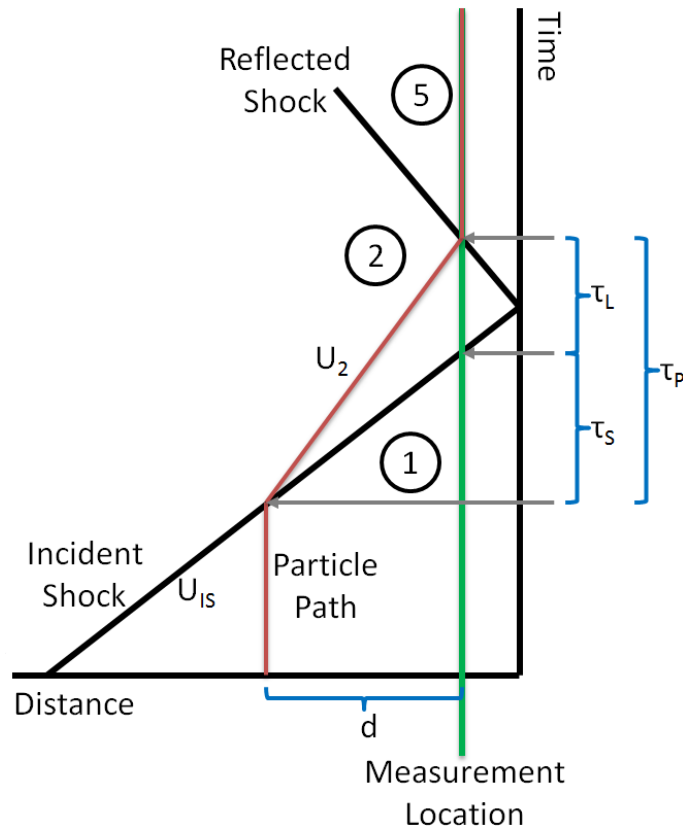


Figure B.1: Explanation of terms used in the derivation of the relationship between lab and particle time. After encountering the incident shock traveling at lab-frame velocity U_{IS} , a particle travels at lab-frame velocity U_2 a distance d to the measurement location, where three time intervals, τ_L , τ_S , and τ_P can be identified.

Three time intervals can be identified: τ_P is the time taken by the particle to travel distance d ,

τ_S is the time between the incident shock encountering the particle and the incident shock reaching the measurement location a distance d away, and τ_L is the time seen from a lab reference frame between the incident shock wave passing and the particle reaching the measurement location (and of course being stagnated by the reflected shock).

Naturally, the sum of lab time interval τ_L and shock time interval τ_S is the particle time interval, τ_P :

$$\tau_P = \tau_L + \tau_S \quad (\text{B.1})$$

The distance d can be expressed in terms of the velocities and time intervals involved.

$$d = U_2 \tau_P = U_{IS} \tau_S = U_{IS} (\tau_P - \tau_L) \quad (\text{B.2})$$

Recalling from Equation A.5 that $u_1 = U_{IS}$ and from a rearrangement of Equation A.6 that $U_2 = U_{IS} - u_2$, it follows that the ratio of lab and particle time intervals can be expressed as a ratio of shock-frame velocities before and after the incident shock.

$$\frac{\tau_P}{\tau_L} = \frac{u_1}{u_2} \quad (\text{B.3})$$

Invoking the continuity equation (Equation 4.1) gives the final expression for particle time in terms of lab time (Equation A.11).

$$\frac{t_{particle}}{t_{lab}} = \frac{\rho_2}{\rho_1} \quad \blacksquare \quad (\text{A.11})$$

B.3 Summary

The relationship between lab and particle time (Equation A.11) has been derived. This equation will allow better understanding of shock wave gasdynamics and of the interaction between shock waves and evaporating aerosols. It will also allow greater confidence in the frozen chemistry assumption employed by the FROSH and AEROFROSH algorithms.

Appendix C

Droplet properties

C.1 Introduction

Droplet curvature causes the properties of liquids in droplet (aerosol) form to differ from those of the liquid in bulk form. Fortunately, thermodynamics can be used to determine the extent of these property changes. In this section, these effects are discussed.

C.2 Literature review

It is well known that the properties of a fluid within a spherical droplet are different to the properties of that fluid in bulk form (*e.g.*, in a beaker). Multiple studies, both numerical and experimental, have been performed to quantify these changes. Importantly, nearly all papers in the literature employ the assumption that droplets are perfectly spherical, due to the strong surface tension forces present in micron-sized liquid droplets.

Laplace developed a relationship relating the interface pressure increase across a droplet surface to the surface tension of that drop (this is sometimes attributed to Kelvin). Gibbs extended this theory by realizing that surface tension was dependent on droplet radius, and Tolman set forth a method for determining the radius dependence of that surface tension [448–450]. Tolman’s results show that surface tension decreases as droplet diameter decreases, but the effect is not appreciable unless droplet diameters approach the order of several Angstroms. Hemingway and Hadjiagapiou

produced more detailed analyses of these effects [451, 452].

Crowe conducted an energy balance on a droplet, adjusting the energy of the fluid from its original enthalpy value by including terms for kinetic energy and surface energy [453]; see also Reference [205]. The terminal velocity of a droplet, necessary to compute the kinetic energy in Crowe's expression, can be obtained by applying Stokes flow to the droplet (see Section 3.6) [184, 185].

Gibbs and Thompson developed a relationship between droplet radius and an increase in vapor pressure of that droplet; a similar effect for the increase of vapor pressure of a fluid in the presence of a non-condensable (*i.e.*, noble) gas was developed by Poynting [454]. (Young and Guha chose to ignore these effects on vapor pressure and enthalpy in their analysis of shocks in aerosols [202].) Kelvin and Helmholtz developed an expression specifying the difference in vapor or droplet temperature from the saturation temperature for the case where aerosol droplets are formed via nucleation from a saturated vapor. (Young and Guha also found this effect to be very small [202]; see also Reference [455].)

The sound speed in an aerosol is different to in a pure gas, and extensive theoretical work has been undertaken to quantify the change. Wood reported an expression for the speed of sound propagating through an aerosol [456]. This expression was subsequently critiqued by a number of authors, notably Temkin and Chu, who improved the model and identified two limiting cases where the frequency-dependent sound speed in an aerosol can easily and reliably be determined [214–217]. The first is the equilibrium (low-frequency) limit where thermodynamic equilibrium can always be applied, and the second is the so-called frozen (high-frequency) limit where suspended particles are essentially at rest. In general, the frozen sound speed is higher than the equilibrium sound speed. Between these two limits lies the actual speed of sound for the mixture. See Section 4.6.2 for more details concerning the speed of sound in aerosols.

C.3 Thermodynamic expressions

C.3.1 Surface tension and density

The surface tension is known to be a function of droplet diameter (surface tension decreases as droplet diameter decreases), but the difference from bulk surface tension is only relevant for particles on the order of several Angstroms [450]. The fluid density is not known to change significantly with droplet radius; thus an incompressible fluid approximation is appropriate.

C.3.2 Total energy

The total energy of a droplet e_{drop} includes the fluid enthalpy at its temperature and pressure, the droplet's kinetic energy of motion, and its surface energy [453]. This can be written on a unit-mass basis in Equation C.1, where h_{drop} is the droplet enthalpy at the droplet temperature and pressure, $u_{terminal}$ is the terminal velocity of the droplet, $A_{surface} = \pi d^2$ is the droplet surface area for a droplet with diameter d , and $m_{drop} = \frac{1}{6}\pi d^3 \rho_{drop}$ is the mass of a droplet with density ρ_{drop} .

$$e_{drop} = h_{drop} + \frac{1}{2} u_{terminal}^2 + \varsigma \frac{A_{surface}}{m_{drop}} \quad (\text{C.1})$$

In a stagnant mixture, the net motion of particles is downward due to gravity, and the particles' terminal velocity can be computed by balancing forces of gravity and drag (see Section 3.6) [184, 185]. Applying this concept, and the incompressible liquid assumption in order to realize the pressure dependence of the liquid enthalpy, the equation can be written in terms of more fundamental variables (Equation C.2).

$$e_{drop} = (h_{bulk} + v_{drop} (P_{drop} - P_{ref})) + \frac{1}{2} \left(\frac{\mu_{gas} Re}{\rho_{gas} d} \right)^2 + \frac{6\varsigma}{\rho_{drop} d} \quad (\text{C.2})$$

In this new form, h_{bulk} is the enthalpy of the bulk fluid at the droplet temperature T_{drop} and the reference pressure P_{ref} , v_{drop} is the droplet's specific volume, μ_{gas} is the carrier gas dynamic viscosity, Re is the Reynolds number for the flow around the spherical droplet, ρ_{gas} is the carrier gas density, and ς is the bulk fluid surface tension.

C.3.3 Inner-droplet pressure

The pressure inside a droplet P_{drop} relative to the carrier gas pressure P_{gas} can be described by Laplace's law, expressed in Equation C.3 [452].

$$P_{drop} = P_{gas} + \frac{4\varsigma}{d} \quad (\text{C.3})$$

C.3.4 Vapor pressure

Droplet vapor pressure $P_{vap,drop}$ can be described relative to bulk vapor pressure $P_{vap,bulk}$ by the Gibbs-Thompson effect (Equation C.4).

$$P_{vap,drop} = P_{vap,bulk} \left(\exp \left(\frac{4\varsigma}{\rho_{drop} R_{g,fuel} T d} \right) \right) \quad (\text{C.4})$$

The vapor pressure of a fluid $P_{vap,incond}$ in the presence of a non-condensable gas of total pressure P_{total} can be described by the Poynting effect (Equation C.5) [454].

$$P_{vap,incond} = P_{vap,bulk} \left(\exp \left(\frac{1}{\rho_{drop} R_{g,fuel} T} (P_{total} - P_{vap,bulk}) \right) \right) \quad (\text{C.5})$$

In these equations, $R_{g,fuel}$ is the gas constant for the fuel vapor, *i.e.*, $R_{g,fuel} = \frac{\hat{R}_u}{\hat{M}_{fuel}}$.

C.3.5 Droplet temperature

When droplets are formed via nucleation from a saturated vapor, the temperature of the droplets and their vapor T_{act} differs from their saturation temperature T_{sat} according to the Kelvin-Helmholtz expression in Equation C.6.

$$T_{act} = T_{sat} \left(1 - \frac{4\varsigma}{\rho_{drop} h_{fg} d} \right) \quad (\text{C.6})$$

Here, h_{fg} is the enthalpy of vaporization at T_{sat} [202]. This effect is quite small, and ultimately the temperature of the droplet and vapor will relax to the saturation temperature.

C.3.6 Sound speed

A discussion of the sound speed in aerosols is provided in Section 4.6.2. Especially relevant are Equations 4.6 through 4.9.

C.4 Results

Clearly, aerosol droplets have properties that are different to those of their bulk fluid. This has implications for calculations of conditions following shock-heating of aerosols. If changes due to droplet curvature are less significant than other uncertainties in the shock condition calculation (for example, the uncertainty in incident shock velocity), the properties of aerosol droplets may be approximated by the properties of the bulk fluid. If, however, changes are significant, these changes must be taken into account. Droplet properties are normally correlated with their diameter, and the diameters of individual aerosol droplets can often be described by a lognormal distribution (Equation 3.26) [151, 186–188]. Properties of these distributions can be derived using laser diagnostics or scattering techniques [151], but characterizing these reliably can be difficult. Therefore, it would be convenient if the changes in droplet properties from bulk fluid properties were small; indeed this is what the following analysis will show.

An analysis was conducted to investigate the importance of these effects for an aerosol composed of methyl decanoate droplets ($C_{11}H_{22}O_2$) in argon with a nominal temperature and pressure of 298.15 K and 200 Torr. The results are displayed in Figure C.1. The ratio of total droplet energy to bulk fluid enthalpy as a function of droplet diameter according to Equation C.2 is shown in Subfigure (a). The ratio of inner-droplet pressure to gas pressure according to Equation C.3 is shown in Subfigure (b). The ratio of droplet vapor pressure to bulk fluid vapor pressure according to Equation C.4 is shown in Subfigure (c). The ratio of droplet vapor temperature to saturation temperature (for droplets formed by condensation) from Equation C.6 is shown on Subfigure (d). Subfigure (e) shows the fractional change in vapor pressure in the presence of an inert gas according to Equation C.5. Finally, Subfigure (f) shows the ratio of frozen sound speed to gas (conventional) sound speed as a function of droplet volume fraction according to Equation 4.6.

It is evident that the effect of surface tension and terminal velocity on droplet energy (Subfigure

(a)) is trivial, so this may be safely ignored. Likewise, the Gibbs-Thompson, Kelvin-Helmholtz, and Poynting effects (Subfigures (c), (d), and (e)) are small and can be overlooked for droplets larger than $2 \mu\text{m}$ in diameter and Region 1 pressures less than 1 atm. Subfigure (b) indicates that the pressure of the droplets is substantially higher than that of the surrounding gas (Laplace effect). Subfigure (f) shows that for high particle volume fractions, the frozen sound speed deviates significantly from that of the bath gas.

The results shown in Subfigures (b) and (f) have implications for the AEROFROSH algorithm introduced in Chapter 4. Importantly, the pressure discussed in Region 1 and the beginning of Region 2 only refers to that of the gas, rather than the droplets. Additionally, the sound speed used to compute the incident shock Mach number must be adjusted slightly away from that of the pure gas sound speed.

C.5 Summary

The properties of liquid aerosol droplets have been examined. These properties included surface tension, density, total energy, inner-droplet pressure, vapor pressure, droplet temperature, and sound speed in an aerosol. Important findings included the fact that the aerosol droplet vapor pressure can be approximated by the bulk fluid vapor pressure for droplets with diameters larger than $2 \mu\text{m}$, that the pressure inside an aerosol droplet is higher than that of the bulk carrier gas, and that the sound speed in an aerosol differs from that of the bulk carrier gas.

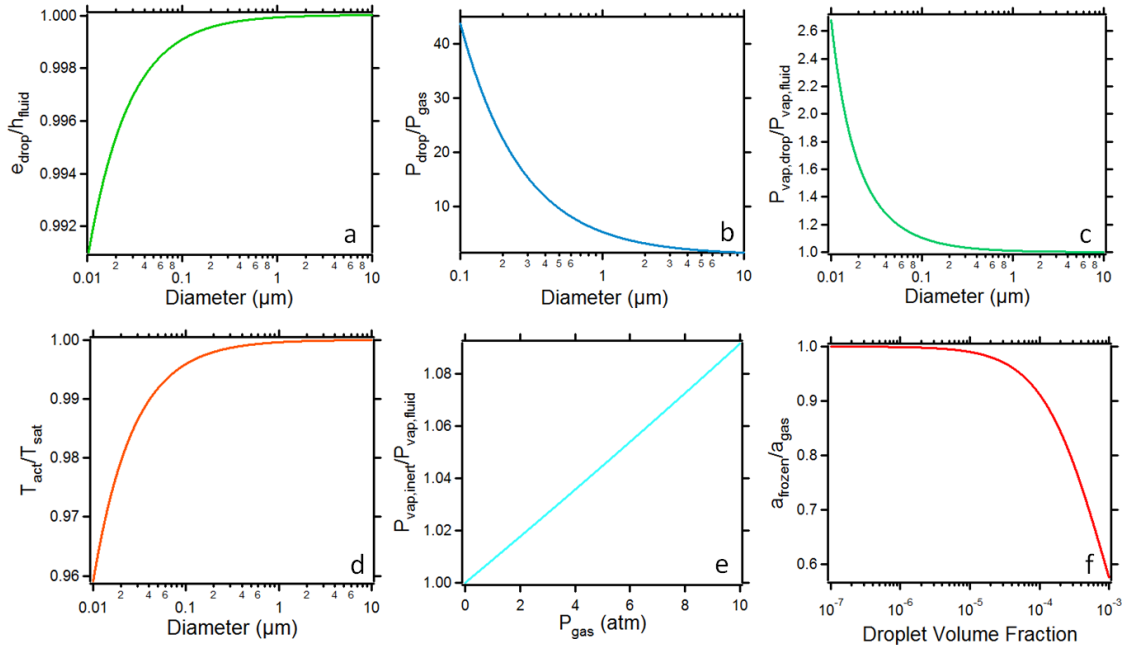


Figure C.1: Comparison of droplet properties to bulk fluid properties for methyl decanoate ($\text{C}_{11}\text{H}_{22}\text{O}_2$) at 298.15 K and 200 Torr in argon. Changes to surface tension with droplet size are small and have been ignored in calculations, as has the effect of fuel vapor on gas viscosity. The number mean diameter for aerosols of large hydrocarbons produced using ultrasonic nebulizers is $d \sim 3 \mu\text{m}$, a typical droplet volume fraction is on the order of $F_v = \phi_v \sim 10^{-6}$, and the pure-gas sound speed in 100%Ar at these conditions is $a_{gas} = 321.597 \text{ m/s}$. Parts (a), (b), (c), (d), (e), and (f) are computed according to Equations C.3 through C.6 and Equations 4.6 through 4.9. The ratio $\frac{e_{drop}}{h_{fluid}}$ decreases with decreasing diameter because both values (relative to the reference state) are negative; e_{drop} is simply less negative than h_{fluid} due to the increase in energy from surface, velocity, and pressure effects.

Appendix D

Arrhenius ignition delay expression

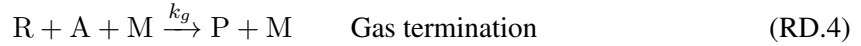
D.1 Introduction

The ignition delay time of a gas mixture is a function of its composition and initial temperature/pressure. In designing practical combustion devices, the ignition delay time of a mixture is a critical parameter; for example, it is used to time fuel injection into a diesel engine, and to determine the size of an afterburner flame holder in a high-performance jet engine. Gas-phase ignition delay times are commonly measured using shock tubes; five excellent sources that describe this process are References [120, 121, 280, 325, 457]. This section will explore the temperature dependence of ignition delay times and their dependence on the rates of multiple simple (elementary) reactions; it follows the derivation set forth in Reference [183] (see also Reference [458]). Ultimately, Equation 6.1 will be obtained.

D.2 Derivation

Consider a reacting system with the following general reactions [183]:





Reaction RD.1 states that each reactant molecule A in a system can form a radical R (initiation). For the hydrogen-oxygen mechanism, $n = 2$ because there are two reactant molecules [57]. Reaction RD.2 states that a reactant can react with a radical to form x radicals and one product P. When $x = 1$ this is a propagation reaction, and when $x > 1$ this constitutes branching. Wall terminations are accomplished when a radical hits the wall and forms a product species (Reaction RD.3). Gas-phase termination can take place in a collision with another molecule M (Reaction RD.4). In these expressions, k_i , k_b , k_w , and k_g are the rate constants for initiation, branching, wall termination, and gas-phase termination reactions, respectively. These take the general form of Equation D.1 where B and m are constants, \hat{R}_u is the universal gas constant, and \hat{E}_B is the elementary reaction's activation energy.

$$k = BT^m \exp\left(\frac{-\hat{E}_B}{\hat{R}_u T}\right) \quad (\text{D.1})$$

Given the simplified system described by Reaction RD.1 through RD.4, the product formation rate can be expressed as

$$\frac{d[P]}{dt} = k_b[A][R] + k_w[R] + k_g[A][M][R] \quad (\text{D.2})$$

$$= [R](k_b[A] + k_w + k_g[A][M]) \quad (\text{D.3})$$

where the brackets [] denote molar concentration [mol/cm³]. Similarly, the radical formation rate can be expressed

$$\frac{d[R]}{dt} = k_i[A]^n + xk_b[A][R] - k_b[A][R] - k_w[R] - k_g[A][M][R] \quad (\text{D.4})$$

$$= [R](k_b[A](x - 1) - k_w - k_g[A][M]) + k_i[A]^n \quad (\text{D.5})$$

Defining the following terms allows this expression to be simplified:

$$a = k_b[A](x - 1) - k_w - k_g[A][M] \quad (\text{D.6})$$

$$b = k_i[A]^n \quad (\text{D.7})$$

$$\frac{d[R]}{dt} = a[R] + b \quad (\text{D.8})$$

At time zero, the concentration of radical species is zero. Also, at early times, [A] and [M] are approximately constant. Hence, the differential rate law can be solved to find the integrated rate expression:

$$[R] = \frac{b}{a} \exp(at) - \frac{b}{a} \quad (\text{D.9})$$

If the ignition point is defined as the time where the radical concentration reaches a critical value $[R] = [R]_{crit}$, this equation may be solved for the ignition delay time τ_{ign} .

$$\tau_{ign} = \frac{1}{a} \ln\left(\frac{a[R]_{crit} + b}{b}\right) \quad (\text{D.10})$$

Substituting the original parameters a and b gives

$$\begin{aligned} \tau_{ign} &= \frac{1}{k_b[A](x - 1) - k_w - k_g[A][M]} \\ &\times \ln\left(\frac{(k_b[A](x - 1) - k_w - k_g[A][M])[R]_{crit} + k_i[A]^n}{k_i[A]^n}\right) \end{aligned} \quad (\text{D.11})$$

This expression may be further simplified by realizing that k_w is small for sizable experimental reactors (for instance, a large-bore shock tube), and the term inside the natural logarithm is relatively constant. Thus, the entire logarithm term can be denoted as C , which is approximately constant. Also, note that at initial times, concentrations have not changed significantly, such that $[A] \approx [A]_0$ and $[M] \approx [M]_0$. Thus, for this simplified, approximate model,

$$\tau_{ign} = \frac{C}{k_b[A]_0(x - 1) - k_g[A]_0[M]_0} \quad (\text{D.12})$$

Often, for simplicity, a simple Arrhenius-like form (similar to Equation D.1) using global parameters A and \hat{E}_A for the reaction mechanism is employed in fitting ignition delay time data. The expression has the form

$$\tau_{ign} = A \exp\left(\frac{\hat{E}_A}{\hat{R}_u T}\right) \quad (6.1)$$

where again it should be emphasized that A and \hat{E}_A are *global fitting parameters for the ignition mechanism*. Thus, the simplified model described above, and Equation D.12, provide a means of interpreting the values of A and \hat{E}_A in Equation 6.1. However, the sign on the global activation energy \hat{E}_A inside the exponential term for ignition delay times is *opposite* to that for elementary reaction rate constants \hat{E}_B (Equation D.1; positive rather than negative). This reflects the fact that, at most temperatures, ignition delay times decrease as temperature increases.

D.3 Summary

The Arrhenius expression for ignition delay times (Equation 6.1) has been derived based on a basic elementary reaction framework. This process illustrated the competing forces of radical generation and termination, showing that this balance, in part, determines the ignition delay time of a reactive gas mixture. Also, the derivation helped explain the temperature dependence of ignition delay times at high temperatures, namely, that ignition times tend to decrease as temperature increases.

Appendix E

Practical considerations for obtaining constant-pressure post-reflected-shock conditions

E.1 Introduction

In Chapter 7, general procedures were presented for achieving long, constant-pressure post-reflected-shock conditions in shock tube experiments. This appendix serves to elaborate on some of these ideas, as well as to introduce additional best-practices. Several topics will be discussed. These can be roughly divided into the following categories: gas tailoring, driver inserts, staged driver gas filling, and diaphragms.

E.2 Gas tailoring

E.2.1 Driver gas tailoring

Recent articles by Amadio *et al.* [277] and Hong *et al.* [278] presented the equations and general algorithm for predicting the driver gas mixture required (for a specified driven gas mixture) in order to achieve ideal tailoring (see Sections 7.1.3 and 7.3.2 for a discussion of driver gas tailoring). The

algorithm developed by these scientists predicts the necessary driver gas composition very closely for simple binary driven gas mixtures that consist primarily of argon. However, the equations set forth in these references assume that heat capacity values (\hat{c}_p , \hat{c}_v , and γ) are constant, and also that shock attenuation is negligible. For this reason, the predicted driver gas tailoring can differ significantly from that determined experimentally, when mixtures contain large fractions of diatomic and polyatomic molecules.

Fortunately, the correct driver gas tailoring can be estimated based on prior experiments at similar temperature/pressure conditions. This is exemplified in Figure E.1, which shows the experimentally-determined driver gas tailoring necessary in comparison with several predictions [277, 278]. Once the experimental best-fit curve (in this case, a second-order polynomial) has been determined for the given buffer gas, the tailoring at new temperatures can be easily ascertained.

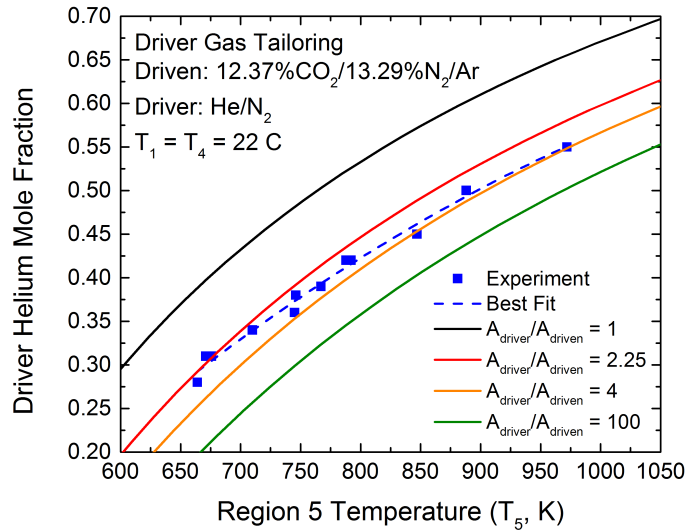


Figure E.1: Comparison of actual to theoretical driver gas tailoring, for several driver/driven area ratios. Driver: He/N₂ (tailored), driven: 12.37%CO₂/13.29%N₂/Ar. $T_1 = T_4 = 22$ °C. For these experiments, the driver-to-driven section area ratio was $\frac{A_{\text{driver}}}{A_{\text{driven}}} \approx 1$, made possible by a series of conical driver inserts (see Section 7.5 and Reference [171]). Theoretical driver tailoring was computed using the method of References [277, 278]. The fit to the data is a second-order polynomial ($R^2 = 0.987$).

In Section 7.3.2, it was mentioned that a sustained pressure rise in Region 5 of a shock experiment indicates the need for more helium in the driver gas mixture (and that likewise, a sustained pressure drop indicates the need for a higher driver section nitrogen mole fraction). Importantly, as the driver helium mole fraction increases, stronger shock waves will result [111]; this causes the Region 5 temperature T_5 to increase as well. Unfortunately, at the new elevated temperature, even more driver gas helium is required for correct driver gas tailoring (see Figure E.1), meaning that a tailoring bump could still be seen in the pressure record even with a higher driver helium content. In order to counteract this trend, the Region 1 pressure P_1 should be slightly increased whenever the helium mole fraction is to be increased, since T_5 scales inversely with P_1 [111]. The amount of increase can be predicted using the method of References [277, 278], or estimated empirically.

In Chapter 7, it was mentioned that the tailored binary driver gas mixture was achieved by alternately filling helium and nitrogen directly into the driver section. When the primary driver fill port (that which is used for the binary mixture) is located about halfway between the diaphragm and the driver section end cap, 2-3 filling cycles (*i.e.*, three cycles would be He-N₂-He-N₂-He-N₂) followed by a 2-3 minute pause before rupturing the diaphragm, are sufficient to ensure mixing. If the primary driver fill port is located close to the diaphragm or close to the end cap, more cycles may be required. Experiment initiation can be accomplished by either filling the low-sound-speed gas until the diaphragm breaks, or (in the case of backfilling) by filling the backfill gas from the port near the end cap until diaphragm rupture.

Also, note that in CRV shock tube operation with correct buffer gas tailoring, either the buffer gas or the test gas can be used in the algorithm of References [277, 278] to solve for the correct driver gas tailored mole fractions. This is because the driver gas tailoring method assumes that heat capacities (specifically, heat capacity ratio value γ) remain constant as temperature changes. Since the γ values of the test and buffer gases were matched at the Region 1 temperature T_1 for the ideal tailoring condition (Section 8.3.1), identical tailoring predictions will be computed using either mixture as the input to the algorithm.

E.2.2 Buffer gas tailoring

In CRV operation, the equations set forth in Section 8.3.1 determine the ideal three-component buffer gas mole fractions required in order to match both γ and \hat{M} for the test and buffer gases. In the absence of fuel loss to the shock tube walls, these equations result in no discontinuity in velocity U_{IS} or attenuation rate Γ as the incident shock enters the test gas from the buffer gas. However, some fuel loss does sometimes occur to the shock tube walls. While passivation (filling the test section with test gas to initial pressure P_1 , mechanically pumping to about 1 Torr, and re-filling to P_1) can reduce this loss, the resulting mole fractions in the test gas will differ slightly from those of the buffer gas. Occasionally, this difference is significant enough that a modified buffer gas tailoring, which matches the post-fuel-loss test gas mixture, is needed. The new buffer gas mixture can be formulated using the average experimentally-measured (using a HeNe laser diagnostic, as in Section 8.2.3) test gas mole fractions (after fuel loss) in the tailoring equations. Alternatively, it can be determined experimentally by iteration; typically this is done by modifying the proportion of the two lesser components (*e.g.*, CO₂ and N₂ in CO₂/N₂/Ar mixtures or CO₂ and CH₄ in CO₂/CH₄/N₂ mixtures) while holding the mole fraction of the third (major) component fixed.

E.3 Driver inserts

As discussed in Chapter 7, the use of driver inserts can greatly reduce the non-ideal pressure increase $\frac{dP^*}{dt}$ (caused by shock attenuation and boundary layer growth) observed in Region 5 of shock experiments, by prematurely reflecting part of the expansion fan back to the test section. The original proposal for the driver insert concept was set forth by Dumitrescu [170] and was later adopted by Stotz *et al.* [171]. Later, Hong *et al.* [172] developed a semi-theoretical framework for predicting the driver insert geometry needed to achieve level pressure profiles. While the method of Hong *et al.* serves to promote understanding of the complex wave interactions during shock experiments, its predictions sometimes still result in residual $\frac{dP^*}{dt}$. The resulting differences from theory are likely the result of non-ideal effects in shock tubes, including the finite time necessary for the diaphragm to open.

In the presence of residual $\frac{dP^*}{dt}$, modifications to the driver insert are possible to correct the

pressure profile. As pointed out by Hong *et al.* [172], the primary two variables in the production of a driver insert are the amount of area change it produces, and the location (as a function of distance from the diaphragm) where the area change takes place. Changes in the insert near the diaphragm affect early Region 5 times, while changes near the driver end cap affect late Region 5 times. By holding all other shock conditions constant (diaphragm thickness, test gas, driver gas, T_1 , T_4 , P_1 , P_4 , etc.) and only making one modification to the driver insert at a time, Region 5 pressure records from shock experiments can be mapped to changes in driver insert geometry. In this way, the driver insert needed to achieve a flat pressure record can be developed systematically.

There are two types of driver inserts (Figure E.2). “Positive” inserts, as recommended by Hong *et al.* [172], are formed by placing solid plastic/PVC or metal cylinders (wood is not advisable because it can result in splinters in the shock tube), held in place by a metal rod, in the middle of the driver section; the diameter of the driver insert is varied by changing the outer diameter of these pieces. “Negative” inserts, as recommended by Stotz *et al.* [171], involve hollow cylinders (plastic/PVC or metal) placed inside the driver section along its outer edge; the diameter of the insert is varied by changing the hole size drilled into these pieces. In either method, a driver insert configuration can quickly be recorded (and rebuilt) by numbering each individual insert section and noting the order in which modules are inserted into the driver section.

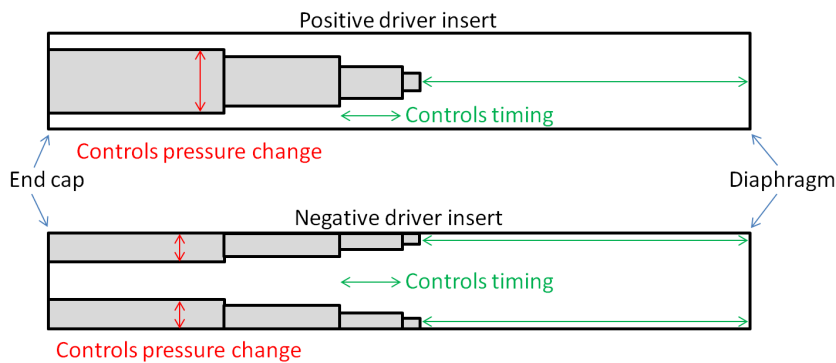


Figure E.2: Diagram showing positive (Hong *et al.* [172]) and negative (Stotz *et al.* [171]) driver inserts.

The geometry of driver inserts depends on the driver gas, test gas, T_5 , and P_5 . In general, if the test gas mixture is changed, a new driver insert will be required. Also, if experiments are to be

conducted over a wide temperature-pressure range, several driver inserts will be needed to achieve satisfactory pressure traces. A helpful rule of thumb is that for higher desired T_5 values, the driver insert will need to cause a greater area change, and also that the insert will need to begin the area change the closer to the diaphragm. The effect of P_5 on the driver insert is slightly more difficult to specify, though in general, a slightly larger driver insert will be required for a higher P_5 .

As detailed in Section 7.2, the first 3.63 m of the driver section on the CRVST have an internal diameter of 17.8 cm, and the following sections, which extend the driver section to a total length of 13.42 m, have an internal diameter of 15.4 cm. Furthermore, as shown in Figure E.3 (see also Figure 8.1), the driver section includes a U-joint that turns the driver section back on itself toward the shock tube endwall (note that in Figure E.3, the total driver length shown is 9.57 m, rather than the full 13.42 m distance). The driver diameter change occurs at the beginning of the U-joint (the side close to the diaphragm).

The resulting driver area change and the U-joint present interesting problems for controlling the Region 5 pressure. First, when the expansion wave encounters the area decrease near the U-joint, it sends an expansion fan back to the test section, causing a slight pressure decrease. Fortunately, at most test conditions explored in the course of the work that is included in this dissertation, the positive driver insert installed in the 17.8 cm section resulted in a driver area near the U-joint that was close to the driver area of the 15.4 cm driver section. As a result, only a small discontinuity in area was experienced by the expansion wave at this junction. Second, the interaction of the expansion wave with the U-joint itself has been found to be unimportant; however, it is difficult to place a solid driver insert in the U-joint because the curved volume inhibits the installation of rigid objects. To solve this issue, a flexible driver insert for the U-joint, consisting of round PVC pieces hung on a twisted half-inch nylon rope, was developed to control the Region 5 pressure profile corresponding to the time at which the expansion wave head passed through this section (see Figure E.4).

In Section 7.5, it was mentioned that in long test time experiments, an area mismatch between the driver and driven sections (near the diaphragm) can cause problems. This is because, in case of the Stanford CRVST, a reflected expansion fan is generated and sent propagating toward the test section when the reflected shock moves from the driven section into the driver section and encounters the area increase from the 11.53 cm driven section to the 17.8 cm driver section (similarly, an area

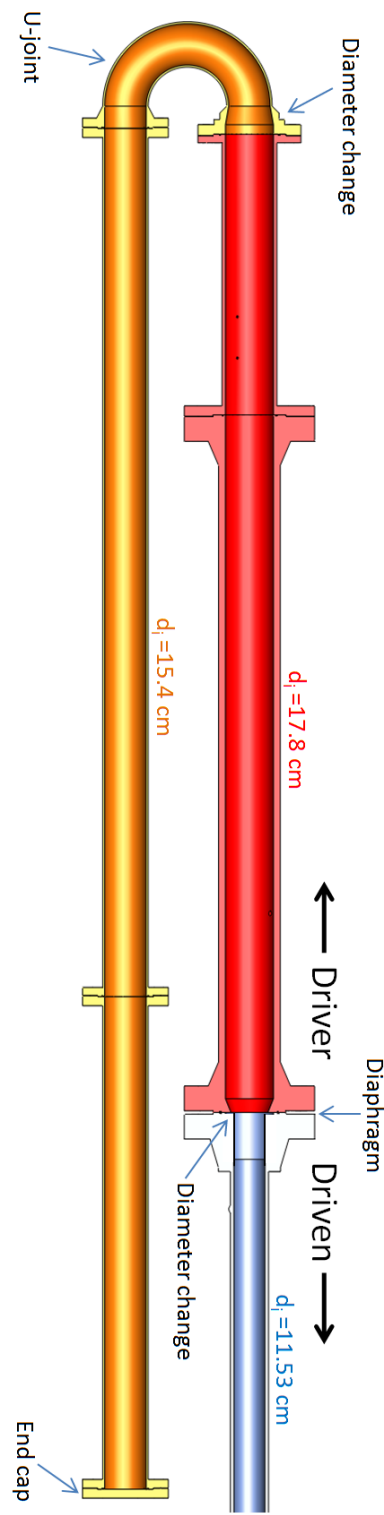


Figure E.3: Section view of the CRVST driver section. The total driver length shown is 9.57 m, rather than the full 13.42 m distance.

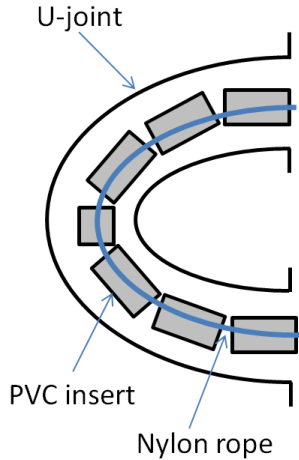


Figure E.4: Driver insert for U-joint.

decrease experienced by the reflected shock wave would send a shock wave back to the test section). This was remedied by using concentric PVC pipes, acting as effective negative inserts [171], in the 17.8 cm driver section to decrease the practical internal diameter from 17.8 cm to about 11.5 cm (see Figure E.5). Within these concentric PVC pipe negative inserts, a smaller positive insert [172] was used to control $\frac{dP^*}{dt}$. Also, positive inserts in the 15.4 cm diameter driver section were employed to control the pressure at later times.

The interaction of the reflected shock with these positive driver inserts caused additional issues to arise. Importantly, as the reflected shock entered the driver section and encountered the small positive insert located inside the PVC pipes, a pressure wave was sent down to the test section, causing the Region 5 pressure to increase at a greater rate (higher $\frac{dP^*}{dt}$) than would be caused in the absence of this small positive driver insert. In other words, the small positive driver insert near the diaphragm, which enabled flat Region 5 pressures to be achieved at early times, resulted in highly undesirable pressure increases toward the end of the Region 5 test time. To combat this, a large positive driver insert was developed and installed in the end of the 15.4 cm section (near the driver end cap), which eliminated the pressure increase. For quickly manipulating pressure profiles, positive inserts were generally found to be favorable compared to negative inserts, due to their lower material cost, smaller storage size, lighter weight, and relative ease of installation.

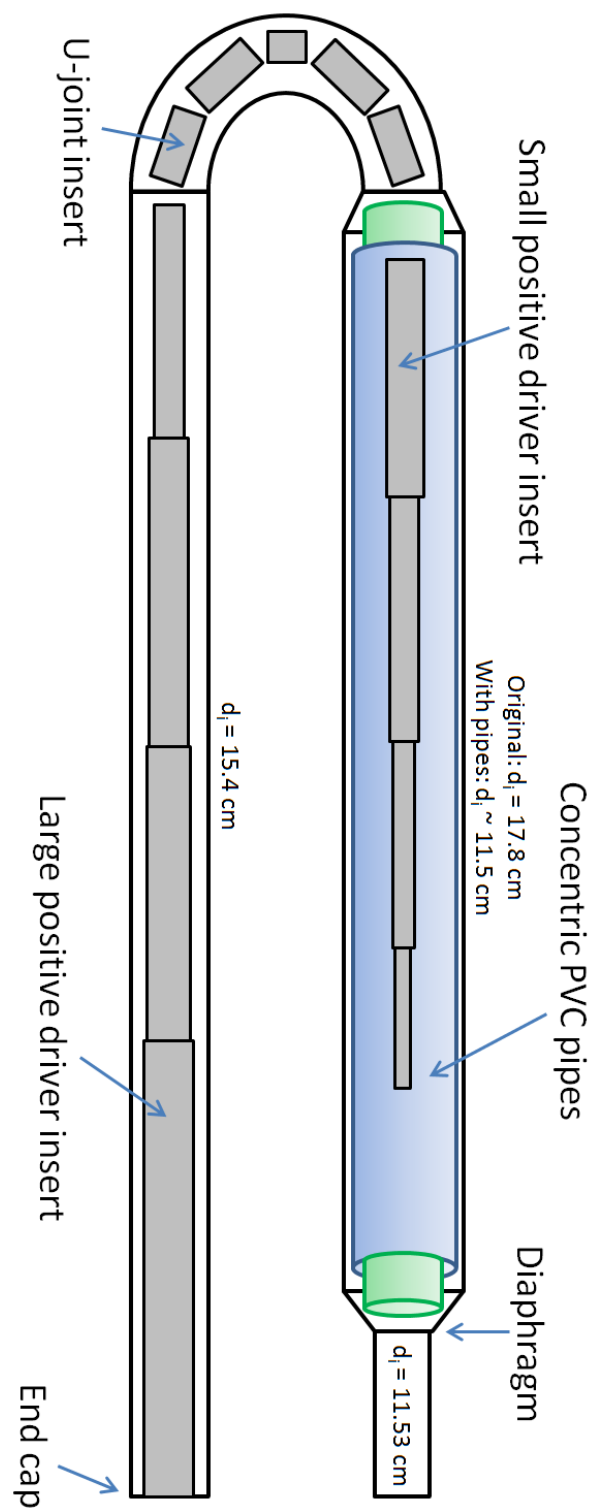


Figure E.5: Schematic of driver inserts employed to achieve long test times. Diagram is not drawn to scale.

In the future, a more robust design that involves permanently decreasing the driver diameter in both the 17.8 cm and 15.4 cm sections to \sim 11.5 cm using negative inserts made of PVC may be worth consideration. Once this large negative insert was installed, the entire length of the driver section would have a uniform diameter of \sim 11.5 cm; this would make experimental driver insert design more straightforward by removing the possible influence of driver section diameter on observed pressure records. Within this large uniform negative insert, smaller positive inserts that can be modified quickly and easily to achieve flat pressure profiles could be installed as well.

Alternately, as mentioned in Chapter 10, a flexible driver section geometry could also be employed, which involves attaching a flexible hose to the end of the rigid driver end cap. Such a hose could be coiled so that it requires little laboratory space, but still allows great driver section overall lengths to be achieved. In this setup, only a small hose diameter would be required, because the open area of the driver section near the driver end cap is quite small due to the large positive driver inserts required for the achievement of flat pressure profiles.

Finally, as noted in Section 7.1.2, various numerical codes have been developed in order to predict gasdynamic interactions within shock tubes [123, 285, 286]. In the future, these programs could be used to aid in the design of driver inserts, reducing the time required for experimental iteration.

E.4 Staged driver gas filling

The staged driver gas filling (*i.e.*, backfilling) technique was introduced in Section 7.4. This method of driver section filling was shown to increase test times significantly, while reducing the high-pressure helium required for each shock experiment. Three variables have been discussed previously: the length of the binary gas L_{binary} (Section 7.4.4), the backfilling time (Section 7.4.5), and the backfill gas sound speed (Section 7.4.6). In this section, additional details about staged driver gas filling will be presented, including the effect of the binary gas partial pressure P_{4a} on the pressure trace and the location of the backfill gas port.

E.4.1 Effect of P_{4a}

In general, as P_{4a} decreases, test time increases, since the length of the low-sound-speed backfill gas $L_{backfill} = L_{driver} - L_{binary}$ increases as well (see Equation 7.4, repeated below).

$$\frac{P_{4a}}{P_4} = \frac{L_{binary}}{L_{driver}} \quad (7.4)$$

However, secondary wave interactions present for some values of P_{4a} can occasionally cause gradual, premature pressure declines that are observable at the test section. This can be seen in Figure E.6, where the pressure record corresponding to $P_{4a} = 34$ psi shows a decrease over time. Changing the value of P_{4a} can remedy this issue; the second record in Figure E.6, corresponding to $P_{4a} = 47$ psi, is relatively level. Typically, some experimentation is necessary in order to determine the ideal value of P_{4a} for a set of shock tube measurements using a certain test gas in a desired temperature and pressure regime.

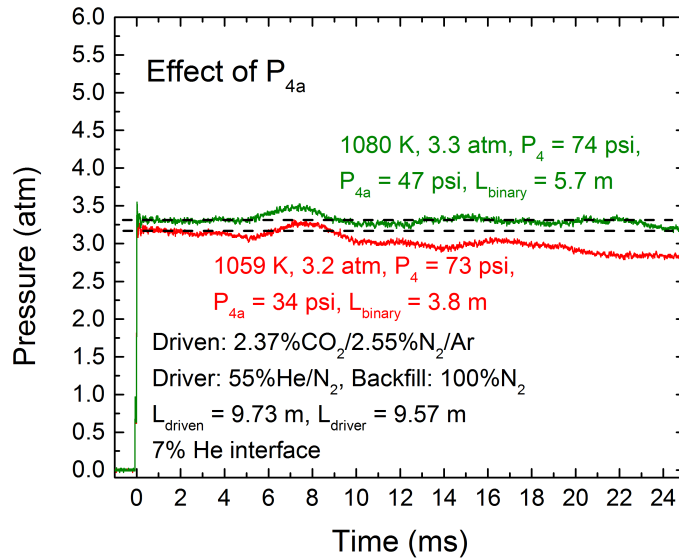


Figure E.6: Effect of P_{4a} on Region 5 pressure. In this case, a higher value of P_{4a} (longer L_{binary}) resulted in improved pressure uniformity across the test time. Conditions: $\frac{A_{driver}}{A_{driven}} = 1$, $L_{driven} = 9.73$ m, $L_{driver} = 9.57$ m. Driver: 55%He/N₂; driven: 2.37%CO₂/2.55%N₂/Ar; backfill: 100%N₂; 7%He interface gas. A series of driver inserts was used to mitigate non-ideal pressure increases.

E.4.2 Effect of backfill port location

In Section 7.4.2, the backfill port, from which the low-sound-speed gas is filled into the driver section, was said to be located very near to the driver section end cap. In theory, this allows for the maximum increase in test time to be obtained. This is because the binary/backfill gas mixing zone necessitates a minimum L_{binary} value to ensure a pure binary gas mixture in contact with the diaphragm such that a strong shock is obtained. If the backfill port is located very close to the driver end cap, when the low-sound-speed gas is filled, all of the binary gas is pushed toward the diaphragm. However, if the backfill port is located away from the driver section end cap, some of the binary gas will be pushed toward the diaphragm (forming the minimum required binary length corresponding to no binary gas dilution at the diaphragm), and some will be pushed toward the driver section end cap. Since not all the binary gas is pushed toward the diaphragm in this case, a higher value of P_{4a} is required to achieve the minimum L_{binary} value, causing the maximum theoretical test time to drop.

There are cases, however, where locating the backfill port away from the end cap may be advantageous. Notably, the time required to reconfigure the driver section for new test conditions can take up to several hours. If only one or two experiments are required at long test times, the additional driver extension tubing can be attached but the backfill port left in its original location; this reduces the time needed to reconfigure the shock tube while still yielding somewhat longer test times. Experiments performed using this shortcut have reliably produced uniform test times.

E.4.3 Recommendations for backfill gas

Current best practices for staged driver gas filling involve the use of either nitrogen or carbon dioxide as the backfill gas. Both of these offer the advantages of having a low sound speed, being inexpensive, and being readily available. However, as noted in Section 7.4.7, other backfill gas choices should be considered in the experiment design process as well.

E.5 Diaphragms

For most low-pressure shocks on the CRVST, plastic (polycarbonate) diaphragms are used. In general, plastic diaphragms have the advantages (compared to metal diaphragms) of being low-cost, having high shock-to-shock repeatability, and being quick/easy to change between experiments. Despite these advantages, plastic diaphragms pose some unique challenges that should be noted.

First, plastic diaphragms are typically purchased in 2-foot-by-4-foot sheets and are subsequently cut into eight 12-inch squares for use. Each plastic piece has a nominal thickness, often with a tight tolerance. In order to decrease shock-to-shock variation in burst pressure, the eight squares taken from each sheet should be used in sequence and not mixed with those from another sheet.

Second, in order to ensure consistent rupture, diaphragms are often burst using a four-bladed cutter (this produces four diaphragm petals that open toward the shock tube endwall). (Note that another option for thick (0.040-inch) plastic diaphragms is to score the diaphragm prior to installation and not use the four-blade cutter.) On the CRVST, a cutter consisting of an electric discharge-machined steel cross that was sharpened on a milling machine has been found to work well (see Figure E.7). In this configuration, each of the four blades puts equal pressure on the diaphragm, causing the four petals to burst simultaneously. By conducting experiments in which the driver section was filled to pressures just less than those that would cause diaphragm rupture and then quickly evacuating the driver gas (again, without rupturing the diaphragm), it was found that even a small (<1 mm) difference in the height of the blades produced uneven pressure on the diaphragm (as evidenced by the depth of the impressions made by the blades in the polycarbonate). Hence, it is thought to be critical that the plane formed by the four blades is absolutely level and parallel to the diaphragm surface. Also, experiments using an arrowhead-shaped cutter (pointed tip) were thought to burst the diaphragm unevenly. Future experiments to photograph the diaphragm rupture process, such as those in References [459–462], may be useful to further-refine new cutter designs.

Third, the distance between the cutter and the diaphragm has a significant effect on the burst pressure P_4 . A change of just 1 mm can result in a 4-5% difference in the resulting value P_4 value. As such, when removing the cutter for sharpening, care should be taken to note the previous cutter distance and orientation such that it can be returned close to its original state.

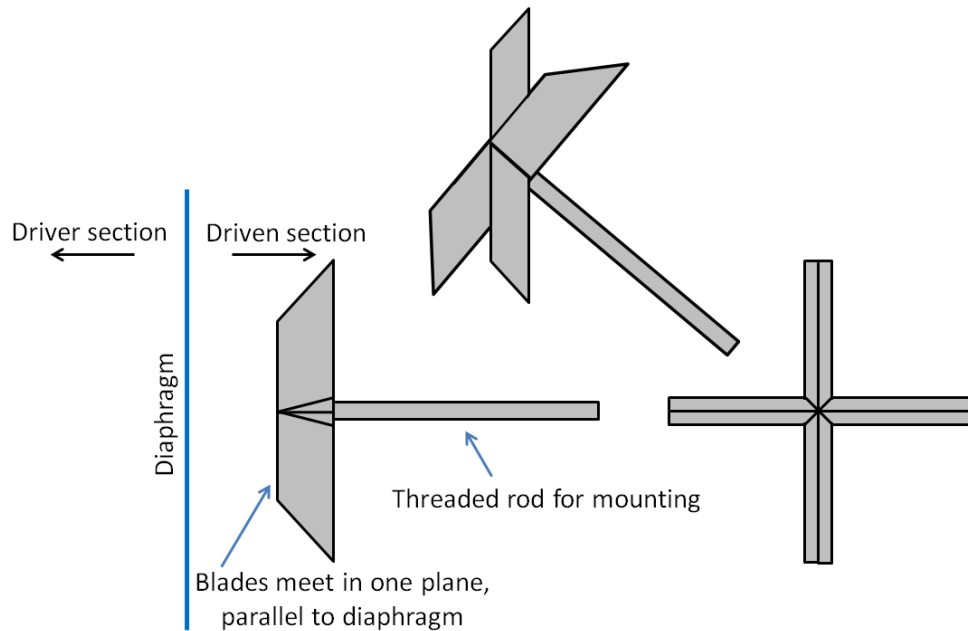


Figure E.7: Schematic of diaphragm cutter used in the CRVST.

Fourth, the plastic petals formed upon diaphragm rupture can flap open and shut rapidly as the driver gas rushes out into the driven section. This phenomenon produces a series of shock waves that quickly increase the test section pressure P_5 , followed by expansion waves that subsequently allow the pressure to fall (see Figure E.8). While the average pressure tends to stay constant in the midst of this flapping, the actual pressure profile is unsuitable for experiments.

Several techniques have been identified for reducing diaphragm flapping. In general, thinner diaphragms were found to flap less, presumably since they are more flexible and hence have less propensity to spring shut. For the experiments conducted in the course of the work constituting this dissertation, diaphragms less than 0.020-inch thick were found to work well. (Placing two thinner diaphragms side-by-side to achieve the desired overall diaphragm thickness was not tested sufficiently to fully understand the effects of this option.) Also, moving the cutter away from the diaphragm has been found to reduce flapping; this may be evidence that the diaphragm actually hits the cutter as it flaps. Moreover, ensuring that all cutter blades correspond to one plane that is parallel to the diaphragm, as discussed above, seemed to decrease flapping as well. Other possible

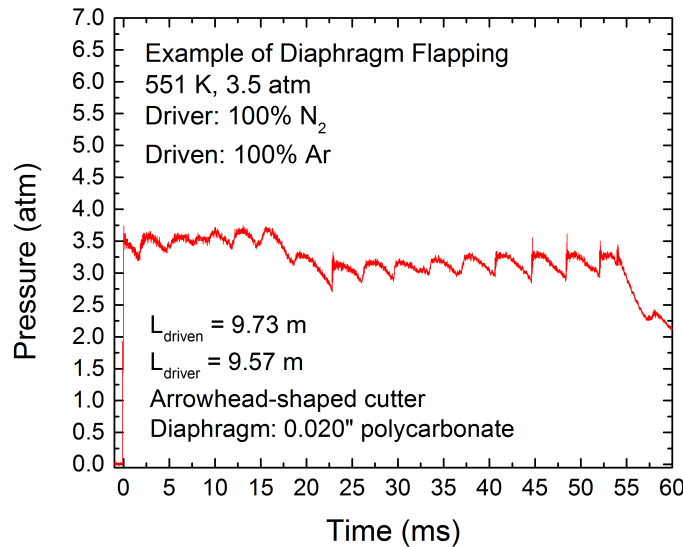


Figure E.8: Example of diaphragm flapping. Conditions: $T_5 = 551$ K, $P_5 = 3.5$ atm, $\frac{A_{driver}}{A_{driven}} = 2.38$, $L_{driven} = 9.73$ m, $L_{driver} = 9.57$ m. Driver: 100%N₂; driven: 100%Ar; no He interface gas. No driver insert was used in this experiment; this resulted in the slight overall $\frac{dP^*}{dt}$ observable. The pressure drop near 17 ms may be attributed in part to the expansion wave head passing into the smaller-diameter section of the driver near the U-joint (a pressure drop like this can also indicate the need for more nitrogen in the He/N₂ binary gas mixture, but in this case the driver was already 100% nitrogen). The pressure drop near 55 ms is likely due to the reflected shock entering the driver section and experiencing an area increase, sending an expansion wave back to the test section.

avenues, which could be explored in future work, include the use of metal diaphragms (these deform as they open so that they do not spring shut) or small hooks inside the shock tube to catch the plastic diaphragm petals and hold them open. Alternatively, several designs for diaphragmless shock tubes have recently been demonstrated [463–465], which may eliminate the flapping problem altogether.

E.6 Summary

In this appendix, several factors that are important to attaining constant-pressure post-reflected-shock test times have been introduced. These included gas tailoring, driver inserts, staged driver gas filling, and diaphragms. An empirical method for determining the correct driver gas tailoring, shown in Figure E.1, was demonstrated, and recommendations for tuning the buffer gas tailoring were also presented. Details concerning both positive and negative driver insert configuration were given, including recommendations for future CRVST driver section modifications. Also, the binary gas partial pressure P_{4a} was said to have an effect on the Region 5 pressure profile, but the location of the backfill port was said to have little effect on the profile (though the longest test times will be achieved when this port is near the driver end cap). Finally, best practices for diaphragm thickness values and cutter design/geometry were set forth in order to minimize non-ideal pressure effects.

Appendix F

Shock tube design

F.1 Introduction

In this appendix, several general principles regarding shock tube design will be set forth. This is not meant to be a comprehensive guide for the design of a shock tube, but rather a summary of the several important ideas determined in the course of this dissertation work. Topics introduced include safety factors, pressure vessel design, window plug design, and o-ring groove design.

F.2 Safety factor

The most important design criteria in developing a shock tube is safety. Safety factors F_s in design compare the strength of a material (often taken to be the yield strength, S_y) to the allowable design stress σ_{allow} (Equation F.1).

$$F_s = \frac{S_y}{\sigma_{allow}} \quad (\text{F.1})$$

In general, safety factors for the parts of a shock tube that may experience detonations should have a safety factor of $F_s = 2.0$ at a minimum. For windows, safety factors should ideally be about $F_s = 4.0$. The allowable stress in a pressure vessel, such as a shock tube, should be computed using the maximum pressure that the volume could experience. In shock tube experiments, this should be taken as the maximum detonation (spike) pressure expected in a shock experiment. The peak

pressure during an explosion can be estimated using Chapman-Jouguet detonation calculations. One computer code capable of such calculations is STANJAN [410]. Alternatively, a general rule of thumb is that the detonation peak pressure will be about twelve times the nominal Region 5 pressure. For instance, in a shock tube that is designed for a nominal maximum Region 5 pressure of 100 atm, the detonation pressure spike may be approximately 1200 atm. Therefore, a conservative design will use 1200 atm as the maximum pressure in design safety factor calculations.

F.3 Pressure vessels

F.3.1 Equations

Since shock tubes are meant to achieve a wide range of experimental conditions, including both low and high pressures, the equations of pressure vessel design for thick-walled cylindrical chambers are of utmost importance. The equations for the principal stresses σ_c (circumferential stress, also known as hoop stress), σ_r (radial stress), and σ_l (longitudinal stress) in terms of radius r are repeated below in Equations F.2 through F.4. An upper bound to the stress in the center of a round, flat plate (the end cap stress, σ_e) with thickness t and bolt circle radius r_b is given in Equation F.5 (note that this assumes the internal pressure acts over the entire area encompassed by the bolt circle; in reality, the pressure acts only over the smaller area encompassed by the sealing o-ring). In these equations, r_i and r_o are the internal and external tank radii, respectively, P_i and P_o are the internal and external vessel pressures, respectively, and ν is Poisson's Ratio (a property of the material; $\nu \sim 0.3$ for stainless steel #304). A diagram showing the various stresses is also provided in Figure F.1. These equations are called Lamé's solution, and they are taken from Lindeburg [466].

$$\sigma_c = \frac{r_i^2 P_i - r_o^2 P_o + \frac{r_i^2 r_o^2}{r^2} (P_i - P_o)}{r_o^2 - r_i^2} \quad (\text{F.2})$$

$$\sigma_r = \frac{r_i^2 P_i - r_o^2 P_o - \frac{r_i^2 r_o^2}{r^2} (P_i - P_o)}{r_o^2 - r_i^2} \quad (\text{F.3})$$

$$\sigma_l = \frac{r_i^2 (P_i - P_o)}{r_o^2 - r_i^2} \quad (\text{F.4})$$

$$\sigma_e^{max} = \frac{3}{8} \left(\frac{r_b}{t} \right)^2 (P_i - P_o)(3 + \nu) \quad (F.5)$$

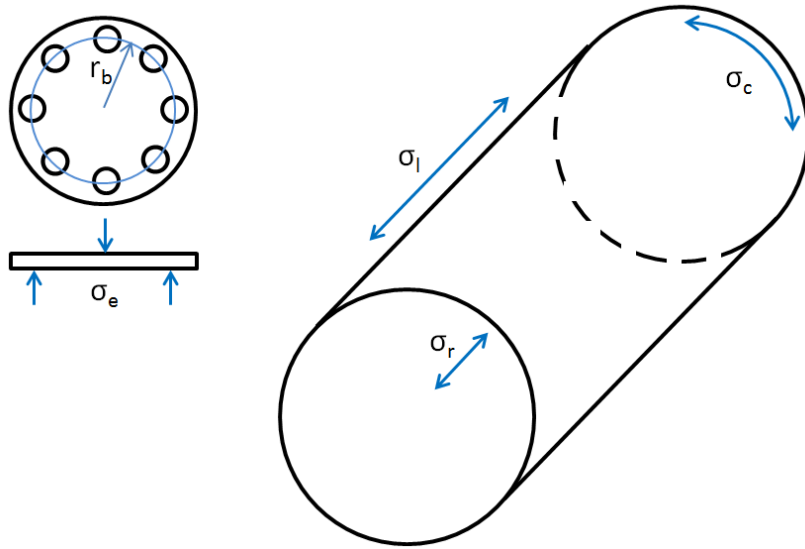


Figure F.1: Principal stresses in a cylindrical pressure vessel.

Both internal pressurization ($P_i > P_o$) and vacuum (external pressure; $P_o > P_i$) conditions should be checked in the vessel design process. The radius at which the most extreme stress occurs depends on the type of stress and the pressurization (external versus internal). For both internal and external pressurization, radial stress values are always compressive ($\sigma_r < 0$). However, for internal pressurization, $\sigma_c > 0$, $\sigma_l > 0$, and $\sigma_e > 0$, whereas for external pressurization, $\sigma_c < 0$, $\sigma_l < 0$, and $\sigma_e < 0$. Table F.1 can be used as a guide to determine which conditions to check. Since these are principal stresses, they can be directly compared to the yield strength of the metal S_y in order to determine the safety factor F_s .

The driver and test sections of a shock tube experience slightly different pressure loadings. Test sections must be designed to contain brief (<10 ms) explosions in high-fuel-loading experiments. However, sustained pressure loading in driven sections is rare. In contrast, in helium/nitrogen-pressure-driven shock tubes, the driver section will never experience an explosion. However, the driver section may be required to contain a high-pressure gas for several minutes prior to diaphragm

Table F.1: Locations of extreme values of principal stresses in pressure vessels. When stresses are compressive ($\sigma < 0$), extreme values are taken as those that are most *negative*.

Principal Stress	Internal Pressure ($P_i > P_o$) Type	Location of Extreme	External Pressure ($P_o > P_i$) Type	Location of Extreme
σ_r	$\sigma_r < 0$	$r = r_i$	$\sigma_r < 0$	$r = r_o$
σ_c	$\sigma_c > 0$	$r = r_i$	$\sigma_c < 0$	$r = r_i$
σ_l	$\sigma_l > 0$		$\sigma_l < 0$	
σ_e	$\sigma_l > 0$		$\sigma_l < 0$	

rupture. Despite these differences, a conservative shock tube design will treat all pressures as sustained (this requires thicker pressure vessel walls) in order to avoid catastrophic failure.

F.3.2 Flanges

The American Society of Mechanical Engineers (ASME) maintains standard flange sizes that correspond to different operating pressure and temperature conditions; these are maintained by standard ASME B16.5-2013 [467]. To select a flange, the operating temperature and pressure are used to determine a pressure class (150, 300, 400, 600, 900, 1500, or 2000 lb.). (Here, the nominal temperature of the shock tube should be used, for instance 25 °C or 100 °C in the case of heating; however, the maximum pressure to be experienced by the component should ideally be used here to ensure maximum safety.) Once the pressure class has been determined, the dimensions for the flange, including its diameter and bolt hole size, can be found tabulated as a function of the nominal diameter of the pipe that is to be welded to the flange.

F.3.3 Bolts

The force experienced by a bolt that mates two components of a pressure vessel is due to the pressure differential across the components and the weight of the components themselves. Once the total combined force F_{tot} on the components has been determined, the resulting force per bolt (assuming a multi-bolt junction) F_{bolt} can be computed by dividing the total combined force by the number of bolts N_{bolt} .

$$F_{bolt} = \frac{F_{tot}}{N_{bolt}} \quad (\text{F.6})$$

For bolts with ultimate strength values $S_u > 100000$ psi that experience primarily tensile stress (along their primary axis), the effective tensile strength area A_t [in²] undergoing stress can be calculated by Equation F.7,

$$A_t = \pi \left(\frac{E_{s,min}}{2} - \frac{0.16238}{N_{tpi}} \right)^2 \quad (\text{F.7})$$

where N_{tpi} is the number of threads per inch and $E_{s,min}$ is the minimum pitch diameter of the external thread. Values for $E_{s,min}$ are tabulated in standard ASME B1.1-2003 [468] and ASME B1.13M-2005 [469].

The tensile stress σ_t experienced by a bolt due to a tensile force $F_{bolt,t}$ can be computed by

$$\sigma_t = \frac{F_{bolt,t}}{A_t} \quad (\text{F.8})$$

Finally, the safety factor F_s for a bolt can be determined by comparing the bolt's proof strength S_p to the tensile stress it experiences,

$$F_s = \frac{S_p}{\sigma_t} \quad (\text{F.9})$$

where the proof strength can be obtained from the material yield strength S_y .

$$S_p = 0.95S_y \quad (\text{F.10})$$

F.3.4 Effect of temperature

The ultimate and yield strength values of metals generally decrease as temperature increases [470]. Therefore, if a shock tube or mixing tank is to be heated significantly, the reduced strength of the metals must be used in stress analyses. Note that shock tubes experience brief (<100 ms) intervals of very high temperature during experiments; such temperatures need not be considered in stress calculations because, due to the transient nature of the heating and the large thermal mass of the metal, the shock tube wall temperature remains low.

F.3.5 CRVST constraints

The operating pressure ranges for the various components of the Constrained Reaction Volume Shock Tube (CRVST) are detailed in Table F.2.

Table F.2: Maximum operating pressures P_{max} for CRVST components, based on σ_r , σ_c , and σ_l (but not on σ_e). Safety factors F_s for these calculations are also provided. All values are computed at room temperature (25 °C) using $S_y = 205$ MPa for stainless steel #304. The length L , internal diameter d_i , and cylinder wall thickness $r_o - r_i$ values for each component are provided. *Note: For the mixing tank and the driver section, which have flat end caps, the actual maximum pressure values will be less than those in the table below; these depend on the end plate thickness t chosen (for this reason, end plate thickness values are not included in this table).*

Pressure Vessel	L [m]	d_i [cm]	$r_o - r_i$ [cm]	P_{max} [atm]	F_s
Mixing tank	1.5	19.4	1.27	70	2
Driver section	2.6	17.8	2.54	170	3
Driver section	1.0	17.8	1.27	135	2
Driver extension	9.8	15.4	0.71	90	2
Low-pressure buffer section	6.7	11.53	1.27	100	4
High-pressure buffer section	2.6	11.53	2.54	175	4
Test section	0.4	11.53	4.64	270	4

F.4 Window plug design

F.4.1 Equations

The primary diagnostics employed on shock tubes are optically-based, meaning that windows, which provide optical access, are a critical shock tube component. Windows are typically situated in plugs, which are inserted into shock tube ports. The seal between the window and the plug is accomplished via epoxy, and the seal between the plug and the shock tube via an o-ring.

When designing a window plug/port, there are three important dimensions: the window thickness t_w , the window diameter d_w , and the port's clear aperture diameter d_c (that which is available for optical transmission). These dimensions are shown in Figure F.2. The window thickness needed to withstand a pressure differential $\Delta P = P_i - P_o$ (in the case of internal pressurization) for a window with a modulus of rupture M_r is given in Equation F.11 (usually, $F_s = 4$ for windows) [471]

(see also References [472, 473]). Modulus of rupture and transmission range data for several common window materials are provided in Table F.3. The pressure differential should be the maximum expected, including the peak pressure spike expected during detonation events.

$$t_w = d_c \sqrt{\frac{11}{40} \frac{\Delta P}{M_r} F_s} \quad (\text{F.11})$$

Once the required window thickness is known, the window slot length L_s cut into the plug can be determined (see Figure F.2). Alternatively, if a window with a known thickness t_w is to be used, the necessary clear aperture diameter d_c can be determined instead. Finally, the diameter of the window slot d_s should be a few thousandths of an inch (for instance, 0.015-inch) larger than the nominal window diameter d_w (plus its maximum tolerance value) in order to provide sufficient room for epoxy for the pressure seal.

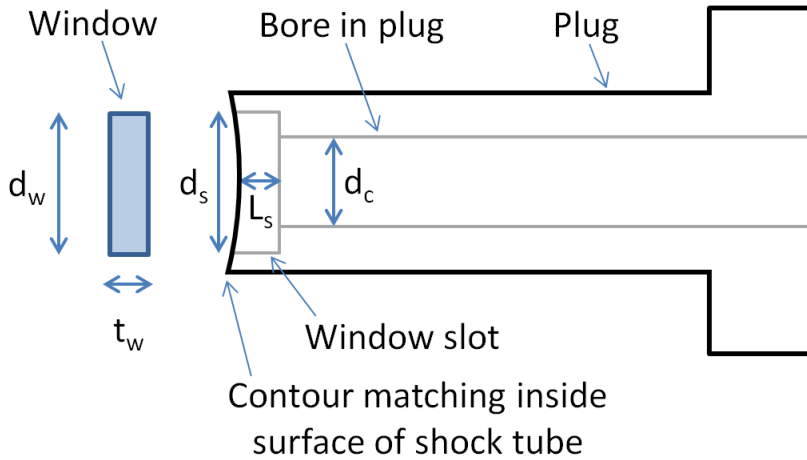


Figure F.2: Important dimensions for window plug design. These are shown for the case of a round shock tube, where the plug's internal contour matches that of the shock tube bore.

F.4.2 Transmission

In shock tube design, the window material selected is dependent on several factors. These include the anticipated stresses (through the modulus of rupture M_r) and the optical diagnostics to be employed. Table F.3 provides data for the transmission range of several materials at room

Table F.3: Window material properties at room temperature (25 °C). Data obtained from Reference [471].

Material	M_r [psi]	Transmission Range [μm]
BaF ₂	3900	0.15-12.5
CaF ₂	5300	0.15-9.0
Fused Silica (IR Grade)	7000	0.18-3.5
GaAs	20000	1-15
Quartz (SiO ₂)	7000	0.15-3.3
Sapphire	65000	0.17-5.0
ZnSe	8000	0.55-20

temperature. Importantly, the transmission range of many windows is temperature-dependent; often, as temperature increases, the transmissivity of window materials decreases [242].

F.4.3 Glue

Epoxy is typically used to cement windows into optical plug window slots. Since there is little room for excess glue in a plug in order to maximize the available clear aperture, the epoxy must be applied with great care. Using a thermally-cured epoxy is advantageous in this regard because it allows more time for the glue to be painted in place, as compared to traditional five-minute epoxy, which quickly cures at room temperature. However, the temperature change required for curing can introduce thermal stresses in the window/plug junction (usually, the plug/window are heated to ~150 °C and held there for 30 minutes in this process). As such, heating should be performed slowly (about 50 °C every 30 minutes), and cooling should be performed over the course of several hours.

In the event that windows must be removed, the window/plug combination can be baked (~300 °C) for 1-2 hours. This will allow the window to be gently tapped out in one piece using a metal reamer whose diameter is as close to the plug's clear aperture diameter d_c as possible (this spreads the force over a larger area, reducing the risk of shattering the window). After scraping out the old glue using a razor blade and re-sanding the window slot, a new window may be installed.

F.5 O-rings

Proper seals are critical in shock tube design. Most seals are accomplished using o-rings, which sit in grooves machined on the faces of mating components. There are two types of seals common in shock tube design: male seals, where the o-ring surrounds an object that is inserted into a hole (*e.g.*, the o-ring on a window plug), and face seals, where the o-ring is compressed between two plates (*e.g.*, the junction of two shock tube pipe flanges).

O-rings sizes are specified in SAE standard AS568 (revision D) [474] and in ISO standard ISO 3601-1:2012 [475]. Each o-ring is typically assigned a “dash number,” such as AS568-XYY, where the X number is an index for the o-ring thickness t , and the YY number is an index for the internal diameter d_i (note that other conventions use 2-XYY).

Material selection for o-ring design is important, as some fuels, such as biodiesel, studied in shock tubes can degrade certain rubbers. A fifteen-day trial was conducted in which several o-rings (AS568-214 size, which nominally has $t = 0.139 \pm 0.004$ inch and $d_i = 0.984 \pm 0.010$ inch) were submerged in methyl decanoate (MD) and in the methyl oleate blend (MOB), two fuels discussed in Chapter 6. The percent changes in these o-rings’ thicknesses and internal diameters (relative to the nominal values) are shown in Figure F.3. In this chart, the 70, 75, 80, and 90 numbers denote Shore A Rubber Durometer Hardness Scale values, where hardness increases with the Shore A number. It appears that MD and the MOB affected the o-rings differently, but overall the Viton ETP and Kalrez rubbers were least susceptible to degradation. In shock tubes, since most fuels are only encountered in the gas phase in low concentrations, such o-ring enlargement is not expected; however, understanding these effects is important. Generally, the Viton 75 material/hardness combination is preferred due to its low cost and widespread availability.

Many references exist to aid in the selection of o-rings and the design of o-ring grooves (*e.g.*, Reference [476]). Therefore, the relevant equations will not be repeated here. However, it should be stated that two of the most important quantities in o-ring selection/groove design are the “o-ring compression” (the amount the o-ring is squeezed in the groove) and the “gland fill” (the amount of the o-ring groove that is occupied by the o-ring). Also, since all o-ring dimensions can vary within their allowable tolerances, and o-ring grooves are also machined to finite precision, rigorous

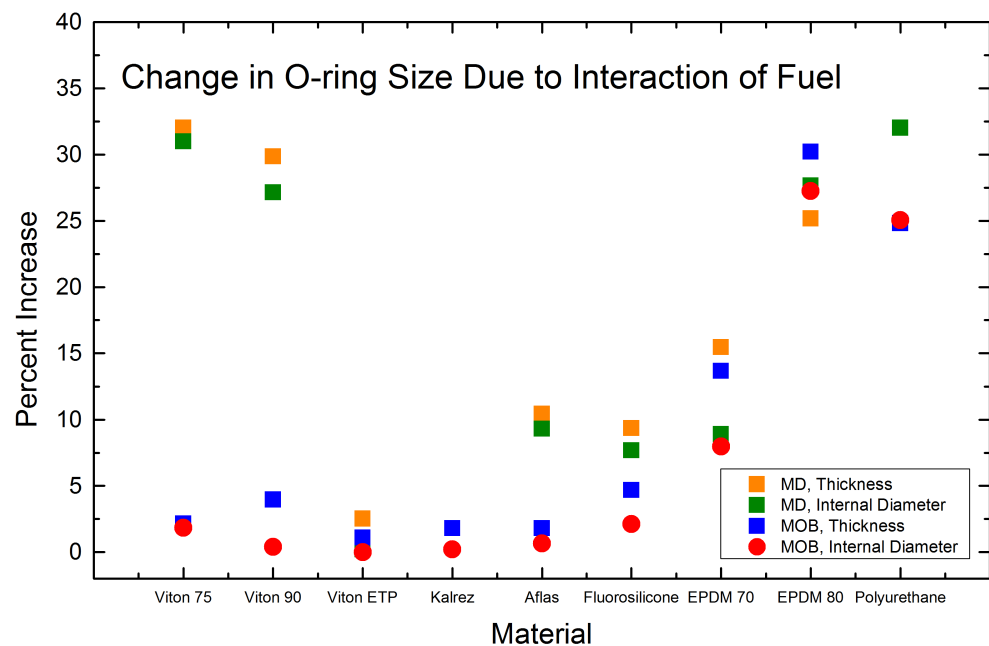


Figure F.3: Change in o-ring size (as compared to nominal values) due to interaction with methyl decanoate and the methyl oleate blend (two fuels discussed in Chapter 6). O-rings were submerged in the fuels for 15 days and then measured using digital calipers. The nominal o-ring dimensions (AS568-214 size) are $t = 0.139 \pm 0.004$ inch and $d_i = 0.984 \pm 0.010$ inch. The 70, 75, 80, and 90 numbers denote Shore A Rubber Durometer Hardness Scale values, where hardness increases with the Shore A number.

analysis must be conducted to ensure that even at the extremes of all tolerance values (for both the o-rings and the grooves), good compression/gland fill will still be achieved.

F.6 Summary

Topics including safety factors, pressure vessel design, window selection/plug design, and o-ring selection/groove design have been discussed in this appendix. The Lamé equations for thick-walled pressure vessels were given, and information regarding the selection of flanges and bolts was presented. Operating pressure limits for the CRVST components were also supplied. Window plug design was covered, including Equation F.11, which can be used to determine the appropriate window thickness for an optical port. Finally, a brief overview of o-rings was given, including recommendations concerning o-ring materials for use in corrosive environments.

Appendix G

Determining the fraction of fuel remaining after first stage ignition

G.1 Introduction

The helium-neon (HeNe) laser diagnostic is a simple yet powerful technique for observing fuel decay *in situ* during shock tube experiments. However, HeNe laser absorbance profiles show absorption by more than just the parent fuel; they also contain contributions from all fuel fragments and radicals present in the system that absorb at 3.39 μm . In order to obtain the mole fraction time history of fuel alone, corrections to the measured HeNe absorbance must be performed.

In this appendix, the methodology followed in order to correct the measured HeNe absorbance records from Chapter 9 is presented. The goal of this method was to determine the fraction of fuel remaining after first stage ignition during the experiments that were conducted at Negative Temperature Coefficient (NTC) region conditions. Note that alternate correction methods have also been recommended elsewhere [477, 478].

G.2 Procedure

The following procedure was followed in order to determine the fraction of fuel remaining after first stage ignition during the *n*-heptane oxidation experiments of Chapter 9. First, the Lawrence Livermore National Laboratory (LLNL) mechanism of Mehl *et al.* [328] was used in Chemkin-Pro [263] under constant enthalpy-pressure (H-P) constraints to estimate the *n*-heptane and intermediate hydrocarbon mole fractions during and after the first stage ignition event. These simulations were performed at 6.5 atm in *n*-heptane/15%O₂/5%CO₂/Ar ($\phi = 0.75$) mixtures at 25 K increments between 600 K and 825 K. Chemkin-Pro was asked to provide output data for the top 60 species in this analysis. In order to ensure that this was a sufficiently large number of intermediates, an estimation was performed using the top 80 species as well, revealing that the additional 20 species contributed minimally to the interference absorption at 3.39 μm .

In addition, the mechanism was used to compute the temperature and volume increase upon first stage ignition as a function of the initial temperature of the simulation (note that the H-P constraint implies that pressure remains constant through first stage ignition). The time at which the post-first-stage temperature and volume were taken was roughly specified as the instant when the derivative of the *n*-heptane mole fraction $\frac{dx_{\text{heptane}}}{dt}$ reached some small percentage of its maximum (most negative) value during the first stage ignition event (see Figure G.1). At 650 K, this percentage was 1%, and at 800 K, the percentage was 5%. The temperature increase $T_{\tau_1} - T_i = \Delta T$ and fractional volume increase $\frac{V_{\tau_1}}{V_i}$ were found to vary linearly with the initial simulation temperature (here, subscript *i* denotes initial properties, and subscript τ_1 denotes post-first-stage-ignition values; see Figure G.2).

Second, using cross section values measured by Klingbeil *et al.* [225, 226, 241] and the model-derived mole fraction and temperature data, absorbance profiles of each species *j* were simulated according to Equation G.1 (this equation was derived by rearranging Equation 9.1, wherein $n = \frac{x_j P}{R_u T}$).

$$\alpha_{sim,j} = x_j \sigma_{\nu,j} \frac{PL}{R_u T} \quad (\text{G.1})$$

In this equation, x_j is the simulated mole fraction, $\sigma_{\nu,j}$ is the temperature-dependent absorption

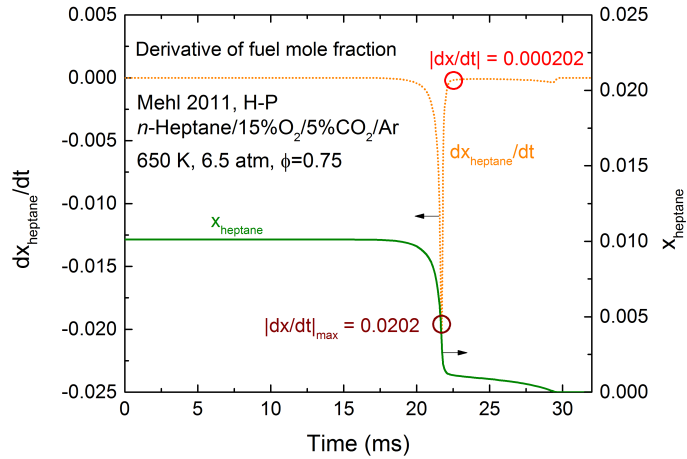


Figure G.1: Determination of the time at which the post-first-stage-ignition quantities (temperature, volume, and computed absorbance) were evaluated in the *n*-heptane oxidation simulation (LLNL mechanism [328] under H-P constraints). Conditions: *n*-heptane/15%O₂/5%CO₂/Ar, $\phi = 0.75$, $T = 650$ K, $P = 6.5$ atm.

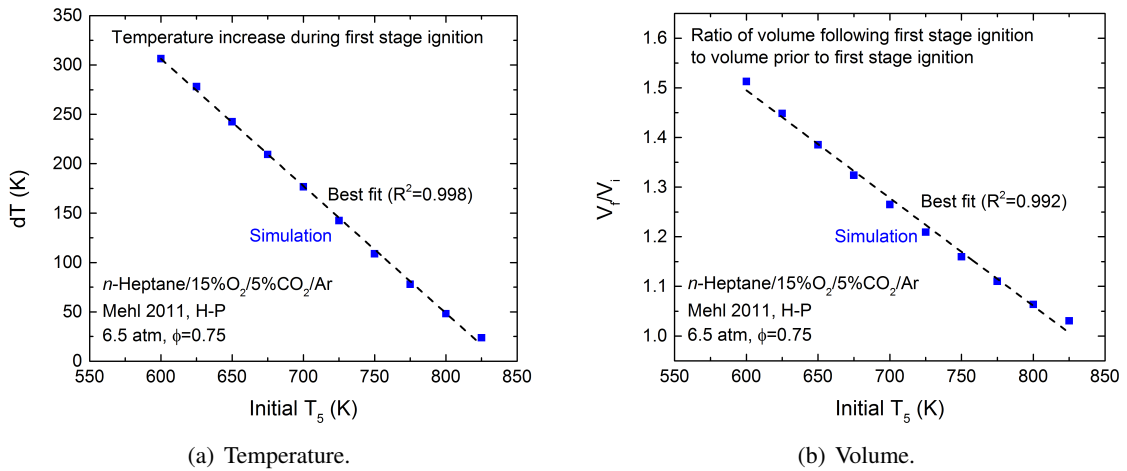


Figure G.2: Simulated a) temperature increase ($T_{\tau_1} - T_i = \Delta T$) and b) fractional volume increase ($\frac{V_{\tau_1}}{V_i}$) at first stage ignition as a function of initial simulation temperature T_5 using the LLNL mechanism [328] under H-P constraints. Conditions: *n*-heptane/15%O₂/5%CO₂/Ar, $\phi = 0.75$, $P = 6.5$ atm.

cross section at $3.39 \mu\text{m}$ of each species, P is the experimental pressure (constant), L is the optical path length, \hat{R}_u is the ideal gas constant, and T is the time-dependent experimental temperature. Example profiles (with similar species grouped together) are shown at 650 K and 800 K in Figure G.3, and example profiles showing total and *n*-heptane absorption are provided in Figure G.4.

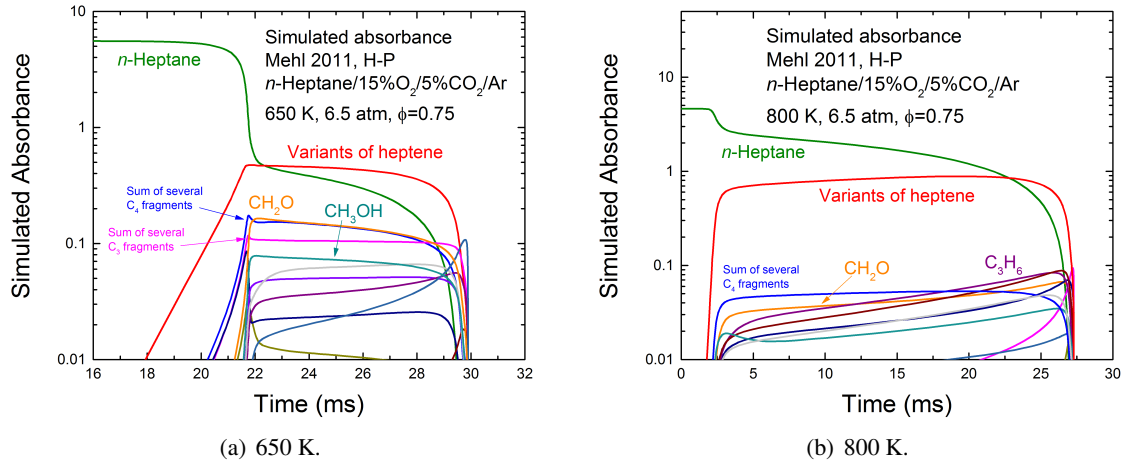


Figure G.3: Simulated absorbance profiles (with similar species grouped together) at a) 650 K and b) 800 K during *n*-heptane oxidation, created using the LLNL mechanism [328] under H-P constraints. Conditions: *n*-heptane/15%O₂/5%CO₂/Ar, $\phi = 0.75$, $P = 6.5$ atm, $L = 11.53$ cm.

Third, the fraction of simulated absorbance attributable to *n*-heptane, ξ , was computed according to Equation G.2, and the value immediately following first stage ignition, ξ_{τ_1} , was noted (in this equation, C is the number of interfering species). The time at which this value was taken is demonstrated in Figure G.1.

$$\xi = \frac{\alpha_{sim, heptane}}{\sum_{j=1}^C \alpha_{sim,j}} \quad (G.2)$$

This analysis was performed at several NTC temperatures, and the results showed, within the uncertainty of this method, a linear relationship between the initial experiment temperature T_i and ξ_{T_1} (Figure G.5). The majority of interference was found to come from C₇ fuel fragments, such as the heptene isomers (C₇H₁₄).

Fourth, for each experiment, the post-first-stage $3.39 \mu\text{m}$ total absorbance value, $\alpha_{exp,total,\tau_1}$, was noted and then corrected according to Equation G.3 to obtain the absorbance attributable only

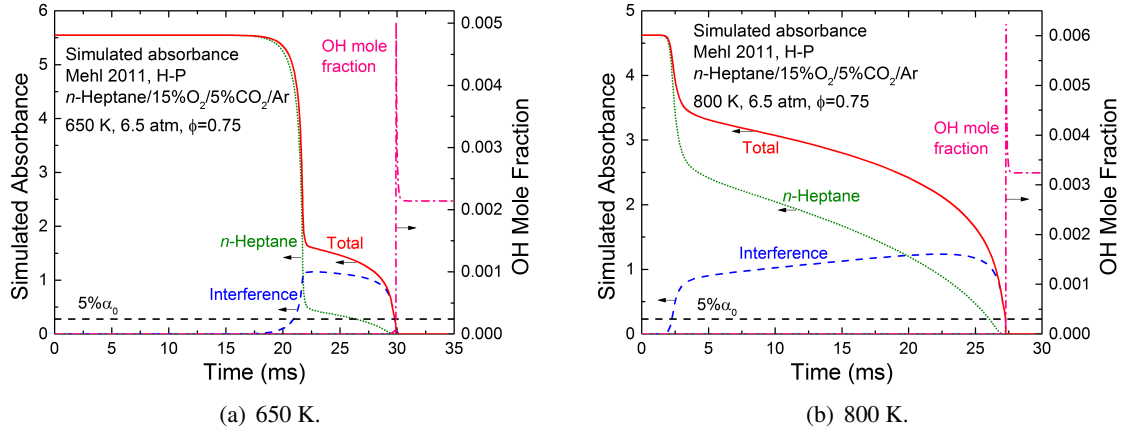


Figure G.4: Simulated *n*-heptane, interfering species, and total absorbance profiles at a) 650 K and b) 800 K during *n*-heptane oxidation, created using the LLNL mechanism [328] under H-P constraints. Also shown are the mole fraction of OH and a line denoting 5% of the initial ($t = 0$) absorbance. Notice that when the total absorbance drops to 5% of its initial value, the OH mole fraction rapidly increases, denoting the second-stage ignition event. Conditions: *n*-heptane/15%O₂/5%CO₂/Ar, $\phi = 0.75$, $P = 6.5$ atm, $L = 11.53$ cm.

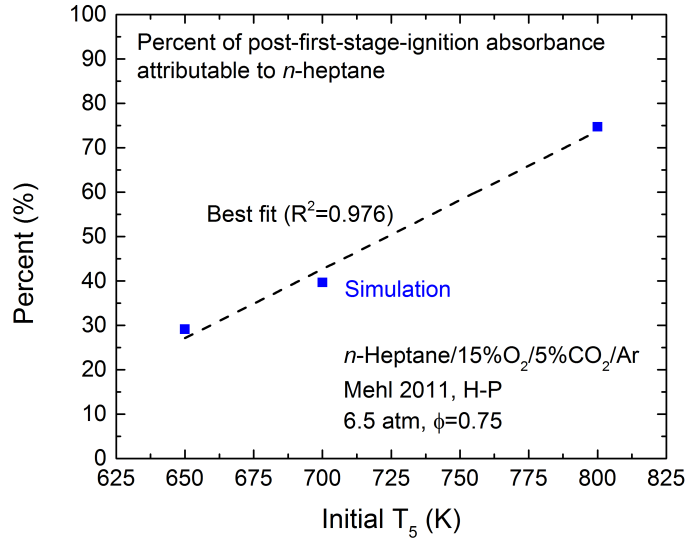


Figure G.5: Fraction of simulated absorbance attributable to *n*-heptane as a function of initial simulation temperature T_5 (LLNL mechanism [328] under H-P constraints). Conditions: *n*-heptane/15%O₂/5%CO₂/Ar, $\phi = 0.75$, $P = 6.5$ atm.

to *n*-heptane, $\alpha_{exp,heptane,\tau_1}$. Figure 9.3 shows examples of when these values were taken from the experimental data records.

$$\alpha_{exp,heptane,\tau_1} = \xi_{\tau_1} \alpha_{exp,total,\tau_1} \quad (\text{G.3})$$

This was then converted to the experimentally measured mole fraction of *n*-heptane $x_{exp,heptane,\tau_1}$ using Equation G.4 (here, T_{τ_1} is the temperature following first stage ignition (obtained from the simulation), and $\sigma_{\nu,heptane,\tau_1}$ is the absorption cross section of *n*-heptane at this temperature).

$$x_{exp,heptane,\tau_1} = \frac{\alpha_{exp,heptane,\tau_1} \hat{R}_u T_{\tau_1}}{P \sigma_{\nu,heptane,\tau_1} L} \quad (\text{G.4})$$

Finally, the fraction of *n*-heptane remaining after first stage ignition η_{exp,τ_1} was computed according to Equation G.5 (here, $N_{heptane,\tau_1}$ is the total number of moles of *n*-heptane remaining after first stage ignition, V_{τ_1} is the total gas volume following first stage ignition (obtained from the simulation), and quantities denoted *i* refer to those at the beginning of the experiment).

$$\eta_{exp,\tau_1} = \frac{N_{heptane,\tau_1}}{N_{heptane,i}} = \frac{x_{exp,heptane,\tau_1} V_{\tau_1} T_i}{x_{exp,heptane,i} V_i T_{\tau_1}} \quad (\text{G.5})$$

Likewise, the fraction of fuel remaining after ignition according to the mechanism η_{sim,τ_1} was computed for several T_i values according to Equation G.6 (here, $x_{sim,heptane,\tau_1}$ is the simulated mole fraction of *n*-heptane remaining after stage one ignition).

$$\eta_{sim,\tau_1} = \frac{N_{heptane,\tau_1}}{N_{heptane,i}} = \frac{x_{sim,heptane,\tau_1} V_{\tau_1} T_i}{x_{sim,heptane,i} V_i T_{\tau_1}} \quad (\text{G.6})$$

The results of this analysis are presented in Figure 9.4. Uncertainty values shown as error bars in the figure are computed by varying $x_{exp,heptane,i}$ ($\pm 2\%$), $\alpha_{exp,heptane,\tau_1}$ ($\pm 1\%$), $T_{5,i}$ ($\pm 0.3\%$), $P_{5,i}$ ($\pm 2\%$), ΔT ($\pm 2\%$), $\frac{V_{\tau_1}}{V_i}$ ($\pm 2\%$), $\sigma_{\nu,heptane,\tau_1}$ ($\pm 4\%$), and ξ ($\pm 14\%$).

G.3 Summary

A method for determining the fraction of fuel remaining after first stage ignition using the HeNe laser diagnostic has been presented. This algorithm relies upon predictions by kinetic mechanisms

to account for interfering absorption by fuel decomposition products. The results of this method can be used to better understand the low-temperature fuel consumption pathways for hydrocarbon fuels.

Appendix H

Ignition delay time data

H.1 Ignition delay time data

All raw ignition delay time data discussed in this dissertation are included here. Table H.1 contains data for methyl decanoate (MD) [65, 67, 68]. Table H.2 contains data for methyl laurate (MLA) [67, 68]. Table H.3 contains data for methyl myristate (MM) [67, 68]. Table H.4 contains data for methyl palmitate (MP) [67, 68]. Table H.5 contains data for methyl oleate (MO) [105, 258]. Table H.6 contains data for methyl linoleate (ML) [105, 258]. Table H.7 contains data for the methyl oleate/FAME blend (MOB) [65, 67, 68]. Finally, Table H.8 contains data for *n*-heptane [289].

Table H.1: Ignition delay time data for methyl decanoate [65, 67, 68].

Shock	Fuel	T_5 [K]	P_5 [atm]	ϕ	x_{Ar}	x_{O_2}	x_{fuel}	τ_{ign} [μs]
99154	MD	1335	6.64	0.66	0.98959	0.01000	0.00042	494
99155	MD	1368	6.56	0.67	0.98958	0.01000	0.00042	214
99156	MD	1388	6.42	0.81	0.98949	0.00999	0.00052	225
99158	MD	1331	6.86	0.72	0.98955	0.01000	0.00046	559
99159	MD	1278	6.74	0.66	0.98959	0.01000	0.00041	673
99160	MD	1262	6.93	0.65	0.98959	0.01000	0.00041	1077
99163	MD	1213	7.06	0.36	0.78635	0.20903	0.00462	285
99166	MD	1169	7.01	0.29	0.78706	0.20922	0.00372	642
99167	MD	1102	7.12	0.33	0.78662	0.20910	0.00427	1259
99168	MD	1059	7.22	0.36	0.78637	0.20903	0.00460	2226

Table H.1: (continued)

Shock	Fuel	T_5 [K]	P_5 [atm]	ϕ	x_{Ar}	x_{O_2}	x_{fuel}	τ_{ign} [\mu s]
99169	MD	1162	7.09	0.40	0.78593	0.20892	0.00515	621
99170	MD	1113	7.07	0.36	0.78631	0.20902	0.00468	995
99171	MD	1069	7.14	0.60	0.78385	0.20836	0.00779	1164
99172	MD	1026	7.15	0.55	0.78428	0.20848	0.00725	1944
99177	MD	1062	7.20	0.57	0.78415	0.20845	0.00740	1343

Table H.2: Ignition delay time data for methyl laurate [67, 68].

Shock	Fuel	T_5 [K]	P_5 [atm]	ϕ	x_{Ar}	x_{O_2}	x_{fuel}	τ_{ign} [\mu s]
299	MLA	1194	6.61	1.24	0.95741	0.03989	0.00270	1660
300	MLA	1230	6.65	1.24	0.95741	0.03989	0.00270	970
301	MLA	1247	6.64	1.30	0.95726	0.03989	0.00286	747
302	MLA	1249	6.47	1.25	0.95737	0.03989	0.00273	749
303	MLA	1197	6.64	1.22	0.95743	0.03989	0.00267	1159
304	MLA	1171	6.63	1.36	0.95714	0.03988	0.00298	1707
305	MLA	1281	6.63	1.34	0.95717	0.03988	0.00295	526
306	MLA	1309	6.65	1.35	0.95716	0.03988	0.00295	483
307	MLA	1332	6.75	1.41	0.95701	0.03988	0.00312	407
308	MLA	1354	6.69	1.38	0.95708	0.03988	0.00304	284
309	MLA	1332	6.60	1.24	0.95740	0.03989	0.00270	328
310	MLA	1264	6.42	0.80	0.95836	0.03993	0.00171	599
311	MLA	1250	6.56	0.67	0.95864	0.03994	0.00141	754
312	MLA	1218	6.65	0.74	0.95850	0.03994	0.00156	1105
314	MLA	1163	6.70	0.78	0.95841	0.03993	0.00166	2139
315	MLA	1321	6.67	0.80	0.95835	0.03993	0.00172	253
316	MLA	1287	6.51	0.75	0.95847	0.03994	0.00159	391
317	MLA	1300	6.66	0.81	0.95835	0.03993	0.00172	369
318	MLA	1179	6.69	0.83	0.95830	0.03993	0.00177	1768
319	MLA	1217	3.59	1.22	0.95744	0.03989	0.00266	1352
320	MLA	1254	3.54	1.02	0.95789	0.03991	0.00220	1166
321	MLA	1282	3.43	0.94	0.95805	0.03992	0.00203	509
328	MLA	1253	3.51	1.20	0.95748	0.03990	0.00262	1065
329	MLA	1278	3.54	1.20	0.95749	0.03990	0.00262	608
330	MLA	1241	6.73	0.75	0.95847	0.03994	0.00159	736
332	MLA	1274	3.43	1.21	0.95746	0.03989	0.00265	592
334	MLA	1297	3.51	1.43	0.95697	0.03987	0.00316	605
335	MLA	1351	3.61	1.44	0.95694	0.03987	0.00318	272

Table H.3: Ignition delay time data for methyl myristate [67, 68].

Shock	Fuel	T_5 [K]	P_5 [atm]	ϕ	x_{Ar}	x_{O_2}	x_{fuel}	τ_{ign} [μs]
336	MM	1212	6.67	1.07	0.95809	0.03992	0.00199	1016
337	MM	1214	6.71	0.98	0.95826	0.03993	0.00182	1013
338	MM	1275	6.66	0.88	0.95844	0.03993	0.00163	379
340	MM	1241	6.69	0.63	0.95890	0.03995	0.00115	653
341	MM	1222	6.68	0.54	0.95907	0.03996	0.00097	732
342	MM	1192	6.72	0.65	0.95886	0.03995	0.00119	1606
343	MM	1194	6.77	0.85	0.95850	0.03994	0.00156	1085
344	MM	1198	6.60	0.68	0.95880	0.03995	0.00125	999
345	MM	1162	6.68	0.69	0.95878	0.03995	0.00127	1807
346	MM	1221	6.64	0.73	0.95871	0.03995	0.00134	914
347	MM	1292	6.71	0.82	0.95855	0.03994	0.00151	387
348	MM	1255	6.62	0.70	0.95877	0.03995	0.00128	410
349	MM	1257	6.54	0.74	0.95869	0.03995	0.00136	509
350	MM	1278	6.45	0.82	0.95855	0.03994	0.00151	353
351	MM	1241	6.82	0.93	0.95835	0.03993	0.00172	679
352	MM	1214	6.71	1.17	0.95790	0.03991	0.00219	898
353	MM	1251	7.00	1.31	0.95763	0.03990	0.00246	828
354	MM	1258	6.84	1.27	0.95770	0.03990	0.00239	654
355	MM	1254	6.55	1.20	0.95785	0.03991	0.00224	629
356	MM	1295	6.86	1.33	0.95759	0.03990	0.00251	388
357	MM	1270	6.47	1.35	0.95755	0.03990	0.00255	519
358	MM	1322	6.69	1.33	0.95760	0.03990	0.00250	362
359	MM	1357	6.61	1.11	0.95802	0.03992	0.00206	203
361	MM	1317	6.61	0.68	0.95880	0.03995	0.00125	209
362	MM	1214	6.71	1.09	0.95804	0.03992	0.00204	790
363	MM	1194	6.66	1.08	0.95807	0.03992	0.00201	1188
365	MM	1195	6.76	1.00	0.95822	0.03993	0.00186	1293
366	MM	1162	6.71	1.15	0.95794	0.03991	0.00214	1987
367	MM	1231	3.37	0.74	0.95869	0.03995	0.00136	1101
374	MM	1297	3.34	0.87	0.95847	0.03994	0.00160	489
375	MM	1313	3.27	0.68	0.95880	0.03995	0.00125	291
376	MM	1312	3.25	0.74	0.95869	0.03995	0.00137	391
377	MM	1260	3.27	0.78	0.95862	0.03994	0.00144	536
378	MM	1244	3.33	0.90	0.95840	0.03993	0.00167	794
379	MM	1225	3.29	0.83	0.95853	0.03994	0.00153	935
380	MM	1207	3.28	0.81	0.95857	0.03994	0.00149	1552
381	MM	1332	3.23	0.71	0.95875	0.03995	0.00130	219

Table H.3: (continued)

Shock	Fuel	T_5 [K]	P_5 [atm]	ϕ	x_{Ar}	x_{O_2}	x_{fuel}	τ_{ign} [μs]
382	MM	1334	3.27	0.69	0.95878	0.03995	0.00127	208

Table H.4: Ignition delay time data for methyl palmitate [67, 68].

Shock	Fuel	T_5 [K]	P_5 [atm]	ϕ	x_{Ar}	x_{O_2}	x_{fuel}	τ_{ign} [μs]
212	MP	1242	6.32	0.29	0.95956	0.03998	0.00046	467
213	MP	1305	6.43	0.27	0.95959	0.03998	0.00042	221
214	MP	1311	6.60	0.30	0.95954	0.03998	0.00048	269
215	MP	1273	6.56	0.35	0.95946	0.03998	0.00056	378
216	MP	1267	6.59	0.36	0.95945	0.03998	0.00057	361
217	MP	1247	6.64	0.35	0.95946	0.03998	0.00056	503
218	MP	1213	6.55	0.34	0.95948	0.03998	0.00054	705
219	MP	1220	6.65	0.31	0.95954	0.03998	0.00048	646
220	MP	1205	6.66	0.36	0.95945	0.03998	0.00057	786
221	MP	1191	6.73	0.30	0.95955	0.03998	0.00047	962
257	MP	1180	3.31	0.78	0.95879	0.03995	0.00126	2199
258	MP	1240	3.36	0.61	0.95906	0.03996	0.00098	627
259	MP	1228	3.42	0.68	0.95896	0.03996	0.00109	1037
260	MP	1257	3.38	0.73	0.95887	0.03995	0.00117	592
261	MP	1251	3.21	0.68	0.95896	0.03996	0.00109	481
262	MP	1280	3.30	0.81	0.95875	0.03995	0.00130	394
263	MP	1309	3.34	0.69	0.95893	0.03996	0.00111	245
264	MP	1238	3.51	0.71	0.95891	0.03995	0.00114	740
265	MP	1196	3.44	0.69	0.95894	0.03996	0.00110	1535

Table H.5: Ignition delay time data for methyl oleate [105, 258].

Shock	Fuel	T_5 [K]	P_5 [atm]	ϕ	x_{Ar}	x_{O_2}	x_{fuel}	τ_{ign} [μs]
38	MO	1242	6.74	1.15	0.95836	0.03993	0.00171	556
39	MO	1248	6.78	1.17	0.95833	0.03993	0.00174	575
40	MO	1187	6.98	2.09	0.95691	0.03987	0.00322	1139
42	MO	1320	6.69	1.18	0.95832	0.03993	0.00175	285
45	MO	1284	6.90	1.08	0.95846	0.03994	0.00160	381
60	MO	1240	6.69	1.54	0.95777	0.03991	0.00232	622
61	MO	1256	6.66	1.47	0.95788	0.03991	0.00221	492

Table H.5: (continued)

Shock	Fuel	T_5 [K]	P_5 [atm]	ϕ	x_{Ar}	x_{O_2}	x_{fuel}	τ_{ign} [μs]
62	MO	1339	6.62	1.30	0.95813	0.03992	0.00195	232
64	MO	1212	6.95	1.41	0.95797	0.03992	0.00211	840
66	MO	1314	6.84	1.38	0.95802	0.03992	0.00206	319
67	MO	1189	6.87	1.34	0.95808	0.03992	0.00200	1110
68	MO	1162	6.75	1.29	0.95816	0.03992	0.00192	1296
69	MO	1182	7.00	1.27	0.95819	0.03992	0.00189	1409
70	MO	1137	6.75	1.20	0.95828	0.03993	0.00179	2137
75	MO	1332	6.47	1.46	0.95789	0.03991	0.00219	233
78	MO	1314	6.68	0.80	0.95888	0.03995	0.00117	193
80	MO	1242	6.84	0.71	0.95900	0.03996	0.00104	544
81	MO	1188	6.78	0.70	0.95902	0.03996	0.00102	869
82	MO	1152	6.70	0.62	0.95914	0.03996	0.00090	1519
84	MO	1316	6.84	2.23	0.95669	0.03986	0.00345	417
85	MO	1229	6.82	2.02	0.95702	0.03988	0.00310	730
86	MO	1203	6.97	1.93	0.95716	0.03988	0.00296	998
87	MO	1159	7.25	2.39	0.95642	0.03985	0.00373	1372
88	MO	1131	6.94	1.69	0.95753	0.03990	0.00257	2533
89	MO	1115	6.73	1.71	0.95751	0.03990	0.00260	2187
93	MO	1143	6.84	1.86	0.95727	0.03989	0.00284	2006
94	MO	1276	6.82	2.11	0.95688	0.03987	0.00325	552
101	MO	1286	3.48	1.87	0.95725	0.03989	0.00286	601
102	MO	1370	3.42	1.41	0.95796	0.03992	0.00212	196
103	MO	1277	3.54	1.35	0.95806	0.03992	0.00202	645
105	MO	1196	3.50	1.30	0.95813	0.03992	0.00195	2129
106	MO	1220	3.47	1.38	0.95802	0.03992	0.00206	1311
107	MO	1337	3.42	1.54	0.95776	0.03991	0.00233	404
166	MO	1272	6.48	0.76	0.95893	0.03996	0.00112	334
167	MO	1160	6.76	0.75	0.95894	0.03996	0.00110	1625
170	MO	1316	6.59	2.10	0.95690	0.03987	0.00322	353
172	MO	1301	6.74	1.98	0.95708	0.03988	0.00304	381
173	MO	1257	6.72	2.01	0.95704	0.03988	0.00308	644
174	MO	1277	6.67	1.96	0.95712	0.03988	0.00300	528
177	MO	1255	3.43	1.46	0.95790	0.03991	0.00219	728
178	MO	1231	3.40	1.26	0.95819	0.03992	0.00188	1367
179	MO	1320	3.32	1.33	0.95810	0.03992	0.00198	432
180	MO	1355	3.37	1.34	0.95807	0.03992	0.00201	216

Table H.6: Ignition delay time data for methyl linoleate [105, 258].

Shock	Fuel	T_5 [K]	P_5 [atm]	ϕ	x_{Ar}	x_{O_2}	x_{fuel}	τ_{ign} [\mu s]
108	ML	1222	6.71	1.13	0.95836	0.03993	0.00170	782
109	ML	1194	6.82	1.11	0.95839	0.03993	0.00168	1066
110	ML	1147	6.72	1.25	0.95817	0.03992	0.00191	1797
113	ML	1143	7.02	1.38	0.95797	0.03992	0.00211	1976
114	ML	1268	6.95	1.45	0.95787	0.03991	0.00222	613
116	ML	1300	6.92	1.39	0.95796	0.03991	0.00213	414
117	ML	1319	6.71	1.40	0.95794	0.03991	0.00214	334
118	ML	1378	6.68	1.40	0.95795	0.03991	0.00213	185
119	ML	1325	6.53	1.44	0.95788	0.03991	0.00221	272
120	ML	1258	6.87	1.33	0.95806	0.03992	0.00202	571
121	ML	1276	6.78	0.86	0.95877	0.03995	0.00128	376
122	ML	1239	6.82	0.75	0.95892	0.03996	0.00112	684
123	ML	1192	6.82	0.74	0.95894	0.03996	0.00110	1028
124	ML	1163	6.93	0.77	0.95890	0.03995	0.00115	1232
125	ML	1141	6.94	0.73	0.95896	0.03996	0.00109	2071
126	ML	1330	6.73	0.70	0.95900	0.03996	0.00104	205
127	ML	1328	6.59	0.68	0.95903	0.03996	0.00101	199
128	ML	1188	7.19	2.00	0.95699	0.03987	0.00313	1020
129	ML	1169	7.25	1.98	0.95704	0.03988	0.00309	1369
130	ML	1219	7.01	1.87	0.95721	0.03988	0.00290	833
131	ML	1239	7.07	2.11	0.95683	0.03987	0.00331	788
132	ML	1128	7.15	1.91	0.95715	0.03988	0.00297	2032
134	ML	1290	6.87	2.35	0.95643	0.03985	0.00372	458
135	ML	1324	7.04	2.30	0.95651	0.03985	0.00364	364
136	ML	1332	6.84	2.24	0.95661	0.03986	0.00353	272
139	ML	1327	6.56	0.79	0.95886	0.03995	0.00119	190
140	ML	1334	6.33	0.75	0.95892	0.03996	0.00112	208
143	ML	1209	6.70	0.65	0.95907	0.03996	0.00097	831
144	ML	1233	6.59	0.78	0.95888	0.03995	0.00116	574
145	ML	1179	3.88	1.88	0.95718	0.03988	0.00293	2168
146	ML	1242	3.63	1.47	0.95783	0.03991	0.00226	935
147	ML	1233	3.68	1.43	0.95791	0.03991	0.00218	987
148	ML	1185	3.69	1.55	0.95771	0.03990	0.00239	2465
149	ML	1320	3.45	1.33	0.95806	0.03992	0.00202	378
150	ML	1297	3.40	1.07	0.95845	0.03994	0.00161	445
151	ML	1350	3.27	1.07	0.95845	0.03994	0.00162	246

Table H.6: (continued)

Shock	Fuel	T_5 [K]	P_5 [atm]	ϕ	x_{Ar}	x_{O_2}	x_{fuel}	τ_{ign} [μs]
152	ML	1334	3.49	1.54	0.95773	0.03991	0.00236	371
153	ML	1258	3.59	1.23	0.95820	0.03992	0.00188	746

Table H.7: Ignition delay time data for the methyl oleate/FAME blend [65, 67, 68].

Shock	Fuel	T_5 [K]	P_5 [atm]	ϕ	x_{Ar}	x_{O_2}	x_{fuel}	τ_{ign} [μs]
99093	MOB	1205	6.57	0.32	0.95952	0.03998	0.00050	827
99094	MOB	1158	6.62	0.42	0.95937	0.03997	0.00065	1653
99095	MOB	1257	6.63	0.42	0.95938	0.03997	0.00065	512
99096	MOB	1209	6.55	0.55	0.95918	0.03997	0.00086	907
99097	MOB	1176	6.63	0.59	0.95911	0.03996	0.00092	1285
99098	MOB	1170	6.68	0.54	0.95918	0.03997	0.00085	1377
99099	MOB	1280	6.85	0.80	0.95878	0.03995	0.00127	443
99100	MOB	1313	6.97	0.99	0.95848	0.03994	0.00158	321
99101	MOB	1338	6.78	1.05	0.95838	0.03993	0.00169	248
99102	MOB	1338	6.50	1.14	0.95825	0.03993	0.00183	267
99103	MOB	1360	6.51	1.38	0.95785	0.03991	0.00224	217
99105	MOB	1242	6.58	0.50	0.95925	0.03997	0.00078	650
99108	MOB	1141	6.78	1.16	0.95821	0.03993	0.00186	1768
99109	MOB	1212	7.07	0.87	0.95867	0.03994	0.00138	925
99110	MOB	1210	6.95	1.16	0.95821	0.03993	0.00186	874
99111	MOB	1331	6.82	0.64	0.95903	0.03996	0.00101	216
99112	MOB	1345	6.55	0.69	0.95895	0.03996	0.00109	192
99113	MOB	1286	6.82	0.55	0.95917	0.03997	0.00086	354
99117	MOB	1200	6.88	1.17	0.95820	0.03992	0.00188	1013
99118	MOB	1271	6.74	1.08	0.95834	0.03993	0.00173	530
99119	MOB	1314	6.67	1.30	0.95798	0.03992	0.00211	325
99121	MOB	1306	6.77	1.13	0.95826	0.03993	0.00181	395
99122	MOB	1235	6.91	1.28	0.95801	0.03992	0.00207	754
99123	MOB	1191	6.88	1.07	0.95835	0.03993	0.00172	1193
99133	MOB	1234	6.73	1.10	0.95831	0.03993	0.00176	705
99134	MOB	1309	6.64	1.42	0.95778	0.03991	0.00231	388
99135	MOB	1175	6.86	1.17	0.95819	0.03992	0.00188	1204
99136	MOB	1181	6.97	1.32	0.95795	0.03991	0.00213	1360
99137	MOB	1234	6.91	0.63	0.95904	0.03996	0.00100	837

Table H.7: (continued)

Shock	Fuel	T_5 [K]	P_5 [atm]	ϕ	x_{Ar}	x_{O_2}	x_{fuel}	τ_{ign} [μs]
99138	MOB	1256	6.88	0.68	0.95897	0.03996	0.00107	642
99139	MOB	1288	6.59	0.67	0.95899	0.03996	0.00105	440
99140	MOB	1358	6.54	0.43	0.95936	0.03997	0.00067	166
99141	MOB	1225	6.92	0.62	0.95906	0.03996	0.00098	836

Table H.8: Ignition delay time data for *n*-heptane [289]. Equivalence ratio (ϕ) values do not include carbon dioxide. η_{exp,τ_1} is the fraction of fuel remaining after first stage ignition (see Equation G.5). Though not at constant pressure, approximate η_{exp,τ_1} values are also provided for conventional (full shock tube) filling data.

Shock	Initial T_5 [K]	Initial P_5 [atm]	x_{Ar}	x_{O_2}	x_{CO_2}	x_{fuel}	ϕ	Filling Method	τ_{ign, OH^*} [μs]	$\tau_{ign,1, HeNe}$ [μs]	$\tau_{ign,1, HeNe}$ [μs]	η_{exp,τ_1}	Uncertainty in η_{exp,τ_1}
331	721	6.7	0.009858	0.148521	0.791124	0.050497	0.73	CRV	6391	24463	0.26	±29%	
333	777	6.2	0.009878	0.148518	0.791107	0.050496	0.73	CRV	4032	20456	0.44	±29%	
335	746	6.4	0.010694	0.148396	0.790455	0.050455	0.79	CRV	4108	27925	0.33	±29%	
338	808	6.4	0.009742	0.148539	0.791216	0.050503	0.72	CRV	4961	23263	0.52	±28%	
342	713	6.7	0.009927	0.148511	0.791069	0.050494	0.74	CRV	6650	27586	0.25	±29%	
345	690	6.6	0.010046	0.148493	0.790973	0.050488	0.74	CRV	9845	29360	0.21	±30%	
348	803	6.1	0.009684	0.148547	0.791262	0.050506	0.72	CRV	6124	33520	0.54	±28%	
349	817	6.2	0.009809	0.148529	0.791162	0.050500	0.73	CRV		47965			
350	660	6.6	0.009875	0.148519	0.791110	0.050496	0.73	CRV	21531	37730	0.14	±30%	
351	758	6.2	0.010034	0.148495	0.790983	0.050488	0.74	CRV	3412	33808	0.38	±29%	
352	1223	6.3	0.010188	0.148472	0.790860	0.050480	0.75	CRV	437				
354	652	6.6	0.009667	0.148550	0.791276	0.050507	0.72	CRV	29476	45867	0.14	±31%	
358	651	7.0	0.009909	0.148514	0.791083	0.050495	0.73	CRV	41105		0.14	±31%	
360	672	6.7	0.008255	0.148987	0.792188	0.050569	0.61	Full	17797	44157	0.20	±30%	
361	721	6.7	0.008335	0.148975	0.792124	0.050565	0.62	Full	5731	34859	0.29	±29%	
418	765	6.4	0.010510	0.148374	0.790577	0.050538	0.78	Full	3846	18340	0.34	±29%	
425	779	6.4	0.010513	0.148423	0.790600	0.050464	0.78	CRV	4027	30204			
441	705	6.6	0.009723	0.148542	0.791231	0.050504	0.72	CRV	8114	26816	0.25	±29%	
442	703	6.5	0.009855	0.148522	0.791126	0.050497	0.73	CRV	8182	26832	0.24	±29%	
446	766	6.4	0.009838	0.148524	0.791139	0.050498	0.73	CRV	3761	28719	0.41	±29%	
447	763	6.3	0.009679	0.148548	0.791266	0.050506	0.72	CRV	3691	28418	0.40	±29%	
449	670	6.8	0.009800	0.148530	0.791170	0.050500	0.73	CRV	18222	35618	0.17	±30%	
450	673	6.9	0.009800	0.148530	0.791170	0.050500	0.73	CRV	16950	34799	0.17	±30%	
451	770	6.4	0.009764	0.148535	0.791199	0.050502	0.72	CRV	3462	32373	0.42	±29%	
452	673	6.9	0.009907	0.148514	0.791084	0.050495	0.73	CRV	16755	32557	0.17	±30%	
453	703	6.5	0.009904	0.148515	0.791087	0.050495	0.73	CRV	7852	25037	0.24	±29%	
454	669	6.8	0.009884	0.148518	0.791103	0.050496	0.73	CRV	17643	33630	0.16	±30%	
457	667	6.7	0.010097	0.148487	0.790927	0.050489	0.75	Full	23082	35189	0.24	±30%	
458	704	6.6	0.010457	0.148433	0.790640	0.050471	0.77	Full	8831	22741	0.25	±29%	
459	814	6.3	0.010921	0.148364	0.790269	0.050447	0.81	Full	6082	23197	0.53	±28%	
479	1099	7.4	0.008145	0.148871	0.792361	0.050623	0.60	CRV	1851				
480	1134	7.1	0.008196	0.148863	0.792320	0.050621	0.61	CRV	1153				
481	1194	7.2	0.008250	0.148855	0.792277	0.050618	0.61	CRV	545				
482	1072	7.3	0.008206	0.148862	0.792312	0.050620	0.61	CRV	2701				

Table H.8: (continued)

Shock	Initial T_5 [K]	Initial P_5 [atm]	x_{Ar}	x_{O_2}	x_{CO_2}	x_{fuel}	ϕ	Filling Method	$\tau_{\text{ign}, \text{OH}^*}$ [μs]	$\tau_{\text{ign}, 1, \text{HeNe}}$ [μs]	$\tau_{\text{ign}, 1, \text{HeNe}}$ [μs]	$\eta_{\text{exp}, \tau_1}$	Uncertainty in $\eta_{\text{exp}, \tau_1}$
483	1173	7.2	0.008368	0.148837	0.792183	0.050612	0.62	Full	664				
484	1116	7.5	0.008419	0.148830	0.792142	0.050609	0.62	Full	1968				
485	1127	7.2	0.008474	0.148822	0.792098	0.050606	0.63	Full	1285				
486	1068	7.2	0.008626	0.148799	0.791977	0.050599	0.64	Full	3090				

Bibliography

- [1] Linda E. Doman, Vipin Arora, Alexander Metelitsa, Michael Leahy, Justine L. Barden, Michael Ford, Michael L. Mellish, Ayaka Jones, Brian T. Murphy, Kevin Lillis, Nancy Slater-Thompson, Behjat Hojjati, David Peterson, Peter Gross, Victoria V. Zaretskaya, Nicholas Chase, Michael Morris, and Perry Lindstrom. International energy outlook 2013. Technical Report DOE/EIA-0484(2013), U.S. Energy Information Administration, U.S. Department of Energy, July 2013.
- [2] James V. Gardner, Larry A. Mayer, and John E. Hughs Clarke. Morphology and processes in Lake Tahoe (California-Nevada). *Geological Society of America Bulletin*, 112(5):736–746, 2000.
- [3] Charles E. Herdendorf. Distribution of the world's large lakes. In Max M. Tilzer and Colette Serruya, editors, *Large Lakes*, Brock/Springer Series in Contemporary Bioscience, pages 3–38. Springer Berlin Heidelberg, 1990.
- [4] EPA. Paving the way toward cleaner, more efficient trucks. Technical Report EPA-420-F-11-032, United States Environmental Protection Agency, Office of Transportation and Air Quality, August, 2011.
- [5] United States White House. Improving the fuel efficiency of American trucks - Bolstering energy security, cutting carbon pollution, saving money and supporting manufacturing innovation. Technical report, The White House, Office of the Press Secretary, February 18 2014.

- [6] EIA. Gasoline and diesel fuel update. Technical report, United States Energy Information Administration, 2014.
- [7] Ray LaHood and Lisa P. Jackson. Greenhouse gas emissions standards and fuel efficiency standards for medium- and heavy-duty engines and vehicles; Final rule. *Federal Register*, 76(179):57106–57513, 2011.
- [8] Ray LaHood and Bob Perciasepe. Heavy-duty engine and vehicle, and nonroad technical amendments; Final rule. *Federal Register*, 78(116):36370–36406, 2013.
- [9] American Society for Testing and Materials (ASTM) standard D6751. Standard specification for biodiesel fuel blend stock (B100) for middle distillate fuels.
- [10] B. Freedman, E. H. Pryde, and T. L. Mounts. Variables affecting the yields of fatty esters from transesterified vegetable oils. *Journal of the American Oil Chemists Society*, 61(10):1638–1643, 1984.
- [11] Fangrui Ma and Milford A Hanna. Biodiesel production: A review. *Bioresource Technology*, 70(1):1–15, 1999.
- [12] Gerhard Knothe. Biodiesel and renewable diesel: A comparison. *Progress in Energy and Combustion Science*, 36(3):364–373, 2010.
- [13] Fengxian Qiu, Yihuai Li, Dongya Yang, Xiaohua Li, and Ping Sun. Biodiesel production from mixed soybean oil and rapeseed oil. *Applied Energy*, 88(6):2050–2055, 2011.
- [14] Gerhard Knothe. Designer biodiesel: Optimizing fatty ester composition to improve fuel properties. *Energy & Fuels*, 22(2):1358–1364, 2008.
- [15] Michael S. Graboski and Robert L. McCormick. Combustion of fat and vegetable oil derived fuels in diesel engines. *Progress in Energy and Combustion Science*, 24(2):125–164, 1998.
- [16] Michael J. Haas, Nadia Adawi, William W. Berry, Elaine Feldman, Stephen Kasprzyk, Brian Ratigan, Karen Scott, and Emily Bockian Landsburg. Butter as a feedstock for biodiesel production. *Journal of Agricultural and Food Chemistry*, 58(13):7680–7684, 2010.

- [17] Takuya Ito, Yusuke Sakurai, Yusuke Kakuta, Motoyuki Sugano, and Katsumi Hirano. Biodiesel production from waste animal fats using pyrolysis method. *Fuel Processing Technology*, 94(1):47–52, 2012.
- [18] A. L. Ahmad, N. H. Mat Yasin, C. J. C. Derek, and J. K. Lim. Microalgae as a sustainable energy source for biodiesel production: A review. *Renewable and Sustainable Energy Reviews*, 15(1):584–593, 2011.
- [19] Jing-Qi Lai, Zhang-Li Hu, Peng-Wei Wang, and Zhen Yang. Enzymatic production of microalgal biodiesel in ionic liquid [BMIm][PF₆]. *Fuel*, 95(0):329–333, 2012.
- [20] Canan Kaya, Candan Hamamci, Akin Baysal, Osman Akba, Sait Erdogan, and Abdurrahman Saydut. Methyl ester of peanut (*Arachis hypogea L.*) seed oil as a potential feedstock for biodiesel production. *Renewable Energy*, 34(5):1257–1260, 2009.
- [21] Bryan R. Moser, Fred J. Eller, Brent H. Tisserat, and Alan Gravett. Preparation of fatty acid methyl esters from osage orange (*Maclura pomifera*) oil and evaluation as biodiesel. *Energy & Fuels*, 25(4):1869–1877, 2011.
- [22] N. Usta. An experimental study on performance and exhaust emissions of a diesel engine fuelled with tobacco seed oil methyl ester. *Energy Conversion and Management*, 46(15–16):2373–2386, 2005.
- [23] Derek R. Vardon, Bryan R. Moser, Wei Zheng, Katie Witkin, Roque L. Evangelista, Timothy J. Strathmann, Kishore Rajagopalan, and Brajendra K. Sharma. Complete utilization of spent coffee grounds to produce biodiesel, bio-oil, and biochar. *ACS Sustainable Chemistry & Engineering*, 1(10):1286–1294, 2013.
- [24] Antoine Osmont, Laurent Catoire, and Philippe Dagaut. Thermodynamic data for the modeling of the thermal decomposition of biodiesel. 1. Saturated and monounsaturated FAMEs. *The Journal of Physical Chemistry A*, 114(11):3788–3795, 2010. PMID: 19694476.
- [25] C. E. Goering, A. W. Schwab, M. J. Daugherty, E. H. Pryde, and A. J. Heakin. Fuel properties

- of eleven vegetable oils. *Transactions of the American Society of Agricultural and Biological Engineers*, 25(6):1472–1477, 1982.
- [26] C. A. W. Allen, K. C. Watts, R. G. Ackman, and M. J. Pegg. Predicting the viscosity of biodiesel fuels from their fatty acid ester composition. *Fuel*, 78(11):1319–1326, 1999.
- [27] W. Yuan, A. C. Hansen, and Q. Zhang. Vapor pressure and normal boiling point predictions for pure methyl esters and biodiesel fuels. *Fuel*, 84(7–8):943–950, 2005.
- [28] Gerhard Knothe, Andrew C. Matheaus, and Thomas W. Ryan, III. Cetane numbers of branched and straight-chain fatty esters determined in an ignition quality tester. *Fuel*, 82(8):971–975, 2003.
- [29] Gerhard Knothe and Kevin R. Steidley. Lubricity of components of biodiesel and petrodiesel. the origin of biodiesel lubricity. *Energy & Fuels*, 19(3):1192–1200, 2005.
- [30] DOE. Just the basics: Biodiesel. Technical report, United States Department of Energy, Office of Energy Efficiency and Renewable Energy, August 2003.
- [31] Ayhan Demirbas. Importance of biodiesel as transportation fuel. *Energy Policy*, 35(9):4661–4670, 2007.
- [32] C. K. Westbrook, C. V. Naik, O. Herbinet, W. J. Pitz, M. Mehl, S. M. Sarathy, and H. J. Curran. Detailed chemical kinetic reaction mechanisms for soy and rapeseed biodiesel fuels. *Combustion and Flame*, 158(4):742–755, 2011. Special Issue on Kinetics.
- [33] EPA. A comprehensive analysis of biodiesel impacts on exhaust emissions. Technical Report EPA420-P-02-001, United States Environmental Protection Agency, Office of Transportation and Air Quality, Assessment and Standards Division, October 2002.
- [34] Gerhard Knothe, Christopher A. Sharp, and Thomas W. Ryan. Exhaust emissions of biodiesel, petrodiesel, neat methyl esters, and alkanes in a new technology engine. *Energy & Fuels*, 20(1):403–408, 2006.

- [35] Magin Lapuerta, Octavio Armas, and Jose Rodriguez-Fernandez. Effect of biodiesel fuels on diesel engine emissions. *Progress in Energy and Combustion Science*, 34(2):198–223, 2008.
- [36] Alessandro Schönborn, Nicos Ladommatos, John Williams, Robert Allan, and John Roger-son. The influence of molecular structure of fatty acid monoalkyl esters on diesel combustion. *Combustion and Flame*, 156(7):1396–1412, 2009.
- [37] Charles K. Westbrook, William J. Pitz, and Henry J. Curran. Chemical kinetic modeling study of the effects of oxygenated hydrocarbons on soot emissions from diesel engines. *The Journal of Physical Chemistry A*, 110(21):6912–6922, 2006. PMID: 16722706.
- [38] Jiafeng Sun, Jerald A. Caton, and Timothy J. Jacobs. Oxides of nitrogen emissions from biodiesel-fuelled diesel engines. *Progress in Energy and Combustion Science*, 36(6):677–695, 2010.
- [39] B. M. Knight, J. A. Bittle, and T. J. Jacobs. The role of system responses on biodiesel nitric oxide emissions in a medium-duty diesel engine. *International Journal of Engine Research*, 12(4):336–352, 2011.
- [40] T. Gouw and J. Vlugter. Physical properties of fatty acid methyl esters. IV. Ultrasonic sound velocity. *Journal of the American Oil Chemists' Society*, 41:524–526, 1964.
- [41] Mustafa E. Tat, Jon H. Gerpen, Seref Soylu, Mustafa Canakci, Abdul Monyem, and Samuel Wormley. The speed of sound and isentropic bulk modulus of biodiesel at 21 °C from atmospheric pressure to 35 MPa. *Journal of the American Oil Chemists' Society*, 77(3):285–289, 2000.
- [42] James P. Szybist, André L. Boehman, Joshua D. Taylor, and Robert L. McCormick. Evaluation of formulation strategies to eliminate the biodiesel NO_x effect. *Fuel Processing Technology*, 86(10):1109–1126, 2005. Biodiesel Processing and Production.
- [43] C. P. Fenimore. Formation of nitric oxide in premixed hydrocarbon flames. *Symposium (International) on Combustion*, 13(1):373–380, 1971. 13th Symposium (International) on Combustion.

- [44] R. L. McCormick, A. Williams, J. Ireland, M. Brimhall, and R. R. Hayes. Effects of biodiesel blends on vehicle emissions. Technical Report NREL/MP-540-40554, National Renewable Energy Laboratory, October 2006 2006.
- [45] A. S. Cheng, A. Upatnieks, and C. J. Mueller. Investigation of the impact of biodiesel fuelling on NO_x emissions using an optical direct injection diesel engine. *International Journal of Engine Research*, 7(4):297–318, 2006.
- [46] Robert L. McCormick, Christopher J. Tennant, R. Robert Hayes, Stuart Black, John Ireland, Tom McDaniel, Aaron Williams, Mike Frailey, and Christopher A. Sharp. Regulated emissions from biodiesel tested in heavy-duty engines meeting 2004 emission standards. Technical Report 2005-01-2200, Society of Automotive Engineers International, 2005.
- [47] George A. Ban-Weiss, J. Y. Chen, Bruce A. Buchholz, and Robert W. Dibble. A numerical investigation into the anomalous slight NO_x increase when burning biodiesel; A new (old) theory. *Fuel Processing Technology*, 88(7):659–667, 2007. Biofuels for Transportation.
- [48] C. K. Westbrook, W. J. Pitz, S. M. Sarathy, and M. Mehl. Detailed chemical kinetic modeling of the effects of C=C double bonds on the ignition of biodiesel fuels. *Proceedings of the Combustion Institute*, 34(2):3049–3056, 2013.
- [49] DOE. Clean cities alternative fuel price report. Technical report, United States Department of Energy, Office of Energy Efficiency and Renewable Energy, January 2014.
- [50] DOE. Alternative Fuels Data Center - Fuel properties comparison. Technical report, United States Department of Energy, Office of Energy Efficiency and Renewable Energy, 2014.
- [51] Robert O. Dunn and Gerhard Knothe. Oxidative stability of biodiesel in blends with jet fuel by analysis of oil stability index. *Journal of the American Oil Chemists' Society*, 80(10):1047–1048, 2003.
- [52] Gerhard Knothe. Some aspects of biodiesel oxidative stability. *Fuel Processing Technology*, 88(7):669–677, 2007. Biofuels for Transportation.

- [53] T. T. Kivevele, M. M. Mbarawa, A. Bereczky, T. Laza, and J. Madarasz. Impact of antioxidant additives on the oxidation stability of biodiesel produced from Croton Megalocarpus oil. *Fuel Processing Technology*, 92(6):1244–1248, 2011.
- [54] Nwadike Isioma, Yahaya Muhammad, O'Donnell Sylvester, Demshemino Innocent, and Okoro Linus. Cold flow properties and kinematic viscosity of biodiesel. *Universal Journal of Chemistry*, 1(4):135–141, 2013.
- [55] Long Liang, Chitralkumar V. Naik, Karthik Puduppakkam, Cheng Wang, Abhijit Modak, Ellen Meeks, Hai-Wen Ge, Rolf Reitz, and Christopher Rutland. Efficient simulation of diesel engine combustion using realistic chemical kinetics in CFD. In *Society of Automotive Engineers 2010 World Congress & Exhibition*, number 2010-01-0178, Detroit, Michigan, April 13–15, 2010 2010. Society of Automotive Engineers.
- [56] Katharina Kohse-Höinghaus, Patrick Oßwald, Terrill A. Cool, Tina Kasper, Nils Hansen, Fei Qi, Charles K. Westbrook, and Phillip R. Westmoreland. Biofuel combustion chemistry: From ethanol to biodiesel. *Angewandte Chemie International Edition*, 49(21):3572–3597, 2010.
- [57] Zekai Hong, David F. Davidson, and Ronald K. Hanson. An Improved H₂/O₂ mechanism based on recent shock tube/laser absorption measurements. *Combustion and Flame*, 158(4):633–644, 2011. Special Issue on Kinetics.
- [58] Tianfeng Lu and Chung K. Law. Toward accommodating realistic fuel chemistry in large-scale computations. *Progress in Energy and Combustion Science*, 35(2):192–215, 2009.
- [59] Charles K. Westbrook, Jürgen Warnatz, and William J. Pitz. A detailed chemical kinetic reaction mechanism for the oxidation of *iso*-octane and *n*-heptane over an extended temperature range and its application to analysis of engine knock. *Symposium (International) on Combustion*, 22(1):893–901, 1989.
- [60] C. S. Chang, Y. Zhang, K. N. C. Bray, and B. Rogg. Modelling and simulation of autoignition

- under simulated diesel-engine conditions. *Combustion Science and Technology*, 113(1):205–219, 1996.
- [61] Patrick Jenny, Dirk Roekaerts, and Nijso Beishuizen. Modeling of turbulent dilute spray combustion. *Progress in Energy and Combustion Science*, 38(6):846–887, 2012.
- [62] Hukam C. Mongia. Recent progress in comprehensive modeling of gas turbine combustion. In *46th AIAA Aerospace Sciences Meeting and Exhibit*, number AIAA 2008-1445, Reno, Nevada, 7-10 January 2008 2008. AIAA, AIAA.
- [63] Man Zhang, Zhenbo Fu, Yuzhen Lin, and Jibao Li. CFD study of NO_x emissions in a model commercial aircraft engine combustor. *Chinese Journal of Aeronautics*, 25(6):854 – 863, 2012.
- [64] L. Y. M. Gicquel, G. Staffelbach, and T. Poinsot. Large eddy simulations of gaseous flames in gas turbine combustion chambers. *Progress in Energy and Combustion Science*, 38(6):782–817, 2012.
- [65] Matthew F. Campbell, David F. Davidson, and Ronald K. Hanson. A second-generation aerosol shock tube and its use in studying ignition delay times of large biodiesel surrogates. In *Proceedings of the 28th International Symposium on Shock Waves, Manchester, United Kingdom*, July 2011.
- [66] Daniel R. Haylett, David F. Davidson, and Ronald K. Hanson. Ignition delay times of low-vapor-pressure fuels measured using an aerosol shock tube. *Combustion and Flame*, 159(2):552 – 561, 2012.
- [67] Matthew F. Campbell, David F. Davidson, and Ronald K. Hanson. Ignition delay times of very-low-vapor-pressure biodiesel surrogates behind reflected shock waves. In *8th United States Combustion Meeting, Park City, Utah*, number 070RK-0008, May 2013.
- [68] Matthew F. Campbell, David F. Davidson, and Ronald K. Hanson. Ignition delay times of very-low-vapor-pressure biodiesel surrogates behind reflected shock waves. *Fuel*, 126(0):271–281, 2014.

- [69] S. Garner and K. Brezinsky. Biologically derived diesel fuel and NO formation: An experimental and chemical kinetic study, Part 1. *Combustion and Flame*, 158(12):2289–2301, 2011.
- [70] Helena Patricia Ramirez Lancheros, Mustapha Fikri, Leonel Rincón Cancino, Gladys Moréac, Christof Schulz, and Philippe Dagaut. Autoignition of surrogate biodiesel fuel (B30) at high pressures: Experimental and modeling kinetic study. *Combustion and Flame*, 159(3):996–1008, 2012.
- [71] B. Rotavera and E. L. Petersen. Ignition behavior of pure and blended methyl octanoate, *n*-nonane, and methylcyclohexane. *Proceedings of the Combustion Institute*, 34(1):435–442, 2013.
- [72] C. Togbé, J.-B. May-Carle, G. Dayma, and P. Dagaut. Chemical kinetic study of the oxidation of a biodiesel-bioethanol surrogate fuel: Methyl octanoate-ethanol mixtures. *The Journal of Physical Chemistry A*, 114(11):3896–3908, 2010. PMID: 20235606.
- [73] C. Togbé, G. Dayma, A. Mze-Ahmed, and P. Dagaut. Experimental and modeling study of the kinetics of oxidation of simple biodiesel-biobutanol surrogates: Methyl octanoate-butanol mixtures. *Energy & Fuels*, 24(7):3906–3916, 2010.
- [74] G. Dayma, S. M. Sarathy, C. Togbé, C. Yeung, M. J. Thomson, and P. Dagaut. Experimental and kinetic modeling of methyl octanoate oxidation in an opposed-flow diffusion flame and a jet-stirred reactor. *Proceedings of the Combustion Institute*, 33(1):1037–1043, 2011.
- [75] H. P. Ramirez, K. Hadj-Ali, P. Diévert, G. Dayma, C. Togbé, G. Moréac, and P. Dagaut. Oxidation of commercial and surrogate bio-Diesel fuels (B30) in a jet-stirred reactor at elevated pressure: Experimental and modeling kinetic study. *Proceedings of the Combustion Institute*, 33(1):375–382, 2011.
- [76] S. Garner, T. Dubois, C. Togbé, N. Chaumeix, P. Dagaut, and K. Brezinsky. Biologically derived diesel fuel and no formation: Part 2: Model development and extended validation. *Combustion and Flame*, 158(12):2302–2313, 2011.

- [77] Pascal Diévert, Sang Hee Won, Jing Gong, Stephen Dooley, and Yiguang Ju. A comparative study of the chemical kinetic characteristics of small methyl esters in diffusion flame extinction. *Proceedings of the Combustion Institute*, 34(1):821–829, 2013.
- [78] J. Biet, V. Warth, O. Herbinet, P. A. Glaude, and F. Battin-Leclerc. Modelling study of the low-temperature oxidation of large methyl esters. In *Proceedings of the European Combustion Meeting 2009*, 2009.
- [79] Weijing Wang and Matthew A. Oehlschlaeger. A shock tube study of methyl decanoate autoignition at elevated pressures. *Combustion and Flame*, 159(2):476–481, 2012.
- [80] Zhenhua Li, Weijing Wang, Zhen Huang, and Matthew A. Oehlschlaeger. Autoignition of methyl decanoate, a biodiesel surrogate, under high-pressure exhaust gas recirculation conditions. *Energy & Fuels*, 26(8):4887–4895, 2012.
- [81] Weijing Wang, Sandeep Gowdagiri, and Matthew A. Oehlschlaeger. Comparative study of the autoignition of methyl decenoates, unsaturated biodiesel fuel surrogates. *Energy & Fuels*, 27(9):5527–5532, 2013.
- [82] Pierre Alexandre Glaude, Olivier Herbinet, Sarah Bax, Joffrey Biet, Valérie Warth, and Frédérique Battin-Leclerc. Modeling of the oxidation of methyl esters - Validation for methyl hexanoate, methyl heptanoate, and methyl decanoate in a jet-stirred reactor. *Combustion and Flame*, 157(11):2035–2050, 2010.
- [83] Olivier Herbinet, Pierre-Alexandre Glaude, Valorie Warth, and Frédérique Battin-Leclerc. Experimental and modeling study of the thermal decomposition of methyl decanoate. *Combustion and Flame*, 158(7):1288–1300, 2011.
- [84] Kalyanasundaram Seshadri, Tianfeng Lu, Olivier Herbinet, Stefan Humer, Ulrich Niemann, William J. Pitz, Reinhard Seiser, and Chung K. Law. Experimental and kinetic modeling study of extinction and ignition of methyl decanoate in laminar non-premixed flows. *Proceedings of the Combustion Institute*, 32(1):1067–1074, 2009.

- [85] Pascal Diévert, Sang Hee Won, Mruthunjaya Uddi, Stephen Dooley, Frederick L. Dryer, and Yiguang Ju. Measurements of extinction limits of methyl decanoate diffusion flames and a kinetic study. In *49th AIAA Aerospace Sciences Meeting including the New Horizons Forum and Aerospace Exposition, Orlando, Florida, January 4-7, 2011*, number AIAA-2011-697, 2011.
- [86] Yang L. Wang, Qiyao Feng, Fokion N. Egolfopoulos, and Theodore T. Tsotsis. Studies of C₄ and C₁₀ methyl ester flames. *Combustion and Flame*, 158(8):1507–1519, 2011.
- [87] S. M. Sarathy, M. J. Thomson, W. J. Pitz, and T. Lu. An experimental and kinetic modeling study of methyl decanoate combustion. *Proceedings of the Combustion Institute*, 33(1):399–405, 2011.
- [88] Qiyao Feng, Aydin Jalali, Adam M. Fincham, Yang Lee Wang, Theodore T. Tsotsis, and Fokion N. Egolfopoulos. Soot formation in flames of model biodiesel fuels. *Combustion and Flame*, 159(5):1876–1893, 2012.
- [89] Timothy Vaughn, Matthew Hammill, Michael Harris, and Anthony J. Marchese. Ignition delay of bio-ester fuel droplets. Technical Report 2006-01-3302, 2006.
- [90] James P. Szybist, André L. Boehman, Daniel C. Haworth, and Hibiki Koga. Premixed ignition behavior of alternative diesel fuel-relevant compounds in a motored engine experiment. *Combustion and Flame*, 149(1-2):112–128, 2007.
- [91] Seth R. Hoffman and John Abraham. A comparative study of *n*-heptane, methyl decanoate, and dimethyl ether combustion characteristics under homogeneous-charge compression-ignition engine conditions. *Fuel*, 88(6):1099–1108, 2009.
- [92] Anthony J. Marchese, Timothy L. Vaughn, Kenneth Kroenlein, and Frederick L. Dryer. Ignition delay of fatty acid methyl ester fuel droplets: Microgravity experiments and detailed numerical modeling. *Proceedings of the Combustion Institute*, 33(2):2021–2030, 2011.

- [93] Yu Cheng Liu, Tanvir Farouk, Anthony J. Savas, Frederick L. Dryer, and C. Thomas Avedisian. On the spherically symmetrical combustion of methyl decanoate droplets and comparisons with detailed numerical modeling. *Combustion and Flame*, 160(3):641–655, 2013.
- [94] Olivier Herbinet, William J. Pitz, and Charles K. Westbrook. Detailed chemical kinetic oxidation mechanism for a biodiesel surrogate. *Combustion and Flame*, 154(3):507–528, 2008.
- [95] Zhaoyu Luo, Tianfeng Lu, Matthias J. Maciaszek, Sibendu Som, and Douglas E. Longman. A reduced mechanism for high-temperature oxidation of biodiesel surrogates. *Energy & Fuels*, 24(12):6283–6293, 2010.
- [96] Olivier Herbinet, William J. Pitz, and Charles K. Westbrook. Detailed chemical kinetic mechanism for the oxidation of biodiesel fuels blend surrogate. *Combustion and Flame*, 157(5):893–908, 2010.
- [97] Olivier Herbinet, Joffrey Biet, Mohammed Hichem Hakka, Valérie Warth, Pierre-Alexandre Glaude, André Nicolle, and Frédérique Battin-Leclerc. Modeling study of the low-temperature oxidation of large methyl esters from C₁₁ to C₁₉. *Proceedings of the Combustion Institute*, 33(1):391–398, 2011.
- [98] Pascal Diévert, Sang Hee Won, Stephen Dooley, Frederick L. Dryer, and Yiguang Ju. A kinetic model for methyl decanoate combustion. *Combustion and Flame*, 159(5):1793–1805, 2012.
- [99] Roberto Grana, Alessio Frassoldati, Chiara Saggese, Tiziano Faravelli, and Eliseo Ranzi. A wide range kinetic modeling study of pyrolysis and oxidation of methyl butanoate and methyl decanoate - Note II: Lumped kinetic model of decomposition and combustion of methyl esters up to methyl decanoate. *Combustion and Flame*, 159(7):2280–2294, 2012.
- [100] Zhaoyu Luo, Max Plomer, Tianfeng Lu, Sibendu Som, Douglas E. Longman, S. Mani Sarathy, and William J. Pitz. A reduced mechanism for biodiesel surrogates for compression ignition engine applications. *Fuel*, 99(0):143–153, 2012.

- [101] Weijing Wang and Matthew A. Oehlschlaeger. The shock tube autoignition of biodiesels and biodiesel components. In *ASME 2013 Heat Transfer Summer Conference collocated with the ASME 2013 7th International Conference on Energy Sustainability and the ASME 2013 11th International Conference on Fuel Cell Science, Engineering and Technology. Volume 2: Heat Transfer Enhancement for Practical Applications; Heat and Mass Transfer in Fire and Combustion; Heat Transfer in Multiphase Systems; Heat and Mass Transfer in Biotechnology*, volume 2, page V002T05A006, Minneapolis, Minnesota, 2013. ASME. July 14–19.
- [102] Mohammed Hichem Hakka, Pierre-Alexandre Glaude, Olivier Herbinet, and Frédérique Battin-Leclerc. Experimental study of the oxidation of large surrogates for diesel and biodiesel fuels. *Combustion and Flame*, 156(11):2129–2144, 2009.
- [103] Chiara Saggese, Alessio Frassoldati, Alberto Cuoci, Tiziano Faravelli, and Eliseo Ranzi. A lumped approach to the kinetic modeling of pyrolysis and combustion of biodiesel fuels. *Proceedings of the Combustion Institute*, 34(1):427–434, 2013.
- [104] C. V. Naik, C. K. Westbrook, O. Herbinet, W. J. Pitz, and M. Mehl. Detailed chemical kinetic reaction mechanism for biodiesel components methyl stearate and methyl oleate. *Proceedings of the Combustion Institute*, 33(1):383–389, 2011.
- [105] Matthew F. Campbell, David F. Davidson, Ronald K. Hanson, and Charles K. Westbrook. Ignition delay times of methyl oleate and methyl linoleate behind reflected shock waves. *Proceedings of the Combustion Institute*, 34(1):419–425, 2013.
- [106] Sarah Bax, Mohammed Hichem Hakka, Pierre-Alexandre Glaude, Olivier Herbinet, and Frédérique Battin-Leclerc. Experimental study of the oxidation of methyl oleate in a jet-stirred reactor. *Combustion and Flame*, 157(6):1220–1229, 2010.
- [107] D. Archambault and F. Billaud. Experimental and modelling study of methyl oleate pyrolysis between 500 and 650 °C. *Journal de Chimie Physique*, 96(5):778–796, 1999.
- [108] D. Archambault and F. Billaud. Non alimentary rapeseed oil upgrading: A parametric study of methyl oleate pyrolysis. *Industrial Crops and Products*, 7(2-3):329–334, 1998.

- [109] William Payman and Wilfred Charles Furness Shepherd. Explosion waves and shock waves. VI. The Disturbance produced by bursting diaphragms with compressed air. *Proceedings of the Royal Society of London. Series A, Mathematical and Physical Sciences*, 186(1006):293–321, 1946.
- [110] Walker Bleakney, D. K. Weimer, and C. H. Fletcher. The shock tube: A Facility for investigations in fluid dynamics. *Review of Scientific Instruments*, 20(11):807–815, 1949.
- [111] A. G. Gaydon and I. R. Hurle. *The Shock tube in high-temperature chemical physics*. Reinhold Publishing Corporation, New York, 1963.
- [112] Craig T. Bowman and Ronald K. Hanson. Shock tube measurements of rate coefficients of elementary gas reactions. *The Journal of Physical Chemistry*, 83(6):757–763, 1979.
- [113] R. E. Mitchell and R. J. Kee. A General-purpose computer code for predicting chemical kinetic behavior behind incident and reflected shocks. Technical Report SAND82-8205, Sandia National Laboratories, Livermore, CA, 94550, 1982.
- [114] Irvine I. Glass and J. P. Sislian. *Nonstationary Flows and Shock Waves*. Clarendon Press, Oxford U.K., 1994. ISBN: 9780198593881.
- [115] George Emanuel. Theory of shock waves: 3.1 Shock waves in gases. In Gabi Ben-Dor, Ozer Igra, and Tov Elperin, editors, *Handbook of Shock Waves*, pages 185–262. Academic Press, Burlington, 2001.
- [116] K. A. Bhaskaran and P. Roth. The shock tube as wave reactor for kinetic studies and material systems. *Progress in Energy and Combustion Science*, 28(2):151–192, 2002.
- [117] David Davidson and R. Hanson. Recent advances in shock tube/laser diagnostic methods for improved chemical kinetics measurements. *Shock Waves*, 19:271–283, 2009. 10.1007/s00193-009-0203-0.
- [118] Ronald K. Hanson. Applications of quantitative laser sensors to kinetics, propulsion and practical energy systems. *Proceedings of the Combustion Institute*, 33(1):1–40, 2011.

- [119] R. K. Hanson and D. F. Davidson. Recent advances in laser absorption and shock tube methods for studies of combustion chemistry. *Progress in Energy and Combustion Science*, 2014, In Press.
- [120] D. F. Davidson and R. K. Hanson. Interpreting shock tube ignition data. *International Journal of Chemical Kinetics*, 36(9):510–523, 2004.
- [121] Marcos Chaos and Frederick L. Dryer. Chemical-kinetic modeling of ignition delay: Considerations in interpreting shock tube data. *International Journal of Chemical Kinetics*, 42(3):143–150, 2010.
- [122] S. Gordon and B. J. McBride. Computer program for calculation of complex chemical equilibrium compositions, rocket performance, incident and reflected shocks, and Chapman-Jouguet detonations. Technical report, Lewis Research Center, 1971. (2nd Edition), NASA SP-273, Available from National Technical Information Service, 5285 Port Royal Road, Springfield, Virginia 22151. N71-37775.
- [123] Burkard Esser. *State variables of a shock tube as a result from an exact Riemann solver (Die Zustandsgrößen im Stoßwellenkanal als Ergebnisse eines exakten Riemannlösers)*. PhD thesis, RWTH Aachen University, 1991.
- [124] David F. Davidson. RGFROSH: A Real gas frozen shock equation solver. Technical Report 1995-001-1.00, Mechanical Engineering Department, Stanford University, Stanford, CA, 94305, October 1995.
- [125] David F. Davidson and Ronald K. Hanson. Real gas corrections in shock tube studies at high pressures. *Israel Journal of Chemistry*, 36:321–326, 1996.
- [126] D. F. Davidson, E. L. Petersen, R. Bates, and R. K. Hanson. Real gas effects at high pressures and temperatures in shock tube studies. In *JANNAF Combustion Subcommittee Meeting*, pages 49–56, 1996. SEE N97- 18659 01-25.
- [127] Chris Morley. GasEq Ver 0.79: A Chemical equilibrium program for windows. Technical report, GasEq, 2005.

- [128] Megan MacDonald, David Davidson, and Ronald Hanson. Decomposition measurements of RP-1, RP-2, JP-7, *n*-dodecane, and tetrahydroquinoline in shock tubes. *Journal of Propulsion and Power*, 5:981–989, 2011.
- [129] Yangye Zhu, David Frank Davidson, and Ronald K. Hanson. 1-Butanol ignition delay times at low temperatures: An application of the constrained-reaction-volume strategy. *Combustion and Flame*, 161(3):634–643, 2014. Special Issue on Alternative Fuels.
- [130] D. R. Haylett, D. F. Davidson, and R. K. Hanson. Second-generation aerosol shock tube: An improved design. *Shock Waves*, 22(6):483–493, 2012.
- [131] H. K. Ciezki and G. Adomeit. Shock-tube investigation of self-ignition of *n*-heptane-air mixtures under engine relevant conditions. *Combustion and Flame*, 93(4):421–433, 1993.
- [132] Ronald K. Hanson, Genny A. Pang, Sreyashi Chakraborty, Wei Ren, Shengkai Wang, and David Frank Davidson. Constrained reaction volume approach for studying chemical kinetics behind reflected shock waves. *Combustion and Flame*, 160(9):1550–1558, 2013.
- [133] D. F. Davidson, S. C. Ranganath, K. Y. Lam, M. Liaw, Z. Hong, and R. K. Hanson. Ignition delay time measurements of normal alkanes and simple oxygenates. *Journal of Propulsion and Power*, 26(2):280–287, 2010.
- [134] A. Farooq, D. F. Davidson, R. K. Hanson, L. K. Huynh, and A. Violi. An experimental and computational study of methyl ester decomposition pathways using shock tubes. *Proceedings of the Combustion Institute*, 32(1):247–253, 2009.
- [135] King-Yiu Lam, David F. Davidson, and Ronald K. Hanson. High-temperature measurements of the reactions of OH with small methyl esters: Methyl formate, methyl acetate, methyl propanoate, and methyl butanoate. *The Journal of Physical Chemistry A*, 116(50):12229–12241, 2012.
- [136] George Mullaney. Shock tube technique for study of autoignition of liquid fuel sprays. *Industrial & Engineering Chemistry*, 50(1):53–58, 1958.

- [137] George Mullaney. Autoignition of liquid fuel sprays. *Industrial & Engineering Chemistry*, 51(6):779–782, 1959.
- [138] Michael A. Nettleton. Ignition and combustion of a fuel of low volatility (hexadecane) in shock-heated air. *Fuel*, 53(2):88–98, 1974.
- [139] Michael A. Nettleton. Influence of preflame reactions on combustion of hydrocarbons in shock-heated air. *Fuel*, 53(2):99–104, 1974.
- [140] P. Roth and R. Fischer. Shock tube measurements of submicron droplet evaporation. In R. D. Archer and B. E. Milton, editors, *Shock Tubes and Waves: Proceedings of the 14th International Symposium on Shock Tubes and Waves*, pages 429–436, Sydney, Australia, August 1984. Sydney Shock Tube Symposium Publishers.
- [141] Paul Roth and Rudiger Fischer. An experimental shock wave study of aerosol droplet evaporation in the transition regime. *Physics of Fluids*, 28(6):1665–1672, 1985.
- [142] H. Goossens, M. Berkelmans, and M. van Dongen. Experimental investigation of weak shock waves propagating in a fog. In Daniel Bershader and Ronald Hanson, editors, *Shock Waves and Shock Tubes, Proceedings of the 15th International Symposium on Shock Tubes and Shock Waves*, pages 721–725, Berkeley, CA, August 1986. Stanford University, Stanford University Press, Stanford, CA.
- [143] H. W. J. Goossens, J. W. Cleijne, H. J. Smolders, and M. E. H. Dongen. Shock wave induced evaporation of water droplets in a gas-droplet mixture. *Experiments in Fluids*, 6:561–568, 1988.
- [144] H. J. Smolders, J. F. H. Willems, H. C. de Lange, and M. E. H. van Dongen. Wave induced growth and evaporation of droplets in a vapour-gas mixture. *AIP Conference Proceedings*, 208(1):802–807, 1990.
- [145] H. J. Smolders and M. E. H. van Dongen. Shock wave structure in a mixture of gas, vapour and droplets. *Shock Waves*, 2:255–267, 1992.

- [146] H. J. Smolders, E. M. J. Niessen, and M. E. H. van Dongen. The random choice method applied to non-linear wave propagation in gas-vapour-droplets mixtures. *Computers & Fluids*, 21(1):63–75, 1992.
- [147] P. Cadman. Shock tube combustion of liquid hydrocarbon sprays of toluene. *Physical Chemistry Chemical Physics*, 3:4301–4309, 2001.
- [148] Hiroyuki Hirahara and Masaaki Kawahashi. Optical measurement of gas-droplet mixture flow in an expansion-shock tube. *JSME International Journal. Ser. B, Fluids and Thermal Engineering*, 41(1):155–161, 1998-02-15.
- [149] J. T. Kashdan, T. C. Hanson, E. L. Piper, D. F. Davidson, and R. K. Hanson. A new facility for the study of shock wave-induced combustion of liquid fuels. In *42nd AIAA Aerospace Sciences Meeting and Exhibit*, number AIAA 2004-468. American Institute of Aeronautics and Astronautics, Inc., January 2004.
- [150] T. C. Hanson, D. F. Davidson, and R. K. Hanson. Shock tube measurements of water and *n*-dodecane droplet evaporation behind shock waves. In *43rd AIAA Aerospace Sciences Meeting and Exhibit*, number AIAA 2005-350. American Institute of Aeronautics and Astronautics, Inc., January 2005.
- [151] Thomas C. Hanson. *The Development of a facility and diagnostics for studying shock-induced behavior in micron-sized aerosols*. PhD thesis, Stanford University, 2005.
- [152] Thomas C. Hanson, David F. Davidson, and Ronald K. Hanson. Shock-induced behavior in micron-sized water aerosols. *Physics of Fluids*, 19(5):056104, 2007.
- [153] Petros Lappas, Daniel R. Haylett, Jason M. Porter, David F. Davidson, Jay B. Jeffries, Ronald K. Hanson, Leslie A. Hokoma, and Kristien E. Mortelmans. Destruction of bacterial-spore-laden aqueous aerosols in shock-heated flows. In *Digital Holography and Three-Dimensional Imaging*, page JMA28. Optical Society of America, 2008.
- [154] Petros Lappas, A. Daniel McCartt, Christopher Strand, Sean D. Gates, David F. Davidson, Jay B. Jeffries, Ronald K. Hanson, Lydia-Marie Joubert, Leslie A. Hokoma, and Kristien E.

- Mortelmans. Dispersion, activation, and destruction of airborne biological threats: Laboratory studies of the interaction of spore-laden aerosols with shock/blast waves. In *Chemical and Biological Defense Physical Science and Technology Conference*, November 2008.
- [155] S. D. Gates, A. Daniel McCartt, P. Lappas, J. B. Jeffries, R. K. Hanson, L. A. Hokama, and K. E. Mortelmans. Bacillus endospore resistance to gas dynamic heating. *Journal of Applied Microbiology*, 109(5):1591–1598, 2010.
- [156] S. D. Gates, A. D. McCartt, J. B. Jeffries, R. K. Hanson, L. A. Hokama, and K. E. Mortelmans. Extension of Bacillus endospore gas dynamic heating studies to multiple species and test conditions. *Journal of Applied Microbiology*, 111(4):925–931, 2011.
- [157] David E. Jackson, David F. Davidson, and Ronald K. Hanson. Application of an aerosol shock tube for the kinetic studies of *n*-dodecane/nano-aluminum slurries. In *44th AIAA/ASME/SAE/ASEE Joint Propulsion Conference & Exhibit*, number AIAA 2008-4767, 2008.
- [158] D. F. Davidson, D. R. Haylett, and R. K. Hanson. Development of an aerosol shock tube for kinetic studies of low-vapor-pressure fuels. *Combustion and Flame*, 155(1-2):108–117, 2008.
- [159] D. R. Haylett, P. P. Lappas, D. F. Davidson, and R. K. Hanson. Application of an aerosol shock tube to the measurement of diesel ignition delay times. *Proceedings of the Combustion Institute*, 32(1):477–484, 2009.
- [160] Daniel R. Haylett, David F. Davidson, and Ronald K. Hanson. A second-generation aerosol shock tube and its application to combustion research. In *48th AIAA Aerospace Sciences Meeting*, number AIAA 2010-196. American Institute of Aeronautics and Astronautics, Inc, 2010.
- [161] D. R. Haylett, R. D. Cook, D. F. Davidson, and R. K. Hanson. OH and C₂H₄ species time-histories during hexadecane and diesel ignition behind reflected shock waves. *Proceedings of the Combustion Institute*, 33(1):167–173, 2011.

- [162] Daniel Robert Haylett. *The Development and application of aerosol shock tube methods for the study of low-vapor-pressure fuels*. PhD thesis, Stanford University, 2011.
- [163] Qin Lao and Sheng Li Xu. The ignition delay measurement of atomized kerosene air mixture in an aerosol shock tube. *Journal of Experiments in Fluid Mechanics*, 23:70–74, 2009.
- [164] Ying Jia Zhang, Zuo Hua Huang, Jun Hua Wang, and Sheng Li Xu. Shock tube study on auto-ignition characteristics of kerosene/air mixtures. *Engineering Thermophysics / Chinese Science Bulletin*, 56(13):1399–1406, 2011.
- [165] Eric L. Petersen, Matthew J. A. Rickard, Mark W. Crofton, Erin D. Abbey, Matthew J. Traum, and Danielle M. Kalitan. A facility for gas- and condensed-phase measurements behind shock waves. *Measurement Science and Technology*, 16(9):1716–1729, 2005.
- [166] Brandon Rotavera, Anthony Amadio, Victorio Antonovski, and Eric Petersen. New approaches for fundamental rocket injector studies using a shock tube. In *42nd AIAA/ASME/SAE/ASEE Joint Propulsion Conference & Exhibit*, number AIAA 2006-4725, Sacramento, CA, 9–12 July 2006 2006. AIAA.
- [167] Brandon Rotavera, Nolan Polley, Eric L. Petersen, Kara Scheu, Mark Crofton, and Gilles Bourque. Ignition and combustion of heavy hydrocarbons using an aerosol shock-tube approach. *ASME Conference Proceedings*, 2010(43970):699–707, 2010.
- [168] Casey Allen, Gaurav Mittal, Chih-Jen Sung, Elisa Toulson, and Tonghun Lee. An aerosol rapid compression machine for studying energetic-nanoparticle-enhanced combustion of liquid fuels. *Proceedings of the Combustion Institute*, 33(2):3367–3374, 2011.
- [169] M. B. Dantas, Marta M. Conceição, V. J. Fernandes, Jr., Nataly A. Santos, R. Rosenhaim, Aldalea L. B. Marques, Iêda M. G. Santos, and A. G. Souza. Thermal and kinetic study of corn biodiesel obtained by the methanol and ethanol routes. *Journal of Thermal Analysis and Calorimetry*, 87(3):835–839, 2007.
- [170] Lucian Z. Dumitrescu. An attenuation-free shock tube. *Physics of Fluids (1958-1988)*, 15(1):207–209, 1972.

- [171] Ingo Stotz, Grazia Lamanna, Harald Hettrich, Bernhard Weigand, and Johan Steelant. Design of a double diaphragm shock tube for fluid disintegration studies. *Review of Scientific Instruments*, 79(12):125106, 2008.
- [172] Zekai Hong, Genny Pang, Subith Vasu, David Davidson, and Ronald Hanson. The use of driver inserts to reduce non-ideal pressure variations behind reflected shock waves. *Shock Waves*, 19:113–123, 2009. 10.1007/s00193-009-0205-y.
- [173] Matthew F. Campbell, Daniel R. Haylett, David F. Davidson, and Ronald K. Hanson. AEROFROSH: A Shock condition calculator for multi-component-fuel aerosol-laden flows. *Shock Waves*, Submitted.
- [174] Alexander Burcat and Branko Ruscic. Third millennium ideal gas and condensed phase thermochemical database for combustion with updates from active thermochemical tables. Technical Report ANL-05/20 TAE 960, Argonne National Laboratory and Technion Israel Institute of Technology, 2005.
- [175] Steven W. Sharpe, Timothy J. Johnson, Robert L. Sams, Pamela M. Chu, George C. Rhoderick, and Patricia A. Johnson. Gas-phase databases for quantitative infrared spectroscopy. *Applied Spectroscopy*, 58(12):1452–1461, 2004.
- [176] Matthew F. Campbell, Keilan G. Freeman, David F. Davidson, and Ronald K. Hanson. FTIR measurements of mid-IR absorption spectra of gaseous fatty acid methyl esters at T=25-500 °C. *Journal of Quantitative Spectroscopy and Radiative Transfer*, 145(0):57–73, 2014.
- [177] Gilbert S. Bahn. *Role of Vaporization Rate in Combustion of Liquid Fuels*, chapter 10, pages 104–115. Americal Chemical Society, 1155 Sixteenth Street, N.W. Washington 6, D. C., 1958.
- [178] G. M. Faeth. Current status of droplet and liquid combustion. *Progress in Energy and Combustion Science*, 3(4):191–224, 1977.
- [179] E. S. Landry, S. Mikkilineni, M. Paharia, and A. J. H. McGaughey. Droplet evaporation: A molecular dynamics investigation. *Journal of Applied Physics*, 102(12):124301, 2007.

- [180] D. Jakubczyk, M. Koiwas, G. Derkachov, K. Koiwas, and M. Zientara. Evaporation of micro-droplets: The “Radius-Square-Law” revisited. *Acta Physica Polonica A*, 122(4):709–716, 2012.
- [181] Kyungchan Chae and Angela Violi. Mutual diffusion coefficients of heptane isomers in nitrogen: A molecular dynamics study. *The Journal of Chemical Physics*, 134(4):044537, 2011.
- [182] Joseph O. Hirschfelder, Charles F. Curtiss, and R. Byron Bird. *The Molecular Theory of Gases and Liquids*. Wiley-Interscience, 1964.
- [183] C. T. Bowman. *Combustion Fundamentals*. Stanford University, 2010.
- [184] Frank M. White. *Viscous Fluid Flow, 2nd Edition*. Number ISBN 0-07-069712-4. McGraw-Hill, New York, NY, 1991.
- [185] Roland Clift, John Grace, and Martin E. Weber. *Bubbles, Drops, and Particles*. Dover Publications, Inc. Mineola, NY, 1978.
- [186] O. N. M McCallion, K. M. G. Taylor, M. Thomas, and A. J. Taylor. Ultrasonic nebulisation of fluids with different viscosities and surface tensions. *Journal of Aerosol Medicine*, 8(3):281–284, 1995.
- [187] C. A. W. Allen and K. C. Watts. Comparative analysis of the atomization characteristics of fifteen biodiesel fuel types. *Transactions of the American Society of Agricultural Engineers*, 43(2):207–211, 2000.
- [188] Balasubrahmanyam Avvaru, Mohan N. Patil, Parag R. Gogate, and Aniruddha B. Pandit. Ultrasonic atomization: Effect of liquid phase properties. *Ultrasonics*, 44(2):146–158, 2006.
- [189] Robert J. Lang. Ultrasonic atomization of liquids. *The Journal of the Acoustical Society of America*, 34(1):6–8, 1962.
- [190] Hendrik C. van de Hulst. *Light Scattering by Small Particles*. Dover Publications, Inc. Mineola, NY, 1981.

- [191] Ronald Panton and A. K. Oppenheim. Shock relaxation in a particle-gas mixture with mass transfer between phases. *American Institute of Aeronautics and Astronautics Journal*, 6(11):2071–2077, 1968.
- [192] H. Miura and I. I. Glass. On a dusty-gas shock tube. *Proceedings of the Royal Society of London. Series A, Mathematical and Physical Sciences*, 382(1783):373–388, 1982.
- [193] S. Kotake and I. I. Glass. Flows with nucleation and condensation. *Progress in Aerospace Sciences*, 19:129–196, 1979.
- [194] Sergei S. Sazhin. Advanced models of fuel droplet heating and evaporation. *Progress in Energy and Combustion Science*, 32(2):162–214, 2006.
- [195] H. Y. Lu and H. H. Chiu. Dynamics of gases containing evaporable liquid droplets under a normal shock. *American Institute of Aeronautics and Astronautics Journal*, 4(6):1008–1011, 1966.
- [196] Frank E. Marble. Some gasdynamic problems in the flow of condensing vapors. *Astronautica Acta*, 14:585–614, 1969.
- [197] Frank E. Marble. Dynamics of dusty gases. *Annual Review of Fluid Mechanics*, 2:397–446, 1970.
- [198] Y. Narkis and B. Gal-Or. Two-phase flow through normal shock wave. *Journal of Fluids Engineering*, 97(3):361–365, 1975.
- [199] Z. Rakib, O. Igra, and G. Ben-Dor. The effect of water droplets on the relaxation zone developed behind strong normal shock waves. *Journal of Fluids Engineering*, 106(2):154–159, 1984.
- [200] O. Igra, G. Ben-Dor, and Z. Rakib. The effect of dust and water droplets on the relaxation zone developed behind strong normal shock waves. *International Journal of Multiphase Flow*, 11(2):121–132, 1985.

- [201] A. Guha and J. B. Young. *Adiabatic Waves in Liquid-Vapour System: Stationary and moving normal shock waves in wet steam*, pages 159–170. Springer Verlag, 1989. ISBN: 3540502033.
- [202] J. B. Young and A. Guha. Normal shock-wave structure in two-phase vapour-droplet flows. *Journal of Fluid Mechanics*, 228:243–274, 1991.
- [203] A. Guha. Structure of partly dispersed normal shock waves in vapor-droplet flows. *Physics of Fluids A*, 4(7):1566–1578, 1992.
- [204] A. Guha. Jump conditions across normal shock waves in pure vapour-droplet flows. *Journal of Fluid Mechanics*, 241:349–369, 1992.
- [205] J. B. Young. The fundamental equations of gas-droplet multiphase flow. *International Journal of Multiphase Flow*, 21(2):175–191, 1995.
- [206] Y. Tambour and S. Zehavi. Derivation of near-field sectional equations for the dynamics of polydisperse spray flows: An analysis of the relaxation zone behind a normal shock wave. *Combustion and Flame*, 95(4):383–409, 1993.
- [207] E. J. Chang and K. Kailasanath. Shock wave interactions with particles and liquid fuel droplets. *Shock Waves*, 12:333–341, 2003.
- [208] S. Sivier, E. Loth, J. Baum, and R. Löhner. Unstructured adaptive remeshing finite element method for dusty shock flow. *Shock Waves*, 4:15–23, 1994.
- [209] M. Sommerfeld. The unsteadiness of shock waves propagating through gas-particle mixtures. *Experiments in Fluids*, 3:197–206, 1985.
- [210] V. Sychevskii. Liquid droplet processing using shock waves. *Theoretical Foundations of Chemical Engineering*, 42:377–385, 2008.
- [211] E. L. Petersen. Shock tube measurements of heterogeneous combustion phenomena. In *Spring 2000 Meeting of the Western States Section of the Combustion Institute*, Golden, CO, March 13-14 2000. Paper No. 00S-45.

- [212] Marinus E. H. van Dongen. Shock wave propagation in multi-phase media: 15.4 Shock wave interaction with liquid gas suspensions. In Gabi Ben-Dor, Ozer Igra, and Tov Elperin, editors, *Handbook of Shock Waves*, pages 747–781. Academic Press, Burlington, 2001.
- [213] MathWorks. *MATLAB*. The MathWorks, Inc., 3 Apple Hill Drive Natick, MA 01760-2098, R2011a edition, 2011. MATLAB is a registered trademark of The MathWorks, Inc.. 508-647-7000.
- [214] B. T. Chu. Thermodynamics of a dusty gas and its application to some aspects of wave propagation in the gas. Technical report, Division of Engineering, Brown University, Providence, RI, 1960. Report No. DA-4761/1.
- [215] S. Temkin. Sound speeds in suspensions in thermodynamic equilibrium. *Physics of Fluids A: Fluid Dynamics*, 4(11):2399–2409, 1992.
- [216] S. Temkin. Attenuation and dispersion of sound in dilute suspensions of spherical particles. *The Journal of the Acoustical Society of America*, 108(1):126–146, 2000.
- [217] G. Rudinger. *Fundamentals of gas-particle flow*. Elsevier Scientific, Amsterdam, Netherlands, 1980. ISBN: 0444418539.
- [218] A. Klingbeil, J. Jeffries, D. Davidson, and R. Hanson. Two-wavelength mid-IR diagnostic for temperature and *n*-dodecane concentration in an aerosol shock tube. *Applied Physics B: Lasers and Optics*, 93:627–638, 2008.
- [219] J. Porter, J. Jeffries, and R. Hanson. Mid-infrared laser-absorption diagnostic for vapor-phase measurements in an evaporating *n*-decane aerosol. *Applied Physics B: Lasers and Optics*, 97:215–225, 2009.
- [220] Wei Ren, Jay B. Jeffries, and Ronald K. Hanson. Temperature sensing in shock-heated evaporating aerosol using wavelength-modulation absorption spectroscopy of CO₂ near 2.7 μm. *Measurement Science and Technology*, 21(10):105603, 2010.
- [221] Carl L. Yaws. Yaws' handbook of thermodynamic properties for hydrocarbons and chemicals. Technical report, Knovel, 2009. Electronic Edition.

- [222] Carl L Yaws, K. Narasimhan, Prasad, and Chaitanya Gabbula. Yaws' handbook of antoine coefficients for vapor pressure. Technical report, Knovel, 2009. 2nd Electronic Edition.
- [223] Carl L. Yaws. Yaws' thermophysical properties of chemicals and hydrocarbons. Technical report, Knovel, 2010. Electronic Edition.
- [224] Carl L. Yaws. Yaws' transport properties of chemicals and hydrocarbons. Technical report, Knovel, 2010. Electronic Edition.
- [225] Adam E. Klingbeil, Jay B. Jeffries, and Ronald K. Hanson. Temperature-dependent mid-IR absorption spectra of gaseous hydrocarbons. *Journal of Quantitative Spectroscopy and Radiative Transfer*, 107(3):407–420, 2007.
- [226] A. E. Klingbeil, J. B. Jeffries, and R. K. Hanson. Temperature- and pressure-dependent absorption cross sections of gaseous hydrocarbons at 3.39 μm . *Measurement Science and Technology*, 17(7):1950–1957, 2006.
- [227] R. Mével, P. A. Boettcher, and J. E. Shepherd. Absorption cross section at 3.39 μm of alkanes, aromatics and substituted hydrocarbons. *Chemical Physics Letters*, 531(0):22–27, 2012.
- [228] Et-touhami Es-sebbar, Majed Alrefae, and Aamir Farooq. Infrared cross-sections and integrated band intensities of propylene: Temperature-dependent studies. *Journal of Quantitative Spectroscopy and Radiative Transfer*, 133(0):559–569, 2014.
- [229] Et-touhami Es-sebbar, Yves Benilan, and Aamir Farooq. Temperature-dependent absorption cross-section measurements of 1-butene (1-C₄H₈) in VUV and IR. *Journal of Quantitative Spectroscopy and Radiative Transfer*, 115(0):1–12, 2013.
- [230] Ayhan Demirbas. Progress and recent trends in biodiesel fuels. *Energy Conversion and Management*, 50(1):14–34, 2009.
- [231] S. W. Sharpe, R. L. Sams, and T. J. Johnson. The PNNL quantitative IR database for infrared remote sensing and hyperspectral imaging. In *Proceedings of the 31st Applied Imagery Pattern Recognition Workshop (AIPR'02)*, pages 45–48, Los Alamitos, CA, USA, 2002. IEEE Computer Society.

- [232] Steven W. Sharpe, Robert L. Sams, Timothy J. Johnson, Pamela M. Chu, George C. Rhoderick, and Franklin R. Guenther. Creation of 0.10-cm^{-1} resolution quantitative infrared spectral libraries for gas samples. *Proceedings of the Society of Photographic Instrumentation Engineers (SPIE)*, 4577:12–24, 2002.
- [233] Timothy J. Johnson, Robert L. Sams, and Steven W. Sharpe. The PNNL quantitative infrared database for gas-phase sensing: A Spectral library for environmental, hazmat, and public safety standoff detection. *Proceedings of the Society of Photographic Instrumentation Engineers (SPIE)*, 5269:159–167, 2004.
- [234] Eiji Tomita, Nobuyuki Kawahara, Atsushi Nishiyama, and Masahiro Shigenaga. *In situ* measurement of hydrocarbon fuel concentration near a spark plug in an engine cylinder using the $3.392\ \mu\text{m}$ infrared laser absorption method: Application to an actual engine. *Measurement Science and Technology*, 14(8):1357, 2003.
- [235] David A. Rothamer, Jordan A. Snyder, Ronald K. Hanson, Richard R. Steeper, and Russell P. Fitzgerald. Simultaneous imaging of exhaust gas residuals and temperature during HCCI combustion. *Proceedings of the Combustion Institute*, 32(2):2869–2876, 2009.
- [236] J. Snyder, R. Hanson, R. Fitzgerald, and R. Steeper. Dual-wavelength PLIF measurements of temperature and composition in an optical HCCI engine with negative valve overlap. *SAE Int. J. Engines*, 2(1):460–474, 2009.
- [237] D. A. Rothamer, J. A. Snyder, R. K. Hanson, and R. R. Steeper. Optimization of a tracer-based PLIF diagnostic for simultaneous imaging of EGR and temperature in IC engines. *Applied Physics B*, 99(1-2):371–384, 2010.
- [238] Adam E. Klingbeil, Jay B. Jeffries, and Ronald K. Hanson. $3.39\ \mu\text{m}$ Laser absorption sensor for ethylene and propane measurements in a pulse detonation engine. In *44th AIAA Aerospace Sciences Meeting and Exhibit*, number AIAA 2006-925, Reno, Nevada, January 2006. AIAA.
- [239] K. Wakatsuki, S. P. Fuss, A. Hamins, and M. R. Nyden. A technique for extrapolating

- absorption coefficient measurements to high temperatures. *Proceedings of the Combustion Institute*, 30(1):1565–1573, 2005.
- [240] Kaoru Wakatsuki, Gregory S. Jackson, Jungho Kim, Anthony Hamins, Marc R. Nyden, and Stephen P. Fuss. Determination of planck mean absorption coefficients for hydrocarbon fuels. *Combustion Science and Technology*, 180(4):616–630, 2008.
- [241] Adam Edgar Klingbeil. *Mid-IR laser absorption diagnostics for hydrocarbon vapor sensing in harsh environments*. PhD thesis, Stanford University, 2007.
- [242] Michael E. Thomas, Richard I. Joseph, and William J. Tropf. Infrared transmission properties of sapphire, spinel, yttria, and alon as a function of temperature and frequency. *Appl. Opt.*, 27(2):239–245, Jan 1988.
- [243] Timothy J. Johnson, Steven W. Sharpe, and Matthew A. Covert. Disseminator for rapid, selectable, and quantitative delivery of low and semivolatile liquid species to the vapor phase. *Review of Scientific Instruments*, 77(9):094103, 2006.
- [244] Peter J. Mohr, Barry N. Taylor, and David B. Newell. CODATA recommended values of the fundamental physical constants: 2010. *Rev. Mod. Phys.*, 84:1527–1605, Nov 2012.
- [245] Peter J. Mohr, Barry N. Taylor, and David B. Newell. CODATA recommended values of the fundamental physical constants: 2010. *Journal of Physical and Chemical Reference Data*, 41(4):043109, 2012.
- [246] Alexander Grosch, Volker Beushausen, Hainer Wackerbarth, Olaf Thiele, and Thomas Berg. Temperature- and pressure-dependent midinfrared absorption cross sections of gaseous hydrocarbons. *Appl. Opt.*, 49(2):196–203, Jan 2010.
- [247] S. S. Penner. *Quantitative molecular spectroscopy and gas emissivities*. Addison-Wesley Pub. Co., 1959.
- [248] D. K. Edwards and W. A. Menard. Comparison of models for correlation of total band absorption. *Appl. Opt.*, 3(5):621–625, May 1964.

- [249] D. K. Edwards and A. Balakrishnan. Thermal radiation by combustion gases. *International Journal of Heat and Mass Transfer*, 16(1):25–40, 1973.
- [250] M. Handke and N. J. Harrick. A new accessory for infrared emission spectroscopy measurements. *Applied Spectroscopy*, 40(3):401–405, 1986.
- [251] J. A. McGuire, B. Wangmaneerat, T. M. Niemczyk, and D. M. Haaland. Modifications to a commercial infrared emission apparatus to permit quantitative applications. *Appl. Spectrosc.*, 46(1):178–180, Jan 1992.
- [252] A. M. Vassallo and M. I. Attalla. Studies of thermal transformations of fulvic acids using fourier transform-infrared emission spectroscopy. *Journal of Analytical and Applied Pyrolysis*, 23(1):73–85, 1992.
- [253] G. A. George, M. Celina, A. M. Vassallo, and P. A. Cole-Clarke. Real-time analysis of the thermal oxidation of polyolefins by FT-IR emission. *Polymer Degradation and Stability*, 48(2):199–210, 1995.
- [254] M. Celina, D. K. Ottesen, K. T. Gillen, and R. L. Clough. FTIR emission spectroscopy applied to polymer degradation. *Polymer Degradation and Stability*, 58(1–2):15–31, 1997.
- [255] T. J. Johnson, R. L. Sams, T. A. Blake, S. W. Sharpe, and P. M. Chu. Removing aperture-induced artifacts from fourier transform infrared intensity values. *Applied Optics*, 41(15):2831–2839, 2002.
- [256] Adam E. Klingbeil, Jay B. Jeffries, and Ronald K. Hanson. Tunable mid-IR laser absorption sensor for time-resolved hydrocarbon fuel measurements. *Proceedings of the Combustion Institute*, 31(1):807–815, 2007.
- [257] James W. Robinson. *Handbook of Spectroscopy*. CRC Press LCC, 1974.
- [258] Matthew F. Campbell, David F. Davidson, Ronald K. Hanson, and Charles K. Westbrook. Ignition delay times of methyl oleate and methyl linoleate behind reflected shock waves. In *Proceedings of the 34th International Symposium on Combustion*, number 3D01. Combustion Institute, 2012.

- [259] Gerhard Knothe, Steven C. Cermak, and Roque L. Evangelista. Cuphea oil as source of biodiesel with improved fuel properties caused by high content of methyl decanoate. *Energy & Fuels*, 23(3):1743–1747, 2009.
- [260] Steven P. Pyl, Kevin M. Van Geem, Philip Puimége, Maarten K. Sabbe, Marie-Françoise Reyniers, and Guy B. Marin. A comprehensive study of methyl decanoate pyrolysis. *Energy*, 43(1):146–160, 2012. 2nd International Meeting on Cleaner Combustion (CM0901-Detailed Chemical Models for Cleaner Combustion).
- [261] Gerhard Knothe. Dependence of biodiesel fuel properties on the structure of fatty acid alkyl esters. *Fuel Processing Technology*, 86(10):1059–1070, 2005.
- [262] Ned A. Porter, Sarah E. Caldwell, and Karen A. Mills. Mechanisms of free radical oxidation of unsaturated lipids. *Lipids*, 30(4):277–290, 1995.
- [263] CHEMKIN-PRO. Chemkin-pro 15131. Technical report, Reaction Design, San Diego, CA, 2013.
- [264] Hsi-Ping S. Shen, Jeremy Vanderover, and Matthew A. Oehlschlaeger. A shock tube study of *iso*-octane ignition at elevated pressures: The influence of diluent gases. *Combustion and Flame*, 155(4):739–755, 2008.
- [265] Antoine Osmont, Laurent Catoire, Iskender Gökalp, and Mark T. Swihart. Thermochemistry of C-C and C-H bond breaking in fatty acid methyl esters. *Energy & Fuels*, 21(4):2027–2032, 2007.
- [266] Edward R. Ritter and Joseph W. Bozzelli. THERM: Thermodynamic property estimation for gas phase radicals and molecules. *International Journal of Chemical Kinetics*, 23(9):767–778, 1991.
- [267] Sinéad M. Burke. *Development of a chemical kinetic mechanism for small hydrocarbons*. PhD thesis, National University of Ireland at Galway, 2014.

- [268] Xiaoqing You, Andrew Packard, and Michael Frenklach. Process informatics tools for predictive modeling: Hydrogen combustion. *International Journal of Chemical Kinetics*, 44(2):101–116, 2012.
- [269] D. C. Horning, D. F. Davidson, and R. K. Hanson. Study of the high-temperature autoignition of *n*-alkane/O₂/Ar mixtures. *Journal of Propulsion and Power*, 18(2):363–371, 2002.
- [270] Wayne G. Burwell and Donald R. Olson. The spontaneous ignition of isoctane air mixtures under steady flow conditions. Technical Report 650510, Society of Automotive Engineers International, 1965.
- [271] D. J. Vermeer, J. W. Meyer, and A. K. Oppenheim. Auto-ignition of hydrocarbons behind reflected shock waves. *Combustion and Flame*, 18(3):327–336, 1972.
- [272] A. Burcat, R. F. Farmer, and R. A. Matula. Shock initiated ignition in heptane-oxygen-argon mixtures. In C. E. Treanor and J. G. Hall, editors, *Shock Tubes and Waves: Proceedings of the 13th International Symposium on Shock Tubes and Shock Waves*, page 826, Niagara Falls, NY, 1982. State University of New York Press, Albany, NY.
- [273] Thomas W. Ryan and Timothy J. Callahan. Engine and constant volume bomb studies of diesel ignition and combustion. Technical Report 881626, Society of Automotive Engineers International, 1988.
- [274] Charles K. Westbrook, William J. Pitz, Henry C. Curran, Janice Boercker, and Eric Kunrath. Chemical kinetic modeling study of shock tube ignition of heptane isomers. *International Journal of Chemical Kinetics*, 33(12):868–877, 2001.
- [275] Matthew F. Campbell, Thomas C. Parise, Andrew M. Tulgestke, R. Mitchell Spearrin, David F. Davidson, and Ronald K. Hanson. Strategies for obtaining long constant-pressure test times in shock tubes. *Shock Waves*, Submitted.
- [276] Hsi-Ping S. Shen, Jeremy Vanderover, and Matthew A. Oehlschlaeger. A shock tube study of the auto-ignition of toluene/air mixtures at high pressures. *Proceedings of the Combustion Institute*, 32(1):165–172, 2009.

- [277] Anthony R. Amadio, Mark W. Crofton, and Eric L. Petersen. Test-time extension behind reflected shock waves using CO₂-He and C₃H₈-He driver mixtures. *Shock Waves*, 16(2):157–165, 2006.
- [278] Zekai Hong, David Davidson, and Ronald Hanson. Contact surface tailoring condition for shock tubes with different driver and driven section diameters. *Shock Waves*, 19:331–336, 2009. 10.1007/s00193-009-0212-z.
- [279] T. Rossmann, M. G. Mungal, and R. K. Hanson. A new shock tunnel facility for high compressibility mixing layer studies. In *37th Aerospace Sciences Meeting, Reno, NV, 1999*, number AIAA 99-0415, 1999.
- [280] G. A. Pang, D. F. Davidson, and R. K. Hanson. Experimental study and modeling of shock tube ignition delay times for hydrogen-oxygen-argon mixtures at low temperatures. *Proceedings of the Combustion Institute*, 32(1):181–188, 2009.
- [281] K.-Y. Lam, Z. Hong, D. F. Davidson, and R. K. Hanson. Shock tube ignition delay time measurements in propane/O₂/argon mixtures at near-constant-volume conditions. *Proceedings of the Combustion Institute*, 33(1):251–258, 2011.
- [282] William J. Hooker. Testing time and contact-zone phenomena in shock-tube flows. *Physics of Fluids (1958-1988)*, 4(12):1451–1463, 1961.
- [283] H. Polacheck and R. J. Seeger. On shock-wave phenomena; Refraction of shock waves at a gaseous interface. *Phys. Rev.*, 84:922–929, Dec 1951.
- [284] C. Frazier, M. Lamnaouer, E. Divo, A. Kassab, and E. Petersen. Effect of wall heat transfer on shock-tube test temperature at long times. *Shock Waves*, 21(1):1–17, 2011.
- [285] P. A. Jacobs. Quasi-one-dimensional modeling of a free-piston shock tunnel. *AIAA Journal*, 32(1):137–145, 1994.
- [286] J. G. Oakley and R. Bonazza. *xt.exe* Wisconsin Shock Tube Laboratory (WiSTL) code. Technical report, University of Wisconsin, Madison, WI, 2004.

- [287] Michio Nishida. Chapter 4.1 - Shock tubes and tunnels: Facilities, instrumentation, and techniques. In Gabi Ben-Dor, Ozer Igra, and Tov Elperin, editors, *Handbook of Shock Waves*, pages 553–585. Academic Press, Burlington, 2001.
- [288] R. A. Alpher and D. R. White. Flow in shock tubes with area change at the diaphragm section. *Journal of Fluid Mechanics*, 3:457–470, 1958.
- [289] Matthew F. Campbell, Shengkai Wang, Christopher S. Goldenstein, R. Mitchell Spearrin, Andrew M. Tulgestke, Luke T. Zaczek, David F. Davidson, and Ronald K. Hanson. Constrained reaction volume shock tube study of *n*-heptane oxidation: Ignition delay times and time-histories of multiple species and temperature. *Proceedings of the Combustion Institute*, 2014, In Press.
- [290] K. A. Heufer and H. Olivier. Determination of ignition delay times of different hydrocarbons in a new high pressure shock tube. *Shock Waves*, 20(4):307–316, 2010.
- [291] Eric L. Petersen and Ronald K. Hanson. Nonideal effects behind reflected shock waves in a high-pressure shock tube. *Shock Waves*, 10:405–420, 2001.
- [292] Matthew A. Oehlschlaeger, David F. Davidson, and Jay B. Jeffries. Temperature measurement using ultraviolet laser absorption of carbon dioxide behind shock waves. *Appl. Opt.*, 44(31):6599–6605, Nov 2005.
- [293] William J. Nuttall, Richard H. Clarke, and Bartek A. Glowacki. Resources: Stop squandering helium. *Nature*, 485(7400):573–575, 2012.
- [294] Assa Lifshitz, S. H. Bauer, and E. L. Resler. Studies with a single-pulse shock tube. I. The *Cis-Trans* isomerization of butene-2. *The Journal of Chemical Physics*, 38(9):2056–2063, 1963.
- [295] Wing Tsang. Thermal decomposition of some *Tert*-butyl compounds at elevated temperatures. *The Journal of Chemical Physics*, 40(6):1498–1505, 1964.
- [296] William McKinley Robinson. *Mass spectrometric studies of ionization precursors ahead of strong shock waves*. PhD thesis, California Institute of Technology, 1969.

- [297] Roger C. Millikan and Donald R. White. Systematics of vibrational relaxation. *The Journal of Chemical Physics*, 39(12):3209–3213, 1963.
- [298] J. P. Appleton. Shock-tube study of the vibrational relaxation of nitrogen using vacuum-ultraviolet light absorption. *The Journal of Chemical Physics*, 47(9):3231–3240, 1967.
- [299] R. K. Hanson and D. Baganoff. Shock-tube study of vibrational relaxation in nitrogen using pressure measurements. *The Journal of Chemical Physics*, 53(11):4401–4403, 1970.
- [300] V. P. Fokeev, S. Abid, G. Dupré, V. Vaslier, and C. Paillard. Domains of existence of the bifurcation of a reflected shock wave in cylindrical channels. In Raymond Brun and Lucien Z. Dumitrescu, editors, *Shock Waves at Marseille IV*, pages 145–150. Springer Berlin Heidelberg, 1995.
- [301] E. Petersen and R. Hanson. Measurement of reflected-shock bifurcation over a wide range of gas composition and pressure. *Shock Waves*, 15:333–340, 2006.
- [302] P. Desgroux, R. Minetti, and L. R. Sochet. Temperature distribution induced by pre-ignition reactions in a rapid compression machine. *Combustion Science and Technology*, 113(1):193–203, 1996.
- [303] E. L. Petersen, M. Lamnaouer, J. de Vries, H. Curran, J. Simmie, M. Fikri, C. Schulz, and G. Bourque. Discrepancies between shock tube and rapid compression machine ignition at low temperatures and high pressures. In Klaus Hannemann and Friedrich Seiler, editors, *Shock Waves*, pages 739–744. Springer Berlin Heidelberg, 2009.
- [304] S. S. Goldsborough, G. Mittal, and C. Banyon. Methodology to account for multi-stage ignition phenomena during simulations of RCM experiments. *Proceedings of the Combustion Institute*, 34(1):685–693, 2013.
- [305] R. M. Spearrin, W. Ren, J. B. Jeffries, and R. K. Hanson. Multi-band infrared CO₂ absorption sensor for sensitive temperature and species measurements in high-temperature gases. *Applied Physics B*, 2014, In Press.

- [306] Matthew F. Campbell, Andrew M. Tulgestke, David F. Davidson, and Ronald K. Hanson. A Second-generation constrained reaction volume shock tube. *Review of Scientific Instruments*, 85(5):055108, 2014.
- [307] H. S. Glick, W. Squire, and A. Hertzberg. A new shock tube technique for the study of high temperature gas phase reactions. *Symposium (International) on Combustion*, 5(1):393–402, 1955.
- [308] B. Rajakumar, K. P. J. Reddy, and E. Arunan. Unimolecular HCl elimination from 1,2-dichloroethane: A Single pulse shock tube and *ab Initio* study. *The Journal of Physical Chemistry A*, 106(36):8366–8373, 2002.
- [309] C. J. Brown and G. O. Thomas. Experimental studies of shock-induced ignition and transition to detonation in ethylene and propane mixtures. *Combustion and Flame*, 117(4):861–870, 1999.
- [310] William Heltsley, Jordan Snyder, Andree Houle, David Davidson, M. Mungal, and Ronald Hanson. Design and characterization of the stanford 6 inch expansion tube. In *42nd AIAA/ASME/SAE/ASEE Joint Propulsion Conference & Exhibit*, number AIAA 2006-4443, 2006.
- [311] Victor A. Miller, Mirko Gamba, M. Godfrey Mungal, and Ronald K. Hanson. Secondary diaphragm thickness effects and improved pressure measurements in an expansion tube. *American Institute of Aeronautics and Astronautics Journal*, 52(2):451–456, 2014.
- [312] R. S. Tranter, K. Brezinsky, and D. Fulle. Design of a high-pressure single pulse shock tube for chemical kinetic investigations. *Review of Scientific Instruments*, 72(7):3046–3054, 2001.
- [313] H. Kellerer, A. Muller, H.-J. Bauer, and S. Wittig. Soot formation in a shock tube under elevated pressure conditions. *Combustion Science and Technology*, 113(1):67–80, 1996.
- [314] Benjamin Akhi-Kumgeh and Jeffrey M. Berghorson. Shock tube study of methyl formate ignition. *Energy & Fuels*, 24(1):396–403, 2010.

- [315] Eric L. Petersen. *A Shock tube and diagnostics for chemistry measurements at elevated pressures with application to methane ignition*. PhD thesis, Stanford University, 1998.
- [316] Shane M. Daley, Andrew M. Berkowitz, and Matthew A. Oehlschlaeger. A Shock tube study of cyclopentane and cyclohexane ignition at elevated pressures. *International Journal of Chemical Kinetics*, 40(10):624–634, 2008.
- [317] Daniel Darcy, Colin J. Tobin, Kenji Yasunaga, John M. Simmie, Judith Würmel, Wayne K. Metcalfe, Tidjani Niass, Syed S. Ahmed, Charles K. Westbrook, and Henry J. Curran. A high pressure shock tube study of *n*-propylbenzene oxidation and its comparison with *n*-butylbenzene. *Combustion and Flame*, 159(7):2219–2232, 2012.
- [318] J. Herzler, M. Fikri, K. Hitzbleck, R. Starke, C. Schulz, P. Roth, and G.T. Kalghatgi. Shock-tube study of the autoignition of *n*-heptane/toluene/air mixtures at intermediate temperatures and high pressures. *Combustion and Flame*, 149(1–2):25–31, 2007.
- [319] Aamir Farooq. Personal Communication, May 30 2014.
- [320] J. de Vries, C. Aul, A. Barrett, D. Lambe, and E. L. Petersen. Shock tube for high-pressure and low-temperature chemical kinetics experiments. In Klaus Hannemann and Friedrich Seiler, editors, *Proceedings of the 26th International Symposium on Shock Waves, Gottingen, Germany*, volume 1, pages 171–176. Springer Berlin Heidelberg, July 15–20 2007.
- [321] M. A. Oehlschlaeger, D. F. Davidson, J. T. Herbon, and R. K. Hanson. Shock tube measurements of branched alkane ignition times and OH concentration time histories. *International Journal of Chemical Kinetics*, 36(2):67–78, 2004.
- [322] Matthew A. Oehlschlaeger. *Shock tube studies of thermal decomposition reactions using ultraviolet absorption spectroscopy*. PhD thesis, Stanford University, June 2005.
- [323] Jihad Badra, Ahmed E. Elwardany, Fethi Khaled, Subith S. Vasu, and Aamir Farooq. A Shock tube and laser absorption study of ignition delay times and OH reaction rates of ketones: 2-Butanone and 3-buten-2-one. *Combustion and Flame*, 161(3):725–734, 2014. Special Issue on Alternative Fuels.

- [324] K. A. Heufer, R. X. Fernandes, H. Olivier, J. Beeckmann, O. Rohl, and N. Peters. Shock tube investigations of ignition delays of *n*-butanol at elevated pressures between 770 and 1250 K. *Proceedings of the Combustion Institute*, 33(1):359–366, 2011.
- [325] Eric L. Petersen. Interpreting endwall and sidewall measurements in shock-tube ignition studies. *Combustion Science and Technology*, 181(9):1123–1144, 2009.
- [326] Stewart Paterson. The reflection of a plane shock wave at a gaseous interface. *Proceedings of the Physical Society*, 61(2):119–121, 1948.
- [327] G. B. Whitham. On the propagation of shock waves through regions of non-uniform area or flow. *Journal of Fluid Mechanics*, 4(4):337–360, 1958.
- [328] Marco Mehl, William J. Pitz, Charles K. Westbrook, and Henry J. Curran. Kinetic modeling of gasoline surrogate components and mixtures under engine conditions. *Proceedings of the Combustion Institute*, 33(1):193–200, 2011.
- [329] G. S. Levinson. High temperature preflame reactions of *n*-heptane. *Combustion and Flame*, 9(1):63–72, 1965.
- [330] Alexander Burcat, Karl Scheller, and Assa Lifshitz. Shock-tube investigation of comparative ignition delay times for C₁-C₅ alkanes. *Combustion and Flame*, 16(1):29–33, 1971.
- [331] A. Burcat, R. C. Farmer, R. L. Espinoza, and R. A. Matula. Comparative ignition delay times for selected ring-structured hydrocarbons. *Combustion and Flame*, 36(0):313–316, 1979.
- [332] C. M. Coats and Alan Williams. Investigation of the ignition and combustion of *n*-heptane-oxygen mixtures. *Symposium (International) on Combustion*, 17(1):611–621, 1979. Seventeenth Symposium (International) on Combustion.
- [333] J. F. Griffiths, P. A. Halford-Maw, and D. J. Rose. Fundamental features of hydrocarbon autoignition in a rapid compression machine. *Combustion and Flame*, 95(3):291–306, 1993.

- [334] K. Fieweger, R. Blumenthal, and G. Adomeit. Shock-tube investigations on the self-ignition of hydrocarbon-air mixtures at high pressures. *Symposium (International) on Combustion*, 25(1):1579–1585, 1994. 25th Symposium (International) on Combustion.
- [335] R. Minetti, M. Carlier, M. Ribaucour, E. Therssen, and L. R. Sochet. A rapid compression machine investigation of oxidation and auto-ignition of *n*-heptane: Measurements and modeling. *Combustion and Flame*, 102(3):298–309, 1995.
- [336] R. Blumenthal, K. Fieweger, K. H. Komp, and G. Adomeit. Gas dynamic features of self ignition of non diluted fuel/air mixtures at high pressure. *Combustion Science and Technology*, 113(1):137–166, 1996.
- [337] R. Minetti, M. Ribaucour, M. Carlier, and L. R. Sochet. Autoignition delays of a series of linear and branched chain alkanes in the intermediate range of temperature. *Combustion Science and Technology*, 113(1):179–192, 1996.
- [338] R. Minetti, M. Carlier, M. Ribaucour, E. Therssen, and L. R. Sochet. Comparison of oxidation and autoignition of the two primary reference fuels by rapid compression. *Symposium (International) on Combustion*, 26(1):747–753, 1996.
- [339] A. Cox, J. F. Griffiths, C. Mohamed, H. J. Curran, W. J. Pitz, and C. K. Westbrook. Extents of alkane combustion during rapid compression leading to single-and two-stage ignition. *Symposium (International) on Combustion*, 26(2):2685–2692, 1996.
- [340] C. V. Callahan, T. J. Held, F. L. Dryer, R. Minetti, M. Ribaucour, L. R. Sochet, T. Faravelli, P. Gaffuri, and E. Rani. Experimental data and kinetic modeling of primary reference fuel mixtures. *Symposium (International) on Combustion*, 26(1):739–746, 1996.
- [341] K. Fieweger, R. Blumenthal, and G. Adomeit. Self-ignition of S.I. engine model fuels: A shock tube investigation at high pressure. *Combustion and Flame*, 109(4):599–619, 1997.
- [342] Åsa T. Ingemarsson, Jørgen R. Pedersen, and Jim O. Olsson. Oxidation of *n*-heptane in a premixed laminar flame. *The Journal of Physical Chemistry A*, 103(41):8222–8230, 1999.

- [343] R. Seiser, H. Pitsch, K. Seshadri, W. J. Pitz, and H. J. Curran. Extinction and autoignition of *n*-heptane in counterflow configuration. *Proceedings of the Combustion Institute*, 28(2):2029–2037, 2000.
- [344] Meredith B. Colket and Louis J. Spadaccini. Scramjet fuels autoignition study. *Journal of Propulsion and Power*, 17(2):315–323, 2001.
- [345] Shigeyuki Tanaka, Ferran Ayala, James C. Keck, and John B. Heywood. Two-stage ignition in HCCI combustion and HCCI control by fuels and additives. *Combustion and Flame*, 132(1–2):219–239, 2003.
- [346] B. M. Gauthier, D. F. Davidson, and R. K. Hanson. Shock tube determination of ignition delay times in full-blend and surrogate fuel mixtures. *Combustion and Flame*, 139(4):300–311, 2004.
- [347] J. Herzler, L. Jerig, and P. Roth. Shock tube study of the ignition of lean *n*-heptane/air mixtures at intermediate temperatures and high pressures. *Proceedings of the Combustion Institute*, 30(1):1147–1153, 2005.
- [348] Emma J. Silke, Henry J. Curran, and John M. Simmie. The influence of fuel structure on combustion as demonstrated by the isomers of heptane: A Rapid compression machine study. *Proceedings of the Combustion Institute*, 30(2):2639–2647, 2005.
- [349] John M. Smith, John M. Simmie, and Henry J. Curran. Autoignition of heptanes; Experiments and modeling. *International Journal of Chemical Kinetics*, 37(12):728–736, 2005.
- [350] D. F. Davidson, M. A. Oehlschlaeger, and R. K. Hanson. Methyl concentration time-histories during *iso*-octane and *n*-heptane oxidation and pyrolysis. *Proceedings of the Combustion Institute*, 31(1):321–328, 2007.
- [351] Subith S. Vasu, David F. Davidson, and Ronald K. Hanson. OH time-histories during oxidation of *n*-heptane and methylcyclohexane at high pressures and temperatures. *Combustion and Flame*, 156(4):736–749, 2009.

- [352] Hsi-Ping S. Shen, Justin Steinberg, Jeremy Vanderover, and Matthew A. Oehlschlaeger. A shock tube study of the ignition of *n*-heptane, *n*-decane, *n*-dodecane, and *n*-tetradecane at elevated pressures. *Energy & Fuels*, 23(5):2482–2489, 2009.
- [353] Chunde Yao, Chuanhui Cheng, Shiyu Liu, Zhenyu Tian, and Jing Wang. Identification of intermediates in an *n*-heptane/oxygen/argon low-pressure premixed laminar flame using synchrotron radiation. *Fuel*, 88(9):1752–1757, 2009.
- [354] D. F. Davidson, Z. Hong, G. L. Pilla, A. Farooq, R. D. Cook, and R. K. Hanson. Multi-species time-history measurements during *n*-heptane oxidation behind reflected shock waves. *Combustion and Flame*, 157(10):1899–1905, 2010.
- [355] Benjamin Akih-Kumgeh and Jeffrey M. Bergthorson. Comparative study of methyl butanoate and *n*-heptane high temperature autoignition. *Energy & Fuels*, 24(4):2439–2448, 2010.
- [356] Genny A. Pang, Ronald K. Hanson, David M. Golden, and Craig T. Bowman. High-temperature measurements of the rate constants for reactions of OH with a series of large normal alkanes: *n*-pentane, *n*-heptane, and *n*-nonane. *Zeitschrift für Physikalische Chemie*, 225:1157–1178, 2011.
- [357] Olivier Herbinet, Benoit Husson, Zeynep Serinyel, Maximilien Cord, Valérie Warth, René Fournet, Pierre-Alexandre Glaude, Baptiste Sirjean, Frédérique Battin-Leclerc, Zhandong Wang, Mingfeng Xie, Zhanjun Cheng, and Fei Qi. Experimental and modeling investigation of the low-temperature oxidation of *n*-heptane. *Combustion and Flame*, 159(12):3455–3471, 2012.
- [358] Yu Zhang and André L. Boehman. Autoignition of binary fuel blends of *n*-heptane and C₇ esters in a motored engine. *Combustion and Flame*, 159(4):1619–1630, 2012.
- [359] Jiaxiang Zhang, Shaodong Niu, Yingjia Zhang, Chenglong Tang, Xue Jiang, Erjiang Hu, and Zuohua Huang. Experimental and modeling study of the auto-ignition of *n*-heptane/*n*-butanol mixtures. *Combustion and Flame*, 160(1):31–39, 2013.

- [360] Darshan M. A. Karwat, Scott W. Wagnon, Margaret S. Wooldridge, and Charles K. Westbrook. Low-temperature speciation and chemical kinetic studies of *n*-heptane. *Combustion and Flame*, 160(12):2693–2706, 2013.
- [361] Goutham Kukkadapu, Kamal Kumar, Chih-Jen Sung, Marco Mehl, and William J. Pitz. Autoignition of gasoline and its surrogates in a rapid compression machine. *Proceedings of the Combustion Institute*, 34(1):345–352, 2013.
- [362] S. Mani Sarathy, Goutham Kukkadapu, Marco Mehl, Weijing Wang, Tamour Javed, Sungwoo Park, Matthew A. Oehlschlaeger, Aamir Farooq, William J. Pitz, and Chih-Jen Sung. Ignition of alkane-rich FACE gasoline fuels and their surrogate mixtures. *Proceedings of the Combustion Institute*, 2014, In Press.
- [363] Jürgen Warnatz. Chemistry of high temperature combustion of alkanes up to octane. *Symposium (International) on Combustion*, 20(1):845–856, 1985. 20th Symposium (International) on Combustion.
- [364] M. Bui-Pham and K. Seshadri. Comparison between experimental measurements and numerical calculations of the structure of heptane-air diffusion flames. *Combustion Science and Technology*, 79(4–6):293–310, 1991.
- [365] C. Chevalier, W. J. Pitz, J. Warnatz, C. K. Westbrook, and H. Melenk. Hydrocarbon ignition: Automatic generation of reaction mechanisms and applications to modeling of engine knock. *Symposium (International) on Combustion*, 24(1):93–101, 1992. 24th Symposium on Combustion.
- [366] A. Chakir, M. Bellimam, J. C. Boettner, and M. Cathonnet. Kinetic study of *n*-heptane oxidation. *International Journal of Chemical Kinetics*, 24(4):385–410, 1992.
- [367] U. C. Muller, N. Peters, and A. Linan. Global kinetics for *n*-heptane ignition at high pressures. *Symposium (International) on Combustion*, 24(1):777–784, 1992. 24th Symposium on Combustion.

- [368] V. Ya. Basevich, A. A. Belyaev, V. Brandshteter, M. G. Neigauz, R. Tashl, and S. M. Frolov. Simulation of auto-ignition of *iso*-octane and *n*-heptane in an internal combustion engine. *Combustion, Explosion and Shock Waves*, 30(6):737–745, 1994.
- [369] Eliseo Ranzi, Paolo Gaffuri, Tiziano Faravelli, and Philippe Dagaut. A Wide-range modeling study of *n*-heptane oxidation. *Combustion and Flame*, 103(1–2):91–106, 1995.
- [370] R. P. Lindstedt and L. Q. Maurice. Detailed kinetic modeling of *n*-heptane combustion. *Combustion Science and Technology*, 107(4–6):317–353, 1995.
- [371] M. Bollig, H. Pitsch, J. C. Hewson, and K. Seshadri. Reduced *n*-heptane mechanism for non-premixed combustion with emphasis on pollutant-relevant intermediate species. *Symposium (International) on Combustion*, 26(1):729–737, 1996.
- [372] A. Linan and F. A. Williams. Asymptotic analysis of *n*-heptane ignition and cool flames with a temperature-explicit model. *Combustion Science and Technology*, 113(1):81–107, 1996.
- [373] G. M. Come, V. Warth, P. A. Glaude, R. Fournet, F. Battin-Leclerc, and G. Scacchi. Computer-aided design of gas-phase oxidation mechanisms – Application to the modeling of *n*-heptane and *iso*-octane oxidation. *Symposium (International) on Combustion*, 26(1):755–762, 1996.
- [374] T. J. Held, A. J. Marchese, and F. L. Dryer. A Semi-empirical reaction mechanism for *n*-heptane oxidation and pyrolysis. *Combustion Science and Technology*, 123(1–6):107–146, 1997.
- [375] H. J. Curran, P. Gaffuri, W. J. Pitz, and C. K. Westbrook. A Comprehensive modeling study of *n*-heptane oxidation. *Combustion and Flame*, 114(1–2):149–177, 1998.
- [376] Abderrahman El Bakali, Jean-Louis Delfau, and Christian Vovelle. Kinetic modeling of a rich, atmospheric pressure, premixed *n*-heptane/O₂/N₂ flame. *Combustion and Flame*, 118(3):381–398, 1999.

- [377] Christine Douté, Jean-Louis Selfau, and Christian Vovelle. Detailed reaction mechanisms for low pressure premixed *n*-heptane flames. *Combustion Science and Technology*, 147(1–6):61–109, 1999.
- [378] R. Fournet, V. Warth, P. A. Glaude, F. Battin-Leclerc, G. Scacchi, and G. M. Côme. Automatic reduction of detailed mechanisms of combustion of alkanes by chemical lumping. *International Journal of Chemical Kinetics*, 32(1):36–51, 2000.
- [379] Guy-Marie Côme. Generation of reaction mechanisms. In *Gas-Phase Thermal Reactions*, pages 201–223. Springer Netherlands, 2001.
- [380] N. A. Slavinskaya and O. J. Haidn. Modeling of *n*-heptane and *iso*-octane gas-phase oxidation in air at low and high temperatures. In *41st Aerospace Sciences Meeting and Exhibit*, number AIAA 2003-662, Reno, Nevada, 6-9 January 2003.
- [381] V. I. Babushok and W. Tsang. Kinetic modeling of heptane combustion and PAH formation. *Journal of Propulsion and Power*, 20(3):403–414, 2004.
- [382] Marcos Chaos, Andrei Kazakov, Zhenwei Zhao, and Frederick L. Dryer. A High-temperature chemical kinetic model for primary reference fuels. *International Journal of Chemical Kinetics*, 39(7):399–414, 2007.
- [383] Bruno Imbert, Fabien Lafosse, Laurent Catoire, Claude-Etienne Paillard, and Boris Khaisanov. Formulation reproducing the ignition delays simulated by a detailed mechanism: Application to *n*-heptane combustion. *Combustion and Flame*, 155(3):380–408, 2008.
- [384] F. Battin-Leclerc. Detailed chemical kinetic models for the low-temperature combustion of hydrocarbons with application to gasoline and diesel fuel surrogates. *Progress in Energy and Combustion Science*, 34(4):440–498, 2008.
- [385] H. Wang, E. Dames, B. Sirjean, D. A. Sheen, R. Tango, A. Violi, J. Y. W. Lai, F. N. Egolfopoulos, D. F. Davidson, R. K. Hanson, C. T. Bowman, C. K. Law, W. Tsang, N. P. Cernansky, D. L. Miller, and R. P. Lindstedt. A high-temperature chemical kinetic model of *n*-alkane

- (up to *n*-dodecane), cyclohexane, and methyl-, ethyl-, *n*-propyl and *n*-butyl-cyclohexane oxidation at high temperatures, JetSurF version 2.0. Technical report, Stanford University, September 19 2010.
- [386] S. M. Sarathy, C. K. Westbrook, M. Mehl, W. J. Pitz, C. Togbe, P. Dagaut, H. Wang, M. A. Oehlschlaeger, U. Niemann, K. Seshadri, P. S. Veloo, C. Ji, F. N. Egolfopoulos, and T. Lu. Comprehensive chemical kinetic modeling of the oxidation of 2-methylalkanes from C₇ to C₂₀. *Combustion and Flame*, 158(12):2338–2357, 2011.
- [387] David A. Sheen and Wing Tsang. A Comparison of literature models for the oxidation of normal heptane. *Combustion and Flame*, 161(8):1984–1992, 2014.
- [388] Sandeep Sharma, Sumathy Raman, and William H. Green. Intramolecular hydrogen migration in alkylperoxy and hydroperoxyalkylperoxy radicals: Accurate treatment of hindered rotors. *The Journal of Physical Chemistry A*, 114(18):5689–5701, 2010. PMID: 20405886.
- [389] Akira Miyoshi. Systematic computational study on the unimolecular reactions of alkylperoxy (RO₂), hydroperoxyalkyl (QOOH), and hydroperoxyalkylperoxy (O₂QOOH) radicals. *The Journal of Physical Chemistry A*, 115(15):3301–3325, 2011.
- [390] Stephanie M. Villano, Lam K. Huynh, Hans-Heinrich Carstensen, and Anthony M. Dean. High-pressure rate rules for alkyl + O₂ reactions. 1. The Dissociation, concerted elimination, and isomerization channels of the alkyl peroxy radical. *The Journal of Physical Chemistry A*, 115(46):13425–13442, 2011.
- [391] Stephanie M. Villano, Lam K. Huynh, Hans-Heinrich Carstensen, and Anthony M. Dean. High-pressure rate rules for alkyl + O₂ reactions. 2. The Isomerization, cyclic ether formation, and β -scission reactions of hydroperoxy alkyl radicals. *The Journal of Physical Chemistry A*, 116(21):5068–5089, 2012.
- [392] C. Franklin Goldsmith, William H. Green, and Stephen J. Klippenstein. Role of O₂ + QOOH in low-temperature ignition of propane. 1. Temperature and pressure dependent rate coefficients. *The Journal of Physical Chemistry A*, 116(13):3325–3346, 2012.

- [393] Akira Miyoshi. Molecular size dependent falloff rate constants for the recombination reactions of alkyl radicals with O₂ and implications for simplified kinetics of alkylperoxy radicals. *International Journal of Chemical Kinetics*, 44(1):59–74, 2012.
- [394] Patrick F. Flynn, Russell P. Durrett, Gary L. Hunter, Axel O. zur Loya, O. C. Akinyemi, John E. Dec, and Charles K. Westbrook. Diesel combustion: An Integrated view combining laser diagnostics, chemical kinetics, and empirical validation. In *1999 Society of Automotive Engineers International Congress and Exposition*, number 1999-01-0509. Society of Automotive Engineers, 1999.
- [395] James P. Szybist, Juhun Song, Mahabubul Alam, and André L. Boehman. Biodiesel combustion, emissions and emission control. *Fuel Processing Technology*, 88(7):679–691, 2007. Biofuels for Transportation.
- [396] D. F. Davidson, M. Roehrig, E. L. Petersen, M. D. Di Rosa, and R. K. Hanson. Measurements of the OH A-X (0,0) 306 nm absorption bandhead at 60 atm and 1735 K. *Journal of Quantitative Spectroscopy and Radiative Transfer*, 55(6):755–762, 1996.
- [397] John T. Herbon, Ronald K. Hanson, David M. Golden, and Craig T. Bowman. A Shock tube study of the enthalpy of formation of OH. *Proceedings of the Combustion Institute*, 29(1):1201–1208, 2002. Proceedings of the Combustion Institute.
- [398] Shengkai Wang, David F. Davidson, and Ronald K. Hanson. High-temperature laser absorption diagnostics for CH₂O and CH₃CHO and their application to shock tube kinetic studies. *Combustion and Flame*, 160(10):1930–1938, 2013.
- [399] K. Sun, X. Chao, R. Sur, C. S. Goldenstein, J. B. Jeffries, and R. K. Hanson. Analysis of calibration-free wavelength-scanned wavelength modulation spectroscopy for practical gas sensing using tunable diode lasers. *Measurement Science and Technology*, 24(12):125203, 2013.
- [400] C. S. Goldenstein, I. A. Schultz, R. M. Spearrin, J. B. Jeffries, and R. K. Hanson.

- Scanned-wavelength-modulation spectroscopy near $2.5\text{ }\mu\text{m}$ for H_2O and temperature in a hydrocarbon-fueled scramjet combustor. *Applied Physics B*, 2014, In Press.
- [401] K. G. P. Sulzmann, D. E. Baxter, M. Khazra, and T. S. Lund. Initiation of methyl acetate pyrolysis in argon-diluted mixtures behind reflected shock waves. *The Journal of Physical Chemistry*, 89(16):3561–3566, 1985.
- [402] Hyun-Mo Yoon, Hwan-Gon Yeo, Suck Sung Yun, Chang-Sik Kim, and Jun-Gill Kang. Ignition delay times in ethylene oxide-oxygen-argon mixtures behind a reflected shock. *Combustion and Flame*, 92(4):481–484, 1993.
- [403] D. A. Bittker and V. J. Scullin. General chemical kinetics computer program for static and flow reactions with applications to combustion and shock-tube kinetics. Technical Report NASA TN D-6586, National Aeronautics and Space Administration, Washington, D.C., 1972.
- [404] Casimir J. Jachimowski. An Experimental and analytical study of acetylene and ethylene oxidation behind shock waves. *Combustion and Flame*, 29:55–66, 1977.
- [405] J. P. Monat, R. K. Hanson, and C. H. Kruger. Kinetics of nitrous oxide decomposition. *Combustion Science and Technology*, 16(1-2):21–28, 1977.
- [406] Allen G. McLain and C. S. R. Rao. A Hybrid computer program for rapidly solving flowing or static chemical kinetic problems involving many chemical species. Technical Report NASA TM X-3403, National Aeronautics and Space Administration, Langley Research Center, Hampton, VA, 23665, July 1976.
- [407] W. C. Gardiner, B. F. Walker, and C. B. Wakefield. *Shock Waves in Chemistry*. Marcel Dekker, New York, 1981.
- [408] W. C. Gardiner, S. M. Hwang, and M. J. Rabinowitz. Shock tube and modeling study of methyl radical in methane oxidation. *Energy & Fuels*, 1(6):545–549, 1987.
- [409] Z. Qin, H. Yang, V. Lissianski, W. C. Gardiner, and K. S. Shin. Shock tube study of the $\text{H} + \text{NO} \rightarrow \text{OH} + \text{N}$ reaction. *Chemical Physics Letters*, 276(1-2):110–113, 1997.

- [410] W. C. Reynolds. The element potential method for chemcial equilibrium analysis: Implementation in the interactive program STANJAN. Technical report, Stanford University, Department of Mechanical Engineering, Stanford, CA, 94305, January 1986.
- [411] Michael V. Johnson, S. Scott Goldsborough, Zeynep Serinyel, Peter O'Toole, Eoin Larkin, Grainne O'Malley, and Henry J. Curran. A shock tube study of *n*- and *iso*-propanol ignition. *Energy & Fuels*, 23(12):5886–5898, 2009.
- [412] Khalid Emilio Noorani, Benjamin Akh-Kumgeh, and Jeffrey M. Bergthorson. Comparative high temperature shock tube ignition of C₁-C₄ primary alcohols. *Energy & Fuels*, 24(11):5834–5843, 2010.
- [413] K. Yasunaga, F. Gillespie, J. M. Simmie, H. J. Curran, Y. Kuraguchi, H. Hoshikawa, M. Yamane, and Y. Hidaka. A Multiple shock tube and chemical kinetic modeling study of diethyl ether pyrolysis and oxidation. *The Journal of Physical Chemistry A*, 114(34):9098–9109, 2010.
- [414] Kenji Yasunaga, Takahiro Mikajiri, S. Mani Sarathy, Tohru Koike, Fiona Gillespie, Tibor Nagy, John M. Simmie, and Henry J. Curran. A Shock tube and chemical kinetic modeling study of the pyrolysis and oxidation of butanols. *Combustion and Flame*, 159(6):2009–2027, 2012.
- [415] George Rudinger. Effect of boundary-layer growth in a shock tube on shock reflection from a closed end. *Physics of Fluids*, 4(12):1463–1473, 1961.
- [416] Ronald K. Hanson and Donald Baganoff. Reflection of a shock wave into a density gradient. *American Institute of Aeronautics and Astronautics Journal*, 8(4):805, 1970. 0001-1452.
- [417] R. K. Hanson. Shock-wave reflection in a relaxing gas. *Journal of Fluid Mechanics*, 45:721–746, 1971.
- [418] Harold Mirels. Test time in low-pressure shock tubes. *Physics of Fluids*, 6(9):1201–1214, 1963.

- [419] Harold Mirels. Shock tube test time limitation due to turbulent wall boundary layer. *American Institute of Aeronautics and Astronautics Journal*, 2(1):84–93, 1964. 0001-1452.
- [420] E. L. Petersen and R. K. Hanson. An Improved turbulent boundary-layer model for shock tubes. In *31st AIAA Fluid Dynamics Conference & Exhibit*, Anaheim, CA, June 11-14 2001. AIAA-2001-2855.
- [421] Eric L. Petersen and Ronald K. Hanson. Improved turbulent boundary-layer model for shock tubes. *American Institute of Aeronautics and Astronautics Journal*, 41(7):1314–1322, 2003. 0001-1452.
- [422] W. H. Parkinson and R. W. Nicholls. Spectroscopic temperature measurements in a shock tube using CN as a thermometric molecule. *Canadian Journal of Physics*, 38(6):715–719, 1960.
- [423] D. H. Napier, M. Nettleton, J. R. Simonson, and D. P. C. Thackeray. Temperature measurement in a chemical shock tube by sodium-line reversal and C₂ reversal methods. *American Institute of Aeronautics and Astronautics Journal*, 2(6):1136–1138, 1964. 0001-1452.
- [424] Soji Tsuchiya and Kenji Kuratani. Temperature measurement of argon gas behind reflected shock wave. *The Journal of Chemical Physics*, 42(8):2986–2987, 1965.
- [425] K. C. Lapworth, L. A. Allnutt, and J. R. Pendlebury. Temperature measurements in shock-heated carbon monoxide by an infrared technique. *Journal of Physics D: Applied Physics*, 4(6):759–768, 1971.
- [426] M. J. Guinee, F. A. Hewitt, D. F. Fussey, B. E. Milton, and T. F. Palmer. The formation of oxides of nitrogen from CH₄/O₂/N₂ mixtures. In *Shock Tubes and Waves, Proceedings of the 12th International Symposium on Shock Tubes and Waves*, pages 495–502. The Magnes Press, Jerusalem, Israel, 1980.
- [427] Edward C. Rea, Jr., Siamak Salimian, and Ronald K. Hanson. Rapid-tuning frequency-doubled ring dye laser for high resolution absorption spectroscopy in shock-heated gases. *Applied Optics*, 23(11):1691–1694, Jun 1984.

- [428] Albert Y. Chang, Edward C. Rea, Jr., and Ronald K. Hanson. Temperature measurements in shock tubes using a laser-based absorption technique. *Applied Optics*, 26(5):885–891, Mar 1987.
- [429] D. F. Davidson, R. Bates, E. L. Petersen, and R. K. Hanson. Shock tube measurements of the equation of state in argon. *International Journal of Thermophysics*, 19(6):1585–1594, 1998.
- [430] Adam E. Klingbeil, Jason M. Porter, Jay B. Jeffries, and Ronald K. Hanson. Two-wavelength mid-IR absorption diagnostic for simultaneous measurement of temperature and hydrocarbon fuel concentration. *Proceedings of the Combustion Institute*, 32(1):821–829, 2009.
- [431] Donald R. White and Roger C. Millikan. Vibrational relaxation in air. *American Institute of Aeronautics and Astronautics Journal*, 2(10):1844–1846, 1964. 0001-1452.
- [432] J. D. Lambert, A. J. Edwards, D. Pemberton, and J. L. Stretton. Intermolecular transfer of vibrational energy. *Discussions of the Faraday Society*, 33:61–70, 1962.
- [433] R. L. Taylor, M. Camac, and R. M. Feinberg. Measurements of vibration-vibration coupling in gas mixtures. *Symposium (International) on Combustion*, 11(1):49–65, 1967.
- [434] Donald Rapp and Thomas Kassal. Theory of vibrational energy transfer between simple molecules in nonreactive collisions. *Chemical Reviews*, 69(1):61–102, 1969.
- [435] T. L. Cottrell and J. C. McCoubrey. *Molecular Energy Transfer in Gases*. Butterworths, London, 1961.
- [436] J. F. Clarke and M. McChesney. *The Dynamics of Real Gases*. Butterworths, London, 1964.
- [437] W. G. Vincenti and Charles H. Kruger. *Introduction to Physical Gas Dynamics*. Krieger Publication Company, 1975. ISBN: 9780882753096.
- [438] Nick M. Marinov. STATTERM: A Statistical thermodynamics program for calculating thermochemical information. Technical Report UCRL-ID-126775, Lawrence Livermore National Laboratory, P.O. Box 808. Livermore, CA, 94550, March 1997.

- [439] D. R. Stull and H. Prophet. JANAF thermochemical tables. Technical report, U.S. Government Printing Office, Washington, D.C., 1971. (2nd Edition), Nat. Stand. Ref. Data Ser. 37, Superintendent of Documents.
- [440] Gilbert Strang. *Linear Algebra and its Applications*. Thomson Brooks/Cole, Belmont, CA, USA, 4th edition, 2006.
- [441] J. S. Coursey, D. J. Schwab, J. J. Tsai, and R. A. Dragoset. Atomic weights and isotopic compositions with relative atomic masses. Technical report, National Institute of Standards and Technology, 2010.
- [442] Y. Hidaka, S. Takahashi, H. Kawano, M. Suga, and W. C. Gardiner. Shock-tube measurement of the rate constant for excited hydroxyl (A2.SIGMA.+) formation in the hydrogen-oxygen reaction. *The Journal of Physical Chemistry*, 86(8):1429–1433, 1982.
- [443] Yoshiaki Hidaka, Kenji Hattori, Tatsuya Okuno, Kohji Inami, Tomoko Abe, and Tohru Koike. Shock-tube and modeling study of acetylene pyrolysis and oxidation. *Combustion and Flame*, 107(4):401–417, 1996.
- [444] Kenji Yasunaga, Tohru Koike, Hiroki Hoshikawa, and Yoshiaki Hidaka. Shock-tube and modeling study of ethyl methyl ether pyrolysis and oxidation. *Proceedings of the Combustion Institute*, 31(1):313–320, 2007.
- [445] E. E. Nikitin and J. Troe. 70 Years of Landau-Teller theory for collisional energy transfer. Semiclassical three-dimensional generalizations of the classical collinear model. *Phys. Chem. Chem. Phys.*, 10:1483–1501, 2008.
- [446] John T. Yates and J. Karl Johnson. *Molecular Physical Chemistry for Engineers*. University Science Books, 1st edition, 2007. ISBN: 9781891389276.
- [447] Zdenek Slanina. On the extremum behaviour of the heat capacity of species with a low-lying excited electronic state and of isomeric mixtures: A Solvable model. *Chemical Physics Letters*, 130(4):346–351, 1986.

- [448] Richard C. Tolman. Consideration of the Gibbs theory of surface tension. *The Journal of Chemical Physics*, 16(8):758–774, 1948.
- [449] Richard C. Tolman. The superficial density of matter at a liquid-vapor boundary. *The Journal of Chemical Physics*, 17(2):118–127, 1949.
- [450] Richard C. Tolman. The effect of droplet size on surface tension. *The Journal of Chemical Physics*, 17(3):333–337, 1949.
- [451] S. J. Hemingway, J. R. Henderson, and J. S. Rowlinson. The density profile and surface tension of a drop. *Faraday Symp. Chem. Soc.*, 16:33–43, 1981.
- [452] Ioannis Hadjiagapiou. Density functional theory for spherical drops. *Journal of Physics: Condensed Matter*, 6(28):5303–5322, 1994.
- [453] Clayton T. Crowe, Martin Sommerfeld, and Yataka Tsuji. *Multiphase flows with droplets and particles*. CRC Press LCC, 2000 N.W. Corporate Blvd., Boca Raton, FL 33431, 1998.
- [454] Kenneth Wark, Jr. *Advanced Thermodynamics for Engineers*. McGraw-Hill, Inc., New York NY, 1995.
- [455] Georg Gyarmathy. Zur Wachstumsgeschwindigkeit kleiner Flüssigkeitstropfen in einer über-sättigten Atmosphäre. *Zeitschrift für Angewandte Mathematik und Physik (ZAMP)*, 14:280–293, 1963.
- [456] A. B. Wood. *Propagation of sound in suspensions*. Bell and Sons, London, 1941.
- [457] R. Mével, S. Pichon, L. Catoire, N. Chaumeix, C.-E. Paillard, and J. E. Shepherd. Dynamics of excited hydroxyl radicals in hydrogen-based mixtures behind reflected shock waves. *Proceedings of the Combustion Institute*, 34(1):677–684, 2013.
- [458] Ronald K. Hanson. *ME362B: Nonequilibrium Processes in High-Temperature Gases*. Stanford University, 2014.
- [459] G. A. Campbell, G. M. Kimber, and D. H. Napier. Bursting of diaphragms as related to the operation of shock tubes. *Journal of Scientific Instruments*, 42(6):381–384, 1965.

- [460] Roy S. Hickman, Larry C. Farrar, and James B. Kyser. Behavior of burst diaphragms in shock tubes. *Physics of Fluids (1958-1988)*, 18(10):1249–1252, 1975.
- [461] Paolo Gaetani, Alberto Guardone, and Giacomo Persico. Shock tube flows past partially opened diaphragms. *Journal of Fluid Mechanics*, 602:267–286, 5 2008.
- [462] L. Houas, L. Biamino, C. Mariani, O. Igra, G. Jourdan, and A. Massol. The Effects that changes in the diaphragm aperture have on the resulting shock tube flow. *Shock Waves*, 22(4):287–293, 2012.
- [463] Y. Takano and T. Akamatsu. A diaphragmless shock tube. *Journal of Physics E: Scientific Instruments*, 17(8):644–646, 1984.
- [464] Robert S. Tranter and Binod R. Giri. A diaphragmless shock tube for high temperature kinetic studies. *Review of Scientific Instruments*, 79(9):094103, 2008.
- [465] M. S. Downey, T. J. Cloete, and A. D. B. Yates. A rapid opening sleeve valve for a diaphragmless shock tube. *Shock Waves*, 21(4):315–319, 2011.
- [466] Michael R. Lindeburg. *Mechanical Engineering Reference Manual*. Professional Publications, Inc., 13th edition, 2013.
- [467] American Society of Mechanical Engineers (ASME) standard B16.5-2013. Pipe flanges and flanged fittings. NPS 1/2 through NPS 24 metric/inch standard.
- [468] American Society of Mechanical Engineers (ASME) standard B1.1-2003. Unified inch screw threads, (UN and UNR thread form).
- [469] American Society of Mechanical Engineers (ASME) standard B1.1-2003. Metric screw threads: M profile.
- [470] J. D. Campbell and W. G. Ferguson. The temperature and strain-rate dependence of the shear strength of mild steel. *Philosophical Magazine*, 21(169):63–82, 1970.
- [471] ISP Optics. Design of pressure window. Technical report, ISP Optics Corporation, 2014.

- [472] H. D. Stromberg and R. N. Schock. A Window configuration for high pressure optical cells. *Review of Scientific Instruments*, 41(12):1880–1881, 1970.
- [473] H. C. Alt and J. Kalus. Stress distribution in cylindrical windows for optical high-pressure cells. *Review of Scientific Instruments*, 53(8):1235–1239, 1982.
- [474] Society of Automotive Engineers (SAE) Aerospace size standard for o-rings AS568D.
- [475] International Standards Organization (ISO) standard ISO3601-1:2012.
- [476] Dichtomatic. O-ring handbook. Technical report, Dichtomatic Americas, 2014.
- [477] Yoshiaki Hidaka, Toshihide Nishimori, Kazutaka Sato, Yusuke Henmi, Rieko Okuda, Koji Inami, and Tetsuo Higashihara. Shock-tube and modeling study of ethylene pyrolysis and oxidation. *Combustion and Flame*, 117(4):755–776, 1999.
- [478] Megan Edwards MacDonald. *Decomposition kinetics of the rocket propellant RP-1 and its chemical kinetic surrogates*. PhD thesis, Stanford University, 2012.